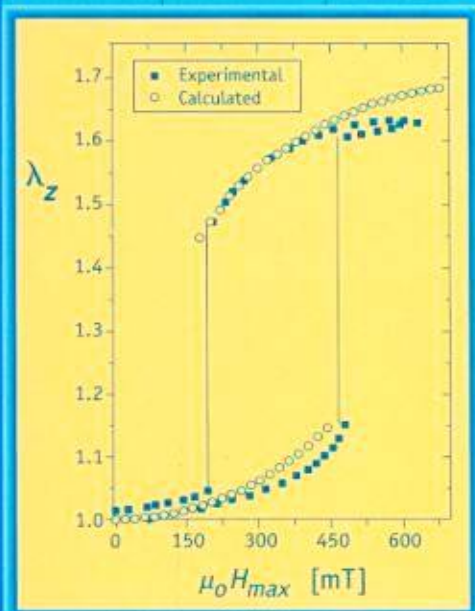


# Polymer Gels and Networks



*edited by*  
Yoshihito Osada  
Alexei R. Khokhlov

# Polymer Gels and Networks

edited by

Yoshihito Osada

*Hokkaido University*

*Sapporo, Japan*

Alexei R. Khokhlov

*Moscow State University*

*Moscow, Russia*



MARCEL DEKKER, INC.

NEW YORK • BASEL

ISBN 0-203-90839-2 Master e-book ISBN

**ISBN: 0-08247-0669-2** (Print Edition)

**Headquarters**

Marcel Dekker, Inc.

270 Madison Avenue, New York, NY 10016

tel: 212-696-9000; fax: 212-685-4540

This edition published in the Taylor & Francis e-Library, 2005.

To purchase your own copy of this or any of Taylor & Francis or Routledge's collection of thousands of eBooks please go to [www.eBookstore.tandf.co.uk](http://www.eBookstore.tandf.co.uk).

**Eastern Hemisphere Distribution**

Marcel Dekker AG

Hutgasse 4, Postfach 812, CH-4001 Basel, Switzerland

tel: 41-61-261-8482; fax: 41-61-261-8896

**World Wide Web**

<http://www.dekker.com>

The publisher offers discounts on this book when ordered in bulk quantities. For more information, write to Special Sales/Professional Marketing at the headquarters address above.

**Copyright © 2002 by Marcel Dekker, Inc. All Rights Reserved.**

Neither this book nor any part may be reproduced or transmitted in any form or by any means, electronic or mechanical, including photocopying, microfilming, and recording, or by any information storage and retrieval system, without permission in writing from the publisher.

Current printing (last digit):

10 9 8 7 6 5 4 3 2 1

# Preface

Polymer networks consist of long macromolecular chains cross-linked with each other by chemical or physical bonding. Polymer networks swollen in a liquid are called polymer gels.

Interest in the behavior of polymer gels and networks has grown significantly over the past decades. The impetus for the rapid scientific development in this field was the first experimental observation of the phenomenon of gel collapse by T. Tanaka in 1978. This phenomenon consists of a sharp decrease in the volume of the gel by several orders of magnitude in response to a small variation in the external parameters (temperature, pH, ionic strength, electric or magnetic field, etc.). It was realized that not only can polymer gels absorb and hold a considerable volume of liquids, but they can also be forced to expel the absorbed liquid in a controlled manner.

Of particular interest are hydrogels, i.e., polymer gels, which swell extensively in water. The most common hydrogels are polyelectrolyte gels: their high degree of swelling in water is due to the exerting osmotic pressure of counterions. Such gels can acquire up to several hundredweight parts of water per one part of a dry polymer. However, some neutral gels—e.g., based on polyacrylamide or poly(ethylene oxide)—also have high affinity to water, but their degree of swelling is always much lower than that of charged gels.

Hydrogels are used extensively as superabsorbents. For this application high swelling capacity is the most important property. However, there are a number of other areas of use for hydrogels as functional materials (e.g., carriers for controlled drug release, membranes with regulated permeability, and sensor devices, artificial muscles). For these purposes, high cooperativity of response to the change in external conditions and developed internal microstructure of the gels is required. Therefore, in addition to high swelling capacity, it is necessary to have a counteracting tendency, which favors the gel contraction.

The most natural physical origin of such a tendency might be hydrophobic interactions. There are several means of enhancing the hydrophobic interactions inside the hydrogels (incorporation of hydrophobic- or temperature-sensitive monomer units, addition of surfactants, addition of linear polymers forming hydrophobic complexes with the gel chains, etc.). For such systems the interplay of hydrophilic and hydrophobic tendencies leads to the very rich picture of conformational and structural changes in hydrogels.

When less polar solvents are used instead of water, the attractive interactions responsible for the gel collapse can be due to the association of polymer-charged groups with counterions, with the formation of ion pairs followed by the aggregation of ion pairs with each other due to dipole-dipole attraction.

In this book we present recent results of the investigation of behavior of polymer gels. We brought together experts from Europe, Japan, and North America to cover topics as diverse as theoretical and experimental study of the formation of physically and

chemically cross-linked polymer gels, as well as the study of the structure and properties of various polymer gels, including gels with embedded metal nanoparticles or surfactant molecules.

The book consists of two parts. The first contains chapters describing gel formation, including the formation of organic/inorganic hybrid gels (H.Urakawa et al), physical gels from biopolymers (D.R.Picout and S.B.Ross-Murphy), physical gels from associating polyelectrolytes (I.I.Potemkin and A.R. Khokhlov), gels composed of polyelectrolyte and catanionic vesicles (E.Marques et al.), as well as the formation of metal nanoparticles inside polyelectrolyte gels (L.M.Bronstein et al).

The second part of the book is dedicated to the structure and behavior of polymer gels. It contains papers describing the structure and properties of polyampholyte gels (G.Nisato and S.J.Candau), the polyelectrolyte/ionomer behavior of ion-containing polymer gels (O.E.Philippova and A.R.Khokhlov), the electrical behavior of charged gels (Y.Osada and J.P.Gong), the behavior of polymer gels responsive to electric and magnetic fields (M.Zrínyi et al), as well as the behavior of rhythmically pulsing gels (R.A.Siegel et al.). Also in Part B are chapters that review studies of the synchrotron X-ray scattering study on nano-structures of polyelectrolyte gel/surfactant complexes (C.Burger et al.) as well as structure and dynamics of polymer gels by NMR spectroscopy (I.Ando et al).

We hope the book will be useful for Ph.D. students and scientific researchers working in the field of polymer science.

*Yoshihito Osada  
Alexei R.Khokhlov*

# Contents

<i>Preface</i>	iii
<i>Contributors</i>	vii

## Part A. Process and Formation of Gels

1. Cascade Formalism Applied to Network Formation in Organic/ Inorganic Hybrid Gel Films	1
<i>Hiroshi Urakawa, Yuko Ikeda, Yoshiaki Yuguchi, Kanji Kajiware, Yoshitaka Hirata, and Shinzo Kohjiya</i>	
2. Thermoreversible and Irreversible Physical Gels from Biopolymers	28
<i>David R. Picout and Simon B. Ross-Murphy</i>	
3. Reversible (Physical) Gelation in the Solutions of Associating Polyelectrolytes	47
<i>Igor I. Potemkin and Alexei R. Khokhlov</i>	
4. Association in Polyelectrolyte-Catanionic Vesicle Systems: From Phase Behavior to Microstructure	67
<i>Eduardo Marques, Rita Dias, Maria Miguel, Ali Khan, and Björn Lindman</i>	
5. Metal Nanoparticle Formation in Polyelectrolyte Gels with Regular Microstructures	101
<i>Lyudmila M. Bronstein, Dmitri I. Svergun, and Alexei R. Khokhlov</i>	

## Part B. Structure and Behaviors of Gels

6. Structure and Properties of Polyampholyte Gels	129
<i>Giovanni Nisato and Sauveur Jean Candau</i>	
7. Polyelectrolyte/Ionomer Behavior of Polymer Gels	161
<i>Olga E. Philippova and Alexei R. Khokhlov</i>	
8. Electrical Behaviors and Mechanical Responses of Polyelectrolyte Gels	175
<i>Yoshihito Osada and Jian Ping Gong</i>	
9. Synchrotron X-Ray Scattering Study on Nanostructures of Polyelectrolyte Gel/Surfactant Complexes	217
<i>Christian Burger, Shuiqin Zhou, and Benjamin Chu</i>	
10. Structural and Dynamic Behavior of Polymer Gels as Elucidated by Nuclear Magnetic Resonance Spectroscopy	234
<i>Isao Ando, Masatoshi Kobayashi, Chenhua Zhao, Shingo Matsukawa, and Shigeki Kuroki</i>	

11. Electrical and Magnetic Field-Sensitive Smart Polymer Gels	309
<i>Miklós Zrínyi, Dénes Szabó, Genovéva Filipcsei, and József Fehér</i>	
12. Rhythmically Pulsing Gels Based on Chemomechanical Feedback Instability	356
<i>Ronald A.Siegel, Gauri P.Misra, and Anish P.Dhanarajan</i>	
<i>Index</i>	371

## Contributors

**Isao Ando** Department of Chemistry and Materials Science, Tokyo Institute of Technology, Tokyo, Japan

**Lyudmila M.Bronstein** Department of Chemistry, Indiana University, Bloomington, Indiana

**Christian Burger** Department of Chemistry, State University of New York at Stony Brook, Stony Brook, New York

**Sauveur Jean Candau** Laboratoire de Dynamique des Fluides Complexes, Université Louis Pasteur, Strasbourg, France

**Benjamin Chu** Department of Chemistry, State University of New York at Stony Brook, Stony Brook, New York

**Anish P.Dhanarajan** Department of Biomedical Engineering, University of Minnesota, Minneapolis, Minnesota

**Rita Dias** Department of Chemistry, Coimbra University, Coimbra, Portugal

**József Fehér** Department of Physical Chemistry, Budapest University of Technology and Economics, Budapest, Hungary

**Genovéva Filipcsei** Department of Physical Chemistry, Budapest University of Technology and Economics, Budapest, Hungary

**Jian Ping Gong** Division of Biological Sciences, Graduate School of Science, Hokkaido University, Sapporo, Japan

**Yoshitaka Hirata** Laboratory for Polymer Condensed State, Institute for Chemical Research, Kyoto University, Kyoto, Japan

**Yuko Ikeda** Department of Chemistry and Materials Technology, Kyoto Institute of Technology, Kyoto, Japan

**Kanji Kajiwara** Department of Chemistry and Materials Technology, Kyoto Institute of Technology, Kyoto, Japan

**Ali Khan** Physical Chemistry 1, Center for Chemistry and Chemical Engineering, Lund University, Lund, Sweden

**Alexei R.Khokhlov** Department of Physics, Moscow State University, Moscow, Russia

**Masatoshi Kobayashi** Department of Biochemistry, National Institute of Agrobiological Sciences, Ibaraki, Japan

**Shinzo Kohjiya** Laboratory for Polymer Condensed State, Institute for Chemical Research, Kyoto University, Kyoto, Japan

**Shigeki Kuroki** Department of Chemistry and Materials Science, Tokyo Institute of Technology, Tokyo, Japan

**Björn Lindman** Physical Chemistry 1, Center for Chemistry and Chemical Engineering, Lund University, Lund, Sweden

**Eduardo Marques\*** Department of Chemistry, Coimbra University, Coimbra, Portugal

**Shingo Matsukawa** Department of Food Science and Technology, Tokyo University of Fisheries, Tokyo, Japan



**Maria Miguel** Department of Chemistry, Coimbra University, Coimbra, Portugal  
**Gauri P.Misra** Department of Pharmaceutics, University of Minnesota, Minneapolis, Minnesota  
**Giovanni Nisato** Department of Materials and Process Technology, Philips Research, Eindhoven, The Netherlands  
**Yoshihito Osada** Division of Biological Sciences, Graduate School of Science, Hokkaido University, Sapporo, Japan  
**Olga E.Philippova** Department of Physics, Moscow State University, Moscow, Russia

\* *Current affiliation:* University of Porto, Porto, Portugal.

**David R.Picout** Biopolymers Group-Division of Life Sciences, King's College London, London, England  
**Igor I.Potemkin** Department of Physics, Moscow State University, Moscow, Russia  
**Simon B.Ross-Murphy** Biopolymers Group-Division of Life Sciences, King's College London, London, England  
**Ronald A.Siegel** Departments of Pharmaceutics and Biomedical Engineering, University of Minnesota, Minneapolis, Minnesota  
**Dmitri I.Svergun** European Molecular Biology Laboratory, Hamburg, Germany, and Institute of Crystallography, Russian Academy of Sciences, Moscow, Russia  
**Dénes Szabó** Department of Physical Chemistry, Budapest University of Technology and Economics, Budapest, Hungary  
**Hiroshi Urakawa** Department of Chemistry and Materials Technology, Kyoto Institute of Technology, Kyoto, Japan  
**Yoshiaki Yuguchi** Department of Chemistry and Materials Technology, Kyoto Institute of Technology, Kyoto, Japan  
**Chenhua Zhao** Department of Biotechnology, Tokyo University of Agriculture and Technology, Tokyo, Japan  
**Shuiqin Zhou** Department of Chemistry, State University of New York at Stony Brook, Stony Brook, New York  
**Miklós Zrínyi** Department of Physical Chemistry, Budapest University of Technology and Economics, Budapest, Hungary



# 1

## Cascade Formalism Applied to Network Formation in Organic/Inorganic Hybrid Gel Films

**HIROSHI URAKAWA, YUKO IKEDA, YOSHIAKI YUGUCHI, and  
KANJI KAJIWARA** *Kyoto Institute of Technology, Kyoto, Japan*

**YOSHITAKA HIRATA and SHINZO KOHJIYA** *Institute for Chemical  
Research, Kyoto University, Kyoto, Japan*

### I. INTRODUCTION

The Flory-Stockmayer model [1] provides the simplest kinetic scheme of polyfunctional polymerization. Although the model has been criticized often for its oversimplification of the network structure, the model survived and is considered to correspond to the ideal state of the network structure. Gordon [2] has applied Good's theory [3] of the cascade process to calculate the statistical quantities of randomly branched polymers described by the Flory-Stockmayer model. His method has an advantage over the previous methods of reducing the combinatorial argument to the joint probability-generating function formulated by Good. Here a simple algebraic procedure yields the statistical parameters of the system without knowing an explicit expression for the molecular weight distribution.

Conventionally, the weight fraction generating function is introduced to calculate the statistical parameters of the system. The weight fraction generating function is defined as a function of  $\alpha$  and  $\theta$

$$W(\alpha, \theta) = \sum_{x=1}^{\infty} w_x(\alpha) \theta^x \quad (1)$$

where  $\alpha$  and  $\theta$  are the fraction of functionalities which have reacted and the dummy variable specifying the generating function, respectively. From the definition of the weight fraction, the weight fraction distribution should satisfy the normalization condition as

$$\sum_{x=1}^{\infty} w_x(\alpha) = 1 \quad (2)$$

when the system is prior to the critical conversion  $\alpha_c$  ( $\alpha < \alpha_c$ ). Here obviously  $W(\alpha, 1)=1$ . The various average degrees of polymerization are obtained by a successive algebraic

procedure of integration/differentiation as

$$DP_n(\alpha) = 1 \Big/ \int_0^1 W d\theta \quad (3)$$

$$DP_w(\alpha) = (\partial W / \partial \theta)_{\theta=1} \quad (4)$$

$$DP_z(\alpha) = \left[ \frac{\partial}{\partial \theta} \left( \theta \frac{\partial W}{\partial \theta} \right) \right]_{\theta=1} / DP_w(\alpha) \quad (5)$$

Here  $DP_n(\alpha)$ ,  $DP_w(\alpha)$ , and  $DP_z(\alpha)$  denote the number-average, weight-average and z-average degrees of polymerization given as a function of the fraction of reacted functionalities, respectively. Although the calculation of  $DP_n(\alpha)$  is trivially done by a simple stoichiometry, Eqs. (3) to (5) provide a systematic way of calculating the average degrees of polymerization once the weight fraction-generating function is formulated. The gel point is defined as the critical conversion  $\alpha_c$  at which the weight average degree of polymerization diverges

$$\lim_{\alpha \rightarrow \alpha_c} DP_w(\alpha) = \infty \quad (6)$$

and  $W(\alpha, 1)$  assumes a nontrivial value yielding the sol fraction at  $\alpha > \alpha_c$ .

The cascade formalism is incorporated in the probability-generating function as follows. The probability generating function is in definition written as

$$F(\theta) = \sum_{i=0}^{\infty} p_i \theta^i \quad (7)$$

where  $p_i$  corresponds to the probability of the occurrence of event  $i$ , so that the sequence  $\{p_i\}$  defines the distribution of such events. When Eq. (8) converges in some interval of the dummy variable  $\theta$ , specified by  $|\theta| < 1$ ,  $F(\theta)$  is called the generating function of the sequence of  $\{p_i\}$  [4]. A simple example will be demonstrated by the probability distribution of the number scored in throwing a perfect die. The probability distribution  $\{p_i\}$  in this case is given by  $1/6$  for all  $i$ 's, since the probability of obtaining any particular number  $i$  is the same for all six numbers. Thus, the probability-generating function for the sequence  $\{p_i\}$  is given by

$$F(\theta) = \sum_{i=1}^6 \frac{1}{6} \theta^i \quad (8)$$

where, for example, the coefficient of  $\theta^3$  gives the probability that a die takes a value of 3

(which is of course equal to 1/6).

The advantage of using the probability-generating function will be shown by a simple product of two probability-generating functions, specifying the sequence  $\{a_i\}$  and  $\{b_i\}$ , respectively, to yield a new probability-generating function specifying the convolution of two sequences. If two sequences  $\{a_i\}$  and  $\{b_i\}$  are specified by the generating functions  $A(\theta) = \sum a_i \theta^i$  and  $B(\theta) = \sum b_i \theta^i$ , then the convolution of  $\{a_i\}$  and  $\{b_i\}$  defined by

$$\{c_i\} = \{a_i\} * \{b_i\} \quad (9)$$

has a generating function given by the product of the generating functions of  $A(\theta)$  and  $B(\theta)$  as

$$C(\theta) = A(\theta)B(\theta) \quad (10)$$

The example is given by throwing a pair of perfect dies, where the scored number is given by the sum of the numbers of thrown dies. The probability-generating function for the sequence representing the probability distribution of the number scored by a pair of dies is calculated by the product of two probability-generating functions for a single die [Eq. (8)] as

$$\begin{aligned} F(\theta) &= \left[ \sum_{i=1}^6 \frac{1}{6} \theta^i \right]^2 \\ &= \frac{1}{36} (\theta^2 + 2\theta^3 + 3\theta^4 + 4\theta^5 + 5\theta^6 + 6\theta^7 + 5\theta^8 \\ &\quad + 4\theta^9 + 3\theta^{10} + 2\theta^{11} + \theta^{12}) \end{aligned} \quad (11)$$

The product in Eq. (10) is not restricted to two sequences, but can be extended to any number of sequences.

The joint distribution for the sizes of the generations in a cascade process is given as a natural extension of Eq. (10) by the iteration of the probability-generating functions as [3]

$$F(\theta) = \theta F_0(\theta F_1(\theta \dots F_{n-1}(\theta) \dots)) \quad (12)$$

for the whole system, including the individuals in the 0th generation. Here  $F_0(\theta)$ ,  $F_1(\theta)$ ,  $F_2(\theta)$ , ... denote the probability-generating functions for the numbers of individuals in the zero-th, first, second, ... generations, respectively. Equation (12) will be intuitively understood by unfolding into the form of a

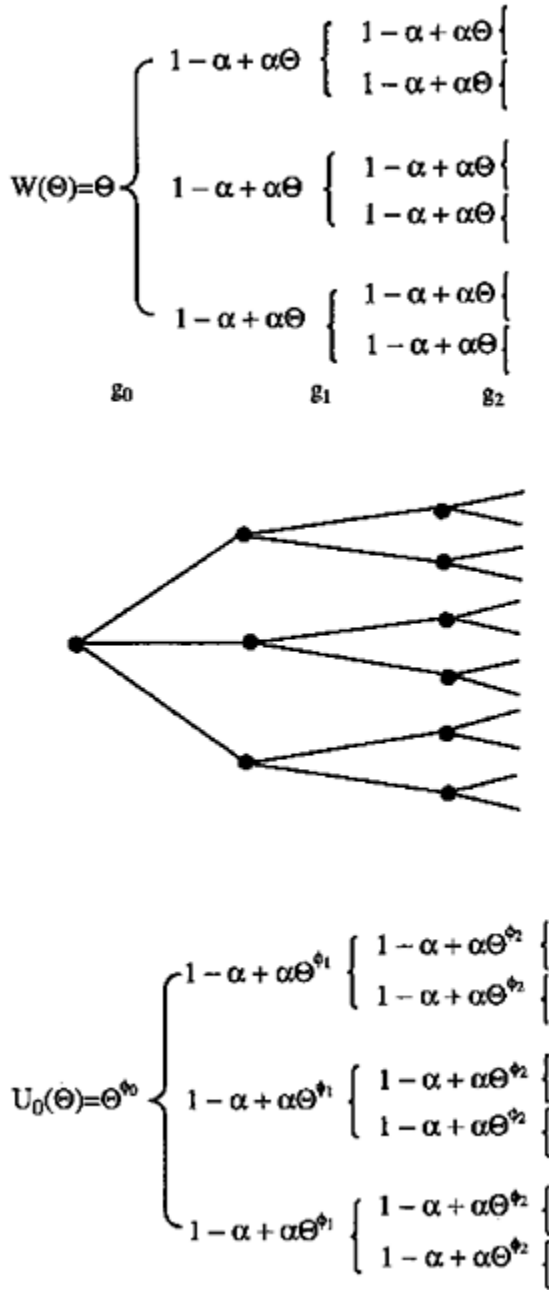


**FIG. 1** A tree (middle) graphically represents a probability-generating function (top) specifying the joint distribution for the sizes of the generations in a cascade process. A tree also corresponds one-to-one to the path-

weighted generating function (bottom).  $g_0, g_1, \dots$ . Denote the zero-th generation, the first generation, .....

cascade as shown in Figure 1. For example, when a maximum number of the events is three, the probability-generating function specifying the number of individuals in the first generation produced in the 0th generation is given by  $F_0(\theta) = \alpha_0 + \alpha_1\theta + \alpha_2\theta^2 + \alpha_3\theta^3$ . Since the number of individuals in the second generation produced by the first generation is specified by the probability-generating function  $F_1(\theta) = \alpha'_0 + \alpha'_1\theta + \alpha'_2\theta^2 + \alpha'_3\theta^3$ , then the probability for the number of individuals in the whole generations is given as

$$\begin{aligned} F(\theta) &= \theta F_0(\theta F_1(\theta)) \\ &= \alpha_0\theta + \alpha_1\theta(\alpha'_0 + \alpha'_1\theta + \alpha'_2\theta^2 + \alpha'_3\theta^3) \\ &\quad + \alpha_2\theta(\alpha'_0 + \alpha'_1\theta + \alpha'_2\theta^2 + \alpha'_3\theta^3)^2 \\ &\quad + \alpha_3\theta(\alpha'_0 + \alpha'_1\theta + \alpha'_2\theta^2 + \alpha'_3\theta^3)^3 \end{aligned} \tag{13}$$

Here, for example, the coefficient of  $\theta^3$  yields the probability that the number of individuals is equal to three in the whole generations.

## II. CASCADE FORMALISM

The difficulties in the basic problems in polymer science are mainly of a combinatorial nature. The most primitive theories of polymer science thus ignore the chain structure and describe the polymer system as an assembly of unconnected segments represented by points, regarding the system as zero-dimensional objects. Connecting points with lines, where one-dimensional objects composed of complexes of points and lines represent molecules, makes the next higher degree of sophistication. The complexes of points and lines are called graphs, and one-dimensional graph-like molecules can be embedded in spaces of higher dimensionality by incorporating a combinatorial and continuum treatment of some averaging process in the space.

Points and lines can represent any chemical system. Let us consider the random condensation of  $f$ -functional monomers, where functionalities are all equally reactive. If cyclization is excluded, the  $x$ -mer molecule is regarded as a tree with  $x$  branches represented by lines. The model is equivalent to the classic Flory-Stockmayer model. Here the tree will grow from a root (a randomly chosen repeat unit corresponding to the zero-th generation) to a first generation, a second generation, and so forth by chemical condensation as schematically shown in Figure 1.

The weight fraction  $w_x$  of  $x$ -mer should be equal to the probability that a repeat unit chosen at random in the system is found to be a part of an  $x$ -mer. In this context, the weight fraction-generating function is given by Eq. (12) specifying the joint distribution for the sizes of the generations in a cascade process as

$$\begin{aligned}
 W(\theta) &= \sum_{x=1}^{\infty} w_x \theta^x \\
 &= \theta F_0(\theta F_1(\theta \cdots F_{n-1}(\theta)) \cdots)
 \end{aligned}
 \tag{14}$$

where the probability-generating function for each generation will be given as

$$F_0(\theta) = (1 - \alpha + \alpha\theta)^f \tag{15}$$

$$F_1(\theta) = F_2(\theta) = F_3(\theta) = \cdots = (1 - \alpha + \alpha\theta)^{f-1} \tag{16}$$

with  $\alpha$  being the fraction of reacted functionalities on a monomeric unit. Equations (15) and (16) are incorporated in Eq. (14) to yield the weight fraction-generating function for the condensation of  $f$ -functional monomers as

$$W(\theta) = \theta(1 - \alpha + \alpha u(\theta))^f \tag{17}$$

$$u(\theta) = \theta(1 - \alpha + \alpha u(\theta))^{f-1} \tag{18}$$

The function  $u(\theta)$  corresponds to the probability-generating function for the size distribution of molecular moieties produced by splitting a link chosen at random in the system of  $f$ -functional random polycondensates. Thus,  $u(\theta)$  generates the probability of  $p_i$  of finding  $i$  descendents in a specified moiety in two split moieties as

$$u(\theta) = \theta F_1(\theta) = \theta F_2(\theta) = \cdots = \sum_{i=1}^{\infty} p_i \theta^i \tag{19}$$

The differentiation of Eq. (17) with respect to  $\theta$  leads to

$$\frac{\partial W(\theta)}{\partial \theta} = F_0(u) + \frac{\theta F_0(u) F'_0(u)}{1 - \theta F'_1(u)} \tag{20}$$

where the prime denotes differentiation and the weight average degree of polymerization is calculated by putting  $\theta=1$  as [see Eq. (4)]



$$\begin{aligned}
 DP_w(\alpha) &= \left( \frac{\partial W(\theta)}{\partial \theta} \right)_{\theta=1} \\
 &= \frac{1 + \alpha}{1 - (f - 1)\alpha}
 \end{aligned} \tag{21}$$

The critical conversion is given by Eq. (6), so that

$$\alpha_c = \frac{1}{(f - 1)} \tag{22}$$

From Eq. (21) as already driven by Stockmayer and Flory in 1944 [1].

### III. PATH-WEIGHTED GENERATING FUNCTION

The spatial correlation can be incorporated in the generating function by distinguishing each point in the graph. Dobson and Gordon [5] performed the first extension within the framework of the cascade formalism to calculate the configurational averages of  $f$ -functional random polycondensates. Here the variously averaged mean-square radii were calculated by means of Kramers' theorem [6], which requires counting the number of paths passing through a particular point. Take an  $x$ -mer and split it in two moieties by cutting an arbitrary bond,  $i$ . Then the number of such paths passing through the  $i$ -th bond is given by the product of  $N_i(x - N_i)$  where  $N_i$  and  $x - N_i$  correspond to the numbers of points found in the two moieties split by the  $i$ th bond. Since the mean-square distance is proportional to the number of bonds consisting of a path according to random flight statistics, the mean-square radius of gyration of an  $x$ -mer,  $R_{G,x}$  is given by [7]

$$\langle R_{G,x}^2 \rangle = \frac{b^2}{x^2} \sum_{i=1}^{x-1} N_i(x - N_i) \tag{23}$$

with  $b$  being the bond length. As seen from the physical meaning of probability-generating function  $u(\theta)$  [see Eq. (19)], the probability-generating function specifying the number of the paths passing through the  $i$ th bond in the  $f$ -functional random polycondensates is given by the self-convolution of  $\theta u'(\theta)$  as

$$[\theta u'(\theta)]^2 = \sum_{x=2}^{\infty} \sum_{i=1}^{x-1} p_i p_{x-i} i(x - i) \theta^x \tag{24}$$

where two moieties belonging to an arbitrary chosen bond have the same distribution without any correlation, so that

$$\sum_{x=2}^{\infty} \sum_{i=1}^{x-1} p_i p_{x-i} = 1 \quad (25)$$

Thus, the  $z$ -average mean-square radius of gyration for the  $f$ -functional random polycondensates is calculated from Eq. (24) as

$$\begin{aligned} \langle R_G^2 \rangle_z &= \sum_x w_x x \langle R_{G,x}^2 \rangle / DP_w \\ &= \frac{b^2 (DP_n - 1) [u'(1)]^2}{DP_n DP_w} \\ &\cong b^2 \frac{f-1}{f} DP_w \quad DP_w \gg 1 \end{aligned} \quad (26)$$

The result shows that  $\langle R_G^2 \rangle_z$  is insensitive with respect to the functionality when  $DP_w \gg 1$ .

The more systematic way is provided to calculate the statistical parameters of the system by introducing the path-weighted functions in connection with scattering theory [8, 9]. Here the path-weighted function  $\phi_n$  is an arbitrary function of a path of length  $n$ , which corresponds to a linear progression of  $n$  links (or  $n$  segments) in a molecule. The path-weighted generating function for  $f$ -functional random polycondensates is given as

$$u_0(\theta) = \theta^{\phi_0} (1 - \alpha + \alpha \theta^{\phi_1} (1 - \alpha + \alpha \theta^{\phi_2} (\dots)^{f-1})^{f-1})^f \quad (27)$$

The path-weighted generating function corresponds one-to-one to a tree-like graph as schematically shown in Figure 1. When  $\phi_0 = \phi_1 = \phi_2 = \dots = 1$ , Eq. (27) reduces to the weight fraction-generating function, so that Eq. (27) can be rewritten as

$$u_0(\theta) = \sum_{x,k} w_{xk} x^{-1} \sum_{l=1}^x \theta^{\sum_{n=1}^l N_{ln,xk} \phi_n} \quad (28)$$

where the limits of the summation in the exponent of  $\theta$  are from  $n=0$  to  $x-1$ , and  $w_{xk}$  denotes the weight fraction of the  $k$ th isomer in the  $x$ -mer fraction, which is normalized as

$$\sum_x \sum_k w_{xk} = 1 \quad (29)$$

$N_{ln,xk}$  is the number of distinct paths of length  $n$  in the  $k$ th isomer in  $x$ -mer fraction, of which the  $l$ th repeat unit forms one end.

The path-weighted generating function is applied to calculate the moments of the

distribution for  $f$ -functional random polycondensates [9] by replacing the path-weighted function with the  $N$ th power of the average path length. The average of the  $N$ th power of the end-to-end distance of a path of length  $n$ ,  $\langle r_n^N \rangle$ , is by assuming a Gaussian statistic as

$$\langle r_n^N \rangle = A_N n^{N/2} \quad (30)$$

where

$$A_N = \left[ \frac{(N+1)!}{(N/2)!} \right] \left( \frac{b^2}{6} \right)^{N/2} \quad (31)$$

for  $N=0$  and positive even integer, or

$$A_N = \left( \frac{2}{\sqrt{\pi}} \left[ \left( \frac{N+1}{2} \right)! \right] \left( \frac{2b^2}{3} \right) \right)^{N/2} \quad (32)$$

for  $N=-1$  and positive odd integers.  $b^2$  Is the mean square of the effective bond length. Let

$$\phi_n = \langle r_n^N \rangle = A_N n^{N/2} \quad (33)$$

then the  $z$ -average radius of gyration is calculated from Eqs. (28) and (33) as

$$\begin{aligned} \langle R_G^2 \rangle &\equiv \frac{1}{2} \sum_{x,k} w_{xk} x^{-1} \sum_{l=1}^x \sum_{n=1}^{x-1} N_{ln,xk} n / DP_w \\ &= \frac{b^2 f \alpha}{2(1 + \alpha)[1 - (f - 1)\alpha]} \end{aligned} \quad (34)$$

which reduces to Eq. (26) when  $DP_w \gg 1$ .

#### IV. CASCADE FORMALISM FOR ELECTROMAGNETIC SCATTERING

The normalized angular intensity distribution for the particle scattering of monodisperse molecules is given as [10]

$$P_x(\partial) = \frac{1}{x^2} \sum \sum \left\langle \frac{\sin(qr_{ij})}{qr_{ij}} \right\rangle \quad (35)$$

with  $q$  being the magnitude of the scattering vector:

$$q = \left( \frac{4\pi}{\lambda} \right) \sin\left(\frac{\theta}{2}\right) \quad (36)$$

where  $\theta$  denotes the scattering angle,  $\lambda$  the wavelength of the incident electromagnetic wave in solution,  $r_{ij}$  the distance between two scattering units  $i$  and  $j$ , and  $x$  the number of the scattering units. In most cases, the scattering units are considered to be identical to the segments or monomer units. Equation (35) is averaged over ensemble to yield the observable  $z$ -average particle-scattering factor for the polydisperse system as

$$\overline{P_z(\theta)} = \frac{1}{DP_w} \sum w_{xk} x^{-1} \sum_i \sum_j \left\langle \frac{\sin(qr_{ij})}{qr_{ij}} \right\rangle \quad (37)$$

and the configurational average of  $\sin(qr_{ij})/qr_{ij}$  is given for Gaussian subchains (the random spatial correlation between scattering units) by using Debye's approximation as

$$\left\langle \frac{\sin(qr_{ij})}{qr_{ij}} \right\rangle = \exp \frac{-|i-j|q^2 b^2}{6} \quad (38)$$

Thus, let  $\phi_n = \exp(-nq^2 b^2/6)$ , where  $n=|i-j|$ , the scattering intensity is calculated for  $f$ -functional random polycondensates from Eq. (28) as a function of the reaction probability  $\alpha$ :

$$I(q) = A^2(q)(1 + \alpha\phi)/[1 - (f-1)\alpha\phi] \quad (39)$$

$$\phi = \exp(-b^2 q^2/6) \quad (40)$$

$A(q)$  is scattering amplitude, which is assumed to be the same for all scattering units.  $A(q)$  is equal to 1 when the scattering unit is a point. Equation (39) holds even when gelation takes place as far as  $1 - (f-1)\alpha\phi < 1$  [11]. Equation (37) can be extended to more general cases if the configurational average of  $\sin(qr_{ij})/qr_{ij}$  is calculated as a function of the distance between two scattering units. Another simple example is demonstrated for a random flight chain, where the configurational average of  $\sin(qr_{ij})/qr_{ij}$  is given as

$$\left\langle \frac{\sin(qr_{ij})}{qr_{ij}} \right\rangle = \left( \frac{\sin(qb)}{qb} \right)^{|i-j|} \quad (41)$$

so that Eq. (39) holds by replacing Eq. (40) with

$$\phi = \left( \frac{\sin(qb)}{qb} \right) \quad (42)$$

If the  $f$ -functional random polycondensation proceeds ideally to form tree-like molecules as represented schematically in Figure 1, the scattering units are composed of branching points, and the scattering profile from such a system is directly calculated for a Gaussian subchain and a random flight chain by Eq. (39) with  $A(q)=1$  as shown in Figure 2. In a real gelling system, however, the scattering units are not necessarily point-like, but may be composed of a condensed phase (domain) of a finite volume. The domains of a finite volume are linked into a tree-like structure as the most primitive network model, and the resulting network will possess a hierarchical structure.

In order to analyze the scattering profiles from such a gelling system quantitatively, we may assume that the random association (in the case of physical gel) or the initial stage of cross-linking reaction (in the case of chemical gel) results in the formation of the multifunctional domains which link together to form a tree-like network. In the case of chemical gel, the domains formed in the initial stage of reaction may be highly branched and broadly distributed in size and shape. The domain formation can be described in general by the Smolu-chowski equation [12, 13], where the forward reaction rate will be given in various ways according to a specified mode of association. That is, the density distribu

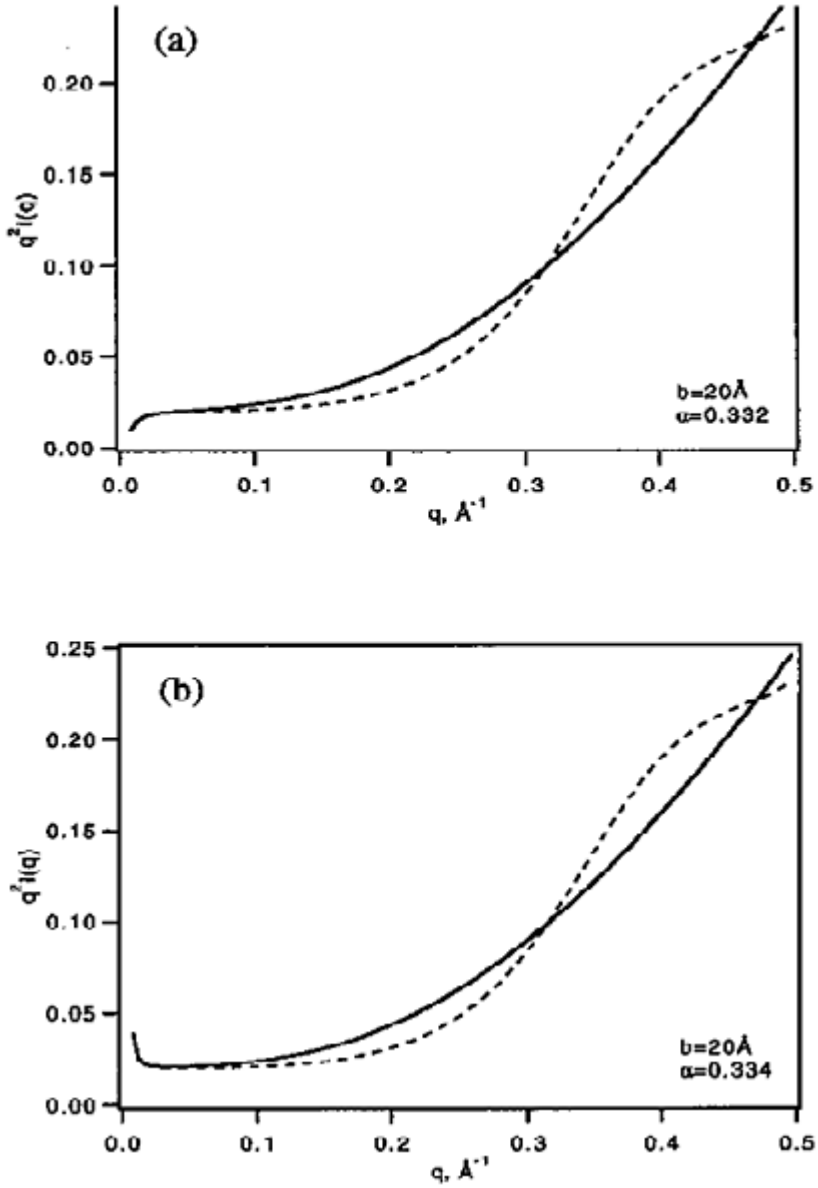


**FIG. 2** Scattering profiles from the system [solid lines; a Gaussian subchain model Eq. (40), and dotted lines; a random flight subchain model Eq. (42)] undergoing an ideal  $f$ -functional random polycondensation.  $f=4$  in the present example. (a) Before gelation, and (b) after gelation.

tion (the density correlation function) in the domain will be given by a generalized Ornstein-Zernike form [14, 15] as

$$\gamma(r) \approx \left(\frac{\xi}{r}\right)^{3-D} \exp\left(\frac{-r}{\xi}\right) \quad (43)$$

where  $D$  ( $1 \leq D < 3$ ) and  $\xi$  denote the fractal dimension and the correlation length specifying the density fluctuation in the domain, respectively. Equation (43) yields the scattering amplitude in Eq. (1) by the Fourier transform [11, 15] as

$$A^2(q) \approx \frac{1}{[1 + (D+1)\xi^2 q^2/3]^{D/2}} \quad (44)$$

Since  $D=2$  for a Gaussian chain, Eq. (43) reduces to a Lorentzian form [14]:

$$A^2(q) \approx \frac{1}{1 + \xi^2 q^2} \quad (45)$$

**TABLE 1** Density Correlation Function and Corresponding Scattering Function

Specification	Density correlation function $\gamma(r)$	Scattering function $P(q)$
1. Sphere <sup>a</sup>	$1 - \frac{3}{4}\left(\frac{r}{R}\right) + \frac{1}{16}\left(\frac{r}{R}\right)^3$	$\left[\frac{3(\sin qR - qR \cos qR)}{(qR)^3}\right]^2$
2. Ornstein-Zernicke	$\frac{\xi}{r} \exp\left(-\frac{r}{\xi}\right)$	$\frac{1}{1 + \xi^2 q^2}$
3. Generalized Ornstein-Zernicke <sup>b</sup>	$\left(\frac{\xi}{r}\right)^{3-D} \exp\left(-\frac{r}{\xi}\right)$	$\frac{1}{[1 + (D+1)\xi^2 q^2/3]^{D/2}}$
4. Debye-Bueche	$\exp\left(-\frac{r}{\xi}\right)$	$\frac{1}{(1 + \xi^2 q^2)^2}$
5. Guinier	$\exp\left(-\frac{r^2}{\xi^2}\right)$	$\exp\left(-\frac{\xi^2 q^2}{4}\right)$
6. Combined	$\frac{1}{2}\left(1 + \frac{\xi}{r}\right) \exp\left(-\frac{r}{\xi}\right)$	$\frac{1}{(1 + \xi^2 q^2)^3}$

<sup>a</sup>  $R$  denotes the diameter of the sphere.

<sup>b</sup>  $D$  denotes the fractal dimension.

Debye and Bueche [16] gave the simplest case for the correlation function  $\exp(-r/\xi)$  in order to account the inhomogeneities in solid due to random associates as

$$A^2(q) \approx \frac{1}{(1 + \xi^2 q^2)^2} \quad (46)$$

The Debye-Bueche density correlation function corresponds to the case that  $D=3$  in Eq. (5), which is equivalent to the rigid body having a smooth boundary distinct from the medium. Equation (46) indicates the  $q^{-4}$  dependence of the scattering intensity (the Porod region) at  $q \rightarrow \infty$ . The density correlation function and its corresponding scattering function are summarized in Table 1.

## V. INTERFERENCE EFFECT

The scattering profile is calculated for the individual domains according to Eq. (39). If the interdomain interaction is appreciable as the concentration is increased or the interaction is extremely strong, the spatial correlation between domains appears on the scattering profile in the form of a peak at the  $q$  region corresponding to the interaction distance [17]. When the interdomain interaction is isotropic and represented approximately by a hard-sphere repulsion, the scattering profile is decomposed into the product of two terms  $P(q)$  and  $S_I(q)$  due to the particle scattering factor from an individual (isolated) domain and the interference between domains, respectively, as

$$I(q) \approx P(q) \cdot S_I(q) \quad (47)$$

Here  $P(q)$  is identical to Eq. (39), and the interference term is written as

$$S_I(q) \approx \frac{1}{1 + 8(v_0/v_1)\epsilon\Phi(2qR)} \quad (48)$$

where  $v_0$  denotes the volume of the sphere,  $v_1$  the average volume allocated to each domain, and  $\epsilon$  a constant close to unity.  $\Phi(r)$  is a potential function and is given for the hard-sphere repulsion by the scattering amplitude of a sphere of the radius,  $r$ , as

$$\Phi(r) = \frac{\sin qr - qr \cos qr}{3(qr)^3} \quad (49)$$

Considering the size distribution and the average effect of particular motions, a single hard sphere cannot represent the interdomain interaction in the solution or gel, but the average oversize distribution and molecular motion should be taken into account in the interdomain interaction. Let us assume the average effect is incorporated by a random process, and the Gaussian-type potential specifies the interaction. Then Eq. (48) is rewritten in terms of the correlation length of interaction  $R$  as



$$S_I(q) = \frac{1}{1 + C \exp(-R^2 q^2)} \quad (50)$$

A constant  $C$  in Eq. (50) includes the second virial coefficient  $A_2$ , the molecular weight, and the concentration, as known by adjusting the second term in the virial expansion of Eq. (47) to a general expression of the osmotic pressure [18].

## VI. NETWORK FORMATION IN ORGANIC/INORGANIC HYBRID GEL IN THE FRAMEWORK OF CASCADE FORMALISM

Organic/inorganic hybrid gels have been prepared and investigated for a decade as being expected as a novel functional material. Organic/inorganic hybrids investigated so far are mostly composed of tetraethoxysilane (TEOS) as an inorganic component. Those organic polymer/silica hybrids are roughly classified into two groups according to the bonding between organic component and silica. Here the interpenetrated polymer network (IPN) and the hydrogen-bonded composite represent the physical hybrid, where the network is constituted of the physical (nonbonded) interaction of the organic component with silica (or siloxane network). The other type is classified as the chemical hybrid where the organic component and silica are covalently bonded. Organic polymers having a functional group such as an ethoxysilyl group are chosen to react with TEOS. In either case of physical or chemical hybrid, the sol-gel process is an effective way for the preparation of such organic/inorganic hybrid gels [19, 20].

The sol-gel process consists of hydrolysis of alkoxymetal and subsequent polycondensation of metal hydroxide. The polymerization of TEOS by the sol-gel process has been extensively investigated, and the characteristic of resulted siloxane network was found to depend heavily on the nature of gelling catalyst [21, 22]. Because of the incompatibility between the inorganic and organic component, inorganic or organic components will form the independent phases rich in either component, which constitute the cross-linking domains. Although the network formation in the sol-gel process proceeds not as a simple  $f$ -functional random polycondensation, the cascade model may describe the system approximately by assuming that the cross-linking domain acts as a new functional group. Here the cascade model provides the spatial distribution of domains, which are not necessarily linked as a tree. Incorporating the density distribution of domains into the cascade model, the structural characteristics of hybrid network can be quantitatively evaluated in terms of the domain size and its interspatial distance. We examine the validity of the cascade formalism to specify the structural characteristics of organic/inorganic hybrid gels prepared from triethoxysilyl-terminated poly(oxytetramethylene) (ET-PTMO) and TEOS by acid or base catalysis.

### A. Experimental

Organic/inorganic hybrid gel was prepared from ET-PTMO and TEOS. ET-PTMO ( $M_n=1.35 \times 10^3$ ) was synthesized from poly(oxytetramethylene) glycol by end-group

modification [23]. 1 M hydrochloric acid or 0.2 M butylamine was used for the catalyst of the sol-gel process, respectively, in Series A, Series B, and Series C. The reaction conditions are summarized in Table 2 for each series. The sol-gel process and the preparation of hybrid gel are schematically shown in Figure 3. ET-PTMO, TEOS, and ethanol (solvent) were mixed and stirred at room temperature for 2 min. A hydrochloric acid and water were added to the reaction

**TABLE 2** Concentration of Each Component in the Reaction Mixture (in Terms of Molar Ratio)

Code	Polymer	TEOS	Solvent			
	$[(\text{Si})\text{-OEt}]_{\text{PTMO}}$	$[(\text{Si})\text{-OEt}]_{\text{TEOS}}$	EtOH	H <sub>2</sub> O	HCl	BuNH <sub>2</sub>
Series A						
SG2F	1.00	0	6.67	6.67	0.060	–
SG7F	0.767	0.233	6.67	6.67	0.060	–
SG8F	0.700	0.300	6.67	6.67	0.060	–
SG15F	0.567	0.433	6.67	6.67	0.060	–
SGI8F	0.500	0.500	6.67	6.67	0.060	–
Series B						
SG11F	1.00	0	13.3	13.3	0.010	0.013
SG16F	0.833	0.167	13.3	13.3	0.010	0.013
SG12F	0.667	0.333	13.3	13.3	0.010	0.013
SG17F	0.500	0.500	13.3	13.3	0.010	0.013
SG13F	0.333	0.667	13.3	13.3	0.010	0.013
Series C						
SGGO	1.0	0	14	13	0.010	–
SGG1	1.0	0	14	13	0.010	0.028
SGG2	1.0	0	14	13	0.010	0.020
SGG3	1.0	0	14	13	0.010	0.015
SGG4	1.0	0	14	13	0.010	0.013
SGG5	1.0	0.23	14	13	0.010	0.013
SGG6	1.0	0.48	14	13	0.010	0.013
SGG7	0.60	1.7	14	13	0.010	0.015
SGG8	0.60	1.7	14	13	0.010	0.013

mixture in Series A, and the solution was stirred at room temperature for 10 min. In Series B, a small amount of hydrochloric acid was added in order to avoid precipitation of silicate, and the solution was stirred for 10 min at room temperature. Then butylamine and water were added dropwise, and the solution was stirred for 1 min. The gel films were prepared from Series A and Series B by casting each solution onto a mold made of Teflon and covering with Parafilm in order to prevent evaporation of TEOS and solvent. The mold was kept at 50°C for 50 h, and gel was formed after a few hours as the sol-gel process proceeded. The resulted transparent hybrid gels were dried under nitrogen atmosphere at 50°C for 4 or 5 days and to a constant weight at 50°C under vacuum. Since BuNH<sub>2</sub> was employed for catalyst in Series C except for SGG0 as in Series B, the

reaction proceeded under the basic condition. The reaction mixture was prepared as Series B. The resulted solution (the reaction mixture) was capsulated in the capillary cell ( $\phi = 2\text{ mm}$ ), inserted in the cell holder maintained at  $50^{\circ}\text{C}$ , and the time-resolved small-angle x-ray scattering was observed immediately from the solution undergoing sol-gel reaction.

The hybrid gel ifims were subjected to the measurements of small-angle x-ray scattering (SAXS) and dynamic mechanical analysis (DMA), while a structural change during the network formation in the sol-gel process was observed by time-resolved SAXS from Series C.

SAXS was observed from the hybrid gel films (Series A and B) and the mixed solution (Series C) undergoing sol-gel reaction with the SAXES equipment installed at BL-10C in the Photon Factory, Tukuba, Japan. SAXS was observed from the hybrid gel films sandwiched with the square cell with a window of  $2.0 \times 0.5\text{ cm}$  at room temperature. The excess scattering intensity was calculated by subtracting the scattering intensity from the empty cell. The time-resolved SAXS measurement was started immediately after the cell was inserted in the cell holder block kept at  $50^{\circ}\text{C}$ . Ninety-eight measurements with an appropriate interval were repeated during the course of hydrosilylation, where each measuring time was 3 min. The excess scattering intensity at each reaction time was calculated by subtracting the scattering intensity at time 0.

DMA was performed on DVE-V4 FT Rheospectra (Rheology Co. Ltd., Kyoto, Japan) with a compression mode at the frequency of 1 Hz while the temperature increased at the rate of  $2^{\circ}\text{C}/\text{min}$ .

## B. Results and Discussion

SAXS profiles from Series A and Series B are shown in Figures 4 and 5. All the profiles exhibited an interference peak except for SG2F. The interference peak is considered as being due to the microphase separation, which results in the formation of the cross-linking domain mainly composed of inorganic components. As the molar ratio of ethoxysilyl group in TEOS increases, the interference

# 1st Step

## Hydrolysis

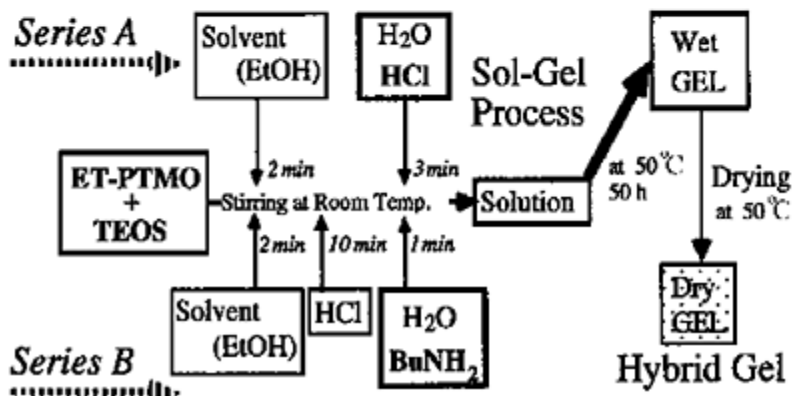
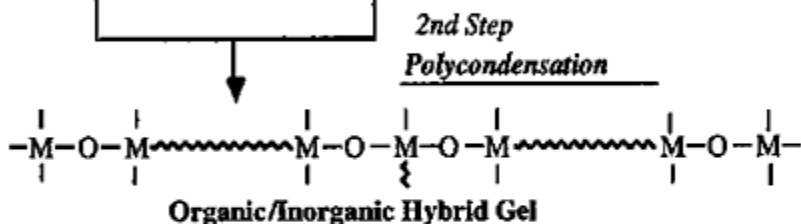
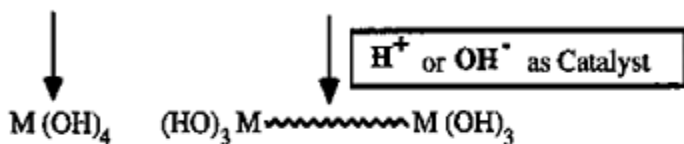
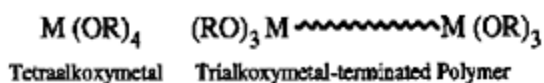
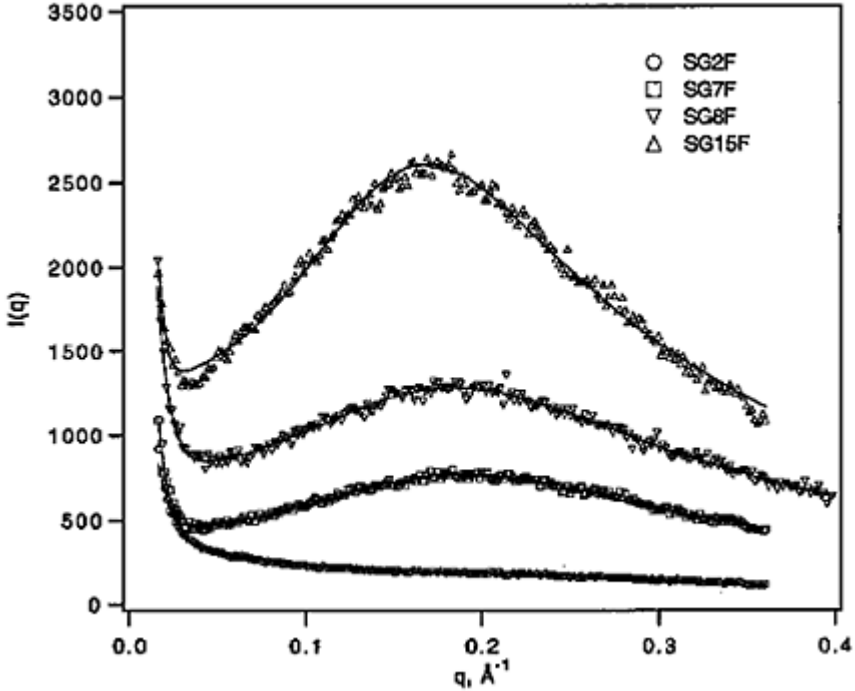


FIG. 3 Sol-gel process (schematic) and preparation of hybrid gel.

peak becomes more marked and shifts to a lower  $q$ . Since the interference peak is more enhanced in Series B than in Series A, the base-catalysis promotes the microphase separation, and no apparent interference peak was observed in the profile of acid-catalyzed hybrid gel SG2F prepared without TEOS.

The scattering profiles were analyzed according to Eq. (39) with Eq. (45) or Eq. (46) by taking into account the repulsive interaction between inorganic domains. The results

were summarized in Table 3. Although the inconsistent value of the branching degree  $(f-1)\alpha$  may indicate the inadequacy in the



**FIG. 4** SAXS profiles observed from hybrid gel films (Series A) (see Table 2). Solid lines represent the scattering profiles calculated according to Eqs. (45), (48), and (59).

calculation of the excess scattering by subtracting the scattering from an empty cell, the profile in the larger  $q$  region is approximately given by Eq. (46) in the case of Series B (base-catalyzed hybrid gel), which represents the Debye-Bueche-type density correlation function. That is, the inorganic domain formed in Series B has a distinct boundary with the matrix. The Ornstein-Zernicke-type density correlation function was found to fit better to the scattering profiles from Series A (acid-catalyzed hybrid gel), as the inorganic components are randomly incorporated in the organic matrix.

The DMA revealed the different mechanical behavior between Series A and Series B, reflecting the microstructure difference as shown in Figures 6 and 7. The mechanical behavior is almost identical for all acid-catalyzed hybrid gel films (Series A) (Figure 6). This result confirms a relatively homogeneous network structure in Series A, where the inorganic component is incorporated randomly in the network. On the contrary, the mechanical behavior changes with increasing the molar ratio of TEOS in Series B (Figure 7). Here the glass transition temperature,  $T_g$ , shifts to a higher temperature as the molar ratio of TEOS increases. Since a larger inorganic domain is formed in the base-catalyzed

hybrid

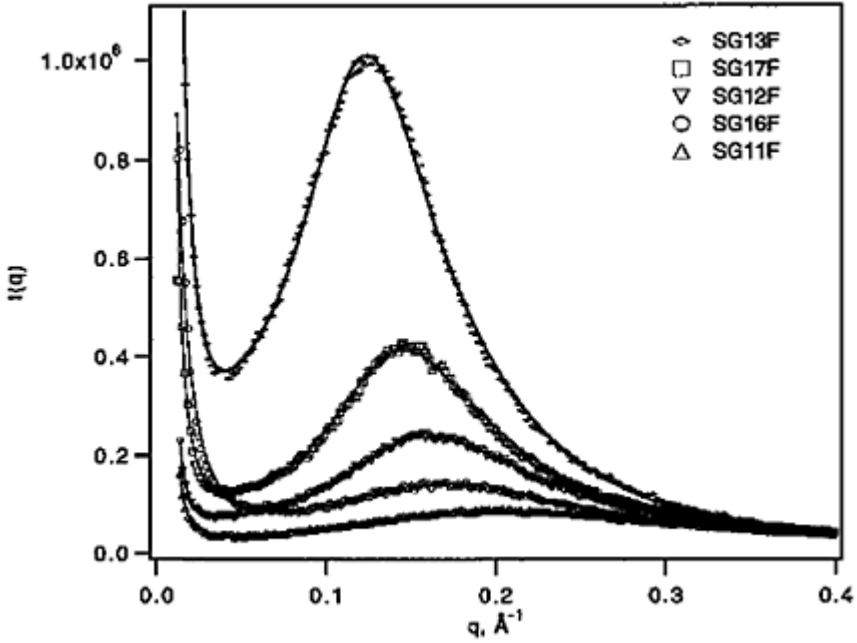


**FIG. 5** SAXS profiles observed from hybrid gel films (Series B) (see Table 2). Solid lines represent the scattering profiles calculated according to Eqs. (46), (48), and (50).

**TABLE 3** Evaluated Parameters  $\xi$ ,  $(f-1)\alpha$ ,  $b$ , and  $R$  (the correlation length of interaction) According to Eq. (45), Eq. (48) [or Eq. (46), Eq. (48)], and Eq. (50)

Sample code	$\xi$ (Å)	$(f-1)\alpha$	$b$ (Å)	$R$ (Å)
Series A <sup>a</sup>				
SG2F	10.3	0.804	100.7	6.4
SG7F	4.1	1.203	136.2	8.5
SG8F	4.2	0.924	120.3	8.5
SG15F	5.5	1.365	187.4	10.1
Series B <sup>b</sup>				
SG11F	2.6	1.173	117.4	9.2
SG16F	3.9	0.987	55.9	10.3
SG12F	4.9	1.206	137.9	12.3
SG17F	6.9	1.098	103.0	14.2
SG13F	9.2	1.113	112.3	16.4

<sup>a</sup> Eqs. (45) and (48).

<sup>b</sup> Eqs. (46) and (48).

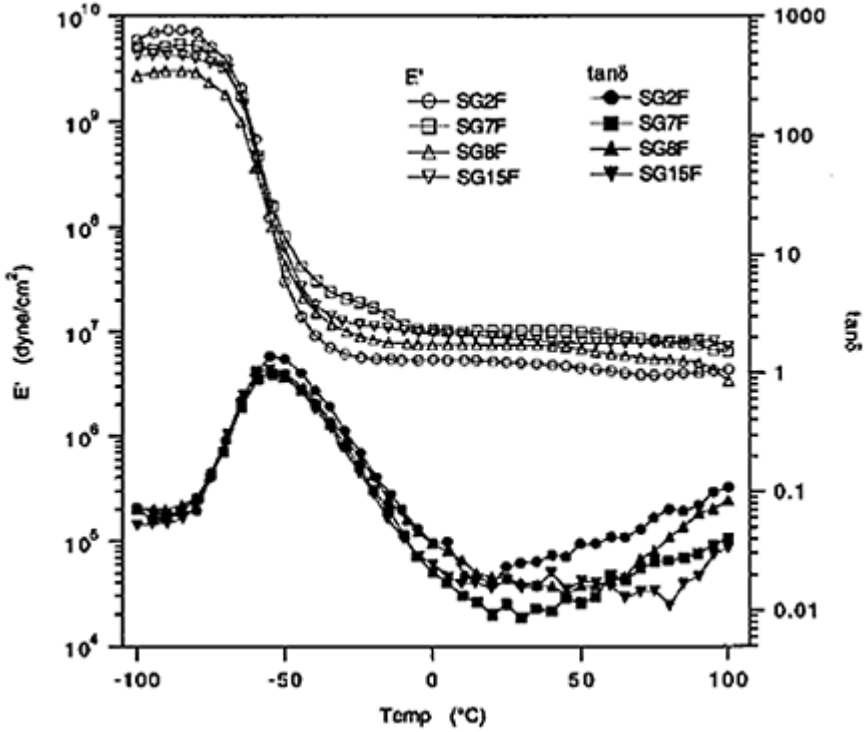


**FIG. 6** Dynamic modulus and  $\tan \delta$  of Series A hybrid gel films as a function of temperature, where the temperature was increased from  $-100$  to  $+100^\circ\text{C}$  at the rate of  $2^\circ\text{C}$ .

gel with a higher TEOS content, the inorganic domain seems to suppress the molecular motion of polymer chain. SG11F (the base-catalyzed hybrid gel with no TEOS content) exhibits two-step decrease of  $E'$  as the temperature increases from  $-100$  to  $0^\circ\text{C}$ . The phenomena could be attributed to the recrystallization of PTMO chains, where no inorganic domain is formed.

Both time-resolved SAXS profiles from the ET-PTMO/TEOS mixtures (Series C) show the upturn at  $q \rightarrow 0$  in the Kratky plots [ $q^2 I(q)$  plotted against  $q$ ] when the sol-gel reaction proceeds. The reaction time of the initial upturn corresponds to the gel point of the system as expected from the Flory-Stockmayer tree-like model according to Eq. (39). The examples of time-resolved SAXS profiles (SGG1 and SGG6) are shown in Figure 8, where the gel points are observed at 30 min and 120 min, respectively. The interference peak was not observed in the wet state because of the dilution effect.

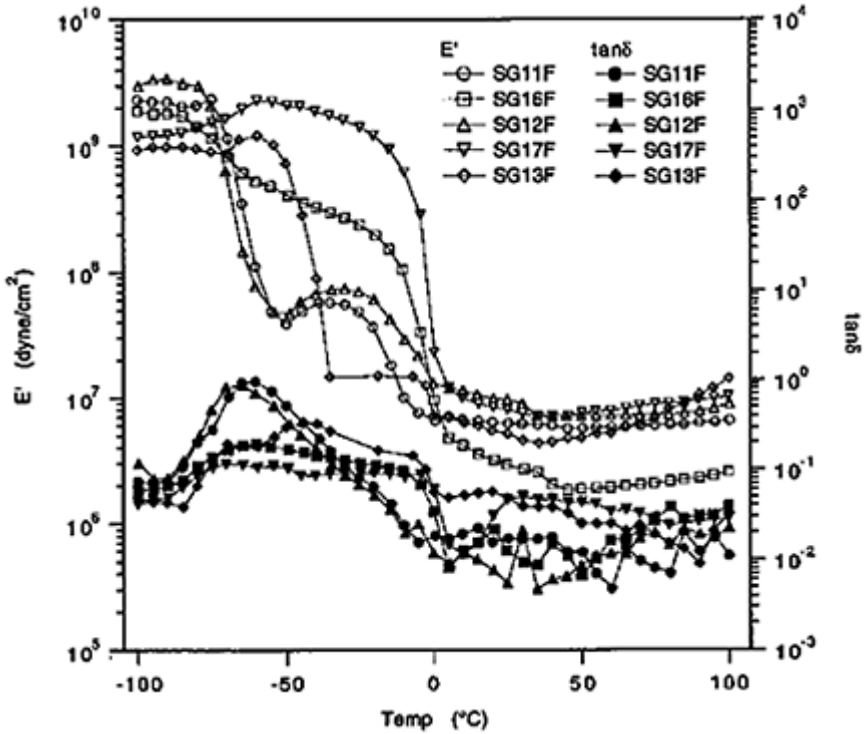


**FIG. 7** Dynamic modulus and  $\tan \delta$  of Series B hybrid gel films as a function of temperature, where the temperature was increased from  $-100$  to  $+100^\circ\text{C}$  at the rate of  $2^\circ\text{C}$ .

The scattering profiles were analyzed in terms of three parameters  $(f-1)\alpha$ ,  $b^2$ , and  $\xi$  specifying the modified Flory-Stockmayer model by curve fitting. The fitting results are demonstrated in Figures 9 and 10, and the results are summarized in Table 4. The gel point was evaluated from the reaction time when  $(f-1)\alpha$  exceeds. After gelation takes place,  $(f-1)\alpha$  hardly increases in all the series, indicating the further intermolecular reaction is suppressed by gelation.  $b$  and  $\xi$  increase with reaction before reaching the gel point but remain almost constant with the value of  $(f-1)\alpha$  becoming invariant (Fig. 10). Here no shrinkage of gel was observed in the wet state, different from the network formation of polysiloxane [24], where the shrinkage of gel due to the intramolecular reaction was observed after gel point.

The gelation model considered here is similar to the model proposed by Landry et al. [25] Their model comprises a liquid-like arrangement among



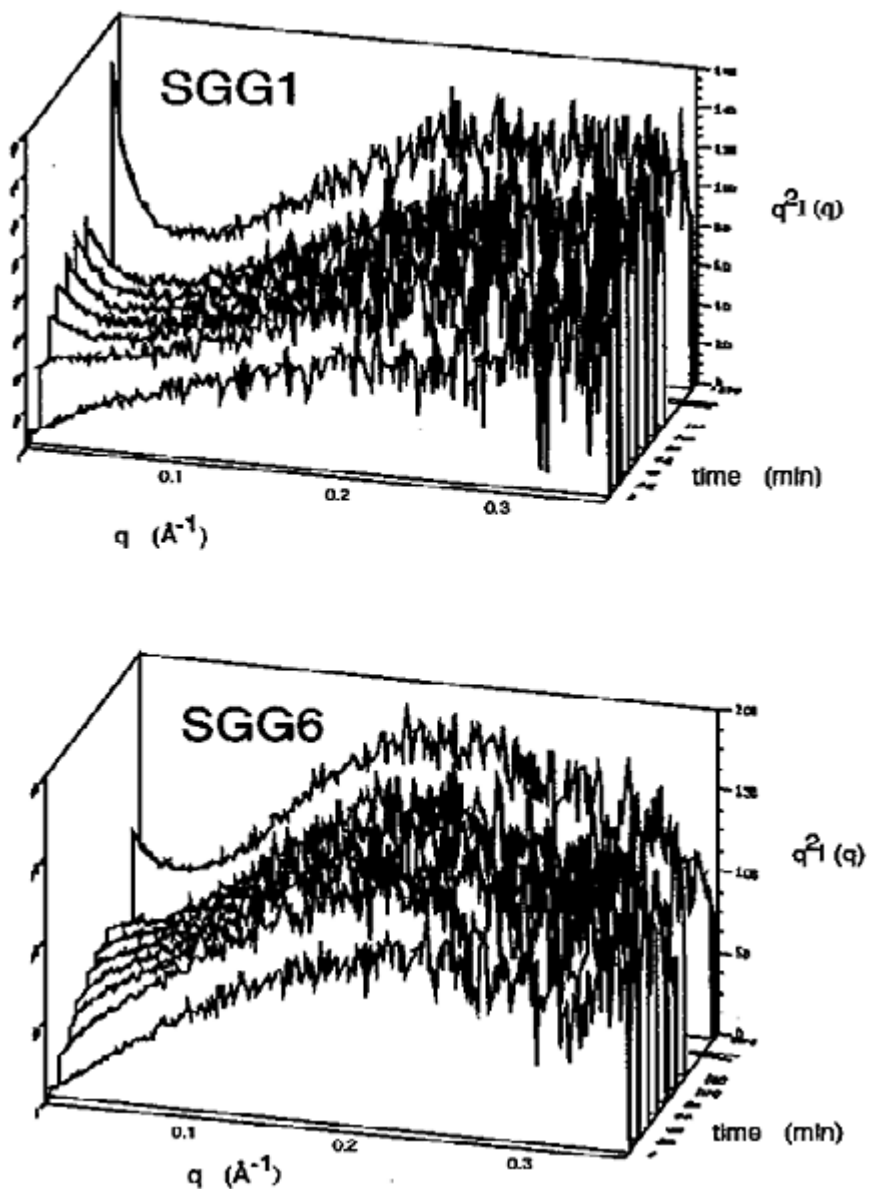


**FIG. 8** Time-resolved SAXS observed from the ET-PTMO/TEOS mixtures (Series C) (see Table 2) during the sol-gel process.

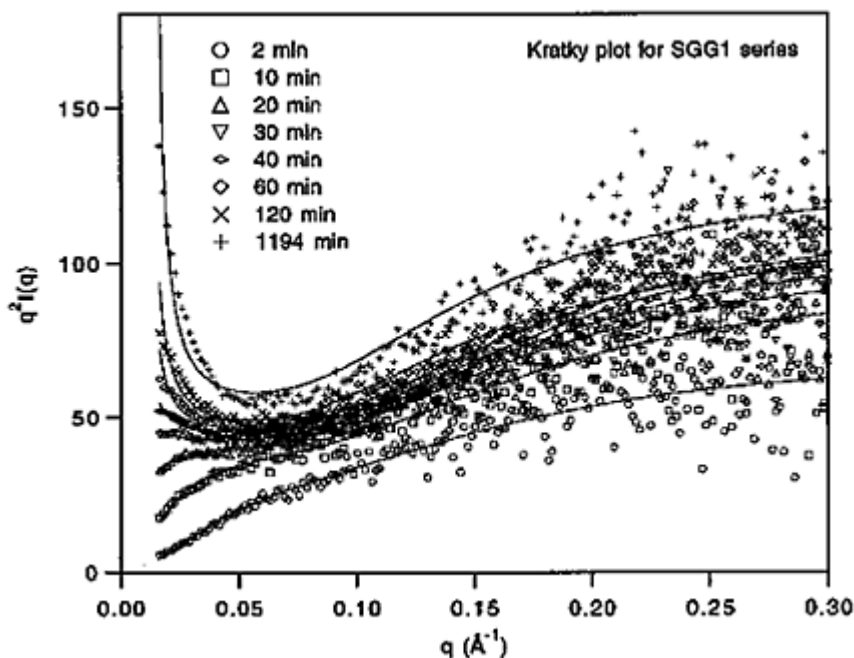


**FIG. 9** Observed SAXS profiles (SGG1) and calculated profiles according to Eqs. (39) and (45) for SGG1 as a function of the reaction time (shown in this figure).

noninterpenetrating fractal clusters, whereas in the present model, noninterpenetrating fractal clusters are spatially distributed and linked as described by the Flory-Stockmayer model. Here a correlation length,  $\xi$ , specifies the noninterpenetrating fractal clusters according to Eq. (45) or Eq. (46) in the present instance.

The evaluated parameters by curve fitting were summarized in Table 4. SGG0 (without TEOS under acidic condition) undergoes no gelation. When no TEOS is added (SGG1–4), the resulted gel is rather homogeneous, and the domain is characterized by a Gaussian-type density distribution. Decreasing the amount  $\text{BuNH}_2$  (catalyst) reduces the gelation time, but no appreciable change was observed in the gel structure. The formation of relatively hard domain described by the Debye-Bueche-type correlation function was observed by adding TEOS in SGG5–8 synthesized under basic condition. The size of the domain increases and the gelation time reduces as increasing the amount of added TEOS. The domain is considered to be composed mainly of inorganic components, as illustrated in Figure 11. The gel structure is schematically shown in Figure 11.

In conclusion, TEOS promotes the formation of Si-rich domains under the basic condition, but the reaction is suppressed after gelation in the wet state. Further reaction takes place where the intramolecular cross-linking induces the shrinkage of hybrid gel in the drying process.

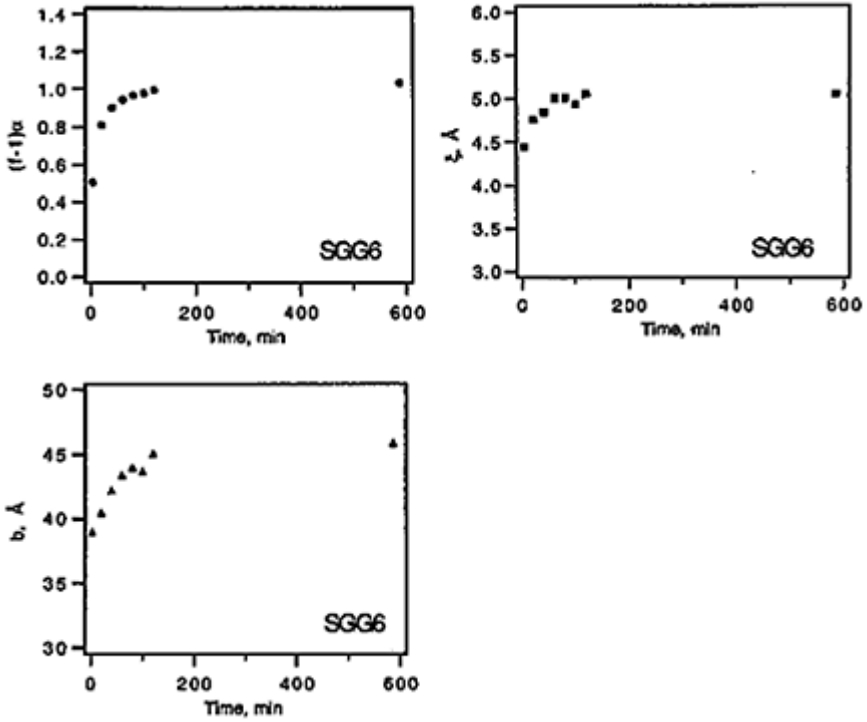


**FIG. 10** Evaluated parameters  $\xi$ ,  $(f-1)\alpha$ , and  $b$  according to Eqs. (39) and (46) for SGG6 as a function of the reaction time.

**TABLE 4** Evaluated Parameters  $\xi$ ,  $(f-1)\alpha$  and  $b$  in the Steady State (at the Final Reaction Time) According to Eqs. (39) and (45) [or Eqs. (39) and (46)], and a Gel Point

Sample code	$\xi(\text{\AA})$	$(f-1)\alpha$	$b(\text{\AA})$	Gel point (min)
SGG0 <sup>a</sup>	3.0	0.803	12.0	—
SGG1 <sup>a</sup>	9.7	1.059	42.2	30
SGG2 <sup>a</sup>	8.9	1.049	40.9	40
SGG3 <sup>a</sup>	9.4	1.052	42.1	130
SGG4 <sup>a</sup>	8.5	1.019	37.2	222
SGG5 <sup>b</sup>	4.6	1.041	41.9	>120
SGG6 <sup>b</sup>	5.1	1.036	45.9	120
SGG7 <sup>b</sup>	8.0	1.018	64.0	90
SGG8 <sup>b</sup>	8.2	1.021	64.4	>120

<sup>a</sup> Eqs. (39) and (45).

<sup>b</sup> Eqs. (39) and (46).

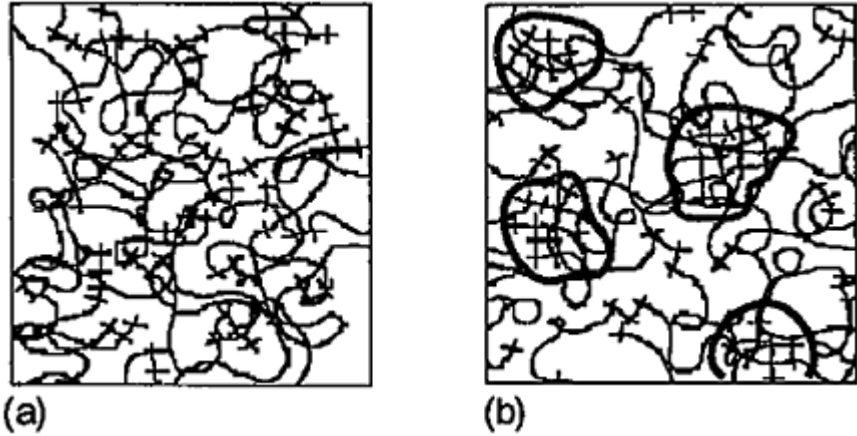


**FIG. 11** Schematic structure of the PTMO/TEOS hybrid gel. (a) The acid-catalyzed hybrid gel and (b) the base-catalyzed hybrid gel where the inorganic domain is distinct from the matrix network.

## VII. SUMMARY

Although the combinatorial approach requires a cumbersome calculation in the Flory-Stockmayer model, the cascade formalism has been proven to provide a systematic way of calculating statistical parameters of the branched system. Here the Flory-Stockmayer model is based on the assumption of no ring formation, and the ring formation may cause the deviation of the gel point and the size distribution from an ideal case. The incorporation of the concept of the domain in the scattering theory implies neglecting the connectivity in the Flory-Stockmayer model, and the domains specified by a density correlation function are considered to distribute spatially as prescribed by the model. Although the model is primitive, the consistency of the fitting to the observed scattering profiles in many cases implements the modified Flory-Stockmayer model for the analysis of the gel structure.

## ACKNOWLEDGMENTS

This work was performed under the approval of the Photon Factory Advisory Committee (Proposal No. 91-217). Y.Y. thanks the Japan Society for the Promotion of Science for the Research Fellowship for Young Scientists. Part of the work was financially supported by Grant-in-Aid for COE Research No. 10CE2003 (Ministry of Education, Science, Sports and Culture, Japan).

## REFERENCES

1. See, for example, PJ Flory, Principles of Polymer Chemistry. Cornell University Press, Ithaca, NY, 1953.
2. M Gordon. Proc R Soc (Lond), A268:240, 1962.
3. IJ Good. Proc Cambridge Phil Soc 51:240, 1955.
4. See, for example, W Feller, An Introduction to Probability Theory and Its Application. Wiley, New York, 1957.
5. GR Dobson M Gordon J Chem Phys 41:2389, 1964.
6. HA Kramers J Chem Phys 14:415, 1946.
7. BH Zimm, WH Stockmayer J Chem Phys 17:1301, 1949.
8. K Kajiwara, W Burchard, M Gordon Br Polym J 2:110, 1970.
9. K Kajiwara J Chem Phys 54:296, 1971.
10. P Debye. In: Light Scattering from Dilute Polymer Solutions. D McIntyre, F.Gornick, eds., Gordon & Breech, New York, 1964, p. 139.
11. K Kajiwara, S Kohjiya, M Shibayama, H Urakawa. In Polymer Gels. D.De Rossi, K Kajiwara, Y Osada, A Yamauchi, eds., Plenum Press, New York, 1991, p. 3.
12. JL Spouge. Macromolecules 16:121, 1983.
13. R Botet, R Jullien, M Kolb. Phys Rev A30:2150, 1984.
14. P-G De Gennes. Scaling Concepts in Polymer Physics. Cornell University Press, Ithaca, NY, 1979.
15. M Shibayama, H Kurokawa, S Nomura, M Muthkumar, RS Stein. Polymer 33:2883, 1984.
16. P Debye, AM Bueche J Appl Phys 20:518, 1949.
17. A Guinier, G Fournet. Small-Angle Scattering of X-Rays. Wiley, New York, 1955.
18. M Shimode, M Mimura, H Urakawa, S Yamanaka, K Kajiwara. Sen'i Gakkaishi 52:301, 1996.
19. C Sanchez, F Ribot NJ Chem 18:1007, 1994.
20. L Mascia. Trends in Polym Sci 3:61, 1995.
21. KD Keefer. Mat Res Soc, Symp Proc 32:15, 1984.
22. CJ Brinker, KD Keefer, RA Schaefer, RA Assink, BD Kay, CS Ashley J Non-Cryst Solids 63:45, 1984.
23. S Kohjiya, K Ochiai, S Yamashita J Non-Cryst Solids 119:132, 1990.
24. S Yamanaka, Y Yuguchi, H Urakawa, K Kajiwara, S Kohjiya. J Network Polym 20:157, 1999.
25. MR Landry, BK Coltrain, CJT Landry, JM O'Reilly J Polymer Sci (Polym Phys) B33:637, 1995.

## 2

# Thermoreversible and Irreversible Physical Gels from Biopolymers

DAVID R.PICOUT and SIMON B.ROSS-MURPHY *King's College London,  
London, England*

## I. INTRODUCTION

In a number of key industries, including the pharmaceuticals, photographic, paper, and food industries, gels and gelling processes have for many years occupied a position of prime importance, fulfilling many functions from controlled release, surface coatings, and consumed products. Although many definitions have been suggested and attributed to gels in the literature [1]–[3], it is accepted that gels are notoriously difficult to define as a class of materials. They represent a state of matter somehow intermediate between solid and liquid, and they are usually considered as showing solid character overall, although some features of a liquid may also be present. Even though a gel may consist of 99.9% liquid, it can still behave as a solid. Under normal conditions of observation, gels are able to store the work employed in their deformation, and to recover their original shape, and it is this property of “elasticity” that is the essence of a solid. Generally, a simple gel consists of a solid network, which is interspersed (swollen) by a liquid. This network, in the case of biopolymer gels, is built of biological macromolecules and the liquid is usually water. Biopolymer gels may range from so-called weak-gel systems, actually just structured liquids which break down under shear to flow like viscous fluids, to rigid solids, but they are typically soft and resilient or simply jelly-like. In what has later proved to be one of the most quoted articles on gels and gelation, Paul Flory in 1974 proposed in his introduction to a “Faraday Discussion on Gels and Gelation” a classification of gels established on the following basis:

1. Well-ordered lamellar structures, including gel mesophases
2. Covalent polymeric networks, completely disordered
3. Polymer networks formed through physical aggregation, predominantly disordered but with regions of order
4. Particulate disordered structures

In this chapter, these gels will be called, respectively, Flory I, II, III, and IV. A more recent definition of a gel has been proposed from the rheological point of view by Almdal and coworkers in 1993 [4]. This states that a gel is a soft, solid, or solid-like material, which consists of two or more components, one of which is a liquid, present in substantial quantity. The gel shows a flat mechanical spectrum in an oscillatory-shear experiment. This requires that  $G'$  exhibits a plateau extending to times of the order of

seconds, whereas  $G''$  is considerably smaller. This follows earlier suggestions, for example, by Winter and Chambon [5] that the gel point, the discontinuity when sol  $\rightarrow$  gel, can be associated with a common power-law dependence of  $G'$  and  $G''$ .

This chapter will give first a brief overview of the different gel network types existing, focusing on physical gels, thermoreversibility, and irreversibility. We will also introduce the viscoelastic techniques used by the physical chemist to characterize physical gels, and then relate the properties to the underlying structure at the macromolecular and junction zone level.

The gelation of different biopolymer systems will be discussed here, and some of our recent studies on novel cold-set gels of gelatins derived from both mammalian and piscine sources, and work on the heat-set gelation of globular proteins (Flory IV gels) will then be described. Finally, we will also briefly describe some of our recently published work on biopolymer mixed gel systems (i.e., starch-pectate systems).

## II. GEL NETWORK TYPES

Historically, polymer networks can be divided into two main classes: covalent materials, which include bulk elastomers formed from cross-linked materials (usually synthetic polymers but also natural polymers) commonly referred to as chemical networks (e.g., Flory II gels), whereas gel systems having noncovalent interactions are described as physical networks (Flory I, III, IV). Flory I gels cover a wide range of systems, including liquid-crystalline materials, but because the properties tend not to be macromolecular, they will not be discussed here. The formation of a gel involves the association of the polymer segments in solution in such a way as to form a three-dimensional network that contains solvent in the interstices. In this three-dimensional network, chains are usually linked either by junction zones, which extend along a region of the participating chains, by chemical cross links acting at single points, or by aggregation into random clumps (particle association). Chemical gels (covalent network materials) can be formed in a number of ways, including cross-linking high molecular weight linear chains, either chemically or by radiation, by the polymerization of oligomeric multifunctional precursors, or by end linking reactant chains with branching units. They are considered as being true macromolecules, having a molecular weight that is nominally infinite, and consequently they swell rather than dissolve if immersed in a good solvent. They possess an infinite relaxation time and an equilibrium modulus.

Physical gels or networks share much in common with their covalent analogues, but because their cross links are not permanent, they will also show some differences. For instance, they will have the tendency to exhibit rheological creep behavior at long times and also some will dissolve (to form a more dilute polymer solution) rather than swell when placed into a good solvent. Physical gels formed from synthetic polymers include isotactic polymers in certain solvents (i-polystyrene in decalin), ionomer systems in solvents of low dielectric constant, and a number of A-B-A-type block copolymers—aggregation of heterostructural chains is often a common feature of such materials. In this case, block A is compatible with a solvent and block B is incompatible. Under these circumstances, in solution the B-B interaction between units on adjacent chains forms the

physical cross links.

As far as biopolymers, in particular, are concerned, noncovalent cross links are formed by one or more of the mechanisms listed above, usually combined with more specific and complex mechanisms involving junction zones of known, ordered secondary structure. These junction zones hold the chains together through physical forces as, for example, Coulombic, dipole-dipole, charge transfer, and hydrophobic interactions, and hydrogen or van der Waals bonding. Among the biopolymer physical gels, examples of those with cross linking include the double helices in gels from the polysaccharide agar, the triple helices in gelatin gels, and the ion-mediated junction zones in alginate where divalent calcium ions occupy sites between laterally associated regions of chain [6], whereas particulate gels include those formed by heating globular protein solutions. Some physical gels, such as gelatin gels, form on cooling a heated solution, whereas others form only on heating, as for instance those formed from globular proteins as mentioned above or from the polysaccharides curdlan and certain cellulose derivatives, such as cellulose ethers. Also, some, but by no means all, such gels are thermoreversible [7], which means they can be melted out and then will reform without any real hysteresis; others are formed essentially irreversibly.

Thermoreversibility and irreversibility of a gel depend on the type of material. For example, "storage" materials possess highly ordered structures even after extraction and purification (e.g., starch granules), and in order to gel aqueous solutions or dispersions, it is usually necessary first to heat the samples to rupture partially the ordered structure. Cooling will then lead to gelation with a new intermolecular network being formed. The original ordered structure cannot be recovered and, as with heat-set mechanisms, the process is generally irreversible. The gelation of "structural" polymers, by contrast, is accompanied typically by a reversible disorder-order transition, with high-methoxy pectin being an exception to this rule. Such gels are usually thermoreversible, because the junction binding is rather weak. Conversely, chemically cross-linked gels are thermally irreversible (except in the rare cases when cross links are designed to be labile) as the cross links are strong, permanent point-junctions held together by covalent bonding.

It is interesting to note that in physical gels the length of disordered chain between junction zones is generally shorter and less flexible than the regions of "random coil" in chemical gels. Gel networks of the association type (physical) indicated in Figure 1a and the point cross-link situation (chemical) shown in Figure 1b are by no means the only structures involved in gel formation. Indeed, as mentioned above, networks often described as particulate arise when macro-molecules in a compact, semirigid conformational form, aggregate into random clumps and chains to give a continuous network as shown in Figure 1c (Flory IV). In the case of particulate biopolymer gels, however, the gel-forming material is



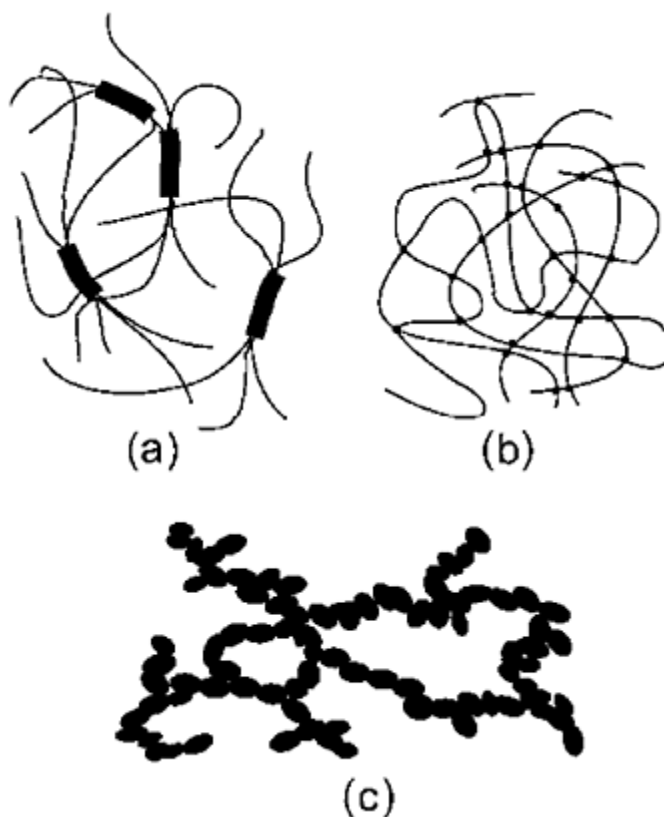


**FIG. 1** Schematic representation of a gel network involving (a) physical junction zones; (b) permanent point-like chemical cross links, and (c) particle association.

usually a protein such as albumin or  $\beta$ -lactoglobulin [8–12]. As defined before, gels can range from single-component networks to complex, multicomponent structures, and in order to manipulate, for instance, gel formation and rheology (“texture”) in such systems, it is necessary to understand the underlying structural features and their effects on mechanical properties.

### III. CHARACTERIZATION OF BIOPOLYMERS BY SHEAR MEASUREMENTS IN OSCILLATORY RHEOLOGY

Over the last two decades, the dynamic oscillatory shear experiment [13] has become nearly routine. Indeed, the improvements in equipment design and computer software have turned such experiments from being the realm of the specialist rheologist into becoming a more common established procedure. Nevertheless, it is still considered to be

the best technique for characterizing the rheological properties of soft solids and viscous fluids, which are viscoelastic by nature. In oscillatory shear experiments, the strain is applied as a periodic oscillation and the resulting sinusoidal stress wave is recorded. In the case of a Hookean solid (perfectly elastic material), where the stress is proportional to strain, the resulting stress wave is completely in phase with the strain wave (i.e., phase angle,  $\delta=0^\circ$ ). However, since stress is proportional to the rate of strain for a Newtonian liquid (purely viscous systems), the stress and strain waves are exactly 90 degrees out of phase. For a viscoelastic material (usually the case), which has elements of both solid-like and liquid-like character,  $\delta$  will be between 0 and 90 degrees [13].

Just as a modulus is defined as the stress/strain ratio in any constant deformation experiment, then for a dynamic sinusoidal experiment, it follows that two moduli can be defined: Stress in phase with strain/strain and stress 90 degrees out of phase with strain/strain. These are the storage modulus ( $G'$ ) and loss modulus ( $G''$ ), respectively.  $G'$  is a measure of the energy stored in the material and recovered from it per cycle. It is taken as an indication of the solid or elastic character of the material under test.  $G''$  represents a measure of the energy dissipated or lost (as heat) per cycle of sinusoidal deformation. The loss modulus  $G''$  therefore, is taken as an indication of liquid or viscous behavior. The  $\omega$ -dependent elastic and viscous components,  $G'$  and  $G''$ , respectively are then separable by software correlation analysis, and the resultant complex viscosity  $\eta^*$  calculated, in the instrument.

As far as viscoelastic measurements are concerned, the coupling of strain and strain rate (frequency) can be a serious problem. This is because only in the small strain limit will the correct  $G'$  and  $G''$  profiles be obtained. The design of an instrument with good minimum strain resolution and good stress detection sensitivity is not routine, and the purchase of such an instrument can be costly.

Considering the preparation of a linear polymer in the melt above a certain molecular weight,  $M_w$  (typically  $> \sim 2 \times 10^4$ ), enhanced viscosity will be observed owing to the presence of entanglements. The same characteristics are true for a solution when the product of concentration and molecular weight ( $CM_w$ ) is greater than this figure. These entanglement networks are therefore formed by the topological interactions of polymer chains either in the melt or in solution when the product of concentration and molecular weight becomes greater than some critical molecular weight,  $M_e$ . In this case, they behave as "pseudogels" at frequencies higher (shorter time scales) than the lifetime of the topological entanglements. For linear chains, this depends on  $M_w^3$ , where  $M_w$  is the (weight average) molecular weight. The typical "mechanical spectrum" of an entangled polymer solution or melt shows the following features: At very low frequencies, in the "terminal zone," it flows as a high-viscosity liquid, with  $G' \propto \omega^2$  (in the usual  $\log G'$  vs  $\log \omega$  representation this gives a slope=2; see Fig. 2) and  $G'' \propto \omega^1$  (slope=1). As the frequency is increased, there is a "crossover" in  $G'$  and  $G''$ . At high frequencies, the entangled molecules behave more like a permanent gel network (elastic response dominating in this region). This means  $G'$  and  $G''$  are parallel, with  $G' > G''$  and with a largely frequency-insensitive spectrum; i.e., both  $G'$  and  $G''$  are  $\propto \omega^0$ , giving an equilibrium modulus (slope~0) referred to as the plateau region.

From, for example, reptation theory, it can be shown that the extent of the low-frequency plateau of  $G'$  should depend on  $M_w^3$ . Consequently as the molecular weight increases, the plateau region will move to lower and lower frequencies, as

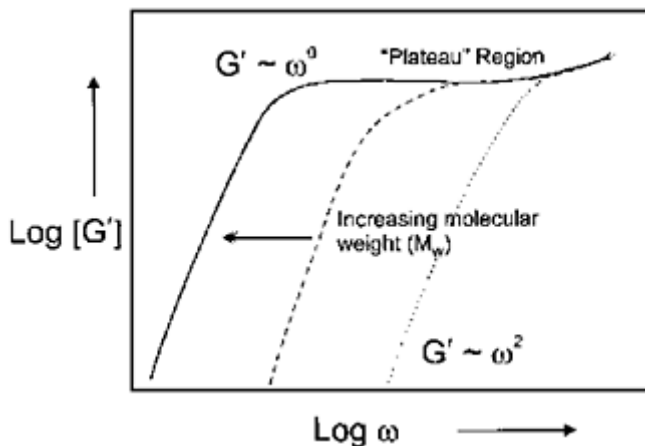


**FIG. 2** Effect of the  $M_w$  increase for linear polymer on the modulus  $G'$  plotted against frequency,  $\omega$ .

shown in Figure 2. If the molecular weight becomes extremely large, then the end of plateau frequency can be well below the instrument measurement range (in  $\text{rad s}^{-1}$ ,  $=2\pi \times$  frequency in hertz, typically 0.01–50.0). For a branched cross-linked microgel particle, it is easy to estimate the molecular weight to be of the order of  $10^{12}$ . For a true megamolecule, such as a macroscopic cross-linked network, or a swollen gel, the apparent molecular weight is  $>10^{16}$ . In this case, the longest relaxation time will be well outside any instrument range, and only the plateau modulus or gel spectrum is seen. (The relaxation spectrum for a branched system is much broader than for a linear system, since there are many more “chain paths” for relaxation.) A typical mechanical spectrum for a biopolymer hydrogel is illustrated in Figure 3 (although the curvature in  $G''$  may also be more pronounced than is seen here). For lower concentration gels, the slope is slightly greater, although measurements close to or below the critical gel concentration are quite difficult, since such systems usually gel from the dilute rather than semidilute region [5].

Biopolymer gels and solutions can be strain insensitive, but this is usually not the case, unlike most synthetic polymer solutions, melts, rubber networks, and glasses. Small and intermediate oscillatory shear strain sweep measurements have enabled a better distinction to be made between what have been called “strong” and “weak” gels [15]. At very small strains, both systems show practically the same (plateau modulus) mechanical spectrum, with  $G'$  being greater than  $G''$ , and with both moduli frequency independent over the frequency range. In other words, they respond as solids. However, the strain dependence of these two

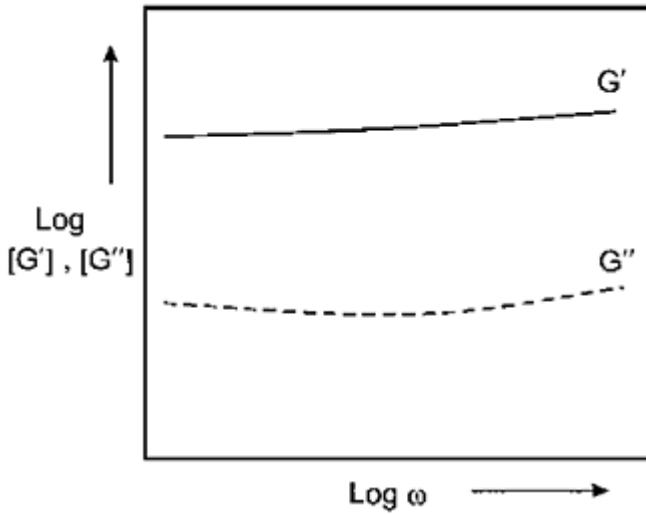


**FIG. 3** Typical mechanical spectrum observed for a true gel, with  $G' > G''$  and both moduli showing little frequency dependence.

classes of materials may be very different. Indeed, usually for strains  $\gamma_{lin} \geq$  say 0.25, the moduli for strong gels are strain independent (linearly viscoelastic), whereas on the contrary, weak gels start being strain dependent when  $\gamma_{lin} > \sim 0.05$ . Therefore, these behave more like colloidal particle networks (where  $\gamma_{lin}$  may be  $< 0.001$ ) [16]. Indeed merely employing the term *weak gel* is liable to generate some confusion, since it is by nature qualitative. (How weak is weak?) It may be safer just to regard such system as structured liquids.

Xanthan is the prime example of such a system: a free flowing solution that is yet capable of suspending material for long (but not infinite!) times. Its flow curve is a straight line, of slope  $\sim -0.9$ , on log-log plots of steady shear viscosity ( $\eta$ ) versus shear rate over several decades, implying that, at zero shear rate, it has infinite viscosity and does not flow. These are consistent with the properties of solids, and indeed the mechanical spectrum of a xanthan solution can be similar to that of a true gel. At a simplistic level, it can be said to form shear-reversible network junctions, providing the solid-like character, which are readily disrupted by mechanical stress or strain, allowing the bulk flow to occur. Subjecting a sample to large deformations can discriminate further between true gels and these structured liquids. Large deformation tests, by contrast to small deformation measurements where the amplitude of the applied sinusoidal stress or strain can be so small that the structure of the material is virtually unaffected by the measurements, involve tension or compression of a sample until fracture. In this case, strong gels will rupture and fail, and they cannot reform unless reheated through the order-disorder temperature. By contrast, and like polymer melts, the so-called weak gels will recover given sufficient time—typically say 1–50 s—(they will flow rather than fail) at large deformations. Under appropriate conditions, the latter can also be measured,

without apparent fracture, under steady shear flow. This distinction between strong and weak physical gel must be somewhat arbitrary, since, if the noncovalent junction zones can be ruptured by mechanical perturbation, they must have bond energies of only a few  $kT$  units (where  $T$  is temperature and  $k$  is Boltzmann's constant), and therefore may also melt on heating. Ultimately, such discussion serves only to focus attention on the inadequacy of using the term *weak gel* to describe a range of different phenomena. Rheologically, this means that although such a system lies within the linear (stress proportional to strain) viscoelastic regime, the maximum strain for linear behavior,  $\gamma_0$ , is very small. For strong gels, we can say that  $\gamma_0 \sim 20\%$ , whereas for weak gels, it can be up to 1000 times smaller. Colloidal and particulate networks (Flory IV) are often of this type.

A complete characterization of gel (and gel-like) materials therefore requires both strain and frequency sweeps to be carried out. Indeed, since, in general, the two parameters are coupled, the ideal experiment would require a strain sweep to be carried out at all frequencies in order to determine the value of  $\gamma_{lin}$ , prior to making a frequency sweep. In practice, it is usually deemed to be sufficient to choose a frequency in the middle of the experimental range and then vary the strain. In this case, it is important to appreciate that because of the sample and instrument response,  $\gamma_{lin}$  may decrease at both higher and lower frequencies.

#### IV. KINETIC CONTROL OF GELATION

Gelation is, of course, a kinetic process, and with modern equipment it is very simple to place an ungelled solution on the instrument and adjust conditions (i.e., for physical gels, e.g., the temperature, for chemical gels the amount of cross linker) and follow the behavior of  $G'$  and  $G''$  as a function of time. The trace observed shows a characteristic shape "cure" curve of  $\log(G', G'')$  against time. For the fluid state,  $G''$  will be greater than  $G'$ . After the start of the cure experiment there is an initial lag time. Subsequently both  $G''$  and  $G'$  begin to increase, but with  $G'$  increasing faster than  $G''$ . Consequently, at a given time, there should be a crossover where  $G'$  becomes greater than  $G''$ , sometimes associated with the gel(ation) time (although this does not necessarily occur at the same time). Subsequently  $G'$  continues to increase, before levelling off, whereas  $G''$  ideally passes through a parabolic maximum and then decreases to zero. The maximum in  $G''$  is an effect which can be associated with the relaxation of "dangling chain ends." The  $G'$  (strictly  $G$ ) versus time kinetic behavior has been calculated by Clark in terms of the branching model [17]. This form of behavior is illustrated in Figure 4 in a typical experiment when  $G'$  is monitored at a constant frequency. As the concentration of polymer is increased, the gelation time falls, but the value of  $G'$  at long (actually asymptotic) times increases.

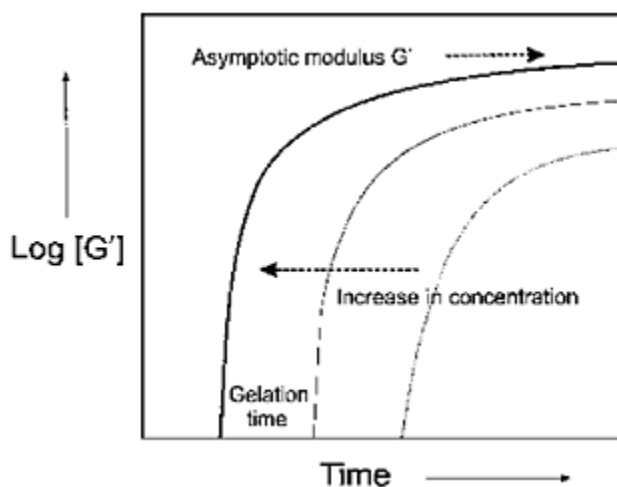


**FIG. 4** Time dependence of  $G'$  for a gelling system. As the concentration increases, the asymptotic modulus is increased, but the gelation time is decreased.

## V. GELATIN

Over the years gelatin, a thermoreversible gelling biopolymer, has proved to be one of the most popular hydrocolloids for use in industry. The unique characteristics that distinguish it from other gelling agents are its melt-in-the-mouth texture and its brilliant clarity. Although widely used in foods such as confectionery, jellied meats, and chilled dairy products, other important applications are in the pharmaceutical industry—in the manufacture of capsules and in the photographic industry, where it is used to suspend particles of silver halide. Gelatin is a proteinaceous material derived by the hydrolytic degradation (by either acid or alkaline treatment) of collagen, the principal protein component of white, fibrous connective tissue (e.g., skin, tendon, bone).

Traditional gelatins normally dissolve in warm water ( $\geq 40^\circ\text{C}$ ). Above this temperature, the polypeptide exists largely as flexible, single random coils. When cooled to below room temperature, clear gels are formed, providing that the concentration is greater than about 0.5%. The gels contain extended physical junction zones (Flory III gels) formed by a partial reversion to ordered, triple-helical collagen-like sequences separated along the chain contour by peptide residues in the disordered conformation [18, 19].

It is thought that the coil to triple-helix propagation rate is limited by the presence of *cis*-proline residues in the backbone. The subsequent reversion of these to the *trans* form allows the helix to propagate only slowly; the overall growth rate is typically four to six orders of magnitude less than for double-helical systems, such as the carrageenans (discussed later). One recent model has suggested that the triple helix is formed from two chains, one of which has an intramolecular  $\beta$  chain, rather than from three separate chains

[20].

In the past, it was assumed that initial helix formation was followed by substantial lateral aggregation, leading to extended quasicrystalline junctions, as described historically in the fringed micelle model of polymer crystallization. However, since long-time measurements of optical rotation increase slowly, but apparently without limit (even when plotted on a log-time axis), the proportion of residues in the ordered, helical conformation must also be increasing. This suggests a considerable degree of conformational flexibility, even postgel, that is rather unlikely to occur if the junction zones are formed of rigid crystallites. More direct evidence comes from small-angle neutron scattering by Djabourov and coworkers [21]. They found that in the sol state the cross-sectional chain radius,  $R_c$ , was  $0.32 \pm 0.1$  nm, a value in good agreement with the calculated side-group extension of a collagen chain, whereas in a relatively concentrated gel (5%),  $R_c$  was  $0.43 \pm 0.1$  nm, not much greater than this. Now it is widely accepted that the junction zones consist of (largely) isolated triple helices. This, albeit simpler, hypothesis helps to explain how and why of all the physical gels, gelatin behaves, at least isothermally, most like an ideal rubber.

Almost all published work in the scientific literature has concentrated on gelatins derived from traditional collagen sources (mammalian), and therefore few studies have been carried out on alternative (piscine) sources. It is well known [22] that the melting and gelling temperature of gelatin correlate with the proportion of imino acid residues in the original collagen (typically ~24% for mammals and 16–18% for most fish species). Coldwater fish, say cod, have a very low hydroxyproline content, and it has been shown that the gelatin issued from these sources has very low gelling and melting temperatures compared to the gelatin obtained from pigskin or cowhide. For example, 10% mammalian gelatin forms a gel at room temperature, whereas 10% cod gelatin will just about gel at ~2°C. In some recent work, we examined single-component fish gelatins as well as some mixtures to investigate how the properties of the single systems are altered in the blends. The gelling and melting temperatures as well as the gel modulus have been characterized by using rheological measurements, which have benefited greatly by improvements in instrumentation in the last few years. Fish samples studied were tilapia, tuna, megrim and cod, ranging in order from tropical to coldwater species [23].

## VI. PLANT POLYSACCHARIDES

Pectin, extracted from plant cell walls, particularly from apples and citrus fruits, and starch, extracted, for example, from cereals and tubers (potato), are the most important members of this group. The former consists predominantly of sequences of D-galacturonic acid residues joined in chains by means of  $\alpha$ -(1–4) glycosidic linkages. Inserted into the main uronide chain are occasional rhamnose units introducing a kink into the otherwise straight chain. At least some of the carboxyl groups are methyl esterified, with the precise distribution depending upon the plant source and age. Reasonably, in view of their structural similarity, pectins of a low degree of esterification behave like alginates and gel with divalent ions, and the structure has been termed the “egg-box” model [24]. The more highly esterified materials gel under conditions of low

pH and decreased water activity; that is, where intermolecular electrostatic repulsions are reduced, in this case, the junction zones are thermoreversible at, say, 40°C [6].

Starch, by contrast, consists of two chemically very similar polysaccharides, one predominantly linear and of relatively low molecular weight ( $<2 \times 10^6$ ), amylose, and the other, branched and of much higher  $M_w$  ( $>5 \times 10^7$ ), amylopectin. Amylopectin usually predominates ( $>70\%$  by weight), but the precise proportions of the two polymers, their chain length, and the branching frequency depend upon the source (e.g., potato, maize, wheat, rice). The polymers themselves are laid down in a highly structured semicrystalline supramolecular granule ( $\sim 2\text{--}100\ \mu\text{m}$  diameter). On heating, the granules swell and rupture (at temperatures  $>60^\circ\text{C}$ ). After this, it is believed that the amylose leaches out, and at concentrations greater than, say, 20%, the mixture of granular residues and amylose forms a viscoelastic paste. On cooling, this sets, and the result has been described as a composite of amylose gel filled with swollen granules [25]. This is, however, by no means the whole picture, since amylopectin solutions can also gel, albeit extremely slowly [26], and much of the subtlety of starch behavior is undoubtedly related to the limited compatibility and mutual gelation of the two polymeric components.

## VII. MARINE POLYSACCHARIDES

The most important of these forming gels are ( $\iota$ - and  $\kappa$ -) carrageenan, agar(ose), and the alginates. All three are extracted from different species of seaweed. Much evidence suggests that the first two form thermoreversible gels by an extension of the gelatin mechanism and, although some details are still disputed, the general principles are as follows. On heating above the helix-coil transition temperature (for charged carrageenans, this depends crucially on ionic strength and cation species but lies typically in the range of 20–50°C), they apparently undergo an order-to-disorder (helix-to-coil) transition. On recooling, they revert, at least partly, to a double helix [27]. Compared with that for gelatin, this is a very fast process, taking only a second or two under most conditions. More recently, it has been suggested that a superhelical structure is involved [28]. It seems that the common view now is that all of these systems probably form quite small intertwined fibrils, and it is the aggregation of these that gives the gel. Evidence comes from small-angle X-ray scattering, atomic force microscopy, and some small-angle neutron scattering work.

Subsequently, at lower temperatures, the behavior becomes less ideal; so for agarose there is then substantial side by side aggregation (confirmed by the measurements of  $R_c$  by small-angle X-ray scattering) [29]. For the carrageenans, gelation is known to depend crucially on the cations present; for  $\text{Na}^+$  little is seen, whereas high-modulus gels are formed, for example, with  $\text{K}^+$  and  $\text{Ca}^{2+}$ . The precise details of network formation in these systems is still being actively researched [28].

Alginate gels, by contrast, are not thermoreversible; in fact, they appear to be heat stable up to  $>100^\circ\text{C}$ , and their formation can only be induced in the presence of certain, specifically divalent, cations. Alginates are anionic block copolymers composed of two very similar saccharide units, guluronate (G) and mannuronate (M). If  $\text{Ca}^{2+}$  ions are introduced into a solution of sodium alginate, gelation occurs extremely rapidly. Gelation



is induced by specific ion binding, accompanied by conformational changes, with evidence for  $\text{Ca}^{2+}$  ions binding cooperatively to G blocks. In one model, the junction zones involve two chains and chelated ions giving the so-called egg-box structure [24].

### VIII. MICROBIAL POLYSACCHARIDES

A number of polysaccharides of interest occur outside the cells of certain cultured microbes either covalently attached to the cells or secreted into the growth media. They are the microbial exopolysaccharides and, over the past few years, a great number of them have been described. Currently, on a volume-production basis, the two major members of this group are gellan, an anionic polysaccharide produced by *Auromonas elodea*, and xanthan, also anionic, from *Xanthomonas campestris*. Gellan has a complex, tetrasaccharide repeat unit and gels in the presence of multivalent cation, via a double-helical intermediate, in a way analogous to the gelling carrageenans. The bulk, mechanical properties are sensitive to the degree of acylation of the chain [30, 31]. There have been quite a number of published viscoelastic data for gellan, but many of the published observations appear to be rather obvious; quantitative conclusions based on, for example, results for different molecular weight samples appear to be lacking. Xanthan, which has a pentasaccharide sequence, forms strong gels only with trivalent, for example, aluminium  $3^+$ , ions [32]. It is, however, the archetypal weak-gel structurant that has been employed in a number of industries because of its unusual rheological properties [33, 34].

### IX. HEAT SET GELS FORMED FROM GLOBULAR PROTEINS

A distinction can be made between gel networks formed from initially disordered random coil biopolymers (as seen in the previous sections) and those formed and maintained in an essentially ordered state, such as heat-set globular protein gels. These gels from globular proteins have been extensively investigated over many years, although in the great majority of studies, rather crude and/or mixed samples of protein have been considered rather than pure systems. Most previous work has concentrated on examining structural and rheological properties of fully cured gels. In this section, we will discuss heat-induced gelation of the globular proteins, bovine serum albumin (BSA), and  $\beta$ -lactoglobulin ( $\beta$ -Lg) not far from critical gel conditions together with aspects of kinetic gelation theory.

For systems heated to not much greater than the protein unfolding temperature ( $T_c \sim 70^\circ\text{C}$ ), many studies, using electron microscopy, X-ray scattering, and spectroscopic techniques, have confirmed that the globular conformation of the native protein is only slightly perturbed [35–37]. It appears that denaturation partially disrupts the protein without modifying the overall shape very significantly, but it exposes some intraglobular hydrophobic residues. At low enough concentrations, these can refold all but reversibly, but above a certain concentration, there is competition between intramolecular and intermolecular  $\beta$ -sheet formation. If the latter predominates, gels are formed which are fibrillar and whose fibrils are approximately 1–2 times the width of the original globule,

as illustrated in Figure 5. The parallels between these fibrils and the insoluble protein fibrils being formed and laid down in disease states (so-called  $\beta$ -amyloid fibrils) are of considerable interest. The latter exist, as one example, in the brains of patients with Alzheimer's disease, although similar structures are formed in other dementias such as Huntington's chorea [38]. The balance between linear and branched chain growth and the precise mode of aggregation, for example, random clumping, more directed rod-like fibrillar, etc., depend upon the pH and external ionic strength. The higher the ionic strength and the closer the pH to the isoelectric point, the more unspecific the aggregation (coagulation), and turbid syneresing gels are formed. Conversely, transparent gels are formed when the pH is far from the isoelectric point, and they are formed at intermediate salt levels. Experimental "phase" diagrams can be constructed showing the boundary between sols, clear gels, and turbid gels as a function of protein concentration, pH, and I. In fact, boiled egg white is only white because of the concentration of salt in the ovalbumin solution, and suitable dialysis can produce a transparent egg white. Prolonged heating of protein gels to  $>85^{\circ}\text{C}$  produces a more drastic change, and some intermolecular covalent disulfide bonds are formed; these gels can no longer be regarded as being merely physical networks [39].

By interpolating the gel time determined at a range of concentrations, it is possible to construct a phase diagram (strictly a state diagram) of gelation

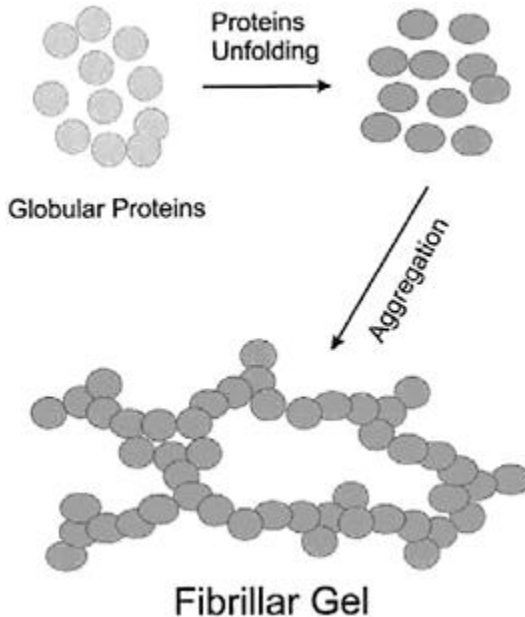


**FIG. 5** Corpuscular gel formation illustrated for heat-set protein gels—the "molten globules" mechanism.

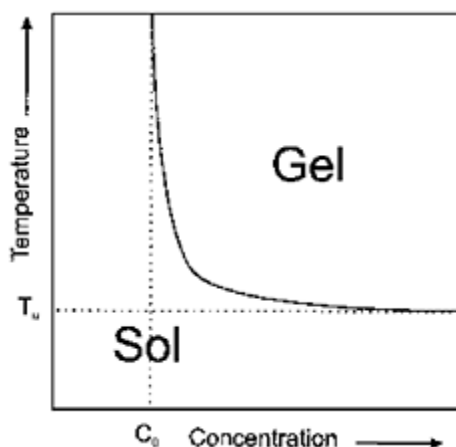


**FIG. 6** Temperature vs concentration in the lower critical solution temperature (LCST) type phase diagram.

temperature versus concentration. This clearly illustrates the qualitative similarity between thermal gelation of globular proteins and the lower critical solution temperature (LCST) type phase diagram (Fig. 6) seen for certain fluid (and polymer solution) systems.

## X. MIXED PHYSICAL GELS

Phase separation in polymer mixtures is a well-understood phenomenon, that differs from the behavior of small molecules which are free to move independently in solution, and which can normally remain intimately mixed (entropy of mixing favoring single-phase systems). In solutions of biopolymers, where there are far fewer independently moving species, the entropic advantage of mixing is greatly reduced and the enthalpy of interaction becomes dominant [40]. Therefore, when different polymers are mixed in solution, we expect the two systems to phase separate. For biopolymers, behavior is often dominated by the enthalpy of segment-segment interactions; in other words, by the energies of interactions between chains [41]. The simplest systems are when no phase separation occurs and the solutions remain homogeneous. This may happen because the two biopolymers are compatible, at least in the solvent, and therefore are completely miscible, or because they form a complex which is soluble in the solvent. In the latter case, the biopolymers may be separated under conditions where such complex formation is inhibited. However, in polymer mixtures, complete miscibility is the exception rather than the rule, and the mixture of two different biopolymers often becomes turbid on mixing owing to phase incompatibility and, over a period of time, separates into two phases, each containing most of one polymer and little of the other, with solvent partitioned between them.

Interactions can either be of the associative or segregative type. Associative

interactions are favorable, such as those in polyanion-polycation systems in which two different polymers can associate with one another by charge-charge attraction. An example is typically between an anionic polysaccharide (e.g., low-methoxy pectin or sodium alginate) and a protein (e.g., gelatin) below its isoelectric point under conditions where the polysaccharide alone does not gel [41, 42]. Normally, however, charge-charge attraction results in precipitation of the neutral complex (complex coacervate) rather than in formation of a hydrated gel. The two biopolymers collect together in one of the phases, which therefore becomes polymer rich, whereas the other consists mainly of solvent. In most cases, however, the interactions are unfavorable and can lead to thermodynamic incompatibility (or segregative interactions) between chains of dissimilar biopolymers. This tends to cause each to exclude the other from its polymer domain so that the effective concentration [43] of both is raised. At high concentration, there is partitioning of the system into two separate discrete phases, with one forming a continuous matrix and the other being dispersed through it. The effect of segregative interactions can, however, also be seen at polymer concentrations below the binodal where the mixture remains single phase. In systems where one component can undergo a transition from an expanded coil conformation to a more compact ordered form, the presence of low concentrations of a second polymer within the same phase may cause a large increase in the rate and/or extent of conformational ordering [44]. In some cases, one component may drive the other out of solution. For example, mixtures of maltodextrins (low molecular weight starch fractions) and gelatin prepared at concentrations in the single-phase region and held at a temperature above the onset of conformational ordering and gelation of either component showed massive precipitation of maltodextrin [45], with the fraction precipitated increasing in direct proportion to the protein concentration. In mixtures of maltodextrin with whey proteins, the converse effect was observed [46], with precipitation of protein in direct proportion to maltodextrin concentration.

This section will describe some recent work showing evidence of an analogous precipitation process during formation of calcium pectate gels in the presence of oxidized starch, leading to progressive collapse of the calcium pectate network structure with increasing starch concentration [47]. This qualitative interpretation is supported by quantitative analysis of gel moduli [48].

The effect of partially depolymerized starch products (oxidized starch and gelling maltodextrin) on the gels formed by low-methoxy pectin on cooling in the presence of  $\text{Ca}^{2+}$  has been investigated by rheological measurements under low-amplitude oscillatory shear. The central aim of this work was to gain a better understanding of the effect of segregative interactions in this particularly complex gelling mixture.

The first paper [47] of a series of four related publications showed that the storage modulus,  $G'$  of the calcium pectate network, could be increased, decreased, or remain unaffected by the presence of oxidized starch, depending on the concentration of  $\text{Ca}^{2+}$  used. The  $\text{Ca}^{2+}$  concentration at the transition from enhancement to depletion of network strength was independent of starch concentration, and increased with increasing degree of esterification (DE) of the pectin component (across the DE range of 31.1–55.8%). Decrease in gel strength at high concentrations of  $\text{Ca}^{2+}$  was found to arise from sharp reductions in  $G'$  during cooling, and was accompanied by development of a grossly heterogeneous network structure (as visualized by light microscopy with iodine staining

for starch). It was tentatively suggested that (1) segregative interactions between the two polymers promote conversion of pectin to a progressively more compact structure as the starch concentration is increased; (2) low concentrations of  $\text{Ca}^{2+}$ , the network is enhanced by formation of additional intermolecular junctions; and (3) at higher  $\text{Ca}^{2+}$  concentrations, where there is already extensive intermolecular association in the absence of starch, gel strength is reduced by further association of pectin chains into large aggregated bundles that make little contribution to the overall connectivity of the network (effectively precipitation of ordered pectin in response to thermodynamic incompatibility with starch).

In the second paper [48], the concept of reduction in gel strength by a precipitation mechanism was explored further by quantitative analysis of  $G'$  values for 2 wt% pectin with stoichiometric  $\text{Ca}^{2+}$  after cooling to  $5^\circ\text{C}$  in the presence of increasing concentrations of oxidized starch (0–40 wt%). The experimental results were matched with good precision by an analysis based on the following postulates. (1) Thermodynamic incompatibility between the two polymers causes partial precipitation of pectin chains into aggregated bundles within a supporting calcium pectate network. (2) The extent of precipitation is controlled by a solubility product ( $K$ ), defined as the starch concentration multiplied by the square of the concentration of unprecipitated pectin. (3) The volume occupied by the precipitated pectin fraction is directly proportional to the amount precipitated (constant of proportionality,  $k$ ). The system was regarded as comprising a continuous phase of oxidized starch and unprecipitated pectin surrounding a dispersed phase of precipitated pectin, and overall moduli were calculated using an appropriate rheological blending law. The moduli of the individual components at their effective concentration within the appropriate phase were determined from calibration curves for calcium pectate and oxidized starch alone. The overall modulus of the continuous phase was estimated by simple addition of the separate contributions from unprecipitated pectin and oxidized starch. The modulus of the dispersed particles of precipitated pectin was effectively infinite in comparison with that of the continuous phase, allowing a simplified form of the isostress equation to be used. The discrepancies between observed and fitted values were virtually within experimental scatter of the results, suggesting that the assumptions made in the analysis may be physically realistic.

A related investigation and analysis of calcium pectate gelation in the presence of potato maltodextrin has also been reported [49, 50].

## XI. SUMMARY

The detailed study of physical gelation of biopolymers is a comparatively young area of research but one which is growing in importance. The potential shortage of petropolymers makes studies of renewable resource (“green”) polymers of even increasing importance. We anticipate this area will continue to grow and will become economically more and more significant in the future.

## REFERENCES

1. DJ Lloyd. The problem of a gel structure. In: Colloid Chemistry 1. J Alexander, ed. Chemical Catalogue Co. New York, 1926, pp. 767–782.
2. PH Hermans. Gels. In: Colloid Science. Vol II, HR Kruyt, ed. Elsevier, Amsterdam, 1949, p. 483.
3. PJ Flory. Introductory lecture. Faraday Discussions 57:7–18, 1974.
4. K Almdal, J Dyre, S Hvidt, O Kramer. Polym Gels Netw 1:5, 1993.
5. HH Winter, F Chambon. Analysis of linear viscoelasticity of a cross-linking polymer at the gel point. J Rheol 30:367–382, 1986.
6. AH Clark, SB Ross-Murphy. Structural and mechanical properties of bio-polymer gels. Adv Polym Sci 83:57, 1987.
7. K te Nijenhuis. Thermoreversible networks. Viscoelastic properties and structure of gels. Adv Polym Sci 130:1–193, 1997.
8. AH Clark, FJ Judge, JB Richards, JM Stubbs, A Suggett. Electron microscopy of network structures in thermally induced globular protein gels. Int J Peptide Protein Res 17:380–392, 1981.
9. AM Hermansson. Gel characteristics-structure as related to texture and water-binding of blood plasma gels. J Food Sci 47:1965–1972, 1982.
10. AM Harwalker, M Kalab. Thermal denaturation of  $\beta$ -lactoglobulin in solution. Electron microscopic study. Milchwissenschaft 40:65–68, 1985.
11. AM Hermansson, O Harbitz, M Langton. Formation of Two Types of Gels from Bovine Myosin. J Sci Food Agric 37:69–84, 1986.
12. M Langton, AM Hermansson. Fine-stranded and particulate gels of  $\beta$ -lactoglobulin and whey protein at varying pH. Food Hydrocolloid 5:523–539, 1992.
13. JD Ferry. Viscoelastic Properties of Polymers. 3rd ed. Wiley Interscience, New York, 1980.
14. M Doi, SF Edwards. The Theory of Polymer Dynamics. Clarendon Press, Oxford, UK, 1986.
15. SB Ross-Murphy, KP Shatwell. Polysaccharide strong and weak gels Biorheology 30:217–227, 1993.
16. JW Goodwin, RW Hughes. Particle Interactions and Dispersion Rheology In: Technology for Waterborne Coatings. ACS Symposium Series. Vol 663, 1997, pp. 94–125.
17. AH Clark. Biopolymer gelation—comparison of reversible and irreversible cross-link descriptions. Polym Gels Netw 1:139–158, 1993.
18. M Djabourov, J Maquet, H Theveneau, J Leblond, P Papon Br Polym J 17:169, 1985.
19. SB Ross-Murphy. Structure and rheology of gelatin gels—recent progress. Polymer 33:2622, 1992.
20. JP Busnel, ER Morris, SB Ross-Murphy. Interpretation of the renaturation kinetics of gelatin solutions. Int J Biol Macromol 11:119, 1989.
21. I Pezron, T Herning, M Djabourov, J Leblond. Conformation of gelatin chains in aqueous-solutions. 1. A light and small angle neutron-scattering study. 2. A quasielastic light scattering study. In: Physical Networks—Polymers and Gels, W Burchard, SB Ross-Murphy, eds. Elsevier, London, 1990, p. 231.
22. A Veis. The Macromolecular Chemistry of Gelatin. Academic Press, New York, 1964.

23. PM Gilsenan, SB Ross-Murphy. Viscoelasticity of thermoreversible gelatin gels from mammalian and piscine collagens. *J Rheol* 44:871–883, 2000.
24. GT Grant, ER Morris, DA Rees, PJC Smith, D Thom. *FEBS Lett* 32:195, 1973.
25. MJ Miles, VJ Morris, PD Orford, SG Ring. *Carbohydr Res* 135:257, 1985.
26. CM Durrani and AM Donald. *Polymer Gels and Networks*, 3:1, 1995.
27. DA Rees. *Adv Carbohydr Chem Biochem* 24:215, 1969.
28. IS Chronakis, L Piculell, J Borgström. Rheology of kappa-carrageenan in mixtures of sodium and cesium iodide: two types of gels. *Carbohydr Polym* 31:215, 1996.
29. M Djabourov, AH Clark, DJ Rowlands, SB Ross-Murphy. Small-angle X-ray-scattering characterization of agarose sols and gels. *Macromolecules* 22:180, 1989.
30. R Moorhouse, GT Colegrove, PA Sandford, JK Baird, KS Kang. A new gel-forming polysaccharide. In: *Solution Properties of Polysaccharides*, DA Brant, ed., American Chemical Society, Washington, DC, 1981, p. 111.
31. G Robinson, CA Manning, ER Morris. Conformation and physical properties of the bacterial polysaccharides gellan, welan and rhomsan . In: *Food Polymers, Gels and Colloids* E Dickinson, ed. Royal Society of Chemistry, London, 1991, p. 22.
32. AB Rodd, DE Dunstan, DV Boger. Characterization of xanthan gum solutions using dynamic light scattering and rheology. *Carbohydr Polym* 42:159–174, 2000.
33. M Milas, M Rinaudo, M Knipper, JL Schuppiser. Flow and viscoelastic properties of xanthan gum solutions. *Macromolecules* 23:2506, 1990.
34. SB Ross-Murphy, VJ Morris, ER Morris. *Faraday Discussions. Chem Soc* 18:115, 1983.
35. AH Clark, CD Lee-Tuffnell. Gelation of globular proteins. In: *Functional Properties of Food Macromolecules* JR Mitchell, DA Ledward, eds. Elsevier, London, 1986, pp. 203–272.
36. P Aymard, JC Gimel, T Nicolai, D Durand. Experimental evidence for a two-step process in the aggregation of beta-lactoglobulin at pH 7. *J Chimie Physique Physico-Chimie Biologique* 93:987–997, 1996.
37. P Aymard, T Nicolai, D Durand, AH Clark. Static and dynamic scattering of betalactoglobulin aggregates formed after heat-induced denaturation at pH 2. *Macromolecules* 32:2542–2552, 1999.
38. M Sunde, CCF Blake. From the globular to the fibrous state: protein structure and structural conversion in amyloid formation. *Q Rev Biophys* 31:1, 1998.
39. SB Ross-Murphy. Formation, structure and properties of physical networks . In: *Polymer Networks: Principles of their Formation, Structure and Properties* RFT, Stepto, ed. Chapman & Hall, Glasgow, 1998, pp. 290–318.
40. ER Morris. Mixed polymer gels. In: *Food Gels* P Harris, ed. Elsevier, London, 1990, pp. 291–359.
41. VB Tolstoguzov. Functional properties of protein-polysaccharide Mixtures . In: *Functional Properties of Food Macromolecules* JR Mitchell, DA Ledward, eds. Elsevier, London, 1986, p. 385.
42. MA Muchin, ES Wajnermann, VB Tolstoguzov. Complex gels of proteins and acidic polysaccharides. *Die Nahrung* 20:313–319, 1976.
43. AH Clark, RK Richardson, SB Ross-Murphy and JM Stubbs. Structural and mechanical properties of organo-gelatine co-gels. Small deformation studies . *Macromolecules* 16:1367–1374, 1983.
44. VB Tolstoguzov, VP Belkina, VJa Gulov, VJa Grinberg, EF Titova, EM Belavzeva. State of phase, structure and mechanical properties of the gelatinous system wategelatin-dextran. *Die Stärke* 26:130–137, 1974.

45. S Kasapis, ER Morris, IT Norton, MJ Gidley. Phase equilibria and gelation in gelatin/maltodextrin systems. Part II. Polymer incompatibility in solution . Carbohydr Polym 21:249–259, 1993.
46. P Manoj, S Kasapis, MWN Hember, RK Richardson, ER Morris. Complex interactions in co-gelation of whey protein isolate or bovine serum albumin with potato .Food Hydrocolloids maltodextrin. Submitted.
47. DR Picout, RK Richardson, C Rollin, RM Abeysekera, ER Morris. Ca<sup>2+</sup> -induced gelation of low-methoxy pectin in the presence of oxidized starch. Part 1. Collapse of network structure. Carbohydr Polym 43:113–122, 2000.
48. DR Picout, RK Richardson, ER Morris. Ca<sup>2+</sup> -induced gelation of low-methoxy pectin in the presence of oxidized starch. Part 2. Quantitative analysis of moduli Carbohydr Polym 43:123–131, 2000.
49. DR Picout, RK Richardson, ER Morris. Co-gelation of calcium pectinate with potato maltodextrin. Part 1. Network formation on cooling. Carbohydr Polym 43:133–141, 2000.
50. DR Picout, RK Richardson, ER Morris. Co-gelation of calcium pectinate with potato maltodextrin. Part 2. Analysis of co-gel moduli. Carbohydr Polym 43:143–153, 2000.



# Reversible (Physical) Gelation in the Solutions of Associating Polyelectrolytes

IGOR I.POTEMKIN and ALEXEI R.KHOKHLOV *Moscow State University, Moscow, Russia*

## I. INTRODUCTION

Associating polyelectrolytes (APEL) are molecules consisting of water-soluble charged units (hydrophilic blocks) and insoluble (hydrophobic) groups (stickers) distributed along the chain. At high enough attraction between the stickers, they can aggregate to each other and form reversible junctions. In this chapter, we will focus our attention on the behavior of weakly charged APEL; that is, molecules containing a small fraction of the charged units. We consider APEL solutions in polar media where charged groups of the chain are completely dissociated and mobile counterions are freely in the solution.

During the past two decades, much attention has been paid to the theoretical study of various systems of neutral associating polymers [1–10]. In particular, it was established that phase behavior of such polymers in dilute and more concentrated solutions is determined mainly by a competition between attraction of the stickers, on one hand, and repulsion of the molecules caused by intermolecular excluded volume interactions and their translational motion on the other hand. The presence of the charged groups on the chain and their mobile counterions leads to additional nonlocal interactions of the chains and changes mechanism responsible for the phase behavior, as well as enriches the properties of polymer solutions. Many of the effects considered in this chapter, that is (1) stabilization of the clusters at certain finite size, (2) the possibility of dissolution of the physical gel with the increase of the number of associating groups, and (3) microphase separation in the physical gel, have purely polyelectrolyte nature.

The physical properties of dilute solutions of APEL are determined mainly by the interplay between attraction of the stickers and repulsion originated by both unscreened charges of the chains and motion of counterions [11, 12]. The formation of finite-size clusters (sol-phase) or physical gel (infinite cluster) in such solution becomes possible if the attraction energy of the stickers,  $\varepsilon$ , exceeds significantly the thermal energy,  $kT$ ,  $\varepsilon \gg kT$ . The aggregation of the chains into the finite-size cluster requires a very large gain in the attraction energy to overcome both strong Coulomb repulsion of the charges and entropy losses of those counterions, which are localized within the cluster to compensate partially its charge: The electrostatic energy of the mesoscopic particle in dilute solution is too small to trap all “own” counterions. Because of this, counterions are distributed inhomogeneously in the system [13–15]. The fraction of inner and outer counterions is determined by the balance between Coulomb energy and entropy of their

translational motion. The formation of macroscopic physical gel in dilute solution requires full compensation of macroscopic charge of the gel that is achieved by the entry of all counterions into the gel. In this case, the gain in the attraction energy of the stickers should be larger than entropy losses of counterions.

In contrast to dilute solutions of APEL, where Coulomb interactions between finite-size clusters are mainly screened by counterions, the aggregates of sol-phase in semidilute and more concentrated solutions interact with each other. At certain conditions, such interaction can lead to the formation of physical gel with an internal ordered microstructure [16]. In contrast to dilute solutions, association of the chains into the physical gel in concentrated solutions occurs at smaller energy,  $\varepsilon$ ,  $\varepsilon > kT$ , because, in this case, counterions practically do not lose their entropy.

The rheological properties of APEL solutions are multivarious. For instance, depending on polymer concentration and strength of the sticker interactions, the viscosity of such solutions can be both decreased (small concentrations) in comparison with the equivalent solution of nonaggregating molecules or increased significantly (by a few orders of magnitude) at physical gelation (high concentrations). As a result of a weak enough attraction between the stickers, the APEL solutions are very sensitive to external influences and similar viscosity variations are observed at fixed concentrations under shear flow.

In this chapter, we will review some theoretical and experimental results obtained for the solutions of APEL and consider phase separation in dilute solutions (Sec. II and III), microphase separation in semidilute solutions (Sec. IV), and rheological behavior of the solutions under shear flow (Sec. V).

## II. PHASE SEPARATION OF ASSOCIATING TELECHELIC POLYELECTROLYTES IN DILUTE SOLUTIONS

A polymer chain with only two associating groups located on its ends is called telechelic. The first simple theory of weakly charged telechelic polyelectrolytes in dilute solution was developed by Potemkin et al. [11] and Vasilevskaya et al. [12]. The possibility of sol- and gel-phase formation in a good solvent was considered by Potemkin et al. [11]. It was assumed that the clusters have a gel-like internal structure: All stickers form reversible junctions owing to the strong interactions between them, and all chains contribute to the elasticity of the cluster. The shape of the cluster was chosen to be spherical on the basis of a simple symmetry consideration. Free energy of the cluster containing  $m$  chains was written as a sum of four terms

$$F_m = F_a + F_{el} + F_{tr} + F_C \quad (1)$$

accounting for the gain in energy due to association of the stickers ( $F_a$ ), elastic energy of the chains swollen in a good solvent ( $F_{el}$ ), energy of translational motion of counterions within and outside the clusters ( $F_{tr}$ ), and Coulomb energy of charges ( $F_C$ ). Free energy of dilute solution of the clusters having some size distribution,  $c_m$  (the volume fraction of

the clusters consisting of  $m$  chains), is a sum of the energies of translational motion of the clusters and their self-energies

$$F = \sum_{m=1}^{\infty} c_m \ln \frac{c_m}{e} + \sum_{m=1}^{\infty} c_m F_m \quad (2)$$

One of the main results obtained in Ref. 11 was the conclusion about the possibility of an *optimum-size* cluster formation. It was shown that at certain conditions (values of average polymer volume fraction,  $\phi$ , and attraction energy per sticker,  $\varepsilon$ ), the distribution function,  $c_m$ , can have maximum at some aggregation number,  $m=m^*>1$ . The presence of such maximum means that the cluster formation of  $m^*$  size (optimum size) is the most probable, whereas the probability of the formation of considerably different clusters is exponentially small. The onset of the cluster formation can be determined as the appearance of the inflexion point of the distribution function (Fig. 1a). The increase of the attraction energy,  $\varepsilon$ , at the same polymer volume fraction leads to the increase of the size of the optimum clusters (Fig. 1b).

The stabilization mechanism of the optimum-size clusters can be explained as follows. In the dilute solution of nonaggregated chains, counterions tend to occupy the whole volume of the system to maximize their entropy of motion. Aggregation of the chains into the cluster requires partial localization of counterions within the cluster to reduce its charge: The electrostatic energy of mesoscopic cluster is too small to overcome the energy of motion of counterions and to trap all of them. The increase of the aggregation number requires a further increase of the fraction of inner counterions. This can become unfavorable for entropic reasons. Therefore, if the attraction energy of the stickers is smaller than a certain threshold value, the growth of the clusters can be prevented. Note that this kind of stabilization is connected with the classic Rayleigh problem of the charged droplet [17] in the sense that the size of the cluster is determined by the

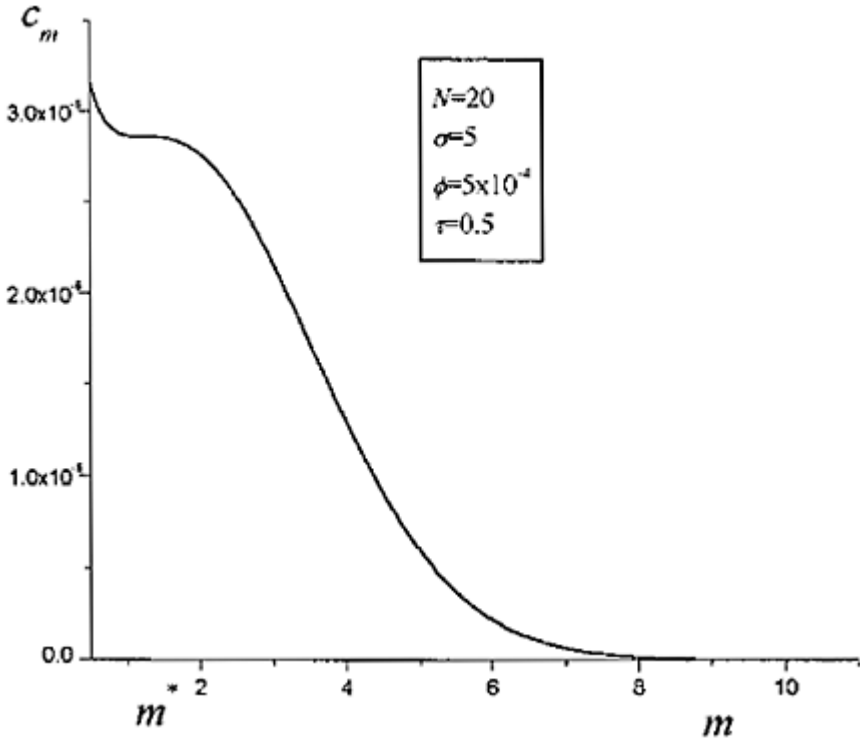


**FIG. 1a** Volume fraction of the clusters,  $c_m$ , as a function of the number of constituent chains,  $m$ , for different values of the association energy,  $\epsilon$ . Onset of aggregation process at  $\epsilon=10.7$ .

charge and surface tension of the cluster. However, the charge is fully controlled by escaped counterions, and the stabilization occurs at larger length scales in contrast to the “pure” Rayleigh stabilization in the absence of counterions.

At the attraction energies exceeding some threshold value, macroscopic phase separation can take place when part of the clusters or nonaggregated chains form a physical gel. A phase diagram of the telechelic polyelectrolyte in dilute solution is presented in Figure 2 [11]. Such a diagram was obtained by equating chemical potentials of sol and gel phases (BC curve), as well as from the conditions for the inflexion point of the distribution function (AC curve). Below the AC curve, that is, at small attraction energy,  $\epsilon$ , and polymer volume fraction,  $\phi$ , a homogeneous solution of nonaggregated chains is the most stable. With the increase of polymer concentration at  $\epsilon < \epsilon_c$ , the solution is separated in two coexisting phases: concentrated gel-phase and more diluted solution of the chains. The optimum clusters are formed with the increase of polymer concentration, when the attraction energy exceeds the critical value  $\epsilon > \epsilon_c$ ; they grow up to curve BC where phase separation occurs.

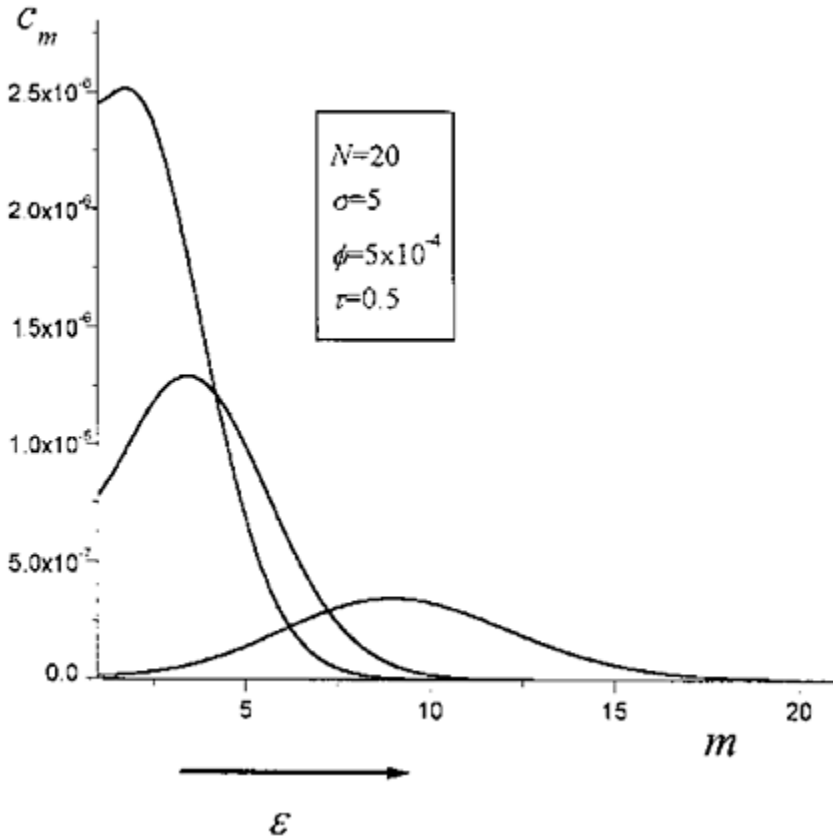


**FIG. 1b** Volume fraction of the clusters,  $c_m$ , as a function of the number of constituent chains,  $m$ , for different values of the association energy,  $\epsilon$ . Optimum clusters at  $\epsilon=11, 12, 15$ . Arrow shows direction of the increase of  $\epsilon$ ;  $m^*$  is the coordinate of the inflexion point.

Dotted lines in Figure 2 correspond to the phase diagram [12]. Here the influence of the supernatant phase on the swelling and collapse of the physical gel was considered on the basis of a more simple model accounting for only two states of telechelic polyelectrolyte: a physical gel and a solution of nonaggregated chains. It is seen in Figure 2 that at small polymer concentrations and high attraction energy,  $\epsilon$ , the physical gel practically does not sense the presence of a small amount of supernatant and swells like an equivalent chemically cross-linked one. However, with the increase of concentration and the decrease of attraction energy, the supernatant becomes more dense, and extraosmotic pressure of its counterions compresses the physical gel. Under poor solvent conditions, when attractive forces between neutral monomeric units prevail, a dense globular state of the associative gel becomes more favorable [12]. This effect is illustrated

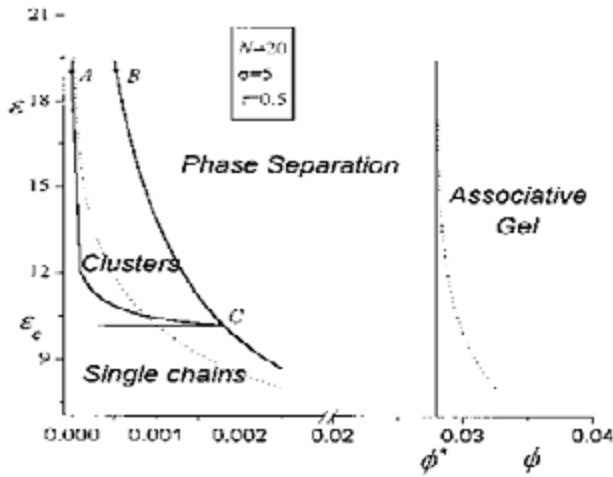


**FIG. 2** Phase diagram of a dilute solution of weakly charged associating telechelic polyelectrolytes in variables volume fraction of polymer,  $\phi$ , versus attraction energy of the stickers,  $\varepsilon$ . The notation  $\phi^*$  corresponds to the overlap volume fraction. Dotted lines show the diagram obtained by Vasilevskaya et al. [12].

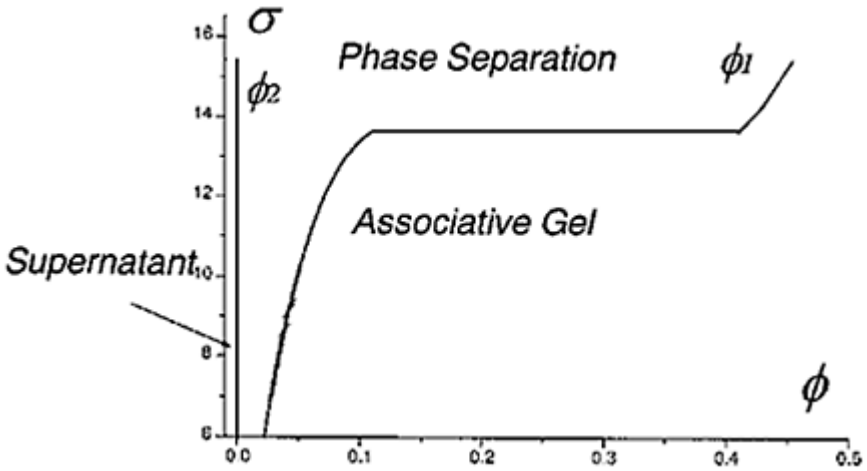


**FIG. 3** Phase diagram of weakly charged associating telechelic polyelectrolyte under poor solvent conditions in variables: volume fraction,  $\phi$  and degree of ionization of the chain,  $1/\sigma$  ( $\sigma$  is a number of neutral monomer units between two neighbor charged ones). Curves  $\phi_1$  and  $\phi_2$  depict coexisting gel and supernatant phases, respectively

by a phase diagram in variables volume fraction of polymer versus degree of ionization of the chain ( $1/\sigma$ ) (Fig. 3).

At a high degree of ionization (small values of  $\sigma$ ) counterions of the gel create a high osmotic pressure which dominates over hydrophobic attraction and leads to the swelling of the physical gel similar to the case of chemical gels [18, 19]. The decrease of the degree of ionization reduces osmotic pressure of counterions and stimulates an increase of polymer density: At a certain critical value of  $a$ , the volume fraction of the polymer in physical gel can be increased and become of the order of unity by jump-like phase transition. Simultaneously, the concentration of the supernatant is decreased drastically which evidences the additional association of supernatant molecules not only due to the attraction of the stickers but due to hydrophobic forces as well.

The influence of low molecular salt on association of telechelic polyelectrolytes was studied by Vasilevskaya et al. [12]. From the physical point of view, the presence of the salt means the appearance of an additional equal amount of mobile, positively and negatively charged ions. Therefore, phase equilibrium of the gel and supernatant should depend on the distribution of salt ions between these two phases. In the dilute solution, the gel sample occupies a small volume of the system trapping all “own” counterions to compensate for the macroscopic charge. Additional essential penetration of salt ions into the gel is unfavorable, because they should lose their entropy without energetic gain: The gel with counterions is electrically neutral. Therefore, a dominant fraction of the salt ions concentrates in the supernatant phase, which creates additional osmotic pressure and compresses the gel (Fig. 4).

On the other hand, the excess of the salt in the supernatant phase stimulates the association of the chains into the gel (decrease of volume fraction of the supernatant; see Fig. 4). This effect can be explained as follows. Note that gel-supernatant phase equilibrium in the absence of salt is determined by the balance between attraction of the stickers and repulsion caused by entropy of counterions. The growth of the gel stops when the chains become unable to draw in “own” counterions into the gel. In the presence of salt, when there are ions of the same sign as counterions, the entropy of such particles is significantly increased, and entropic losses at the association of the chains into the gel become smaller: The chains can draw into the gel both “own” counterions and “foreign” salt ions.

These theoretical predictions were confirmed in a recent experiment [20], which Tsitsilianis et al. studied the equilibrium and rheological properties of aqueous solutions of polystyrene-poly(tertiary-butyl acrylate)-polystyrene triblock copolymers.

In particular, it was shown that addition of salt (NaCl) in a 0.5% solution of the polymer, where physical gel is formed (gelation concentration is  $c \approx 0.2\%$  at the temperature  $T=20^\circ\text{C}$ ), decreases the relative volume of the gel,  $V_{\text{gel}}/V_{\text{tot}}$  (Fig. 5).

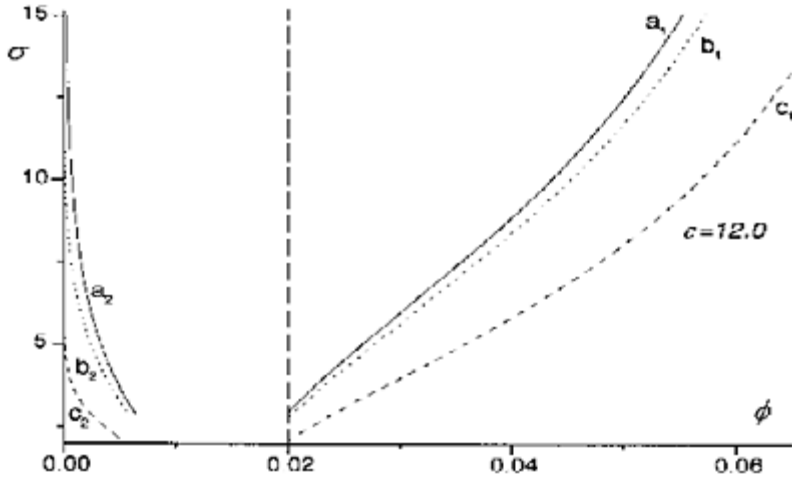


FIG. 4 ( $\phi$ ,  $\sigma$ )-diagram of state of weakly charged telechelic polyelectrolyte in good solvent at a different salt fraction: (a)  $n_s=10^{-6}$ ; (b)  $10^{-5}$ ; (c)  $10^{-4}$ . Dashed vertical line corresponds to the volume fraction of polymer in the system,  $\phi_{\text{tot}} = 0.02$ .

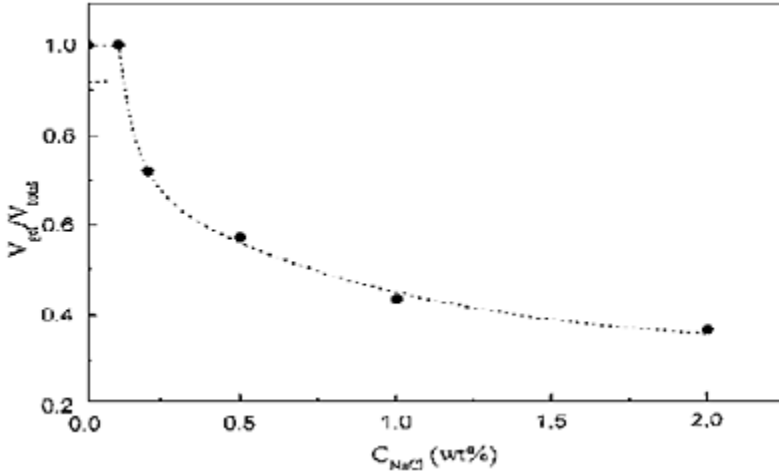


FIG. 5 Effect of salt (NaCl) on the relative volume,  $V_{\text{gel}}/V_{\text{tot}}$ , of the gel-phase for a 0.5% aqueous solution of PS-PANa-PS copolymer at  $T=20^\circ\text{C}$ .



### III. ASSOCIATING POLYELECTROLYTES WITH LARGE NUMBER OF STICKERS IN DILUTE SOLUTION. NORMAL AND ANOMALOUS GELATION

Interesting effects connected with phase behavior of APEL having many stickers homogeneously distributed along the chain were predicted by Potemkin et al. [21]. From the physical point of view, it is connected with the appearance of an additional parameter—distance between the stickers,  $l$ , the presence of which can have an essential influence on both the conformation of the chains and the boundaries of the stability of different phases. For instance, one can expect that the conformation of an individual molecule is more compact in comparison with one of an equivalent telechelic chain: Additional stickers create intramolecular reversible junctions and the internal structure of such chain can be close to gel-like if attraction between the stickers is high enough.

The case of weakly charged APEL having a smaller number of ionized groups than stickers and surrounded by  $\theta$ -solvent was considered by Potemkin et al. [21]. It was assumed that the chains could aggregate and form physical gel as well as optimum clusters of spherical shape and gel-like structure (high  $\epsilon$ ). Because in this model Coulomb interactions and osmotic pressure of counterions only weakly perturb Gaussian statistics of the chains, one could assume that the polymer volume fraction in both the gel and clusters is approximately the same,  $\phi^* \approx 1/l^{1/2}$ . Similar to the case of telechelic polyelectrolytes, the free energy of the cluster of  $m$  chains has the form of Eq. (1) except for the contribution of elastic energy, which is of the order of unity per one subchain (fragment of the chain between two neighbor stickers) for all considered phases.

One of the main conclusions of Ref. [21] is the independence of the size of the cluster on the length of constituent chains. Only degree of ionization and number of stickers of the chain determine the size of the clusters. This is in agreement with the stabilization mechanism reported in the previous section. On the other hand, the aggregation number of the cluster,  $m$ , is essentially dependent on the chain length,  $N$ : The larger is  $N$ , the smaller is  $m$ . Furthermore, at very large  $N$ , the aggregation number can become less than unity. It means that intramolecular optimum cluster formation is possible; that is, few optimum clusters can be formed within one molecule. First, the existence of a similar necklace-like conformation was predicted by Kantor and Kardar [22, 23] for polymer chains with short-range attraction and long-range repulsion and then for the case of polyelectrolytes in poor solvent by Dobrynin et al. [24].

A phase diagram of APEL with many stickers is presented in Figure 6 in variables: polymer volume fraction,  $\phi$ , versus distance between the stickers,  $l$ , at high-attraction energy. The bottom curve corresponds to the boundary of stability of dilute solution of single chains and the onset of optimum-size cluster formation. The middle and upper curves depict the phase separation region of coexisting optimum clusters and physical gel, respectively.

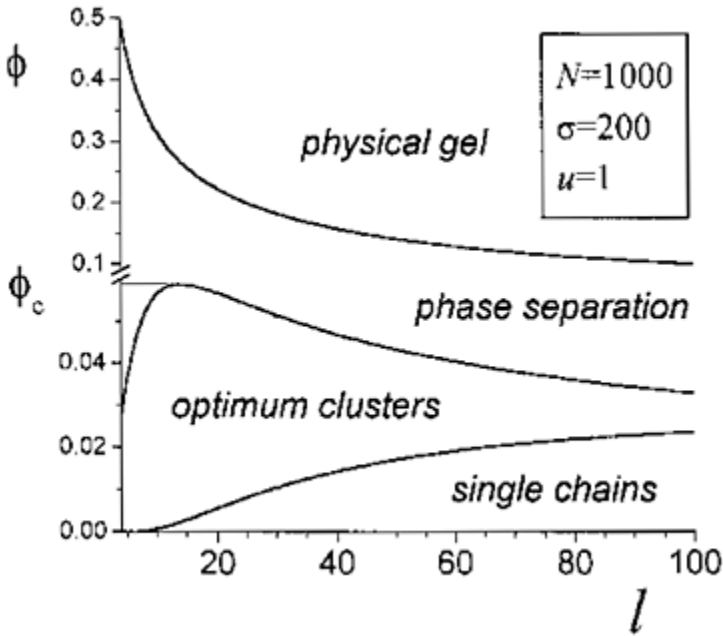


**FIG. 6** Phase diagram of APEL with many stickers per chain in coordinates volume fraction of polymer,  $\phi$ , versus number of monomer units between two neighbor stickers,  $l$ .  $\phi_c$  corresponds to the maximum of the upper boundary of the cluster-phase.

Thus, at a fixed value of  $l$ , the increase of polymer concentration leads first to the formation of optimum clusters and then to phase separation. This scenario is similar to the phase behavior of the solution of associating telechelic polyelectrolytes at high-attraction energy ( $\epsilon > \epsilon_c$ ; see Fig. 2) and is intuitively predictable. Much more interesting and counterintuitive (at the first glance), phase behavior can be extracted from the diagram in Figure 6 by fixing of the polymer concentration and variation of the number of stickers. The increase of the number of stickers (decrease of  $l$ ) at concentrations  $\phi < \phi_c$  in the region of phase separation leads first to the compaction of the physical gel because of shortening of subchains. However, upon the further decrease of  $l$ , the gel can be dissolved with the formation of several finite-size clusters. Seemingly, the increase of the number of stickers should lead to the increase of surface energy and prohibit the dissolution. But in this case, counterions begin to play the key role. An explanation of such an effect is illustrated in Figure 7.

Physical gel occupies small volume of the system in the dilute solution of APEL. Counterions, which are localized within the gel, undergo large losses in entropy. Because the increase of the number of stickers should require the decrease of the gel volume and stimulate further losses in entropy of counterions, this situation can become unfavorable, and the gel is dissolved with the formation

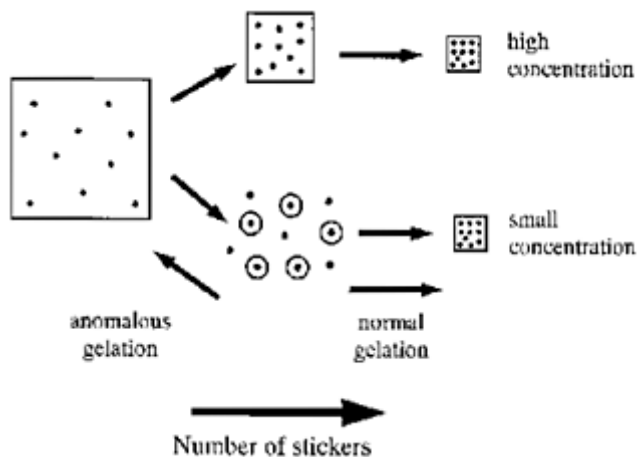


**FIG. 7** Schematic representation of the physical gel behavior for different polymer concentration. Squares and circles depict physical gel and optimum clusters, respectively. Small black circles represent counterion location. Bottom arrow shows direction of the increase of the number of stickers.

of finite-size clusters releasing part of the counterions in outer solution, which is favorable entropically. Only when the number of stickers is too large and the surface energy of the clusters dominates over the entropy of counterions is coalescence of the clusters possible. So one can say that there are two kinds of reversible gelation in dilute solution of APEL: The clusters can form (1) dense gel with the increase of the number of associating groups (normal gelation mechanism) and (2) loose gel with the decrease of the number of associating groups (so-called anomalous gelation mechanism). The permanent compaction of physical gel with the decrease of  $l$  (upper portion of Fig. 7) happens at polymer concentrations exceeding the critical value, because losses in entropy of counterions in more concentrated solutions are smaller.

Recent experimental results obtained for the solutions of hydrophobically modified polyelectrolytes [25, 26] can be explained on the basis of the theory of anomalous gelation. Turbidity of aqueous solutions of modified N-isopropylacrylamide (NIPAM)-based copolymers with hydrophobic side chains of different lengths was studied by Bokias et al. [26]. The measured magnitude (turbidity) in such experiments is proportional to the characteristic size of inhomogeneities in the visible light spectrum: The larger inhomogeneities are, the higher is turbidity. Unusual dependence of the turbidity on the length of hydrophobic blocks was observed (Fig. 8).

It turns out that the shorter the blocks are, the higher is the turbidity of the solution or the size of inhomogeneities (clusters). An explanation of such behavior is the following. The increase of the length of the side chains effectively

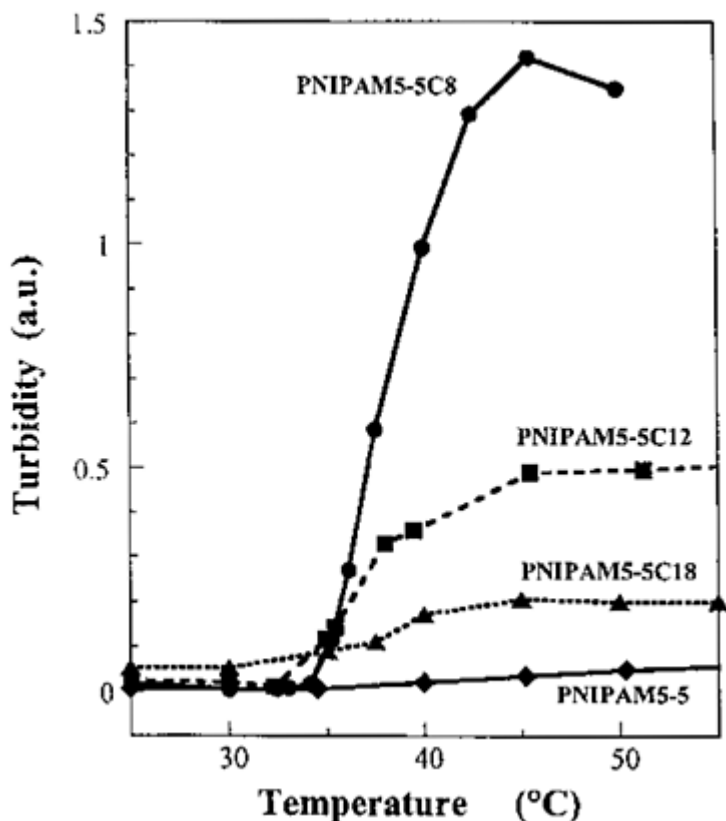


**FIG. 8** Influence of the alkyl length on the turbidity behavior of the NIPAM-based copolymers containing 5 mol% amphiphilic units. A modified polymer denoted, for instance, PNIPAM5-5C18 is a NIPAM-MADAP copolymer containing 5 mol% MADAP fully quaternized with octadecyl bromide.  $C_p=0.02\text{g}/\text{cm}^3$ .

leads to the increase of the number of stickers. The arguments in favor of such a statement can be drawn from the theories of micelle formation in block copolymers [27–29]. According to such theories, the aggregation number of the micelle in a strong segregation regime is proportional to the length of the block which forms core of the micelle. For hydrophobically modified copolymers, it means that the longer the side chains are, the larger number of the chains constitute the micelle (reversible junction), and gel or clusters occupy the smaller volume because the number of the micelles is decreased while the distance between them remains the same. Therefore, we can expect that the curve of maximum turbidity in Figure 8 corresponds to large and loose clusters. The increase of the density of the clusters (charge density) with the increase of the length of hydrophobic blocks leads to the decomposition of the clusters (decrease of turbidity) accompanied by the release of counterions to the outer solution.

#### IV. ASSOCIATING POLYELECTROLYTES WITH LARGE NUMBER OF STICKERS IN SEMIDILUTE SOLUTION. MICROPHASE SEPARATION

In the previous sections, we considered association of polyelectrolytes in dilute solutions where both nonaggregated chains and optimum clusters do not interact with each other at large length scales because long-range Coulomb interactions are basically screened by counterions moving between them. Also, it was assumed that the dense gel-phase is homogeneous. However, it is well known in polymer physics that a spatially homogeneous state of concentrated polymer systems with a short-range segregating tendency and long-range stabilizing factors can be unstable with respect to the density fluctuations at finite wave vector,  $q$  [30–32], and microphase separation occurs which is characterized by the periodic density profile of certain symmetry (e.g., lamellar, hexagonal, bcc). For instance, the stabilizing factor is a connectivity of segregating monomer units in blocks for the case of block copolymer melts [30–34] or long-range Coulomb interactions—for weakly charged polyelectrolytes in poor solvent [35, 36]. In particular, the effect of microstructure formation in semidilute solution of weakly charged polyelectrolytes in poor solvent [35] has universal character and is valid for many charged polymer systems [37–40]. The origin of this effect is the following. The aggregating molecules tend to occupy a minimum volume to minimize the surface energy. The large decrease of the volume, that is, the formation of macroscopic, very dense phase leads to large losses in entropy of counterions. Instead, a compromise state of alternating more and less dense regions occurs: such phase has a larger volume than the macroscopic one and results in minimum entropy losses. Long-range Coulomb interactions between inhomogeneities are not screened in such dense polymer systems, therefore their ordering occurs at large length scales. The existence of such a periodic structure was first theoretically predicted by Borue and Erukhimovich [35] and then confirmed experimentally [41, 42].

All above-mentioned arguments can be applied for microphase separation in concentrated enough solutions of APEL. Indeed, it was predicted recently that both macrophase and microphase separation can occur in such systems even under good or  $\theta$ -solvent conditions [16]. The density-density correlation function and spinodal of APEL with a large number of stickers have been analyzed [16]. The influence of the solvent quality and attraction energy of the stickers was studied. If spinodal is attained at finite wave vector  $q$ , the homogeneous state of the solution becomes unstable with respect to microphase formation of periodicity,  $D=2\pi/q$ . The instability at  $q=0$  means macroscopic separation (infinite periodicity). The point on spinodal dividing these two types of instabilities is called the Lifshitz point. The spinodal of APEL in variables polymer volume

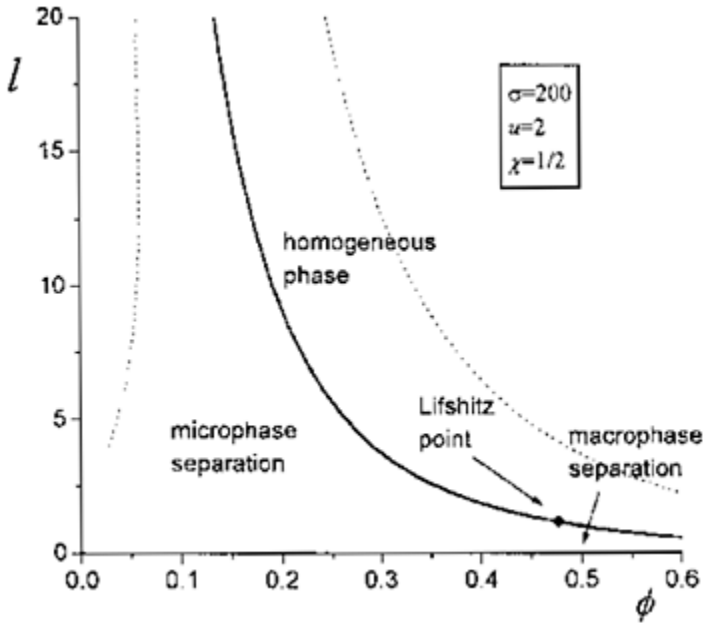


**FIG. 9** Spinodal of associating polyelectrolyte with many stickers in  $\theta$ -solvent in  $(\phi, l)$ -coordinates (solid line). Dotted lines correspond to the binodals of dilute solution presented in Figure 6: left and right curves are the boundaries of the cluster- and gel-phase, respectively.

fraction,  $\phi$  versus distance between the stickers,  $l$ , is presented in Figure 9 by a solid curve.

This curve corresponds to  $\theta$ -solvent conditions (Flory parameter  $\chi=1/2$ ) and high attraction energy of the stickers ( $\varepsilon \gg kT$ ). The homogeneous state, that is, physical gel of constant density, is stable to the right of the spinodal. The microscopically separated state of the gel, that is, the gel of periodically modulated density, is stable to the left of the spinodal above the Lifshitz point. Macroscopic separation below the Lifshitz point means the coexistence of two homogeneous gels of different density. However, the spinodal just shows where the homogeneous phase loses its stability. The determination of real areas of thermodynamic stability of above-mentioned phases requires the calculation of binodals from the conditions of equality of chemical potentials and pressures of different phases.

The phase diagram of APEL in dilute solution presented in the previous section is shown in Figure 9 by dotted lines. We can see that the spinodal lies in the region of phase separation where left and right dashed curves correspond to cluster and gel phases, respectively. On the basis of such a mutual position of the spinodal and binodals, one can conclude that the region of microphase separation can exist somewhere in the phase separation region. In other words, the scenario is possible when with the increase of the polymer concentration part of the optimum clusters is connected by bridges and forms gel

with a microstructure. At higher concentrations, the coexistence of gel with a microstructure and homogeneous gel can be possible. Similar phase behavior was predicted for a semidilute solution of polyelectrolytes in poor solvent [39]. Another important conclusion, which comes from the possibility of the coexistence of optimum clusters and gel with a microstructure, is the universal nature of stabilization of mesoscopic aggregates (optimum clusters in dilute solution and more dense regions in the gel with a microstructure). In both cases, counterions prevent macroscopic phase formation maximizing its entropy and characteristic length scale (cluster size or periodicity of the microstructure) is determined by the competition of the short-range attraction of stickers and partially screened long-range Coulomb repulsion.

## **V. RHEOLOGICAL PROPERTIES OF ASSOCIATING POLYELECTROLYTE SOLUTIONS. SHEARTHICKENING EFFECT**

Another very interesting and important for industrial applications effects, which are the result of the intramolecular and intermolecular interaction of stickers, were observed in rheological studies of associating polyelectrolyte solutions [25, 26, 43–49]. At small polymer concentrations, attraction between the stickers leads basically to the formation of intramolecular junctions and compaction of the molecules. As a result, the viscosity of such a solution becomes smaller in comparison with the equivalent solution of nonassociating molecules [25, 43–45]. At high enough concentrations, when intermolecular aggregation of the chains and physical gel formation are possible, a strong increase of the viscosity is observed. The rheological properties of APEL solutions are very sensitive to the external actions (in particular, to the shear rate) due to high lability of physical junctions: They can easily break and combine under applied external forces. The most characteristic behavior of many solutions of APEL is a shear-thinning one, when with the increase of the shear rate, the viscosity of the solution is monotonously decreased owing to the break of intermolecular junctions. However, as an intermediate stage of the shear-thinning behavior, a drastic (by few orders) increase of the viscosity (shear-thickening) can be observed at the increase of the shear rate in both charged and neutral hydrophobically modified copolymers [26, 46–49]. In particular, a shear-thickening effect was found recently in the solutions of hydrophobically modified copolymers based on *N*-isopropylacrylamide (NIPAM) [26]. The dependence of viscosity on the shear rate of such a copolymer containing 10 mol% MADAP at the temperature  $T=25^{\circ}\text{C}$  and concentration  $C_p=0.05\text{g/cm}^3$  is presented in Figure 10.

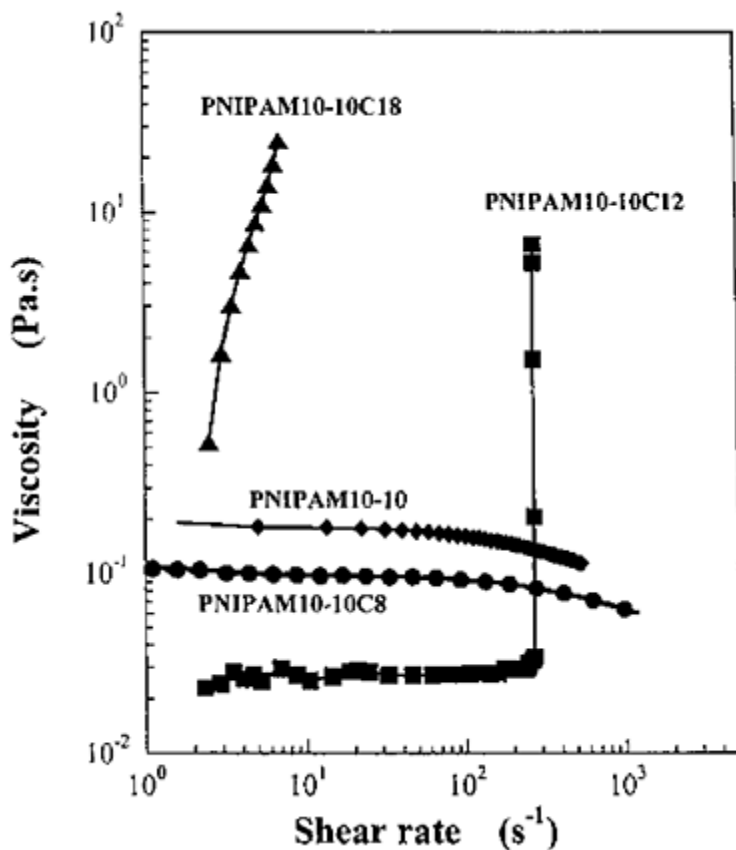


**FIG. 10** Viscosity as a function of shear rate for the NIPAM-based copolymers modified at 10 mol% with alkyl groups of various length.  
 $C_p=0.05\text{g/cm}^3$ .

Unmodified PNIPAM10–10 demonstrates the behavior typical for semidilute solutions: The decrease of the viscosity with the increase of shear rate is observed after the Newtonian plateau. The behavior of modified PNIPAM10–10C8 copolymer having short enough hydrophobic blocks is similar to the behavior of PNIPAM10–10 with the only difference being that the viscosity is smaller owing to intramolecular aggregation of the hydrophobic blocks (shear thinning) (see Fig. 10). However, with the increase of the length of alkyl blocks, an unusual picture is observed. The viscosity of PNIPAM10–10C12 is smaller than for the above-mentioned copolymers at small shear rates. Such an effect is quite expected, because it was shown in the previous section that the increase of the length of hydrophobic blocks leads to the compaction of single chains; that is, to the decrease of viscosity. At the achievement of a certain threshold shear rate, a rheological transition occurs when the viscosity of the solution is increased by few orders (shear-thickening effect). The longer hydrophobic blocks are, the smaller is the threshold shear



rate (see Fig. 10).

So far there is no clear understanding of the mechanism responsible for the giant shear-thickening behavior in the solutions of APEL. It follows from the experiment [26] that shear can induce intermolecular reversible junctions. However, the variation of which microscopic characteristics is responsible for this effect, and what is the role of charges and their counterions remains still an open question. Various mechanisms of the shear-thickening effect have been proposed [50–53]. In particular, it was assumed [50, 51] that shear increases the probability of intermolecular junction formation in comparison with an intramolecular one and increases effectively the molecular weight of the chain. Similarly, but in the context of the temporal network theory [52], shear thickening was explained in terms of coagulation of free chains under shear leading to the increase of the number of chains which form the gel. Another idea has been proposed [53] where strong, non-Gaussian stretching of the chains under shear was considered, whereas the fraction of elastically active chains, that is, the relation between intramolecular and intermolecular junctions, was assumed to be constant. According to Marrucci et al. [53], the mechanism of non-Gaussian stretching of the chains is not alternative of other investigations [50–52]; they might coexist.

Associating polymers are not a unique class of the systems where shear thickening is observed [54]. In addition, dense suspensions display an increase of viscosity with an increasing shear rate. Such an effect can be either smooth or discontinuous [55, 56] and depends on the nature of interaction between particles, polydispersity, particle size, and volume fraction. The basic mechanism of shear thickening in hard-sphere suspensions involves an increase in the hydrodynamic contribution to the stress due to shear-induced dynamic clustering [57–59].

In many aqueous surfactant solutions, where amphiphiles assemble reversibly into worm-like micelles that can become very long and flexible, shear thickening is very pronounced [60–64]. It is caused by the formation of large shear-induced structures.

## VI. CONCLUSIONS

We have shown that the competition of different types of interactions (short-range attraction and long-range repulsion) in the solutions of APEL leads to some unusual effects. Forecited examples demonstrate that this field is important not only for applications but also from a fundamental viewpoint as well. Experimental studies of new effects reported in this chapter should be very interesting.

## ACKNOWLEDGMENTS

This work is supported by INTAS and the Russian Foundation for Basic Research.

## REFERENCES

1. A Coniglio, HE Stanley, W Klein. *Phys Rev Lett* 42:518–522, 1979.
2. A Coniglio, HE Stanley, W Klein. *Phys Rev B* 25:6805–6821, 1982.
3. F Tanaka. *Macromolecules* 22:1988–1994, 1989.
4. F Tanaka, M Ishida. *Macromolecules* 29:7571–7580, 1996.
5. M Ishida, F Tanaka. *Macromolecules* 30:3900–3909, 1997.
6. AV Ermoshkin, IYa Erukhimovich. *J Chem Phys* 110:1781–1793, 1999.
7. IYa Erukhimovich, A Ermoshkin. *JETP* 115:979, 1999.
8. PG Khalatur, AR Khokhlov. *Macromol Theory Simul* 5:877–899, 1996.
9. PG Khalatur, LV Men'shikova, AR Khokhlov. *Macromol Theory Simul* 6:317–338, 1997.
10. AN Semenov, JF Joanny, AR Khokhlov. *Macromolecules* 28:1066–1075, 1995.
11. Potemkin, VV Vasilevskaya, AR Khokhlov. *J Chem Phys* 111:2809–2817, 1999.
12. VV Vasilevskaya, II Potemkin, AR Khokhlov. *Langmuir* 15:7918–7924, 1999.
13. NP Shusharina, MV Saphonov, IA Nyrkova, PG Khalatur, AR Khokhlov. *Ber Bunsenges Phys Chem* 100:857–862, 1996.
14. NP Shusharina, IA Nyrkova, AR Khokhlov. *Macromolecules* 29:3167–3174, 1996.
15. EYu Kramarenko, AR Khokhlov, K Yoshikawa. *Macromolecules* 30:3383–3388, 1997.
16. AN Kudlay, IYa Erukhimovich, AR Khokhlov. *Macromolecules* 33:5644–5654, 2000.
17. Rayleigh Lord. *Philos Mag* 14:184, 1882.
18. M Shibayama, T Tanaka. *Adv Polym Sci* 109:1–62, 1993.
19. AR Khokhlov, SG Starodubtzev, VV Vasilevskaya. *Adv Polym Sci* 109:123–171, 1993.
20. C Tsitsilianis, I Iliopoulos, G Ducouret. *Macromolecules* 33:2936–2943, 2000.
21. II Potemkin, KB Zeldovich, AR Khokhlov. *Polym Sci C Russia* 42:154–171, 2000.
22. Y Kantor, M Kardar. *Europhys Lett* 27:643–646, 1994.
23. Y Kantor, M Kardar. *Phys Rev E* 51:1299–1312, 1995.
24. AV Dobrynin, M Rubinstein, SP Obukhov. *Macromolecules* 29:2974–2979, 1996.
25. L Guillaumont, G Bokias, I Iliopoulos. *Macromol Chem Phys* 201:251–260, 2000.
26. G Bokias, D Hourdet, I Iliopoulos. *Macromolecules* 33:2929–2935, 2000.
27. E Helfand, ZR Wasserman. *Macromolecules* 9:879–888, 1976.
28. AN Semenov. *Soy Phys JETP* 6 1:733–747, 1985.
29. FS Bates, GH Fredrickson. *Annu Rev Phys Chem* 41:525–557, 1990.
30. PG de Gennes. *Faraday Disc Chem Soc* 68:96, 1979.
31. L Leibler. *Macromolecules* 13:1602, 1980.
32. IYa Erukhimovich. *Polym Sci USSR* 24:2223–2232, 1982.
33. M Olvera de la Cruz, I Sanchez. *Macromolecules* 19:2501–2508, 1986.
34. H Benoit, G.Hadziioannou. *Macromolecules* 21:1449–1464, 1988.
35. VYU Borue, IYa Erukhimovich. *Macromolecules* 21:3240–3249, 1988.
36. JF Joanny, L Leibler. *J de Phys France* 51:545, 1990.
37. AR Khokhlov, IA Nyrkova. *Macromolecules* 25:1493–1502, 1992.
38. IA Nyrkova, AR Khokhlov, M Doi. *Macromolecules* 27:4220–4230, 1994.
39. EE Dormidontova, IYa Erukhimovich, AR Khokhlov. *Macromol Theory Simul* 3:661, 1994.

40. KB Zeldovich, EE Dormidontova, AR Khokhlov, TA Vilgis. *J de Phys* 11 7:627–635, 1997.
41. F Schosseler, F Ilmain, SF Candau. *Macromolecules* 24:225–234, 1991.
42. M Shibayama, T Tanaka, CC Han. *J Chem Phys* 97:6842–6854, 1992.
43. DN Schulz, JJ Kaladas, JJ Maurer, J Bock, SJ Pace, WW Schulz. *Polymer* 28:2110–2115, 1987.
44. Y Uemura, J McNulty, PM McDonald. *Macromolecules* 28:4150–4158, 1995.
45. E Volpert, J Seib, F Candau. *Polymer* 39:1025, 1998.
46. J Eliassaf, A Silberberg, A Katchalsky. *Nature* 176:1119, 1955.
47. JM Maerker, SW Sinton. *J Rheology* 30:77, 1986.
48. S Biggs, J Selb, F Candau. *Polymer* 34:580–591, 1993.
49. Y Chang, CL McCormick. *Polymer* 35:3503–3512, 1994.
50. TA Witten, MH Cohen. *Macromolecules* 18:1915–1918, 1985.
51. TA Witten. *J Phys France* 49:1055, 1988.
52. S-Q Wang. *Macromolecules* 25:7003–7010, 1992.
53. G Marrucci, S Bhargava, SL Cooper. *Macromolecules* 26:6483–6488, 1993.
54. JW von Egmond. *Current Opinion in Colloid and Interface Science* 3:385–390, 1998.
55. AB Metzner, M Whitlock. *Trans Soc Rheol* 11:239, 1958.
56. RL Hoffman. *Trans Soc Rheol* 16:155, 1972.
57. P D’Haene, J Mewis, GG Fuller. *J Colloid Interface Sci* 156:350–358, 1993.
58. WJ Frith, P D’Haene, R Buscall, J Mewis. *J Rheol* 40:531, 1996.
59. J Bender, NJ Wagner. *J Rheol* 40:899, 1996.
60. H Rehage, H Hoffmann. *Rheol Acta* 21:561, 1982.
61. HW Brewersdoeff, B Frings, P Lindner. R Oberthür. *Rheol Acta* 25:642, 1986.
62. I Wunderlich, H Hoffmann, H Rehage. *Rheol Acta* 26:532, 1987.
63. V Schmitt, F Schosseler, F Lequex. *Europhys Lett* 30:31–35, 1995.
64. CH Liu, DJ Pine. *Phys Rev Lett* 77:2121–2124, 1996.



# Association in Polyelectrolyte-Catanionic Vesicle Systems: From Phase Behavior to Microstructure

EDUARDO MARQUES,\* RITA DIAS, and MARIA MIGUEL *Coimbra University, Coimbra, Portugal*

ALI KHAN and BJÖRN LINDMAN *Lund University, Lund, Sweden*

## I. INTRODUCTION

Mixed surfactant-surfactant [1–5] and polymer-surfactant systems [6–10] have been in the past decade in the forefront of significant basic research, often with strong implications in applied areas, since they display a number of very versatile interfacial and aggregation properties. Systems comprising polymers and surfactant vesicular aggregates, in particular, are reviewed in this chapter, with special reference to mixtures where oppositely charged cosolutes are present. Features such as associative phase separation, formation of thermodynamically stable vesicles, and polymer-vesicle aggregation are herein addressed, which are based on a number of reports [11–16]. The experimental work includes phase diagram determination, self-diffusion nuclear magnetic resonance (NMR), light and electron microscopy, and rheology. With regard to phase behavior, there is a close analogy between polyelectrolyte-vesicle mixtures and previous studies of polyelectrolyte-micelle mixtures, with an associative phase separation in a wide range of charge stoichiometries. Interesting novel gels are identified in phase maps and their structures discussed with reference to cryo-transmission electron microscopic (cryo-TEM) results. The interactions between DNA and mixed cationic-anionic vesicles, only recently investigated, are also addressed, with direct imaging evidence for the adsorption configuration of the macromolecule.

\* *Current affiliation:* University of Porto, Porto, Portugal.

## II. POLYMER-SURFACTANT MIXTURES: OVERVIEW

The physicochemical principles underlying the phase behavior and association mechanisms of polymer-surfactant systems are a theoretical challenge and often have also direct technical implications [9, 17]. This type of colloidal system can be used for colloidal stability, emulsification, structuring, and suspending properties of various materials as well as control of their rheological properties.

### A. Critical Aggregation Concentration

If there is a net attractive interaction between a water-soluble polymer and a surfactant, the surfactant will display a critical aggregation concentration (CAC) in the presence of polymer, which is lower than the critical micellar concentration (CMC) for the neat surfactant in water (Fig. 1). Polymer-surfactant interactions can be looked at in two alternative ways: (1) as a strongly cooperative binding of the surfactant to the polymer chain and (2) as a micellization process of the surfactant in the vicinity of the polymer chains (pearl-necklace model). Ionic surfactants show a marked interaction with most water-soluble homopolymers (in particular, anionic surfactants) and the micellar formation picture is more relevant in this type of system. Electrostatic interactions between polymer and surfactant, in oppositely charged systems, greatly enhance the association. Nonionic surfactants only rarely have distinct interactions with water-soluble homopolymers, but they may interact with slightly hydrophobic homopolymers or if the polymer has grafted hydrophobic parts.

### B. Mixed Micelle Formation

If water-soluble polymer bears hydrophobic chains grafted onto its backbone—hydrophobically modified polymer (HMP)—there is a strong association between

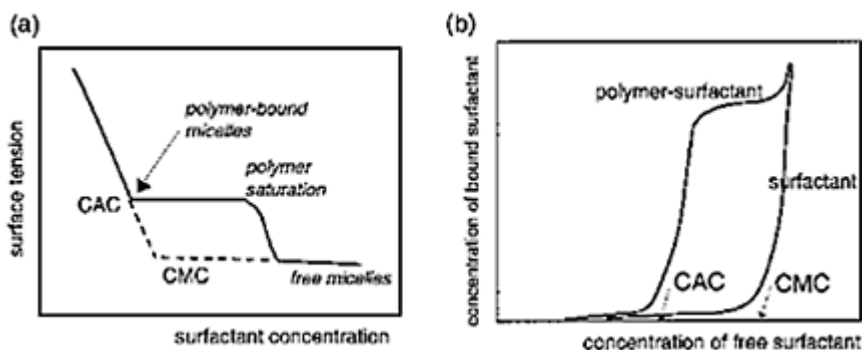


**FIG. 1** Polymer effects on surfactant self-association: (a) CAC for the surfactant in the mixed solution; (b) binding isotherm for the surfactant in presence or absence of polymer.

any type of surfactant, ionic or nonionic, and polymer. The polymer itself may have a tendency to self-associate in solution and increase the viscosity of the solution. Upon addition of surfactant, formation of mixed micelles between polymer and surfactant occurs. A CAC is also obtained for the mixture and the binding model is rather useful for picturing the interaction. At low surfactant concentration, the mixed micelles reinforce the cross links between the polymers, and there is a pronounced increase of viscosity. At sufficiently high surfactant concentration, there is about one polymer hydrophobe per mixed micelle, and thus no cross links exist between the chains; consequently, the

viscosity is reduced.

For the case of the binding of an ionic surfactant to a water-soluble HMP, three distinct regions can be seen in a binding isotherm [18]: a noncooperative region, an anticooperative region, and a cooperative region (Fig. 2). For the corresponding homopolymer, where no hydrophobic modification exists, there is only cooperative binding, as mentioned above. If the HMP is a polyelectrolyte, the association with an oppositely charged surfactant will have stronger viscosity effects as compared to nonionic or similarly charged surfactants.

### C. Phase Behavior: Association Versus Segregation

Comparative phase behavior studies of different types of polymer-surfactant systems have greatly improved the understanding of polymer-surfactant interactions [6, 7, 10]. Features characterizing the phase behavior of mixed polymer-polymer systems can be qualitatively conveyed to polymer-surfactant systems, as essentially the same driving forces are present in both types of systems. Indeed, a surfactant micelle can be regarded to some extent as a macromolecule except that it has a variable “degree of polymerization,” as the micelle aggregation number may change with different factors such as temperature and ionic strength.

The entropic driving force for mixing a polymer and a surfactant is weak, similar to the case of two different polymers in a solvent. Whether miscibility or

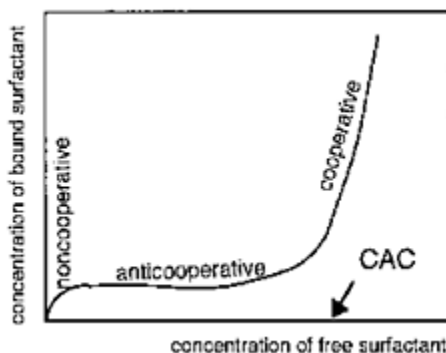


**FIG. 2** Binding isotherm for an ionic surfactant to a hydrophobically modified polymer.

phase separation occurs depends on the net interaction between the polymer and surfactant:

1. No attractive interaction leads to separation into a phase enriched in polymer and another phase enriched in surfactant—*segregative* phase separation.
2. A moderate attractive interaction leads to a *complete miscibility* with the formation of a single phase.
3. A strong attractive interaction leads to the formation of one phase concentrated in both polymer and surfactant and another phase diluted in both components—*associative*

phase separation.

The tie-lines of the two-phase region in ternary phase diagrams will be different in the case of segregation or association, as can be seen in Figure 3.

The general trends for polymer-surfactant interactions depending on the charge of the two cosolutes are summarized in Table 1.

#### D. Mixtures of Polyelectrolyte and Oppositely Charged Surfactant

A polyelectrolyte dissolves in water into a polyion and  $n$  counterions. The dissociation of the counterions gives a large contribution to the entropy of mixing, since  $n+1$  particles exist in solution as compared with one for the dissolution of a nonionic polymer. Thus, polyelectrolytes derive their higher solubility in water, as compared with uncharged polymers, from the entropically driven release of counterions. The confinement of the large number of counterions in one phase would involve a large entropic penalty. Hence, polyelectrolytes tend to mix with both nonionic surfactants and nonionic polymers in the absence of salt. Addition of high amounts of salt eliminates the gain in counterion entropy associated with miscibility, and therefore the polyelectrolyte usually segregates from the nonionic surfactant/polymer—two phases can be formed with similar concentrations of small ions.

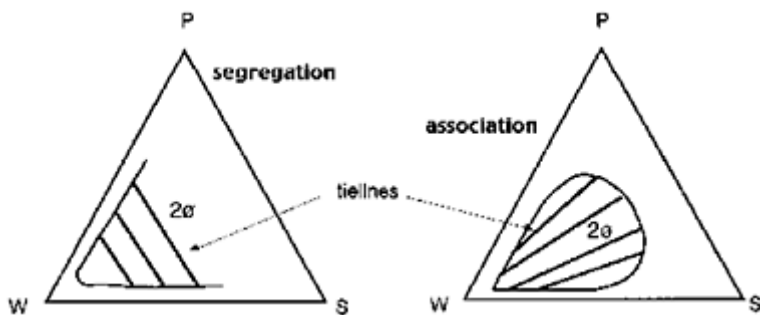


**FIG. 3** The two types of phase separation in polymer-surfactant systems: segregation and association. The tie-lines in the two-phase region are indicated.

**TABLE 1** Interactions Between Polymers and Surfactants

Polymer-surfactant system	Phase behavior	Main driving force
Nonionic-nonionic	<i>Segregation<sup>a</sup></i>	Low entropy of mixing, no net attractions
Nonionic-ionic	<i>Total miscibility</i> without salt	Entropic penalty for counterion confinement, hydrophobic



		interactions
Ionic-nonionic	<i>Association or segregation</i> may occur with salt	Variable
Ionic-ionic of similar charge	<i>Segregation</i>	Low entropy of mixing, no net attraction
Ionic-ionic of opposite charge	<i>Association</i> without salt	No counterion entropy gain
	<i>Association-miscibility- segregation</i> pattern with increasing salt	Larger counterion entropy Salt eliminates contribution of counterion entropy

---

<sup>a</sup> Association may take place with slightly hydrophobic water-soluble polymers.

Mixtures of polyelectrolytes and oppositely charged surfactants show similar effects and have been extensively investigated [6, 7, 19]. In general, it has been observed in these systems that:

- (1) A strong associative phase separation occurs; that is, a concentrated phase forms which is in equilibrium with a very dilute phase. The driving force for this strong polymer-surfactant association is again the release of the counterions, which involves a large entropy gain. The charged surfactant micelles and the polyelectrolytes are enriched with counterions at the surface (*counterion condensation*). With association, the counterions of both solutes are transferred to the bulk with a consequent large increase in entropy.
- (2) The CAC is much lower than the CMC for the neat surfactant; by orders of magnitude in the case of long-chain surfactants. This is borne out from the work done in mixtures of sodium hyaluronate and alkyltrimethylammonium bromide ( $C_n$ TAB) with increasing chain length [20].

The polymer-surfactant complex that separates in the concentrated phase can be a precipitate (crystalline or amorphous), a coacervate (a concentrated liquid phase), or a gel depending on the specific composition of the polymer.

### 1. Effect of Salt Addition

Addition of salt has large consequences in the polymer-surfactant phase behavior. The following effects are observed:

- (1) There is an increase in the CAC of the system owing to a reduction of the electrostatic interactions between surfactant and polyelectrolyte. This effect is opposite to that observed for surfactant micellar solutions, where addition of salt lowers the CMC and induces micellar growth.
- (2) At moderate addition of salt, the polymer-surfactant complex may even become soluble. Thus, at enough salt addition, there can be formation of an extensive one-phase region (total miscibility).
- (3) Further addition of salt to high concentrations totally eliminates the counterion

entropy effects, and thus the system may evolve to segregation if the polymer and surfactant are intrinsically segregating. Both phases have large concentrations of small counterions, and thus no entropic penalty arises.

## 2. Effect of Hydrophobic Grafting of the Polyelectrolyte

For hydrophobically modified polyelectrolytes, the number of charges per polymer is at least equal to the number of hydrophobes, but in general it is much larger. A simple system to study is that for which the HMP has equal number of charges and hydrophobes, in particular when the charge is placed in the hydrophobe [18]. An example of this type of polymer is LM200, a cationic derivative of hydroxyethylcellulose with charges placed in hydrophobic side chains. The polymer strongly associates with the surfactant owing to electrostatic interactions and hydrophobic interactions, leading to mixed micellar formation. Two stoichiometries are important here: (1) the alkyl chain stoichiometry and (2) the charge stoichiometry. The associative phase separation occurs only for a restricted concentration region of both surfactant and polymer. At high enough excess of surfactant in the mixture, the associative complex redissolves and further addition of surfactant results in a single-phase region. At an excess amount of polymer, the complex loses its charge stoichiometry and tends to swell, which leads to the formation of gels.

## III. VESICLE FORMATION IN MIXTURES OF CATIONIC AND ANIONIC SURFACTANTS

### A. Catanionic Mixtures: Background

Mixed systems comprising oppositely charged surfactants in water exhibit a wealth of physicochemical properties that has attracted continual interest over the years [1–5]. A broad division of these properties can be made in terms of interfacial properties and phase behavior properties.

#### 1. Interfacial Properties

For several decades, most of the research concentrated on the solution properties, since the mixtures present large deviations from ideal behavior [3, 9]. Synergistic interfacial properties are in effect observed: (1) Reduction in the CMC of the mixture as compared to the individual surfactants (e.g., see Refs. 21 and 22). For most systems, there is a minimum in the CMC in the vicinity of the equimolar ratio between amphiphiles. (2) Enhancement in surface activity resulting in a decrease of surface tension values and in higher adsorption to surfaces (e.g., see Refs. 23–25) as compared to the individual surfactants.

Large negative values of  $\beta$ , the molar interaction parameter from the regular solution theory, in the range of  $-25$  and  $-10$ , are typical for catanionic mixtures [3]. For such large negative values of  $\beta$  the regular solution theory predicts that:

1. The mixtures exhibit a drastic drop in the CMC value relative to  $\text{CMC}_1$  and  $\text{CMC}_2$  at

different mixing ratios between the surfactants (synergistic effects).

2. The minimum in CMC value ( $CMC_{min}$ ) occurs for a bulk composition close to equimolarity depending on  $\beta$  and on the relative values of  $CMC_1$  and  $CMC_2$ .
3. For increasingly negative values of  $\beta$ , the composition of the mixed micelles tends to be a mixing ratio of 50/50 and to be practically constant over a wide range of bulk mixing ratios.

## 2. Phase Behavior

Phase behavior studies on catanionic mixtures over wide concentration ranges have been carried out over the last two decades [11, 26–31]. Behind this interest is the fact that the complex interplay between electrostatic and chain-packing interactions between the amphiphiles leads in many systems to rich and often unexpected phase behavior. Also, the global picture gained from the investigation of the phase behavior for concentrated mixtures can be valuably conveyed to dilute mixtures, which are of more direct relevance for applied goals (detergency, microemulsions, vesicles). At higher surfactant concentration, a variety of liquid-crystalline phases are formed [30, 31]. At lower surfactant concentration, equimolar catanionic mixtures often produce a crystalline precipitate in water [32–34]. However, coacervation [35], formation of liquid-crystalline phases, mixed micelles [36, 37], or even vesicles [38] may also occur at equimolar ratios for systems where the surfactants interactions are not able to stabilize crystalline solids. If a crystalline precipitate is obtained and made salt free, it gives rise to new surfactants—*catanionic surfactants*, typically of the swelling type [39–42].

When an excess amount of ionic surfactant is present in the aqueous mixture, the precipitate is rendered soluble to form mixed micelles—denoting higher aggregation numbers than the individual micellar solutions [33, 43, 44], and, in some systems, regions of stable vesicles.

The phase behavior for the catanionic mixture sodium dodecylsulfate (SDS) and didodecyldimethylammonium bromide (DDAB) in water will be used as an illustration [11]. SDS is a widespread water-soluble, micelle-forming amphiphile at room temperature. DDAB in turn is a water-insoluble, swelling surfactant, which forms bilayer structures in water (two lamellar phases and vesicle dispersions at high dilution). The surfactant parameter for SDS in a neat micelle is close to 0.33, whereas for DDAB the value of  $P_s$  has been calculated to be about 0.8. When both surfactants are mixed in water, a strong associative behavior is expected owing to head group electrostatic attractions and, above all, the large counterion entropy gain. At the same time, the two molecules with very different molecular shapes have to pack together in an aggregate. The interplay *electrostatics/geometrical shape* in the mixed system is seen to result in rich phase behavior.

### B. Phase Behavior Representation

One complexity presented by catanionic mixtures (and as well by polymer-surfactant systems of opposite charge) is that of the dimensionality of their phase behavior depiction. If one considers a system composed of a cationic surfactant  $C^+X^-$ , an anionic

surfactant  $A^-X^+$ , and water, with no common ion, there are four components according to the Gibbs' phase rule. This is due to the possibility of having the salts  $C^+A^-$  (catanionic surfactant) and  $X^+X^-$  (simple electrolyte), in addition to the cationic and anionic surfactant salts, bearing in mind electro-neutrality. In principle, all four of these salts are present; in particular when  $C^+A^-$  ion pair formation is favored. Thus, a third dimension is required, and the conventional triangular phase diagram does not optimally convey the phase behavior. This can be achieved by using a trigonal bipyramid representation [45], shown in Figure 4a, or a pyramid representation [6, 10], shown in Figure 4b-c. In either case, the ternary diagram constitutes a particular two-dimensional (2-D) slice through the three-dimensional (3-D) body.

When inspecting a triangular phase diagram for such four-component systems, one should then bear in mind that (1) one-phase regions are in reality 3-D onephase bodies in the pyramid; (2) thus, the same phase can be cut at distinct regions on the plane, so two such cuts are not distinct homogeneous phases; (3) phase-separating samples may have constituent phases absent from the triangular plane chosen; and (4) the shape of three-phase regions is not limited to triangles. However, if supported by experimental data, triangular phase diagrams provide a satisfactory depiction of the phase behavior of catanionic mixtures and are a good starting point for discussions on the phase behavior.

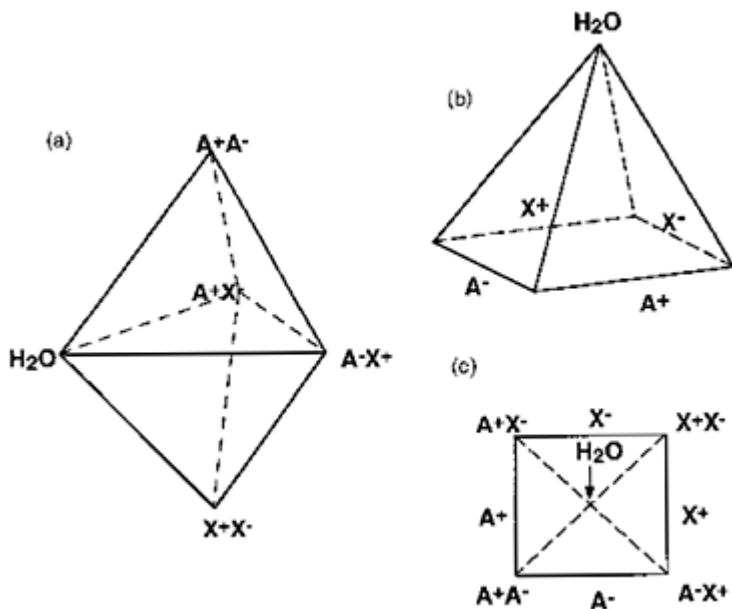


**FIG. 4** Two possible types of representing phase diagrams for catanionic mixtures as four-component systems: (a) trigonal bipyramid and (b) pyramid, seen in top view (c).

These considerations should then be borne in mind prior to a discussion of the phase behavior of the pseudoternary SDS-DDAB-water mixture presented here. Denoting the

didodecyldimethylammonium cation by  $\text{DDA}^+$  and the dodecylsulfate anion by  $\text{DS}^-$ , the amphiphilic electrolytes  $\text{Na}^+\text{DS}^-$ ,  $\text{DDA}^+\text{Br}^-$ ,  $\text{DDA}^+\text{DS}^-$ , and the simple salt  $\text{Na}^+\text{Br}^-$  are all present in the system. In the pyramid-shaped diagram shown in Figure 5, the sides of the base can be assigned to the four different ionic species and the height above the base is proportional to the water content of the samples. The 2-D triangular phase diagram shown in

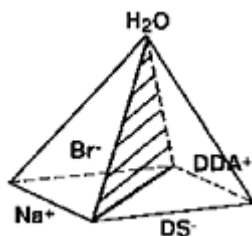


**FIG. 5** Pyramidal phase diagram for the four-component system of  $\text{Na}^+$ , dodecylsulfate ( $\text{A}^-$ ),  $\text{Br}^-$ , didodecyldimethylammonium ( $\text{A}^+$ ), and  $\text{H}_2\text{O}$ . The base vertexes correspond to the four ionic species  $\text{A}^+$ ,  $\text{Na}^+\text{Br}^-$ ,  $\text{Na}^+\text{A}^-$ , and  $\text{A}^+\text{Br}^-$ . The shaded diagonal plane corresponds to the two-dimensional triangular phase diagram shown in Figure 6. (From Ref. 11.)

Figure 6 constitutes the shaded diagonal symmetry plane in Figure 5. The one-phase regions pictured therein are thus cuts of 3-D bodies in the pyramid. Some indications of the possible phases in equilibrium in heterogeneous regions, as supported by experimental data, will be given.

### C. Concentrated Catanionic Systems

The observed ternary phase diagram is shown in Figure 6a where sample compositions are presented in weight percent concentrations. The triangle sides correspond to the different binary systems (SDS-water, DDAB-water, and DDAB-SDS) and the straight line drawn to equimolar composition. Therefore, compositions lying above the line have an excess of DDAB, whereas the ones lying below have an excess of SDS.

Several interesting features of phase behavior are apparent in the phase diagram in Figure 6. (1) A large number of lamellar phases (four) is present, including two novel ones ( $\text{D}_{\text{III}}$  and  $\text{D}_{\text{IV}}$ ). (2) The lamellar phase  $\text{DI}$  incorporates only minute amounts of SDS, whereas the lamellar phase  $\text{DII}$  can accommodate substantial amounts of SDS. (3) The equimolar mixture forms a precipitate at low concentration and, at much higher surfactant concentration, a cubic liquid-crystalline phase and a lamellar phase with a very small region of existence ( $\text{D}_{\text{IV}}$ ). (4) The SDS-rich solution and hexagonal phases are destabilized by a small amount of the double-chained amphiphile, and a hexagonal to lamellar phase transition ( $\text{E} \rightarrow \text{D}_{\text{III}}$ ) is induced upon addition of DDAB.

The observed phase behavior can be fruitfully analyzed on the basis of electrostatic effects and molecular packing considerations. The mixing of two oppositely charged

surfactants makes the variation in electrostatic interactions especially pronounced and this is reflected, for example, in the low stability of D<sub>I</sub> upon addition of SDS. The definition of an effective surfactant parameter ( $P_{S,\text{eff}}$ ) for this mixture is to a great extent misleading. It can be said that  $P_{S,\text{eff}}$  is expected to attain its maximal value at equimolarity; for nonequimolar mixtures, a nonmonotonic variation of  $P_{S,\text{eff}}$  with the surfactant mixing ratio occurs.

On the basis of  $[^2\text{H}]\text{NMR}$  and polarizing microscopy, the various multiphase regions have been tentatively defined. Noting the limitations of this representation, the multiphase regions are indicated in Figure 6b. The assignment of phases is essentially based on the  $[^2\text{H}]\text{NMR}$  spectra of the samples and their position in relation to the single-phase regions. We note that the shape of the three-phase regions is not limited to triangles and that no four-phase region has been identified.

The results obtained here can be put into a broader context, bearing in mind other concentrated catanionic systems [30, 31, 39]. If one considers an effective surfactant parameter,  $P_{S,\text{eff}}=a_{\text{hc,eff}}/a_{\text{hg,eff}}$  for a catanionic surfactant (or an equimolar mixture of the surfactants, where salt is present), this parameter is

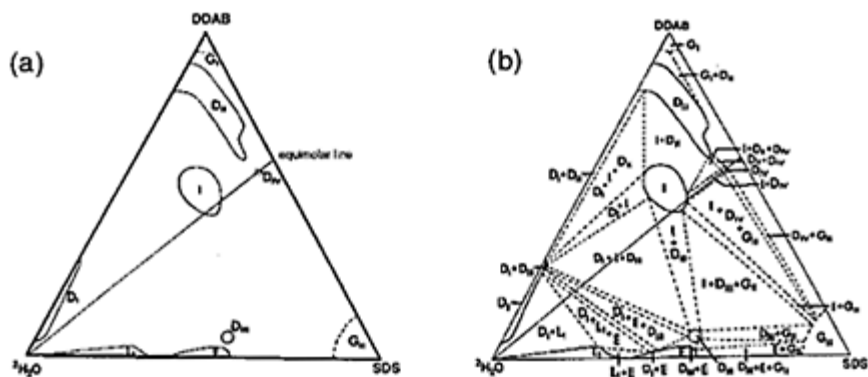
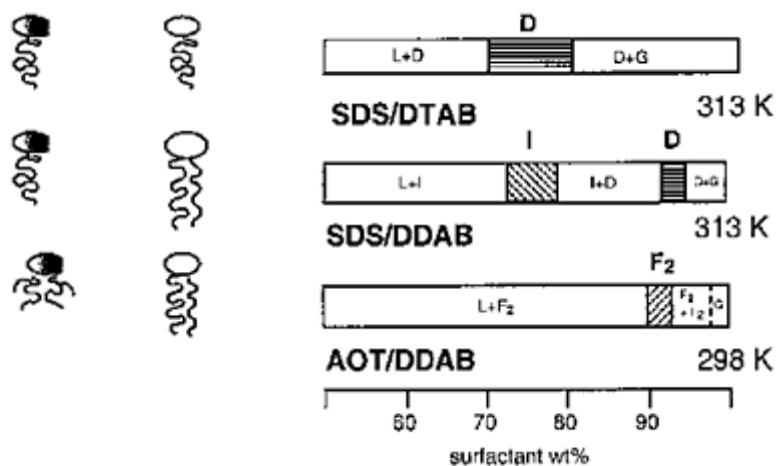


**FIG. 6** (a) Isothermal pseudoternary phase diagram of the SDS-DDAB–water system at 40°C showing single-phase regions. Notations are: L<sub>I</sub>, isotropic solution; E, hexagonal; I, cubic; D<sub>I</sub>, D<sub>II</sub>, D<sub>III</sub>, D<sub>IV</sub>, lamellar liquid crystalline phases; G<sub>I</sub> and G<sub>II</sub>, surfactant crystals. The drawn straight line contains all the points with an equimolar ratio of SDS and DDAB. (b) The complete phase diagram of the SDS-DDAB–water system at 40°C, where the two- and three-phase regions are approximately shown. (From Ref. 11.)

**TABLE 2** Effect of the Geometry of the Catanionic Surfactant on Phase Behavior<sup>a</sup>

Number of alkyl chains in the surfactants		
Anionic	Cationic	Phase behavior for equimolar mixtures



<sup>a</sup> Phase notations: D, lamellar phase; I, cubic phase; F<sub>2</sub>, reverse hexagonal phase.

Source: From Ref. 3.

determined by two opposing effects: the electrostatic attraction between the head groups and steric interactions between the tails. The parameter increases with the number of tails of the parent surfactants. In terms of the flexible surface model, the spontaneous curvature of the catanionic surface becomes increasingly negative (i.e., it curves toward water). This qualitative picture is supported from the phase diagrams of the systems single-/single-chained, single-/double-chained, and double-/double-chained surfactants (Table 2). A lamellar phase (of zero average curvature) occurs for the single-chain-single-chain system, a cubic phase of reversed curvature occurs for the single-chain-double-chain one, and a reversed hexagonal phase (of high negative curvature) exists for the double-chain-double-chain system. These studies indicate generally how a suitable blending of surfactants in water can dictate microstructure and stability regions, an observation that may be useful for theoretical modeling and practical applications.

## D. Vesicle Formation in Dilute Systems

### 1. The Question of Vesicle Stability

Vesicles are closed bilayer aggregates of variable average size. They can thus be used as *in vitro* cell models for biochemical studies, as agents for the transport of substrates (in drug and gene delivery), and as microreactors for specialized chemistry, among other uses. There is great demand for truly stable vesicle systems; strictly for thermodynamically stable vesicles. Since the early 1990s, experimental investigations on the phase behavior and aggregated structures of several mixed surfactant systems, in particular catanionic systems, have revealed that equilibrium vesicle formation is a typical feature.

A solution of vesicles can be experimentally obtained by choice of an appropriate

surfactant system and a preparation method [46]. These two factors in principle dictate the characteristics of the vesicles: mean size, polydispersity, and stability. However, the existence of the vesicle as a true thermodynamically stable phase is theoretically challenging and, to a great extent, debatable [47, 48]. The question resides in accounting for the factors that stabilize the vesicle rather than competing geometries; that is, the flat bilayer state (a lamellar phase), the sponge phase, or the micellar phase. A detailed discussion of the theories for vesicle stability is outside the scope here, but we will briefly mention (1) the conditions for vesicle stability within the framework of the flexible surface model and (2) the type of amphiphilic systems where vesicles are formed.

When considering the curved bilayer in a vesicle, it is to be realized that the outer monolayer has positive curvature,  $c_{\text{out}} > 0$ , whereas the inner one has a negative curvature,  $c_{\text{in}} < 0$ , which is slightly smaller in absolute value. As the radius of the vesicle increases,  $c_{\text{out}} - |c_{\text{in}}| > 0$ . This asymmetry in curvature for a single-component vesicle dictates a situation of curvature energy frustration. The relief of this frustration in the planar bilayer state, where  $c_{\text{out}} = c_{\text{in}}$ , implies that as a general rule the lamellar phase is favored over the vesicle phase. In many systems, although not the equilibrium state, it may happen that the vesicles are kinetically stable for a long time before they flocculate, fuse, and reach the lamellar state. There are, however, conditions within the flexible surface model for which the vesicle is the stable aggregate; that is, the state for curvature energy minimization. It has been shown [49] that the curvature free energy of forming a vesicle from a flat bilayer (for which the spontaneous curvature  $c_0 = 0$ ) is given by  $E_c = 8\pi(k + (1/2)\bar{k})$ .

The bending constants  $k$  (bending modulus) and  $\bar{k}$  (saddle-splay modulus) are usually expressed in terms of  $k_B T$  units ( $k_B$  = Boltzmann constant). A significant consequence of this equation is that the curvature energy of a vesicle does not depend on its radius but only in the bending constants. The planar membrane has  $E_c = 0$ . It can be shown that if:

1.  $k + \bar{k}/2 > 0$  and  $\bar{k} < 0$ , the planar state is favored. Curvature instability is produced if one of these conditions is violated.
2. If  $k < -\bar{k}/2$ , the formation of a vesicle is favored, since  $E_c < 0$ .
3. If  $\bar{k} > 0$ , the formation of a sponge phase is favored.

The question of the curvature stabilization of a vesicle is therefore dependent on the sign of  $k + \bar{k}/2$ . Normally  $k$  assumes large values for phospholipids and double-chained surfactants; in the range of  $k = 5\text{--}20 k_B T$  (these molecules are said to form *rigid* bilayers).

The  $\bar{k}$  values are usually low (only a few  $k_B T$ ) and negative. Therefore, since  $k \gg |\bar{k}|/2$  and solely on the basis of curvature energy, the formation of vesicles is unfavored for the common double-chained amphiphiles.

Entropy changes also play a role in the assembly of vesicles. There is an entropy increase associated with the formation of many finite-sized vesicles from an infinite bilayer. It is possible to present an expression for the free energy density of a vesicle solution accounting for curvature energy and the effects of entropy of mixing at high dilution. Within this approach, the formation of vesicles can be seen essentially as a



competition between curvature energy and entropy of mixing. The total curvature energy is proportional to the number of vesicles, so upon vesicle fusion, it decreases; therefore, larger vesicles are energetically favored. Entropy favors instead a large number of small vesicles. Whereas  $E_c$  is in the order of 50–300  $k_B T$  for each vesicle, entropic contributions are in the order of a few  $k_B T$ . Vesiculation is thus generally unfavorable. Still, the formation of stable vesicles should be possible:

1. Entropically—in the case of bilayers where  $k$  is extremely low

( $k < |k|/2$ ,  $E_c \approx k_B T$ ) or if the surfactant concentration is very low [50];

2. Energetically—if the bilayer has nonzero spontaneous curvature  $c_0 \neq 0$ , which in principle requires the presence of at least two components.

Several mixed surfactant vesicles have been theoretically investigated from both the perspective of energetic or entropic stabilization [51–54]. Experimentally, the formation of equilibrium vesicles has been reported in several mixed systems. Dialkyldimethylammonium surfactants form stable vesicle phases at very low concentrations; namely, with bromide, acetate, and hydroxide counterions [55–58]. Mixtures of surfactant-cosurfactant (alcohol) with and without added salt, where the spontaneous curvature of the bilayer can be finely tuned also yield stable vesicles [54, 59–62]. In a mixed system formed by nonionic-ionic surfactant at low charge concentration, the addition of octanol can induce the formation of a phase of very small monodisperse vesicles [63].

For catanionic mixtures, the presence of excess ionic surfactant is thought to break the symmetry of the monolayers and through different mechanisms (of entropic or energetic origin) to stabilize the vesicle bilayer with respect to competing geometries; in particular, the planar bilayer. In general, the vesicles have properties that correlate with thermodynamic stability and show a variable degree of polydispersity (from tens of nanometers to a few microns). The equimolar precipitate is usually in equilibrium with vesicles at low surfactant volume fraction and with dilute lamellar phases at high volume fraction. In most systems, a region with only vesicles is observed. Phase diagram studies illustrate these observations [64–72], and below we consider the case for the SDS-DDAB system in more detail [12, 13].

## 2. Catanionic Vesicles from Single-Chained/Double-Chained Surfactants

Vesicles form spontaneously in the very dilute water-rich part of the SDS-DDAB-water phase diagram [12, 13], for more than 97 wt% of water (Fig. 7). The region for vesicle formation in the anion-rich side of the mixture occurs for a molar fraction of DDAB in the range of 0.25–0.34 and is limited between 0.2 and 1.2 wt% SDS.

The vesicles are essentially spherical and unilamellar, with a size distribution falling in the range 20–200 nm (Fig. 8a). The size range is biased toward a narrower width of 20–70 nm. A very small fraction of giant vesicular aggregates (1–40  $\mu\text{m}$ ), mainly giant unilamellar vesicles below 2  $\mu\text{m}$ , is also present. Dilution within the vesicle region ( $C_s=5\text{--}50\text{ mM}$ ) does not induce any detectable structural changes in shape and average size of the vesicles (Fig. 8b). Thus, a dilution path induces a gradual reduction of the volume fraction of vesicles by a decrease in concentration of aggregates with essentially

constant size [12]. The

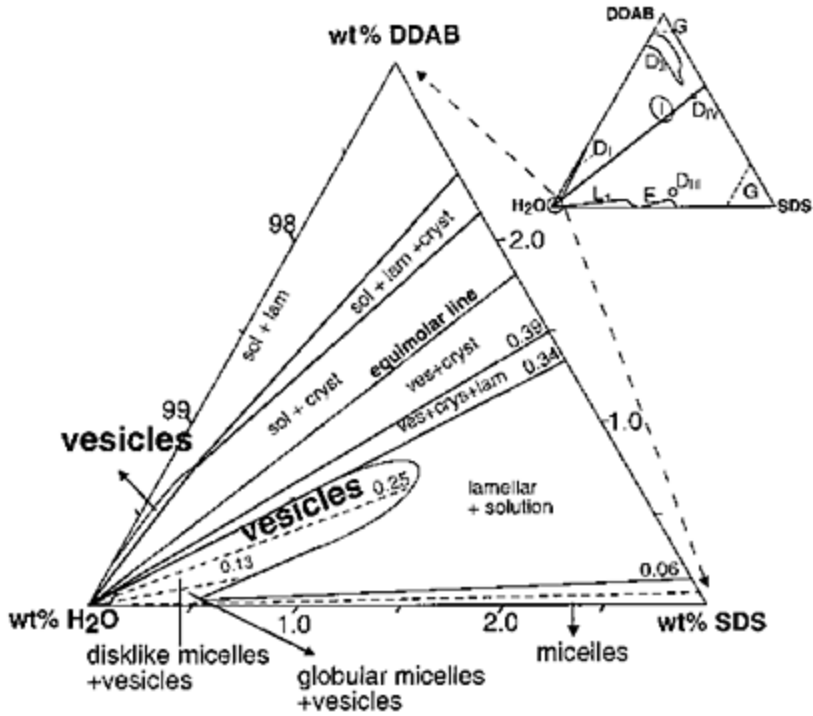
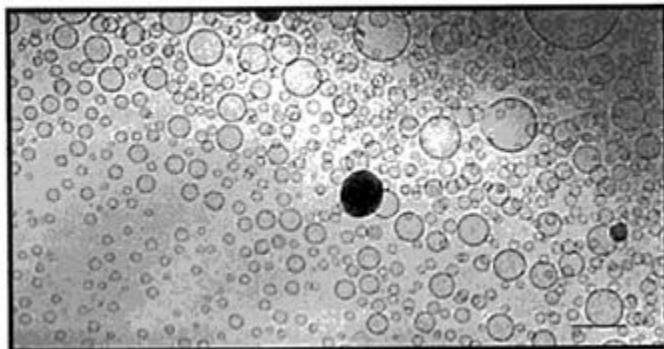


**FIG. 7** Phase behavior in the dilute region of the SDS-DDAB-water system at 25°C. Numbers over lines indicate  $X_{DDAB}$  values for relevant phase boundaries or regions where different aggregate structures are found. Two vesicle lobe regions are found. (Adapted from Ref. 12.)

(a)



(b)

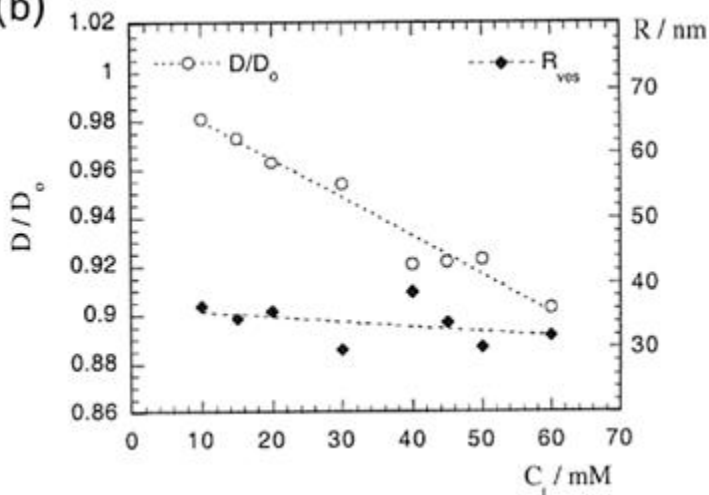


**FIG. 8** The anionic SDS-DDAB vesicles: (a) Cryo-TEM micrograph showing small unilamellar vesicles (for SDS 1 wt% and  $X_{DDAB}=0.3$ ); bar=100 nm. (b) Estimation of the average size of SDS-rich vesicles (◆) from the water-reduced self-diffusion coefficients (○). Samples at constant  $X_{DDAB}=0.3$  along a dilution path,  $C_t=10$ –60 mM ( $C_t=C_{SDS}+C_{DDAB}$ ). (From Ref. 12.)

maximal volume fraction enclosed by the vesicles is approximately 0.10 (at  $C_s \approx 60$  mM).

A vesicular lobe is also present in the cation-rich side of the phase diagram [13]. A rich diversity of vesicular aggregates occurs in this area in contrast to the anion-rich side, in which mostly unilamellar vesicles were detected. Both unilamellar vesicles and multilamellar vesicles are generally observed in the DDAB-rich vesicular solutions and the size range is often broad (0.1–5.0  $\mu$ m). The fact that the average vesicle's size and

degree of polydispersity are much larger than for the SDS-rich vesicles is a direct consequence of the difference in the packing parameter of the two surfactants.

Overall, the DDAB-SDS catanionic pair, comprising a single- and a double-chained surfactant, provides a system in which the net charge, mean size of the vesicles, and vesicular volume fraction are to some extent controllable through surfactant concentration and mixing ratio. Below we will consider in some detail the interaction between thermodynamically stable vesicles and oppositely charged polymers. We note here that the thermodynamically stable vesicles have an excess of either surfactant; that is, they are net anionic (SDS-DDAB system) or net cationic (CTAB-SOS system).

## IV. INTERACTIONS BETWEEN CATANIONIC VESICLES AND POLYELECTROLYTES

### A. Polymer-Vesicle Systems: Background

Aqueous polymer-vesicle systems are a type of mixed colloidal system under intensive current investigation. In general, these mixtures are model systems for living cells, as these are composed of lipid membranes interacting with a variety of biopolymers (proteins, polysaccharides, and DNA). They may also lead to novel and interesting phase behavior, such as the formation of gels and networks, with potential rheological applications. The polymer can act as a liposome stabilizer and controller of membrane permeability in liposomal systems for drug delivery. The vesicle can act as carrier of DNA in systems designed for gene therapy and delivery.

It has been shown that in the presence of nonadsorbing polymers (with respect to the bilayer interface), such as poly(ethylene)glycol (PEG), aggregation and fusion of phospholipid or synthetic surfactant vesicles occur [73–75]. The effects stem from a polymer-induced attractive depletion force between the vesicles. Polymers can interact directly with the vesicle bilayer by means of (1) hydrophobic interactions (due to the incorporation of hydrophobic moieties in the polymer chain) [76–79], (2) electrostatic interactions in charged systems [78, 80–82], or (3) both hydrophobic and electrostatic interactions simultaneously. Thermal gelation has been observed in systems of hydrophobically modified polymer and nonionic surfactant bilayers, and it has been referred to as vesicular cross linking by the polymer chains with hydrophobes anchored in the bilayer [76]. The stabilization of double-chained surfactant vesicles by polymers containing terminally placed hydrophobes has also been observed [77, 83]. These polymers can anchor in different aggregates and bridge them, leading to transient polymer gels of rheological interest [77].

Mixed systems of DNA and amphiphilic molecules have also received much attention from biochemical and pharmaceutical sciences in recent years [84]. In particular, liposomes consisting of positively charged and zwitterionic lipids were found to be optimal vehicles for medical applications; that is, *in vitro* and *in vivo* delivery of genetic material [85]. Several physicochemical methods were used for the examination of DNA-amphiphile interactions in solutions [86]. Although unveiling important information on the interactions, these methods do not answer the question of the behavior of single DNA

molecules. Recently, the interaction between single large DNA molecules in aqueous environment and amphiphilic molecules has been studied by means of fluorescence microscopy [87]. The conformational behavior of individual DNA molecules stained with a fluorescence marker has been detected with respect to the activity of amphiphilic molecules; that is, cationic and neutral lipids and synthetic surfactants. It has been found that isolated DNA chains undergo a discrete coil-globule transition upon the increase of the concentration of amphiphiles in the solution [88]. This process starts at very low concentrations of a positively charged surfactant; that is, approximately two orders of magnitude lower than the critical micellization concentration (CMC) of the individual surfactant in polyelectrolyte-free solutions [89]. If nonionic surfactant is added to the DNA solution, collapse occurs at much higher surfactant concentrations owing to a weaker associative behavior [90].

Despite numerous studies of DNA interaction with oppositely charged amphiphiles, the conformational behavior of DNA in the presence of mixtures of two oppositely charged surfactants has never been addressed. Nevertheless, this system presents a certain interest for pharmaceutical applications, since variation of the molar ratio between the two amphiphiles may strongly affect linear dimensions and the charge of individual DNA molecules and, consequently, influences the process of a transmembrane DNA delivery.

## **B. Polycation-Anionic Vesicles**

### **1. Experimental Conditions**

In this section, we will discuss the phase behavior and microstructural effects resulting from the addition of modified polysaccharides to a solution of catanionic vesicles [15]. The aim with this study has been to (1) characterize the mean features of the phase behavior of the system (a multicomponent polymer-surfactant-surfactant system); (2) probe the effect of the macromolecule on the structure and stability of vesicles at low polymer concentration; (3) search for the possibility of vesicle-polymer gel formation at high polymer concentrations.

The current systems have some fundamental differences with respect to the oppositely charged polymer-surfactant systems available in the literature. Here (1) polymer is added to a solution of preformed aggregates (vesicles) where the surfactant monomer concentration is low, and thus kinetic aspects may play an important role; (2) the surfactant consists of a mixture of anionic and cationic

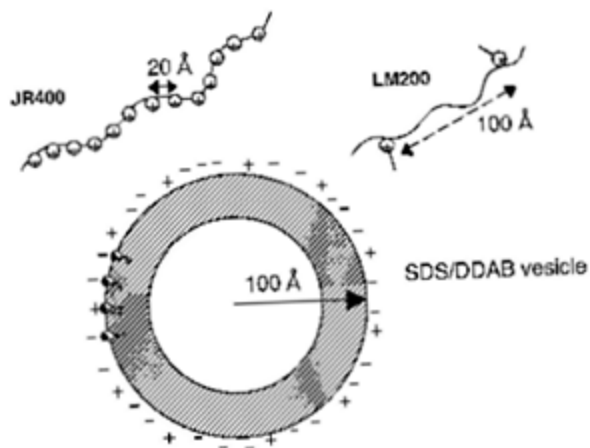


**FIG. 9** Schematic representations of the interacting polymer and vesicle structures; length scales involved in the system are also shown. The mean contour length between charges (not the mean linear repeat distance) is given in angstroms (Å) for both polymers. A net negatively charged SDS-DDAB vesicle is also shown with a typical radius of 100 Å, drawn approximately in scale with polymer length scales. (From Ref. 15.)

surfactant at a fixed mixing ratio; and (3) both polymer-surfactant and surfactant-surfactant systems of opposite charges are simultaneously present.

Two cationic polyelectrolytes, both based on hydroxyethylcellulose, JR400 (homopolymer) and Quatrisoft LM200 (modified with hydrophobic chains), were investigated. They will be referred henceforth as the  $P^+$  and the  $HMP^+$ , respectively. The colloidal structures and length scales involved in the current polymer-surfactant systems are schematically presented in Figure 9. A vesicle with a typical diameter of 20 nm is shown in scale with the mean charge-to-charge contour lengths of both polyelectrolytes. The  $HMP^+$  has on average 20 hydrophobic side chains; meaning that the average contour length of one  $HMP^+$  chain is approximately 200 nm. The  $P^+$  has on average 500 charges per chain, which implies a mean contour length for the molecule of about 1  $\mu\text{m}$ .

The polymer-surfactant samples were mixed by weight from a polyelectrolyte solution and a surfactant solution containing catanionic SDS/DDAB vesicles, taking precautions to ensure miscibility and equilibration.

## 2. Phase Maps

The determination of phase behavior was carried out by gradual addition of cationic polyelectrolyte to the surfactant solution containing previously assembled aggregates [15]. The surfactant solution contains initially catanionic SDS-rich vesicles, and is henceforth simply referred to as  $V^-$  solution. The procedure is schematically depicted in Figure 10. The total surfactant concentration in the polymer-vesicle mixture,  $C_s$ , was

varied in the range of 5–50 mm,

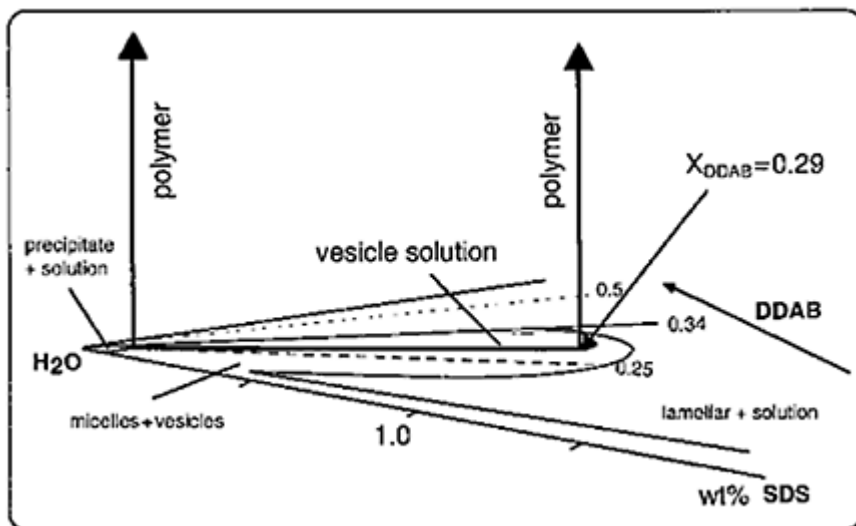


**FIG. 10** Schematic representation of the approach used for the phase behavior study of polymer-vesicle systems. (From Ref. 15.)

corresponding to a dilution path between 1.0 and 0.1 wt% SDS spanning the vesicle-only solution region (Fig. 10). The composition lies midway in the range for the occurrence of the vesicular region.

The difficulty in presenting the phase behavior for the multicomponent polymer-surfactant systems is evident from Figure 10. The vesicular solution consists of a catanionic surfactant mixture. This mixture already is a four-component system (see above) for which the triangular phase diagram is an approximate representation (strictly accurate only for the location of single-phase regions). The presence of an additional component, the cationic polyelectrolyte, which can associate electrostatically with one of the surfactants, the anionic SDS, brings about further complexity to the dimensionality of the system in terms of the phase rule. Thus, a generic phase behavior is best presented in *phase maps*, where the single phase and heterogeneous regions experimentally found are indicated.

As can be seen in Figure 11, three main regions are found: (1) a solution surfactant-rich single phase, which can only take up a relatively small amount of polymer; (2) a wide region of phase separation, containing a precipitate and a solution, present up to a slight excess of polymer charge in the system; (3) a gel region after “redissolution” of the precipitate (*polymer-rich phase*).

The phase separation observed in this system is of the associative type: A concentrated phase in both polymer and surfactant (precipitate) is in equilibrium with a solution dilute with respect to both species.

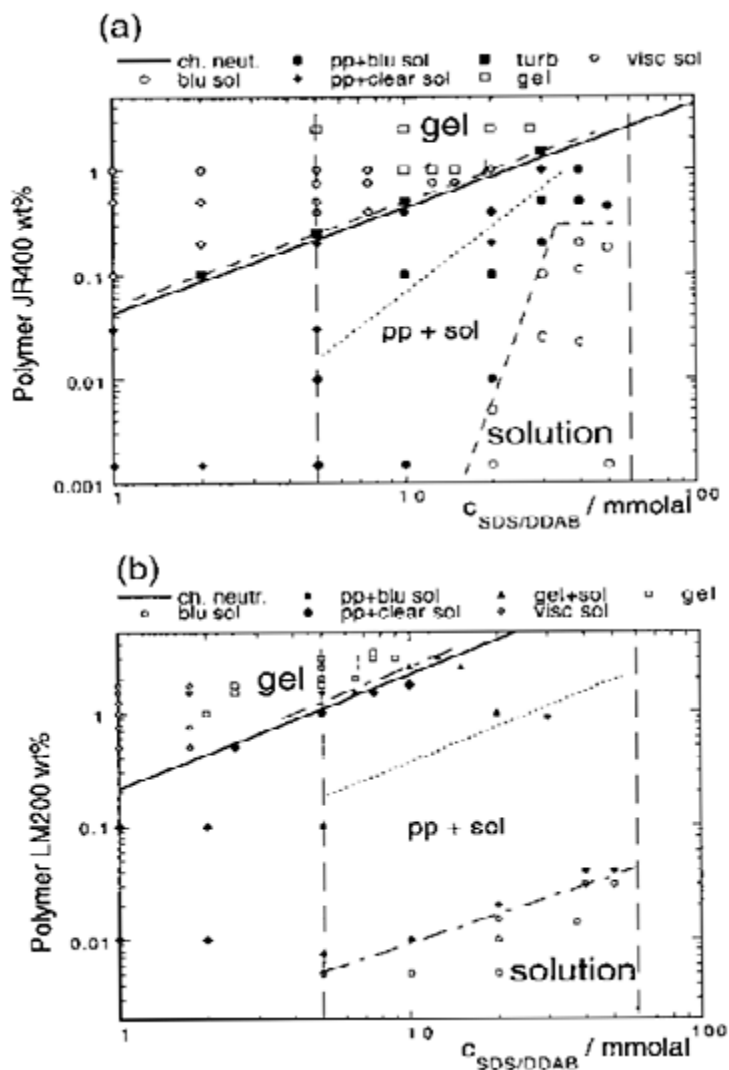


**FIG. 11** Phase map for the polymer-vesicle aqueous systems: (a)  $P^+-V^-$  and (b)  $HMP^+V^-$ . The catanionic vesicle system has a fixed composition of  $X_{DDAB}=0.29$ . Vertical dashed lines mark the available range of surfactant concentration for the vesicular solution. Line denoted by ch. neutr. indicates charge neutrality. Phase notations: sol, bluish low-viscous solution; pp, precipitate; clear sol, clear solution; turb, two-phase sample (coacervate); visc sol, viscous solutions; gel, bluish gel-like samples. (From Ref. 15.)

It should be noted that in oppositely charged polymer-surfactant mixtures, two main types of associative phase separation occur—coacervation and precipitation.



Coacervation consists of a liquid-liquid phase separation, for which one of the liquids is highly concentrated in both polymer and surfactant and the other is a very dilute solution. Precipitation involves a concentrated phase of solid-like character with either crystalline or amorphous structure.

In the polymer-rich single phase, the samples display slightly different macroscopic behavior depending on their relative content in polymer and surfactant. For lower surfactant concentrations, the samples consist of highly viscous solutions, which flow slowly under gravity. At higher polymer or surfactant content, the samples are best described as gels, flowing very slowly under gravity. A striking feature of these solution/gel samples is their bluish translucence, giving indication that they contain aggregates or colloidal domains large enough to scatter visible light. Another significant observation is that for  $C_s = 15 \text{ mM}$ , where the surfactant-only system precipitates, addition of polymer also induces the formation of highly viscous solutions above the neutralization line. The solubilization of the catanionic precipitate in the presence of polymer confirms the strong character of the polymer-surfactant interactions in this system.

A common feature for all the mixtures shown in Figure 12 is the occurrence of an extensive region of phase separation of the associative type. The polymer charge is plotted versus the surfactant charge as (1) the polyelectrolytes have different charge densities and (2) for a given surfactant concentration, there is a net charge concentration in the catanionic system which is lower than that in the micellar system. Boundaries separating one- and two-phase regions are shown. The boundaries for the  $P^+$ -SDS system were calculated on the basis of the phase diagrams presented elsewhere [91]. For the  $HMP^+$ -SDS system, we replot the values from Guillemet and Piculell [18]. The concentrated phase in the two-phase region consists of a precipitate in the  $P^+$ -SDS system [91]. In the  $HMP^+$ -SDS system, a coacervate is formed that is characterized as a gel-like liquid containing a high degree of cross-linking polymer due to the formation of mixed hydrophobe-SDS micelles [18]. For these polymer-SDS systems, the phase behavior is usually described from the point of view of surfactant addition to polymer solution. Thus, the boundary at lower surfactant charge concentration is termed coacervation or precipitation boundary, which at higher surfactant charge, is referred to as redissolution boundary.

### 3. Rheological Data

Oscillatory measurements were made for samples in the  $P^+-V^-$  system in the viscous solution/gel region [15]. Plots of the rheological parameters  $G'$  and  $G''$ , the shear storage, and the shear loss modulus, respectively, versus the oscillation frequency are shown in Figure 13. It can be seen that, within the studied

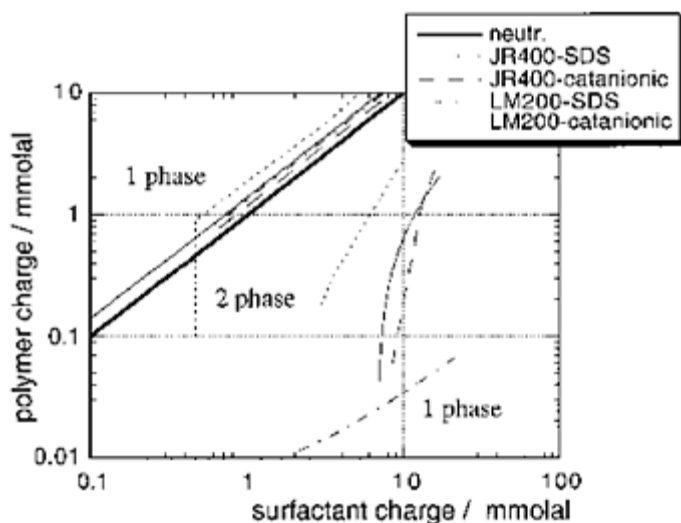


**FIG. 12** Comparative phase map for mixed polyelectrolyte-surfactant systems (from Ref. 15). Lines at lower surfactant charge: coacervation/precipitation boundaries; lines at higher surfactant charge: redissolution boundaries. For any given system, the region between the two boundaries is a two-phase region. The catanionic system is composed of SDS-DDAB at fixed surfactant mixing ratio of  $X_{\text{DDAB}}=0.29$ . Values for HMP<sup>+</sup>-SDS lines from Ref. 18; for P<sup>+</sup>-SDS lines from Ref. 19.

frequency range, both moduli show a strong frequency dependence and  $G'$  values are always higher than  $G''$ , indicating that the samples have a viscoelastic character. The magnitude of  $G'$  and  $G''$  is quite low, and at any frequency the highest values occur at 0.75 wt% polymer. This fact points to the highest network organization for this concentration. The network seems to be destabilized when the polymer concentration is further increased to 1 wt%.

This rheological study shows that the samples have a viscoelastic behavior which is dependent on both polymer and surfactant concentration in a complex way. The changes are more pronounced when the surfactant concentration is varied rather than the polymer concentration. It is possible that such a behavior is directly connected with changes in the global microstructure (dominant aggregate shape and aggregate diversity) of the gels. The dynamic properties of the polymer-surfactant network must be distinctive if vesicles, disk-like aggregates, or planar membranes are present (see below). If small and low polydisperse disks are the dominant type of aggregate, a less heterogeneous type of polymer-aggregate network is likely to be present as compared to a vesicular network in which the polydispersity is probably higher and also the aggregates can be deformed under shear. Therefore, the strength of the network is likely to be higher in the former case.

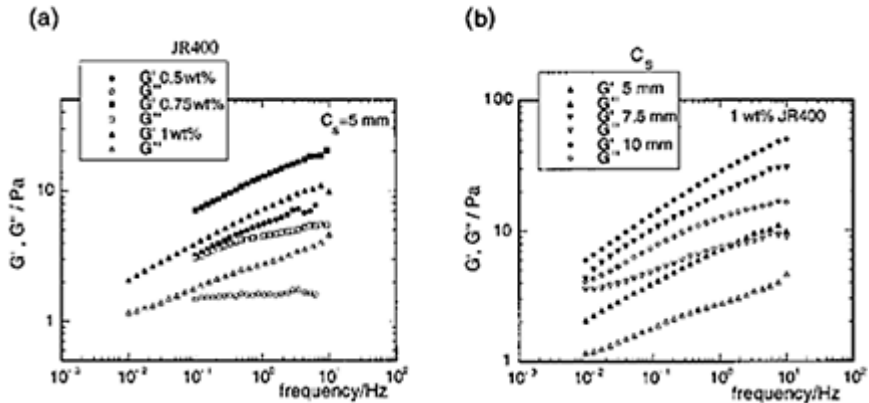


**FIG. 13** The elastic modulus  $G'$  and the loss modulus  $G''$  versus oscillation frequency for samples in the  $P^+-V^-$  systems at 25°C: (a) at constant total surfactant concentration,  $C_s = 5$  mM, and increasing polymer concentration; (b) at constant polymer concentration, 1 wt%, and increasing surfactant concentration,  $C_s$ . (From Ref. 15)

#### 4. Microstructural Effects

Investigation of the aggregation microstructure in the bluish solution phase and in the viscos/gel phases observed in the polymer-catanionic systems was done by direct imaging with the Cryo-TEM method [15]. For the surfactant-rich phase, the goal was to probe the structural effect of the polyelectrolyte on the surfactant vesicular bilayer, which eventually leads to phase separation with the formation of a solid-like precipitate. For the polymer-rich phase, it was of interest to investigate the presence of vesicular or other type of surfactant aggregates responsible for the gel-like behavior.

Whereas at a macroscopic scale, each sample displays a single isotropic phase, at a microscopic level, there is in general a polydispersity of self-assembled structures not only in size for a particular geometry but, significantly, in terms of the variety of coexisting aggregate geometries. However, in most cases, it is possible to identify the dominant type of aggregate form and its characteristic size. So, upon polymer addition, there is typically a progressive evolution from a given state of aggregation to another accompanied or not with the replacement of the dominant structure. Since the addition of the charged polymer results in partial neutralization of the oppositely charged surfactant bilayer, it is natural to consider electrostatics as the main driving force for the observed structural transitions, and we adopt this view in the description that follows. Other factors like molecular weight and hydrophobic modification, in the case of the  $HMP^+$ , also affect the observed microstructural evolution.

Addition of the  $HMP^+$  to the vesicular solution induces structural effects on the vesicular bilayer comparable to those observed with the  $P^+$ . In fact, as the polymer concentration increases (and, concomitantly, charge neutralization in the system), there is a gradual formation of faceted vesicles and disk-like aggregates. Moreover, the variety of

coexisting aggregate forms increases.

The interaction of hydrophobically modified polycation with the vesicles can involve molecular contact. The hydrophobic side chains (bearing the charge) can anchor in the oppositely charged vesicular bilayer, opening the possibility of vesicular cross linking. Since the mean contour length between the hydrophobes, 10 nm, is of the order of the diameter of the small vesicles, 20–30 nm, it is reasonable to picture that even one HMP<sup>+</sup> molecule can make cross links between several small vesicles. An illustration of this type of “network” is shown in Figure 14, where both faceted and round vesicles are seen interconnected by the polymer chains. It should be noted that the polymer chain itself is invisible in the TEM micrographs, since its diameter is below the resolution of this imaging technique.

When the concentration of polymer is doubled for the same surfactant concentration, the cross-linking effect becomes evident. Clusters of relatively large size containing many bilayer aggregates are observed, suggesting that the

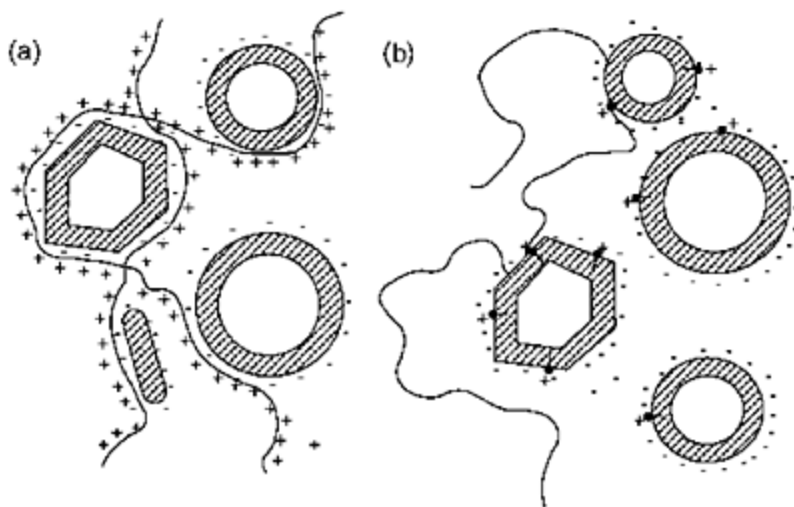


**FIG. 14** Schematic view of the possible vesicle cross-linking effects by the polymers P<sup>+</sup> and HMP<sup>+</sup>; both faceted and round vesicles are shown, on the basis of the cryo-TEM micrographs (see Fig. 15).

constituent aggregates are strongly interconnected. The occurrence of the interconnected vesicles and dense clusters is thus a novel feature of the HMP<sup>+</sup>-V<sup>-</sup> system as compared to the P<sup>+</sup>-V<sup>-</sup> system.

We note that vesicle-polymer networks have been previously suggested for some systems containing hydrophobically modified polymers [76, 77]. Here we note the following specific aspects of the different homogeneous regions of the phase map.

(a) *Surfactant-Rich Phase.* Strong polymer-aggregate interactions are expected when polyelectrolyte is added to a solution containing oppositely charged vesicles. The polyelectrolyte will have a general screening effect in the electrostatics of the system:

intrabilayer effects (decreasing headgroup repulsions) promoting structural changes; interbilayer effects (weakening double-layer repulsions) promoting a decrease in the stability of the aggregates. At lower polymer concentration, the decreased surfactant head group repulsions can promote an evolution to structures of lower curvature. In the investigated polymer-catanionic systems, the closed vesicular structure is essentially preserved at low polymer content. However, there is formation of faceted vesicles, where the bilayer has a different structural appearance (Fig. 15a). A qualitative difference seems to exist between the effects induced by the  $P^+$  and the  $HMP^+$  as the polymer concentration is further increased. One can sum up the observations in the following way. The  $P^+$  has higher charge density (thus being a stiffer molecule) and no grafted chains. Prior to phase separation, it induces two effects: (1) initial formation of

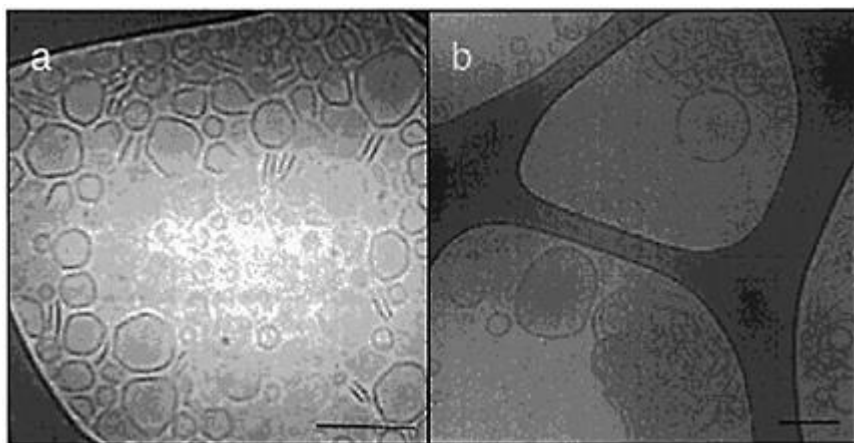


**FIG. 15** Cryo-TEM micrographs of the bluish solution region illustrating the polyelectrolyte effects on vesicles. (a) JR400 vesicular system: The polymer induces the formation of faceted vesicles and disk-like aggregates (Composition: 0.11 wt% JR400,  $C_s=40$  mM). (b) LM200 vesicular system: formation of vesicle clusters due to polymer bridging (Composition: 0.01 wt% LM200,  $C_s=20$  mM). Bars: 100 nm. (Adapted from Ref. 15.)

faceted vesicles and (2) breakage of the vesicles into small disk-like aggregates at higher polymer content. The  $HMP^+$  has lower charge density and the possibility of anchoring directly onto the bilayer due to its alkyl side chains. In this case, the polymer adsorption involves molecular contact between the polymer and the vesicle. The formation of disk aggregates seems to be less favored in this system. Two main effects are induced: (1) formation of ruptured, faceted vesicles and (2) formation of clusters of vesicles and other bilayer structures due to polymer cross linking, as seen in Figure 15b.

*(b) Polymer-Rich Phase.* The occurrence of gel-like samples in the  $HMP^+-V^-$  and  $P^+-V^-$  systems, at high polymer content, displaying a characteristic bluish appearance suggested the presence of large aggregates. The existence of the aggregates was confirmed by the cryo-TEM method. The formation of gels occurs for roughly similar

values of the molar fraction of polymer charge in both systems; thus implying that electrostatics is the driving force for gel formation. Cryo-TEM data and preliminary rheological measurements in the  $P^+-V^-$  system suggest that the structure of the gel may in reality involve a different type of surfactant aggregates—vesicles, disks, or large membrane fragments—depending on polymer-surfactant charge stoichiometry. For the case of the  $HMP^+-V^-$  system, comparatively stronger gels were macroscopically observed. For this system, the alkyl chains of the polymer can anchor hydrophobically to the oppositely charged bilayer. Thus, the gel can be intuitively pictured as a network of vesicles, or other type of bilayered aggregates, cross linked by the polymer backbone. The hydrophobic interactions in the system would considerably increase the viscosity of the gels as compared to the  $P^+$  system (where they are absent) for similar values of charge stoichiometry. It is likely that for the  $HMP^+$  system, the ratio between surfactant tails and polymer hydrophobes is also a determining factor on the dynamic properties of the gel.

### 5. Other Investigated Systems

A number of other vesicle-polymer systems has been investigated recently [5]. Binding models for polyelectrolyte-vesicle association have been proposed [81, 92]. When bilayers composed of mixed nonionic/ionic lipids are used, the polyelectrolyte induces lateral phase separation in the membrane due to electrostatic interactions between the polyelectrolyte and the oppositely charged lipid [82]. An insoluble complex is formed when DDAB is mixed with an oppositely charged polyelectrolyte; if the precipitate is heated above room temperature, network domains containing giant vesicles can be imaged in a light microscope [80].

The formation of segregated domains in vesicles formed by mixed zwitter-ionic-anionic lipids, due to interaction with a polycation, is demonstrated by  $[^2H]$  quadrupolar splitting nuclear magnetic resonance [93]. The polycation is able to segregate laterally the anionic lipid into domains, and, furthermore, it has been demonstrated that the conformation of the adsorbed polymer into a collapsed or a random coil is dependent on the charge density of the bilayer. An anionic hydrophobically modified copolymer is seen to interact strongly with positively charged multilamellar vesicles formed by neutral lipids and cationic surfactants. The interactions are dominated by the electrostatic attractions between the cationic lipid and the glycine residues of the polymer and, at high binding levels, regions of high local curvature are formed in the lipid bilayer. In mixtures of cardiolipin (an anionic lipid)-phosphatidylcholine vesicles and a cationic polyelectrolyte [95], it is seen that the integrity of the vesicles is dependent on the molar fraction of negative charge in the mixed vesicle. Beyond a certain charge density of the vesicle, the polymer induces a disruption of the structure into nonvesicular polymer-lipid complexes. Polycations adsorbed to negatively charged vesicles are shown to be desorbed by addition of anionic polyelectrolyte, which thus acts as a competitor with the vesicle aggregate [97]. If the polycation is made hydrophobically modified, the addition of the polyanion is much less effective in the desorption process. A thermosensitive anionic polymer containing octadecyl side chains is able to bind to different types of mixed amphiphilic vesicles through electrostatic, hydrophobic, and hydrogen-bonding interactions [98].

## C. DNA-Cationic Vesicles

### 1. Experimental Conditions

The vesicular system used in the work briefly reviewed here is the aqueous mixture of cetyltrimethylammonium bromide (CTAB) and sodium octyl sulfate (SOS), studied by E. Kaler and coworkers [67, 96]. By varying the mixture composition, the head group interactions along with hydrophobic interactions between surfactant tails can be tuned to produce aggregates with different charges and geometries ranging from spherical to cylindrical and planar. Coliphage T4 DNA ( $M=1.1 \times 10^8$  D) was used. The fluorescence technique has been used to observe large DNA molecules in the presence of both positively and negatively charged catanionic mixtures. The conformational behavior of fluorescence-labeled DNA molecules at different molar ratios between cationic and anionic surfactants in the mixture has been directly visualized in aqueous solution by fluorescence microscopy. To better understand the mechanism of DNA interaction with catanionic vesicles, the diffusion of individual DNA molecules was quantified for different compositions of catanionic mixtures also by dynamic light scattering and cryo-TEM experiments, as shown in detail elsewhere [16].

### 2. Microstructural Effects

(a) *DNA-Negatively Charged Catanionic Vesicles.* Experimental investigations have shown that since the equilibrium interaction constant of CTAB-SOS association is higher than that of CTAB-DNA association, DNA is unable to remove cationic surfactant from catanionic vesicles [16]. It remains in the coiled state, as in buffer solution in the absence of other cosolutes. Since the net charge of catanionic vesicles is negative, the strong electrostatic repulsion between DNA and vesicles also oppose their association. Thus, the presence of anion-rich catanionic vesicles in aqueous DNA solutions does not lead to any associative interaction and does not affect the DNA conformational behavior.

(b) *DNA-Positively Charged Catanionic Vesicles.* Contrary to the results obtained for anion-rich catanionic mixtures, the addition of oppositely charged mixtures to DNA solution leads to the collapse of individual DNA chains, which were detected by fluorescence microscopy in a compact globular conformation with apparent long-axis length values of 0.6–0.8  $\mu\text{m}$  [16]. The dimensions and fluorescence intensities of single DNA globules were quite similar to those reported previously for DNA compaction in the presence of various condensation agents [87]. However, the fluorescence microscopy experiments revealed that in some compositions, DNA globules exhibited a much slower Brownian motion compared to that in DNA-cationic surfactant system [88].

A very significant observation that has been made by means of fluorescence microscopy is the direct imaging of adsorption of DNA globules on the surface of catanionic vesicles. Figure 16 demonstrates images of DNA globules adsorbed

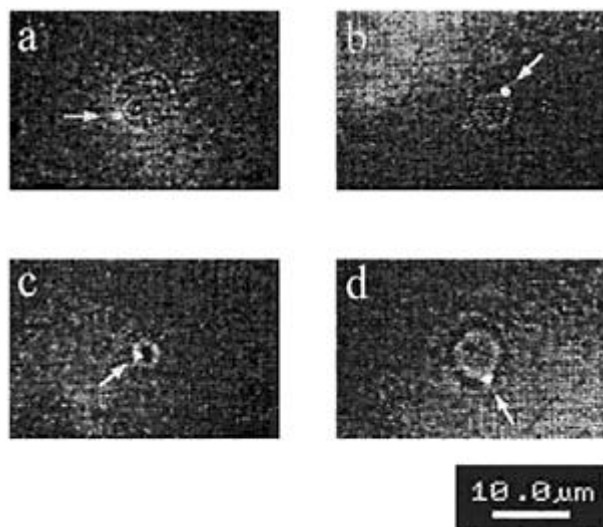


**FIG. 16** Imaging by fluorescence optical microscopy of single T4 DNA globules adsorbed onto the surface of positively charged catanionic vesicles. Arrowheads indicate single DNA globules. (From Ref. 16.)

onto the surface of CTAB-SOS vesicles. In this particular experiment, the sample has been illuminated with both ultraviolet and visible light simultaneously. Therefore, the observation of both fluorescently labeled DNA and large catanionic vesicles was possible. The vesicles were quite polydisperse, and some of them were big enough to be detected with the use of the light microscope.

If DNA is added to a vesicular solution at higher concentration, compared to that in fluorescence microscopy experiments, DNA molecules adsorbed onto the catanionic vesicles can also be visualized by cryo-TEM, similarly to DNA chains enclosed between liposomes observed by Templeton et al. [99], confirming data of optical microscopic experiments (Fig. 17).

## V. SUMMARY

In this chapter, we have briefly reviewed polymer-vesicle interactions with emphasis on the associative phase behavior resulting from electrostatic interactions between the two cosolutes. We have also given a general description of the phase behavior of mixed solutions of a cationic and an anionic surfactant, focusing on one system, a mixture of double-chain cationic and a single-chain anionic surfactant. We have stressed the complex and rich phase behavior with several liquid crystalline phases. In particular, we noted the appearance of two regions of thermodynamically stable vesicles, one with an excess of anionic and one with an excess of cationic surfactant. The interaction of the anionic vesicles



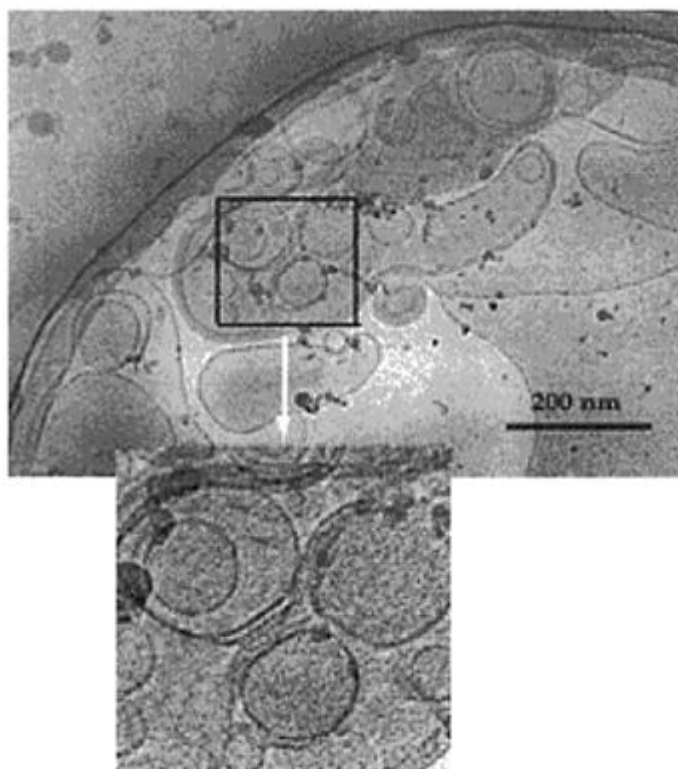


**FIG. 17** Imaging by cryo-TEM of a sample containing DNA and catanionic vesicles with suggesting evidence for DNA-vesicle complex formation. (From Ref. 16.)

with cationic polymers was investigated with respect to phase behavior, rheology, and microstructure. This first entry into the field of polymer-catanionic surfactants proved to be most fruitful with the observation of various microstructures and novel gels.

In the DNA-vesicle systems, it has been shown that the positively charged catanionic vesicles may be successfully applied to induce the folding transition in a large single linear DNA and adsorption of DNA globules onto the surface of the vesicles. Recharging of the vesicles through the change of the molar ratio between cationic and anionic lipids in the solution leads to the DNA unfolding and release to the bulk solution. Therefore, these observations might be of interest from the perspective of a controlled DNA delivery *in vitro* and *in vivo*. For this purpose, the conditions for the formation of catanionic vesicles from the mixtures of oppositely charged biocompatible lipids should be additionally studied.

In conclusion, mixed charged vesicles are shown to interact strongly with polyelectrolytes. Lateral domain formation in membranes, changes in vesicular shape, formation of disk-like aggregates and networks, and membrane adsorption are

phenomena that have been reported, drawing increasing interest to such types of polymer-surfactant systems.

## ACKNOWLEDGMENTS

EFM was a former Ph.D. student of Coimbra University and Lund University, supported by PRAXIS XXI, CAP and TFR. RD is a current joint Ph.D. student of Coimbra/Lund Universities, supported by PRAXIS XXI and NFR. MM held a visiting professorship in Lund supported by CAP. AK was supported by CAP and TFR. BL was a visiting professor in Coimbra. Oren Regev is thanked for discussions and part of the cryo-TEM work.

## REFERENCES

1. K Ogino, A Masahiko. *Mixed Surfactant Systems*. Marcel Dekker, New York, 1993.
2. PM Holland, DN Rubingh. *Mixed Surfactant Systems*. ACS, Washington, DC, 1992.
3. A Khan, E Marques. *Catanionic Surfactants*. In: *Specialists Surfactants* ID Robb, ed. London, Blackie Academic and Professional, an imprint of Chapman & Hall, 1997, pp 37–76.
4. B Kronberg. *Curr Opin Colloid Interface Sci* 2:456–463, 1997.
5. A Khan, EF Marques. *Curr Opin Colloid Interface Sci* 4:402–410, 2000.
6. K Thalberg, B Lindman. *Polyelectrolyte-ionic surfactant systems*. In: *Surfactants in Solution*. K Mittal, OO Shah, eds. Plenum Press, New York, 1991.
7. L Piculell, B Lindman. *Adv Colloid Interface Sci* 41:149–178, 1992.
8. ED Goddard, KP Ananthapadmanabhan. *Interactions of Surfactants with Polymer and Proteins*. CRC Press, Boca Raton, FL, 1993.
9. B Jönsson, B Lindman, K Holmberg, B Kronberg. *Surfactants and Polymers in Aqueous Solution*. Wiley, New York, 1998.
10. L Piculell, B Lindman, G Karlström. *Phase behavior of polymer/surfactant systems*. In: *Polymer-Surfactant Systems*. JCT Kwak, ed. Marcel Dekker, New York, 1998.
11. E Marques, A Khan, MG Miguel, B Lindman. *J Phys Chem* 97:4729–4736, 1993.
12. EF Marques, O Regev, A Khan, M Miguel, B Lindman. *J Phys Chem B* 102:6746–6758, 1998.
13. EF Marques, O Regev, A Khan, MG Miguel, B Lindman. *J Phys Chem B* 103:8353–8363, 1999.
14. EF Marques. *Langmuir* 16:4798–4807, 2000.
15. EF Marques, O Regev, A Khan, MG Miguel, B Lindman. *Macromolecules* 32:6626–6637, 1999. (b) O Regev, EF Marques, A Khan. *Langmuir* 15:642–645, 1999.
16. SM Mel'nikov, R Dias, Y Mel'nikova, EF Marques, MG Miguel, B Lindman. *FEBS Lett* 453:113–118, 1999.
17. DF Evans, H Wennerstrom. *The Colloidal Domain: Where Physics, Chemistry, Biology and Technology Meet*. 2nd ed. Wiley-VCH, New York, 1999.
18. F Guillemet, L Piculell. *J Phys Chem* 99:9201–9209, 1995.
19. ED Goddard. *Polymer-Surfactant Interaction. Part II. Polymer and Surfactant of Opposite Charge*. In: *Interactions of Surfactants with Polymers and Proteins* ED Goddard, KP Ananthapadmanabhan, eds. CRC Press, Boca Raton, FL, 1993.

20. K Thalberg. Polyelectrolyte-Surfactant Interactions. PhD dissertation, University of Lund, Sweden, 1990.
21. A Graciaa, MB Ghoulam, G Marion, J Lachaise. *J Phys Chem* 93:4167–4173, 1989.
22. Z-J Yu, G-X Zhao. *J Colloid Interface Sci* 156:325–328, 1993.
23. Z Huang, Z Yan, T Gu. *Colloids Surfaces* 36:353–358, 1989.
24. L Capovilla, P Labbé, G Reverdy. *Langmuir* 7:2000–2003, 1991.
25. D Góralczyk. *Colloid Polym Sci* 272:204–210, 1994.
26. L Hecker, LW Reeves, AS Tracey. *Mol Cryst Liq Cryst* 53:77–87, 1979.
27. P Boonbrahm, A Saupe. *Mol Cryst Liq Cryst* 109:223–232, 1984.
28. CL Mesa, A Khan, K Fontell, B Lindman. *J Colloid Interface Sci* 103:373–391, 1985.
29. K Tamori, K Kihara, H Sanda, K Esumi, K Meguro, C Thuning, H Hoffmann. *Colloid Polym Sci* 270:885–893, 1992.
30. A Caria, A Khan. *Langmuir* 12:6282–6290, 1996.
31. H Edlund, A Sadaghiani, A Khan. *Langmuir* 13:4953–4963, 1997.
32. JC Amante, JF Scamehorn, JF Harwell. *J Colloid Interface Sci* 144:243–253, 1991.
33. KL Herrington, EW Kaler, DD Miller, JA Zasadzinski, S Chiruvolu. *J Phys Chem* 97:13792–13802, 1993.
34. N Filipovic-Vincekovic, M Bujan, D Dragcevic, N Nekic. *Colloid Polym Sci* 273:182–188, 1995.
35. MS Vethamuthu, M Almgren, W Brown, E Mukhtar. *J Colloid Interface Sci* 174:461–479, 1995.
36. J Eastoe, P Rogueda, D Shariatmadari, R Heenan. *Colloids Surfaces* 117:215–225, 1996.
37. O Regev, A Khan. *J Colloid Interface Sci* 182:95–109, 1996.
38. PA Hassan, BS Valaulikar, C Manohar, F Kern, L Bourdieu, SJ Candau. *Langmuir* 12:4350–4357, 1996.
39. P Jokela, B Jönsson, A Khan. *J Phys Chem* 91:3291–3298, 1987.
40. P Jokela, B Jönsson. *J Phys Chem* 92:1923–1927, 1988.
41. B Jönsson, P Jokela, A Khan, B Lindman, A Sadaghiani. *Langmuir* 7:889–895, 1991.
42. AS Sadaghiani, A Khan. *J Colloid Interface Sci* 146:69–78, 1991.
43. A Malliaris, W Binana-Limbele, R Zana. *J Colloid Interface Sci* 110:114–120, 1986.
44. MS Vethamuthu, M Almgren, E Mukhtar, P Bahadur. *Langmuir* 8:2396–2404, 1992.
45. P Jokela, B Jönsson, H Wennerstrom. *Progr Colloid Polym Sci* 70:17–22, 1985.
46. DD Lasic. *Liposomes: From Physics to Applications*. Elsevier, Amsterdam, 1993.
47. BW Ninham, DF Evans. *Faraday discussions. Chem Soc* 81:1–17, 1986.
48. JN Israelachvili. *Intermolecular and Surface Forces*. 2nd ed. Academic Press, San Diego, 1992.
49. W Helfrich. *Z Naturforsch* 28 C:683–703, 1973.
50. SA Safran, P Pincus, A Andelman, FC Mackintosh. *Phys Rev* 43:1071–1078, 1991.
51. SA Safran, PA Pincus, DA Andelman. *Science* 248:354–356, 1990.
52. M. Bergström. *Langmuir* 12:2454–2463, 1996.
53. PK Yuet, D Blankshtein. *Langmuir* 12:3802–3818, 1996.
54. J Oberdisse, G Porte. *Phys Rev E* 56:1965–1975, 1997.
55. Y Talmon, DF Evans, BW Ninham. *Science* 221:1047–1048, 1983.
56. JE Brady, DF Evans, B Kachar, BW Ninham. *J Am Chem Soc* 106:4279–4280, 1984.
57. DF Evans, BW Ninham. *J Phys Chem* 90:226–234, 1986.
58. O Regev, C Kang, A Khan. *J Phys Chem* 98:6619–6625, 1994.
59. P Hervé, D Roux, A-M Belloq, F Nallet, T Gulik-Krzywicki. *J Phys II France* 3:1255–1270, 1993.

60. H Hoffmann, C Thunig, U Munkert. *Langmuir* 8:2629–2638, 1992.
61. H Hoffmann, U Munkert, C Thunig, M Valiente. *J Colloid Interface Sci* 163; 217–228, 1994.
62. H Hoffmann, C Thunig, P Schmiedel, U Munkert. *Langmuir* 10:3972–3981, 1994.
63. J Oberdisse, O Regev, G Porte. *J Phys Chem B* 102:1102–1108, 1998.
64. EW Kaler, AK Murthy, BE Rodriguez, JA Zasadzinski. *Science* 245:1371–1374, 1989.
65. EW Kaler, KL Herrington, AK Murthy, JA Zasadzinski. *J Phys Chem* 96:6698–6707, 1992.
66. KL Herrington, EW Kaler, DD Miller, JA Zasadzinski, S Chiruvolu. *J Phys Chem* 97:13792–13802, 1993.
67. MT Yacilla, KL Herrington, LL Brasher, EW Kaler. *J Phys Chem* 100:5874–5879, 1996.
68. O Söderman, KL Herrington, EW Kaler, DD Miller. *Langmuir* 13:5531–5538, 1997.
69. M Ambühl, E Bangerter, PL Luisi, P Skrabal, HJ Watzke. *Progr Colloid Polym Sci* 93:183–184, 1993.
70. Y Kondo, H Uchiyama, N Yoshino, K Nihyama, M Abe. *Langmuir* 11:2380–2384, 1995.
71. II Yaacob, A Bose. *J Colloid Interface Sci* 178:638–647, 1996.
72. RA Salkar, D Mukesh, SD Samant, C Manohar. *Langmuir* 14:3778–3782, 1998.
73. A Caria, O Regev, A Khan. *J Colloid Interface Sci* 200:19–30, 1998.
74. T Kuhl, YQ Guo, JL Alderfer, AD Berman, D Leckband, J Israelachvili, SW Hui. *Langmuir* 12:3003–3014, 1996.
75. JC Van de Pas, CJ Buytenhek. *Colloids Surfaces* 68:127–139, 1992.
76. K Løyn, I Iliopoulos, R Audebert, U Olsson. *Langmuir* 11:1053–1056, 1995.
77. W Meier, J Hotz, S Günther-Ausborn. *Langmuir* 12:5028–5032, 1996.
78. J Kevelam, JFL Breemen, W Blokzijl, JBFN Engberts. *Langmuir* 12:4709–4717, 1996.
79. A Polozova. *Biochim Biophys Acta* 1326:213–224, 1997.
80. MD Everaars, AC Nieuwkerk, S Denis, ATM Marcelis, EJR Sudhölter. *Langmuir* 12:4042–4043, 1996.
81. I Porcar, R Garcia, C Gómez, A Campos, C Abad. *Polymer* 38:5107–5113, 1997.
82. A Raudino, F Castelli. *Macromolecules* 30:2495–2502, 1997.
83. A Murphy, A Hill, B Vincent. *Ber Bunsen Phys Chem* 100:963–971, 1996.
84. DD Lasic. *Liposomes in Gene Delivery*. CRC Press, Boca Raton, FL, 1997.
85. DD Lasic, NS Templeton. *Adv Drug Del Rev* 20:221–266, 1996.
86. K Hayakawa, JCT Kwak. *Interactions Between Polymers and Cationic Surfactants*. In: *Cationic Surfactants: Physical Chemistry* DN Rubingh, PM Holland, eds. Marcel Dekker, New York, 1991, pp 189–248.
87. SM Mel'nikov, VG Sergeyev, K Yoshikawa. *Visualization of DNA-Surfactant Interactions with Fluorescence Microscopy*. In: *Recent Research Developments in Chemical Sciences* SG Pandalai, ed. Trivandrum, 1997, pp 69–113.
88. SM Mel'nikov, VG Sergeyev, K Yoshikawa. *J Am Chem Soc* 117:2401–2408, 1995.
89. SM Mel'nikov, VG Sergeyev, K Yoshikawa. *J Am Chem Soc* 117:9951–9956, 1995.
90. SM Mel'nikov, VG Sergeyev. *Biochem Biophys Res Commun* 230:514–517, 1997.
91. ED Goddard, RB Hannan. *J Am Oil Chem Soc* 54:561–566, 1997.
92. I Porcar, R Garcia, V Soria, A Campos. *Polymer* 38:3553–3560, 1997.
93. KJ Crowell, PM Macdonald. *J Phys Chem B* 102:9091–9100, 1998.
94. CM Franzin, PM Macdonald, A Polozova, FM Winnik. *Biochim Biophys Acta*

1415:219–234, 1998.

95. AA Yaroslavov, EA Kiseliova, OY Udalykh, VA Kabanov. *Langmuir* 14:5160–5163, 1998.

96. LL Brasher, KL Herrington, EW Kaler. *Langmuir* 1:4267–4277, 1995.

97. AA Yaroslavov, VE Koulikov, EG Yaroslavova, MO Ignatiev, VA Kabanov, FM Menger. *Langmuir* 14:5999–6004, 1998.

98. A Polozova, FM Winnik. *Langmuir* 15:4222–4229, 1999.

99. NS Templeton, DD Lasic, PM Frederik, HH Strey, DD Roberts, GN Pavlakis. *Nat Biotechnol* 15:647–652, 1997.



## 5

# Metal Nanoparticle Formation in Polyelectrolyte Gels with Regular Microstructures

**LYUDMILA M.BRONSTEIN** *Indiana University, Bloomington, Indiana*

**DMITRI I.SVERGUN** *European Molecular Biology Laboratory, Hamburg,  
Germany, and Institute of Crystallography, Russian Academy of Sciences,  
Moscow, Russia*

**ALEXEI R.KHOKHLOV** *Moscow State University, Moscow, Russia*

## I. METAL NANOPARTICLE FORMATION IN NANOSTRUCTURED ENVIRONMENT

Nanosized metal particles have huge surface areas and possess unique properties that can be employed in a wide range of chemical and physical applications: catalysis, nonlinear optics, semiconductors, microelectronics, and others [1–4]. Properties of metal colloids depend strongly on the particle shapes, size distributions, and chemical environment. The use of a polymeric matrix as a medium for metal nanoparticle formation not only allows one to stabilize the particles and to control the nanoparticle growth but also to impart new properties to the matrix itself. A better control of the nanoparticle growth is achieved in nanostructured matrices such as amphiphilic block copolymers in bulk or block copolymer micelles [5–10]. Most well-defined amphiphilic block copolymers (most efficient in nanoparticle control) are still synthesized by anionic polymerization demanding a high degree of purification at all the steps of synthetic procedure. A very robust alternative way for the preparation of metal nanoparticles in an ordered polymeric environment in aqueous media is discussed in this chapter. Here we consider polyelectrolyte gels forming nanostructures under particular conditions as an external template controlling the nanoparticle growth. The charged groups in the hydrogel are able to attract the metal ions of interest, whereas the internal structure of the gel controls the nanoparticle formation. The metal-nanoparticle-containing hydrogels may serve as nonconventional actuators, sensors, catalysts, or controlled delivery systems.

## II. INCORPORATION OF METAL IONS OR METAL NANOPARTICLES IN POLYELECTROLYTE GELS

Polyelectrolyte gels are extensively studied as ion-exchange systems capable of taking up different kinds of ions [11–13]. The influence of pH on chromium ion retention and

desorption was analyzed using  $\text{CrCl}_3$  in polyacrylic acid gels [12]. *N*-isopropyl acrylamide (NIPA) copolymers containing acidic groups were studied in Zn, Ni, and Cr uptake [11]. A peculiar feature of these block copolymers is their ability to collapse; that is, to form microstructures owing to a phase transition between the hydrated and dehydrated states of the polymer chains, which occurs at around 32°C for homopolymer NIPA. The study of the ion uptake displayed no temperature dependence of the microphase separation, although for metal nanoparticle formation such a dependence might be expected.

Another approach for incorporating metals (broadly discussed for polyelectrolyte gels) deals with anchoring metal colloids [14–16]. In this way, magnetic field-sensitive gels, called ferrogels, can be prepared. Ferrogels are chemically cross-linked polymer networks swollen by a ferrofluid [14, 16]. These ferrogels can be prepared either by swelling the preliminary cross-linked gels or by cross linking the polymer chains in the solution of magnetic particles. Neither way allows control over the properties of the particles formed in nonpolymeric media. A similar approach was described by Dauben et al. [15] for preparation of catalytically active materials. Thus, the above advantages of the polyelectrolyte gel structure were not realized in the development of metal-containing polymer gels.

Based on published results and on our own experience in metal nanoparticle formation in polymeric systems, we believed that development of microstructures or nanostructures in the polymeric environment should provide necessary control over the metal particle growth and, as a consequence, over the properties of the material in general. Moreover, strict limitations on particle sizes are required for development of catalytically active systems (the smaller the particles, the higher the catalytic activity). In this chapter, we will describe two approaches using two microsegregated polymeric systems to solve the problem of control of nanoparticle growth in polyelectrolyte gels. These two approaches are microgels and complexes of polyelectrolyte macrogels with oppositely charged surfactants.

### III. METAL NANOPARTICLE FORMATION IN POLYSTYRENE SULFONATE MICROGELS

Microgels are spherical polymer gel particles [17, 18] with a well-defined diameter in the nanometer range. Their limited size along with cross linking within the microgel particles allow considering them as nanoreactors; that is, structure-directing molecular containers for the nanoparticle growth. Using reduction of a gold salt to gold nanoparticles as a model reaction allowed us to observe regularities in the metal nanoparticle formation [19]. Influence of the reduction rate and microgel characteristics have been studied. Three typical morphologies obtained by varying the reduction conditions are possible. Fast reduction with  $\text{NaBH}_4$  in water produced small Au nanoparticles (4.5 nm, as revealed by wide-angle x-ray scattering [WAXS]) located in the microgels. Decrease of the reduction rate by addition of  $\text{NaBH}_4$  in 0.1N NaOH resulted in another morphology: long gold threads containing particles of 7 nm in diameter (by WAXS and transmission electron microscopy [TEM]). Use of a sluggish reducing agent, hydrazine, results in larger



particles (25 nm), which are combined in selected microgels. Moreover, analytical ultracentrifugation showed that for slower nucleation only 15% (for hydrazine) and 20% (for  $\text{NaBH}_4$  in 0.1N NaOH) of the microgels are filled with gold particles, whereas others are empty at the end of reduction. Formation of larger, complex colloids shows that rate of nucleation is lower than the rates of mass transfer and growth. This results in transfer of gold ions from neighboring microgels and uneven growth of colloids.

Another factor strongly affecting the colloid and sample morphology is the microgel cross-linking density. The higher the cross-linking density, the higher the probability of formation of spherical particles embedded in microgels (under a wider range of reaction conditions). The high-resolution TEM revealed a remarkable correlation of the crystallographic Au(111) planes in gold nanoparticles, which is only slightly disturbed by the outer particle curvature. This confirmed that the particles grew from one nucleus, whereas the microgel environment determined the outer shape of the particles. The growth of the particles under  $\text{NaBH}_4$  reduction is restricted by the elastic forces of the surrounding gel matrix. This means that the particles grow along a given direction until the surrounding polymer chains are fully stretched in this direction. The system thus provides “cage”-like effect, although, in this case, the “cage” is not a rigid environment.

Besides the gold nanoparticles, Pd and Pt ones were prepared using a similar procedure. Further, after the nanoparticles were formed in the microgel environment, the microgels were used as cotemplates along with polystyrene-block-poly(ethylene oxide) block copolymer (SE10/10, Goldschmidt AG) in mesoporous silica formation [20]. Here, the microgels fulfill two tasks: They serve as nanoreactors for metal nanoparticle formation and as templates for mesoporous material casting.

#### **IV. POLYELECTROLYTE GEL/SURFACTANT COMPLEXES AS NANOSTRUCTURED MEDIUM FOR INTERACTION WITH METAL IONS AND METAL NANOPARTICLE FORMATION**

Complexes of polyelectrolyte gels with oppositely charged surfactants have intensively been studied in recent years [21–29]. This is mainly because these complexes exhibit highly regular self-assembled nanostructures as revealed by small-angle x-ray scattering (SAXS) studies [24–29]. Both the complexes of anionic gel/cationic surfactants and cationic gel/anionic surfactants were found to exhibit extremely sharp and intensive SAXS peaks which manifest a high degree of order in the spatial arrangement of surfactants within the gel. The statistical disorder of the gel does not destroy the regular arrangement of surfactant aggregates: It was shown that the average mesh size of the gel is much smaller than the spatial scale over which the surfactant aggregates are arranged in a perfect crystalline order [27, 28]. Moreover, the surfactants within the oppositely charged gels are better ordered than in the pure aqueous medium (at the same concentration of the surfactants) [28]. The spatial order of the gel/surfactant complexes may provide a nanostructured environment for the metal nanoparticle formation. One could expect that the size, shape, and size distribution of the emerging nanoparticles will be controlled by the state of the surrounding polymer/surfactant matrix, which can be easily varied by changing the external parameters. The stability of the resulting metal

colloidal particles will be ensured by embedding them in the body of a hydrogel.

However, polyelectrolyte gel/oppositely charged surfactant complexes appear to be “self-sufficient”; that is, too stable for any additional reactions. Indeed, they are stabilized by two types of interactions: (1) electrostatic interactions between surfactant head groups and charged groups of hydrogel and (2) strong hydrophobic interactions between surfactant tails providing the ordering in the system. In order to interact with metal ions, either surfactant ions or hydrogel-charged groups should be replaced, which demands a strong driving force. If such an interaction does occur, several questions arise:

Do noble and transition metal cations and anions penetrate in such well-defined structures as hydrogel/surfactant complexes?

What is the structure of hydrogel/surfactant complex after the interaction with monovalent and bivalent metal ions and after metal nanoparticle formation. Is the ordering preserved?

What particles are formed in such hydrogel/surfactant systems?

Three polyelectrolyte gel/surfactant systems were studied: a complex of the anionic gel of poly(methacrylic acid) (PMA) with the cationic surfactant cetylpyridinium chloride (CPC) and complexes of the cationic gel of poly(diallyldimethylammonium chloride) (PDADMACl) with two anionic surfactants: sodium dodecyl sulfate (SDS) and sodium dodecylbenzenesulfonate (SDBS).

### **A. Probing the Nanostructure by Small-Angle X-Ray Scattering**

As discussed above, physical and chemical properties (e.g., catalytic and optical ones) of the nanoparticle-containing systems are largely determined by the particle size and particle size distributions. As most of such systems are designed for use in aqueous media, nondestructive analysis methods are required to probe the size distributions under native conditions. The methods like electron and atomic force microscopy employ special treatment of the specimen, which may distort the structure of the sample [30]. In contrast, SAXS allows one to study native systems in aqueous environment. This technique is widely used to analyze disperse systems of different physical nature; for example, solutions of biological macromolecules, polymers in solution and in bulk, microemulsions, alloys, and ceramics [31].

First, we shall briefly outline the basics of the technique. In a SAXS experiment, the sample is irradiated by x-rays of wavelength  $\lambda$ , and the scattering intensity,  $I$ , is recorded. The scattering from disordered or weakly ordered disperse systems is usually isotropic, and the signal depends only on modulus of the scattering vector  $s=4\pi \sin \theta/\lambda$ , where  $2\theta$  is the scattering angle. The intensity  $I(s)$  is mostly concentrated at small angles and provides information about the structural elements with characteristic sizes much larger than the wavelength. The x-rays suitable for the structural studies have the wavelength approximately  $\lambda=0.1$  nm, so the SAXS permits us to characterize the samples at the resolution ranging from approximately 1–100 nm.

The scattering of the x-rays emerges because of inhomogeneities of the electron density distribution in the object. Figure 1 schematically shows a sample consisting of a partially ordered polymer matrix with embedded nano-particles. The scattering pattern from this system consists of two major components. The former, particle scattering, appears to be due to the difference between the electron density of particles and that of the matrix. This term usually dominates the scattering at smaller angles and bears information about the particle sizes. The latter component containing scattering from the internal inhomogeneities within the matrix is more significant at higher angles and may display one or several distinct maxima (Bragg peaks) providing information about the internal ordering in the polymer matrix. Separation of these two terms permits

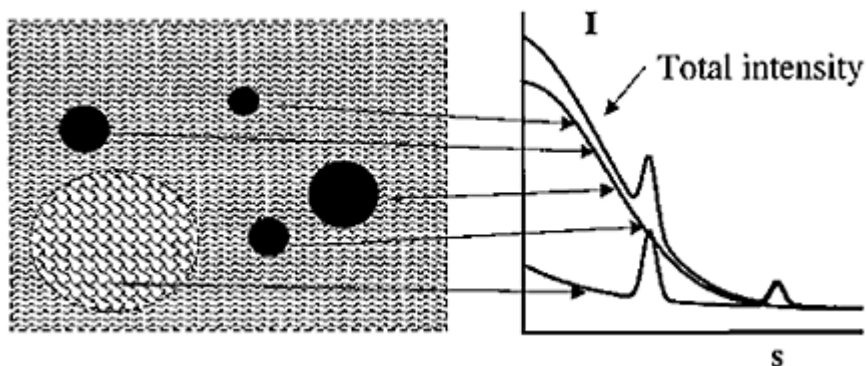
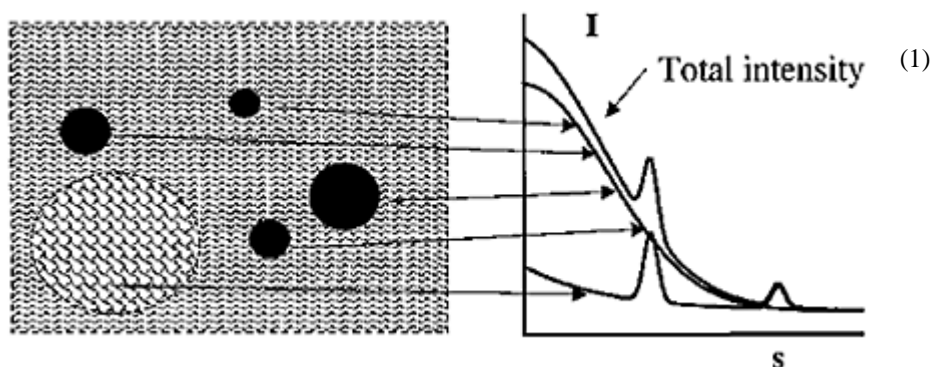


**FIG. 1** Schematic representation of an ordered polymer matrix with embedded nanoparticles and its major scattering components.

one to characterize both the nanoparticles and the internal structure of the polymer matrix.

Let us consider the scattering from an ensemble of nanoparticles with different sizes but similar shape (we assume a spherical shape for simplicity). Introducing the volume distribution function  $D_V(R)=N(R)V(R)$ , where  $N(R)$  is the number of particles with radius,  $R$ , and  $V(R)=(4\pi/3)R^3$  is the volume of a sphere, the scattering intensity from the ensemble can be written as [31]



where  $R_{\max}$  is the maximum particle radius in the ensemble,  $i_0(x) = \{[\sin(x) - x\cos(x)]/x^3\}^2$  is the sphere form factor, and the contrast  $\Delta\rho$  is the electron density difference between the particles and the matrix. An estimate of the average particle size is given by the radius of gyration  $R_g = (3/5)^{1/2} \langle R \rangle$ , where  $\langle R \rangle$  denotes an average sphere radius in the system. Given the intensity  $I(s)$ , Eq. (1) can be solved with respect to  $D_V(R)$  yielding the size distribution of particles in the system. Solving this equation is not a trivial task, as the result is sensitive with respect to the experimental errors. We employed an indirect transformation program, GNOM [32], that uses a regularization method to provide a stable solution. The value of the maximum radius is usually not known in advance but can be estimated by running the program several times with different values of  $R_{\max}$ .

The scattering from an ordered matrix is analyzed using the Bragg peaks in the scattering pattern. The position of the first peak  $s_{\max}$  yields the spacing between the neighboring periodic motifs as  $\bar{d} = 2\pi/s_{\max}$ . The width of the peak provides the long-range order dimension,  $L$ , and the degree of disorder,  $\Delta/\bar{d}$ , following the equations [33].

$$L = \frac{\lambda}{\beta_s \cos \theta} \quad (2)$$

$$\Delta/\bar{d} = \frac{1}{\pi} \cdot \sqrt{\frac{\beta_s \cdot \bar{d}}{\lambda}} \quad (3)$$

where  $\beta_s$  is the full width at a half-maximum intensity of the peak (in radians) observed at a mean scattering angle of  $2\theta$ . Physically,  $L$  estimates the size of quasicrystalline zones in the sample, whereas  $\Delta/\bar{d}$  estimates the relative mean square deviation of the repeating. In general, better-ordered systems yield sharper peaks; that is, larger  $L$  and smaller  $\Delta/\bar{d}$  (the Bragg peaks are nearly absent if  $\Delta/\bar{d} > 0.25$ ).

In the following sections, we shall present several examples of the use of SAXS to study particle size distributions and internal structures of different nanoparticle-containing polymer systems.

## B. Interaction of Polyelectrolyte Gel Surfactant Complex with Metal Ions

Figure 2 illustrates the collapse of both anionic and cationic gels upon addition of oppositely charged surfactants. Curves 4 and 5 show that collapse is connected with the absorption of surfactants. The mole ratio of the absorbed surfactant molecules and network monomer units in the collapsed phase is close to 1:1. The elemental analysis data in Table 1 show that for the complex PMA/CPC, this ratio reached 1:1; for the system PDADMACI/SDS, the molar ratio was 1/0.92; for PDADMACI/SDBS, it approached 1:1.2. For the preparation of the metalcontaining gel/surfactant complexes, a uniformly

collapsed piece of gel/surfactant complex was placed in an aqueous solution of a metal compound for 3 days at room temperature (concentration of metal ions was  $10^{-2}$  M) followed by washing with water and treatment with  $\text{N}_2\text{H}_4 \cdot \text{H}_2\text{O}$  or  $\text{NaBH}_4$  (in 10-fold excess toward metal ions) after degassing procedure [30, 34].

Figure 3 (curve 1) demonstrates the SAXS results for the PMA/CPC complex. Similar to [24, 25], we see here sharp peaks; that is, self-assembly of surfactants within the gel results in the formation of ordered structure. The PMA/CPC complexes were allowed to swell in the aqueous solutions of  $\text{H}_2\text{PtCl}_6$  and  $\text{AgNO}_3$ , which dissociate in water giving bivalent anion  $\text{PtCl}_6^{2-}$  and monovalent cation  $\text{Ag}(\text{H}_2\text{O})_2^+$  respectively. By elemental analysis (Table 2), a small fraction of bivalent anions of  $\text{PtCl}_6^{2-}$  penetrates into the PMA/CPC complex. For a homogeneous distribution of all the components, the content of Pt inside the gel would be 0.88 wt%, which fits well to Pt content found (Table 2). Therefore, in

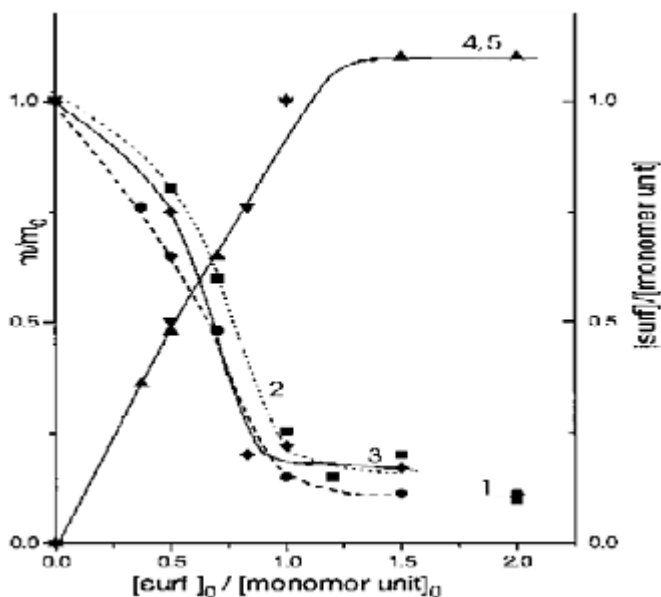


**FIG. 2** Dependence of relative mass of gel,  $m/m_0$  (curves 1, 2, 3), and the amount of absorbed surfactant (4, 5) on the initial surfactant concentration (mole ratio between the added surfactant molecules and network monomer units  $[\text{Surf.}]/[\text{monomer unit}]$ ) for complexes PMA/CPC (1, 4), PDADMACI/SDS (2), and PDADMACI/SDBS (3, 5). The amount of the absorbed surfactant is characterized by the mole ratio between absorbed CPC or SDBS molecules and PMA or PDADMACI network monomer units ( $[\text{Surf.}]/[\text{monomer unit}]$ ). Reprinted with permission from Ref. 34. Copyright (1998) American Chemical Society.

this case, there is no driving force for penetration of  $\text{PtCl}_6^{2-}$  inside the gel. Moreover, from the elemental analysis data in Table 2, one can notice that  $\text{H}_2\text{PtCl}_6$  in the outer solution induces a slight release of CPC by the gel: After exposure of the PMA/CPC complex to the  $\text{H}_2\text{PtCl}_6$  solution, the molar ratio PMA: CPC becomes 1.0:0.9. This can be explained by an increased acidity of the medium, which depresses the charge of the PMA carboxylic groups. In the case of  $\text{AgNO}_3$ , the molar ratio in the complex PMA/CPC was not disturbed and the amount of  $\text{Ag}^+$  ions penetrating the gel was much higher [34]. Because surfactant molecules were not replaced by metal ions, one may suggest that metal

**TABLE 1** Elemental Analysis Data for Complexes PMA/CPC, PDADMACI/SDS, and PDADMACI/SDBS in the Collapsed Phase

Element	PMA-CPC <sup>a</sup>		PDADMACI-SDS <sup>a</sup>		PDADMACI-SDBS <sup>a</sup>	
	(Wt%)		(wt%)		(wt%)	
	Found	Calculated	Found	Calculated	Found	Calculated
C	70.32	70.54	57.70	57.16	65.22	64.86
H	10.41	10.90	9.69	10.50	9.97	9.82
N	3.64	3.29	3.30	3.50	2.36	2.55
S	—	—	6.69	7.36	7.30	7.01
Cl	1.35	0.84	0.50	0.71	—	—
Na	0.30	0.54	—	—	0.60	0.84
Composition $(\text{PMA}_n + \text{CPCat})^+{}^b$ $(\text{PDADMACat} + 0.088\text{Cl}^- + {}^c(\text{PDADMACat} + {}^d$ $0.1\text{NaCl} + 1.7\text{H}_2\text{O}$ $0.92\text{DSAn}) + 1.5\text{H}_2\text{O}$ $1.2\text{DBMSAn} + 0.2\text{Na}^+)$ $+ 1.5\text{H}_2\text{O}$						

<sup>a</sup> Surfactant concentration in outer solution is  $5 \cdot 10^{-3}$  M for CPC,  $5 \cdot 10^{-4}$  M for SDS, and  $5 \cdot 10^{-3}$  M SDBS.

<sup>b</sup> PMA<sub>n</sub>: poly(methacrylic acid) anion, CPCat: cetylpridinium cation.

<sup>c</sup> PDADMACat: polydiallyldimethylammonium cation, DSAn: dodecyl sulfate anion.

<sup>d</sup> DBSAn: dodecyl benzenesulfonate anion.

Source: Ref. 34.

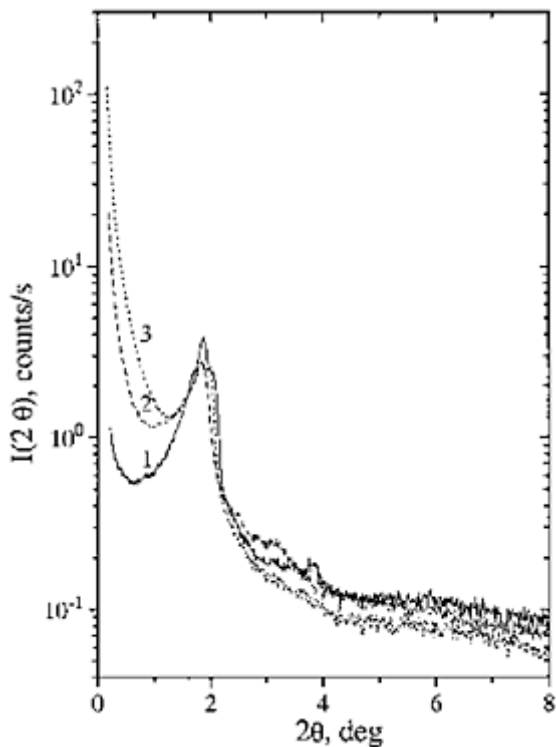


**FIG. 3** SAXS profiles of PMA/CPC complex (1), of PMA/CPC+AgNO<sub>3</sub> (2), and after subsequent reduction of Ag<sup>+</sup> cations with UV irradiation (3). (From Ref. 34.)

**TABLE 2** Elemental Analysis Data for PMA/CPC Complex After Interaction with H<sub>2</sub>PtCl<sub>6</sub> and AgNO<sub>3</sub>

Element	H <sub>2</sub> PtCl <sub>6</sub> (wt%)		AgNO <sub>3</sub> (wt%)	
	Found	Calculated	Found	Calculated
C	70.82	70.68	67.64	67.41
H	10.42	10.73	10.08	9.91
N	3.26	3.24	3.84	3.77
Cl	2.21	2.01	0.73	0.79
Met	1.06	1.01	4.03	4.81
Na	—	—	0.20	0.10
Charged gel units/ metal ion (mol)	50:1		5:1	
Composition	(PMA <sub>n</sub> +0.9CPCat + 0.1H <sup>+</sup> ) +0.1HCl + 0.02H <sub>2</sub> PtCl <sub>6</sub> +H <sub>2</sub> O		(PMA <sub>n</sub> +CPCat) + 0.01NaCl+0.2AgNO <sub>3</sub> +	

---

Salt concentration in outer solution is 10 M.

*Source:* Ref. 34.

ions along with their counterions form a bilayer between hydrogel-charged groups and surfactant head groups.

Similar studies on the PDADMACI/SDS and PDADMACI/SBDS complexes showed that noticeable penetration of the metal ions in the hydrogel/surfactant complexes (4–6 wt% metal in dry sample) occurs only when metal ions are oppositely charged with respect to the charged groups of hydrogel. Moreover, comparison of Figures 4 and 5 presenting the SAXS profiles after incorporation of the metal compound, and metal particle formation for all three systems suggests that different structural changes take place [34]. For the PMA/CPC system, incorporation of oppositely charged metal ions and metal particle formation in the gels does not destroy the surfactant ordering despite the high degree of penetration of metal cations in the gel. This means that the PMA/CPC complex produces very well-defined and stable structures. In contrast, the PDADMACI/SDS complex is rather unstable, and its internal nanostructure is influenced by growing metal nanoparticles. On the other hand, highly ordered nanostructures formed by SBDS in PDADMACI gel are more stable, and Pt



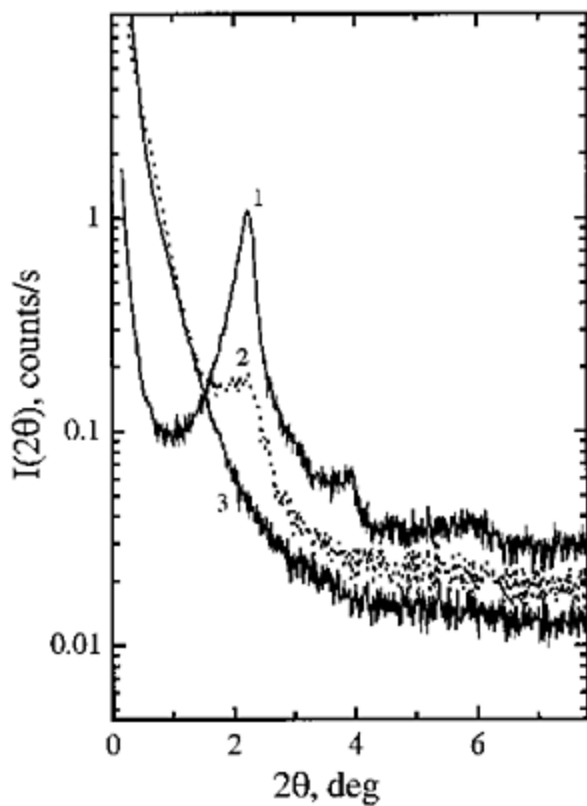


**FIG. 4** SAXS profiles of PDADMACI/SDS complex (1), of PDADMACI/SDS+ $\text{H}_2\text{PtCl}_6$  (2), and after its subsequent reduction with  $\text{NaBH}_4$  (3). (From Ref. 34.)

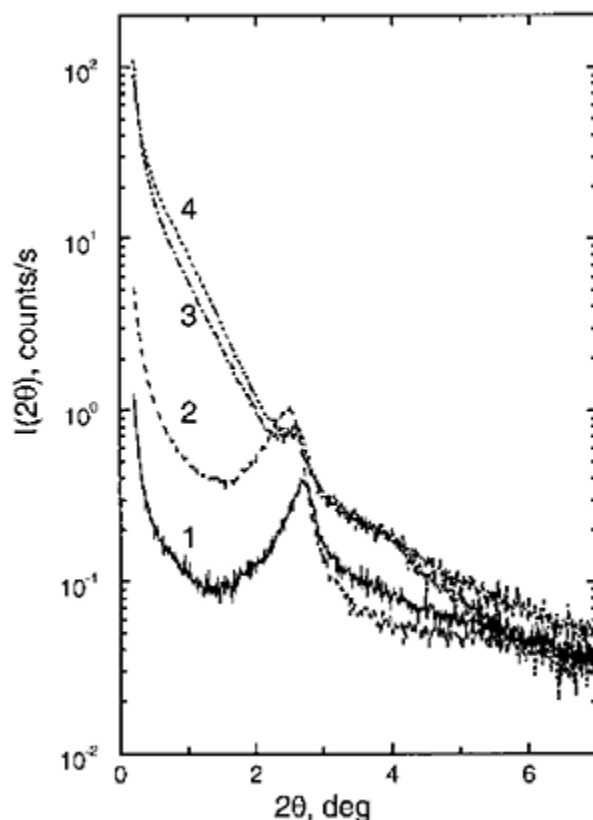


**FIG. 5** SAXS profiles of PDADMACl/SDBS complex (1), of PDADMACl/SBDS+H<sub>2</sub>PtCl<sub>6</sub> system (2), and after its subsequent reduction with N<sub>2</sub>H<sub>4</sub> (3) and NaBH<sub>4</sub> (4). (From Ref. 34.)

particle growth disturbs them only partially. The cause of this different behavior may be connected with different mechanisms of hydrophobic interactions between surfactant molecules in each system. An optimum situation corresponds to the exact fitting of the distance between the charges on the chain ( $S$ ) and the distance between hydrocarbon tails ( $l$ ) in the surfactant layers. In the orthorhombic unit cell of high-density polyethylene, the two main distances between polymer chains are  $l_1=4.45$  Å and  $l_2=4.93$  Å [35].

On the other hand, from Figure 6, one can see that the distance between two PMA carboxylic groups in *cis* position,  $a$ , is 5.06 Å, whereas the distance between two neighboring charged groups in PDADMACl,  $b$ , is about 7.2 Å. The PMA/CPC complex is closer to the exact matching situation. In contrast, for PDADMACl/SDS, the values  $l_2=4.93$  Å and  $b=7.2$  Å are far from matching, and the optimum complex providing maximum hydrophobic interactions of hydrocarbon surfactant tails cannot be realized. Therefore, the highest stability

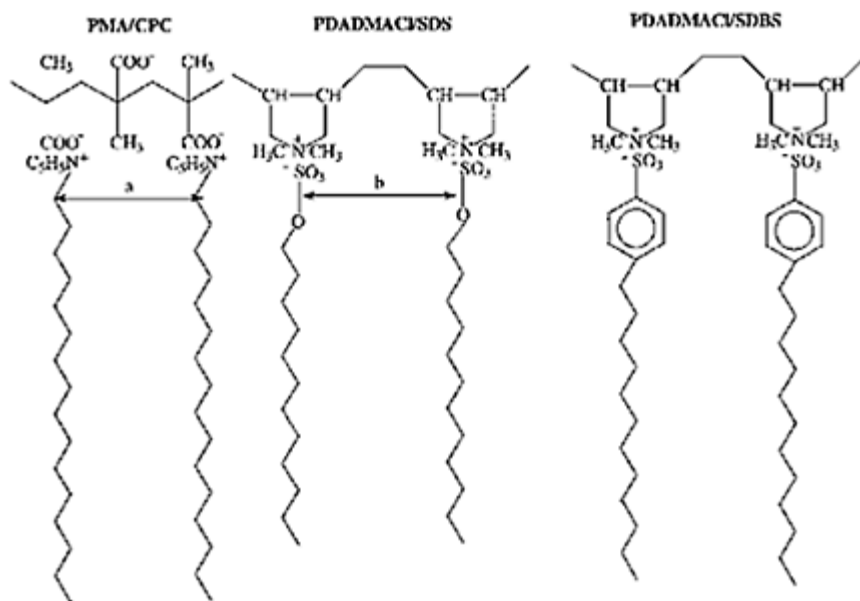


**FIG. 6** Schematic representation of PMA/CPC, PDADMAC/SDS, and PDADMAC/SDBS complexes. (From Ref. 34.)

of PMA/CPC sounds reasonable. As to the PDADMAC/SDBS complex, one can assume that strong  $\pi$ - $\pi$  interaction between benzene rings of SDBS molecules located mainly parallel to each other results in additional hydrophobic interaction between surfactant molecules, providing the relatively higher stability of PDADMAC/SDBS complex [34]. Thus, the PDADMAC/SDS complex should be the weakest one among all the systems studied, which is indeed observed. The quantitative structural characterization of the metal-containing hydrogel/surfactant complexes by SAXS and anomalous SAXS (ASAXS) showed remarkably striking results on the degree of ordering and are discussed at the end of this chapter.

### C. SAXS Studies of Metal Nanoparticle Formation in Polyelectrolyte Gels

As the complexes of polyelectrolyte gels with oppositely charged surfactants exhibit regular internal nanostructure, one can expect that the shapes, sizes, and stability of the metal particles incorporated in the body of the hydrogels will be controlled by the state of the surrounding polymer-surfactant matrix which can be varied by changing the external parameters. A systematic study of the metal nanoparticle formation in such systems would yield information required to design a system with desired nanoparticle size distributions.

#### 1. Ordered Gel Environment Controls the Growth of Nanoparticles

Figure 7 presents experimental scattering data from a collapsed gel/surfactant complex of a cationic gel of poly(diallyldimethylammonium chloride) with an anionic surfactant sodium dodecyl sulfate (PDADMACI/SDS), recorded on a laboratory x-ray diffractometer, AMUR-K (Institute of Crystallography, Moscow) at a wavelength of  $\lambda=0.15$  nm [36]. The curve 2 from the collapsed gel PDADMACI/SDS displays virtually no central scattering (which would indicate the presence of nanoparticles), but a characteristic peak at  $s=1.7$  nm<sup>-1</sup> corresponding to a spacing of 3.7 nm in the ordered gel structure. Addition of H<sub>2</sub>AuCl<sub>4</sub> to the PDADMACI/SDS system (curve 3) diminishes the peak and noticeable central scattering appears. These effects indicate that the addition of the gold compound partially disrupts the gel/surfactant structure and promotes formation of nanoscale clusters. Further reduction of the gold ions with NaBH<sub>4</sub> (curve 4) increases the central scattering significantly and the peak disappears completely. This means that the cluster structure is enhanced, whereas the order in

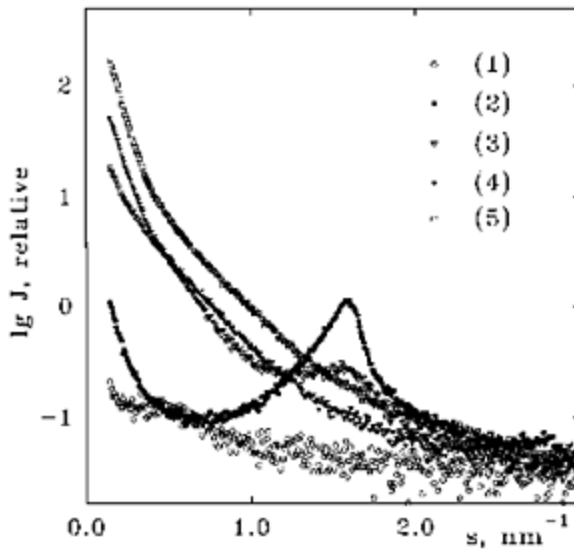


**FIG. 7** Experimental scattering curves for the system PDADMACI: empty cell (1); collapsed gel PDADMACI/SDS (2); PDADMACI/SDS with H<sub>2</sub>AuCl<sub>4</sub> added (3); PDADMACI/SDS with gold ions reduced by NaBH<sub>4</sub> (4), noncollapsed gel PDADMACI without SDS containing gold nanoparticles after NaBH<sub>4</sub> reduction (5). The curves are scaled to match the scattering from the empty cell at  $s>3$  nm<sup>-1</sup>. (From Ref. 36.)

the gel/surfactant complex is disrupted. These data are in agreement with those presented in Figure 4. Even higher central scattering is observed in curve 5 corresponding to the reduced gold particles in the initial (noncollapsed) gel without the surfactant.

In order to evaluate the particle size distributions using Eq. (1), net scattering from the nanosized particles should be obtained from the experimental data; that is, scattering

from the matrix should be properly subtracted from the total signal (see Fig. 1). For the  $\text{HAuCl}_4$ -containing system, the gel/surfactant complex structure is largely preserved, and this can be done by subtracting the gel/surfactant scattering from that of the  $\text{HAuCl}_4$ -gel complex. For the systems after the metal ions reduction, the gel/surfactant structure is completely disrupted so that the appropriately normalized scattering from the empty sample holder is subtracted. Although this approach does not hold over the entire angular range, it ensures proper matrix subtraction for the initial portions of the scattering curves ( $s < 12 \text{ nm}^{-1}$ ) sufficient to compute the particle size distributions.

Figure 8 presents the volume distribution functions computed by GNOM from the difference curves thus obtained. Addition of  $\text{HAuCl}_4$  to the PDADMACI/SDS complex (curve 1) yields clusters with an average  $R_g = 11.6 \pm 0.5 \text{ nm}$ , and their major fraction has radii of less than 10 nm. Presumably, these clusters are aggregates of the metal compound. After reduction of the metal ions (curve 2), the volume distribution still displays a maximum at approximately  $R = 5 \text{ nm}$ , but a significant amount of larger particles ( $R = 10\text{--}20 \text{ nm}$ ) appears and the radius of gyration increases to  $R_g = 15.5 \pm 0.8 \text{ nm}$ . Moreover, the magnitude of the function  $D_V(R)$  increases as compared to that for the  $\text{HAuCl}_4$ -gel complex (distribution 1 was multiplied by a factor of 5 for better visualization). As seen from Eq. (1), the numerically computed distribution function is proportional to the particle contrast  $\Delta\rho$ . As the contrast of the gold particles is much higher than that of the  $\text{HAuCl}_4$  compound clusters, the distributions in Figure 8 suggest that the clusters in the  $\text{HAuCl}_4$ /gel complex are formed by the gold compound, whereas the reduced samples contain pure metal nanoparticles. The noncollapsed PDADMACI gel without SDS is not structured and thus does not control the growth of the nanoparticles. This is clearly reflected in the corresponding distribution function (curve 3 in Fig. 8) displaying a significant portion of larger particles ( $R_g = 19.9 \pm 1.5 \text{ nm}$ ). Moreover, the size distributions further changes with aging as yet larger particles with the radii up to 40 nm are formed (curve 4,  $R_g = 22.5 \pm 0.6 \text{ nm}$ ). The aging effect is absent for the nanoparticles in the collapsed gel/surfactant complexes indicating that the aggregation of metal colloids is prevented by the surfactant structure in the collapsed gel.

## 2. Fast Reduction Yields Smaller Particles

It has recently been found [5, 37] that the type of the reducing agent strongly influences particle sizes of the metal colloids prepared in block copolymers

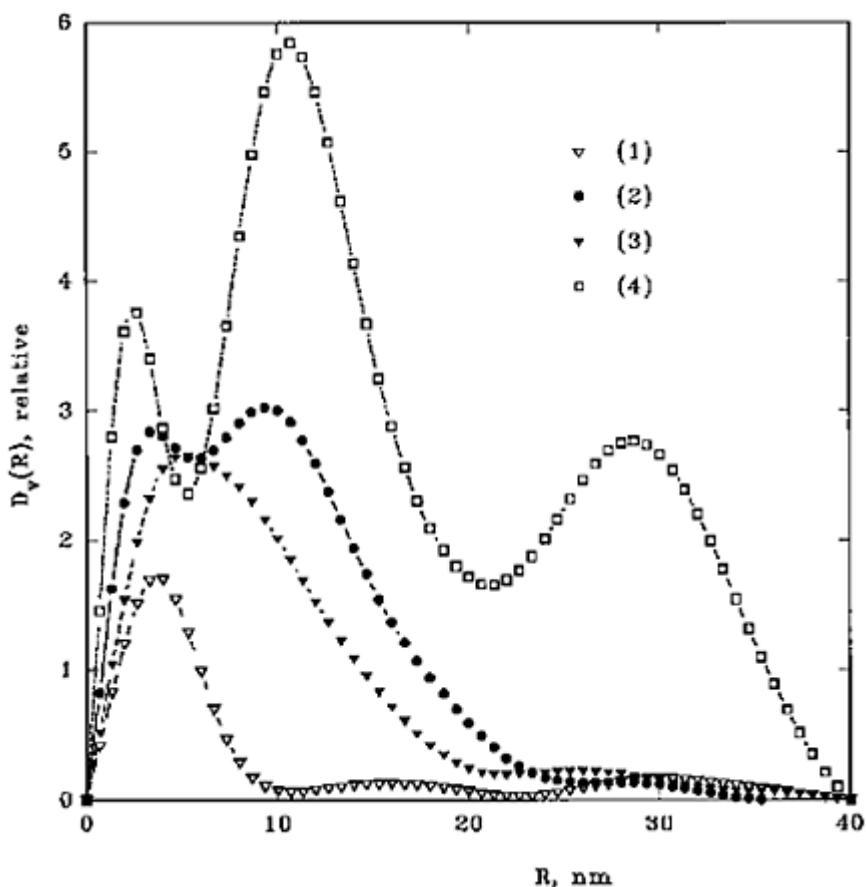


**FIG. 8** Volume distribution functions evaluated by GNOM: the PDADMACI/SDS system with added  $\text{HAuCl}_4$  (1); the PDADMACI/SDS system after the metal ions reduction (2); the PDADMACI gel after the metal ions reduction without SDS (measurements done just after preparation) (3); the same as (3) after 35 days' aging (4). Curve 1 was multiplied by a factor of 5 for better visualization. (From Ref. 36.)

micelles in selective solvents. Sluggish reducing agents such as hydrazine-hydrate  $\text{N}_2\text{H}_4 \cdot \text{H}_2\text{O}$  and triethylsilane initiate slow nucleation and growth of large particles, whereas sodium borohydride  $\text{NaBH}_4$  and superhydride allow the nucleation of many active sites at the same time and are thus expected to yield smaller particles [37]. To analyze the effect of the reducing agent type on the particle size distribution, two reducing agents,  $\text{NaBH}_4$  and  $\text{N}_2\text{H}_4 \cdot \text{H}_2\text{O}$ , were applied to the hydrogel/surfactant complexes loaded with  $\text{PtCl}_4$ . The latter compound forms  $\text{H}_2\text{Pt}(\text{OH})_2\text{Cl}_4$  after dissolution in water, and the  $\text{Pt}(\text{OH})_2\text{Cl}_4^{2-}$  ion has an octahedral geometry typical for the Pt(IV)

ions [38]. The x-ray scattering curves are presented in Figure 9 and the volume distribution functions in Figure 10. The distribution of the platinum compound clusters (curve

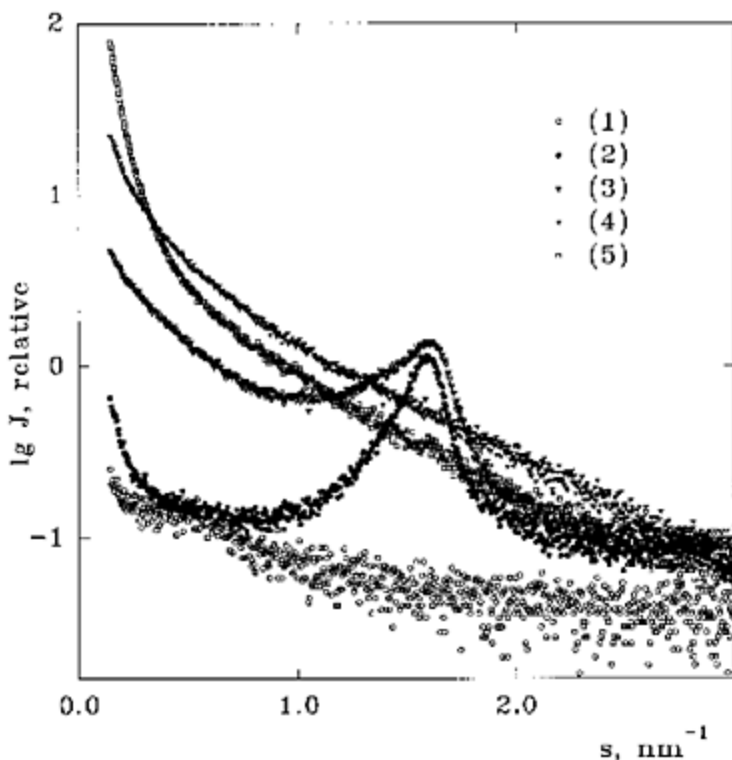


**FIG. 9** Experimental scattering curves for the Pt-loaded system  
 PDADMACI/SDS: empty cell (1); collapsed gel PDADMACI/SDS  
 (2); PDADMACI/SDS with added  $\text{H}_2(\text{OH})_2\text{PtCl}_4$  (3);  
 PDADMACI/SDS with platinum ions reduced with  $\text{NaBH}_4$  (4) and  
 $\text{N}_2\text{H}_4 \cdot \text{H}_2\text{O}$  (5). The curves are scaled as in Figure 7. (From Ref. 36.)

1) displays a maximum at  $R=3$  nm, yields an average  $R_g=7.6\pm0.1$  nm, and contains particles with the radii less than 15 nm. The reduction of the metal ions with  $\text{NaBH}_4$  (curve 3) results in particles with the radii up to 25 nm and the  $R_g$  increases to  $12.7\pm0.2$  nm. The maximum at small radii is preserved and significantly increased in curve 2 owing to the enhanced contrast of the metal particles compared to that of the compound clusters (see above). The metal compound clusters can thus be considered as centers of nucleation of metal nanoparticles. The volume distribution is significantly different for the system reduced with  $\text{N}_2\text{H}_4 \cdot \text{H}_2\text{O}$  (curve 3). In this case, larger particles with radii up to 30 nm constitute a major part of the  $D_V(R)$  distribution yielding an average  $R_g=16.2\pm0.1$  nm. So we do observe the dependence of particle size and particle size distribution on type of reducing agent: A slowly acting reducing agent yields much larger particles.

Comparing the size distributions of the Au and Pt nanoparticles in PDADMAC1/SDS (curves 2 in Figs. 8 and 10, respectively), it is seen that the Au distribution displays a somewhat higher proportion of larger particles. As the

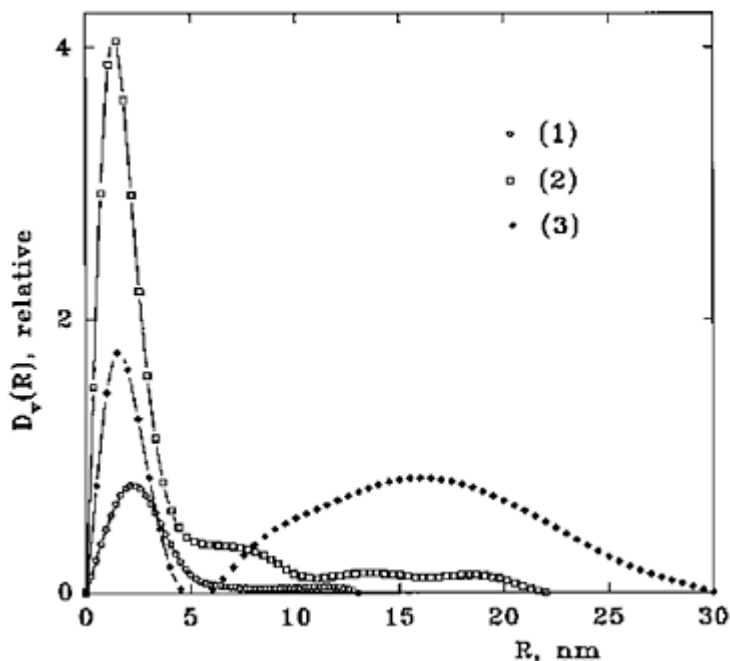


**FIG. 10** Volume distribution functions for the Pt-loaded PDADMAC1/SDS gel evaluated by GNOM: the system with added  $H_2(OH)_2PtCl_4$  (1); the system after the metal ions reduction with  $NaBH_4$  (2) and  $N_2H_4 \cdot H_2O$  (3). (From Ref. 36.)

$Pt(OH)_2Cl_4^{2-}$  ion is bivalent and  $AuCl_4^-$  monovalent, one may conclude that the metal particle formation is also influenced by the ion charge. Indeed, assuming that the metal ions are located at the border between the polymer chain and the surfactant head groups, the ion charge and structure become significant factors in the particle growth.

### 3. Particle Sizes Depend on the Type of Metal Compound

To analyze the influence of the metal compound type, three different platinum compounds,  $H_2PtCl_6$ ,  $(NH_4)_2PtCl_4$ , and  $Na_2PtCl_6$ , were added to the PDADMAC1/SDS system followed by a rapid reduction with  $NaBH_4$  [39]. The choice of these compounds aimed at clarifying the influence of acidity of the reaction medium (comparison of  $H_2PtCl_6$  and  $Na_2PtCl_6$ ) and Pt ion geometry (comparison of  $(NH_4)_2PtCl_4$  and  $Na_2PtCl_6$ ) on the Pt nanoparticle formation. Figure 11 presents the SAXS patterns from the gel/surfactant complexes after addition of platinum compounds. To obtain difference



scattering from the compound clusters, the latter curve was subtracted from the three others yielding the average radii of gyration of  $8.9\pm0.2$ ,  $9.4\pm0.3$ , and  $9.0\pm0.2$  nm for the  $\text{H}_2\text{PtCl}_6$ ,  $(\text{NH}_4)_2\text{PtCl}_4$  and  $\text{Na}_2\text{PtCl}_6$  clusters, respectively. The difference data were too noisy to compute the size distribution functions of the clusters.

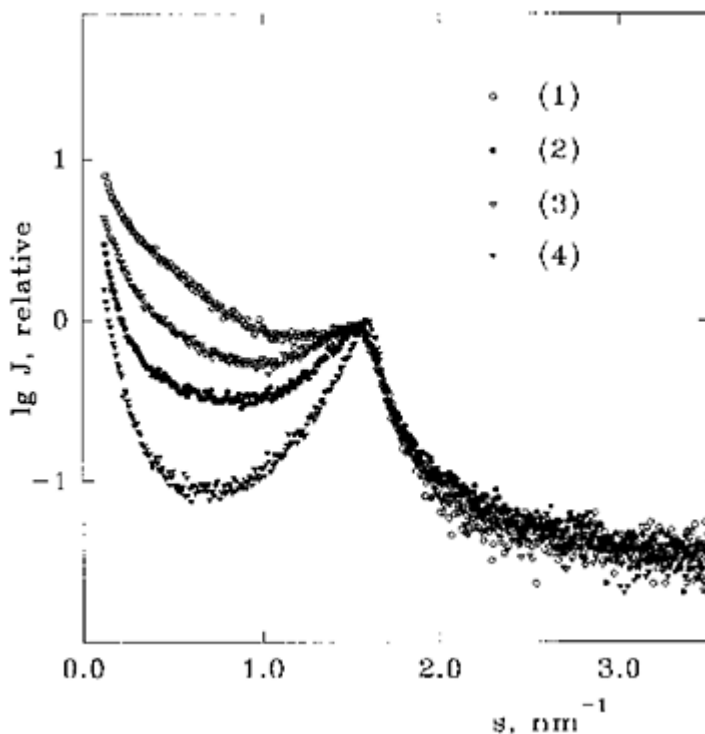


**FIG. 11** Experimental SAXS curves from the PDADMACI/SDS gel containing  $\text{H}_2\text{PtCl}_6$  (1),  $(\text{NH}_4)_2\text{PtCl}_4$  (2) and  $\text{Na}_2\text{PtCl}_6$  (3). The curves are scaled to match the scattering from the initial collapsed gel (4) at  $s > 3 \text{ nm}^{-1}$ . (From Ref. 39.)

The scattering curves from the reduced samples presented in Figure 12 display pronounced central scattering owing to metal nanoparticles. The weakest scattering is observed for the sample containing  $\text{Na}_2\text{PtCl}_6$ , (curves 3 and 4) where the peak at about  $s = 1.5 \text{ nm}^{-1}$  emerging from the ordering in the gel/surfactant structure can still be observed. Comparison of the curves 3 and 4 (the latter was recorded 1 month later than the former) shows that the magnitude of the peak is reduced with time indicating further rearrangements in the gel structure. The initial parts of the two curves nearly coincide suggesting that the metal particles remain stable. The average radius of gyration for the  $(\text{NH}_4)_2\text{PtCl}_4$  system ( $8.5\pm0.4$  nm) differs only marginally from that of this system before the metal reduction, suggesting that the Pt nanoparticles are formed from the compound clusters serving as “embryos” for the particle growth. The radius of gyration of the

system containing  $\text{Na}_2\text{PtCl}_6$  ( $12 \pm 0.4$  nm) is close to that for the  $(\text{NH}_4)_2\text{PtCl}_4$ , but the value found for the  $\text{H}_2\text{PtCl}_6$  system ( $32 \pm 0.5$  nm) is significantly larger. Note that the  $\text{Na}_2\text{PtCl}_6$  sample has the lowest Pt content among the three so that the weaker scattering observed for this sample should be

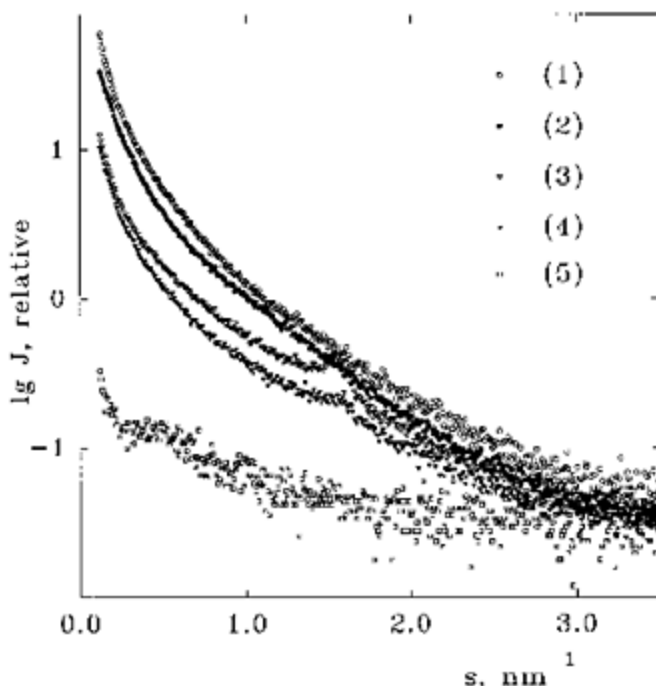


**FIG. 12** Experimental SAXS curves from the PDADMACI/SDS gels after reduction with  $\text{NaBH}_4$  of the platinum compounds:  $\text{H}_2\text{PtCl}_6$  (1),  $(\text{NH}_4)_2\text{PtCl}_4$  (2),  $\text{Na}_2\text{PtCl}_6$  just after reduction (3), and after 30 days' aging (4). The curves are scaled to match the scattering from the empty cell (5) at higher angles. (From Ref. 39.)

attributed not to smaller nanoparticles but to their smaller volume fraction in the gel.

To compute the size distributions of the nanoparticles, the background scattering (curve 5 in Fig. 12) was subtracted from that of the reduced samples. The difference curves were processed by GNOM yielding the size distributions in Figure 13. All  $D_V(R)$  functions display characteristic profiles with the major contribution of small particles. However, whereas for the  $(\text{NH}_4)_2\text{PtCl}_4$  and  $\text{Na}_2\text{PtCl}_6$  systems, particles with the radii larger than 15 nm are nearly absent, the  $\text{H}_2\text{PtCl}_6$  system displays a relatively small but detectable population of larger (up to  $R=40$  nm) particles with a broad size distribution. Attempts to restrict the evaluation range for the  $D_V(R)$  distributions in GNOM to smaller  $R_{\text{max}}$  lead to systematic deviations between the experimental and calculated data.

The pH of the solutions containing  $\text{H}_2\text{PtCl}_6$  (2.2) is much lower than that of the  $\text{Na}_2\text{PtCl}_6$  solutions (6.9). The mean radii of the small particle fraction for  $\text{H}_2\text{PtCl}_6$  and

$\text{Na}_2\text{PtCl}_6$  in the PDADMACI/SDS system are of about 3 and 2 nm, respectively, whereas large particles are present only for  $\text{H}_2\text{PtCl}_6$ . This suggests that the lower pH of the reaction medium promotes the formation of larger

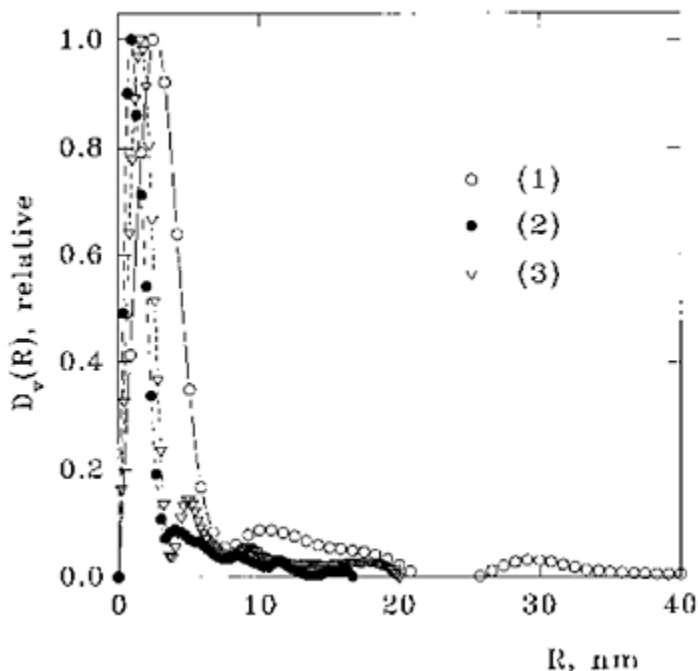


**FIG. 13** Volume distribution functions evaluated by GNOM for the PDADMACI/SDS gel containing Pt nanoparticles derived from  $\text{H}_2\text{PtCl}_6$  (1),  $(\text{NH}_4)_2\text{PtCl}_4$  (2), and  $\text{Na}_2\text{PtCl}_6$  (3). The distributions are normalized to a maximum value of unity. (From Ref. 39.)

particles, which agrees with the pH influence found for other systems [40]. The  $(\text{NH}_4)_2\text{PtCl}_4$ - and  $\text{Na}_2\text{PtCl}_6$ -containing systems provide comparison of different geometrical structures of the Pt ions (Pt[II] and Pt[IV], respectively). The plane  $\text{PtCl}_4^{2-}$  ions can be densely packed already in the  $(\text{NH}_4)_2\text{PtCl}_4$  compound clusters and they seem to produce smaller particles ( $R \approx 1$  nm in the small particle fraction) than those prepared by reduction of the octahedral  $\text{PtCl}_6^{2-}$  ions.

#### 4. Anomalous Scattering Permits In Situ Separation of the Contribution from Nanoparticles

As discussed above, to evaluate the size distributions in the conventional SAXS studies, matrix scattering had to be subtracted from that of the particle-containing sample. This operation is not always entirely justified, as the gel structure (and thus its scattering) may

change during the sample preparation. ASAXS near the absorption edge of the metal enables an in situ separation of the particle and matrix contributions [41, 42]. The ASAXS experiments involve measurements of the scattering curves at different x-ray radiation wavelengths  $\lambda$ ; that is, for different energies of the incident beam  $E$  [41, 43, 44]. The atomic scattering factor is

$$f(E) = f_0 + f'(E) + if''(E) \quad (4)$$

where the anomalous dispersion corrections  $f'(E)$  and  $f''(E)$  to  $f(E)$  become significant if the energy of the incident beam is close to that of an x-ray absorption edge of the atom. Therefore, performing measurements at the wavelengths around the absorption edges of the metal atoms and analyzing differences between the scattering patterns at different wavelength, net scattering from the nanoparticles can be extracted in situ.

We employed ASAXS to compare the two reducing agents  $N_2H_4 \cdot H_2O$  and  $NaBH_4$ , in situ in the PDADMACI/SDBS/ $H_2Pt(OH)_2Cl_4$  system. The experimental scattering profiles measured at the beam energy far from the Pt absorption edge are presented in Figure 14 [39]. They resemble the changes observed for PDADMACI/SDS system after incorporation or metal compounds and their reduction (see Fig. 9). To obtain the scattering from the Pt particles, differences

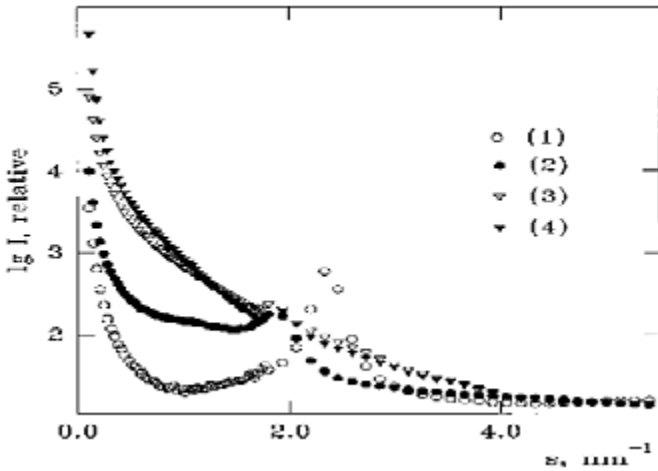


**FIG. 14** SAXS curves from the PDADMACI/SDBS/ $H_2Pt(OH)_2Cl_4$  system far from the absorption edge: (1) scattering after addition of the compound; (2) and (3) after reduction of platinum ions by  $NaBH_4$  and  $N_2H_4 \cdot H_2O$ , respectively; (4) scattering from the initial collapsed gel. The statistical error bars in the data are smaller than the symbol size. The curves are scaled to match the scattering from the collapsed gel at  $s > 4 \text{ nm}^{-1}$ . (From Ref. 34.)

between SAXS intensities at different energies were calculated as described above. The

difference curves in Figure 15 corresponding to  $k=3$  (maximum anomalous signal) were processed with the program GNOM to evaluate the size distribution functions shown in Figure 16. Two criteria were used to verify that the difference signal was indeed due to the Pt particles: (1) the difference,  $\Delta_k(S)$ , should be proportional to the squared anomalous correction for the  $k$ th energy and (2) the peak due to the internal gel structure should disappear. These conditions were met for all the samples except for the  $\text{H}_2\text{Pt}(\text{OH})_2\text{Cl}_4$ -containing system before metal reduction. Here the anomalous signal was obviously too small and the peak due to the gel structure did not disappear completely (Fig. 15, curve 1), producing artificial oscillations in the corresponding distribution function (Fig. 16, curve 1). The distribution of  $\text{H}_2\text{Pt}(\text{OH})_2\text{Cl}_4$  clusters displays a major fraction of small particles with radii about  $R \approx 2$  nm. The average radius of gyration,  $R_g = 9.50 \pm 0.2$  nm, points to the presence of larger particles in the system, although they cannot be clearly seen in the distribution because of the oscillations. Fast reduction with  $\text{NaBH}_4$  (curve 2) yields  $R_g = 15.1 \pm 1.2$  nm, and

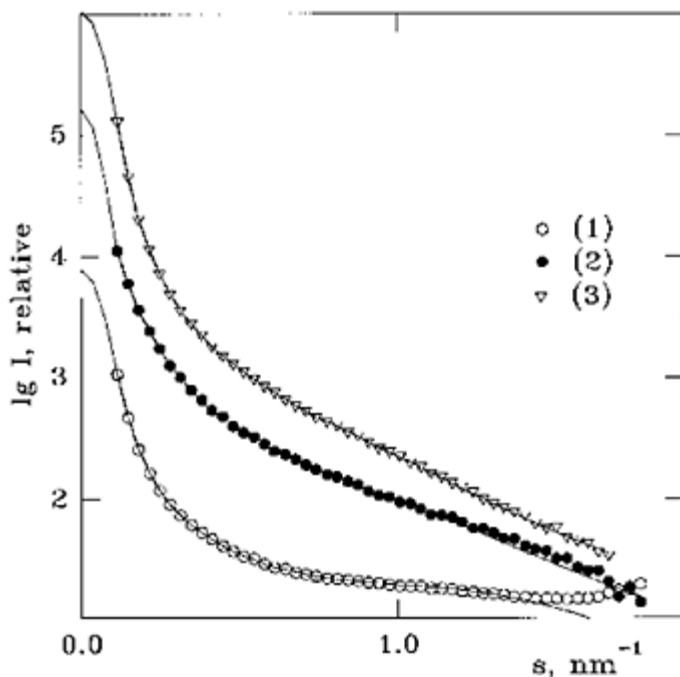


**FIG. 15** Difference ASAXS data (anomalous signal) from the PDADMACI/SDBS system containing  $\text{H}_2\text{Pt}(\text{OH})_2\text{Cl}_4$ : (1) Scattering from the compound clusters; (2) and (3) scattering from the Pt nanoparticles reduced with  $\text{NaBH}_4$  and  $\text{N}_2\text{H}_4 \cdot \text{H}_2\text{O}$ , respectively. Symbols: experimental points; solid lines: backtransformed curves from the volume distribution functions computed by GNOM. Only the low angle data (setting A2) used to compute the distribution functions are displayed. (From Ref. 39.)

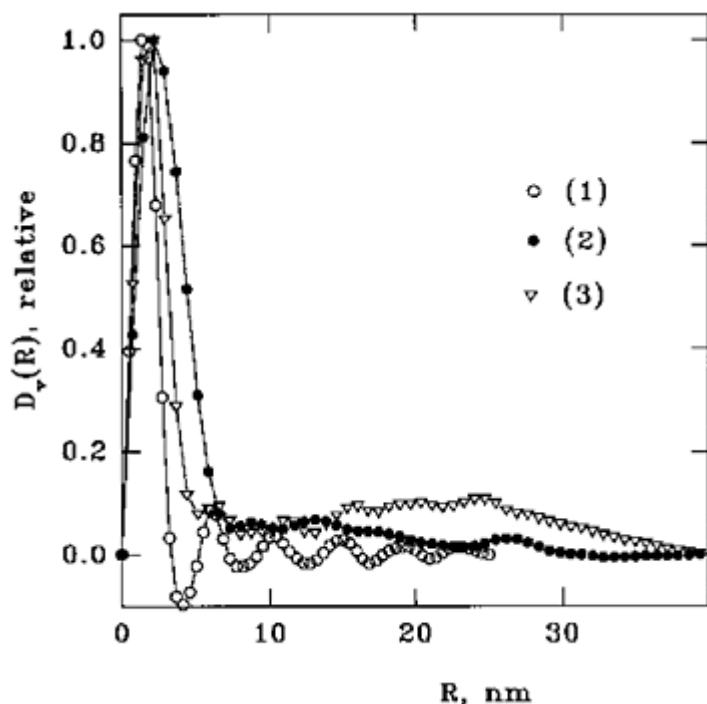


**FIG. 16** Volume distribution functions for the PDADMACl/SDBS gels containing  $H_2Pt(OH)_2Cl_4$ : (1) compound clusters; (2) and (3) Pt nanoparticles reduced with  $NaBH_4$  and  $N_2H_4 \cdot H_2O$ , respectively. The distributions are normalized to a maximum value of unity. (From Ref. 39.)

the small particles with radii about 2 nm still comprise the major fraction of the distribution function. Slow reduction using  $N_2H_4 \cdot H_2O$  leads to a different  $D_v(R)$  (curve 3) where larger particles with radii up to 40 nm make a more significant contribution yielding an average  $R_g = 21.6 \pm 1.1$  nm.

The sluggish reducing agent ( $N_2H_4 \cdot H_2O$ ) was found to produce larger particles than the rapid one ( $NaBH_4$ ), which is in agreement with the results obtained for the Au and Pt nanoparticles in the PDADMACl/SDS system [36]. The average sizes of the small particles fraction in the volume distributions of compound clusters and Pt nanoparticles obtained with rapid reduction practically coincide (about 2 nm). This corroborates the hypothesis [36] that the compound clusters embedded between the charged groups of the polymer chain and the head groups of surfactant molecules serve as centers of nucleation of metal nanoparticles, and the growing particles are protected from aggregation by the surrounding matrix during the fast reduction. When the nucleation is slow, the metal ions and smaller particles migrate unevenly to the areas of the hydrogel where their aggregation is possible, resulting in larger particles with broader size distribution.

## 5. Enhanced Ordering in the Hydrogels upon Metal Reduction

As discussed above, for anionic gel/cationic surfactant complexes, after metal nanoparticle growth, Bragg peaks either disappear or their intensity strongly decreased. Table 3 presents the structural parameters characterizing the internal order in the collapsed gel/surfactant complexes calculated from the Bragg peaks in the SAXS and ASAXS data. The mean long-range order dimension,  $L$ , estimating the size of quasicrystalline zones in the sample, and the radius of interaction,  $r_m$ , yielding maximum separation between spatially correlated structural motifs, should increase with increasing order in the system. In contrast, the relative mean square deviation of the distance between the neighboring periodic motifs,  $\Delta/\bar{d}$  (degree of disorder), should decrease if the system becomes more ordered, whereas the Bragg peaks nearly disappear if  $\Delta/\bar{d} > 0.25$ .

A striking feature observed for the both cationic gel/anionic surfactant systems is that the metal-containing samples appear to be not less ordered than the initial gels despite the diminished amplitudes of the peaks. For the PDADMAC1/SDBS system, the average distance between the ordered structure motifs,  $\bar{d}$ , increases from 2.7 to about 3.4 nm after the addition of the metal compounds compared to the initial gel, but the parameters describing the degree of order remain practically unchanged. The internal order is even enhanced after the metal reduction with both sluggish and fast reducing agents. The PDADMAC1/SDS system displays a similar tendency, but the periodicity in the system (spacing about 4 nm) does not change for the metal-containing samples compared to the initial gel. The mean long-range order dimension,  $L$ , is around 30 nm for the

**TABLE 3** Structural Characteristics of the Hydrogel/Surfactant Complexes Obtained from the SAXS and ASAXS Data

Sample	$s_{\max}(\text{nm}^{-1})$	$\bar{d}(\text{nm})$	$L(\text{nm})$	$\Delta/\bar{d}$
PDADMAC1/SDBS				
Collapsed gel	2.34	2.68	27	0.100
Gel+H <sub>2</sub> Pt(OH) <sub>2</sub> Cl <sub>4</sub>	1.88	3.34	38	0.094
Gel+H <sub>2</sub> Pt(OH) <sub>2</sub> Cl <sub>4</sub> +NaBH <sub>4</sub>	1.87	3.36	74	0.066
Gel+H <sub>2</sub> Pt(OH) <sub>2</sub> Cl <sub>4</sub> +N <sub>2</sub> H <sub>4</sub>	1.94	3.24	60	0.074
PDADMAC1/SDS				
Collapsed gel	1.53	4.10	3	0.116
Gel+H <sub>2</sub> PtCl <sub>6</sub>	1.52	4.13	29	0.118
Gel+(NH <sub>4</sub> ) <sub>2</sub> PtCl <sub>4</sub>	1.51	4.17	32	0.114
Gel+Na <sub>2</sub> PtCl <sub>6</sub>	1.52	4.13	38	0.105
Gel+H <sub>2</sub> Pt(OH) <sub>2</sub> Cl <sub>4</sub>	1.58	3.98	39	0.101
Gel+Na <sub>2</sub> PtCl <sub>6</sub> +NaBH <sub>4</sub>	1.56	4.02	98	0.064

Source: Ref. 39.

initial gel/surfactant complexes and those after the metal compound addition. For the reduced samples, much higher  $L$  values are found ranging from 50 to more than 100 nm.

The degree of disorder,  $\Delta/\bar{d}$ , decreases from 0.10 to 0.11 for the initial gels to 0.06–0.08 for the reduced samples also indicating higher internal ordering in the latter.

The magnitude of a Bragg peak emerging from the internal structure is proportional to the degree of order in the crystalline (ordered) phase and to its volume fraction in the sample. The parameters characterizing the internal order depend on the ratio of the integral peak width to its magnitude (see Eqs. [3–5]). For all the PDADMAC1/SDBS (SDS) samples above, both the magnitude and the width of the peak decrease upon metal

reduction, but the values of  $L$  and  $\Delta/\bar{d}$  indicate a significant increase in the degree of order in the crystalline phase. One concludes that an evenly distributed surfactant/gel network is redistributed in the gel during reduction forming highly localized ordered structures that occupy only a small volume fraction in the sample. From comparison of the magnitude of the peaks, this fraction is estimated to be about a few percent. It is conceivable that the highly ordered portions surround the metal nanoparticles formed in the gel.

## V. SUMMARY

As seen from the above results, the complexes of polyelectrolyte gels with oppositely charged surfactants permit one to stabilize the process of metal nanoparticle formation. The uptake of metal ions by hydrogel/surfactant complexes occurs successfully when the ions are oppositely charged with respect to hydrogel-charged groups. The incorporated ions form the compound clusters embedded between the charged groups of the polymer chain and the head groups of surfactant molecules. These compound clusters serve as centers of nucleation of metal nanoparticles. The increased order around the growing nanoparticles (despite the decrease of the crystalline phase volume) enhances the control over the nanoparticle sizes and yields narrow particle size distributions. This effect is observed for different metal compounds and hydrogel/surfactant complexes if the reduction is carried out with a rapid reducing agent (i.e.,  $\text{NaBH}_4$ ). If the nucleation of the nanoparticles is slow, small clusters and metal ions migrate unevenly to the nonordered areas of the hydrogel where their aggregation is possible, resulting in larger particles with broader size distribution. Polyelectrolyte gels without internal order are unable to control metal nanoparticle formation.

## REFERENCES

1. A Henglein. *Chem Rev* 89:1861–1873, 1989.
2. CNR Rao, GU Kulkarni, PJ Thomas, PP Edwards. *Chem Soc Rev* 29:27–35, 2000.
3. JH Fendler, ed. *Nanoparticles in Solids and Solutions. Preparation, Characterization and Utilization*. Dordrecht, The Netherlands, Kluwer, Boston-London, 1996, pp 10–565.
4. J Bradley. The chemistry of transition metal colloids. In: G Schmid, ed. *Clusters and*



- Colloids. Wiley, New York, 1994, pp 459–544.
5. M Antonietti, E Wenz, L Bronstein, M Seregina. *Adv Mater* 7:1000–1005, 1995.
6. YNC Chan, RR Schrock, RE Cohen. *Chem Mater* 4:24–30, 1992.
7. M Antonietti, S Henz. *Nachr Chem Lab Tech* 40:308–314, 1992.
8. M Moffit, L McMahon, V Pessel, A Eisenberg. *Chem Mater* 7:1185–1192, 1995.
9. JP Spatz, A Roescher, M Möller. *Adv Mater* 8:337–340, 1996.
10. LM Bronstein, SN Sidorov, PM Valetsky, J Hartmann, H Cölfen, M Antonietti. *Langmuir* 15:6256–6262, 1999.
11. J Leht, K Vaaramaya, E Vesterinen, H Tehnu. *J Appl Polym Sci* 68:355–362, 1998.
12. C Heitz, W Binana-Limbele, J Francois, C Biver. *J Appl Polym Sci* 72:455–466, 1999.
13. T Tanaka, CN Wang, V Pande, AY Grossberg, A English, S Masamune, H Gold, R Levy, K King. *Faraday Dis* 101:201–206, 1995.
14. D Szabo, G Szeghy, M Zrinyi. *Macromolecules* 31:6541–6548, 1998.
15. M Dauben, K Platkowski, KH Reichert. *Angew Makromol Chem* 250:67–83, 1997.
16. M Zrinyi, D Szabo, L Barsi. *J Intell Mater Sys Struct* 9:667–671, 1998.
17. M Antonietti. *Angew Chem Int Ed Engl* 27:1743–1747, 1988.
18. M Antonietti, W Bremser, M Schmidt. *Macromolecules* 23:3796–3805, 1990.
19. M Antonietti, F Grohn, J Hartmann, L Bronstein. *Angew Chem Int Ed Engl* 36:2080–2083, 1997.
20. NT Whilton, B Berton, L Bronstein, HP Hentze, M Antonietti. *Adv Mater* 11:1014–1018, 1999.
21. AR Khokhlov, SG Starodubtsev, VV Vasilevskaya. *Adv Polym Sci* 109:123–171, 1993.
22. AR Khokhlov, EYU Kramarenko, EE Makhaeva, SG Starodubtsev. *Macromolecules* 25:4779–4783, 1992.
23. AR Khokhlov, EYU Kramarenko, EE Makhaeva, SG Starodubtsev. *Macromol Theory Simul* 1:105–118, 1992.
24. YuV Khandurina, AT Dembo, VB Rogacheiva, AB Zezin, VA Kabanov. *Vysokomol Soed* 36A:235–240, 1994.
25. H Okuzaki, Y Osada. *Macromolecules* 28:380–382, 1995.
26. B Chu, F Yeh, EL Sokolov, SG Starodubtsev, AR Khokhlov. *Macromolecules* 28:8447–8449, 1995.
27. F Yeh, EL Sokolov, AR Khokhlov, B Chu. *J Am Chem Soc* 118:6615–6618, 1996.
28. AT Dembo, AN Yakunin, VS Zaitsev, AV Mironov, SG Starodubtsev, AR Khokhlov, B Chu. *J Polym Sci: Phys* 34:2893–2898, 1996.
29. S Zhou, B Chu. *Adv Mater* 12:545–556, 2000.
30. LM Bronstein, OA Platonova, AN Yakunin, IM Yanovskaya, PM Valetsky, AT Dembo, ES Obolonkova, EE Makhaeva, AV Mironov, AR Khokhlov. *Colloids Surf A* 147:221–231, 1999.
31. LA Feigin, DI Svergun. *Structure Analysis by Small-Angle X-ray and Neutron Scattering*. Plenum Press, New York, 1987, pp 28–125.
32. DI Svergun. *J Appl Crystallogr* 25:495–503, 1992.
33. BK Vainshtein. *Diffraction of X-Rays by Chain Molecules*. Elsevier, Amsterdam, 1966, pp 5–69.
34. LM Bronstein, OA Platonova, AN Yakunin, IM Yanovskaya, PM Valetsky, AT Dembo, EE Makhaeva, AV Mironov, AR Khokhlov. *Langmuir* 14:252–259, 1998.
35. HF Mark, NM Bikales, CG Overberger, G Menges, JI Kroschwitz, ed. *Encyclopedia of Polymer Science and Engineering*. Vol 6. Wiley, New York, 1986, pp 410–456.

36. DI Svergun, EV Shtykova, AT Dembo, LM Bronstein, OA Platonova, AN Yakunin, PM Valetsky, AR Khokhlov. *J Chem Phys* 109:11109–11116, 1998.
37. LM Bronstein, PM Valetsky, M Antonietti. In: JH Fendler, ed. *Nanoparticles and Nanostructured Films*. Wiley, New York, 1998, pp 145–171.
38. H Remy. *Lehrbuch Der Anorganischen Chemie II*. Akademische Verlag, Leipzig, 1961, pp 343–345.
39. DI Svergun, EV Shtykova, MB Kozin, VV Volkov, AT Dembo, EV Shtykova Jr, LM Bronstein, OA Platonova, AN Yakunin, PM Valetsky, AR Khokhlov. *Phys Chem B* 104:5242–5250, 2000.
40. SN Sidorov, LM Bronstein, PM Valetsky, J Hartmann, H Coelfen, H Schnablegger, M Antonietti. *J Colloid Interface Sci* 212:197–211, 1999.
41. HB Stuhmann, G Goerigk, B Munk. In: E Rubenstein, S Ebashi, M Koch, ed. *Handbook on Synchrotron Radiation*. Elsevier, Amsterdam, 1994, pp 555–572.
42. HG Haubold, XH Wang, G Goerigk, W Schilling. *J Appl Crystallogr* 30:653–658, 1997.
43. HG Haubold, R Gebhardt, G Buth, G Goerigk. In: G Materlik, CJ Sparkks, K Fischer, eds. *Resonant Anomalous X-ray Scattering*. Elsevier, Oxford, UK, 1994, pp 295–304.
44. HG Haubold. *J Phys IV C8 J Phys I 3(Suppl):475–79*, 1993.

## 6

# Structure and Properties of Polyampholyte Gels

**GIOVANNI NISATO** *Philips Research, Eindhoven, The Netherlands*

**SAUVEUR JEAN CANDAU** *Université Louis Pasteur, Strasbourg, France*

## I. INTRODUCTION

Polyampholytes constitute a particular class of polyions containing both positively and negatively charged units. The properties of these complex systems are essentially ruled by electrostatic interactions. As a rule, the synthesis of polyampholytic copolymers or terpolymers leads to samples containing the inorganic counterions associated with the cationic and anionic monomer units. However, it is possible to dialyze the excess ions and to obtain zero net-charge polyampholytes without counterions. A schematic representation of a linear polyampholyte is given in Figure 1.

The first studies on synthetic polyampholytes, which date back to the 1950s [1], were partially motivated by the hope to cast a new light on the behavior of more complicated biological systems such as proteins. Since the 1980s, there is an increased amount of activity in the field of polyampholytes, thanks to new synthetic methods, as well as theoretical and experimental tools [2, 3].

There are two large families of polyampholytes (PA); namely, weak PA (annealed) and strong PA (quenched). Annealed PA are synthesized from weak acid and/or base monomers; their net charge depends on the pH of the solution (negative net charge in a basic solution, positive net charge in acid solution, zero net charge at the isoelectric point). Quenched PA are obtained from strong base and acid monomers. Their net charge is directly linked to the polymer composition and remains constant in a large pH range.

Theoretical models [4–6] and numerical simulations [5, 7] give a description of the PA chain as a function of net charge and salt concentration. When the net charge is very small, the conformation of the molecule is collapsed at very low ionic strength because of the strong attractive interactions between monomers

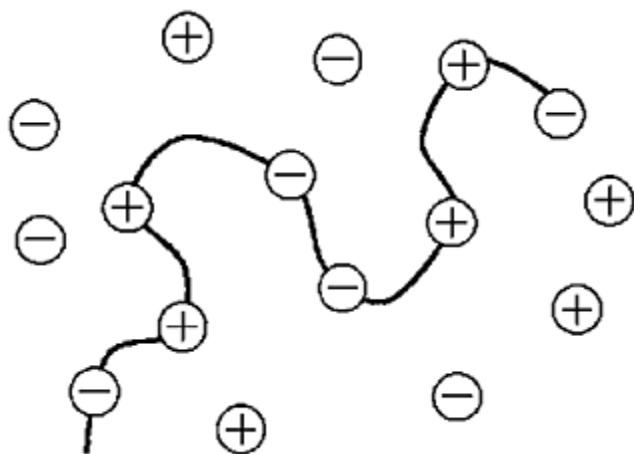


**FIG. 1** A linear PA chain and its counterions.

carrying charges of opposite signs. At high ionic strength, these attractive interactions are screened and the molecule adopts a more extended conformation. When the net charge is high, the molecule behaves as a polyelectrolyte at low ionic strength and as a PA at high ionic strength. In both cases, the conformation of the chain is rather extended, and the transition between the two regimes is characterized by a partial collapse of the molecule.

The models proposed so far were developed for terpolymers; that is to say for polymers containing neutral and charged units (both positive and negative). Nevertheless, several experimental studies [8] showed that the behavior of copolymers containing only charged monomers were in qualitative agreement with these models.

Since the models aim to describe the conformation of single chains, the more convincing experimental studies should deal with diluted PA solutions. However, such diluted solutions are experimentally very difficult to prepare owing to the difference in the reactivity ratios of the monomers during polymerization [9]. This difference leads to a large distribution of charges carried by the macromolecules resulting in a complex behavior. It is possible, at least partially, to solve the problem of net-charge polydispersity by stopping the reaction at low conversion rates [10]. Another approach to obtain truly neutral PA involves the polymerization of zwitterionic monomers (C.Oeschlager, personal communication) [11, 12].

More concentrated PA systems present a rather complex behavior. The theoretical models that were developed for single chains lead to predictions about the phase diagram starting from the assumption [4] that the collapse of each PA molecule causes a phase separation in systems at finite concentration. Later on it was realized both theoretically [13] and experimentally [14] that PA solutions with small global charge offsets are subject to precipitation by pairing of chains in the tail of the net-charge distribution and oppositely charged majority chains. This phenomenon was confirmed by molecular dynamics studies of several chains of weakly charged PA [15, 16]. The swelling behavior of a neutral PA strand as well as the reentrant behavior of nonneutral PA with ionic

strength, which was experimentally observed for solutions and gels, was also reproduced by the simulations.

Polyampholytic gels have been the subject of relatively few experimental studies which focused essentially on their swelling behavior [12, 17–21]. The results are in qualitative agreement with the predictions of the models describing single chains in solution. In particular, balanced PA gels collapse in low ionic strength conditions and swell at high salt concentration. As the net charge increases, polyelectrolyte behavior is observed, and equilibrium swelling decreases with increasing salt concentration. For PA near the balance point, the polyelectrolytic effect is dominant at low salt concentration, whereas the PA behavior appears at high salt concentration.

Swelling models entirely based on the classic Donnan theory cannot predict a PA swelling behavior, because the electrostatic forces between ions are not considered directly. To account for these Coulombic interactions, several approaches have been proposed that describe qualitatively the general swelling behavior, including the characteristic PA effect (swelling at high salt concentration). However, fitting of the swelling equilibrium data to the existing models requires several adjustable parameters. Furthermore, the problems mentioned above linked to the difference between the reactivity rates of the monomers cannot be avoided.

During the synthesis of a gel it is not possible to stop the reaction at low conversion rates, which results in a large distribution of net charge carried by the different chains of the network. This difficulty is overcome when using zwitterionic monomers, however in this case only globally neutral gels can be prepared.

The study of the variation of the shear modulus of neutral gels as a function of the equilibrium swelling degree reduces the number of adjustable parameters and minimizes the effect of structural imperfections [22]. This classic approach has recently been applied to PA gels leading to the intriguing observation that a PA gel with a weak net charge can reach the same degree equilibrium swelling with widely different salt contents, but it is then characterized by two different values of the shear modulus [23]. This is mainly due to screening effects that influence differently the attractive (polyampholyte) and repulsive (polyelectrolyte) interactions. Polyampholytic gels are therefore well suited to investigate the effect of electrostatic interactions on the elastic properties of gels. Such effects have been experimentally studied in polyelectrolytic gels and are not yet totally understood [24].

The complexity of the structure of PA gels is also revealed by scattering experiments. Such experiments are scarce, but they complement the elasticity studies and show that a given PA gel under two different salt conditions leading to the same swelling equilibrium exhibits a totally different spatial spectrum of frozen-in concentration fluctuations [23].

The structure of the chapter is as follows. In the first section, a brief survey of the properties of PA solutions is given. Both the predictions of the current models describing the single-chain behavior and the conclusions of recent molecular dynamics simulations concerning multichain systems are recalled. Some experimental results are reported and compared to the theory. In the second section, we describe the results obtained for PA gels. The Flory-type swelling models, including Coulombic interactions, are presented. Experimental results on the swelling equilibrium of both highly and weakly charged PA gels are discussed in terms of single-chain behavior and of the models describing gels.

Light scattering and elastic modulus data are reported. The possible effects of the different reactivity rates of the monomers on the structural properties of PA gels are also discussed.

## II. CONFORMATION OF PA CHAINS IN SOLUTION

The conformation of PA chains is for the most part dictated by the electro-statically charged monomers. The fundamental difficulty for the theoretical description of polyampholyte chains and gels resides essentially in the modeling of the strong and long-range Coulombic interactions.

### A. Single-Chain Properties

The conformation of a PA carrying a net charge results from a competition between the attractive electrostatic interactions, which favor a compact configuration of the polymer, and the repulsion of monomers carrying the same type of charge which favors a stretched configuration of the polymer. In an ideal PA chain constituted of  $N$  monomers, the fraction of positively and negatively charged monomers are  $f_+=N_+/N$  and  $f_-=N_-/N$ , respectively. The total fraction of charged monomers is  $f$  and the net charge fraction is  $\Delta f=(f_+-f_-)$ .

The conformation of PA in the absence of salt is governed by the total charge,  $f$ , and the net charge,  $\Delta f$ . In the case of weakly charged PA [3], repulsive effects are dominant when the net charge,  $\Delta f$ , is greater than  $\Delta f_1$ , defined by:

$$\Delta f_1 = \left( \frac{l_B}{a} \right) f^{3/2} \quad (1)$$

In this case, the molecule adopts a very stretched, polyelectrolyte-like conformation; the chain is a linear assembly of electrostatic blobs of size  $\xi_e \sim a(a/l_B))^{1/3} \Delta f^{-2/3}$  and has for length:

$$R \sim Na \left( \frac{l_B}{a} \right)^{1/3} \Delta f^{2/3} \quad (2)$$

When  $\Delta f$  is smaller than  $\Delta f_1$ , the dominant interactions are attractive and the chain adopts a globular conformation. The shape of the globule is determined by the repulsion between charges of opposed signs and changes following  $\Delta f$ . The regime changes when  $\Delta f$  is smaller than  $\Delta f_2$ :

$$\Delta f_2 \sim \left( \frac{f}{N} \right)^{1/2} \quad (3)$$

Polyampholytic chains adopt then a globular configuration of radius  $R_G \sim N^{1/3} a (a/f l_B)^{1/3} \Delta f_2^{2/3}$ . The value of  $\Delta f_2$  given by Eq. (3) corresponds exactly to the net charge of statistical origin carried by the chains of a globally neutral PA solution obtained by random copolymerization.

Addition of salt screens both attractive and repulsive intramolecular electro-static interactions, which confer a great richness of conformations to PA chains. The effect of electrostatic interactions in the presence of salt can be described by the excluded volume term  $v^*$  introduced by Higgs and Joanny [4]:

$$v^* = -\frac{\pi(f l_B)^2}{\kappa_s} + \frac{4\pi l_B \Delta f^2}{\kappa_s^2} \quad (4)$$

where  $l_B$  is the Bjerrum length and  $\kappa_s$  is the Debye-Hückel parameter. The first term of Eq. (4) is the excluded volume,  $v_{PA}$ , associated with the attractive PA effect. This term dominates at high  $\kappa_s$  values (high ionic strength). The second term is the excluded volume,  $v_{PE}$ , associated with the repulsive polyelectrolyte effect, which is predominant at low  $\kappa_s$  values (low ionic strength). The excluded volume,  $v^*$ , is minimum when:

$$\kappa_s^m = 8/l_B (\Delta f/f)^2 \quad (5)$$

The total effective excluded volume is  $v_{\text{eff}} = v^* + v$ , where  $v$  is the second virial coefficient of the neutral polymer. Figure 2 summarizes qualitatively the salt dependency of the mean square end to end distance of a chain and the conformations of a linear PA for three different net charge fractions as a function of the external salt concentration  $C_s$ .

A polyampholyte chain with a net charge fraction close to one behaves essentially like a polyelectrolytic chain. When polyelectrolytes are in the presence of salt, a Donnan equilibrium is established between the polymer and the solvent. The salt concentration inside the chain is lower than the imposed salt

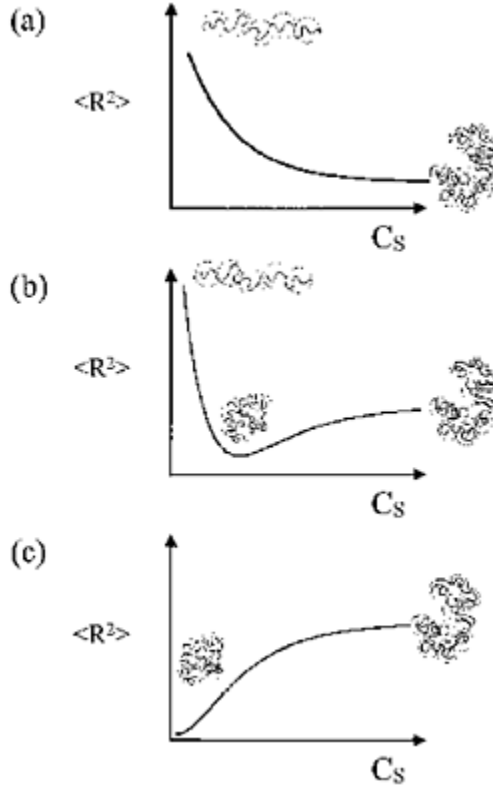


**FIG. 2** Conformations of a linear PA as a function of the salt concentration,  $C_s$ , for three different net charge fractions corresponding to (a) strong net charge (PE behavior); (b) intermediate net charge; (c) zero net charge (antipolyelectrolytic behavior).  $\langle R^2 \rangle$  is the mean square end to end distance of a chain.

concentration. When the salt concentration increases, the radius of the chain decreases, because the osmotic pressure of the salt inside the chain is smaller than outside. As for polyelectrolytes, a Donnan equilibrium is established between the interior and the exterior of globally neutral PA chains. However, in this case, the salt concentration inside the chain,  $C_{sint}$ , is *larger* than the salt concentration outside the chain, and the higher osmotic pressure of the salt inside the chain increases the chain radius. Higgs and Joanny [4] derived the following expression for the salt concentration difference  $\delta = (C_{sint} - C_s)/C_s$ .

$$\delta = \frac{\gamma \kappa_0}{(1 - \kappa_0)} - \gamma^2 \kappa_0 \frac{(1 - 2\kappa_0)}{4(1 - \kappa_0)^3} \quad (6)$$



where  $\gamma = fC_P/C_S$  and  $\kappa_0 = \kappa_S l_B/4$ ;  $C_P$  is the polymer concentration. Figure 3 shows the variation of  $\delta$  with external salt concentration for different values of  $fC_P$ .

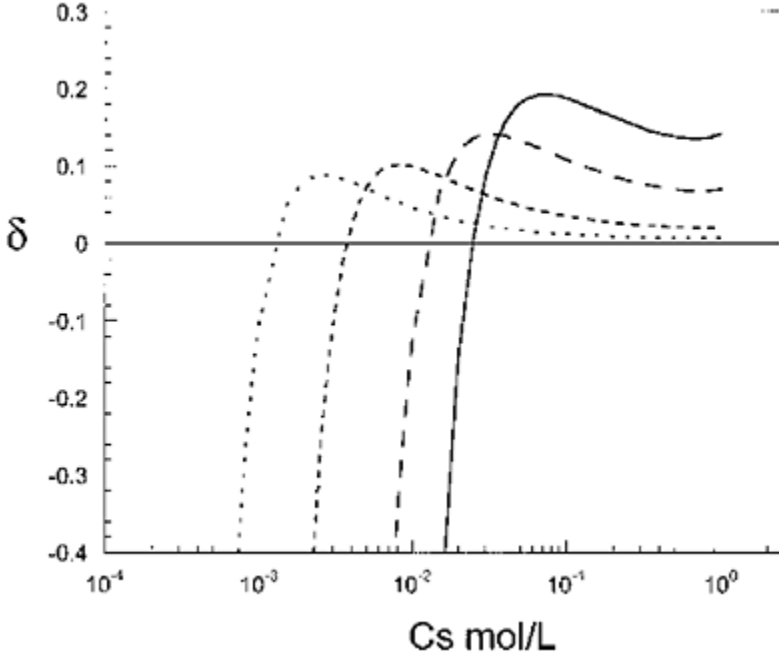


**FIG. 3** Evolution of the relative salt concentration difference between the exterior and the interior of a globally neutral polyampholyte chain  $\delta = (C_{Sint} - C_S)/C_S$  calculated from Eq. 6. The curves correspond to the following molar charge concentrations,  $fC_{PA}$ : 0.005 (*dotted line*); 0.015 (*short dashed line*); 0.05 (*dashed line*), and 0.1 (*continuous line*).

## B. Multichain Effects

The single-chain picture has been applied to explain qualitatively the behavior of solutions of finite concentration [3]. However, the experimental observations were often marred by effects originating from net charge polydispersity. It was found that samples containing mixtures of oppositely charged chains partially precipitate even though the average net charge is much higher than the one of perfectly soluble samples with a narrower net charge distribution [10, 25]. These effects were discussed by Everaers et al. [13], who analyzed the equilibrium between a homogeneous, dense polymer solution phase and its dilute supernatant. The analysis was based on the description of PA in solutions at low ionic strength adopting an elongated globular conformation. It was found that PA with a charge imbalance ( $|\Delta f| > 0$ ) have a strong tendency to form neutral complexes and to precipitate. Neutral samples are almost insoluble, whereas samples with low net charge behave like a mixture of an insoluble neutral part with a soluble part

consisting of the most strongly charged chains and the corresponding counterions. Highly nonneutral PA with narrower net charge distribution are entirely soluble.

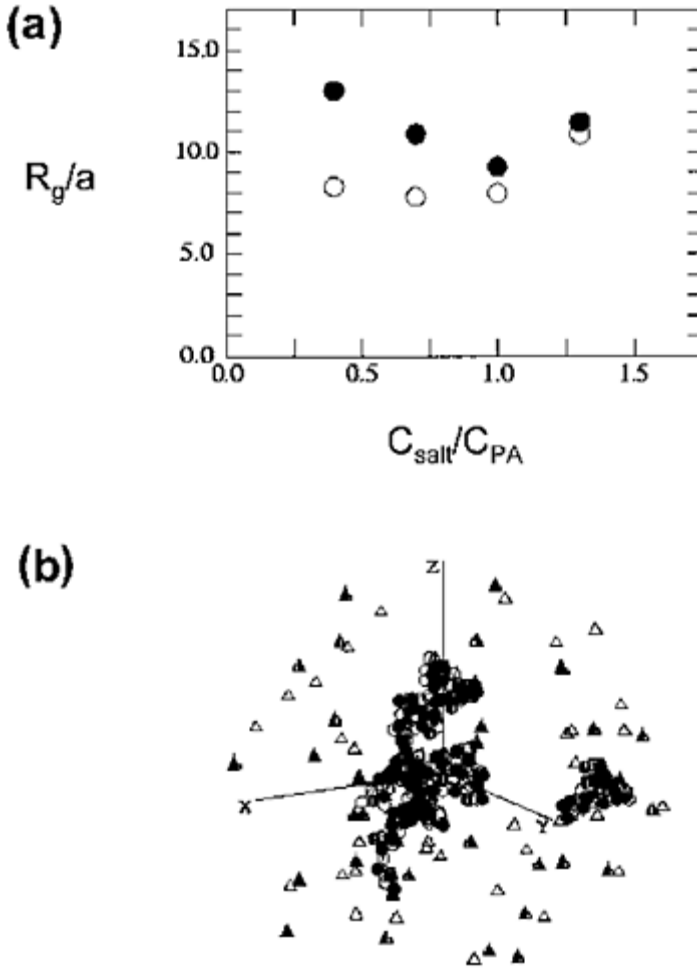


**FIG. 4** (a) Salt dependency of the average radius of gyration (normalized by the monomer size,  $a$ ) of neutral and charged PA. The systems consist of six PA 32 mers with 0% ( $\circ$ ) and 40% ( $\bullet$ ) global charge effect. The neutral PA are collapsed at low ionic strength and swell when the charge density of the added salt (and counterions) is comparable to that of the polyampholyte. (b) Bird's-eye view of neutral, random PA. The monomers of the PA are depicted with circles, counterions are depicted with triangles (open=positive, closed=negative). (From Ref. 15.)

The same behavior was also seen in molecular dynamics simulations that were recently

performed by Tanaka and Tanaka [15]. The effect of salt on the swelling behavior of multichain PA was qualitatively similar to that of a single chain, as illustrated in Figure 4. Figure 4 illustrates the salt dependency of the average radius of gyration of neutral and charged PA. The systems consist of six PA 32 mers with 0 and 40% global net charge, respectively. The neutral PA are collapsed

at low ionic strength and swell when the charge density of the added salt (and counterions) is comparable to that of the PA. In the case of nonneutral PA, the effect of salt addition occurs in two steps. The salt first screens the polyelectrolytic interactions, which causes the collapse of the PA chain leading to a transition from PA to noncharged polymer regimes, with the latter resulting in reswelling of the chains.

### C. Experimental Results

The solution properties of annealed PA are controlled by the strength of the acid or base groups and the pH, whereas the solution properties of quenched PA are controlled by the copolymer composition. Most studies focused on the solubility behavior of the polymers. In pure water, most of the PA become insoluble around the isoelectric point owing to the predominance of the PA effect. Away from the neutral point, the PA are soluble because of their polyelectrolytic character. In the presence of salt, the electrostatic interactions are screened and the copolymers become soluble again.

The solubility of the PA in aqueous media is closely related to their conformation. The conformational changes induced by a variation of the net charge and/or by the ionic strength have been probed by viscometry and, to a lesser extent, by light scattering. The intrinsic viscosity of a dilute solution, which is a measure of the hydrodynamic volume of the chain, was found to exhibit a sharp minimum in pure water close to the neutral point associated with chain contraction. Upon addition of salt, the viscosity is strongly dependent on the net charge. The intrinsic viscosity exhibits the same type of variations with the salt concentration as those reported schematically in Figure 2b for the average end to end distance of the chain.

A quantitative comparison with the theory can be done only for terpolymers with low net charge. A major problem encountered in such a study concerns the distribution of the net charges among the polymer chains. As the polymerization reaction proceeds, the different reactivity ratios of the cationic and the anionic monomers produce a drift in the composition of the copolymer. This difficulty can be overcome by optimizing the stoichiometry to compensate for the differences in reactivity ratios and by stopping the polymerization at very low degree of conversion. Such a method was used by Ohlemacher et al. [10] to prepare low-charge-density terpolymers AA/Na AMPS/MADQUAT by micro-emulsion polymerization (see Table 1 for the abbreviation). Figure 5 shows the variation of the intrinsic viscosity as a function of salt concentration for aqueous solutions of two samples obtained at degrees of conversion equal to 2.3 and 4.4%. One observes a minimum whose position depends on the characteristics of the samples (global and net charge). Table 2 shows the comparison between the experimental values of the Debye-Hückel parameter,  $\kappa_{0\min}$ , at the minimum of the

**TABLE 1** Molecules and Abbreviations

AA	Sodium acrylate
ADAMQUAT	Acryloyloxy-ethyltrimethyl ammonium chloride
AM	Acrylamide
HEMA	2-Hydroxyethyl methacrylate
MADQUAT	2(methacryloyloxy)-ethyltrimethylammonium chloride
MAPTAC	(Methacrylamino propyl)trimethylammonium chloride
NaAMPS	Sodium 2-acrylamido-2-methylpropane sulfonate
NDAPA	<i>N</i> -3-dimethylaminopropyl acrylamide
NIPAM	<i>N</i> -Isopropyl acrylamide
SB	<i>N</i> -(3-sulfopropyl) <i>N</i> -ethacrylamidopropyl <i>N,N</i> -dimethylammonium betaine
SPE	<i>N,N</i> -dimethyl- <i>N</i> -methacryloyloxyethyl- <i>N</i> -(3-sulfopropyl) ammonium betain
SSS	Sodium styrene sulfonate
VAEE	Vinyl 2-amino ethyl ether

viscosity and the predictions of Eq. (5). In Table 2 are also reported results for two other samples prepared at higher degrees of conversion which are expected to exhibit a broader net charge distribution. The agreement between the experiment and the theory is rather satisfactory. It must be stressed that these results are, up to now, the only ones available to perform a quantitative verification of the model of Higgs and Joanny [4].

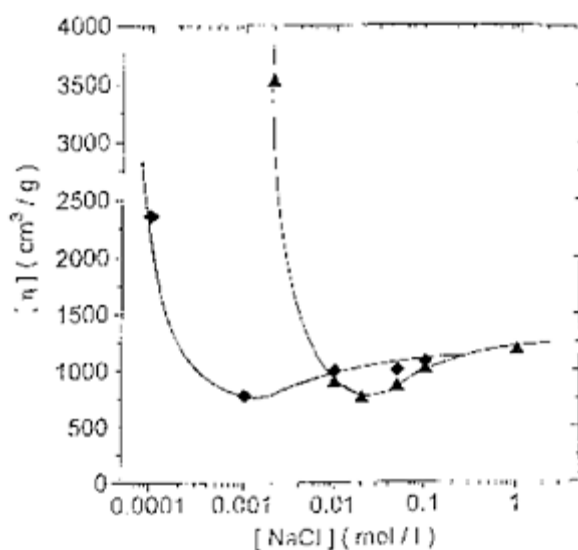


**FIG. 5** Intrinsic viscosity of linear polyampholyte terpolymers as a function of the salt concentration reported by Ohlemacher et al. (From Ref. 10.)

**TABLE 2** Minima of the Swelling vs.  $\kappa_S$  curves. The Last Two Columns Report Calculated and Experimental Values ( $\kappa_{0\min}$ ), Respectively

Degree of conversion	$10^2 f$	$10^2 \Delta f$	$\frac{\Delta f}{f}$	$\frac{8}{l_B} \frac{\Delta f^2}{f^2} (10^{-3} \text{ \AA}^{-1})$	$\kappa_{0\min} (10^{-3} \text{ \AA}^{-1})$	
	2.3	7.3	0.62	0.08	8	10
	4.4	9	1.14	0.13	18	45
	14.8	17.3	6.45	0.27	85	100
	26.8	12.9	3.47	0.38	155	140

### III. PROPERTIES OF PA GELS

#### A. Swelling Models

The equilibrium swelling of PA gels can be described with a Flory-Huggins-type model [18, 19] which takes into account the electrostatic interactions. The free energy of PA gels can be written as a sum of four independent terms:

$$F = F_{\text{elast}} + F_{\text{Flory}} + F_{\text{ion}} + F_{\text{electro}} \quad (7)$$

The elastic free energy of the gel  $F_{\text{elast}}$  gives rise to a negative swelling pressure which opposes the swelling of the network and which varies monotonously with the polymer concentration  $C_{\text{PA}}$ . Flory's mixing free energy [26]

$$\frac{F_{\text{Flory}}}{k_B T} \sim (1 - C_{\text{PA}}) \ln(1 - C_{\text{PA}}) - \chi C_{\text{PA}} (1 - C_{\text{PA}}) \quad (8)$$

The sign of this term can change depending on the values of the concentration and the polymer-solvent interaction parameter,  $\chi$ . In good solvent conditions, this term leads to a positive pressure, which promotes the swelling of the gel.

The entropic free energy of the counterions is

$$\frac{F_{\text{ion}}}{k_B T} \sim C_{\text{ion}} \quad (9)$$

The concentration of counterions  $C_{\text{ion}}$  is calculated assuming that a Donnan equilibrium is established between the gel and the surrounding solvent. The osmotic pressure associated with this term is always positive (low ionic strength) or zero (high ionic strength) and tends to swell the gel. In these models, this is the dominant term at low

ionic strength. The presence of both attractive and repulsive intramolecular as well as intermolecular interactions is a challenge for the modeling of the electrostatic interactions in gels.

### 1. Weakly Charged PA Gels

The polymer volume fraction of a neutral gel at swelling equilibrium is given by the classic expression [27]:

$$\phi_C = \left(\frac{A}{u}\right)^{3/5} \phi_0^{2/5} N_C^{-3/5} \quad (10)$$

where  $u=1/2-\chi$  is proportional to the classic (Flory) excluded volume. For weakly charged PA gels,  $u$  is replaced by the effective electrostatic excluded volume given by Eq. (4). The equilibrium swelling as a function of salt concentration is characterized by a minimum occurring at the monovalent salt concentration  $C_s^m$  given by:

$$C_s^m \sim \frac{2}{\pi l_B^3} \left(\frac{\Delta f}{f}\right)^4 \quad (11)$$

### 2. Strongly Charged PA Gels

The free energy of the electrostatic interactions in the case of strongly charged systems can, up to now, probably be best described by the model proposed by English et al., [19] which considered that charges of the network interact through a screened Coulomb potential and introduced a free-energy term analogue to Madelung energy in ionic crystals:

$$\frac{F_{\text{network}}}{k_B T} = -A l_B \left(\frac{f}{2} - |\Delta f|\right) \frac{\exp(-\kappa r)}{r} \quad (12)$$

$A$  is a constant of order unity (akin to the Madelung constant),  $N$  is the total number of monomers in the network, and  $r$  is the average distance between two charged first neighbor sites. This term is attractive when  $|\Delta f| < f/2$  ("polyampholyte" gel) and becomes repulsive when  $|\Delta f| > f/2$  ("polyelectrolyte" gel).

The first three terms of the free energy in Eq. (7) can describe qualitatively or semiquantitatively the swelling behavior of PA gels in the low ionic strength domain. In this region, the swelling behavior is essentially ruled by the entropy of the counterions and the elastic pressure of the polymer network. On the other hand, the typical PA behavior (increased swelling at high ionic strength), cannot be described correctly by these three terms. In the model proposed by Baker et al., [18] the electrostatic interaction term appears as a nonlinear corrective term. According to the numerical analysis

performed by the investigators, the contribution of this term describes qualitatively the experimental results.

Even though the models presented by Baker et al. and English et al. reproduce the experimental trends, it appears very clearly that quantitative comparisons with the experimental results are very delicate, among other things because of the number of fitting parameters involved.

## B. Experimental Results

Most of the studies have been performed on quenched PA copolymers or terpolymers for which the composition of the polymer network is expected to be that of the monomer feed. However, the microstructure of the polymeric network might be affected by the reactivity of the monomers. Contrary to the case of the solutions, it is not possible to stop the reaction at its early stage, and thus the gels investigated so far were obtained after full conversion of the monomers. As a consequence, the charge characteristics  $f$  and  $\Delta f$  at the mesoscopic scale might deviate significantly from the average ones. In particular, if one considers overall neutral gels in the absence of salt, the only systems for which the electroneutrality can be ensured at all spatial scales are those formed from zwitterionic monomers. Some illustrations of the influence of the microstructure of PA gels on their properties are given in the following sections. Different monomers have been used to prepare the PA gels. These monomers, with their abbreviated symbols, are listed in Table 2.

### 1. Swelling Equilibrium

In the absence of salt, the swelling ratio of gels at the swelling equilibrium is controlled by the presence of charged monomers and their counterions. For large charge offset,  $\Delta f$ , the gels must behave as polyelectrolytes, and high swelling ratios are expected owing to the translational entropy of the counterions. As  $\Delta f$  tends toward zero, the attractive interactions between oppositely charged monomeric units become predominant, thus producing a collapse of the network chains. Apart from possible effects arising from physicochemical differences in the charged monomers, one expects that the swelling properties will depend on  $f$  and  $\Delta f$  irrespective of the sign of the latter. However, the behavior observed experimentally is more complex as illustrated by Figure 6 that shows the variation of the swelling ratios at the equilibrium as a function of  $\Delta f$  for two systems with different overall charge fractions. Figure 6a refers to weakly charged AA/MAPTAC/SSS gels ( $f=0.045$ ) [12, 18]. Figure 6b shows the results obtained with fully charged NaAMPS/MADQUAT gels ( $f=1$ ). In these two systems, an asymmetrical swelling behavior was observed: the maximum swelling ratios are not the same for  $\Delta f$  of the same magnitude but of different signs. A possible explanation of this behavior might be related to solvent effects. Different hydrophobicities of the two charged monomers could account for the observed behavior. A skewed swelling ratio distribution, flattened toward the anionic side, was also reported for the MAPTAC/AMPS copolymer gels [19]. This behavior was attributed to the hydrogen-ion association to AMPS, but this hypothesis was not confirmed by observation of other NaAMPS-based systems.

Another intriguing observation, first reported by Baker et al. [12] and recently confirmed, refers to the difficulty of preparing moderately charged PA gels (e.g.,

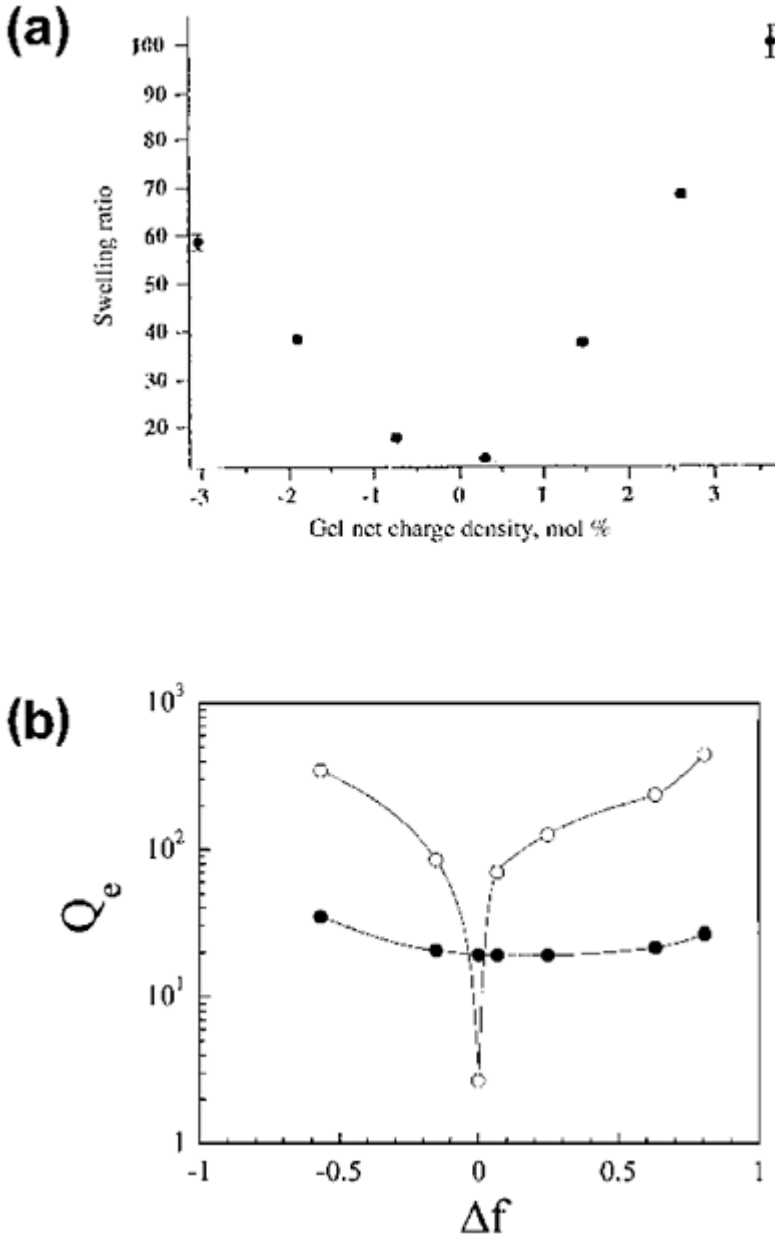


**FIG. 6** Effect of the net charge on the swelling behavior of different types of PA gels swollen in pure water. (a) Weakly charged



AA/MAPTAC/SSS gels ( $f=0.045$ ) reported by Baker et al. [12, 18]. The cross linker to monomer (molar) ratio is  $R_c=2\times 10^{-3}$ . The polymer concentration in the preparation state  $C_{PA}^0 = 0.16 \text{ g/mL}$ . (From Ref. 18.) (b) Fully charged NaAMPS/MADQUAT gels ( $f=1$ ). Closed symbols refer to gels at the swelling equilibrium in 2 mol/L NaCl solutions. The swelling ratios are taken with respect to the dried state.  $R_c=2\times 10^{-2}$  and  $C_{PA}^0 = 0.1 \text{ g/mL}$ . Solid lines are guides to the eye. (From Ref. 23.)

$f=0.1$ ) showing the behavior predicted for globally neutral gels. For instance, the minimum of the swelling ratio of AA/MADQUAT/NaAMPS gels with  $f=0.1$  was not obtained for an equimolecular content of ionic and cationic monomers but for a three to two ratios of MADQUAT to NaAMPS (C. Oelschlager, personal communication). Other effects which were not considered until now could also play a role. The samples previously mentioned were obtained by gelation in a Teflon tube. Recent experiments showed that the swelling behavior of weakly and moderately charged PA gels depends on the nature of the substrate (hydrophilic or hydrophobic), on the nature of the charged monomers, and on the cross-link density (C.Oelschlager, personal communication). It must be noted that the results of Figure 6a showing a minimum of the swelling ratio for  $\Delta f=0$  were obtained on gels prepared in glass tubes. These results suggest the possibility of a "template" effect. Gels are often prepared in glass tubes, pushed out of the tubes with a piston, and subsequently cut in smaller pieces for swelling or mechanical measurements. Samples prepared in Teflon containers are easier to extract from their mold than samples prepared in glass tubes and present much less damage due to fractures. Strong template effects have been reported by Osada et al. [28], which have shown that polyelectrolytic gels prepared in contact with a hydrophobic surface such as Teflon exhibit cross sections with concentration gradients ranging up to 1.6 mm. In the case of PA gels, the more hydrophobic monomer (e.g., MADQUAT) might concentrate close to the hydrophobic surface, and the final cylindrical gel would exhibit a net charge gradient from the periphery toward the axis. The gel as a whole would then swell as a mixture of two polyelectrolytic gels. This effect does not seem to be significant for fully charged gels obtained by copolymerization of two oppositely charged monomers, since one observes a sharp minimum of the swelling ratio for an equimolar composition of the monomer feed (Fig. 6b). Template effects could also explain in part the asymmetrical swelling behavior discussed above (see Fig. 6).

Although PA gels have a well-defined macroscopic  $\Delta f$  value which depends from the monomer feed composition, large domains with different net charges can still exist throughout the gel, and this can also contribute to an anomalous swelling behavior. In the case of solutions of linear PA, it was shown, both experimentally and theoretically, that the net charge distribution along the chains strongly influences their overall properties [3]. In this respect, it must be remembered that the synthesis of PA copolymers in solution promotes the formation of alternating sequences of monomers and that the kinetics of incorporation of the monomers (MADQUAT and NaAMPS) is not identical, with the reactivity ratio of MADQUAT being higher than the one of NaAMPS [29]. Therefore, monomer sequences in the PA chains are not going to be constant throughout

the synthesis. For example, in an equimolar mixture of the two monomers, the polymerization reaction has a tendency to form positively charged chains at the beginning of the synthesis and negatively charged ones at the end of the synthesis. These chains form neutral complexes and precipitate.

In PA gels, different preparation effects lead to samples with large spatial fluctuations of the net charge. Very crudely, a network having an average zero charge could be considered as a composite system in which there are domains with opposite signs of  $\Delta f$ . The presence of cross links limits considerably the possibility of forming complexes between oppositely charged chains. When the gels are washed out, the counterions associated with the charge offset of each domain are likely to be retained. Under salt-free conditions, these counterions will provide an osmotic pressure able to swell the gel as in the case of polyelectrolytic gels. Upon visual inspection, globally neutral MADQUAT/NaAMPS gels ( $\Delta f=0$ ) swollen in pure water are turbid, and become clearer when swollen in brines. This fact appears more clearly in Figure 7a, which shows two samples swollen in pure water and a 2 mol/L NaCl solution illuminated by a He-Ne laser. It is clear that the gel swollen in pure water scatters light the most. Heterogeneous structures reminiscent of phase separation were also observed by optical microscope [23]. Figure 7b shows the internal structure of a MADQUAT/NaAMPS gel with  $\Delta f=0.04$  at the local minimum of the swelling ratio obtained for  $C_s=0.1$  mol/L of sodium chloride.

Another observation concerns the minimum swelling ratio at equilibrium, or the extent to which the polymer network collapses. The minimum swelling ratio is relatively large for terpolymer gels, which can be accounted for by the contribution of the neutral monomeric units to the excluded volume. For copolymer-based gels, the collapse is more marked, but the swelling ratio is still significantly larger than unity (on the order of three times with respect to the dry state). This could be due to the here above-mentioned existence of domains with different  $\Delta f$ .

Let us turn now to the effect of the salt. Figure 6b shows the variation of the swelling ratio as a function of  $\Delta f$  for AMPS/MADQUAT copolymer gels at high ionic strength (2 M NaCl). We note that the swelling ratio at very high ionic strength varies very slightly with the net charge. Since, in principle, all the electrostatic interactions are screened at this ionic strength, the small variation of  $Q_e$  can be attributed to structural differences of the gels and/or to solvent effects. In fact, we observe the same trend as at low ionic strength, namely, a larger swelling ratio for gels containing predominantly NaAMPS, the more soluble monomer. The evolution of  $Q_e$  as a function of salt concentration for fully charged gels carrying a wide range of net charges is represented in Figure 8. We identify three characteristic behaviors. When the net charge of the gels is important (Fig. 8a) the equilibrium swelling decreases with the salt concentration. This is classic polyelectrolytic behavior [24, 30, 31]. The swelling pattern of a globally neutral PA gel is shown in Figure 8b. In this case, the swelling ratio at equilibrium increases with the salt concentration, following the exact opposite trend observed in polyelectrolytic gels (antipolyelectrolytic behavior). When PA

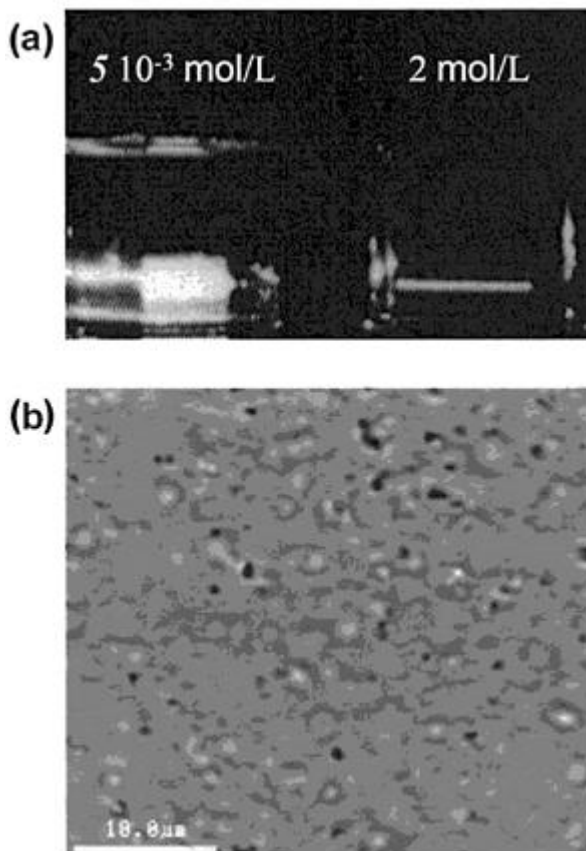


**FIG. 7** (a) Photograph of two NaAMPS/MADQUAT gels with  $\Delta f=0$  illuminated by a He-Ne laser ( $Rc = 2 \times 10^{-2}$  and  $C_{PA}^0 = 0.1 \text{ g/mL}$ ). The samples are in equilibrium with their swelling solvent: pure water (left-hand side) and 2 mol/L NaCl (right-hand side). (b) Differential interference contrast micrograph of a thin (<1 mm) NaAMPS/MADQUAT gel at swelling equilibrium in 0.1 mol/L NaCl solution [23]. The scale of the image is indicated by the 10- $\mu\text{m}$  bar [23].

gels carry a small net charge, we remark that it is possible to describe the swelling equilibrium as a simple superposition of polyelectrolytic behavior (at low ionic strength) and PA behavior (at high ionic strength). Swelling curves as a function of salt concentration are then characterized by a distinct minimum (Fig. 8c).

The same type of variations of  $Q_e$  with the ionic strength have been reported for weakly charged gels, but it is difficult to establish a correlation with  $\Delta f$  because of the uncertainty in the effective value of the latter parameter. Referring back to the template effect reported above, one observes quite different swelling behaviors depending on the

nature of both the monomers and the substrate used for the sample preparation. Figure 9 shows the comparison between the salt

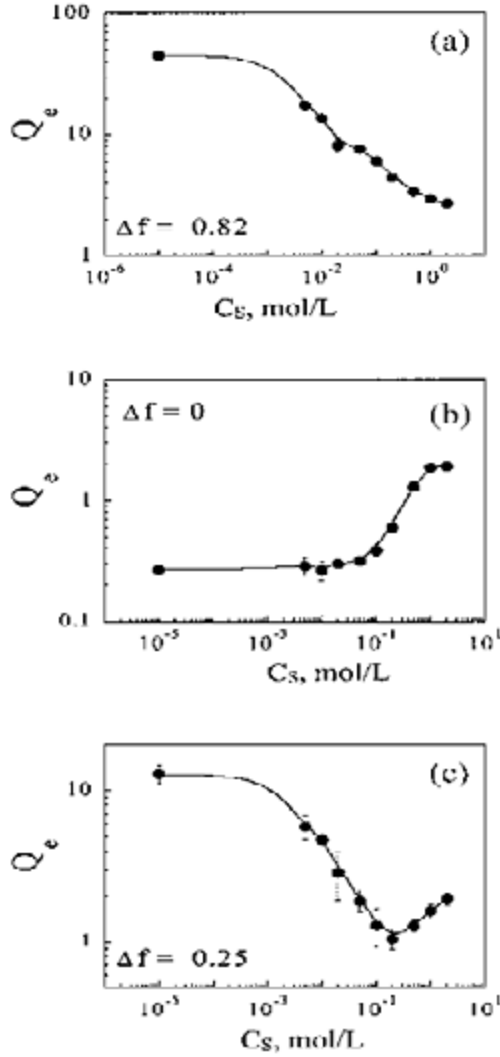


**FIG. 8** Variation of the swelling ratio at equilibrium,  $Q_e$ , as a function of the salt concentration for NaAMPS/MADQUAT gels having different net charges  $\Delta f$ .  $R_c = 2 \times 10^{-2}$  and  $C_{PA}^0 = 0.1 \text{ g/mL}$ . (a) PE behavior,  $\Delta f = 0.82$ . (b) Neutral PA behavior,  $\Delta f = 0.0$ . (c) Intermediate PA behavior,  $\Delta f = 0.25$ . Solid lines are guides to the eye [23].

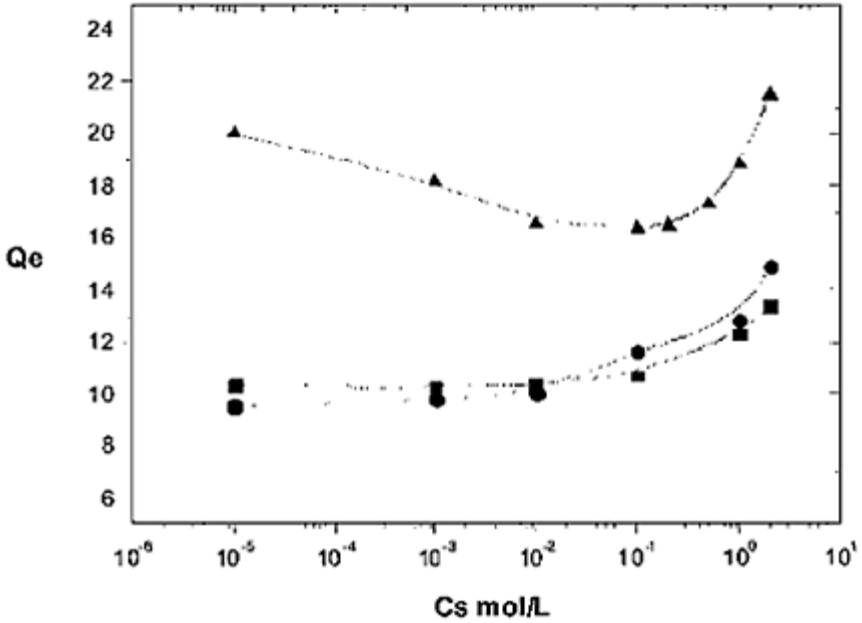


**FIG. 9** (a) Swelling ratio at equilibrium,  $Q_e$ , versus salt concentration for gels prepared with a stoichiometry ensuring  $\Delta f=0$  and  $f=0.1$ : AM/NaAMPS/MADQUAT prepared in a Teflon tube (▲), AM/NaAMPS/MADQUAT (●), and AM/SB (■) gels prepared in a glass tube.  $R_c=2 \times 10^{-2}$  and  $C_{PA}^0 = 0.1$  g/mL. Note the nonneutral PA behavior of the samples prepared in a Teflon tube.

concentration dependencies of the swelling ratio for two identical gels, one prepared in a Teflon container and the other in a glass tube. The latter displays the typical swelling pattern of an electroneutral gel characterized by a collapse at low ionic strength and reswelling at high salt concentration, whereas the former behaves as an unbalanced PA. Gels formed by copolymerization of AM with a zwitterionic monomer (sulfobetain) also exhibit the swelling behavior of an electroneutral gel [18] independently on the nature of the substrate (Fig. 9).

The general features of the swelling behavior of PA gels can be qualitatively reproduced with the existing models, but a quantitative comparison is difficult. In particular, the prediction of Eq. (11) concerning the effect of  $\Delta f$  on the position of the minimum in the  $Q_e$  versus  $C_s$  curves could not be verified because of the uncertainty in the effective  $\Delta f$  for moderately charged gels for which the prediction is made. Still, this minimum was found to shift to higher salt content as the net charge of fully charged gels is increased, as illustrated by Figure 10.

Another interesting property of PA gels concerns the Donnan equilibrium which is established between the gel and its surrounding solvent. Neutral PA gels immersed in a

brine should extract salt from the surrounding solution; see, for

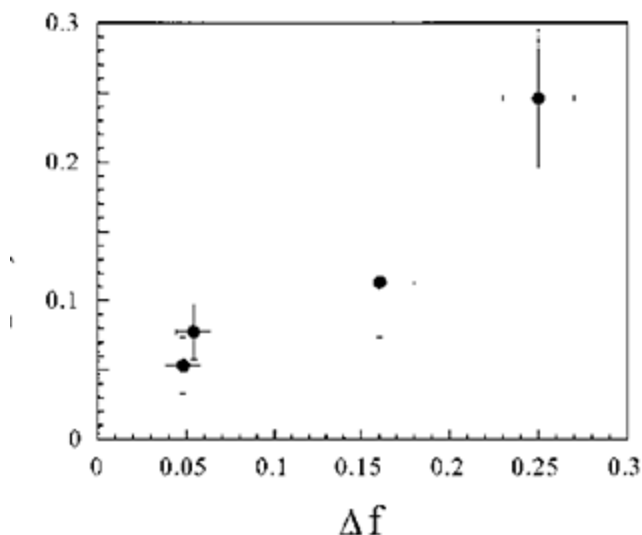


**FIG. 10** The salt concentration  $C_s^{\min}$  corresponding to the minima of the swelling curves of NaAMPS/MADQUAT PA gels (see Fig. 8c) increases a function of  $\Delta f$ .  $R_c = 2 \times 10^{-2}$  and  $C_{PA}^0 = 0.1 \text{ g/mL}$ . This behavior is in qualitative agreement with Eq. (11). (From Ref. 23.)

instance, Eq. (6). Again, a quantitative comparison with the models is difficult for the same reasons as before. Furthermore, the effect should be weak for moderately charged gels (see Fig. 3). Huglin and Rego [11] have performed an extensive study of the effect of salt on the properties of hydrogels of 2-hydroxyethyl methacrylate (HEMA) with sulfobetaine (SBE) comonomers. The swelling ratio of these gels is quite small (of the order of 1) because of the hydrophobicity of the methacrylate monomers. Figure 11 shows the variation of the salt partitioning coefficient between the gel and the surrounding solution as a function of copolymer composition of gels immersed in a 1-M KCNS (potassium thiocyanate) aqueous solution. It can be seen that for the optimal copolymer composition there is an uptake of about 20% of salt in the gel.

Yet another aspect of the properties of gels concerns the reversible and discontinuous volume changes in response to the variations of environmental physicochemical conditions. To date, the volume phase transition of monoionic gels have been extensively studied, whereas only few experimental works have reported a discontinuous swelling behavior of polyampholyte gels. Katayama et al. reported that an acrylamide-based polyampholyte gel exhibits a volume phase transition in a water-acetone mixture, and the swelling volumes of the gels change linearly from an equimolar gel (50/50) with respect to the residual concentration of ionic constituents [20, 32]. The effect of the net charge on the volume phase transition in water-acetone mixtures of an annealed gel (VAEE/AA) has also

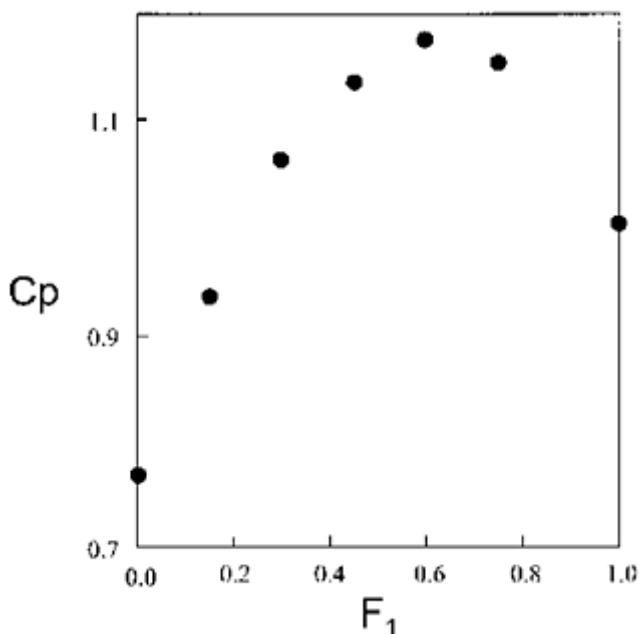


**FIG. 11** Partitioning coefficient,  $C_p$ , of salt (ratio of the molality of salt in the gel swollen at equilibrium to that of the external solution) as a function of the mole fraction of SPE (zwitterionic) in the HEMA/SPE gels immersed in a 0.1 potassium thiocyanate aqueous solution. The cross-linking ratio,  $R_c=5 \times 10^{-3}$  and the polymer concentration in the preparation state is on the order of 1 g/mL but varies as function of monomer feed. (From Ref. 11.)

been reported [33]. NIPAM-based amphoteric gels have also been synthesized and their swelling behavior investigated as a function of the temperature. NIPAM gels are known to be thermosensitive gels; namely, they undergo a volume phase transition in water which is triggered by temperature. The swelling behaviors of the NIPAM/NDAPA/NaAMPS gels were found to be strongly dependent on the NDAPA/NaAMPS ratio, as illustrated in Figure 12. The gel containing an equimolar NDAPA and NaAMPS ratio showed transition temperatures and swelling ratios close to those of NIPAM gels. Only the amplitude of the discontinuous volume change was less for the amphoteric gel. A similar result was obtained for electroneutral NIPAM/betaine acrylamide gels. Upon an increase of the net charge of the gel, both the transition temperature and the swelling ratio increase. These results show that only polyelectrolytic effects are important for the features of the volume phase transition [34].

## 2. Light Scattering

The turbidity of PA gels observed under some ionic strength conditions (see Fig. 7)

indicates the presence of a microstructure at the scale of visible light. Light

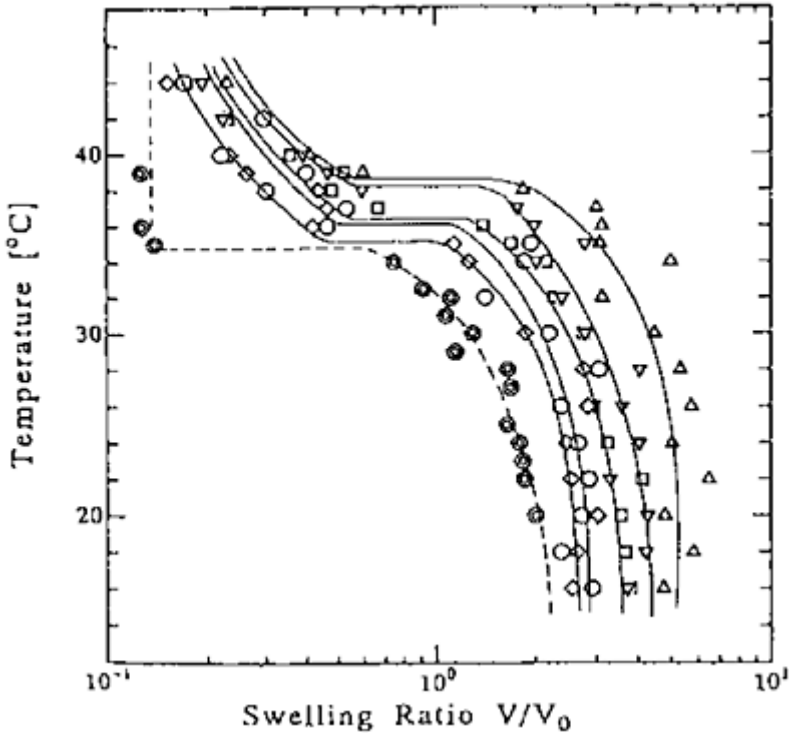


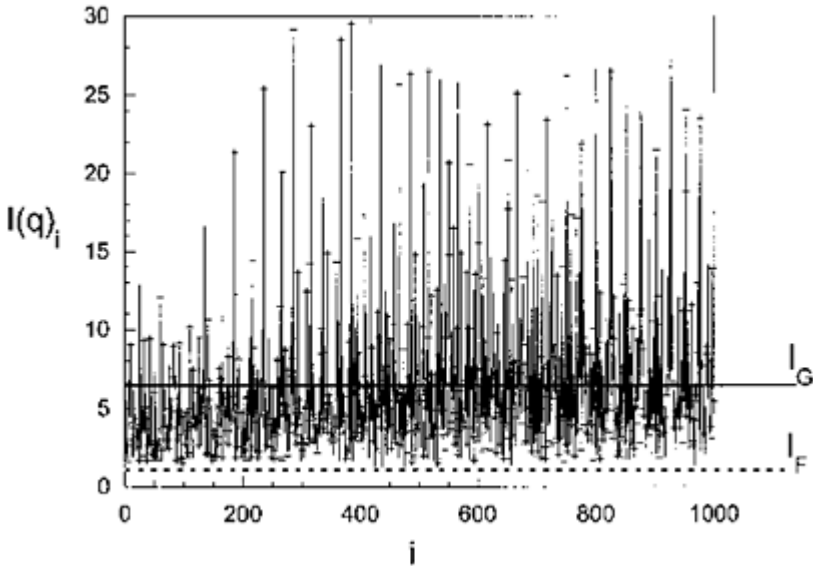
**FIG. 12** Swelling equilibrium curves of NIPA/NDAPA/NaAMPS PA gels and NIPA (⊙) gels in water. The total ionic density of the amphoteric gels are fixed at 1 mol%. The molar ratios of NaAMPS/NDAPA are (Δ) 100/0, (□) 75/25, (◇) 50/50, (○) 25/75, and (▽) 0/100.  $R_c = 2 \times 10^{-2}$  and  $C_{PA}^0 = 700 \text{ mmol/L}$ . (From Ref. 20.)

scattering experiments can provide information on this microstructure as was shown in a recent study [23]. In a polymeric gel, the polymer segments are restricted by the cross links to particular regions of the sample and are only able to perform limited Brownian motion about fixed average positions. As a result, one particular sample of a gel is trapped in a restricted region of phase space defined by its average configuration and the extent of the fluctuations about this configuration. To investigate the domain of the phase space that is actually explored by the system, ensemble averages over a representative number of all possible spatial configurations need to be performed. The dynamic properties of polymeric gels have been investigated using dynamic light scattering (DLS) [35]. The scattered intensity was found to be the sum of a random thermal component and a quenched term that depends on the location of the scattering volume inside the gel. The rapidly fluctuating component,  $I_f$  is related to the osmotic compressibility of the gels

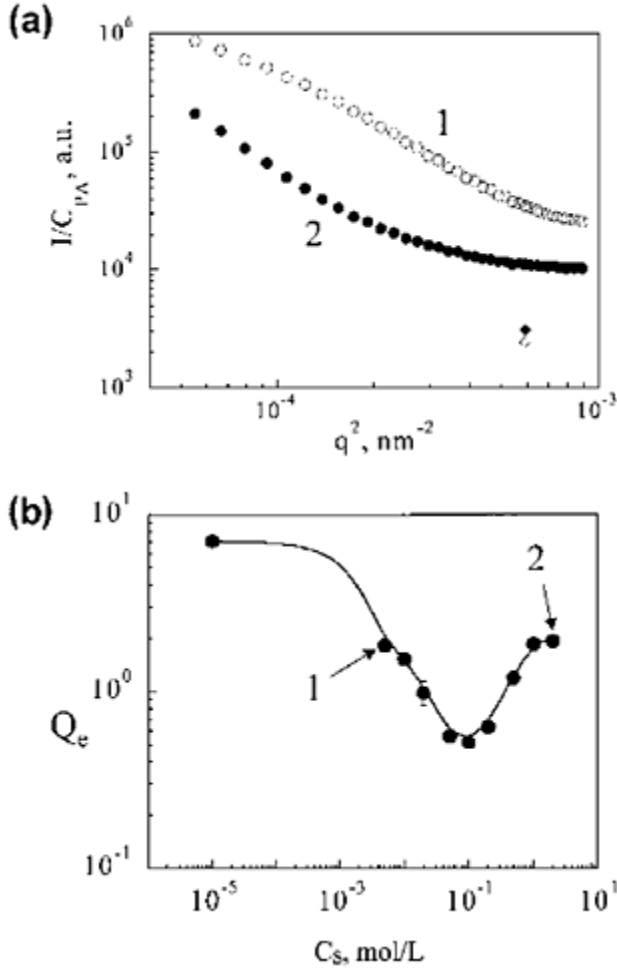


[36], whereas the frozen-in scattered intensity,  $I_0$ , reflects long-range static density fluctuations of the polymer network [37]. The latter result from microstructural effects.

Light-scattering experiments were performed on fully charged NaAMPS/ MADQUAT gels. Samples for light-scattering measurements were swollen at equilibrium then sealed into cylindrical light-scattering cells. The light-scattering experimental set-up has been described previously [38]. The intensity of light scattered by a gel as well as its autocorrelation function depend on the sample position and the diffusing volume considered [35, 39]. Ensemble averages of the static intensity scattered at each diffusing angle,  $\theta$ , were obtained by rotating the sample with continuous current motor. The total measured intensity for each scattering angle results from the average of a hundred different measurements. Each data set corresponded to at least 200 different scattering angles. For each angle, the total scattered intensity as a function of time,  $I(t)$ , can be written as  $I(t)=I_F(t)+I_G$  where  $I_F(t)$  and  $I_G$  denote the rapidly fluctuating and the frozenin (gel) components of the scattered intensity, respectively [37]. Figure 13 shows a typical variation of scattered intensity when scanning over 1000 positions in the sample. The large fluctuations from one location to the other result from the frozen-in intensity, whereas the constant background is due to the rapid thermal fluctuations. Alternatively, the decomposition into frozen and fluctuating components were achieved by measuring averages of at least 1000 autocorrelation functions of the scattered intensity corresponding to different positions of the gel. Figure 14 shows the ensemble average scattered intensity as a function of the



**FIG. 13** Intensity scattered from a PA gel ( $R_c=2\times 10^{-2}$  and  $C_{PA}^0 = 0.1 \text{ g/mL}$ ) as a function of position (1000 data points are displayed). The solid line indicates the ensemble averaged scattered intensity,  $I_G$ . The dotted line shows the fluctuating scattered intensity,  $I_F$ .

$I_F$ 


**FIG. 14** (a) Static structure factors of fully charged NaAMPS/MADQUAT gels ( $\Delta f=0.048$ ) swollen at equilibrium (1) in 0.005 mol/L NaCl ( $\circ$ ) and (2) 2 mol/L NaCl ( $\bullet$ ). Diamonds indicate the level of fluctuating scattered intensity,  $I_F$  for samples swollen in 2 mol/L NaCl ( $\blacklozenge$ ) and 0.005 mol/L NaCl ( $\diamond$ ).  $Rc=2 \times 10^{-2}$  and  $C_{PA}^0 = 0.1 \text{ g/mL}$ . The error bars are smaller than the symbols. (b) Swelling curve of the NaAMPS/MADQUAT gel shown in (a). The gels reach the same equilibrium swelling for two different salt concentrations, the static structure factors shown in (a) correspond to these two conditions [23].

scattering vector  $q=4\pi n/\lambda \sin(\theta/2)$  for two NaAMPS/MADQUAT gels with a small net charge at the swelling equilibrium and at different ionic strengths. It can be seen that for a given swelling equilibrium ratio, the gel scatters considerably more in low ionic strength conditions than in concentrated salt solutions. Furthermore, the scattering arises mainly from the frozen-in component, which is associated with static density fluctuations. The strong upturn of the scattered intensity at low angle is related to the presence of dense regions in the gel having a characteristic size outside of the range accessible to the light-scattering spectrometer (greater than  $0.2 \mu\text{m}$ ). This microstructure has been associated with the creation during the preparation of the gel of domains having different net-charge values, some with  $\Delta f$  close to zero (PA) and others where  $\Delta f$  differ from zero (polyelectrolytes, PE). At low ionic strength, the PA domains are collapsed, whereas the PE domains are swollen owing to the combined effects of the entropy of the counterions and the intrachain electrostatic repulsion of the network chains. In these conditions, the gel would exhibit a microsegregated structure [40] showing dense and dilute polymer regions. On the other hand, electrostatic interactions are screened at high ionic strength, and in this case the entropic term associated with the counterions is practically equal to zero. Therefore, in these conditions, the gel behaves almost as a neutral system and the structural differences between the predominantly PE and the predominantly neutral PA domains have to decrease. Figure 14 shows the scattering patterns of the same gel sample swollen at equilibrium in a highly concentrated salt solution (2 Mol/L) and in a moderately concentrated brine (0.05 Mol/L). In both cases, it is clear that the scattering is

essentially resulting from the frozen-in density fluctuations, since  $I_G \gg I_F$ . The same gel sample scatters more light when swollen in the low ionic strength solution. The attractive interactions dominate once they are no longer screened by the presence of salt, driving a local collapse of the gel and enhancing the frozen-in component of the scattered intensity. As far as the fluctuating component  $I_F$  is concerned, Figure 14 shows that  $I_F$  decreases when the gel is swollen in a low ionic strength brine (0.05 Mol/L). The osmotic compressibility of a gel swollen in a low ionic strength solvent is expected to be lower than for a gel swollen in a high ionic strength solvent. This is essentially due to the difference in counterion entropy. As  $I_F$  and the osmotic compressibility are directly related, this is in qualitative agreement with the observations.

### 3. Shear Modulus

Up to now, only one study on the elastic properties of PA gels has been reported [23]. The study concerns fully charged NaAMPS/MADQUAT gels with various  $\Delta f$  values. The elastic shear moduli,  $G$ , of PA gels were determined from uniaxial compression measurements. (For details concerning experimental set-up and protocol, see, for example, Refs. 22 and 36.) Non-Gaussian elasticity effects appear at high swelling ratios [31, 36, 41].

The variation of the shear modulus of PA gels at swelling equilibrium presents a very rich behavior, shown in Figure 15. The observed patterns can be divided in three qualitatively different cases. The first case, shown in Figure 16a, corresponds to gels carrying a large majority of anionic or cationic groups (polyelectrolytic behavior). The shear modulus varies in a nonmonotonous way as a function of the swelling ratio at

equilibrium  $Q_e$ , decreasing at first following a

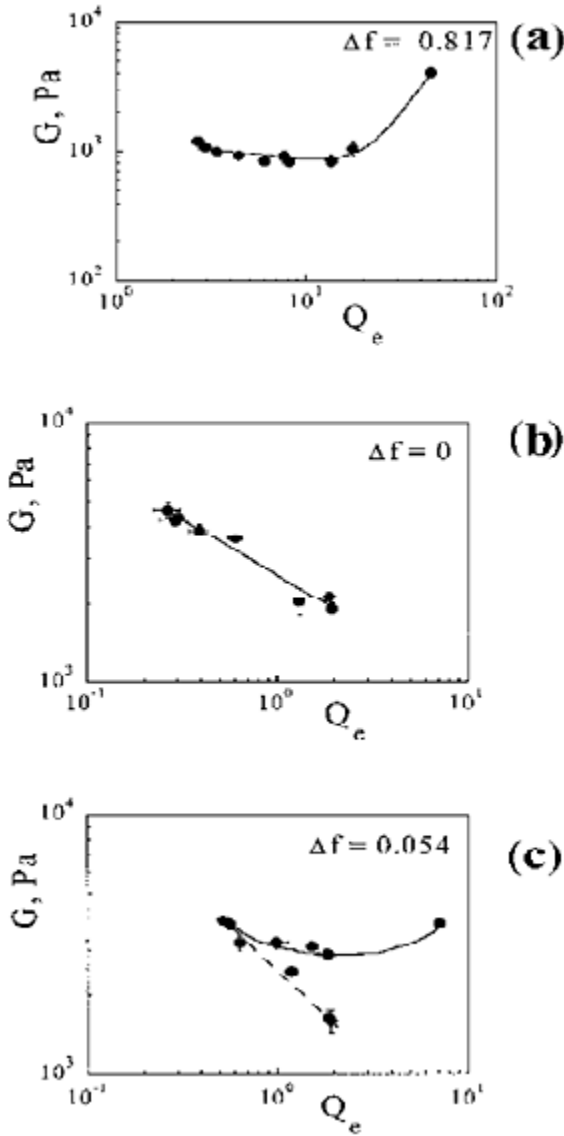


**FIG. 15** Shear moduli at swelling equilibrium of PA gels having different net charges,  $\Delta f$  (indicated in the figures).  $Rc=2 \times 10^{-2}$  and  $C_{PA}^0 = 0.1 \text{ g/mL}$ . Lines are guides to the eye. Solid lines correspond to low ionic strength conditions (PE behavior). The dashed line indicates high ionic strength conditions (PA behavior) [23].

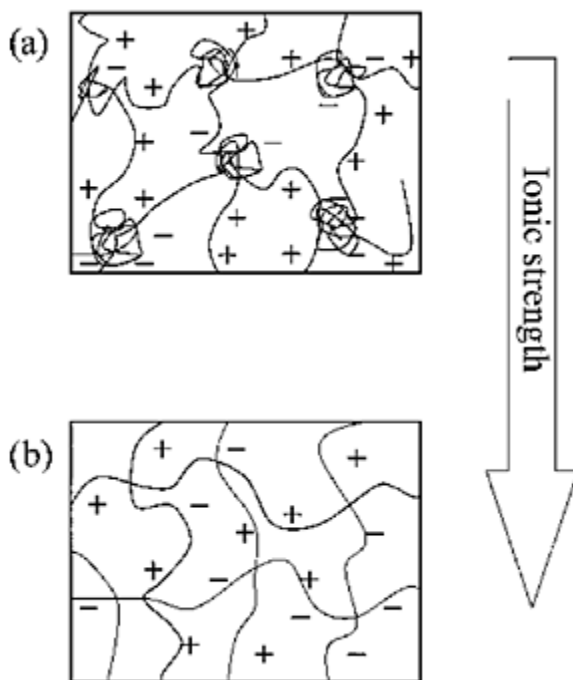


**FIG. 16** Internal structure of a PA gel carrying a small net charge. (a) Low ionic strength: Complexes between oppositely charged chains are formed giving rise to large scale heterogeneities. (b) High ionic strength: Electrostatic interactions are screened and the network is as homogeneous as if it were neutral.

power law with an exponent close to  $-1/3$  and then strongly increasing at high swelling ratios. This behavior is identical to the one observed in polyelectrolytic gels, and the upturn of the elastic modulus is usually interpreted in terms of finite extensibility of the network strands [41]. The second case, shown in Figure 15b, corresponds to globally neutral gels ( $\Delta f=0$ ). In this case, the elastic modulus was found to decrease monotonously with increasing gel volume. If fitted to a power law, the data yielded an apparent exponent of  $-0.4(\pm 0.05)$ . Classic theories of the elasticity of neutral gels [41] predict a

$$G \sim Q_e^{-1/3}$$

behavior. The third case corresponds to PA gels carrying a slight net charge. Again, as for their swelling behavior, it is possible to describe their elastic response as a super-position of a “polyelectrolyte” and a “neutral polyampholyte” branches. The polyelectrolyte branch corresponds to gels swollen in low ionic strength conditions. The polyampholyte branch corresponds to gels swollen in high ionic strength conditions. The elastic modulus was always found to be smaller for gels swollen in concentrated salt solutions (i.e., the polyampholyte branch is always below the polyelectrolyte branch). Ultimately, the most peculiar feature is that same gel having the

same volume (i.e., same swelling ratio) is characterized by two different elastic moduli depending on the salt concentration of the solvent. The elastic modulus can vary up to a factor 2.

The classic approaches of the elasticity of gels cannot account for the observed behavior. According to the recent models by Panyukov [42], Obukov [43], and Rubinstein et al. [44], the shear modulus,  $G$ , of a gel can be written as a function of the swelling ratio with respect to the preparation state  $Q$ , the end to end distance of a network strand in the preparation state,  $R_0$ , and the reference end to end distance of a network chain,  $R_{\text{ref}}$

$$G \sim Q^{-1/3} \left( \frac{R_0}{R_{\text{ref}}} \right)^2 \quad (13)$$

In the case where samples were issued from the same preparation bath (preparation state), for a given swelling ratio, the numerator of Eq. (13) should be a constant. The only difference therefore is in the denominator, or the reference state. A value of the shear modulus which is higher at low ionic strength than at high ionic strength indicates that the conformation of the chain in the reference state has to be more compact at low ionic strength than at high ionic strength. To the best of our knowledge, this is not predicted by any of the models of nonneutral PA chains.

The explanation of the observed behavior might be linked to the existence of the microsegregated structure revealed by the light-scattering experiments, which is schematically represented in Figure 16. It can be assumed that at low ionic strength, the PE domains have a high shear modulus because of the finite extensibility of the network strands (non-Gaussian elasticity) and that these domains dominate the elastic behavior of the gel.

#### IV. SUMMARY

Polyampholytic gels display a wide range of swelling and elastic behaviors as well as complex morphologies. The degree of charge imbalance carried by the network dictates the global properties of the gels. The properties of PA gels carrying a large net charge are analogous to the properties of PE gels; among others, their equilibrium swelling ratio is very large in pure water and decreases monotonously with rising salt concentration. The features of the volume phase transition were also found quite similar to those of PE systems. The variation of the shear modulus as a function of the swelling ratio at equilibrium  $Q_e$  is also identical with the one observed in PE gels. Namely, upon increasing the salt content, the shear modulus varies in a nonmonotonous way, decreasing at first following a power law with an exponent close to  $-1/3$  and then showing an upturn due to non-Gaussian elastic effects in the high-swelling region. Globally neutral PA gels are characterized by an antipolyelectrolytic behavior. In this case, the gels collapse at low ionic strength and swell monotonously upon rising salt concentration.

Polyampholytic gels carrying a small net charge show a characteristic minimum in

their swelling curves, and the same gel can have the same equilibrium volume in two different ionic conditions. The measurement of elastic moduli showed an unexpectedly rich behavior, which can be described in terms of PA and PA "branches." Remarkably, a PA gel can reach the same swelling ratio at equilibrium for two different ionic strengths, but it is then characterized by two different values of the shear modulus. This result is difficult to interpret in the classic theoretical framework, and is likely to be associated with microstructural effects: the volume variations of the gels are accompanied by rearrangements of the gel structure which were detected through light-scattering measurements. At high ionic strength, the gels appear to be more homogeneous at the mesoscopic scale than at low-salt content. This behavior is opposite to the one observed in PE gels. In the latter case, the osmotic pressure due to the entropy of counterions tends to suppress static long-range density fluctuations. In the case of weakly charged PA gels, the domains with different net charges, which are created during synthesis, are revealed at low ionic strength because of different local swelling, whereas the screening effect due to the presence of a large amount of salt tends to smooth down the frozen-in fluctuations.

The general features of swelling equilibrium patterns follow qualitatively the theoretical predictions for conformational changes of single polyampholyte chains. The results are also in qualitative agreement with ad hoc models developed to describe the swelling of PA gels. A major limitation for a quantitative analysis of the experimental data is linked to the difficulty to control the net charge of weakly charged gels for which one has theoretical predictions. Neutral gels can be prepared from zwitterionic monomers. As for weakly unbalanced gels, the different reactivity of the three monomers and/or template effect prevent to attribute to the samples a defined value of  $\Delta f$ . On the other hand, these effects can be used to prepare some composite-like materials susceptible to present interesting responsive properties; in particular, in the presence of applied electric fields [21, 33].

## ACKNOWLEDGMENTS

The authors are grateful to T.Tanaka and to C.Oelschlager for communicating their results prior to publication, and they also wish to thank Y.Osada for stimulating discussions.

## REFERENCES

1. JT Alfrey, H Morawetz, EB Fitzgerald, RM Fuoss. J Am Chem Soc 72:1864, 1950; A Katchalsky, IR Miller. J Polym Sci 13:57, 1954; JT Alfrey, RM Fuoss, H Morawetz, SH Pinner. J Am Chem Soc 74:438, 1952; JT Alfrey, SH Pinner. J Polym Sci 23:533, 1957.
2. EA Bekturov, SE Kudaibergenov, SR Rafikov. Rev Macromol Chem Phys C 30:233, 1990; JC Salamone, WC Rice. In: Encyclopedia of Polymer Science and Engineering. HF Mark, NM Bikales, CG Overberger, G Menges, eds. Wiley, New York, 1987 pp 514.
3. F Candau, J-F Joanny In: Polymeric Materials Encyclopedia. JC Salamone, ed. CRC

Press, Boca Raton, FL, 1996.

4. PG Higgs, J-F Joanny. *J Chem Phys* 94:1543–1555, 1991.
5. Y Kantor, H Lin, M Kardar. *Phys Rev Lett* 69:61–64, 1992.
6. AV Dobrynin, M Rubinstein. *J Phys II* 5:677–695, 1995.
7. D Bratko, AK Chakraborty. *J Phys Chem* 100:1164–1173, 1996; Y Kantor, M Kardar, H Lin. *Phys Rev E* 49:1383–1392, 1994.
8. JM Corpart, F Candau. *Macromolecules* 26:1333–1343, 1992; S Neyret, F Candau, J Selb. *Acta Polymer* 47:323–332, 1996; CL McCormick, CB Johnson. *Macromolecules* 21:694, 1988.
9. S Neyret, A Baudouin, J-M Corpart, F Candau. *II Nuovo Cimento* 16:669–674, 1994; S Neyret, F Candau, J Selb. *Acta Polym* 47:323–332, 1996.
10. A Ohlemacher, F Candau, J-P Munch, SJ Candau. *J Polym Sci: Part B: Polym Phys* 34:2747–2757, 1996.
11. MB Huglin, JM Rego. *Macromolecules* 24:2556, 1991; MB Huglin, JM Rego. *Polymer* 32:3354, 1991; MB Huglin, JM Rego. *Macromolecules* 26:3118, 1993.
12. JP Baker, DR Stephens, HW Blanch, JM Prausnitz. *Macromolecules* 25:1955–1958, 1992.
13. R Everaers, A Johner, J-F Joanny. *Europhys Lett* 37:275–280, 1997.
14. M Skouri, J-P Munch, SJ Candau, S Neyret, F Candau. *Macromolecules* 27:69–76, 1994.
15. M Tanaka, T Tanaka. *Phys Rev E* 62:3803–3816, 2000.
16. M Tanaka, AY Grosberg, V Pande, T Tanaka. *Phys Rev E* 56:5798, 1997.
17. M Annaka, T Tanaka. *Nature* 355:430–432, 1992; LTM Than, EE Makhaeva, AR Khokhlov. *Polym Gels Netw* 5:357–367, 1997; S Mafe, JA Manzanares, AE English, T Tanaka. *Phys Rev Lett* 79:3086–3089, 1997.
18. JP Baker, HW Blanch, JM Prausnitz. *Polymer* 36:1061, 1995.
19. AE English, S Mafe, JA Manzanares, XH Yu, AY Grosberg, T Tanaka. *J Chem Phys* 104:8713–8720, 1996.
20. S Katayama, A Myoga, Y Akahori. *J Phys Chem* 96:4698–4701, 1992.
21. SE Kudaibergenov. *Berichte der Bunsen-Gesellschaft-Physical Chemistry-Chemical Physics* 100:1079–1082, 1996.
22. J Bastide, SJ Candau, L Leibler. *Macromolecules* 14:719–726, 1980.
23. G Nisato, J-P Munch, SJ Candau. *Langmuir* 15:4236–4244, 1999.
24. R Skouri, F Schosseler, J-P Munch, SJ Candau. *Macromolecules* 28:197–210, 1995.
25. M Skouri, JP Munch, SJ Candau, S Neyret, F Candau. *Macromolecules* 27:69–76, 1994.
26. PJ Flory ed. *The Principles of Polymer Chemistry*. Cornell University Press, Ithaca, NY, 1953.
27. See, for instance, J Bastide, SJ Candau, L Leibler. *Macromolecules* 14:719–726, 1980.
28. T Narita, A Hirai, J Xu, JP Gong, Y Osada. *Biomacromolecules* 1:162–167, 2000.
29. JM Corpart, F Candau. *Colloid Polym Sci* 271:1064–1067, 1993.
30. J Hasa, M Ilavsky, K Dusek. *J Polym Sci Polym Phys Ed* X 13:253–262, 1975; G Nisato, F Schosseler, SJ Candau. *Polym Gels Netw* 4:481–498, 1996; A Katchalsky, I Micheli. *J Polym Sci* 15:69–86, 1955.
31. UP Schröder, W Opperman. In: *Physical Properties of Polymeric Gels*. JPC Addad, ed. Wiley, Chichester, UK, 1996 pp 19–38.
32. A Myoga, S Katayama. *Polym Prepr Jpn* 36:2852, 1987.
33. SE Kudaibergenov, VB Sigitov. *Langmuir* 15:4230, 1999.



34. N Wada, Y Yagi, H Inomata, S Saito. *J Polym Sci A* 31:2647, 1993.
35. JGH Joosten, J McCarthy, PN Pusey. *Macromolecules* 24:6690–6699, 1991.
36. G Nisato, Rachid Skouri, F Schosseler, J-P Munch, SJ Candau. *Faraday Discussions*. 133–146, 1995.
37. C Rouf, J Bastide, JM Pugol, F Schosseler, J-P Munch. *Phys Rev Lett* 73:830–833, 1994; C Rouf-George, JP Munch, F.Schosseler et al. *Macromolecules* 30:8344–8359, 1997.
38. R Skouri, F Schosseler, J-P Munch, SJ Candau. *Europhys Lett* 23:635–640, 1993.
39. A Moussaid, J-P Munch, F Schosseler, SJ Candau. *J Phys II France* 1:637–650, 1995; PN Pusey, WV Megen. *Physica A* 157:705–741, 1989; J-Z Xue, DJ Pine, ST Milner, X-L Wu, PM Chaikin. *Phys Rev A* 46:6550–6563, 1992.
40. AR Khokhlov, OE Philippova, N Sitnikova, SG Starodubtsev. *Faraday Discussions* 101 “Gels.” 125–131, 1995.
41. LRG Treloar, ed. *The Physics of Rubber Elasticity*. Clarendon Press, Oxford, UK, 1975.
42. SV Panyukov. *Soviet Phys JETP* 71:372–379, 1990.
43. SP Obukhov, M Rubinstein, RH Colby. *Macromolecules* 27:3191–3198. 1994.
44. M Rubinstein, RH Colby, AV Dobrynin, J-F Joanny. *Macromolecules* 29:398–406, 1995.



# Polyelectrolyte/Ionomer Behavior of Polymer Gels

**OLGA E. PHILIPPOVA and ALEXEI R. KHOKHLOV** *Moscow State University, Moscow, Russia*

## I. BACKGROUND

Electrostatic effects are among the main factors which determine the state of ioncontaining gels. These effects can favor either the gel swelling or the gel collapse [1, 2].

Let us consider a gel with a small fraction of ionizable monomer units. Pronounced gel swelling is usually observed in polyelectrolyte regime; that is, in the case when ion-containing groups are fully dissociated with the formation of charged monomer units and free small counterions, neutralizing the network charges (Fig. 1). Free counterions try to occupy as much volume as possible in order to gain in the translational entropy, but they cannot escape outside the gel because of the condition of macroscopic electroneutrality. As a result they create an exerting osmotic pressure leading to gel swelling. In the polyelectrolyte regimen, the presence of only 5 mol% of charged repeat units in polymer gel chains can induce gel swelling by two orders of magnitude (in comparison with its uncharged state) [3].

An alternative regimen (ionomer regimen) is observed when counterions are condensed on oppositely charged monomer units with the formation of ion pairs (see Fig. 1). An ion pair can be considered to be a strong ionic dipole. Dipole-dipole attraction between different ion pairs can lead to their aggregation with each other to multiplets. In the ionomer regimen, gel is in the collapsed state. This is due to two main causes: (1) the decrease of the intranetwork osmotic pressure because of the binding of mobile counterions and (2) the additional crosslinking of the gel as a result of the aggregation of ion pairs to multiplets.

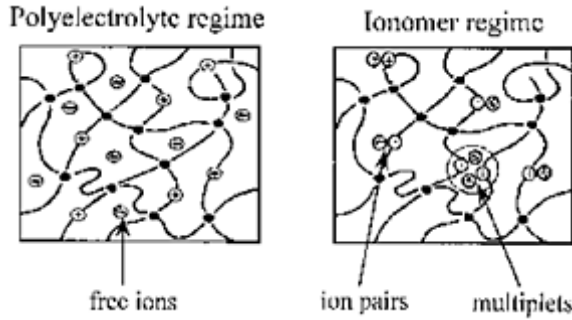


**FIG. 1** Schematic representation of ion-containing gel in polyelectrolyte and ionomer regimes.

What are the conditions for ion pair formation? Association of two opposite charges into an ion pair results in a gain in electrostatic energy. In the case of two monovalent ions, the electrostatic energy,  $E$ , can be written in the following form:

$$E = \frac{e^2}{\epsilon a} \quad (1)$$

where  $e$  is the elementary charge,  $\epsilon$  is the dielectric constant of the medium, and  $a$  is the intercharge distance in the ion pair.

At the same time, the formation of an ion pair leads to a loss of the translational entropy of counterion. The loss of translational entropy is of the order of  $kT$  to the logarithmic factor accuracy.

When the gain in electrostatic energy overcomes the losses in entropy ( $E > kT$ ), the ion pair formation is favorable. In this case, we have the ionomer regimen. In its turn the polyelectrolyte regimen is realized when the electrostatic interactions are weak and cannot overcome the losses in translational entropy ( $E < kT$ ).

The same gel can be either in a polyelectrolyte regimen or in an ionomer regimen depending on the conditions; for example, on the dielectric constant of the medium. The ionomer regimen is usually observed in low polar media. A rough estimation shows [4, 5] that the approach of two point elementary charges of opposite signs within distance of 0.2 nm of each other in a medium with dielectric constant  $\epsilon = 2.5$  leads to the release of energy of the order of 100 kT. At so high a gain in energy which far overcomes possible losses of entropy, all the available charges are aggregated into ion pairs, and almost no free ions remains in the system. But when the polarity of medium increases, the energy gain due to the electrostatic attraction of oppositely charged ions decreases [see Eq. (1)] and finally becomes comparable with the value of  $kT$ . At these conditions, the transition from ionomer to the polyelectrolyte regimen takes place.

Therefore, along with a pure polyelectrolyte regimen (free counterions) and a pure ionomer regimen (bound counterions), a mixed polyelectrolyte/ionomer regimen can be observed. In this case, some of counterions are free, whereas others form ion pairs. This

regimen is rather common, and the existence of ion pairs in this regimen can be responsible for many effects observed in the behavior of polymer gels.

## II. THEORETICAL CONSIDERATION

A theory of polymer gel collapse accounting for the mixed polyelectrolyte/ ionomer behavior, that is, for the partial formation of ion pairs and multiplets, was developed by Khokhlov and Kramarenko [6]. The theory took into account the fact that the dielectric constant,  $\epsilon$ , of the gel depends on the volume fraction of polymer inside the gel (i.e., on the degree of swelling of the gel). In the swollen state, the value of  $\epsilon$  is close to that of the solvent, whereas in the collapsed state, it is close to that of the dry polymer (whose dielectric constant is usually low). Therefore, the amount of ion pairs and multiplets should be much larger for the collapsed gels. In other respects, the consideration followed the usual framework of the theory of polymer gel collapse [7–10].

It turned out [6] that if the formation of ion pairs inside the gel is taken into account, the region of stability for the collapsed state and the volume change at the transition point are larger than in the conventional theory. In addition to this, the theory predicted [6] a quite new effect; namely, the possibility of existence of two states of a collapsed gel: the normal collapsed state where there is enough solvent, so that the amount of ion pairs is not large, and the “supercollapsed” state. In the latter state, the polymer volume fraction within the gel is so large (and the dielectric constant of the gel medium is so low) that numerous ion pairs form a well-defined ionomer multiplet structure. The supercollapsed state is usually separated from the slightly collapsed state by a potential barrier. To overcome this barrier, the following avalanche-type process should be induced: The polymer concentration in some part of the gel must occasionally (i.e., due to fluctuations) become so high and the dielectric constant so low that the amount of new ion pairs formed in this region induces further contraction of this part of the gel, etc.

Further theoretical consideration [11] has shown that in the mixed polyelectrolyte/ionomer regimen a very surprising effect is possible; namely, the collapse induced by the gel ionization. This is indeed unexpected, because one might think that when the degree of charging increases, the gel should swell. But this is true only in the polyelectrolyte regimen when all the counterions are free. The situation is changed when we have ion pairs along with free ions. In this case, with the increase of the gel ionization, the number of both free ions and ion pairs increases. At small charge content, the degree of swelling is determined by the contribution of free ions. But when the concentration of ion pairs becomes high enough so that the ion pairs can meet each other and form multiplets, the collapsed state with the multiplet structure becomes thermodynamically more favorable and the gel shrinks. Therefore, an increasing degree of ionization increases the thermodynamic advantages of the collapsed state with the ionomeric multiplet structure over the swollen polyelectrolyte state.

Therefore, the theory considered the manifestation of the mixed polyelectrolyte/ionomer behavior (1) at the increase of the gel ionization and (2) at the decrease of the polarity of medium inside the gel in the course of collapse transition.

### III. EXPERIMENTAL OBSERVATION OF POLYELECTROLYTE/IONOMER BEHAVIOR IN POLYMER GELS

#### A. Gels with Monovalent Counterions

##### 1. Collapse Induced by Poor Solvent of Low Polarity

To observe a pronounced collapse transition with rather high amplitude of the volume change of the gel, it is first necessary to use a highly swollen gel. A high degree of swelling of gels is mainly due to the osmotic pressure exerted by mobile counterions. Therefore, highly swollen gels are usually polyelectrolyte gels, and they are swollen by water, since true dissociation of an ionizable group with the formation of a charged monomer link and free counterion is possible only in a highly polar medium (water is the best and most common example of such a medium,  $\epsilon=78$ ). One of the most widespread methods used to induce the collapse of water-swollen gels is the addition of a poor organic solvent of low polarity. Upon the gradual addition of a low polar poor solvent to water, the value of the dielectric constant of the medium decreases, and some of the ionizable units of the gel which potentially can dissociate form ion pairs with the corresponding counterions.

The effect of the polarity of poor solvent on the collapse of water-swollen gel was studied for polyacrylamide (PAAm) gels containing 1.8 mol% of charged repeat units of sodium methacrylate [12]. Three poor solvents with different polarity were used: methanol ( $\epsilon=32.6$ ), ethanol ( $\epsilon=24.3$ ), and dioxane ( $\epsilon=2.2$ ). It was shown that the decrease of the polarity of poor solvent leads to two main effects: (1) decrease of the degree of swelling of the gel in a swollen state and (2) shift of the collapse transition toward the lower content of a poor solvent. These results were explained [12] by the increasing tendency toward the formation of ion pairs between network charges and counterions with decreasing polarity of the solvent.

The microstructure of slightly charged PAAm gels collapsed in poor solvent (ethanol) was studied by small-angle X-ray scattering (SAXS) [13]. It was shown that the gel collapse in a water/ethanol mixture is accompanied by an abrupt increase of the value of scattering exponent,  $\mu$ , evaluated from the SAXS intensity curve,  $I(q)$ , according to the fitting of  $I(q) \sim q^{-\mu}$  in the range of scattering vectors,  $0.1 \text{ nm}^{-1} < q < 0.47 \text{ nm}^{-1}$ . The increase of the value of the scattering exponent, which indicates the appearance of microheterogeneities, may be due to the formation of ionomer multiplets.

A pronounced collapse transition can be observed not only for ion-containing gels swollen by water but also for the gels swollen by other solvents with rather high polarity if upon the addition of poor solvent the change in the polarity is sufficiently large [14]. Such experiments were performed for anionic gels of copolymers of N,N-dimethylacrylamide with 2-(acrylamido)-2-methylpropane-sulfonic acid immersed in a mixture of dimethyl sulfoxide ( $\epsilon=48.9$ ) and tetrahydrofuran ( $\epsilon=7.6$ ). The gels undergo a sudden collapse when the content of low polar solvent (tetrahydrofuran) gradually increases. Collapse was attributed to "dipolar attractions of the ion pairs in nonpolar or

low-polarity media" [14].

## 2. Collapse Induced by Gel Ionization

In the previous section, we described the behavior of polymer gels with a constant content of ionizable groups which underwent collapse transition when the solvent quality became poorer. The mixed polyelectrolyte/ionomer behavior can also be observed when the solvent quality remains unchanged, but the content of ionizable groups in the gel increases.

This can be illustrated by the swelling behavior of poly(methacrylic acid) (PMAA) and poly(acrylic acid) (PAA) gels upon ionization in methanol ( $\epsilon=32.6$ ) [15]. The ionization of PAA and PMAA was performed by the addition of a strong base sodium methoxide. It was found that the initial increase of the degree of ionization leads to a usual polyelectrolytic swelling of the gel owing to the exerting osmotic pressure of counterions neutralizing the network charges. When a certain degree of ionization,  $\alpha$ , was reached ( $\alpha \approx 0.1$ ), a pronounced gel collapse was observed (Fig. 2). To demonstrate the fact that the collapse is induced by the formation of ion pairs, the conductivity measurements were performed. It was shown that the gel collapse is accompanied by a significant drop of the reduced conductivity (Fig. 2). This proves that the gel collapse proceeds with the binding of free counterions to ion pairs.

The more the number of charged monomer units in the gel, the more thermodynamically advantageous is the state of the collapsed gel with ionomer multiplet structure because of the great energy gain due to the formation of ion pairs and their subsequent aggregation to multiplets. This leads to the sudden collapse of the gel at some definite degree of ionization. At higher ionization

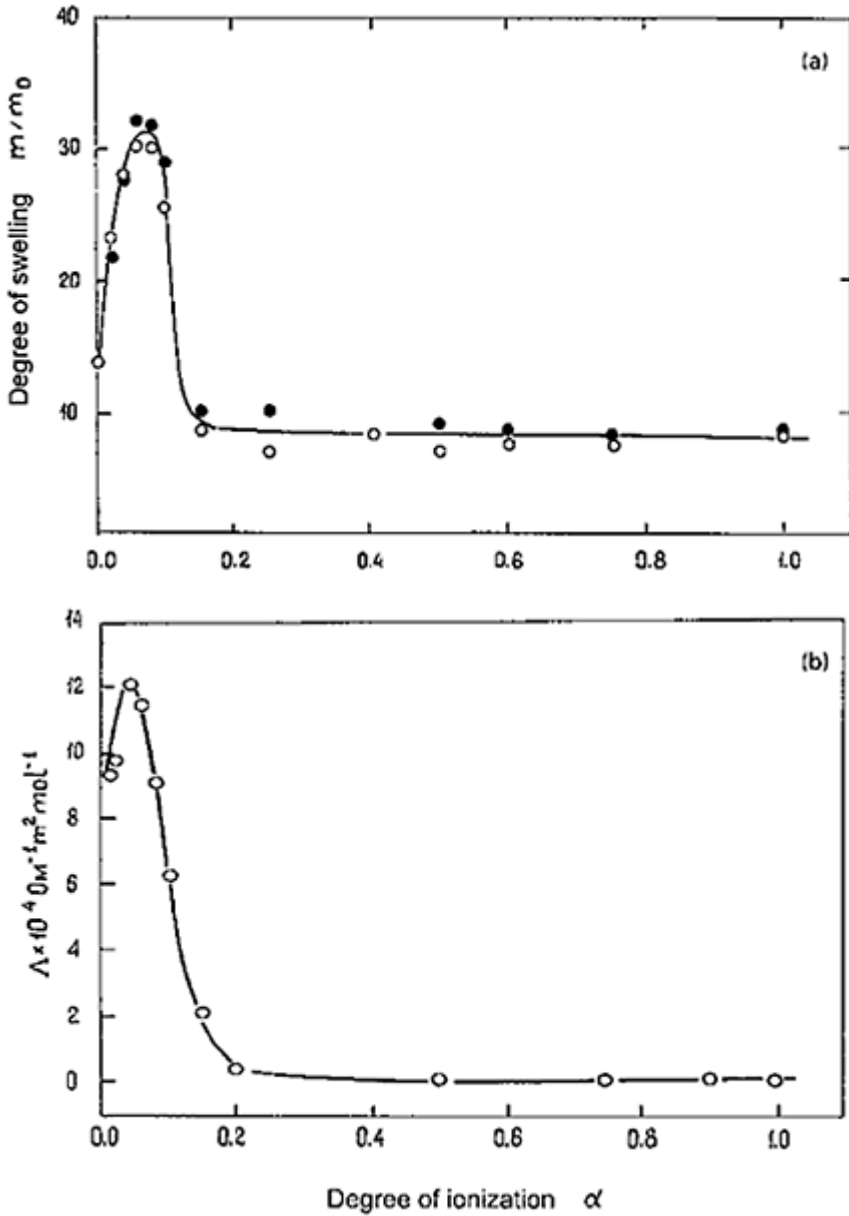


**FIG. 2** Collapse induced by gel ionization. Degree of swelling (a) and the reduced conductivity (b) as a function of the degree of ionization  $\alpha$  for PMAA gel in methanol at 25°C.  $m/m_0$  is the ratio of the mass of the gel equilibrated in solution to the mass of the dried gel. (From Ref. 15.)



degrees, the gel is always in the collapsed state with a developed ionomer multiplet microstructure.

To study the aggregation of ion pairs to multiplets in charged PMAA gels swollen by methanol, the dielectric method was used [16]. It was found that at low frequencies of the applied electric field, the dielectric constant becomes as great as  $10^7$ . According to Deng and Mauritz [17], very high values of the dielectric constant can be due to the aggregation of dipoles with each other into large aggregates with high polarizability, which can be regarded as ionomer multiplets. The change of the external electric field induces a correlated displacement of several dipoles in the direction of the field, which results in a very significant polarization of multiplet. The analogous high values of the dielectric constant were obtained for perfluorosulfonate ionomers [17].

A mixed polyelectrolyte/ionomer behavior of PAA and PMAA gels was observed [15] in media of intermediate polarity ( $20 < \epsilon < 50$ ), where the collapsed state of the gel with the ionomer structure can compete with a swollen state of the gel with free counterions. In more polar media, the pure polyelectrolyte regimen dominates, and the gel swells with an increasing degree of ionization. In less polar media, the gel shows a pure ionomer behavior—it shrinks with increasing degree of ionization.

A collapse induced by ionization was also observed at the titration of linear PAA and PMAA in methanol and ethanol [18, 19]. It was shown that the reduced viscosity of these polymers at first grows and then decreases drastically in a small interval of the degree of ionization of a polyacid. Osmotic pressure and conductance measurements indicate a strong reduction of the net charge during collapse transition and a low degree of charge after the transition. These results were explained by counterion binding to the ions of the chains with the formation of ion pairs. Therefore, the behavior of polymer gels is quite reminiscent of that of linear polymers.

### 3. Collapse Induced by Salt

Another example of the mixed polyelectrolyte/ionomer behavior has been shown in studies by Kudo et al. [20] and Starodoubtsev et al. [21], where the effect of low molecular weight salts on the swelling behavior of cationic gels was investigated.

Kudo et al. [20], studied the interaction of cationic gels of poly(N-n-butyl-N, N-dimethyl-4-vinylbenzylammonium bromide) with different salts, LiBr, NaBr, KBr,  $\text{NH}_4\text{Br}$ , NaCl, NaI, and  $\text{NaClO}_4$ , in aqueous media. The results obtained demonstrate a striking effect of the nature of salt anion:  $\text{I}^-$  and  $\text{ClO}_4^-$  ions lead to the jumpwise collapse of the gel, whereas other anions cause only a slight gradual contraction of the gel. This effect was explained by the higher ability of  $\text{I}^-$  and  $\text{ClO}_4^-$  ions to form ion pairs with positively charged network units.

This suggestion was partially confirmed for the gel collapse induced by iodide ions [20]. From the study of the ion-exchange reaction upon immersion of Br-containing gel in NaI solution, it was shown that the iodide ions are more tightly bound to the gel than bromide ions. More effective binding of iodide ions with cationic gel may be due to a higher polarizability of iodide ions in comparison with bromide ions or to a lower degree of hydration of iodide ions. In addition, the ion pairs formed by  $\text{I}^-$  have a very significant dipole moment, which favors the clustering of the ion pairs in the multiplets. Both effects

(ion pairs formation and their clustering) cause the gel collapse.

A peculiar feature of the salt-induced collapse [21] is that iodide ions can induce the gel collapse only if the network contains a sufficiently high amount of cationic repeat units. This allows one to suggest that the collapsed ionomeric state of the network becomes competitive with the swollen polyelectrolytic state only at high enough fractions of the ion-containing groups because of the tendency of ion pairs to associate.

Of particular interest is the fact that the transition from the polyelectrolyte to ionomer regimen has also affected the kinetics of the gel collapse [21]. It was shown that, in the presence of NaI, the collapse of cationic gel of poly(diallyldimethylammonium chloride) proceeds in two steps (Fig. 3). The first step (also observed in the other salts, e.g., sodium chloride, bromide, or acetate) corresponds to a fast polyelectrolyte contraction due to the usual “screening” effect of the salt. The last step probably corresponds to the slower processes of ion pairs formation. It was suggested that the two-step kinetics of the collapse reflects a potential barrier which separates the two states of the collapsed gel: with and without ionomeric multiplets. These results are in general agreement with the theoretical data [11] which predict the existence of two states of collapsed gels called “collapsed” and “supercollapsed” states.

## B. Gels with Multivalent Counterions

In the case of gels with multivalent counterions, the electrostatic interactions are so strong that we can expect the ion aggregation even in rather polar media; for example, in water. To be able to study the ion aggregates in such gels on a molecular level, the fluorescent counterions, namely, the trivalent europium ions, were chosen [22–24].

$\text{Eu}^{3+}$  ions are widely used as fluorescent probes, because their luminescence is very sensitive to their microenvironment [24]. The most sensitive are fluorescence bands corresponding to the f-f transitions forbidden in electrodipole approximation; for example, the band of electrodipole transition,  $^5\text{D}_0 \rightarrow ^7\text{F}_2$ , at 614 nm. Usually this band is very weak, but the strong and asymmetrical electric field around  $\text{Eu}^{3+}$  ions leads to its significant enhancement. In particular, the enhancement of the forbidden band can be due to the binding of  $\text{Eu}^{3+}$  ions to

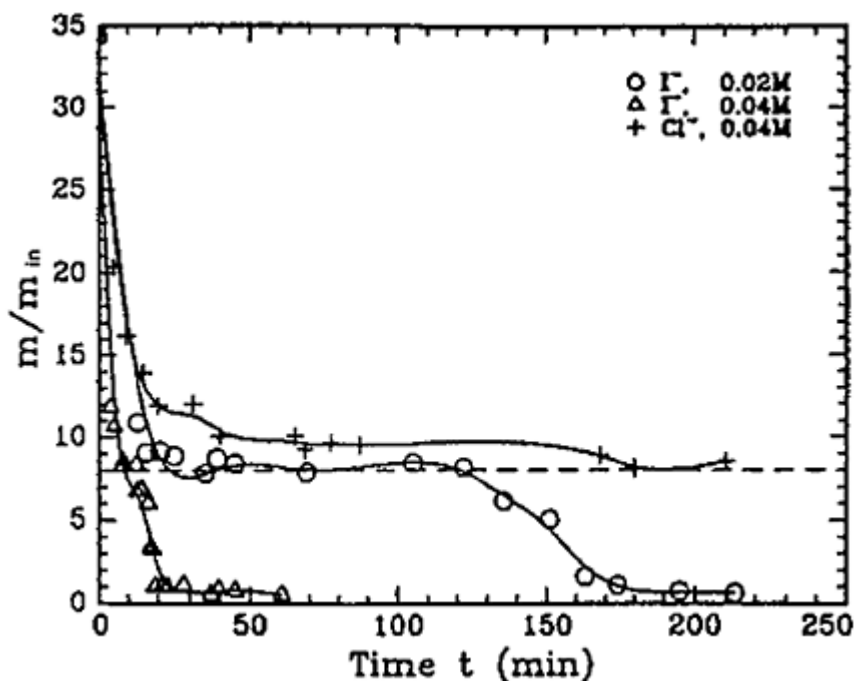


**FIG. 3** A two-step collapse of ion-containing gels induced by salt. Time dependence of the swelling ratio of poly(diallyldimethylammonium chloride) gel in 0.04 and 0.02 M sodium iodide and 0.04 M sodium chloride. The dashed line indicates a volume of the gel sample after being immersed in 0.04 M sodium chloride solution for 2 days.  $m/m_{in}$  is the ratio of the mass of the gel equilibrated in solution to the mass of the gel just after polymerization. (From Ref. 21.)

oppositely charged ligands. In contrast to forbidden bands of electrodipole transitions, the peaks of the allowed magnetodipole transitions (e.g., the peak at 591 nm) show small intensity variations with the change of the microenvironment of the probe. Therefore, the intensity ratio of forbidden bands to allowed ones in the fluorescence spectra of  $\text{Eu}^{3+}$  (e.g.,  $I_{614}/I_{591}$ ) can be used as a measure of the extent of interaction of  $\text{Eu}^{3+}$  ions with surrounding ligands [25].

In the study by Smirnov et al. [24], the fluorescence of europium ions was applied to the investigation of the interaction of hydrogels of poly(sodium acrylate) and of poly(sodium methacrylate) with multivalent ions in aqueous media. The immersion of poly(sodium acrylate) and of poly(sodium methacrylate) gels in aqueous solutions of europium nitrate led to an effective absorption of europium ions by the gel until almost complete ion exchange with network counterions  $3\text{Na}^+ \rightarrow \text{Eu}^{3+}$ .

Figure 4 shows the fluorescence spectrum of  $\text{Eu}^{3+}$  in the gel swollen in water and in aqueous solution of low molecular weight salt of  $\text{Eu}^{3+}$  (at the same

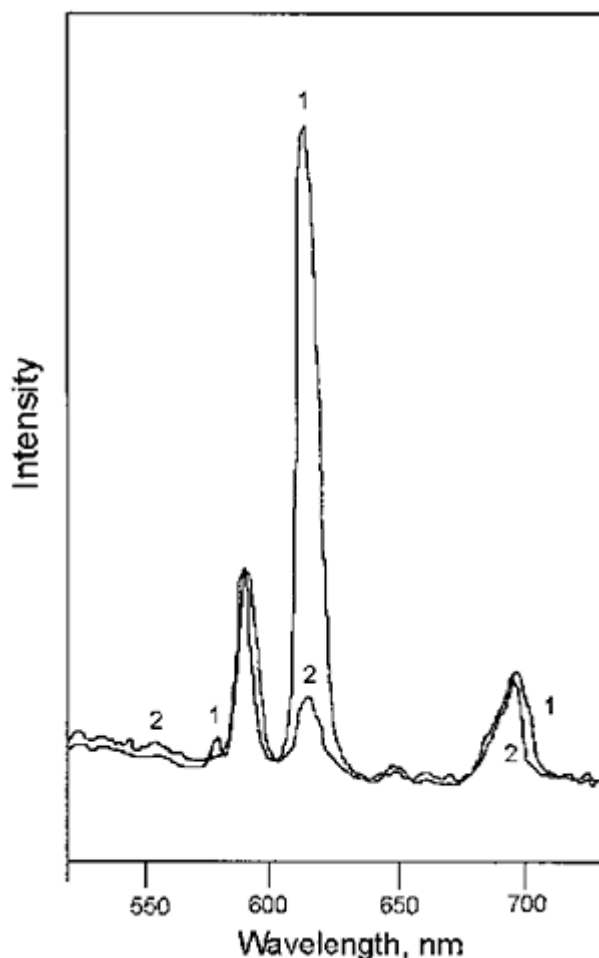


**FIG. 4** Fluorescence emission spectra of the gel of poly(europium acrylate) (1), equilibrated in water, and of aqueous solution of  $\text{Eu}(\text{NO}_3)_3$  (2), obtained under excitation at 395 nm (in both cases the concentration of  $\text{Eu}^{3+}$  was 0.011 mol/L). The spectra are normalized to the intensity of the allowed 591-nm band. (From Ref. 24.)

concentration of europium ions). It is known that, at these conditions, the low molecular weight salt is completely dissociated and we observe the fluorescence of free ions. From Figure 4, it is seen that in the gel the relative intensity of the forbidden band at 614 nm increases dramatically. This indicates that in the  $\text{Eu}^{3+}$  ions are bound to oppositely charged groups of the network [24]. Therefore,  $\text{Eu}^{3+}$  ions are not bound to small ligands, but they are bound to polymer ligands. The reason is that, in the case of a polymer ligand, the formation of ion aggregates leads to much smaller losses of entropy, because the

anions are initially immobilized on the polymer chains.

In water, a free  $\text{Eu}^{3+}$  ion is surrounded by a hydration shell consisting of nine water molecules. At binding, the ligand can expel some of these water molecules. This process should lead to the increase of the lifetime of the excited state of  $\text{Eu}^{3+}$ , because water molecules are effective quenchers of the luminescence of  $\text{Eu}^{3+}$ . The rate of deexcitation via this process is directly proportional to the number of water molecules in the first coordination sphere and does not depend appreciably on the other ligands coordinated around the  $\text{Eu}^{3+}$  ion. This forms the basis of a method of determination of the number of water molecules surrounding rare earth ions from the fluorescence relaxation data [26]. The treatment of the experimental data by means of this method has shown that the binding to polymer chains leads to the release of four to five water molecules from the hydration shell of  $\text{Eu}^{3+}$  ion [24].

Thus,  $\text{Eu}^{3+}$  ions form ion aggregates with the network countercharges. These ion aggregates are characterized by (1) immediate contact of oppositely charged ions which is evident from fluorescence relaxation data and (2) by very asymmetrical arrangement of network countercharges around  $\text{Eu}^{3+}$  ions which is evident from the enhancement of forbidden bands.

Owing to the asymmetrical distribution of charges, the aggregate ( $\text{Eu}^{3+} + 3\text{COO}^-$ ) can be considered to be a dipole. Such dipoles can further self-organize with each other to multiplets owing to dipole-dipole attraction. The multiplet formation was studied by means of energy transfer,  $\text{Eu}^{3+} \rightarrow \text{Nd}^{3+}$ , between different kinds of counterions simultaneously present in the gel [24].

Figure 5 shows the decay curves of the excited state of  $\text{Eu}^{3+}$  in the gel. It is seen that, in the presence of acceptor ( $\text{Nd}^{3+}$ ), the decay rate increases. This is obviously due to the energy transfer,  $\text{Eu}^{3+} \rightarrow \text{Nd}^{3+}$ . If we assume a random distribution of counterions in the system (i.e., the absence of multiplets), the decay rate should be proportional to the average concentration of acceptors. At the same time, the experimental data show [24] that the 60-fold increase of the concentration of acceptors is accompanied by a rather slight increase of the rate of energy transfer (by a factor of approximately 2). Such behavior is possible if ions aggregate with each other to multiplets. In this case, even at low average concentration of acceptors, the decay rate is high enough because of the close contact between donors and acceptors inside the multiplets.

The treatment of the relaxation data as described elsewhere [22, 23] gave the value of the aggregation number of multiplets. It was shown that the multiplets consist of seven rare earth ions together with the corresponding network counter-charges. The aggregation number remains constant upon variation of the overall concentration of rare earth ions in a wide range (from 0.2 to 2.0 mol/L).

The existence of multiplet-like aggregates of ions in a rather polar medium is nontrivial. The reason for the stability of the aggregates can be a high level of polarization of the quadruplets ( $\text{Eu}^{3+} + 3\text{COO}^-$ ), ensuring an enhanced electro-static attraction between them.

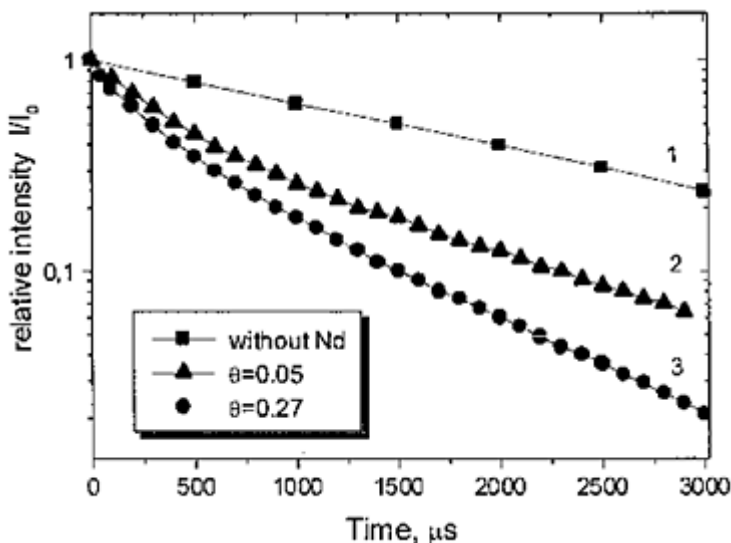


**FIG. 5** Decay curves of fluorescence from  $\text{Eu}^{3+}$  ( $^5\text{D}_0$ ) level in poly(europium acrylate) (PA-Eu) gel at the ratio rare earth ion/ $\text{COO}^-$   $\theta=0.27$  (1) and in PA-Eu, Nd gels at  $\theta=0.05$  (2) and 0.27 (3) at a constant Eu/Nd ratio equal to 9 ( $\lambda_{\text{ex}}=530$  nm,  $\lambda_{\text{em}}=614$  nm). (From Ref. 24.)

The analogous results were obtained for the same gels in less polar solvent methanol [22]. But in this case the “primary” ion aggregates (quadruplets) already exist in the solution of low molecular weight salt of europium. In a polymer gel, the ion aggregation proceeds further up to the formation of multiplets. Probably this is connected with the fact that the primary aggregates are already immobilized on the gel chains, and further aggregation does not lead to significant loss of entropy.

#### IV. SUMMARY

Ion-containing polymer gels show two types of behavior depending on the state of counterions: (1) polyelectrolyte behavior when counterions are free (i.e., the ionogenic groups of polymer chains are dissociated) and (2) ionomer behavior when the counterions are associated with the charged polymer units with the formation of ion pairs and multiplets. In many experimental situations, a mixed polyelectrolyte/ionomer behavior is observed. In this case, some counterions are free, whereas others form ion pairs. In this chapter, some manifestations of the mixed polyelectrolyte/ionomer behavior in polymer gels are described. It was shown that such behavior is common in media of rather low polarity, but in the case of counterions strongly interacting with polymer charges it can be observed even in highly polar media (e.g., in water).

## REFERENCES

1. AR Khokhlov, EE Dormidontova. *Uspekhi Fiz Nauk* 167(2):113–128, 1997.
2. AR Khokhlov, OE Philippova. In: SE Webber, P Munk, Z Tuzar, eds. *Solvents and Self-Organization of Polymers*. NATO ASI Series, Series E. Vol. 327, Kluwer, Dordrecht, The Netherlands 1996, pp. 197–225.
3. OE Philippova, D Hourdet, R Audebert, AR Khokhlov. *Macromolecules* 30(26):8278–8285, 1997.
4. A Eisenberg, JS Kim. *Introduction to Ionomers*. New York, Wiley, 1998, p 327.
5. B Dreyfus. *Macromolecules* 18(2):284–292, 1985.
6. AR Khokhlov, EYu Kramarenko. *Macromol Theory Simul* 3(1):45–59, 1994.
7. T Tanaka. *Phys Rev Lett* 40(12):820–823, 1978.
8. T Tanaka, DJ Fillmore, ST Sun, L Nishio, G Swislov, S Shah. *Phys Rev Lett* 45(20):1636–1639, 1980.
9. AR Khokhlov. *Polymer* 21(4):376–380, 1980.
10. AR Khokhlov, SG Starodoubtsev, VV Vasilevskaya. *Adv Polym Sci* 109:123–171, 1993.
11. AR Khokhlov, EYu Kramarenko. *Macromolecules* 29(2):681–685, 1996.
12. SG Starodoubtsev, AR Khokhlov, VV Vasilevskaya. *Dokl Acad Nauk USSR* 282(2):392–395, 1985.
13. OE Philippova, TG Pieper, NL Sitnikova, AR Khokhlov, SG Starodoubtsev, HG Kilian. *Macromolecules* 28(11): 3925–3929, 1995.
14. X Liu, Z Tong, X Cao, O Hu. *Polymer* 37(26):5947–5949, 1996.
15. OE Philippova, NL Sitnikova, GB Demidovich, AR Khokhlov. *Macromolecules* 29(13):4642–4645, 1996.
16. NL Sitnikova, IA Malysheva, ND Gavrilova, OE Philippova, AR Khokhlov. *Vestnik Moskovskogo Universiteta Ser 3 Fizika Astronomiya* 2:38–43, 1998.
17. ZD Deng, KA Mauritz. *Macromolecules* 25(9):2369–2380, 1992.
18. NTM Klooster, F Van der Touw, M Mandel. *Macromolecules* 17(10):2070–2078, 2078–2086, 2087–2093, 1984.
19. H Morawetz, Y Wang. *Macromolecules* 20:194–196, 1987.
20. S Kudo, N Kosaka, M Konno, S Saito. *Polymer* 33(23):5040–5043, 1992; 34:2370–2374, 1993.
21. SG Starodoubtsev, AR Khokhlov, EL Sokolov, B Chu. *Macromolecules* 28(11): 3930–3936, 1995.
22. VA Smirnov, OE Philippova, GA Sukhadolski, AR Khokhlov. *Macromolecules* 31(4): 1162–1167, 1998.
23. VA Smirnov, GA Sukhadolski, OE Philippova, AR Khokhlov. *Zh Fizicheskoi Khimii* 72(4):710–713, 1998.
24. VA Smirnov, GA Sukhadolski, OE Philippova, AR Khokhlov. *J Phys Chem B* 103(36):7621–7626, 1999.
25. JCG Bunzli. In: JCG Bunzli, GR Choppin, eds. *Lanthanide Probes in Life, Chemical and Earth Sciences. Theory and Practice*. Elsevier, Amsterdam, 1989, pp 219–293.
26. WD Horrocks, DR Sudnick. *J Am Chem Soc* 101(2):334–340, 1979.





## 8

# Electrical Behaviors and Mechanical Responses of Polyelectrolyte Gels

**YOSHIHITO OSADA and JIAN PING GONG** *Hokkaido University,  
Sapporo, Japan*

### I. INTRODUCTION

Polymer gels have attracted considerable attention in recent years [1–10]. A polymer gel consists of an elastic cross-linked network and a fluid filling the interstitial space of the network. The network of long polymer molecules holds the liquid in place and so gives the gel what solidity it has. Gels are wet and soft and look like a solid material, but they are capable of undergoing large deformation. This property is in contrast with most industrial materials such as metal, ceramics, and plastics, which are dry and hard. Living organisms are largely made of gels. Except for bones, teeth, nails, and the outer layers of skin, mammalian tissues are highly aqueous gel materials largely composed of protein and polysaccharide networks in which water contents range up to 90% (blood plasma). This enables the organism to transport ions and molecules more easily and effectively while keeping its solidity

A polyelectrolyte gel is a charged polymer network with macroions fixed on the polymer chains and the microcounter ions that localized in the network frame. The polyelectrolyte gel has the ability to swell in water and absorbs a significant fraction (~2000 times the polymer weight) of water within its structure, but it will not dissolve in water. This chapter describes some of our results on the fundamental aspects and electroresponsive properties of polyelectrolyte gels. In Section II, of this chapter, the electrostatic potential distribution as well as the counterion distribution of the charged network is theoretically estimated by the Poisson-Boltzmann equation using a two-dimensional stacking model. The presence of the potential wells at the cross-linking points is predicted. The electrical conductance and the low-frequency dielectric relaxation of the gel is experimentally measured and compared with the corresponding polymer solution and the effect of the cross-linking points on the counterion conduction is discussed.

In Section III, the specific electrical responses of the polyelectrolyte gels are discussed. When a water-swollen polyelectrolyte gel is interposed between a pair of plate electrodes and a direct current is applied, it undergoes an electrically induced chemomechanical contraction and concomitant water exudation in the air [11]. The electrically induced contraction of the gel is associated with the electrokinetic transportation of hydrated ions and water in the network, and a one-dimensional electrokinetic model for the contractile phenomenon was postulated.

Some kinds of weak polyelectrolyte gels, such as cross-linked poly(acrylic acid), show the mechanoelectric property and produce an electrical potential as large as a few millivolts [12]. A mechanical deformation was supposed to induce a spontaneous ionization of carboxylic acids in a local level.

The polyelectrolyte gel is able to exhibit a repetitive current oscillation that occurs when a direct current voltage is applied to a water-swollen polyelectrolyte gel through a pair of needle electrodes [13]. The amplitude and frequency of the oscillation are strongly associated with the degree of cross-linking, charge density on the network, and temperature.

In Section IV, the recent results on the specific surface frictional properties of gels is presented. It was found that the frictional behaviors of the hydrogels do not conform to Amonton's law,  $F=\mu W$ , which well describes the friction of solids. The frictional force and its dependences on the load are quite different depending on the chemical structures of the gels, surface properties of the opposing surfaces, and the measurement condition [14–18]. At certain conditions, the sliding friction of hydrogels on solid surfaces or on gels is extremely low with a frictional coefficient  $\mu\sim 10^{-3}$ .

## II. ELECTRICAL PROPERTIES OF POLYELECTROLYTE GELS

### A. Electrostatic Potential Distribution

The electrostatic potential distribution,  $\psi(x, y, z)$ , of a polyelectrolyte gel is determined by Poisson-Boltzmann equation:

$$\Delta\psi(x, y, z) = -\frac{\rho_0}{\varepsilon} \exp\left[\frac{e\psi(x, y, z)}{kT}\right] \quad (1)$$

with a boundary condition of

$$\frac{\partial\psi(x, y, z)}{\partial n} = -\frac{\sigma}{\varepsilon} \quad (2)$$

where  $\varepsilon$  is the dielectric constant,  $e$  the charge of an elementary electron,  $k$  the Boltzmann constant,  $T$  the temperature, and  $\rho_0$  the average counterion density. In Eq. (2),  $\sigma$  is the surface charge density of the chains and  $n$  denotes the normal derivation of potential on the surface of polymer chain.

Gels should, in general, be considered to be composed of heterogeneous structures in different orders from a few angstroms to several micrometers (structure hierarchy). This makes it extremely difficult to calculate accurately the electrostatic potential distribution in the gel by the Poisson-Boltzmann equation.

In order to catch the electrical feature due to the cross linkage of the ionic macromolecules, however, we have proposed a periodical model to estimate the electrostatic potential energy distribution in the polyelectrolyte gel [19]. In this model,

the cross-linking points of the gel are supposed to be periodically distributed on the chain segments and the macrocharges are evenly distributed on the chain. Besides, it is supposed that the polymer network is made of the periodical stacking of two-dimensional meshes, each  $2r_0$  distance apart. In addition, a square-shaped cross-section of the meshes with a side length of  $a$ , instead of a circular-shaped cross section of a polymer chain with a radius of  $r_p$  was used for the simulation. We set  $2\pi r_i = 8a$  in order to keep the same surface area as well as the same surface charge density. Therefore, we have

$$\rho_0 = \frac{e}{2b(r_0^2 - 2r_i^2)} \quad (3)$$

and

$$\sigma = \frac{e}{4r_i b} \quad (4)$$

where  $b$  is the distance between two ionizable groups on the polymer chain. Here, we confine to univalent counter ions of a polyanionic gel. With these boundary conditions, a numerical calculation of Poisson-Boltzmann equation gives the electrostatic distribution in the polyelectrolyte gel.

The simulation has been carried out for a poly(2-acrylamido-2-methylpropane sulfonic acid) (PAMPS) gel which is a fully ionized polyelectrolyte having sulfonic groups as macroions and  $H^+$  as counterions. The radius of the polymer chain,  $r_p$ , of the PAMPS is  $r_i = 6.08 \times 10^{-10}$  m. The other constants used are  $b = 2.55 \times 10^{-10}$  m,  $\epsilon_r = 78$  ( $\epsilon = \epsilon_r \epsilon_0$ ,  $\epsilon_0$  is the dielectric constant in vacuum),  $T = 300$  K. The simulation was carried out on a cubic box with a side length of  $r_0$  ( $1/2^3$  of a periodical unit cell) and then copied to the whole periodical unit according to the symmetry. The simulation box was divided into  $10 \times 10 \times 10$  lattice cells. To make the surface of polyions on lattice points,  $r_0 = 10r_i$  was used. Eq. (1) expressed by Poisson's difference equations, and the electrostatic potential on lattice points were calculated by Liebmann's method. A relaxation parameter of 0.5 has been used to accelerate the calculation. An iterative difference value of  $\epsilon = 10^{-7} kT$  was used to determine the accuracy of the calculation. Symmetrical conditions have been used on the walls of the simulation box; that is, the normal derivatives of potential on the walls are zero.

Figure 1 shows a spatial profile of electrostatic potential energy in the unit of  $kT$  on the plates of mesh-like networks. Figure 1 shows that there exist potential energy wells at every cross-linking points and valleys along the polymer chains.

Since the charge density of counterions  $\rho(x, y, z)$  is determined by the Boltzmann distribution,

$$\rho(x, y, z) = \rho_0 \exp \left[ -\frac{e\psi(x, y, z)}{kT} \right] \quad (5)$$

Therefore, counterions are mostly localized around the network knots as well as the

polymer chains because of the deep potential wells and valleys. The charge density of counterions decreased very sharply with an increase in the distance from the polymer chain. Counterions located in the deep potential valley ( $\gg kT$ ) should strongly be bound to the polyion. The amount of these bound counterions would increase with the increase in the cross-linking density.

The deep potential wells and high counterion densities at cross-linking points might bring about an instability and results in the counterion condensation, as predicted by Oosawa and Manning for the linear polyelectrolyte solution [20, 21].

The presence of deep electrostatic potential valley should strongly confine the motion of water molecules which fill the interfacial space of the network and

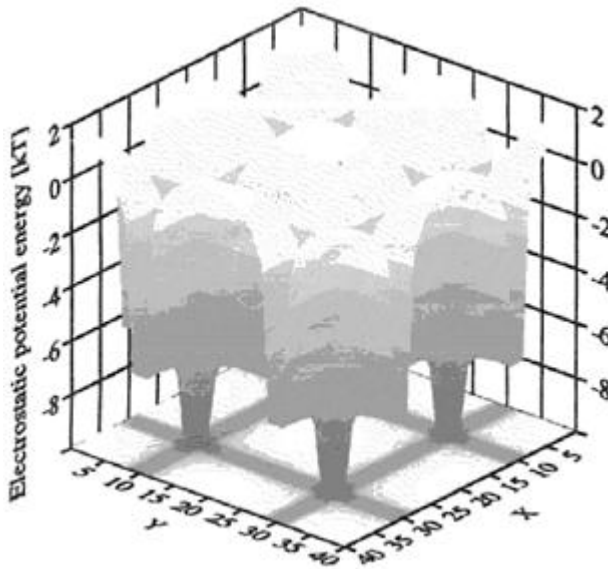


**FIG. 1** Spatial profile of the electrostatic potential energy for the plane within the mesh-like network. x- and y-axes are in unit of  $r_i$  ( $=60.8$  nm). (From Ref. 19.)

restrict the configuration favorable to form a crystalline structure. This might bring about decreased entropic and enthalpic changes of solvent molecules at crystallization owing to enhanced polarization and should decrease the melting temperature of water.

The treatment of a cross-linked polyelectrolyte gel with a rigid periodical structure and the interaction between small ions with a mean field might oversimplify the problem. Since the presence of deep potential wells at cross-linking points could come from this simplification, it would be informative to understand the potential distribution of the polyelectrolyte gels, especially in the case of without the presence of simple salts.

## B. Electrical Conductance

From the calculated potential distribution of the polyelectrolyte gels, some effects of crosslinkage on the conductive behaviors of the gel can easily be expected. One is an enhanced counterion “binding” which should increase with the increase in the cross-linking density [20, 21]. The previous calculation revealed the presence of the deep electrostatic potential wells at the cross-linking point. These potential wells should strongly localize, or “condense”, counterions through strong electrostatic interactions and should affect the conductive behaviors of the gel. The other is a decreased contribution of ion transportation from the “giga” macromolecular network. The macroions also make a contribution to the electrical conduction of polymer solution [22, 23]; this contribution is expected to be depressed in the case of the networked gel.

It must be recognized that there exist several fundamental difficulties in carrying out the measurement of the conductance of water-swollen gels. A gel is a soft and wet material. It contains a large amount of water that does not flow like a liquid but gradually evaporates and changes its size and concentration. A gel keeps a certain shape but is deformable or easily broken. Unnecessary pressure of electrodes on the gel may lead to a break or a change not only of the distance between two electrodes but also the nature of the gel. Methods used for solution and solid are no longer appropriate for a gel. Taking into account the characteristics of the gel, a special methodology to measure the electrical conductance of water-swollen polyelectrolyte gels has been developed [24].

Figure 2 shows the equivalent (molar) conductance of a strong polyelectrolyte gel, PAMPS, at various monomeric concentrations [24]. The equivalent conductance of solutions of corresponding linear polymers (PAMPS) are also shown in Figure 2. It shows that a polyelectrolyte gel has an equivalent conductance approximately equal to that of the corresponding linear polymer solution which showed a slightly increasing tendency in the equivalent conductance with the concentration. Considerable coiling of the polymer chain at such high concentrations was considered to be responsible for the decrease in the fraction of

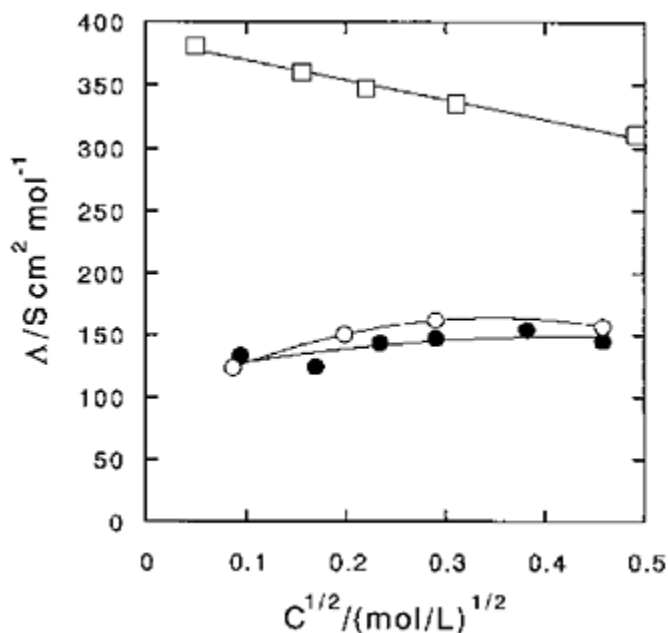


**FIG. 2** Equivalent conductance of monomer AMPS solution (□), linear polymer solutions (○), and polymer gel (●) of PAMPS at various monomeric concentrations  $T=25^\circ\text{C}$ . (From Ref. 24.)

counterions condensed on the polyions, leading to higher values for the counterions mobility and the equivalent conductance.

However, the gels showed almost no distinct concentration dependencies of the equivalent conductance, which was somewhat smaller than that of linear polymer solutions when concentrations were higher than 0.25 M. We consider that the presumable polymer chain-coiling effect that occurs at higher concentrations for polymer solutions may be canceled by the increasing cross-linking points which condense counterions and lead to decreases of counterion mobility and the equivalent conductance of gels.

The activation energy of the conduction of PAMPS as well as its alkali salts gels have been studied, and it has been compared with that of the corresponding monomer solution and polymer solution (Fig. 3). No appreciable differences in the activation energy were observed among the solution of monomer, polymer, and network. This result suggests that the electrical conduction is undergone essentially by the same mechanism for these three different kinds of samples and the transport process of counterions plays a predominant role for the electrical conduction.

According to the condensation theory [20, 21, 25], the electrical conduction of a polyelectrolyte solution is made by the electrical drift of a fraction ( $f$ ) of counterions which are located in a Debye-Huckel atmosphere. The remaining

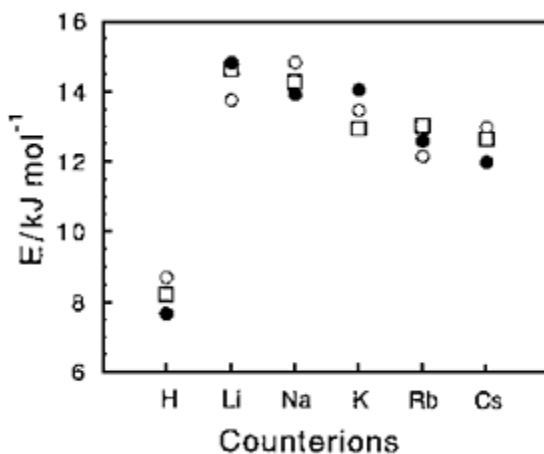


**FIG. 3** Activation energies of electrical conduction of the AMPS monomer solution, PAMPS polymer solution, and PAMPS gel with various counterions. The monomeric concentration is 0.1 M. (□); Monomer solution; (○); polymer solution; (●); polymer gel. (From Ref. 24.)

(1-*f*) fraction of counterions are considered to be bound to the macroions and do not contribute to the direct current conductivity. In the latter case, the results of direct current conductivity measurements are understandable if we take into account that the direct current conductivity of gels and linear polymer solutions is largely dominated by the loosely bound counterions (free counterions). In other words, there should be no large difference in the state of free counterions between a gel and a linear polymer solution. To observe the behavior of bound counterions of gels and linear polymer solutions, the dielectric properties of the two systems were further studied.

### C. Low-Frequency Dielectric Relaxation of Polyelectrolyte Gels

It is well known that the dielectric relaxation spectrum gives us information about ions which move under an alternative electric field. The dielectric relaxation spectroscopy of the polyelectrolyte solutions shows two kinds of relaxation processes: the high-frequency relaxation in the megahertz frequency range and the low-frequency one in the radio-wave frequency range. The high-frequency relaxation is due to the fluctuation of free counterions that exist far from macroions [26–29]. The low-frequency relaxation arises from the fluctuation of bound counterions that exist in the vicinity of macroions [26, 27, 30].

The low-frequency relaxation, which is caused by the bound counterion fluctuation along the polymer chain, should be observed in the polyelectrolyte gels as well as in the polyelectrolyte solutions. Moreover, we are able to speculate

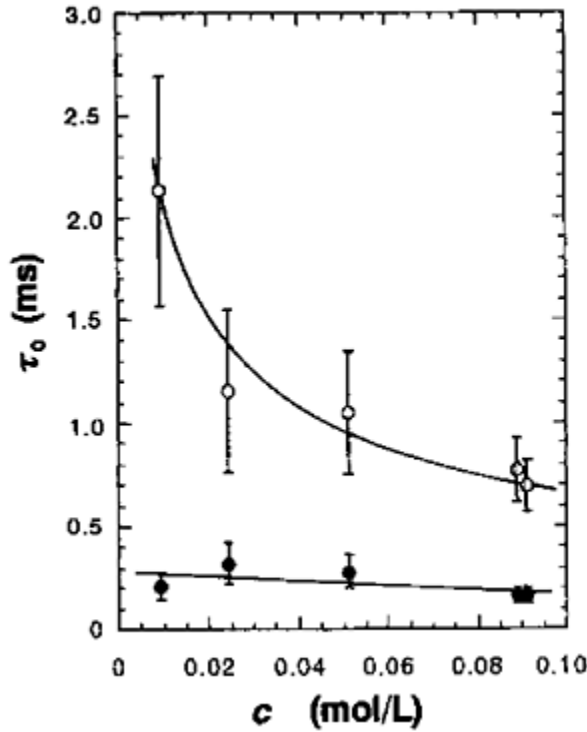


**FIG. 4** Concentration dependencies of the mean relaxation time  $\tau_0$  of PNaAMPS gels and their corresponding linear polymer solutions. (○); polyelectrolyte gels; (●) linear polymer solutions.

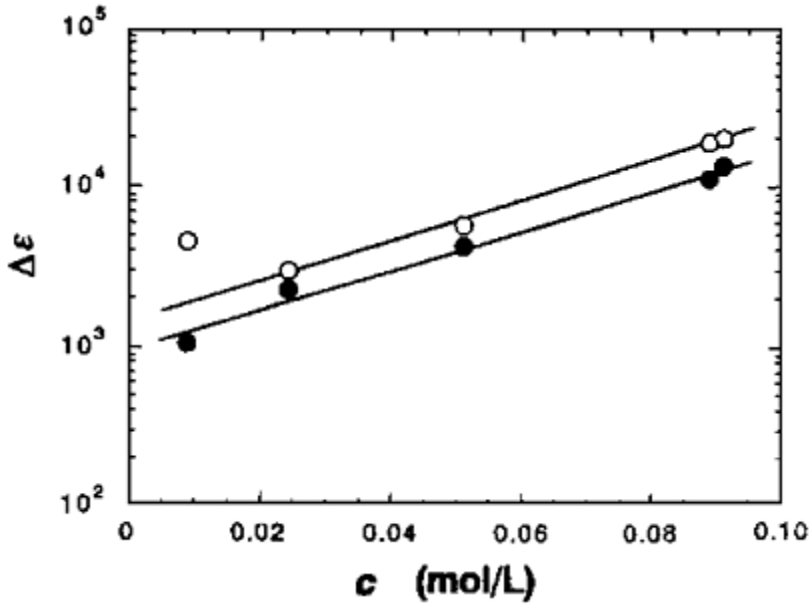
that the polyelectrolyte gel shows a slower relaxation process than the linear polymer solution because of the strong network-counterion interaction, although the loosely bound counterions showed no difference between in the networked gels and in the linear polymer solutions, as elucidated by the results of the electrical conductance.

Figure 4 shows the concentration dependencies of the mean relaxation time,  $\tau_0$ , of sodium salt of poly(2-acrylamido-2-methylpropane sulfonic acid) (PNaAMPS) gels and their corresponding linear polymer solutions. The relaxation time of gels decreases with increasing the concentration, whereas that of linear polymer solutions is almost independent of the concentration.

Figure 5 shows the concentration dependence,  $\Delta\epsilon$ , of gels and their linear polymer solutions. The solid lines in Figure 5 show the exponential fitting ones. Both gels and linear polymer solutions satisfactorily showed the exponential change of  $\Delta\epsilon$  against the concentration except for SIG.

According to the literature [26, 27], the observed low-frequency relaxation of the linear polymer solution is associated with the tightly bound counterion fluctuation along the polymer chain. This low-frequency relaxation strongly





**FIG. 5** Concentration dependencies of the dielectric increments  $\Delta\epsilon$  of PNaAMPS gels and their corresponding linear polymer solutions. ( $\circ$ ); polyelectrolyte gels; ( $\bullet$ ); linear polymer solutions.

depends on the molecular weight but is almost independent of the concentration [31].

Supposing a square-type potential well along the polymer chain,  $\tau_0$ , of the linear polymer solution is given by Eq. (6) [32]

$$\tau_0 = \frac{L_f^2}{D} = \frac{L_c^2}{12D} \quad (6)$$

where  $L_f$  and  $D$  are the fluctuation length and the diffusion constant of the bound counterion, respectively.  $L_c$  is the contour length of the macroion. The dielectric increment  $\Delta\epsilon$  is expressed by following expression

$$\Delta\epsilon \propto \frac{n_B e^2 L^2}{\epsilon_0 k_B T} \quad (7)$$

where  $n_B$  is the number concentration of the bound counterions,  $e$  is the elementary charge, and  $\epsilon_0$  is the vacuum permittivity.

Therefore, using Eqs. (6) and (7), we can estimate the diffusion constant of bound counterions as well as the number concentration of bound counterions for linear polymer solutions. Using the degree of polymerization,  $N$ , as 3100 and the monomer unit length,

$b$ , as  $2.55 \text{ \AA}$ , we get  $L_c$  and  $L_f$  as  $801 \text{ nm}$  and  $231 \text{ nm}$ , respectively. The estimated results of  $D$  and  $n_B$  using Eqs. (6) and (7) are listed in

**TABLE 1** Samples of the PNaAMPS Gels Used in the Present Measurement

Gels <sup>a</sup>	$\rho_m(\text{mol \%})^b$	$q^c$	$c(\text{mol/L})^d$	Polymer solutions <sup>e</sup>
S1G	2	479	$9.1 \times 10^{-3}$	S1P
S2G	3	180	$2.4 \times 10^{-2}$	S2P
S3G	4	85	$5.1 \times 10^{-2}$	S3P
S4G	5	49	$8.1 \times 10^{-2}$	S4P
S5G	6	48	$9.1 \times 10^{-2}$	S5P

<sup>a</sup> Abbreviations of gel samples. <sup>b</sup>  $\rho_m$  Is the cross-linking density. <sup>c</sup>  $q$  Is the degree of swelling. <sup>d</sup>  $c$  Is the monomeric concentration. <sup>e</sup> Abbreviations of linear polymer solution samples.

Table 1. The mean diffusion constant of five samples,  $D_m$ , is determined to be  $2.1 \times 10^{-10} \text{ m}^2/\text{s}$  which is an order of magnitude smaller than the diffusion constant  $D_0 (= 1.22 \times 10^{-9} \text{ m}^2/\text{s})$  of  $\text{Na}^+$  ion in a free medium. This result is in good agreement with the previous data of sodium salts of poly(styrene sulfonate) (PNaPSS) solution reported by Ookubo et al. [33]. The amount of bound counterions for the linear polymer solutions estimated from Eq. (7) are 0.3–0.8% of total counterions.

Dependence of  $\tau_0$  on the cross-linking density of the polyelectrolyte gels seems to suggest that the relaxation time of the gels corresponds to the fluctuation of bound counterions between two neighboring cross-linking points along the polymer chain. If it was true, we would get the relaxation time in the order of  $10^{-7} \text{ s}$ , which is four orders of magnitude smaller than those we have observed. Therefore, the above assumption is apparently not appropriate.

In the contrary, we can consider that the observed relaxation of gels might correspond to the counterion fluctuation along the polymer network by crossing through the cross-linking points as illustrated in Figure 6. If we assume that the observed relaxation time consists of the two relaxation times, that is, the time  $\tau_1$  for fluctuating along the linear part of the polymer network and the time  $\tau_2$  for exceeding the energy barrier which is based on the electrostatic potential well at the cross-linking points, we can write the observed  $\tau_0$  is a linear combination of  $\tau_1$  and  $\tau_2$ .

$$\tau_0 = m^2 \tau_1 + (m-1)^2 \tau_2 \quad (8)$$

Here, the coefficient  $m$  stands for the number of polymer segments that a bound counterion can fluctuate and  $(m-1)$  corresponding to the cross-linking points that a bound counterion can cross through. Because the fluctuation length correlates with the relaxation time in square form, we have the square form of  $m$  or  $(m-1)$  in Eq. (8). Since the average number of monomeric units of a polymer chain segment between two neighboring cross-linking points  $1/2 \rho_m$ , the contour

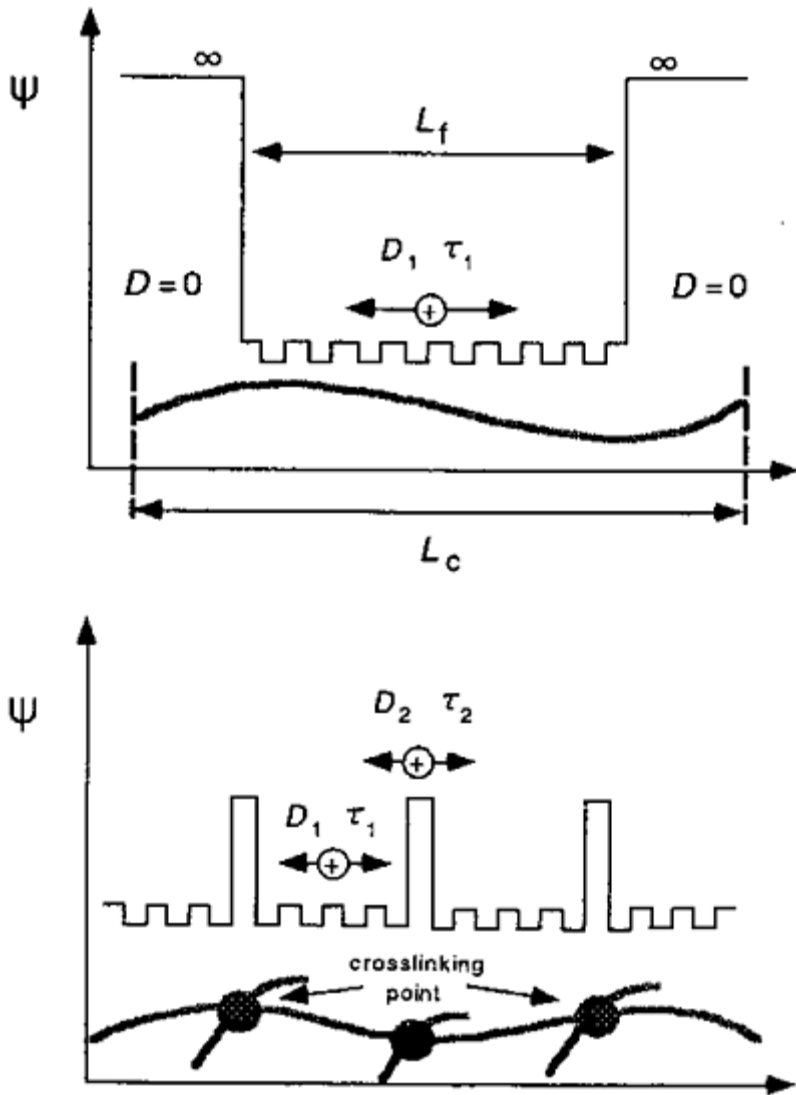


**FIG. 6** Schematic illustration of a possible explanation for the low-frequency relaxation of the polyelectrolyte gel.

length of a polymer chain segment is  $L_c = b/2\rho_m$ . Supposing that the contour length of the energy barrier at the cross-linking points is  $2b$ , we have

$$\tau_1 = \frac{(1/2\rho_m - 2)^2 b^2}{12D_1} \quad (9)$$

and

$$\tau_2 = \frac{(2b)^2}{12D_2} \quad (10)$$

where  $D_1$  and  $D_2$  are the diffusion constants of bound counterions along the polymer chain segment and that at the cross-linking points, respectively.  $D_1$  should be the same as that of a linear polymer solution,  $D_m$ . Thus, we can estimate  $\tau_1$  from  $\rho_m$  and  $D_m$ .

The relationship between  $\tau_0$  and  $\tau_1$  is shown in Figure 7. As seen in Figure 7, the mean relaxation times,  $\tau_0$ , at various cross-linking density are well explained by (9). From the slope and the intersection at the  $\tau_0$  axis of the straight line shown in Figure 7, we get  $m=97$  and  $D_2=10^{-13}$  m<sup>2</sup>/s, which is three orders of magnitude smaller than that of bound counterion in the linear part of the polymer chain. The linearity of the Eq. (9) indicates that the number of the cross-linking points that a bound counterion can cross over is independent of the cross-linking density. Accordingly, the energy barrier of the cross-linking points are neither sensitive to the degree of cross-linking density nor to the polymer concentration. This is in accordance with the fact that the diffusion constant,  $D$ , of bound counterions along a linear polymer chain is not sensitive to the polymer concentration. These results suggest that the state of bound counterions in the vicinity of the polymer chain or in the cross-linking point is not affected by the presence of other polymers or their counterions.

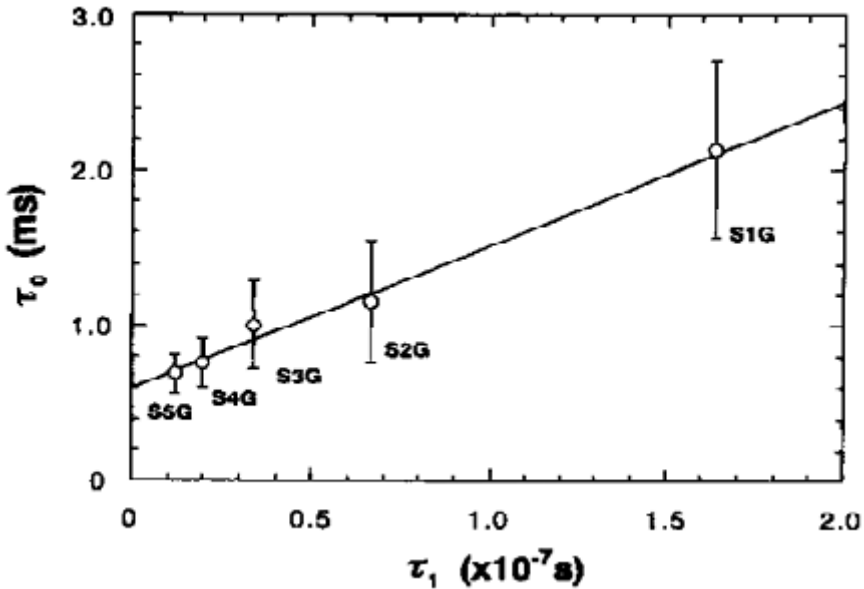
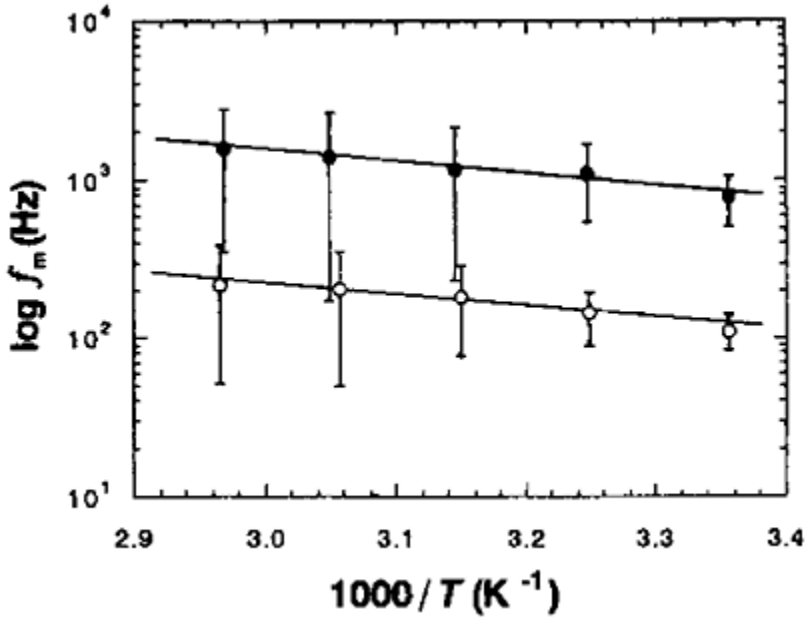


FIG. 7 A linear plot of the observed mean relaxation time,  $\tau_0$ , against the calculated fluctuation time,  $\tau_1$ , between neighboring cross-linking points.

In order to investigate the temperature effect on the electrostatic interaction between macroions and bound counterions, the temperature dependence of the



**FIG. 8** Arrhenius plots of the peak frequency,  $f_m$  of loss curves of PNaAMPS gel and its corresponding linear polymer solution. ( $\circ$ ); polyelectrolyte gel; ( $\bullet$ ); linear polymer solution.

low-frequency dielectrical relaxation was investigated. Figure 8 shows the Arrhenius plots of the peak frequency,  $f_m$ , of the dielectrical loss curves of samples S4P and S4G. The peak frequencies are well fitted by the Arrhenius formula

$$f_m = f_0 \exp\left(-\frac{E}{k_B T}\right) \quad (11)$$

where  $f_0$  is the frequency factor and  $E$  is the activation energy. The activation energy of the gel and its linear polymer solution were determined as 15.0 and 13.7 kJ/mol, respectively. These values are nearly equal to those of electrical conductivity, and might be interpreted by the viscous drag between the bound counterions and water described by the Stokes' law. Owing to the little difference of  $E$  between the gel and the linear polymer solution, we could not determine the appreciable temperature dependence of the electrostatic interaction between macroions and counterions.

Generally, the relaxation time associated with the rotation of main chain of a linear polymer solution is reported in the range of millisecond [33, 34] and coincides with the data we have observed in the polyelectrolyte gels. Accordingly, it seems probable that the

observed relaxation of gels should be ascribed to this rotation. However, it is usually known that the activation energy of rotational relaxation of a polymer chain is much higher than the observed values [35–37]. Furthermore, since the end of the chains are fixed to the cross-linking points, the rotational activation energy of gel might be even higher than that of the linear polymer solution. Therefore, these low values of activation energies,  $E$ , indicate that the observed low-frequency relaxation is not associated with the main chain rotation.

In summary, the dielectrical relaxation time of gels is much longer than that of polyelectrolyte solutions and strongly depends on the cross-linking density and/or the concentration. This behavior of gels is different from that of the linear polyelectrolyte solution, which showed a low-frequency dielectrical relaxation independent of the polymer concentration. The low-frequency relaxation observed on the gels can be explained in terms of the fluctuation of the bound counterions along the polymer network by crossing through the cross-linking points. According to this explanation, the diffusion constant at the cross-linking point is three orders lower in magnitude in comparison with that along the polymer chain. This might be a proof of the presence of deep potential wells at cross-linking points.

### III. ELECTRICAL/MECHANOELECTRICAL

#### A. Electrical Contraction

##### 1. Behaviors

When a water-swollen cross-linked polyelectrolyte gel is inserted between a pair of electrodes and a direct current voltage is applied, it undergoes anisotropic contraction and concomitant fluid (water) exudation [11, 38]. Figure 9 shows the schematic view of the shape change an anionic gel with time under the electrical field [39]. It is found that:

1. The contraction occurs only for polyelectrolyte gels and not for a neutral (noncharged) hydrogel.

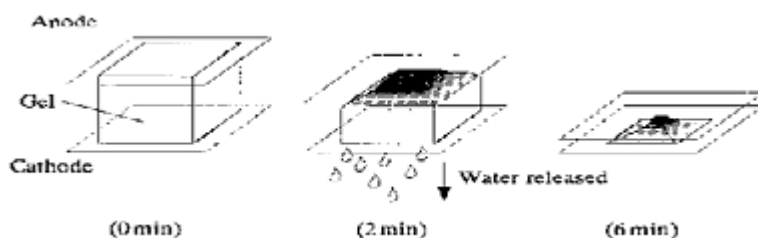


**FIG. 9** Schematic view of shape change of an anionic gel with time under the electric field. (From Ref. 39.)

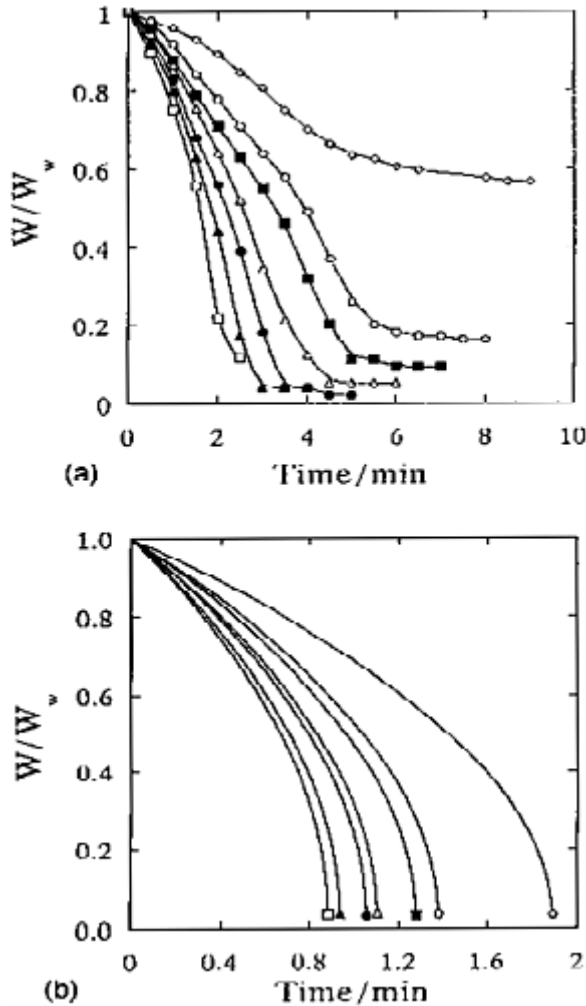
2. The anionic gel slightly swells near the cathode and extensively contracts near the

anode; the reverse occurs for the cationic gel.

3. The rate of contraction is proportional to the electrical current.

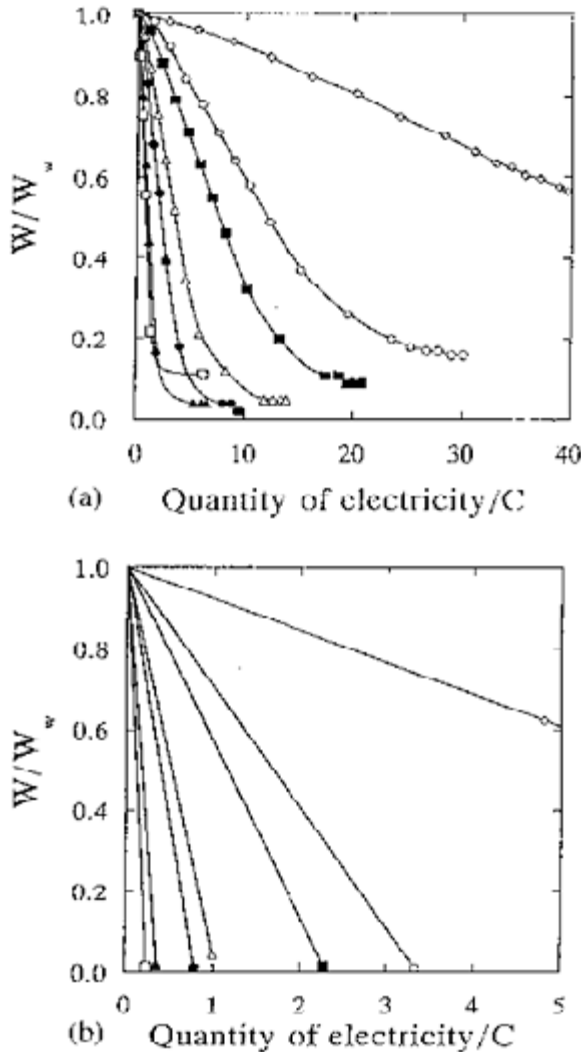
4. The contraction of the gel is reversible; that is, it swells in water after the electricity is turned off.

Figure 10a shows the time profiles of the relative weight change of PAMPS gels with various degrees of swelling under a direct current electrical field. Figure 11a



**FIG. 10** Time profiles of relative weight change of the PAMPS gel for various degree of swelling,  $q$ . (a) experiment, (b) simulation.  $\diamond$ ,  $q=25$ ;  $\circ$ ,  $q=70$ ;  $\blacksquare$ ,  $q=100$ ;  $\triangle$ ,  $q=200$ ;  $\bullet$ ,  $q=256$ ;  $\blacktriangle$ ,  $q=512$ ;  $\square$ ,  $q=750$ . (From Ref. 39.)

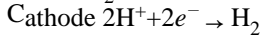
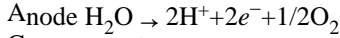
shows the relative weight changes of PAMPS gels as a function of the quantity of electricity which has flowed through the gel for various gels with different degrees of swelling. The PAMPS gel is a strong acid polymer with fully ionized sulfonic groups as macroions and  $\text{H}^+$  as counterions. When an electrical field is applied, hydrated  $\text{H}^+$  ions (more exactly  $\text{H}_3\text{O}^+$ ) migrate toward the cathode and are reduced, liberating  $\text{H}_2$ . The water migrates together with  $\text{H}^+$  ions



**FIG. 11** Relative weight change of the PAMPS gel as a function of the quantity of electricity calculated for various degree of swelling,  $q$ . (a) experiment, (b) simulation. Symbols are the same as those in Fig. 5. (From Ref. 39.)



and exits the gel near the cathode. The overall electrode reactions are expressed as follows:



The oxygen and hydrogen liberated can be observed throughout the course of the contraction. It has been verified that the amount of gases released was consistent with the theoretical value derived by Faraday's law according to the above equations. The overall population of ions should not significantly change during the contraction, because at every moment, the amount of  $\text{H}^+$  generation and consumption should be balanced at both electrodes.

The electrically induced contraction of the gel is caused by a transport of hydrated ions and water in the network, and the contractile behaviors observed are essentially electrochemical phenomena. When an outer electrical field is applied across the gel, both the macroions and the microions get electrical forces in an opposite direction. However, the macroions are stationary phase, since they are chemically fixed to the polymer network, whereas the counterions are mobile capable of migrating along the electrical field and drag water molecules with them. In other words, application of an electrical field causes a pumping of mobile counterions and macro network ions together with the surrounding water in opposite directions until mobile ions reach the electrode, where the velocity of migration and the velocity of gel contraction are governed both by the quantity of mobile ions and the electrical field.

## 2. Theoretical Modeling

In order to model the electrical contraction of the gel, we have supposed that the macroions are evenly distributed along the extended macromolecules with an infinitively long chain compared with its radius. We have considered only the macroions located along the chains parallel to the electrical field applied and neglected the effects of cross-linking points and the chains located perpendicular to the electrical field. Under such a simplification, the problem of water transportation under the electrical field in the polymer network becomes simply a problem of the transportation along the rod-like polymer chain. This problem is analogous to that of liquid flow through a capillary under the influence of an electric field.

Thus, we consider here a tube composed of two concentric cylinders of inner radius,  $r_p$ , and outer radius  $r_0$  which corresponds to the radius of macroion and the distance to the midpoint of two adjacent macroions, respectively (Fig. 12) [39]. When an electrical field is applied across the tube, water molecules in the tube start to move. The frictional force resists this movement and a steady state is quickly obtained. If we suppose that the flow is laminar, the water flow velocity,  $v(r)$  is a function of  $r$ , the distance from the cylindrical axis. The velocity will be

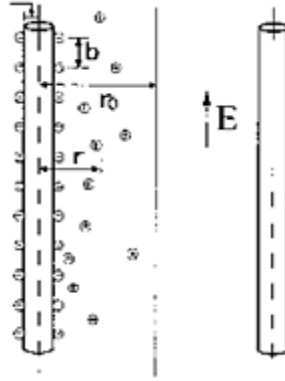


**FIG. 12** Schematic model of the rod-like macroion chains for the polyelectrolyte network. As described in the text, only the macroions parallel to the electric field are considered. (From Ref. 39.)

zero at  $r=r_i$ , the surface of macroion chain, and be a maximum at  $r=r_0$ , which is the midpoint of two adjacent macroions. Under the electric field,  $E$ , the electrostatic force,  $\rho(r)E$ , should be balanced by the frictional force,  $-\eta\Delta v(r)$

$$\rho(r)E = -\eta\Delta v(r) \quad (12)$$

where  $\eta$  is the coefficient of viscosity and  $\rho(r)$  is the charge density which connected with the electrostatic potential,  $\psi(r)$ , by Poisson's equation [Eq. (2)]. Therefore,

$$\Delta\psi(r) = \left[ \frac{\eta}{(\epsilon E)} \right] \Delta v(r) \quad (13)$$

Combining with boundary conditions of

$$v(r_i) = 0, \frac{dv(r_0)}{dr} = 0 \quad (14)$$

we get

$$v(r) = \frac{\epsilon E}{\eta} [\psi(r) - \psi(r_i)] \quad (15)$$

The electrostatic potential,  $\psi(r)$ , is given by the Poisson-Boltzmann equation (Eq. 1) and can be analytically solved in this case. Therefore, the water flow velocity,  $v(r)$ , can be

obtained

$$v(r) = \frac{\varepsilon EkT}{e\eta} \ln \left\{ \left( \frac{r}{r_i} \right) \frac{\sin[-\tan^{-1} \beta + \beta \ln(r/r_0)]}{\sin[-\tan^{-1} \beta + \beta \ln(r_i/r_0)]} \right\}^2 \quad (16)$$

where  $\beta$  is a parameter characterized by the charge density of the macroion. In order to obtain the feature of the contraction process, several approximations have been made:

1. The contraction of a gel occurs only in the direction of the electrical field,  $E$ ; that is, in the direction of water transportation, the cross-sectional area,  $S$ , of the gel keeps constant during the contraction.
2. The degree of swelling of the uncontracted region of gel does not change during the contraction.
3. The counterflow of water due to the contraction is neglected.

The amount of water released from the gel should be equal to the water transported through the cross section of the gel,  $S$ , located near the electrode where the water comes out. The amount of water,  $dw$ , transported through a cross-sectional element,  $dS=2\pi r dr$ , per unit time is

$$dw=v(r)dS=2\pi r v(r)dr \quad (17)$$

The amount of charge,  $dQ$ , flows through the cross-sectional element,  $dS$ , per unit time is

$$dQ=\rho(r)v(r)dS=2\pi r \rho(r)v(r)dr \quad (18)$$

thus, the rate of water transportation to that of charge,  $u(r)$ , in cubic meters per coulomb is

$$u(r) = \frac{dw}{dQ} = \frac{1}{\rho(r)} \quad (19)$$

Taking an average,  $u(r)$ , over one macroion, we get the gel contraction efficiency in cubic meters per coulomb, which means the amount of water transported by 1 C of charges.

$$u_{av} = \left\{ \int_{r_i}^{r_0} \frac{2\pi r}{\rho(r)} dr \right\} / \pi(r_0^2 - r_i^2) \quad (20)$$

$u_{av}$  can also be expressed in grams per coulomb by multiplying a factor of  $10^6$ .

It is clear from the above equation that  $u_{av}$  is independent from the electrical field,  $E$ , and is determined only by the charge density of the gel which is inversely proportional to

the degree of swelling. According to approximation 2 above,  $u_{av}$  is constant during the contraction process. If we denote  $W$  and  $W_w$  as the weight of the gel at  $t$  and  $t=0$ , respectively, the dependence of relative weight  $W/W_w$  on the amount of charge,  $Q$ , flow through the gel is

$$\frac{W}{W_w} = 1 - \int_0^Q \frac{u_{av} dQ}{L_0 S} = \frac{1 - u_{av} Q}{L_0 S} \quad (21)$$

Here  $L_0$  and  $S$  are the initial length and cross-sectional area of the gel, respectively.

When a constant voltage,  $U$ , is applied across the gel,  $E$  would change during the contraction process with time, because the distance between two electrodes is accordingly changed. By denoting  $E$  at time  $t$  as  $E(t)$ ,  $v(r)$  as  $v(r, t)$ , we get

$$E(t) = \frac{U}{L(t)} = \frac{U}{L_0 - \int_0^t v_{av}(t) dt} \quad (22)$$

Thus, we have

$$v(r, t) = \frac{\varepsilon E(t)}{\eta} [\psi(r) - \psi(r_i)] = \frac{v(r, 0) E(t)}{E(0)} \quad (23)$$

Therefore,

$$v_{av}(t) = \frac{v_{av}(0) E(t)}{E(0)} \quad (24)$$

So we have

$$v_{av}(t) [L_0 - \int_0^t v_{av}(t) dt] = \frac{U v_{av}(0)}{E(0)} \quad (25)$$

We find

$$v_{av}(t) = v_{av}(0) \frac{1 - 2v_{av}(0)t}{L_0^{-1/2}} \quad (26)$$

The time dependence of relative weight,  $W/W_w$ , is

$$\frac{W}{W_w} = \frac{L(t)}{L_0} = 1 - \int_0^t v_{av}(t) dt / L_0 \quad (27)$$

The numerical simulation of contraction has been made for PAMPS gel using the following constants:  $r_i=6.08\times10^{-10}$  m,  $b=2.55\times10^{-10}$  m,  $\alpha=1$ ,  $\varepsilon_r=78$  ( $\varepsilon=\varepsilon_r\varepsilon_0$ ,  $\varepsilon_0$  is the dielectric constant in vacuum),  $\eta=0.7973$  mPas,  $\varepsilon=1.6\times10^{-19}$  C,  $T=300$  K.

Figure 10b is theoretically obtained time profiles of the relative weight change of PAMPS gels ( $W/W_w$ ) with various degree of swelling,  $q$ . Comparing Figure 10b with Figure 10a, both figures show that the rate of contraction increases with the increase in the degree of swelling,  $q$ . The theoretical results are convexly curved, indicating the acceleration in the contraction rate, and this acceleration phenomenon in the contraction rate has been also observed experimentally. The acceleration is apparently due to the increase in the current in time that occurred by the contraction of the gel.

The experimental data in Figure 10a shows that there exists a certain value of  $W/W_w$  at which the gel practically stops its contraction, and the higher the degree of swelling of the gel, the lower this value of  $W/W_w$ . We do not have an exact interpretation explaining this phenomenon, but it may possibly be associated with the presence of so-called “bound water.” Water molecules located adjacent to the macroions have a relatively low local velocity or a low relaxation time due to strong interaction with charges located nearby. This indicates that the water molecules surrounding the macroions within a certain distance hardly move under an electrical field. On the other hand, free water (strictly speaking, there is no free water in the sense of pure water solution, and it should be called “more freely moving water”) existing far from the ionic “atmosphere” can easily migrate under the electrical force [40].

According to the electrokinetic contraction model, the rate of the relative weight change is dependent only on the amount of charges being transported through the gel; that is, on the quantity of electricity and is independent of electrical field. Under the assumption that the gel changes its size keeping  $q$  constant in the course of the contraction, we obtain that  $W/W_w$  is proportional to the amount of charges transported through the gel. Figure 11b shows the simulational results of the dependence of the relative weight change on the quantity of electricity. It shows that  $W/W_w$  is almost linearly dependent on  $Q$ , which well coincides with the experimental results shown in Figure 11a.

Here it should be noted that the values obtained by simulation are somehow several times larger than those of experimental data. One reason for this should be attributed to the simplification of the problem to a one-dimensional model, where the effect of cross-linking points and of the macromolecular ions located perpendicular to the electrical field have not been taken into account. At present, we cannot quantitatively evaluate how significant is the cross-linking points' effect on the electrophoretic and electro-osmotic transport processes of counterions and water. However, in the case of a one-dimensional model, the outer electrical field induces the migration of counterions along the capillary-like “channels” formed in parallel to the direction of electrical field, and this does not cause any unnecessary rearrangement of the counterion distribution. While the counterions of a real system, particularly those distributed around the macroions located perpendicular to the electrical field make turbulence or rearrangement of their distribution getting electrostatic force from outside electric field when they are transported, and macroions produces an extra potential barrier through which the microions have to migrate. These make it difficult for electrophoretic and electro-osmotic

migration of ions and water and consequently lower the rate of contraction than that expected from one-dimensional modeling.

In addition, neglect of the counterflow of water might also overestimate the migration ability of water and lead to a large contraction rate.

We consider that this model satisfactorily illustrates the total characteristics of the contraction phenomenon and demonstrates that the contraction of a gel under the electrical field occurs because of an electro-kinetic mechanism.

## **B. Mechanoelectric Effect**

In the previous section, we have shown that a polyelectrolyte gel can contract or deform under an electrical stimulus; that is, a gel can convert electrical energy into mechanical work. The reverse process has also been observed in gels [12]. It has been found that mechanical deformation can produce an electrical potential as large as a few millivolts. This property of gels is similar to that of soft tissue in the mechanically induced biological systems such as the touch-sensing system of the human fingers. It has been proven that stress generates potentials (SGP) in human skin, which are then transmitted to the central nervous system for further processing [41, 42]. Hence, like human skin, a gel is able to convert mechanical energy into electrical energy, behaving like a soft and wet piezoelectric material.

When the ionizable polymer is chemically crosslinked to form a three-dimensional network, an increase in the ionization of the network brings about an extensive swelling of the gel that can visually be observed on the macroscopic level. The expansion of the conformation is due to the increase in the electrostatic potential present on the macromolecules. On the basis of swelling and contraction of a weak polyelectrolyte gel, Katchalsky and Kuhn [43–45] proposed a so-called “muscle” model which was referred to as the “mechanochemical” system or later as the “chemomechanical” system [1, 46].

The reverse process, that is, a mechanically induced shape change of any crosslinked weak polyelectrolyte should cause a change in its ionization state. When a piece of weak polyelectrolyte gel is placed in a cell and compressed from the vertical direction using a glass piston (Fig. 13a), the pH of the gel changes, as shown in Figure 14. When the gel is unloaded, the pH quickly obtains the original pH value with some increase.

Since there is no water outlet in the course of the deformation, the pH change should be associated with an enhanced ionization of carboxyl groups under deformation: Being compressed in one direction, the gel is subject to expand laterally and induces a one-dimensional dilatation of the polymer network in this direction. This brings about an increased chemical free energy (a decrease in entropy) of the polymer chain that should be compensated by the simultaneous increase in its ionization.

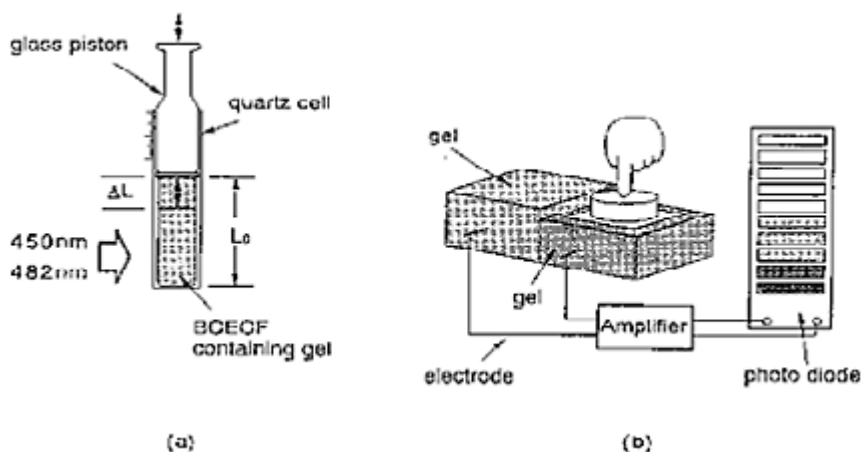


**FIG. 13** Schematics used for measuring the pH change during the deformation of a gel (a) and the artificial tactile sensing system capable of lighting a photodiode array under the deformation (b). In order to avoid any unnecessary electrical interference, the pH change of the gel under the deformation was measured spectroscopically by using 2',7'-bis (carboxyethyl) carboxyfluorescein dye, which changes its absorption maxim at 450 and 482 nm in accordance with the pH in the medium. (From Ref. 12.)

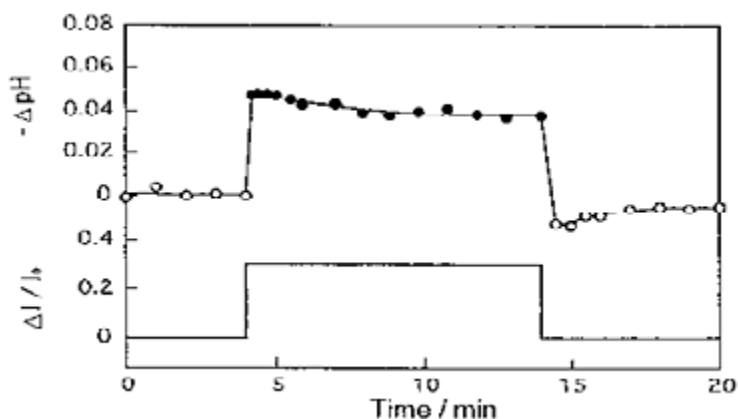


**FIG. 14** Time profile of pH changes of a copolymer gel composed of acrylic acid and acrylamide [poly(AA-co-AAm)] under the deformation; upper trace, pH change; lower trace, deformation ratio. Size of the gel, 15 mm×10 mm×10 mm, degree of swelling, 16; molar fraction of AA, 0.5; at free-standing state, pH=3.01. (From Ref. 12.)

The mechanically induced ionization is observed only for weak polyelectrolyte gels

which are able to change their ionization state sensitively in respect to their conformation and not for the fully ionized strong polyelectrolyte gels.

In order to extract the change in electrical potential caused by the decrease of the pH of the gel, a cell comprising two polymer gels facing each other was made. A pair of needle-like platinum wire electrodes, one as a reference and the other as a working electrode, were inserted to measure the electrical potential. When the gel is deformed, the extra protons migrate to the undeformed gel through the interface until the Donnan equilibrium is reached, and an electrical potential difference was observed during this period. Figure 15 shows the potential difference thus obtained.

On the basis of this principle, a soft and wet tactile-sensing device was constructed by connecting the electrodes with a photoemission diode array through an amplifier (see Fig. 13b). Experiments demonstrated that the tactile-sensing system made of polymer gel could successfully light the array in proportion to the amplitude of the stress applied.

We would like to emphasize that the mechanoelectrical system made of polymer gel has similarities with the tactile perceptions in the living organism. Both of them are dynamic processes in which the macroscopic deformation induces the ionic rearrangement which gives rise to a certain amount of transmembrane potentials. The gel also possesses common features with the natural tissue: softness, wetness, elasticity, and some other rheologically specified characteristics.

Because of these similarities, the soft mechanoelectrical system constructed from a polymer gel may open new possibilities in investigating artificial tissue-like tactile perception for prosthetics and robotics.

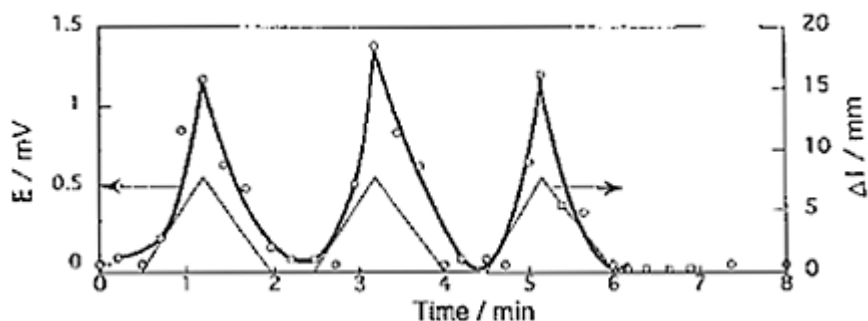


**FIG. 15** Time profile of electrical potential produced at the interface of two poly-(acrylic acid) gels, one of which was deformed and the other was free standing. Upper trace, electrical potential; lower trace, deformation length. Size of the gel, 15 mm×10 mm×10 mm; degree of swelling; 16. (From Ref. 12.)

### C. Electrical Oscillation

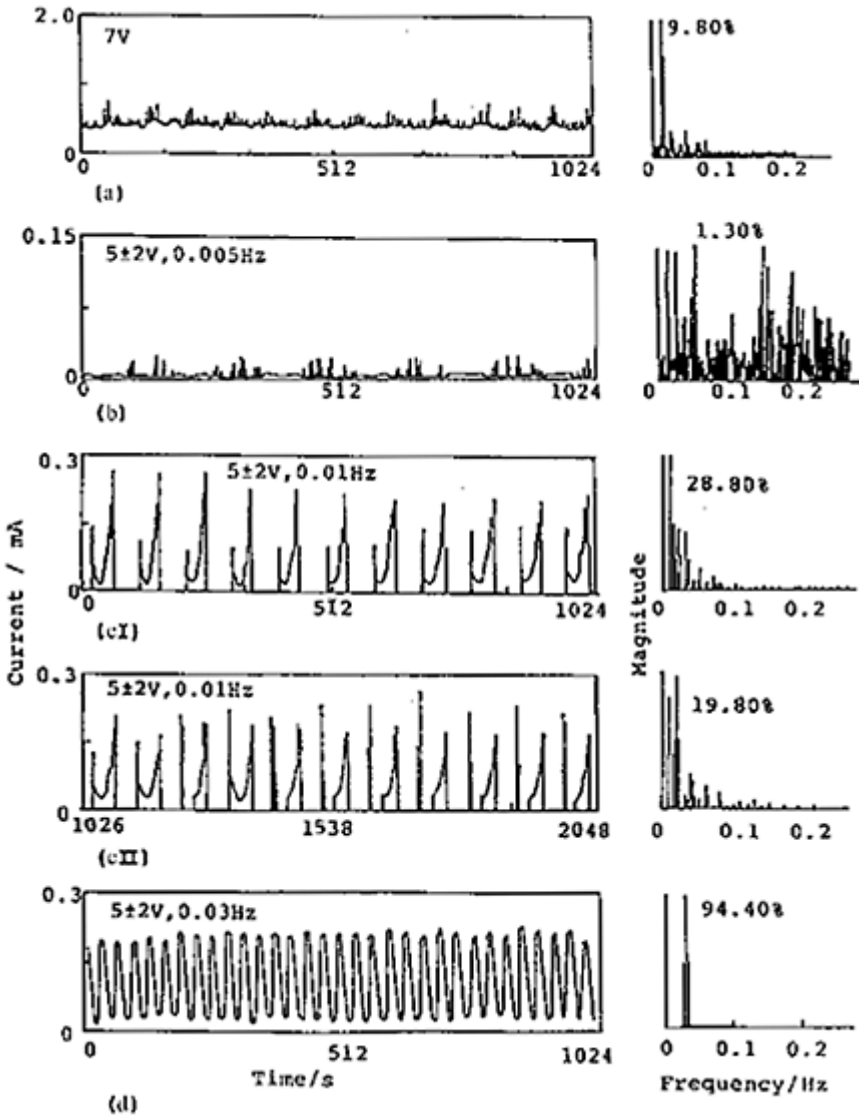
Metal-polymer gel-metal structures, made of a water-swollen polymer gel sandwiched between two platinum wire electrodes, have the property to switch on and off reversibly between two stable states, one characterized by high impedance corresponding to the “off” state and the other to a low impedance corresponding to the “on” state [13, 47, 48].



Figure 16 shows a repetitive curve and its power spectrum of the gel when a direct current (7 V) was applied to a calcium alginate gel. The oscillatory current appeared after a certain induction period, and this oscillation was prolonged for more than several hours. There existed a “threshold” value of potential (in this experiment about 3 V/cm or below) below which practically no oscillation appeared. During the induction period, the undamped oscillations appeared in every cross-linked water-swollen polymeric gel, provided they possessed ionized moieties, regardless of strong or weak polyelectrolytes. The power spectrum of this oscillation shows a main peak at the frequency of 0.013 Hz ( $f_0$ ) with higher harmonics. The magnitude of the main peak was about 9.80% of that total energy within a range of 0.5 Hz. The maximum amplitude of current oscillation was about 0.22 mA.

Figure 16b-d shows the effects of external sinusoidal voltage upon the current oscillation and the power spectra when alternating current frequencies ( $f_i$ ) of 0.005–0.03 Hz and amplitude (V) of 2 V were superimposed afterward to the oscillation induced by direct current voltage ( $V_0=5$  V). Thus, the electrical field by direct current plus alternating current does not exceed the value applied by direct current. When an alternating current of a frequency 0.005 Hz was applied to this oscillating gel, the response of the current oscillation became chaotic, as shown in the power spectrum (Fig. 16b). The magnitude of this alternating current was about 0.08 mA, and this value was much lower than that induced by direct current of 5 V. The power spectrum in this case has many peaks, but the peak induced by direct current (DC) ( $f_0$ ) also remained at 0.013 Hz. The magnitude of  $f_0$  is about 0.85% of the total energy, and that of frequency of alternating current (AC) ( $f_i$ ) is about 0.63%. The frequency of the main peak was shifted to 0.15 Hz, and the magnitude of this peak was about 1.30%.

Figure 16c1 shows the response of current oscillation and its power spectrum when an alternating current of a frequency of 0.01 Hz was applied. The power spectrum has a sharp peak at a frequency of 0.01 Hz, but there is no peak of  $f_0$  this time. The magnitude of this peak is larger and comprises about 28.8% of that of the total within the range of 0.5 Hz; clearly showing that the current oscillation induced by direct current was completely entrained to the oscillation induced by alternating current, although even the magnitude of the latter was much lower. Thus, it was demonstrated that the entrainment of oscillation occurs in the gel.



**FIG. 16** Effects of frequency of external sinusoidal voltage upon the current oscillation. Gel, calcium alginate, 24 mm in diameter, 11 mm long; degree of swelling; 40, electrode distance, 10 mm. (a) DC; 7 V; (b) DC 5 V; AC; 0.005 Hz, 2 V; (cI, cII) DC, 5 V, AC, 0.01 Hz, 2 V; (d) DC, 5 V, AC, 0.03 Hz, 2 V. Figures denoted in the power spectra indicate percentage of magnitude of the main peak of total energy generated within a range from 0 to 0.5 Hz. (From Ref. 48.)

when alternating current with a certain frequency is imposed, and the phenomena were

observed repeatedly for various polymer gels.

It was found that repetitive oscillation also occurs in the electroconductive organogels; for example, poly[(dimethyl amino) propylacrylamide] (PDMA PAA) gel doped with 7,7,8,8-tetracyanoquinodimethane (TCNQ) in *N,N*-dimethylformamide (DMF) [49]. The nature of the oscillation has been associated with the degree of cross linking, the doping ratio of the acceptor molecule, and temperature; an increase of these parameters enhanced both the amplitude and frequency of the oscillation. Note that no oscillation appeared at all in the solution. It is interesting that the base currents of the gel are constant and remain very low, whereas the peak current increased markedly with the increase in the degree of cross linking.

Current oscillation experiments of the TCNQ-doped PDMA PAA organic gel under a wide temperature range were carried out, and it was found that the amplitude as well as the frequency of the oscillation exponentially increase with increasing temperature (Fig. 17). The logarithmic dependence of the amplitude on the reciprocal temperature (Arrhenius-type plot) gave a straight line, as shown in Figure 17 (insert), and the activation energy was estimated as 18.3 kJ/mol for the TCNQ-doped PDMA PAA gel with a doping ratio of 1. This value is in the same order as the activation energy for the ionic conduction of polyelectrolyte gel

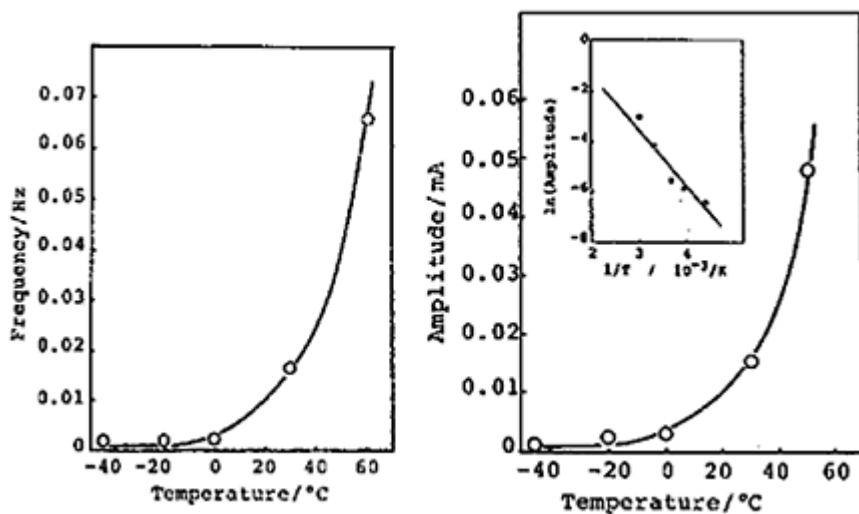


**FIG. 17** Frequency and amplitude of the current oscillation as a function of temperature for a PDMA PAA gel doped with TCNQ in DMF. Cross-linking density, 0.75 mol%; doping ratio, 1; degree of swelling, 25; electrode distance, 10 mm; DC voltage, 10 V. (From Ref. 49.)

estimated from PAMPS gel (see previous section). This result suggests that the oscillation of a polyelectrolyte gel under an electric field is associated with the transfer process of microions and macroions accompanied by the synchronized dynamic segmentational motion of the charged network in the solvent. Thus, the appearance of

periodical current oscillation seems to be an instinctive nature of the cross-linked polymer network. Microions make electrophoretic travel faster than the charged network and the electroconduction is largely dominated by the microions. Since the microions have to travel through an oppositely signed three-dimensional network, they permeate through the sinusoidal potential barriers, coupled with segmental motions of network. Thus, the mobility of microions can be associated with the energy gap of the amorphous network, being attracted by the electrostatic force of the charged network with an activation energy

The elucidation of an oscillation mechanism in the molecular level is still difficult, since the systems are multivariable with a nonlinear kinetic relationship, and complicated coupling mechanism, and many more experiments are required to confirm these ideas conclusively

## IV. SURFACE FRICTION OF POLYMER GELS

### A. Specific Characteristics of Gel Surface Friction

The sliding friction of various kinds of hydrogels has been studied and it was found that the frictional behaviors of the hydrogels do not conform to Amonton's law,  $F = \mu W$ , which well describes the friction of solids. The frictional force and its dependencies on the load are quite different depending on the chemical structures of the gels, surface properties of the opposing substrates, and the measurement condition [14–18]. Figure 18a shows the frictional force,  $F$ , in air for the nonionic synthetic gel, PVA; partially charged polysaccharide gel, gellan; fully charged polyelectrolyte gels poly(2-acrylamido-2-methylpropane) (PAMPS or PHAMPS) and its sodium salt PNaAMPS, on the glass plate. The friction coefficient,  $\mu = F/W$ , is calculated and shown in Figure 18b.  $F$  is almost constant (gellan gel), slightly increases (PVA gel), and strongly dependent (PHAMPS and PNaAMPS) with the load over the observed range of load. The friction coefficient,  $\mu$  for these gels accordingly shows unique load dependencies, which is quite different from those of solids. The  $\mu$  of PNaAMPS gel is constant over the change of the load, similar to that of rubber, but the value of  $\mu$  is as low as 0.002, which is two orders of magnitude lower than those of solids. The  $\mu$  of PVA and gellan gels decreases with the increase of load. These results demonstrate that the gel friction does not simply obey Amonton's law of  $F = \mu W$ , in which  $\mu$  is a material constant, and shows that the chemical structures of gels have a strong effect on the frictional behavior. The specific characteristics of gel friction are summarized as follows:

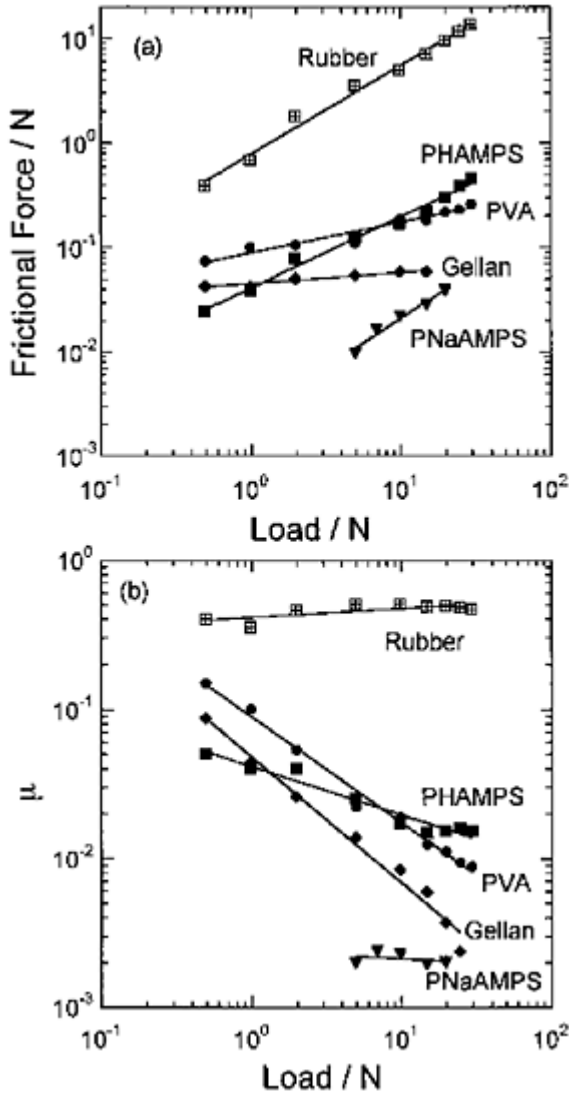


**FIG. 18** Relationship between the load and friction for various kinds of gels slide on glass substrate in air.  $v=30$  mm/min. (From Ref. 16.)

1. Frictional force ( $F$ ) does not obey the Amonton-Coulomb law (1699),

$$F = \mu W.$$

2.  $F$  is proportional to the apparent contact area ( $A$ ), and is a function of normal pressure ( $P$ ) and sliding velocity ( $v$ ),

$$F=Af(P, \nu).$$

3.  $F$  depends on the chemical structure, swelling ratio ( $q$ ), and substrate.

4.  $\mu=F/W$  is extremely low ( $\sim 10^{-3}$ ).

The gel friction is explained in terms of interfacial interaction, either attractive or repulsive, between the polymer chain and the solid surface. According to this model, the friction ascribed to the viscous flow of solvent at the interface in the repulsive case. In the attractive case, the force to detach the adsorbing chain from the substrate appears as friction.

### B. Effect of Electrostatic Interaction at Interface

The effect of interface interaction on the gel friction can be very clearly observed from the frictional behaviors between two gels carrying charges. When a pair of polyelectrolyte gels with opposite charges, for example, the anionic PAMPS gel with cationic poly (quaternized  $N$ -[3-(dimethylamino)propyl]acrylamide) (PDMAAPAA-Q) gel, were slid over each other, the adhesion between the two gel surfaces was so high that the gels were broken in the measurement. This strong adhesion should apparently be attributed to the electrostatic attraction between polyanions and polycations of the gels.

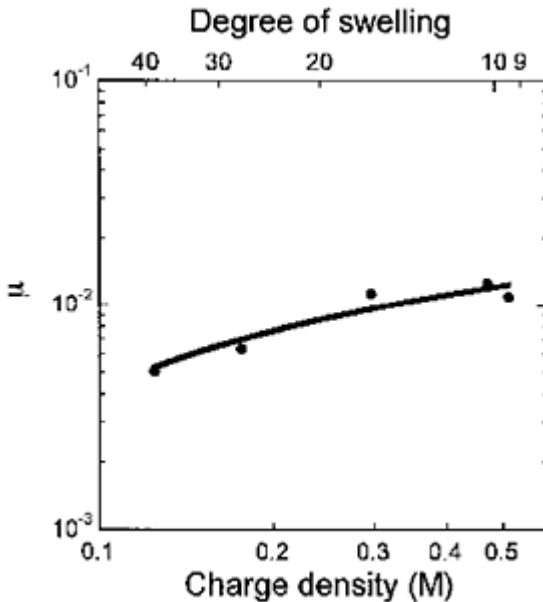


**FIG. 19** Charge density and degree of swelling dependencies of frictional coefficient between two PAMPS gels in water. Sample radius  $R=7.5$  mm; angular velocity,  $\omega=0.05$  rad/s; initial normal force,  $W=3$  N. (From Ref. 17.)

On the other hand, the friction between two polyelectrolyte gels carrying the same sign of charges was extremely low. Figure 19 shows the network charge density dependence of the friction for two pieces of PAMPS gels undergoing relative rotation. The modulation of charge density of the gel has been made by varying the amount of cross-linking agent in the process of gel synthesis, which gives rise to gels of different swelling ability. Since the polyelectrolyte gels used in this work fully dissociate in water, carrying one charge at each monomer unit, the charge density,  $c$  (in units of mol/L), equals the polymer network concentration. Therefore,  $c=1000/qM_w$ , where  $M_w$  is the formula molecular weight of the monomer. As shown in Figure 19, the friction increases modestly with the increase in charge density. That is, the frictional force does not sensitively change with the degree of swelling. Two opposite effects on the frictional force can be considered by examining the increase in charge density. One is the enhanced repulsion between the two gel surfaces, which favors the formation of a thicker solvent layer between the surfaces and decreases the viscous friction. The other is the increased network density, which increases the hydrodynamic resistance of the water in the polymer network and leads to an increase in the frictional force of the gel. A higher water content would lead to a small frictional force, since the fraction of polymer network which is nonflow decreases with the increase in the water content. Therefore, a higher charge density would bring a thicker liquid layer, which leads to a lower friction but gives rise to an increase of nonflow network density, which increases the friction. These two opposite effects on the friction explain why the friction is not sensitive to the network charge density.

An addition of any neutral salt into water can decrease the electrostatic repulsion and favors the approach or the contact of the two repulsive gel surfaces. It was found that the frictional coefficients are almost the same as those in water if the salt concentration is less than  $10^{-2}$  M. However, when the NaCl concentration increases further, the frictional force increases rapidly, and at 1 M of NaCl, it increases about one order [poly(sodium p-styrenesulfate) (PNaSS) gel and PDMAPEAA-Q gel] or two orders (PNaAMPS) of magnitude. Here it should be noted that the degree of swelling of the gel decreases with the increase in salt concentration owing to the screening of the electrostatic repulsion between charged groups on the polymer chain. This experimental result demonstrates that the electrostatic repulsion is effectively screened by the presence of salt, and this allows the polymer chains on the two gel surfaces to approach each other near enough that short distance attraction forces between the polymer networks come into action.

The effect of charge density was also studied by sliding copolymer gels containing different numbers of ionic monomers on homopolyelectrolyte gels. Figure 20 shows the frictional force when the copolymer gels consist of the ionic NaAMPS and the neutral acryl amide (AAm) [(poly(AAm-co-NaAMPS) gels] with various compositions were allowed to slide on a PNaAMPS gel. The friction between two homopolyelectrolyte gels of PNaAMPS showed the lowest values. With the increase of AAm composition, that is, decrease of negative charge density, the friction increases and PAAm homopolymer gel showed the highest

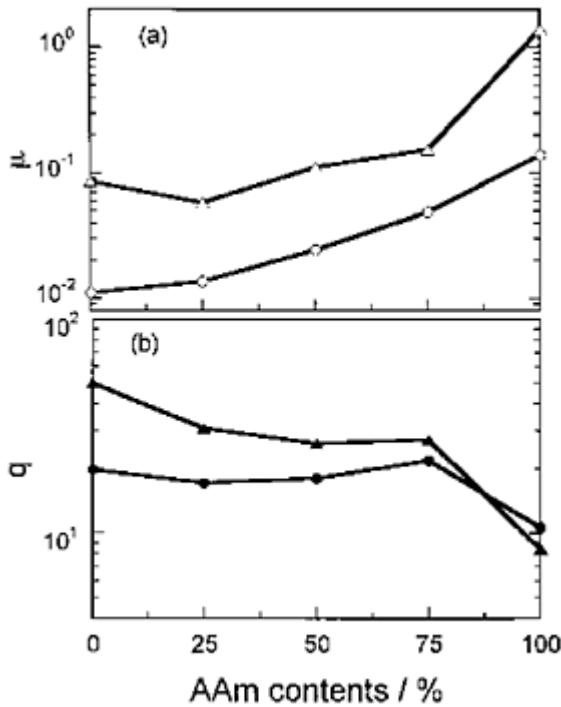


**FIG. 20** Dependencies of the friction coefficient (open symbols) and the degree of swelling (solid symbols) on the copolymer composition. The frictions are the values between poly(AAm-co-NaAMPS) gel and PNaAMPS gel (○, ●) or poly(AAm-co-DMAAPAA-Q) gel and PDMAAPAA-Q gel (Δ, ▲) in water. Sample radius,  $R=7.5$  mm; angular velocity,  $\omega=0.01$  rad/s; initial normal force,  $W=3$  N. (From Ref. 17.)

friction. Similar results were obtained if the poly(AAm-co-DMAAPAA-Q) gels were allowed to slide on the PDMAAPAA-Q gel. Taking into account the change in the swelling ratio brought on by changing the copolymer composition, the charge density of the gel was calculated and the relation between the frictional coefficient and the charge density of the copolymer gels is plotted as shown in Figure 21. Figure 21 clearly shows that the coefficient of friction decreases with the increase in the charge density. So far, we can not explain why the poly(AAm-co-DMAAPAA-Q) gel on PDMAAPAA-Q gel shows a higher friction than the poly(AAm-co-NaAMPS) gel on PNaAMPS gel. It should be related to the stronger interaction between AAm and DMAAPAA-Q.

From the above results, we can demonstrate that the friction of gels is largely dependent on the charge density of the gels. By varying the charge density of the gel or the ionic strength of the solvent, the frictional coefficient of the gel can be varied by about two orders of the magnitude in the examined experimental range.



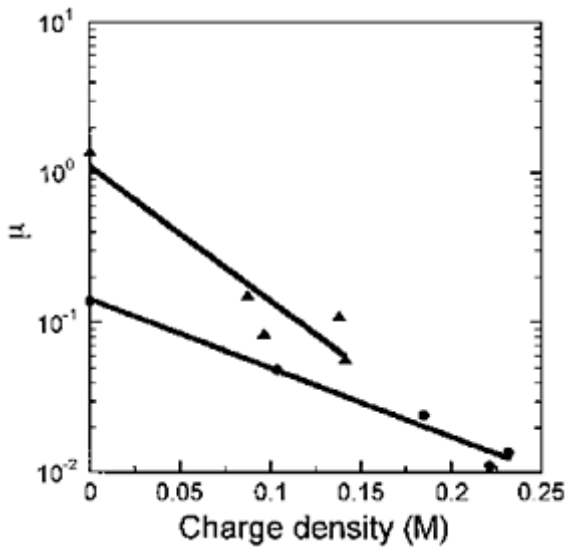


**FIG. 21** Relations between the friction coefficient and the gel charge concentration calculated from Figure 15. (●) poly(AAm-co-NaAMPS)gels; (▲) poly(AAm-co-DMAPAA-Q) gels. (From Ref. 17.)

### C. Theoretical Considerations

The gel friction can be explained in terms of polymer-solid surface repulsion and adsorption. When a polymer gel is placed in contact with a solid wall, the polymer chain would be either repelled from or adsorbed on the solid wall depending on the strength of the interaction between them relative to the solvent. In the former case, a solvent layer is formed at the interface, and the viscous flow of this solvent layer will make a dominant contribution to the frictional force. In the latter case, however, the adsorbing chain will be stretched when the solid surface is in motion relative to the gel. The elastic force increases with the deformation and detaches the adsorbing polymer chain from the substrate; thus it will in turn appear as the frictional force, as shown in Figure 22. According to this consideration, the frictional behavior can be deduced theoretically [16, 17].

#### 1. Repulsive Substrate

The viscous flow of the solvent layer at the interface should obey Newton's law and that of solvent in the polymer network can be expressed by the Debye-Brinkman equation where the effect of polymer network is represented by a distributed force. By solving the Debye-Brinkman equation together with the

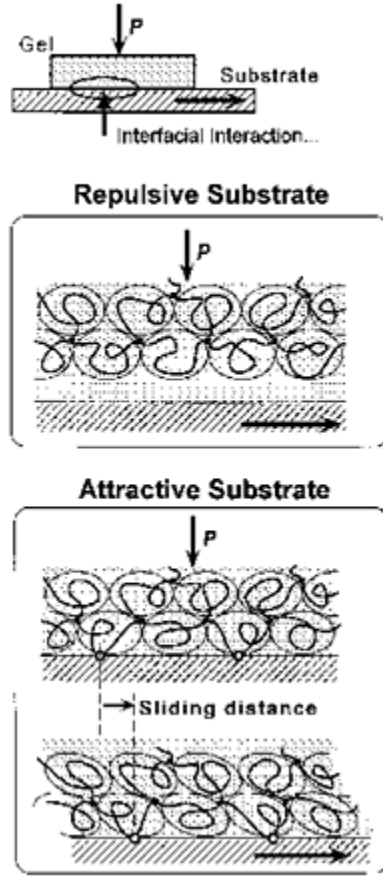


**FIG. 22** Schematic illustration of the mechanism for gel friction on a repulsive or attraction substrate.

Newton equation, the hydrodynamic lubrication between a repulsive solid surface and a gel is obtained:

$$f = \frac{\eta v}{l_g + \sqrt{K_{gel}}} \quad (28)$$

where  $\eta$  is the viscosity of solvent,  $v$  is the sliding velocity,  $l_g$  is the solvent layer thickness or the repelled distance of the gel from the solid surface against the normal pressure,  $P$ , and  $K_{gel}$  is the permeability of the gel. This result indicates that the equivalent nonslippery boundary of a gel surface is located at a depth of  $\sqrt{K_{gel}}$  from the surface.

$l_g$  Can be determined from the interfacial free energy. The work done by the solid

surface to repel the gel from the surface against the normal pressure should be equal to the increase in the interfacial free energy.  $A$ ; that is,

$$A - A_0 \cong Pl_g \quad (29)$$

where  $A_0$  is the interface energy between the substrate and the pure solvent. Supposing that the interfacial free energy between the gel and the substrate is the same as that between a polymer solution with a corresponding concentration and the substrate,

$$A - A_0 \cong \Pi_0 \xi \quad (30)$$

from the scaling theory [50]. Here  $\Pi_0$  is the osmotic pressure and  $\xi$  is the correlation length of the polymer solution. On the other hand,  $K_{gel}$  can be related to  $\xi$  as  $\xi \cong \sqrt{K_{gel}}$ . From the above results, the friction for the repulsive substrate

$$f \cong \eta v \left( \frac{E}{T} \right)^{1/3} \frac{P}{E} \quad (31)$$

in consideration of the deformation of the gel under the pressure,  $P$ . Here  $E$  is the elastic modulus of the gel and  $P/E \ll 1$ .

Eq. (31) suggests that the solvent layer formed between the gel and the repulsive substrate is inversely proportional to the normal pressure applied. We further discuss the thickness of the solvent layer between two charged gel surfaces under a certain load. When the load is not very high, the electrostatic repulsion prevails and the van der Waals interaction between the two surfaces can be neglected. Supposing that the polyions are homogeneously distributed in the bulk gel as well as on the gel surface, then we have an average surface charge density. For a homopolymer gel carrying one charge at each monomer unit, the number surface charge density,  $\sigma$  (in units of  $\text{m}^{-2}$ ), is

$$\sigma = (1000cN_A)^{2/3} = \left( \frac{10^6 N_A}{qM_w} \right)^{2/3} \quad (32)$$

Here,  $c$  is the bulk charge density of the gel or the monomeric concentration (in units of  $\text{mol/L}$ ) and  $N_A$  is Avogadro's number.

We denote the solvent layer thickness between two gel surfaces as  $2l$ , and the gel sample thickness as  $L$ , and we chose the origin of the coordinate system at the middle point between two gel surfaces with the x-axis parallel to and the z-axis vertical to the gel surfaces. Here,  $L \gg l$ . Thus, the electrical potential distribution between the two gel surfaces,  $\psi(x)$ , given by the Poisson equation is expressed as

$$\nabla\psi(z) = -\frac{\rho(z)}{\varepsilon} \quad -1 < z < l \quad (33)$$

where  $\varepsilon$  is the dielectric constant of water and  $\rho(z)$  is the counterion density at position  $z$ , which is given by the Boltzmann distribution. For positively charged counterions which correspond to polyanion gels,

$$\rho(z) = en_0 \exp\left[-\frac{e\psi(z)}{kT}\right] \quad (34)$$

here  $n_0$  is the density of counterions at a position where  $\psi=0$ ,  $e$  is the charge of an elementary electron,  $k$  is the Boltzmann constant, and  $T$  is the absolute temperature. For simplicity, only the case of monovalent ions is considered here. Combining Eqs. (33) and Eq. (34) one has

$$\frac{d^2\psi}{dz^2} = -\frac{en_0}{\varepsilon} \exp\left(-\frac{e\psi}{kT}\right) \quad (35)$$

On the gel surface,

$$\left(\frac{d\psi}{dz}\right)_{z=\pm l} = \mp \frac{e\sigma}{\varepsilon} \quad (36)$$

On the symmetrical plane,

$$\left(\frac{d\psi}{dz}\right)_{z=0} = 0 \quad (37)$$

From the electrical neutrality,

$$\sigma = n_0 \int_0^l \exp\left(-\frac{e\psi}{kT}\right) dz \quad (38)$$

Eq. (35) can be solved analytically. By choosing  $\psi_{z=0}=0$ , one has

$$\frac{e\psi}{kT} = 2 \ln \cos\left(\sqrt{\frac{n_0 r_0}{2z}}\right) \quad (39)$$

where  $n_0$  is a function of the surface number charge density given by

$$\sigma = \sqrt{\frac{2n_0}{r_0}} \tan\left(l\sqrt{\frac{n_0 r_0}{2}}\right) \quad (40)$$

here  $r_0 = e^2/\varepsilon kT$  is a constant with a dimension of length. The repulsive osmotic pressure,  $\Pi$ , between two approaching charged surfaces is determined by the microion charge density at the symmetry plane of  $z=0$ , where the electrostatic attraction on the microions is zero, since  $(d\psi/dz)_{z=0}=0$ , so one has

$$\Pi = n_0 kT \quad (41)$$

In the equilibrium state, this osmotic pressure is counterbalanced by the applied pressure,  $P$ ; that is,  $P=\Pi$ . Thus, the solvent layer thickness under a normal pressure,  $P$ , is obtained by combining Eqs. (40) and (41) and the condition  $p=\Pi$ ,

$$2l = 2\sqrt{\frac{2kT}{Pr_0}} \arctan\left(\sigma\sqrt{\frac{kTr_0}{2P}}\right) \quad (42)$$

When  $\sigma$  is very small and  $P$  is high so that  $\sigma\sqrt{kTr_0/2P} \ll 1$  is satisfied,  $(\sigma\sqrt{kTr_0/2P}) \approx \sigma\sqrt{kTr_0/2P}$ . Accordingly,  $2l \propto P^{-1}$ . This inverse relation between the solvent layer thickness and the pressure agrees with Eq. (4) derived from the scaling rules. When  $\sigma$  is very large and  $P$  is not too high so that  $\sigma\sqrt{kTr_0/2P} \gg 1$ ,  $(\sigma\sqrt{kTr_0/2P}) \approx \pi/2$ . Accordingly,  $2l \propto P^{-1/2}$ . This indicates that highly charged surfaces are able to sustain more pressure.

Figure 23 shows the theoretically calculated relations between the solvent layer thickness and the normal pressure,  $P$ , at various degrees of swelling of the gel. At a high surface charge density, which corresponds to a low degree of swelling, the repulsion distance,  $2l$ , is not sensitive to the pressure when the pressure is not very high. Notice that the experimental investigation in Figure 19 was performed at  $q=10\sim 30$  and  $P \approx 10^4 Pa$ . Under these conditions, the solvent layer thickness,  $2l$ , is not sensitive to the gel surface charge density and it has a value of 30 nm.

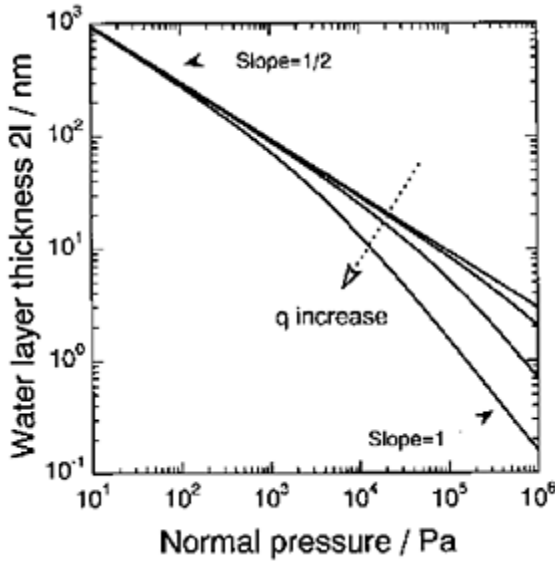


**FIG. 23** Normal pressure dependence of the solvent layer thickness,  $2l$ , for charged gels with various degrees of swelling. Following the direction of the arrow in the figure,  $q=1, 100, 1000, 10,000$ . Parameters used in the calculation:  $\epsilon=78\epsilon_0$ ,  $T=300$  K,  $M_w = 229$  (NaAMPS). (From Ref. 17.)

For two gels carrying the same sign of charges, the frictional force is not sensitively changed with the charge density. Eq. (28) indicates that the friction is inversely proportional to  $l + \sqrt{K_{gel}} \cdot \sqrt{K_{gel}} \cong \xi$  decreases with the increase in the polymer network density. On the other hand, as has been shown,  $l$  increases with the increase of the polymer network density. So the dependence of the parameter,  $\xi/l$  on the degree of swelling as well as on the pressure is very important in determining the frictional behavior. For strong polyelectrolyte, the chain is fully extended at equilibrium swelling in pure water. When  $q$ , the degree of swelling of the gel, is not too large,  $\xi/l \ll 1$  and the effect of  $\xi$  can be neglected. For very high  $q$ ,  $\xi$  becomes important, and  $l + \sqrt{K_{gel}}$  will be insensitive to the degree of swelling of the gel, or the charge density, as shown by the experimental results (see Fig. 19) and the theoretical analysis of Figure 24.

When simple salt is added to the system, the Poisson equation cannot be analytically solved. In addition, for a high salt concentration, the electrostatic repulsion is extensively screened and the polymer chains can approach each other. Therefore, the van der Waals attraction force should be taken into consideration, and the frictional mechanism would change from hydrodynamics to polymer chain detachment.

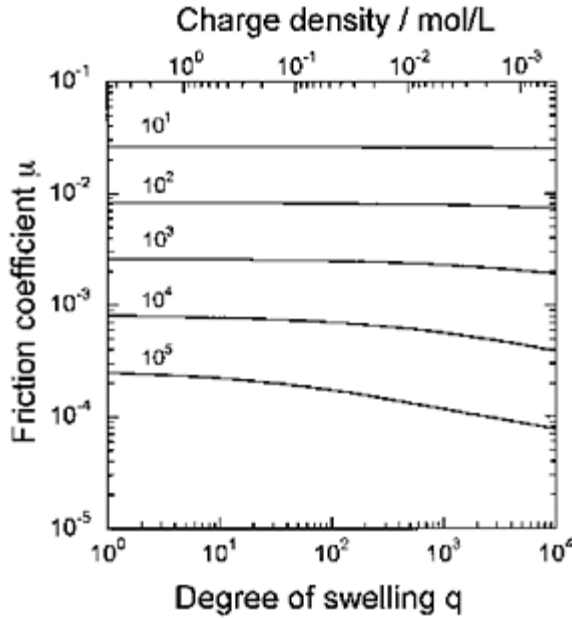


**FIG. 24** Dependencies of the frictional coefficients on the degree of swelling and on the charge density for two charged gels undergoing relative rotation. Numbers in the figure are normal pressure in the unit of Pa. Parameters used in the calculation:  $\omega=0.05$  rad/s,  $R=7.5$  mm,  $\eta=10^3$  Ns/m<sup>2</sup> (bulk water viscosity). (From Ref. 17.)

## 2. Attractive Substrate

The frictional mechanism in this case is quite similar to what occurs when rubber slides against a hard substrate. That is, the friction is due to the polymer chain detachment. We can follow the outline of the model proposed by Schallamach [51] for the case of dynamic rubber friction. The dynamic friction per unit area due to adsorption can be expressed as

$$f \cong \frac{T v \tau_f}{R_F^4} \frac{(\tau_b / \tau_f)^2}{(\tau_b / \tau_f + 1)} \quad (43)$$

where  $\tau_b$  and  $\tau_f$  are the average life-times of the polymer chain in the adsorbing state and in the free state, respectively.  $R_F$  is the radius of the polymer chain. The adsorption and desorption are attributed to thermal fluctuation. The stretching of the chain would favor desorption; that is, it would lower the energy difference between the adsorbing state and the free state by a value of  $F_{el}$ , which is the elastic energy of one stretched chain. So the transition rate from the adsorbing state to the free state becomes

$$\rho = \tau_f^{-1} \exp \left[ -\frac{F_{ads} - F_{el}}{T} \right] \quad (44)$$

The above relation suggests that the adsorption time,  $\tau_b$ , is a function of the deformation rate, or the sliding velocity. Under the normal pressure,  $P$ , the adsorption energy would increase, and it is found

$$F_{ads} \cong \begin{cases} T\phi^{-1/2}\delta\left(\frac{1+P}{E}\right)^{1/3} & \text{for } \delta \ll \phi^{1/2} \\ T\phi^{-5/4}\delta^{5/2} & \text{for } \delta \gg \phi^{1/2} \end{cases} \quad (45)$$

here  $T\delta$  is the effective attraction energy between a monomer unit and the surface in respect to the solvent and  $\phi$  is the volume fraction of the polymer. Different from that of a rubber friction, the hydrodynamic component also exists in this case. The total friction for the attractive substrate of weak adsorption at small pressures is

$$f = \eta v \left( \frac{E}{T} \right)^{1/3} \left[ \frac{1}{2} + \left( 1 + \frac{3}{2} \delta \phi^{-1/2} \right) \left( \frac{1+P}{E} \right)^{1/3} \right] \quad (46)$$

The obtained results are very crucial in understanding the low frictional mechanism of biological organs and serve to construct a comfortable artificial joint using polymer gels.

## REFERENCES

1. Y Osada. Adv in Polym Sci 82:1, 1987.
2. Gels. D De DeRossi, K Kajiware, Y Osada, A Yamauchi, Eds. Polymer Gels. Plenum Press, New York, 1991.
3. Y Osada, JP Gong. Prog Polym. Sci 18:187, 1993.
4. Y Osada, JP Gong. Adv. Mater 10:827, 1998.
5. A Wassermann. Size and Shape Changes of Contractile Polymers. Pergamon Press, New York, 1960.
6. AH Clarke, SB Ross-Murphy. Adv Polym Sci 83:57, 1987.
7. T Tanaka, I Nishio, ST Sun, SV Nishio. Science 218:467, 1973.
8. H Okuzaki, Y Osada. Macromolecules, 27:502, 1994.
9. DE Woessner, BS Snowden. J Colloid Interface Sci 34:290, 1970.
10. Y Osada, H Okuzaki, H Hori. Nature 355:242, 1992.
11. Y. Osada, M Hasebe. Chem. Lett 1285, 1985.
12. K. Sawahata, JP Gong, Y Osada. Macromol Rapid Commun 16:713, 1995.
13. K Umezawa, Y. Osada. Chem Lett 1795, 1987.
14. JP Gong, M Higa, Y Iwasaki, Y Katsuyama, Y Osada. J Phys Chem 101:5487, 1997.
15. JP Gong, Y Osada. J Chem Phys 109:8062, 1998.
16. JP Gong, Y Iwasaki, Y Osada, K Kurihara, Y Hamai. J Phys Chem B 103:6001,



1999.

17. JP Gong, G Kagata, Y Osada. *J Phys Chem B* 103:6007, 1999.
18. JP Gong, Y Iwasaki, Y Osada. *J Phys Chem B* 104:3423, 2000.
19. JP Gong and Y Osada. *Chem Lett* 449, 1995.
20. F Oosawa. *J Polym Sci* 23:421, 1957.
21. GS Manning. *J Chem Phys* 51:924, 1969.
22. M Nagasawa, I Noda, T Takahashi, N Shimamoto. *J Phys Chem* 76:2286, 1972.
23. D Dolar, J Span, A Pretnar. *J Polym Sci* 16(Pt C):3557, 1968.
24. JP Gong, N Komastu, T Nitta, Y Osada. *J Phys Chem* 101:740 1997.
25. GS Manning. *J Phys Chem* 79:262, 1975.
26. M Mandel, T Odijk. *Ann Rev Phys Chem* 35:75, 1984.
27. F Oosawa. *Polyelectrolytes*. New York, Marcel Dekker, 1971.
28. AA Minakata. *Ann NY Acad Sci* 107:303, 1977.
29. K Ito, A Yagi, N Ookubo, R Hayakawa. *Macromolecules* 23:857, 1990.
30. A Minakata, N Imai. *Biopolymers* 11:329, 1972.
31. A Minakata. *Biopolymers* 11:1567, 1972.
32. M Mandel. *Mol Phys* 4:489, 1961.
33. N Ookubo, Y Hirai, K Ito, R Hayakawa. *Macromolecules* 22:1359, 1989.
34. S Takashima. *J Phys Chem* 70:1372, 1966.
35. K Kauzmann. *Rev Mod Phys* 12:34, 1942.
36. H Eyring. *J Chem Phys* 4:283, 1936.
37. RH Ewell. *J Appl Phys* 9:252, 1938.
38. R Kishi, Y Osada. *J Chem Soc Faraday Trans 1*, 85(3):655, 1989.
39. JP Gong, T Nitta, Y Osada. *J Phys Chem* 98:9583, 1994.
40. T Hatakeyama, A Yamauchi, H Hatakeyama. *Eur Polym J* 20:66, 1984.
41. MH Shamos, LS Lavine. *Nature* 213:267, 1967.
42. H Athenstaedt, H Claussen, D Schaper. *Science* 216:1018, 1982.
43. W Kuhn, B Hargitay, A Katchalsky, H Eisenberg. *Nature* 165:514, 1950.
44. IZ Steinburg, A Oplatka, A Katchalsky. *Nature* 210:568, 1966.
45. W Kuhn, A Ramel, DH Walters, G Ebner, HJ Kuhn. *Fortschr Hochpolym Forsch* 1:540, 1960
46. S Maekawa, JP Gong, Y Osada. *Makromol Rapid Commun* 15:73, 1994.
47. Y Osada, K Umezawa. *Makromol Chem* 189:597, 1988.
48. Y Osada, K Umezawa, A Yamauchi. *Bull Chem Soc Jpn* 62:3232, 1989.
49. M Miyano and Y Osada. *Macromolecules* 24:4755, 1991.
50. PG de Gennes. *Scaling Concept in Polymer Physics*. Cornell University Press, Ithaca, NY, 1979.
51. A Shallamach. *Wear* 6:375, 1963.



# Synchrotron X-Ray Scattering Study on Nanostructures of Polyelectrolyte Gel/Surfactant Complexes

CHRISTIAN BURGER, SHUIQIN ZHOU, and BENJAMIN CHU *State University of New York at Stony Brook, Stony Brook, New York*

## I. INTRODUCTION

Polyelectrolyte-surfactant complexes (PSCs) have gained considerable interest in recent years both from a fundamental and from a practical/technological point of view [1–13]. In a similar fashion as block copolymers or microemulsions, these systems are able spontaneously to self-assemble into microphase-separated macrolattices with a high degree of long-range order on a supramolecular length scale. However, PSCs are distinguished from those former systems by the presence of strong electrostatic interactions which usually dominate their structure and property relationships. Polymer chain entropy contributions or weak enthalpic Flory-Huggins-type interactions play a far less prominent role than they do for noncharged systems. A microphase separation into hydrophilic (charged polyelectrolyte backbone, charged surfactant head groups, aqueous solvent with surfactant counter ions) and hydrophobic (aliphatic surfactant chains, neutralized ion-paired hydrophobic backbone) domains shows a considerably higher degree of phase segregation (*superstrong segregation regime* in [14, 15]) with a much narrower interface between the domains than found, for example, between non-charged polymer melts. The introduction of long-range electrostatic interactions leads to a much broader variety in the phase behavior of the PSCs. Note also that the electrostatic interactions can be fine tuned by adjusting the charge density of the polyelectrolytes. A broad variety of highly ordered and highly symmetrical morphologies has been found, many of which are not observed in classic systems.

Apart from their obvious fundamental relevance, PSCs have also been found to have technological interest; for example, in medical, cosmetic, food, painting, and various other applications. Medical applications look especially promising since many important biological molecules can act as polyelectrolytes (e.g., DNA) or as surfactants (e.g., lipids). Thus, apart from providing well-defined model system theoretically to study self-assembly behavior in biological processes, PSCs can also be useful for real-world applications; for example, DNA complexes to be used as drug-delivery systems or in gene therapy applications [16–28].

PSCs are often formed spontaneously from their ingredients. Their preparation can be as simple as mixing the corresponding solutions together. Using stoichiometric quantities of polyelectrolyte and surfactant usually leads to the immediate precipitation of an

insoluble product, whereas the charged complexes obtained from nonstoichiometrically mixed components typically are still soluble in aqueous solution. Although this simple mixing scheme works well for linear polyelectrolytes, the formation of PSCs from cross-linked polyelectrolyte gels require a different technique involving a slow diffusion process of the surfactants into the polyelectrolyte gels. For details, see Section II.

The highly ordered macrolattices on a nanometer-length scale formed by PSCs are ideally suited to be investigated by scattering techniques; namely small-angle x-ray scattering (SAXS) or small-angle neutron scattering (SANS). Analogous to the three-dimensional long-range order on an Angstrom-length scale of low molecular crystals in classic crystallography, the present supramolecular three-dimensional long-range order leads to a scattering pattern consisting of sharp peaks which, due to the relationships of *reciprocal space*, occur at a smaller angular range, leading to the term *small angle* scattering.

In the present study, we investigate polyelectrolyte gel-surfactant complexes of cationic polyelectrolyte gels with anionic surfactants as well as the complementary systems of anionic polyelectrolyte gels with cationic surfactants. We will study the influence of the polyelectrolyte charge density and of the hydrophobic surfactant tail length on the phase behavior. Furthermore, the influence of cross linking in the polyelectrolyte gels will be considered. Finally, the phase behavior of gel PSCs upon drying and redissolving will be investigated.

## II. EXPERIMENTAL

### A. Materials

Methacrylic acid (MAA) monomer (Aldrich, 98.5%) was vacuum distilled. *N*-isopropylacrylamide (NIPAM) monomer (ACROS, 99%) was purified by recrystallization from a toluene/hexane mixture. *N*-(3-aminopropyl) methacrylamide hydrochloride (NAPMACl) monomer (Polyscience), *N,N'*-methylenebisacrylamide (BIS) (Ultragrade, Pharmacia LKB) as a crosslinker, ammonium persulfate (APS) (Aldrich, 98+) as an initiator, and *N,N,N',N'*-tetramethylethylenediamine (TEMED) [electrophoresis grade, Fisher Biotech) as an accelerator were used as received. Linear polymethacrylic acid (PMAA) (Polyscience) with  $M_w=70,000$  and  $M_w/M_n\sim 1.1$  was used as received. The surfactants of alkyltrimethylammonium bromide ( $C_n$ TAB,  $n=10-16$ ) (Lancaster, 98%) and sodium alkyl sulfate ( $SC_nS$ ,  $n=9-16$ ) (Lancaster, 99%) were used without further purification. Deionized water was distilled before use.

### B. Gel Preparation

Gels were prepared by free radical copolymerization. A 15 wt% aqueous solution (5–8 mL) of the reaction mixture with a desired comonomer molar ratio and a cross-linker density of 1 mol% (of total monomers) was bubbled with nitrogen for 15 min to remove oxygen in the reaction mixture. Thirty-five microliters of 10 wt% APS solution was added to the mixture. The final solutions were filtered through a 0.22  $\mu$ m Millipore filter

and injected into the space between two glass plates which were separated by two spacers with a thickness of  $0.63 \pm 0.04$  mm. For the P(MAA/NIPAM) gels, gelation was carried out at  $65^\circ\text{C}$  for 24 h. One portion of the resulting gels was washed in distilled deionized water to remove the unreacted monomers, and was titrated with aqueous sodium hydroxide solution to determine the composition of the copolymer. Another portion of the gels was washed in a large amount of dilute sodium hydroxide solution for 3 weeks in order to neutralize the poly(methacrylic acid) and to remove the unreacted monomers. The dilute sodium hydroxide solution was changed every 1–2 days, and the final pH value was kept at  $\sim 8.2$ . For the P(NAPMACI/NIPAM) gels, 10  $\mu\text{L}$  of TEMED was added to the nitrogen-bubbled reaction mixtures before they were filtered into the space between the two glass plates. Gelation was carried out at room temperature for 24 h. The gels were washed in a large amount of dilute hydrochloric acid solution for 2 weeks in order to remove the unreacted monomers. The dilute hydrochloric acid solution was changed every 1–2 days, and the final pH value was kept at  $\sim 3$ .

### C. Gel-Surfactant Complexation

Complexes were prepared by immersing known amounts of water-swollen PMAA or P(MAA/NIPAM) gel disks (10 mm diameter, 2–3 mm thick) in very dilute aqueous sodium hydroxide solution of  $\text{C}_n\text{TAB}$  (pH $\sim 8$ –9) and by immersing known amounts of P(NAPMACI/NIPAM) gel disks in dilute hydrochloric acid aqueous solutions of  $\text{SC}_n\text{S}$  surfactants (pH $\sim 3$ ). The surfactant concentration was approximately one-third of the critical micelle concentration (CMC) for the corresponding surfactant in the external solution phase. The total volume of the surfactant solution was controlled at such a level that the ratio,  $r$ , defined by  $\langle \text{number of surfactant molecules in solution} \rangle / \langle \text{number of charged groups in the polymer networks} \rangle$ , was in the range of  $r \geq 2$ . It means that the number of surfactant molecules was always in excess of the number of charged groups in the copolymer chains for complexation. The gel disks were equilibrated in the surfactant solution for about 4 weeks before being taken out for SAXS measurements.

### D. Linear PMAA- $\text{C}_n\text{TAB}$ Complexation

Complexes were prepared by adding the PMAA aqueous solution dropwise to the  $\text{C}_n\text{TAB}$  aqueous solutions at adjusted pH values ( $\sim 8.5$ ) and room temperature under stirring condition. The concentration of PMAA was fixed at 0.1 mg/mL, whereas the concentrations of  $\text{C}_n\text{TAB}$  solutions were kept at one third CMC. The volumes of the surfactant solutions were controlled at such a level that the ratio,  $r$ , defined by  $\langle \text{number of surfactant molecules in solution} \rangle / \langle \text{number of charged sites in the polymer chains in solution} \rangle$ , was in the range of  $r = 1.5$ . After complexation between PMAA and  $\text{C}_n\text{TAB}$  solutions, the mixed solution became slightly cloudy. The equilibrated complex particles were collected by centrifugation at 6000 g.

### E. Synchrotron Small-Angle X-Ray Scattering Measurements

Synchrotron small-angle X-ray scattering (SAXS) measurements were performed at the X3A2 State University of New York (SUNY) Beam Line, National Synchrotron Light Source (NSLS) at Brookhaven National Laboratory (BNL), using a laser-aided pre-aligned pinhole collimator. The incident beam wavelength ( $\lambda$ ) was tuned at 0.154 nm. For the two-dimensional detection, Fuji imaging plates have been used in connection with a BAS 2500 imaging plate scanner. The sample to detector distance was 787 mm, corresponding to a  $q$  range of  $0.2 \leq q \leq 4.8 \text{ nm}^{-1}$  for the PMAA or P(MAA/NIPAM) gel- $C_n$ TAB complexes, where  $q = (4\pi/\lambda) \sin(\theta/2)$  with  $\theta$  being the scattering angle between the incident and the scattered beam. The experimental data were corrected for background scattering and sample transmission. Collimation effects were negligible for this setup. Experiments were also performed at the X27C Advanced Polymers Beam Line with  $\lambda = 0.1307 \text{ nm}$  and a sample to detector distance of 918 mm for P(NAPMACI/NIPAM) gel- $SC_nS$  complexes.

## III. RESULTS AND DISCUSSION

### A. Cationic P(NAPMACI/NIPAM) gel- $SC_nS$ Complex Systems

#### 1. Charge-Density Effect

Figure 1 shows small-angle scattering curves for complexes formed by cationic P(NAPMACI/NIPAM) gels with  $SC_{14}S$  surfactant as a function of charge density

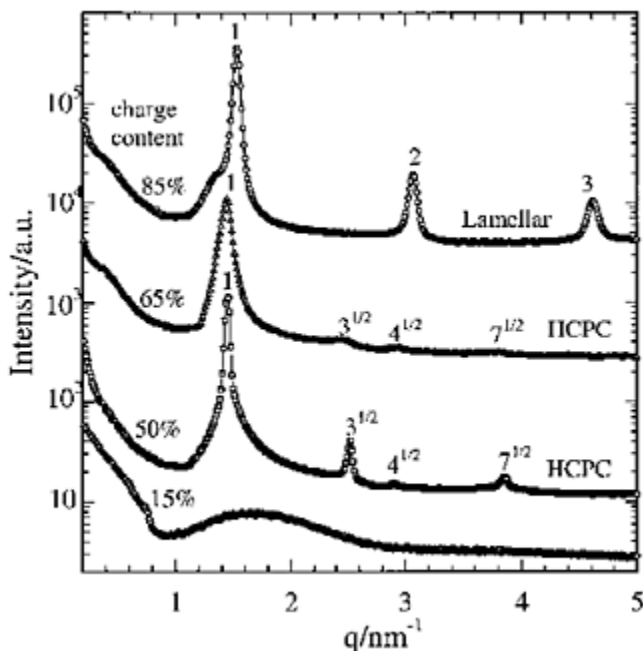


**FIG. 1** SAXS profiles of complexes formed by cationic P(NAPMACI/NIPAM) gels with  $SC_{14}S$  surfactant at various charge contents in the P(NAPMACI/NIPAM) chains.

in the P(NAPMACI/NIPAM) polyelectrolyte chain. At high charge densities, a lamellar (LAM) morphology is observed as indicated by the equidistant peak positions (1:2:3) in the SAXS curve. A decrease in the charge density induces a structural transition from LAM to two-dimensional hexagonally close-packed cylinders (HCPCs) with the typical peak position ratios of  $1:3^{1/2}:2:7^{1/2}$ . For both morphologies, fairly sharp SAXS peaks indicate the existence of a high degree of long range on the present mesoscopic length scales. Further decrease in the charge density destroys this long-range order as expressed by the disappearance of the sharp peaks and by the appearance of a broad “amorphous halo”-like maximum allowing at most a liquid-like order.

## 2. Hydrophobic Tail-Length Effect

Let us now investigate the influence of the length of the hydrophobic surfactant chain at a fixed high charge density in the polyelectrolyte gel. Figure 2 shows SAXS curves of P(NAPMACI/NIPAM) gels with a fixed charge density of 85% complexed with  $SC_nS$  surfactants having  $n=10-16$  carbon atoms in the hydrophobic alkyl chains. For long hydrophobic tails, including the case of  $n=14$  already considered above, a lamellar morphology is observed. Reducing the hydrophobic chain length also induces a structural transition from LAM to HCPCs.

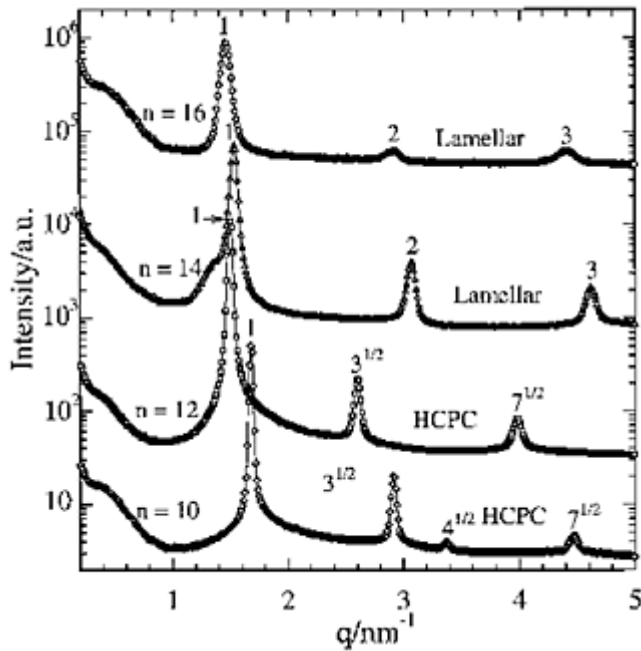


**FIG. 2** SAXS profiles of complexes formed by 85% positively charged P(NAPMACI/NIPAM) gels with surfactants of  $SC_nS$  at different carbon atom numbers in the alkyl chains ( $n=10-16$ ).

It is interesting to note that, for  $n=12$ , the expected peak at position 2 in the peak ratio set  $1:3^{1/2}:2:7^{1/2}$  is not observed. However, since the corresponding peak is also very weak in the SAXS curve for  $n=10$ , and since there are no known reasonable morphologies with peak position ratios of  $1:3^{1/2}:7^{1/2}$ , the structure assignment as HCPCs can be considered with high confidence and the extinction of this peak for  $n=12$  is a coincidental effect of the cylinder form factor.

### 3. Combined Effects

Let us now investigate the transition from the ordered HCPC phase to the disordered (DIS) phase more closely. Figure 3 shows SAXS curves of the P(NAPMACI/NIPAM) gels for various charge densities where the chain lengths of the complexed  $SC_nS$  alkyl chains have been varied in order to locate the HCPC-DIS transition. For the highly charged 85% system, even our shortest available surfactant with  $n=9$  carbon atoms in the hydrophobic alkyl chain was not yet able to destroy the long-range ordered HCPC structure. For an intermediate charge density of 65%, the order-disorder transition occurred between lengths of  $n=9$  and  $n=10$  carbon atoms of the surfactant alkyl chain, respectively. At an even lower charge density of 50%, the order-disorder



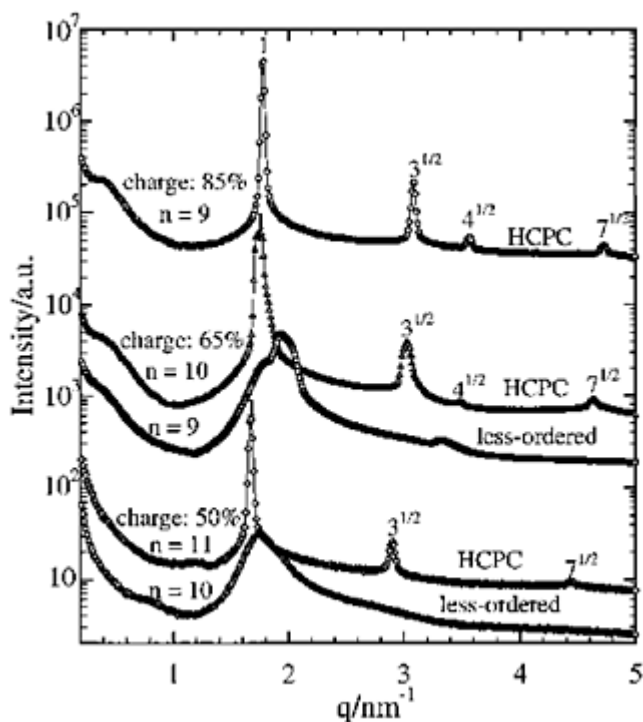


**FIG. 3** Charge content effect of P(NAPMACI/NIPAM) gels on the order-disorder structural transitions of P(NAPMACI/NIPAM) gel- $SC_nS$  complexes induced by a decrease in the alkyl chain length of surfactants  $SC_nS$ .

transition was shifted to hydrophobic chain lengths between  $n=10$  and  $n=11$  C atoms.

We have seen that both electrostatic interactions, which are strong at high charge density, and hydrophobic interactions, which are strong for long alkyl chains of the surfactants, control the phase behavior of these systems. Both effects can stabilize highly ordered macrolattices which, in the present system, are of the LAM and HCPC types. Reducing both of these interactions leads to structural transitions from LAM to HCPC and eventually to poorly ordered morphologies without long-range order. The lower the charge density of gels, the longer the hydrophobic surfactant tails need to be to form the ordered structure [29, 30].

## B. Anionic P(MAA/NIPAM) Gel- $C_n$ TAB Systems

### 1. Pm3n Cubic Network Morphology

Figure 4 shows SAXS curves of fully (100%) charged PMAA gel- $C_n$ TAB complexes.

These scattering curves are shown in dependence of the surfactant

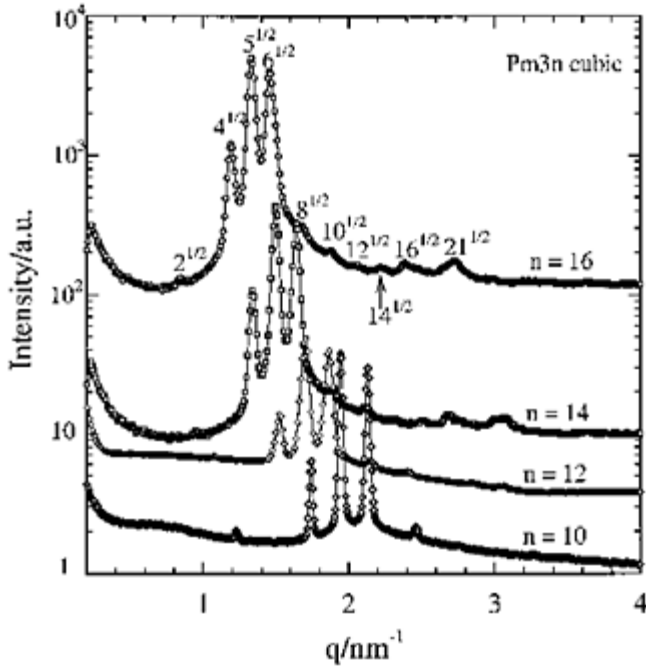


**FIG. 4** Typical SAXS profiles of fully charged PMAA gel-C<sub>12</sub>TAB complexes at different surfactant alkyl chain length ( $n=10-16$ ).

alkyl chain length which is in the range of  $n=10-16$  carbon atoms, but obviously in all cases the same structure is observed which only scales in size.

These scattering patterns look very characteristic with a large number of well-resolved peaks, some of which appear quite closely together. The astonishing weakness of the first observable peak is also typical for this system. It should be noted that a high-resolving well-aligned pinhole collimated experimental setup is mandatory to observe unambiguously this type of scattering pattern. With conventional equipment and especially in slit collimation, closely spaced peaks would be blended together and weak peaks would be smeared out.

The observed reflections occur at position ratios of  $2^{1/2}:2:5^{1/2}:6^{1/2}:8^{1/2}:10^{1/2}:12^{1/2}:14^{1/2}:4:21^{1/2}$ , clearly indicating a cubic symmetry. It can be shown [29-31] that this scattering pattern is best described in terms of a fairly complicated but highly symmetrical cubic Pm3n system consisting of a continuous connected network plus spheres at body-centered positions embedded in a continuous matrix.

## 2. Face-Centered Cubic Morphology

Figure 5 shows the SAXS curves for intermediately (65%) charged P(MAA/NIPAM) gel interacting with surfactants of  $C_{14}$ TAB and  $C_{16}$ TAB, respectively. The scattering patterns with peak position ratios of

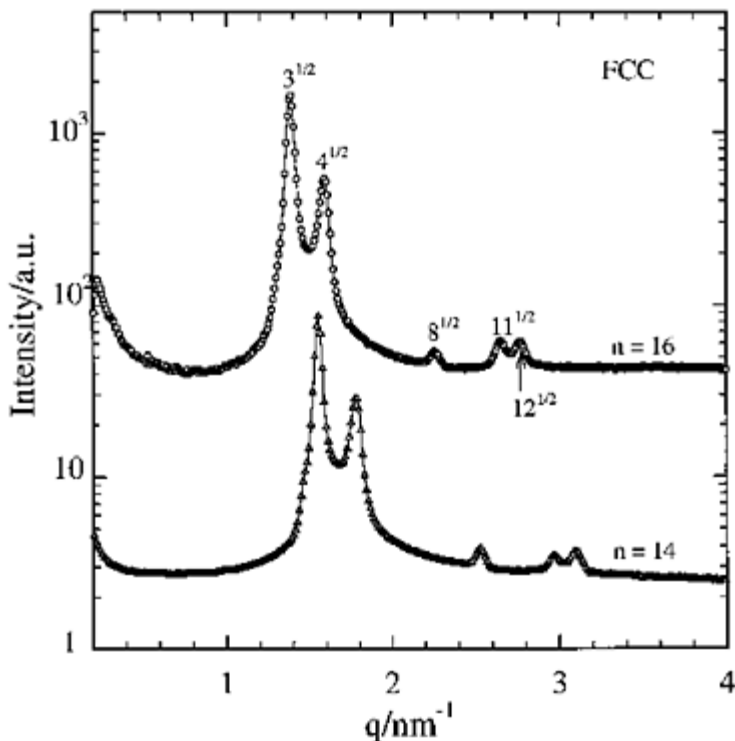


**FIG. 5** Typical SAXS profiles of complexes formed by 67% negatively charged P(MAA/NIPAM) gel interacting with surfactants of  $C_{14}$ TAB and  $C_{16}$ TAB, respectively.

$3^{1/2}:2:8^{1/2}:11^{1/2}:12^{1/2}$  clearly follow a cubic symmetry and can be identified in terms of a face-centered cubic (FCC) packed system of spheres. An alternatively possible Ia3d multiply connected cubic network would share the appearance of the first two peaks but then differ in the higher orders. Again, it must be emphasized that high-resolving experimental equipment is required to distinguish unambiguously these cases.

It should be noted that the occurrence of an FCC system is somewhat unusual in comparison to the ubiquitous body-centered cubic (BCC) systems normally found when soft matter packs spheres in a cubic symmetry. As a rule of thumb, it can be argued that BCC packings are to be expected for weakly interacting, deformable soft spheres, which usually applies to organic matter, whereas an FCC symmetry should be observed for hard

spheres with more complicated interactions. Apparently, the present P(MAA/NIPAM) gel- $C_n$ TAB complex belongs to the latter class.

### 3. Hexagonally Close-Packed Spheres

At an even lower charge density of 50% in the P(MAA/NIPAM) polyelectrolyte gel, again complexed with  $C_{14}$ TAB and  $C_{16}$ TAB, respectively, a very interesting

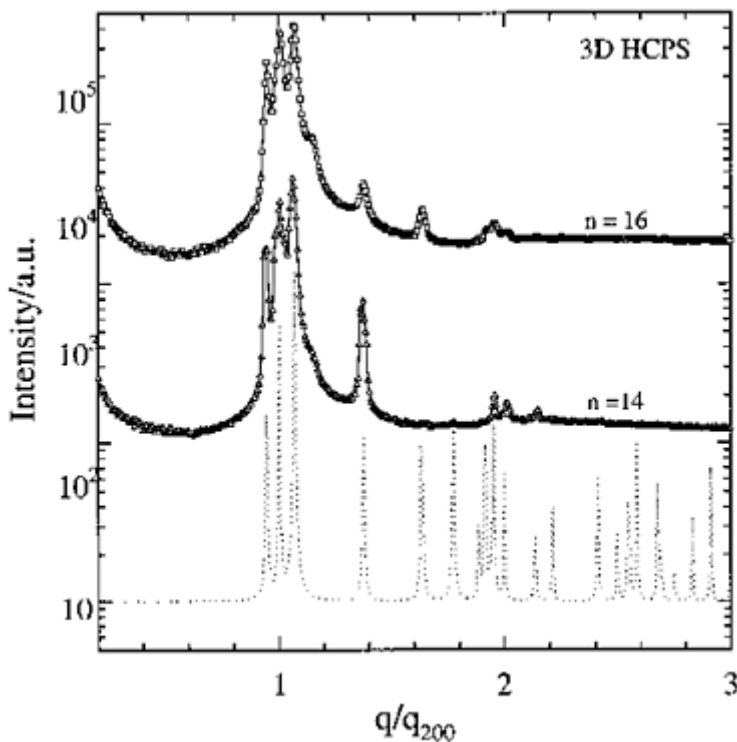


**FIG. 6** Typical SAXS profiles of complexes formed by 50% charged P(MAA/NIPAM) gel interacting with surfactants of  $C_{14}$ TAB and  $C_{16}$ TAB, respectively. The  $q$  scale has been normalized to  $q/q_{200}$  with  $q_{200}=1.40$  and  $1.58\text{ nm}^{-1}$  for  $n=16$  and  $14$ , respectively. The dotted line represents the calculated scattering curve based on the HCPs structure model.

SAXS pattern is observed, as shown in Figure 6. Here, even more than before, the close spacing of the peaks and the required instrument resolution should be stressed. This scattering pattern can be identified in terms of a hexagonally close-packed system of spheres (HCPs). The result is really unusual and sheds some interesting light on the subtleness of the interactions between the spherical structural units involved here. Clearly, the FCC packing observed for higher charge densities and the HCPs

morphology are both close packings of spheres. Envisaging both morphologies in terms of hexagonally close-packed two-dimensional layers of spheres, they only differ in the stacking sequence of these layers, being ABC for FCC and ABA for HCPS, respectively. Thus, both morphologies are closely related, have exactly the same space filling, and differ only very delicately in their higher order interactions between the spheres. This clearly suggests that the P(MAA/NIPAM) gel- $C_n$ TAB system indeed interacts in a very subtle way.

It is even more surprising that very large HCPS monodomains have been observed in this system. Zhou et al. reported an oriented two-dimensional SAXS pattern which could be interpreted in terms of two monodomains filling the total irradiated volume which has a size of a few tenths of a millimetre; once more proving the very long-range nature of the ordering forces in this system.

#### 4. Hydrophobic Chain-Length Effect

In the complexes consisting of the cationic polyelectrolyte P(NAPMACI/ NIPAM) gels with the anionic  $SC_nS$  surfactant we have seen that the structural transitions could be induced both by tuning the electrostatic (via the charge density) and the hydrophobic (via the alkyl chain length) interactions. It turns out that the present complementary system consisting of the anionic polyelectrolyte P(MAA/NIPAM) gel and the cationic surfactant  $C_n$ TAB behaves in a completely analogous fashion.

Figure 7 shows SAXS curves for the P(MAA/NIPAM) gel- $C_n$ TAB complexes at a fixed charge density of 67% and as a function of the hydrophobic surfactant chain length in the range of 12–18 carbon atoms. Indeed, all the three interesting morphologies, Pm3n, FCC, and HCPS, which were observed at fixed hydrophobic chain length as a function of the charge density are now observed at constant charge density as a function of the hydrophobic chain length, emphasizing the previously noted symmetry between electrostatic and hydrophobic interactions.

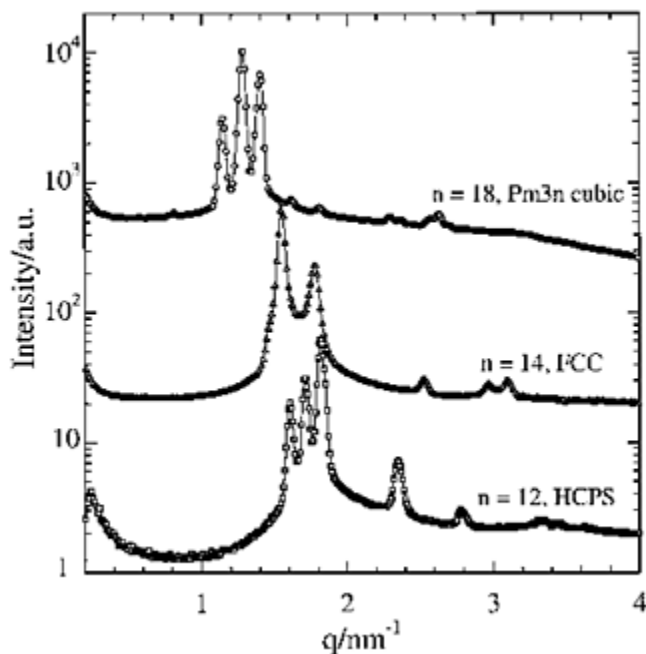


**FIG. 7** Surfactant tail length-induced structural transitions in the 67% charged P(MAA/NIPAM) gel- $C_n$ TAB complexes with  $n$  being decreased from  $n=18$  to 12.

### C. Cross Linker Density Effect

In a previous section we have seen that the system P(MAA/NIPAM) gel- $C_n$ TAB for fully charged polyelectrolyte forms a well-ordered and highly symmetrical Pm3n cubic structure. Let us now consider the related system of a PMAA gel complexed with a  $C_{12}$ TAB surfactant and study it at various concentrations of added  $N,N'$ -methylenebisacrylamide (BIS) which acts as a cross linker for the radical polymerization.

Figure 8 shows SAXS curves for this system for cross-linker densities between 0 and 7%. In the absence of a cross-linker, the highly ordered Pm3n structure continuously degrades as the cross-linker density is increased. Interestingly enough, the characteristic peak triplet typical for the Pm3n morphology is still recognizable in terms of broad peaks at 4% and merely as shoulders at 7% cross-linker density, respectively. Thus, although the long-range coherence of this macro-lattice is lost quickly for high cross-linker concentrations, the overall structure still appears to be of the Pm3n type.

Apparently, the increase in cross-linking in the polyelectrolyte gel reduces the mesh size, so that the surfactant tails can no longer arrange in a highly ordered fashion owing to the space hindrance. However, all other parameters being unchanged, the system still assumes the same morphology, albeit in a less ordered macrolattice.

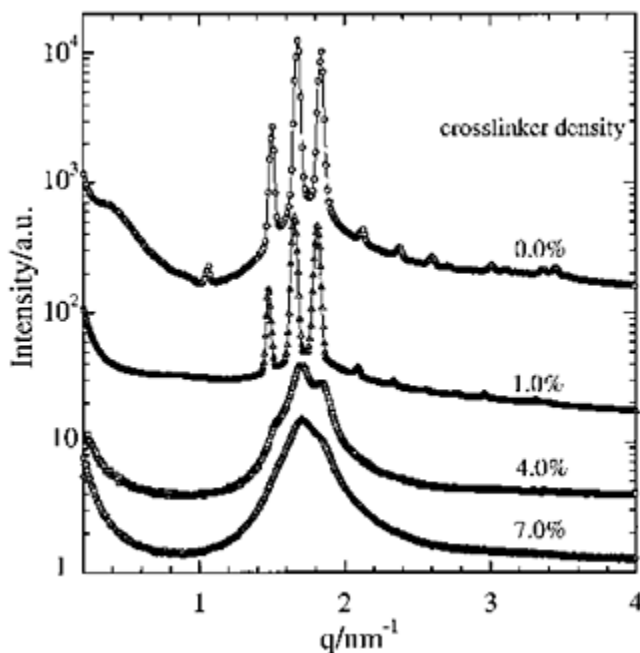


**FIG. 8** Cross linker density effect of fully charged PMAA gel on the structures of PMAA-C<sub>12</sub>TAB complexes.

#### **D. Structures of Polyelectrolyte-Surfactant Complexes (PSCs) in the Dried State**

In this section, we investigate what happens to the highly ordered wet polyelectrolyte gel/surfactant complexes when they are dried and when they are subsequently swollen with water again. Figure 9 shows the SAXS curves of the system PMAA gel-C12 TAB at a water-equilibrated, at a freeze-dried, and at a reswollen state reached from the dry product, respectively. Two interesting observations can be made. Upon drying the original highly symmetrical Pm3n structure collapsed to form a mere HCPC system and, considerably more amazing, upon reswelling with water, the original Pm3n morphology was restored with roughly the same high degree of order it had before drying. This strongly suggests that the occurrence of the Pm3n morphology in this system does not simply occur as a result of being kinetically trapped in some fancy but metastable state but that this complicated cubic structure truly is the thermodynamically stable form for this system.

Although the SAXS curve for the dried state of the system PMAA-C<sub>10</sub>TAB in Figure 9 also shows a hexagonal cylinder packing, the system PMAA-C<sub>14</sub>TAB, as shown in Figure 10, behaves in a somewhat more complicated manner.

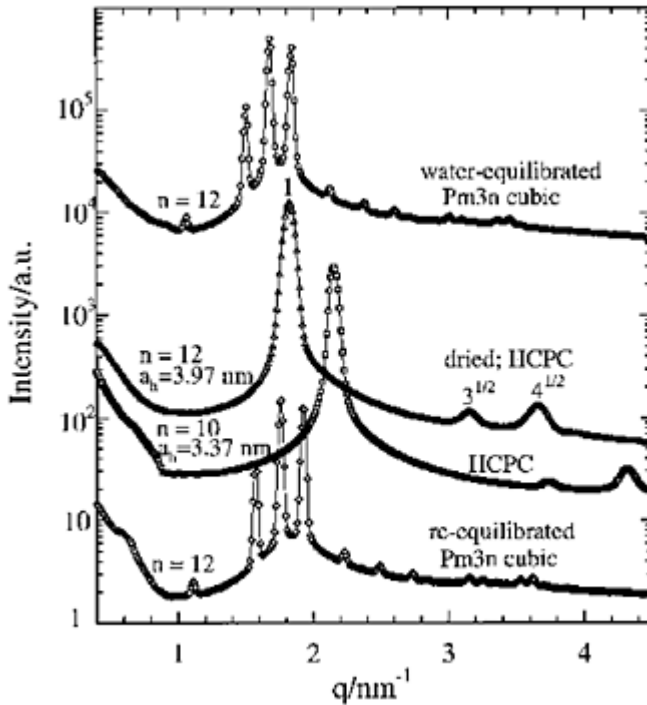


**FIG. 9** SAXS profiles of linear PMAA- $C_{12}$ TAB complexes at water-equilibrated, freeze-dried ( $n=10$  and  $12$ ), and reswollen equilibrium states, respectively.

Corresponding to the previous cases, upon drying, a highly ordered Pm3n system collapsed to a two-dimensional packing of cylinders. Reswelling the dried product completely reconstituted the original Pm3n structure with full long-range order, but in this case the cylinder packing found in the dried state was not hexagonal.

The corresponding scattering curve plotted in Figure 10 shows considerably more peaks at nontrivial position ratios than the simple  $1:3^{1/2}:2:7^{1/2}$  occurring for HCPCs as shown in Figure 9. However, the present scattering curve is closely related to the HCPC curve and can be constructed from the latter by a slight distortion of the hexagonal symmetry. This scattering curve is best described in terms of a two-dimensional unit cell with two equal edges and an enclosed angle which is larger than the hexagonal 120 degrees. This symmetrical distortion causes the first hexagonal peak with a multiplicity of 6 to split up into two distinct peaks, one occurring at lower  $q$  with a multiplicity of 2 and one at higher  $q$  with a multiplicity of 4, implying that the characteristic feature in the SAXS pattern of such a system is that the second peak has roughly twice the intensity of the first peak and appears at an arbitrary position ratio depending on the unit cell angle. It should be noted that this model has only two free parameters, one unit cell edge and the angle. Thus, if all the experimentally observed higher order peaks correspond well to the



calculated ones, the structure can be considered as being identified with high confidence. Inspection of Figure 10 indicates that this is the case, apart from one spurious peak which does not belong to this two-dimensional nonhexagonal packing. It is natural to assume that, for this distorted cylinder packing, the cylinder cross-sections are no longer perfectly circular but will increasingly deform with increasing deviation of the angle from 120 degrees, as shown in the inset of Figure 10.

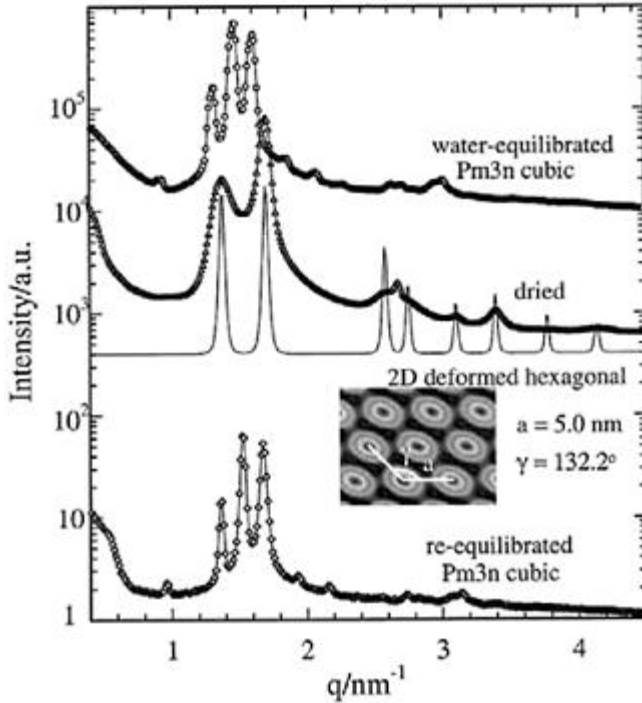


**FIG. 10** SAXS profiles of linear PMAA- $C_{14}$ TAB complex at water-equilibrated, freeze-dried, and reswollen equilibrium states, respectively. The inset shows a structural model of 2D distorted hexagonal packing of deformed cylinders for the dried PMAA- $C_{14}$ TAB complex.

#### IV. SUMMARY

Polyelectrolyte-surfactant complexes and polyelectrolyte gel-surfactant complexes spontaneously form highly ordered macrolattices with various different morphologies, which are ideally suited for the investigation by small-angle x-ray scattering. The PSC morphologies discussed during the present study were lamellar, hexagonally close-packed cylinders, Pm3n cubic, face-centered cubic packed spheres, hexagonally close-packed spheres, two-dimensional non-hexagonally packed cylinders, and poorly ordered

systems lacking three-dimensional long-range order and sharp peaks in the scattering pattern.

We have seen how structural phase transitions from one ordered morphology to another (order-order-transitions) or to a poorly ordered system (order-disorder-transitions) could be induced by various effects, including the fine tuning of the electrostatic interactions by changing the polyelectrolyte charge density, the fine tuning of the hydrophobic interactions by changing the surfactant aliphatic tail length or both, independent of whether backbone and surfactants are cationic or anionic, respectively, or vice versa.

Fine tuning the polyelectrolyte gel mesh size by cross-linking did not induce a phase transition but gradually decreased the degree of long-range order in the observed cubic macrolattice.

The highly ordered cubic networks found in aqueous solution of some polyelectrolyte gel-surfactant complexes could be collapsed upon drying to simple cylinder packings. Redissolution of the collapsed material reversibly reconstituted the highly symmetrical cubic morphology with the same degree of long-range order as before drying; suggesting that these are truly thermodynamically stable states of these systems.

Further work will be necessary to understand completely the mechanisms controlling the structural behavior of PSCs and to make more practical use of these beautiful systems.

## ACKNOWLEDGMENTS

B.C. gratefully acknowledges the support of this research by the National Science Foundation (Polymers Program DMR9984102) and the U.S. Department of Energy (DEFG 0299ER45760). C.B. gratefully acknowledges support of this work by the Alexander von Humboldt Foundation as a Feodor-Lynen Fellow.

## REFERENCES

1. SQ Zhou, B Chu. *Adv Mater* 12:545–556, 2000.
2. B Lindman, K Thalberg. In: ED Goddard, KP Ananthapadmanabham, ed. *Interactions of Surfactants with Polymers and Proteins*. CRC Press, Boca Raton, FL, 1993.
3. W Davydoff, KJ Linow, B Philipp. *Acta Polym* 38:509, 1987.
4. M Antonietti, A Thünemann. *Curr Opin Colloid Interface Sc* 1:667, 1996.
5. M Antonietti, C Burger, J Conrad, A Kaul. *Macromol Symp*. 106:1, 1996.
6. CK Ober, G Wegner. *Adv Mater* 17:9, 1997.
7. M Antonietti, C Burger, A Thünemann, *Trends Polym Sci* 5:262, 1997.
8. WJ Macknight, EA Ponomarenko, DA Tirell. *Ace Chem Res* 31:781, 1998.
9. I Iliopoulos. *Curr Opin Colloid Interface Sci* 3:493, 1998.
10. K.Thalberg, B Lindman. In: KL Mittal, D Shah, ed. *Surfactants in Solution*. Vol. 11. Plenum Press, New York 1991.
11. A.Herslof, LO Sundelof, B Porsch, LValtcheva, S Hjerten. *Langmuir* 12:4628, 1996.
12. T Arnebrant, MC Wahlgren. *Proteins Interfaces II* 602:239, 1995.

13. D Muller, M Malmsten, B Bergenstahl, J Hessing, J Olijve, F Mori. *Imaging Sci J* 45:229, 1997.
14. AN Semenov, IA Nyrkova, AR Khokhlov. *Macromolecules* 28:7491, 1995.
15. AN Semenov, IA Nyrkova, AR Khokhlov. In: S Schick, ed. *Ionomers: Characterization, Theory, and Applications*. CRC Press, Boca Raton, FL, 1996, p. 251.
16. JP Behr. *Bioconjugate Chem* 5:382, 1994.
17. X Gao, L Huang. *Gene Ther* 2:710, 1995.
18. RJ Lee, L Huang. *Crit Rev Ther Drug Carrier Syst* 14:173, 1997.
19. J Monkkonen, A Urtii. *Adv Drug Delivery Rev* 34:37, 1998.
20. N Zhu, D Liggitt, Y Liu, R Debs. *Science* 261:209, 1993.
21. JO Radler, I Koltover, T Salditt, CR Safinya. *Science* 275:810, 1997.
22. I Koltover, T Salditt, JO Radler, CR Safinya. *Science* 281:78, 1998.
23. S May, A Ben-Shaul. *Biophys J* 73:2427, 1997.
24. D Harris, S May, WM Gelbart, A Ben-Shaul. *Biophys J* 75:159, 1998.
25. L Golubonic, M Gloubovic. *Phys Rev Lett* 80:4341, 1998.
26. CS O'Hern, TC Lubensky. *Phys Rev Lett* 80:4345, 1998.
27. N Dan. *Biophys Biochim Acta* 1369:34, 1998.
28. S Bhattacharya, SS Mandal. *Biochemistry* 37:7764, 1998.
29. SQ Zhou, C Burger, FJ Yeh, B Chu. *Macromolecules* 31:8157–8163, 1998.
30. SQ Zhou, FJ Yeh, C Burger, B Chu. *J Phys Chem B* 103:2107–2112.
31. SQ Zhou, FJ Yeh, C Burger, B Chu. *J Polym Sci, Polym Phys Ed* 37:2165, 2000.

## 10

# Structural and Dynamic Behavior of Polymer Gels as Elucidated by Nuclear Magnetic Resonance Spectroscopy

**ISAO ANDO and SHIGEKI KUROKI** *Tokyo Institute of Technology, Tokyo, Japan*

**MASATOSHI KOBAYASHI** *National Institute of Agrobiological Sciences, Ibaraki, Japan*

**CHENHUA ZHAO** *Tokyo University of Agriculture and Technology, Tokyo, Japan*

**SHINGO MATSUKAWA** *Tokyo University of Fisheries, Tokyo, Japan*

## I. INTRODUCTION

Polymer gels have attracted considerable attention from the point of view of various physical and chemical properties [1, 2]. For example, hydroelectrolyte gels show a dramatic change in volume in response to change in solvent composition, pH, ionic strength, and temperature. They contract upon application of an electric field. Further, water-swollen polymer gels can convert chemical energy into mechanical energy. These lead to the vitality of polymer research and the development of a diversity of interests on polymer gel systems. In order to develop new polymer materials, polymer gel design has been performed on the basis of advanced polymer science and technology. The properties of polymer gels are closely related to their structures and dynamics. From such situations, the establishment of methods from determining the structures and dynamics is very important for making reliable polymer gel design and developing new advanced polymer gels.

From such a background, the structure and dynamics of polymer gels by a solid-state nuclear magnetic resonance (NMR) method, diffusion process of polymer gels by a pulse-field-gradient spin-echo NMR method, and spatial information response of hydropolymer gels under stimulus by a  $^1\text{H}$  NMR imaging method have been widely elucidated [3–6]. Details of these research works will be described in this chapter.

## II. MICROSCOPIC STRUCTURE AND DYNAMICS OF POLYMER GELS

Polymer gels sometimes consist of mobile and immobile regions. For this, conventional solution NMR gives useful information on a mobile region but sometimes not on an

immobile region. For example, if one wants to obtain structural information on an immobile region, we need to use a solid-state NMR method. Then, in order to elucidate the structure and dynamics of the immobile and mobile regions in polymer gels, we must use some appropriate NMR methods or we must design special methods.

The chemical shift value ( $\delta$ ), spin-lattice relaxation time ( $T_1$ ), spin-spin relaxation time ( $T_2$ ), and self-diffusion coefficient (ID) as obtained by an appropriate NMR method give information about the microscopic structure and dynamics of some components in polymer gel such as the network polymer, solvent, metal ions, and molecules. From the chemical shift, useful information about the chemical structure, conformation, formation of hydrogen bonds, association and dissociation of functional groups, and so on can be obtained. From the relaxation times  $T_1$  and  $T_2$ , the correlation time ( $\tau_c$ ) in molecular motion can be estimated by using the Bloembergen-Purcell-Pound (BPP) theory [7] when relaxation mechanisms are predominantly affected by dipole-dipole interaction. In this section, some studies of the microscopic structure of some polymer gels by  $^1\text{H}$  pulse NMR method and the high-resolution solid-state  $^{13}\text{C}$  NMR method are reviewed.

### A. Approaches by $^1\text{H}$ Pulse NMR Method

In the pulse NMR experiment, high-power radio frequency (rf) pulses are applied to a sample for rotating the equilibrium longitudinal magnetization, and subsequently, the free induction decay (FID) of the transverse  $T_2$  component is detected as a time-dependent function which becomes a measure of the mobility. The Fourier transform converts FID into the corresponding frequency spectrum, in which the chemical shift gives information about chemical structures. On the other hand, the FID contains information about molecular dynamics, and so the experiment with some rf pulses gives  $T_1$ ,  $T_2$ , and diffusion coefficient ( $D$ ) [3]. The  $T_1$  and  $T_2$  are closely related with the correlation time in molecular motion by BPP theory [7], described above, when they are governed by dipolar interactions, and the  $D$  as obtained by pulse NMR method under field gradient provides information about the translational motion. Therefore, pulse NMR method is a very useful method for the elucidation of molecular dynamics in polymer systems.

#### 1. Gelation of Poly(*N*-Isopropylacrylamide) Aqueous Solution

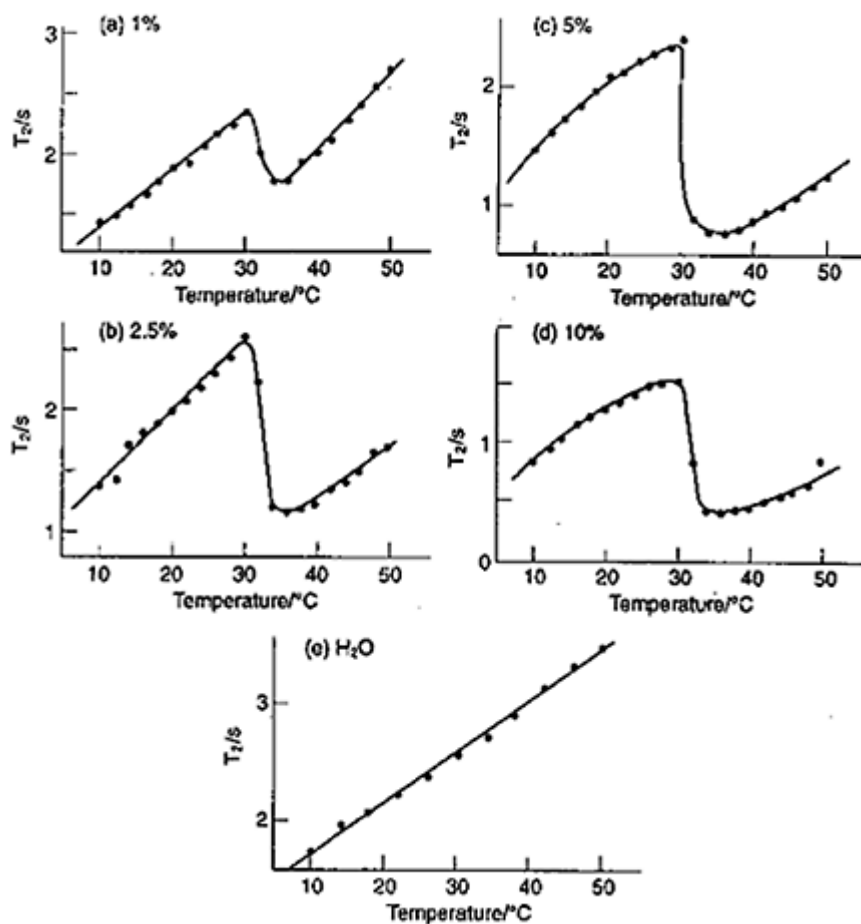
Poly(*N*-isopropylacrylamide) (PNIPAM) in water undergoes a phase transition from sol to gel at around 32°C [8].  $^1\text{H}$  pulse NMR experiments provide useful information about molecular motion of the polymer and solvent in the solution and gel state. The abrupt change in molecular motion for solvent in the gel is caused by the formation of gel structure at the phase transition temperature and, therefore, the change of relaxation times sensitively reflects the change of states.

Figure 1 shows the plots of the  $^1\text{H}$   $T_2$  values for water in 1.0, 2.5, 5.0, and 10.0 wt/v% PNIPAM/water solutions and for neat water against temperature [9]. The  $^1\text{H}$   $T_2$  value increases as the temperature is increased up to 30°C, where an increase in  $T_2$  means an increase in molecular motion according to BPP theory. The  $^1\text{H}$   $T_2$  value of neat water increases linearly with temperature up to 50°C. At the gelation temperature (about 32°C), the  $^1\text{H}$   $T_2$  value in all of the polymer solutions transitionally decreases. As temperature is

further increased, the  $T_2$  value increases again. The mobility of water increases with increasing temperature up to 30°C and then decreases transitionally at about 32°C owing to the gelation of the system and increases again with a further increase of temperature. This trend is very different from that of neat water. Furthermore, Figure 1 shows that the increase in the polymer concentration leads to a decrease in  $^1\text{H } T_2$  for water. The molecular motion of water is restricted by an increase in intermolecular interactions between the polymer chains and water. As the polymer concentration increases up to 5% at the gelation temperature, the magnitude of the decrease for  $^1\text{H } T_2$  value is larger. As the concentration increases further up to 10% wt/v, the magnitude of the decrease for the  $^1\text{H } T_2$  decreases.

The plot of the  $^1\text{H } T_1$  value of water molecules in 5 wt/v% PNIPAM/water solution as a function of temperature is shown in Figure 2. The  $^1\text{H } T_1$  value slowly increases as the temperature is increased. At the gelation temperature, the  $T_1$  value transitionally decreases. As the temperature is further increased, the  $^1\text{H } T_1$  value slowly increases. This behavior is very similar to that for  $T_2$ . As seen from the observed  $^1\text{H } T_1$  and  $T_2$  behaviors, the water molecules are in the fast-motion region ( $\omega\tau_c \ll 1$ , where  $\omega$  is the resonance frequency). At 1.0, 2.5, and 10.0 wt/v% solutions, similar results were obtained. Therefore, the  $^1\text{H } T_1$  and  $T_2$  values for water in the PNIPAM/water system are very sensitive to the phase transition and provide dynamic information.

In PNIPAM/deuterated water solution, the  $^1\text{H } T_2$  signal is composed mainly of two components, a long  $T_2$  component corresponding to the polymer side chains and extremely short  $T_2$  component corresponding to the polymer main chain, as shown in Figure 3. The plot of the  $T_2$  value for the main chain and side chains of PNIPAM in 10 wt/v% PNIPAM/deuterated water solution against temperature is shown in Figure 4. For the main chain, at temperatures from 10 to 30°C, the  $T_2$  value is almost constant, but at the gelation temperature (32°C), it decreases transitionally, and at temperatures of 40–50°C, it returns to constant. This indicates that at the gelation temperature, the molecular motion of the main chain is greatly restricted. On the other hand, for the side chains, at temperatures from 10 to 30°C, the  $T_2$  value remains almost constant, increases transitionally at the gelation temperature, and at temperatures from 40 to 50°C, it becomes a



**FIG. 1** Temperature dependence of  $^1\text{H}$   $T_2$  for water in PNIPAM/water solution with the concentration of (a) 1, (b) 2.5, (c) 5, (d) 10 wt/v%, and (e) neat water.

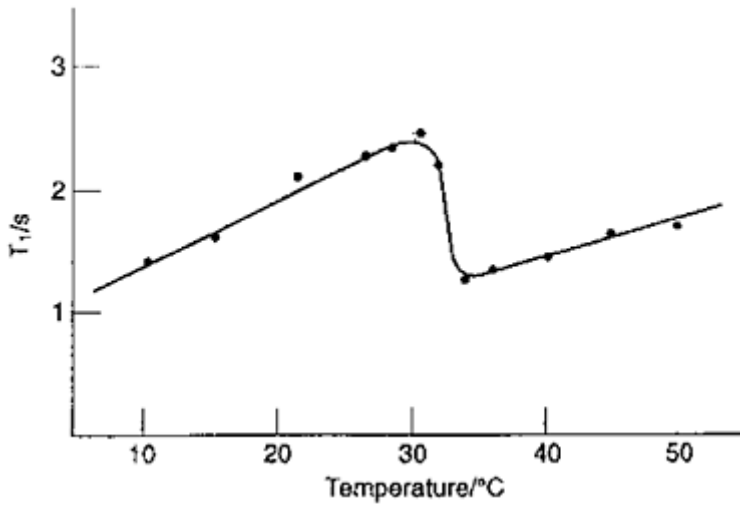


**FIG. 2** Temperature dependence of  $^1\text{H } T_1$  for water in 5 wt/v% PNIPAM/water solution.

constant again. This is evidence that the molecular motion of side chains increases transitionally at the gelation temperature.

By evaporating water slowly from PNIPAM aqueous solution, a PNIPAM gel is obtained. The  $^1\text{H } T_2$  behavior of water for this gel is very similar to that for PNIPAM aqueous solution. This shows that temperature changes of structure and

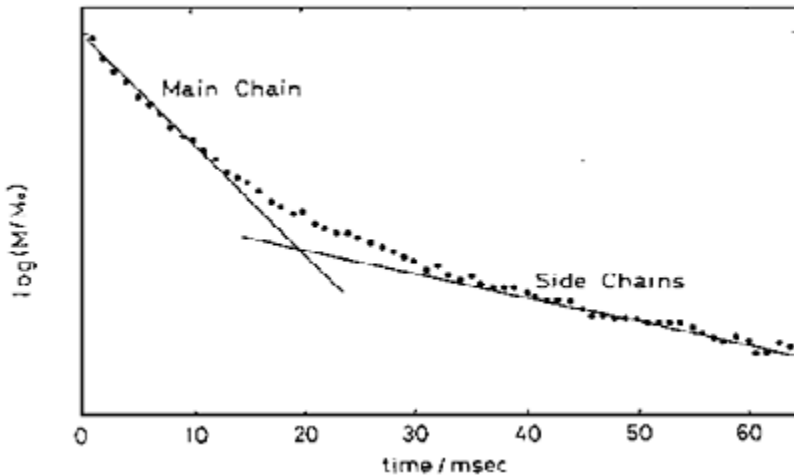


**FIG. 3**  $T_2$  signal from 10 wt/v% PNIPAM/deuterated water solution.



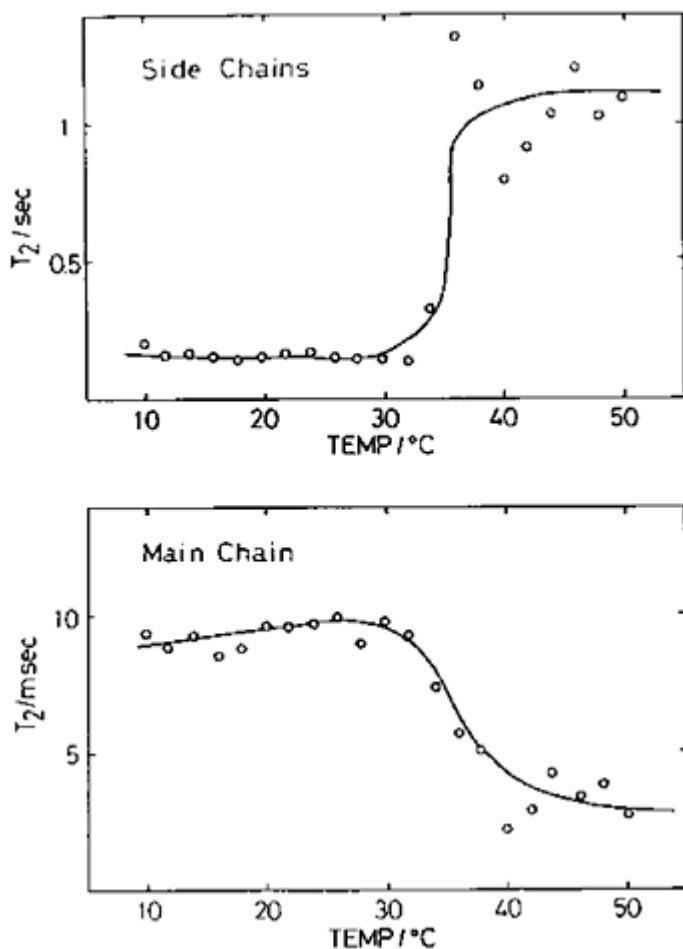


FIG. 4 Temperature dependence of  $T_2$  for the PNIPAM side chains and main chain in 10 wt/v% PNIPAM/deuterated water solution.

dynamics for both of these systems through 32°C are very similar to each other [10].

## 2. Poly(Vinyl Alcohol) Gel

A typical  $^1\text{H}$  spin-echo signal of PVA gel is shown in Figure 5 [30]. This signal curve is composed of three components such as a long  $T_2$  component corresponding to the mobile region (C), a short  $T_2$  component corresponding to the immobile region (A), and an intermediate  $T_2$  component corresponding to the interfacial region (B) which exists between the mobile and immobile regions. It can be said that the mobile region (C) comes from the noncross-linked region, the immobile region (A) comes from the cross-linked region, and the interfacial (B) comes from the vicinity of the cross-linked region in

the gel. With an increase

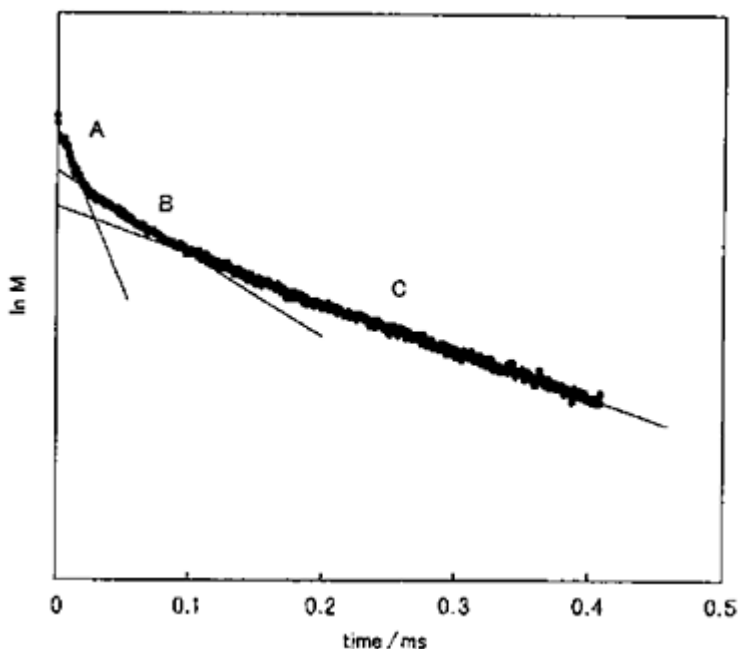


**FIG.5**  $^1\text{H}$   $T_2$  signal of PVA gel at the PVA concentration of 27.4% w/w by the solid echo method.

in the polymer concentration,  $^1\text{H}$   $T_2$  of three regions is slowly decreased. This means that the molecular motion is restrained as the polymer concentration is increased. Figure 6 shows the fractions of the corresponding three regions as a function of polymer concentration. The fractions of the mobile and immobile regions are largely decreased and increased with an increase in the polymer concentration, respectively. The fraction of the intermediate region over a wide range of polymer concentrations is very small.

## B. Approaches by High-Resolution Solid-State $^{13}\text{C}$ NMR Method

### 1. Poly(Vinyl Alcohol) Gel

Poly(vinyl alcohol) (PVA) gel prepared by repeating freeze-thaw cycles from its aqueous solution is one of the physical gels. At the beginning of the gelation of a PVA aqueous solution, the phase separation into polymer-rich and polymer-poor regions occurs with a decrease in temperature [11]. It is suggested that the gel formation is due to the formation of an intermolecular hydrogen bond [12]. The structure and the amount of hydrogen bonds may play an important role in the properties of a PVA gel, and the high-resolution solid-state  $^{13}\text{C}$  NMR method gives useful information about them. Figure 7 shows  $^{13}\text{C}$  NMR spectra for PVA

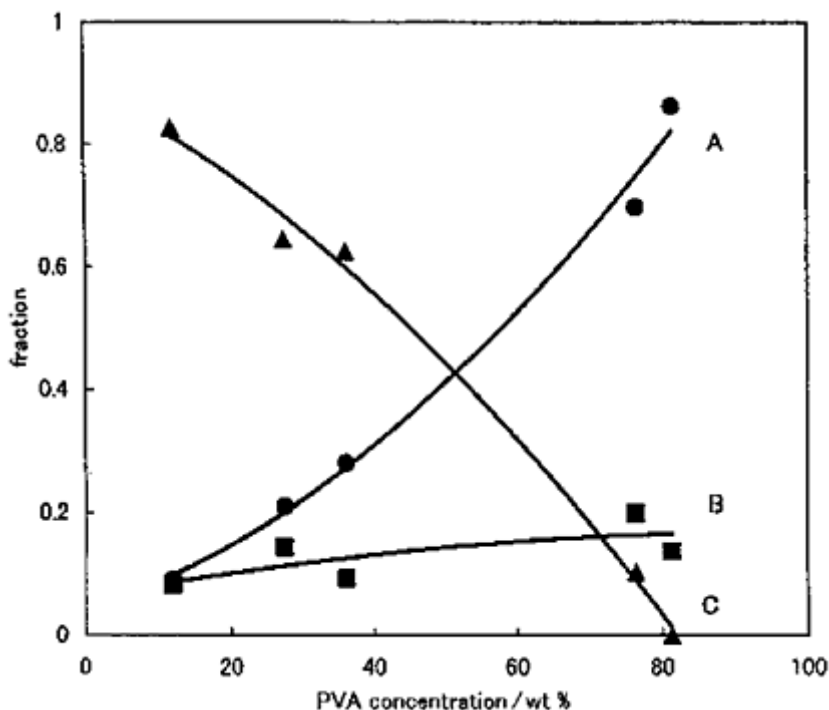


**FIG. 6** The relationship between the fraction of three regions with different molecular motion in PVA chains in the gel and the polymer concentration. ●, region (A) (immobile); ■, region (B) (interfacial); ▲, region (C) (mobile).

in the solution (a), gel (b–d), and solid (e) states as measured by solution and solid-state NMR methods [13]. In conventional solution  $^{13}\text{C}$  NMR spectrum for PVA gel shown in Figure 7(b), the  $^{13}\text{C}$  signal for the CH carbon splits into three peaks assigned to *mm*, *mr*, and *rr* triads from downfield are observed. The signals for the CH and  $\text{CH}_2$  carbons become broader as compared with those for PVA solution (Fig. 7a). This is caused by the increase in dipole-dipole interactions due to a decrease in molecular motion. The  $^{13}\text{C}$  (pulse saturation transfer/magic angle spinning) (PST/MAS) NMR spectrum of the PVA gel shown in Figure 7c is similar to the solution NMR spectrum of Figure 7b. However, the resolution of spectrum (Fig. 7c) is better than that of spectrum (Fig. 7b), because of a MAS and a high-power proton decoupling. The nuclear Overhauser effect (NOE) enhancement is used to obtain more intense  $^{13}\text{C}$  signal in the PST method. The PST method effectively enhances peak intensity for the mobile regions in samples as compared with the cross-polarization (CP) method. This means that the mobile region in the PVA gel is observed in both of the spectra (Fig. 7a, b). The CP method effectively enhances peak intensity for more rigid regions in samples as compared with the PST method. The  $^{13}\text{C}$  signal for the CH carbon of the solid PVA has three-split broad peaks in the  $^{13}\text{C}$  CP/MAS NMR spectrum, as shown in

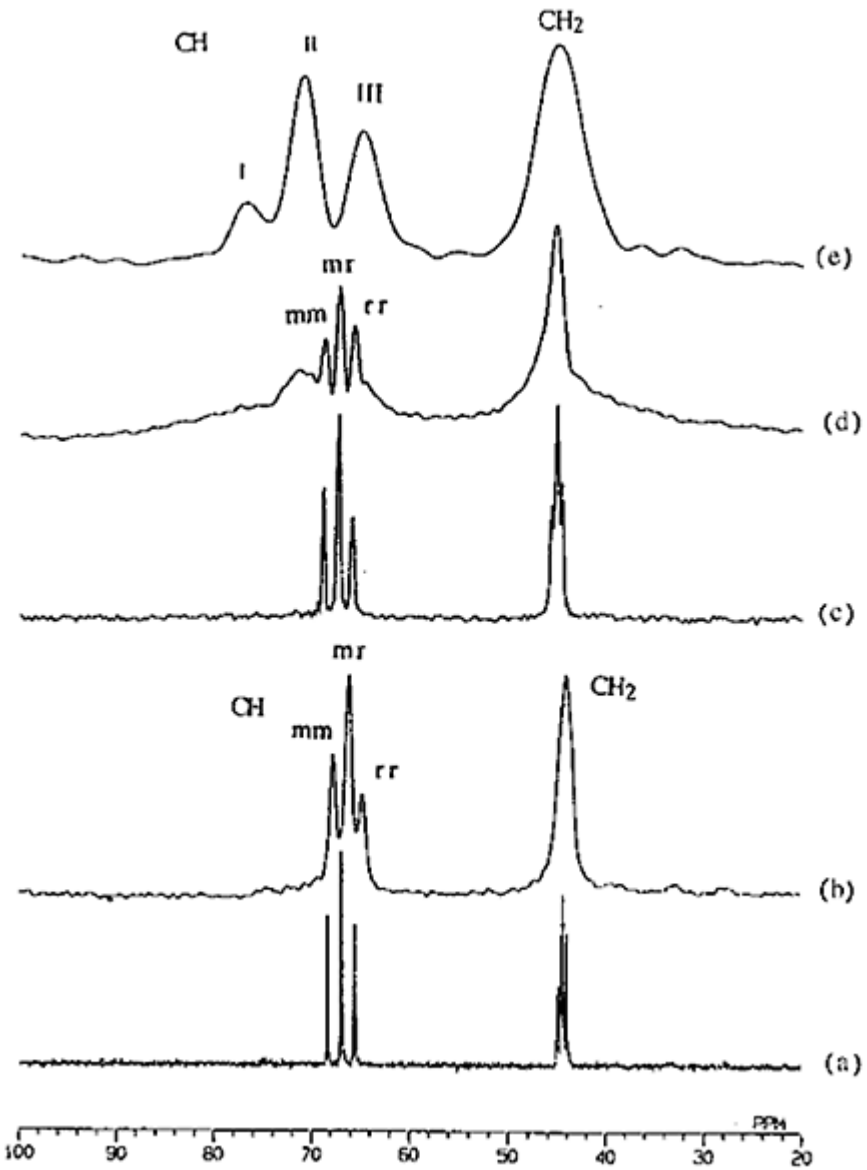


**FIG. 7**  $^{13}\text{C}$  NMR spectra for the PVA in the solution, gel, and solid states as measured by solution and solid-state NMR methods. For solution NMR method: PVA/ $\text{D}_2\text{O}$  solution (a) and PVA gel (b); for solid-state NMR method: PVA gel by PST/MAS (c) and CP/MAS (d), and solid PVA by CP/MAS (e).

Figure 7e. Such a splitting is explained by the number of intramolecular hydrogen bonds

formed among neighboring hydroxyl groups [14]. Assuming that the  $^{13}\text{C}$  chemical shift value for the CH carbon shifts to downfield by 6 ppm per one intermolecular or intramolecular hydrogen bond, the most deshielded peak (peak I) can be assigned to the CH carbon with two hydrogen bonds, the central peak (peak II) to the CH carbon with one hydrogen bond, and the most shielded peak (peak III) to the CH carbon with no hydrogen bonds, respectively. In the  $^{13}\text{C}$  CP/MAS spectrum for the PVA gel as shown in Figure 7d, the CH signal is composed of the three splitting peaks corresponding to the triad tacticity and the broad peaks as found in the solid PVA. This means that both of the immobile and mobile regions of the PVA gel are observed by the CP/MAS method.

Figure 8 shows the  $^{13}\text{C}$  CP/MAS NMR spectra of the PVA gels with different polymer concentrations [13]. The polymer concentrations of samples a–d are 9.1, 11.8, 13.8, and 35.0% (wt/wt), respectively. The intensities of the three-split peaks due to stereochemical configurations decrease and those of peaks I, II, and III increase with a decrease in the water fraction in the gel. The three peaks due to stereochemical configurations completely disappear in sample d. The proposed schematic cross-linked structure of a PVA gel formed by intermolecular and intramolecular hydrogen bonds is shown in Figure 9. The increase in the fraction of the immobile region and the formation of hydrogen bonds are promoted by the increase in the polymer concentration of the gel.

In order to clarify the dynamics of a PVA gel,  $^{13}\text{C}$   $T_1$  measurements were carried out [15]. The  $^{13}\text{C}$   $T_1$  values for the mobile region in a PVA gel were determined by the inversion-recovery method combined with the PST/MAS technique, and the immobile region was also determined by the CP/MAS technique combined with the Torchia's pulse sequence [16]. The  $^{13}\text{C}$   $T_1$  values are summarized in Table 1. The  $T_1$  values for the triads are smaller than those for peaks II and III. The immobile region corresponds to the CH carbons in the cross-linked regions formed by intermolecular and intramolecular hydrogen bonds in the gel and the mobile ones to the regions away from the cross-linked regions which undergo fast molecular motion in the gel [13, 15]. The mobility of the network polymer in the PVA gel is restrained by hydrogen bonds and especially that of the cross-linked region is very low.

In order to elucidate the mechanism of the gelation process for PVA in aqueous solution, high-resolution solid-state  $^{13}\text{C}$  NMR spectra during the freeze-thaw cycles were obtained [17].  $^{13}\text{C}$  CP/MAS NMR spectra of a PVA/water system during the freeze-thaw cycles are shown in Figure 10. There are no signals in the  $^{13}\text{C}$  CP/MAS NMR spectrum of aqueous PVA solution at 40°C, because in the solution state the PVA chains are undergoing much faster molecular motion compared with a frequency of  $^1\text{H}$  decoupling to be approximately 60 kHz used in this experiment, and so the cross polarization efficiency is quite reduced. In the  $^{13}\text{C}$  CP/MAS NMR spectrum of the PVA/water system in the freezing state at

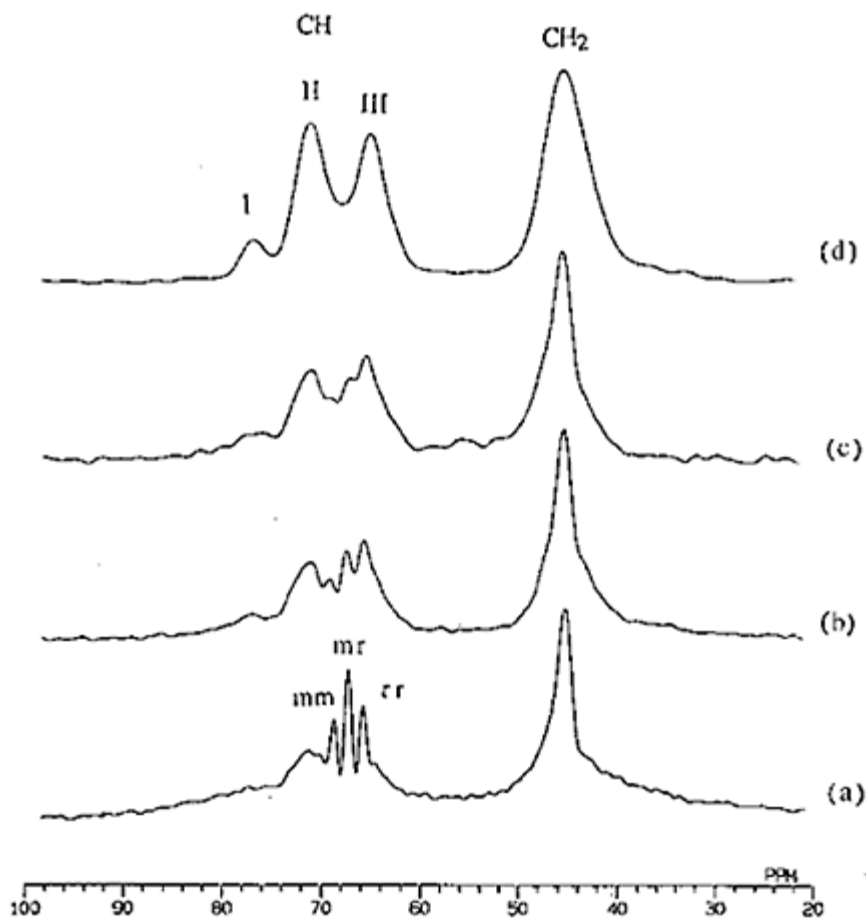


**FIG. 8**  $^{13}\text{C}$  CP/MAS NMR spectra for the PVA gels with different polymer concentrations. The polymer concentrations are 9.1 (a), 11.8 (b), 13.8 (c), and 35.0 (d) % (wt/wt), respectively.

$-30^\circ\text{C}$ , peaks I, II, and III for  $\text{CH}_2$  signal, which come from the formation of hydrogen, appear clearly. From this spectrum, it can be seen that some hydroxyl groups form hydrogen bonds at  $-30^\circ\text{C}$  as in the PVA gel. The temperature is increased from  $-30$  to  $40^\circ\text{C}$  again, peak II at 71 ppm becomes broad, and the three splitting peaks due to the triad configurations (*mm*, *mr*, and *rr*) appear. This shows that the molecular motion of PVA chains is much more decreased compared with that in the original solution state owing to the formation of hydrogen bonds, and so CP efficiency was enhanced. This means that the freezethaw process induces the gel formation. In the  $^{13}\text{C}$  CP/MAS NMR spectrum of the PVA/water system in the second frozen state, the three CH peaks are observed

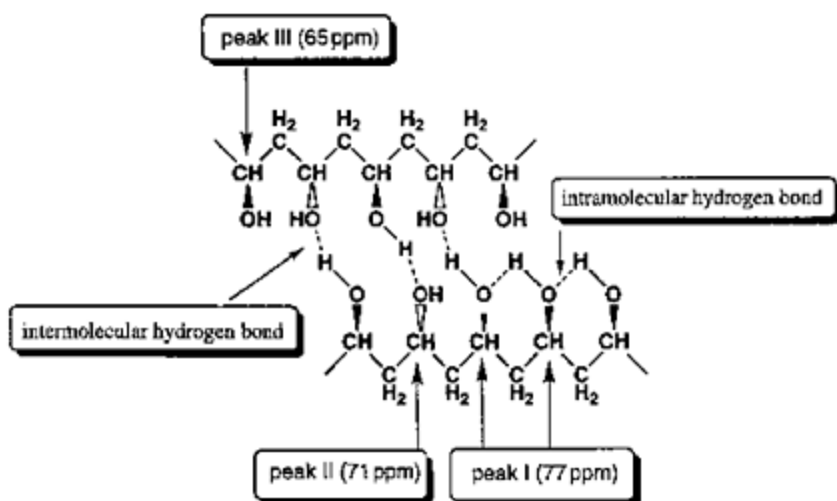


**FIG. 9** Schematic diagram for cross-linked structure of a PVA gel formed by intermolecular and intramolecular hydrogen bondings. The most deshielded peak (peak I) is assigned to the CH carbon with two hydrogen bonds, the central peak (peak II) to the CH carbon with one hydrogen bond, and the most shielded peak (peak III) to the CH carbon with no hydrogen bonds.

as clearly as was the case in first frozen state. The  $^{13}\text{C}$  CP/MAS NMR spectra in the third and fourth frozen states are almost the same as each other. On the other hand, in the  $^{13}\text{C}$  CP/MAS NMR spectrum of the PVA/water system in the thawing state at  $40^\circ\text{C}$ , the intensity of peak II is gradually increased with an increase in the number of freeze-thaw cycles. In the fourth thawing state, peak II clearly appeared. This shows that the amount of hydrogen bonds in the course of the formation of the PVA gel is increased by repeating the freeze-thaw cycles.

**TABLE 1** Determined  $^{13}\text{C}$   $T_1$  Values of PVA Gels

Method	$^{13}\text{C}$ $T_1$ (s)					
	CH					
	<i>mm</i>	<i>mr</i>	<i>rr</i>	II	III	$\text{CH}_2$
Torchia's pulse sequence (CP method)	0.64 <sup>a</sup>	0.25 <sup>a</sup>	0.27 <sup>a</sup>	7.8	7.6	5.2
Inversion-recovery pulse sequence (PST method)	0.37	0.28	0.32			0.16

<sup>a</sup>  $^{13}\text{C}$   $T_1$  values of CH (*mm*, *mr*, *rr*) obtained by Torchia's pulse sequence are not sufficiently accurate because of the poor signal/noise ratio.

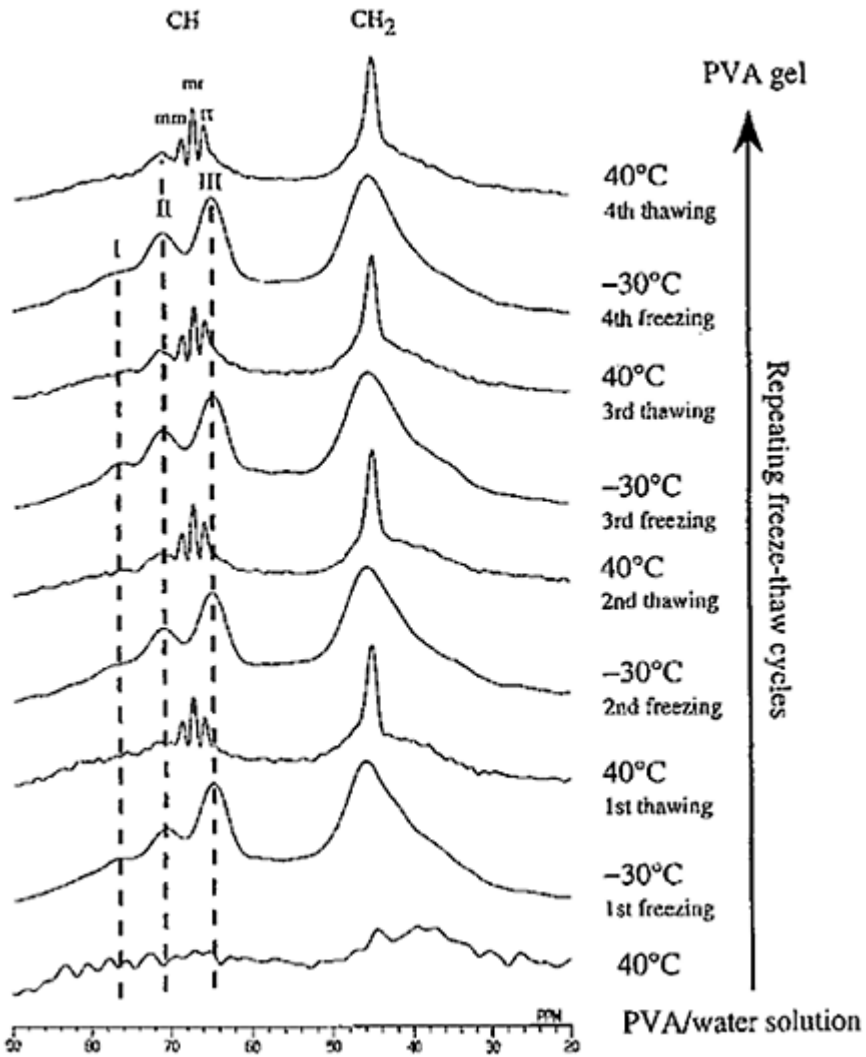


**FIG. 10**  $^{13}\text{C}$  CP/MAS NMR spectra for PVA/water system under the freeze-thaw cycles.

These experimental results mean that the repeating of freeze-thaw cycles induces the gelation of the PVA/water system.

## 2. Poly( $\gamma$ -Methyl L-Glutamate) Gel

The properties of the polymer gels swollen in organic solvents are different from those of hydroswollen gels. Cross-linked poly( $\gamma$ -methyl L-glutamate) (PMLG) is prepared by the ester-amide exchange reaction using diaminododecane as a cross linker and is swollen in



trifluoroacetic acid (TFA) and  $\text{CHCl}_3$ . The PMLG gel was studied by using high-resolution solid-state  $^{13}\text{C}$  NMR spectroscopy [18]. A typical  $^{13}\text{C}$  PST/MAS NMR spectrum of a PMLG gel swollen in  $\text{CHCl}_3$  is shown in Figure 11. The amide and ester carbonyl carbons of PMLG appear at 176.2 and 173.5 ppm, respectively. The  $\text{C}_\alpha$ ,  $\text{OCH}_3$ ,  $\text{C}_\gamma$ , and  $\text{C}_\beta$  carbons appear at 57.6, 52.3, 31.3, and 26.1 ppm, respectively. The peak intensity of the side chain carbons is more intense than that of the main chain carbons. This means that the side chains are undergoing faster molecular motion compared with the main chain.

The  $^{13}\text{C}$  chemical shifts of the individual carbons of a PMLG gel as a function of the TFA content ( $f_{\text{TFA}}$ ) in a mixture of  $\text{CHCl}_3$  and TFA in Figure 12. In the PMLG gel with  $\text{CHCl}_3$ , the  $^{13}\text{C}$  chemical shift values of the main chain amide  $\text{C}=\text{O}$  and  $\text{C}_\alpha$  carbons are 176.2 and 57.6 ppm, respectively. The PMLG chain part in the cross linked network takes the  $\alpha$ -helix conformation as determined by

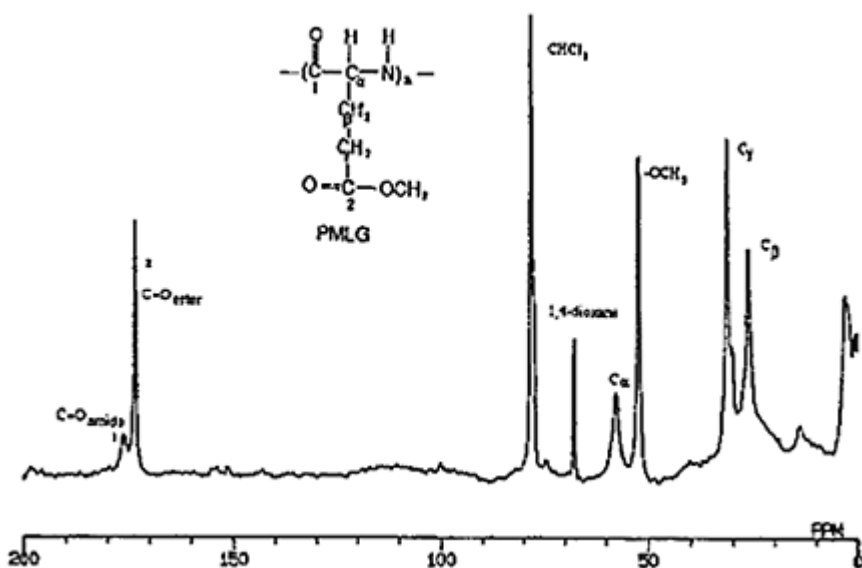


FIG. 11  $^{13}\text{C}$  PST/MAS NMR spectrum of PMLG gel swollen in  $\text{CHCl}_3$ .

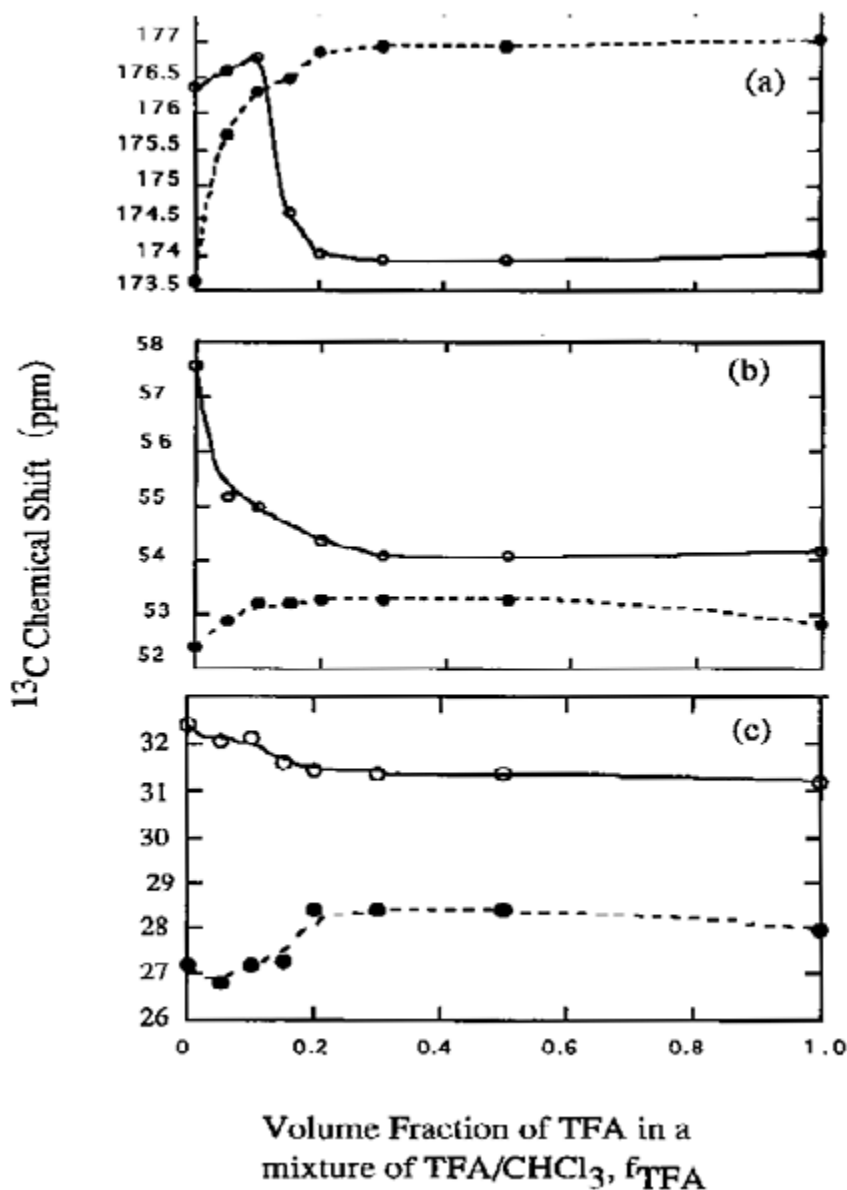


FIG. 12  $^{13}\text{C}$  chemical shifts for PMLG as a function of the TFA content in mixture of  $\text{CHCl}_3$  and TFA: (a) amide carbonyl carbon ( $\circ$ ) and ester carbonyl carbon ( $\bullet$ ); (b)  $\text{C}_\alpha$  ( $\circ$ ) and  $-\text{OCH}_3$  ( $\bullet$ ); and (c)  $\text{C}_\gamma$  ( $\circ$ ) and  $\text{C}_\beta$  ( $\bullet$ ).

reference data [19–21] of solid polypeptide at about 176 and 57 ppm. The amide  $\text{C}=\text{O}$  and  $\text{C}_\alpha$   $^{13}\text{C}$  chemical shifts change transitionally from 176.5 and 57.6 ppm to 174.0 and

54.4 ppm, respectively, and so move upfield with an increase in the TFA content. Such a transitional upfield shift shows that the main chain conformation of the PMLG network changes from the  $\alpha$ -helix to the random coil form. The midpoint of the transition is at about  $f_{TFA}=0.15$ . On the other hand, it is shown that in the side chain carbons the ester C=O carbon shifts downfield at the transition point, but the chemical shifts of the other carbons do not clearly change. The chemical shift of the main chain arises from the conformational change due to the formation of an intramolecular hydrogen bond between the C=O and N—H in the main chain. The main chain chemical shift is considered to be very sensitive to the helix-coil transition. The large shift difference of the ester carbonyl carbons is due to the interaction with TFA. The  $^{13}\text{C}$  chemical shifts of the other side chain carbons also show small change at  $f_{TFA}=0.15$ .

The degree of swelling for the PMLG gel changes by changes of  $f_{TFA}$  (see Fig. 30). The degree of swelling is transitionally decreased at 0–0.05 of  $f_{TFA}$ , it is constant at 0.05–0.2 of  $f_{TFA}$  and is gradually increased  $f_{TFA}>0.2$ . In the range of 0.05–0.2, the fraction of the random coil form is increased gradually with an increase in  $f_{TFA}$  and the degree of swelling is constant. Figure 13 shows the TFA content dependence of the  $^{13}\text{C}$   $T_1$  of amide C=O and ester C=O carbons at 20 and 40°C. As the temperature decreases from 40 to 20°C, the  $^{13}\text{C}$   $T_1$  for the amide O=O carbon increases and that of the ester C=O carbon decreases. The molecular motion of the amide C=O carbon is in the slow-motion region ( $\omega\tau_c \gg 1$ , where  $\omega$  is the resonance frequency) and that of the ester C=O carbon is in the fast motion region ( $\omega\tau_c \ll 1$ ) according to the BPP theory. The decrease in  $^{13}\text{C}$   $T_1$  of the ester C=O carbon in  $f_{TFA}$ , from 0 to 0.05 shows that the decrease in molecular motion of side chain caused by a rapid shrinkage of the gel. In the range of  $f_{TFA}=0.05$  to 0.20,  $^{13}\text{C}$   $T_1$  of the amide C=O carbon decreases with an increase in TFA content. This means that the molecular motion of main chains is increased in going from the  $\alpha$ -helix to the random coil in the constant degree of swelling. On the other hand, the molecular motion of the side chains is not so affected by the helix-coil transition.

### C. Approaches by Pulse Field-Gradient Spin-Echo $^1\text{H}$ NMR

#### 1. Pulse Field-Gradient Spin-Echo $^1\text{H}$ NMR Measurements

In order to determine the diffusion coefficient of solvent and probe molecules in a gel, the pulse field-gradient spin-echo (PFGSE) NMR method is used. This method is very powerful. However, if one wants to determine a small diffusion coefficient with high accuracy, a strong field gradient must be used. We have

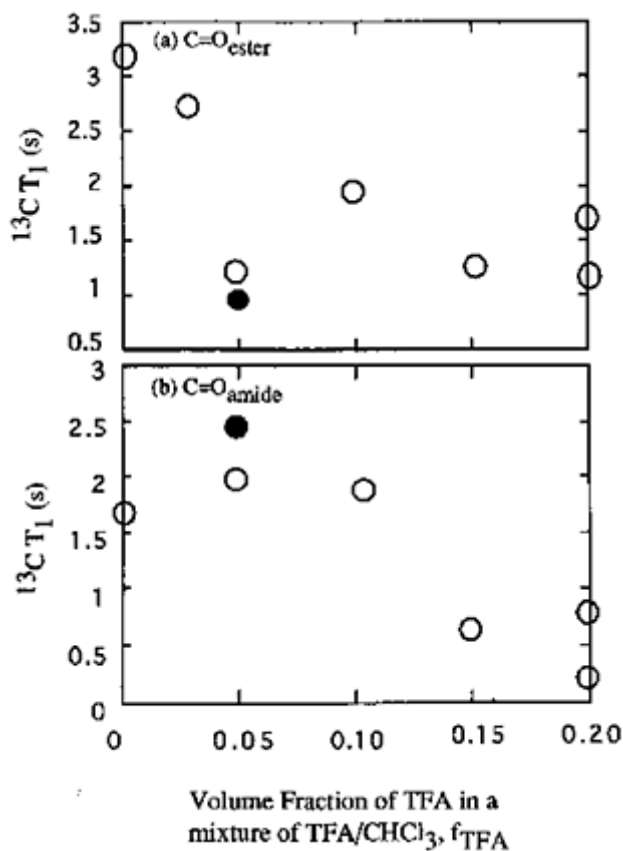


**FIG. 13**  $^{13}C T_1$  of the ester carbonyl (a) and amide carbonyl carbon (b) of PMLG gel as a function of the TFA content in a mixture of  $CHCl_3$  and TFA measured at 20°C (●) and 40°C (○). In the gel with  $f_{TFA}=20\%$ , two  $T_1$  components are observed.

designed two kinds of PFGSE NMR probe systems for generating the strength of the field gradient pulse of 780 and 2280 gauss/cm. This leads to determination of the diffusion coefficient with the order of  $10^{-10}$  cm<sup>2</sup>/s. As the PFGSE pulse sequence, two field gradient pulses are added to the ( $\pi/2$  pulse— $\tau$ — $\pi$  pulse) sequence, in which the first field gradient pulse is added at the mid position between the  $\pi/2$  and  $\pi$  pulses (i.e., at the position of  $\tau^*$  after the  $\pi/2$  pulse), and the second at the position of  $\tau^*$  after the  $\pi$  pulse (Fig. 14) [22–29]. This has been successfully used in our previous work on diffusional behavior in polymer gel systems [31].

The relationship between the echo signal intensity and pulse field gradient parameters is given by

$$\frac{A(\delta)}{A(0)} = \exp \left[ -\gamma^2 G^2 D \delta^2 \left( \frac{\Delta - \delta}{3} \right) \right] \quad (1)$$

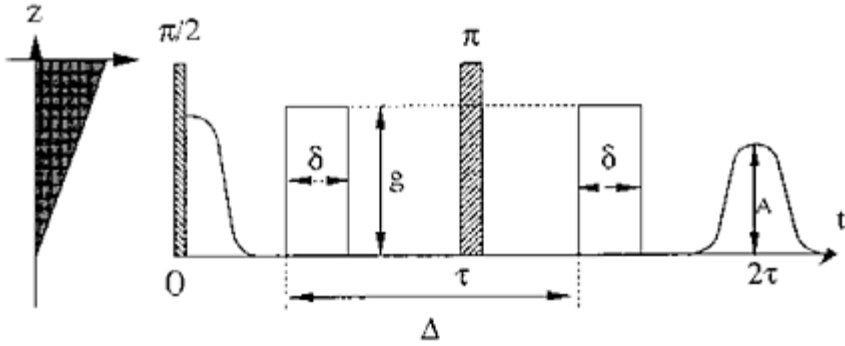


**FIG. 14** Pulse field gradient spin-echo (PGSE) sequence for measuring the diffusion coefficient  $D$ .

where  $A(\delta)$  and  $A(0)$  are echo signal intensities at  $t=2\tau$  with and without the magnetic field gradient pulse, respectively, whose length is  $\delta$ .  $\tau$  is the pulse interval,  $\gamma$  the gyromagnetic ratio of the proton ( $\gamma=2.675 \times 10^4 \text{ rad G}^{-1}\text{S}^{-1}$ ),  $G$  the field gradient strength,  $D$  the self-diffusion coefficient, and  $\Delta$  the gradient pulse interval. The echo signal intensity was measured as a function of  $\delta$ . The plot of  $\ln[A(\delta)/A(0)]$  against  $\gamma^2 G^2 \delta^2 (\Delta - \delta/3)$  gives a straight line with a slope of  $-D$ . Therefore, the  $D$  value can be determined from this slope. The  $\tau$ ,  $\Delta$ , and  $\delta$  values employed in these experiments were 10.0, 10.0, and 0.001–0.12 ms, respectively. The  $D$  value of  $2.5 \times 10^{-5} \text{ cm}^2/\text{s}$  for water at 303 K was used as the calibration of the field gradient strength. The experimental error for the  $D$  value is estimated to be less than approximately 5%.

## 2. Diffusional Behavior and $^1\text{H}$ PFGSE NMR Spectral Behavior

In the PFGSE  $^1\text{H}$  NMR experiments, echo signal intensity decays depending upon the displacement of the proton. For the proton in the molecule undergoing the random movement with a single-component diffusion, which follows Gaussian distribution, the echo signal attenuation is given by [26, 27]

$$\frac{A(\delta)}{A(0)} = \exp(-\gamma^2 G^2 \delta^2 D T_d) \quad (2)$$

where  $T_d$  is the diffusion time. For the random movement, the mean-square displacement in the  $z$  direction  $\langle z^2 \rangle$  after  $T_d$  is given by

$$\langle z^2 \rangle = 2DT_d \quad (3)$$

Therefore, substitution of Eq. (3) into Eq. (2) gives

$$\frac{A(\delta)}{A(0)} = \exp(-\gamma^2 G^2 \delta^2 \langle z^2 \rangle / 2) \quad (4)$$

In the PFGSE experiment with the gradient pulse interval,  $\Delta$ , taking into account the displacement during the time,  $\delta$ , the echo signal attenuation is given by Eq. (1). For the mixture of components with different diffusions which follow individual Gaussian distributions, the total echo attenuation is given by a superposition of the contributions from the individual components. The attenuation for the bimodal mixture is expressed by using Eq. (1) as

$$\frac{A(\delta)}{A(0)} = p_{1,2\tau} \exp\left[-\gamma^2 G^2 D_1 \delta^2 \left(\frac{\Delta - \delta}{3}\right)\right] + p_{2,2\tau} \exp\left[-\gamma^2 G^2 \delta^2 \left(\frac{\Delta - \delta}{3}\right)\right] \quad (5)$$

where  $D_i$  is the diffusion coefficient of  $i$ th component, and  $p_{i,2\tau}$  is given by

$$p_{i,2} = \frac{p_i \exp(-2\tau/T_{2,i})}{[p_1 \exp(-2\tau/T_{2,1}) + p_2 \exp(-2\tau/T_{2,2})]} \quad (6)$$

where  $T_{2,i}$  is  $T_2$  in the  $i$ th region,  $p_i$  is the fractional proton number of  $i$ th component, and  $p_1 + p_2 = 1$ . When the difference in the relaxation time between the individual components is very small, Eq. (5) is reduced to

$$\frac{A(\delta)}{A(0)} = p_1 \exp\left[-\gamma^2 G^2 D_1 \delta^2 \left(\frac{\Delta - \delta}{3}\right)\right] + p_2 \exp\left[-\gamma^2 G^2 D_2 \delta^2 \left(\frac{\Delta - \delta}{3}\right)\right] \quad (7)$$

For the system composed of some regions with different molecular motions, when a diffusant translates into some regions, the observed echo signal attenuation depends on the residence lifetime of the diffusant in each of the regions. For the system composed of two regions with the same chemical shift, the time derivative of the contribution of the molecules in the  $i$ th region  $\Psi_i$  can be described as follows,

$$\frac{d\Psi_1}{dt} = -R_1 \Psi_1 - \Psi_1/\tau_1 + \Psi_2/\tau_2 \quad (8)$$

$$\frac{d\Psi_2}{dt} = -R_2 \Psi_2 + \Psi_1/\tau_1 - \Psi_2/\tau_2 \quad (9)$$

where  $R_i = \gamma^2 G^2 \delta^2 D_i + 1/T_{2,i}$  and  $\tau_i$  is the mean residence lifetime in the  $i$ th region. When the difference in the relaxation time between the individual regions is negligibly small, the attenuation in the PFGSE  $^1\text{H}$  NMR experiment for the system with two regions is given by

$$\frac{A(\delta)}{A(0)} = p_1 \exp \left[ -\gamma^2 G^2 D_1 \delta^2 \left( \frac{\Delta - \delta}{3} \right) \right] + p_2 \exp \left[ -\gamma^2 G^2 D_2 \delta^2 \left( \frac{\Delta - \delta}{3} \right) \right] \quad (10)$$

where  $D'_i$  and  $p'_i$  are the formal diffusion coefficient and fractional population in the  $i$ th region, respectively.  $D'_i$  is given by

$$D' = \frac{1}{2} \left[ D + D + \frac{1}{\gamma^2 G^2 \delta^2} \left( \frac{1}{\tau_1} + \frac{1}{\tau_2} \right) - \left\{ \left[ D - D + \frac{1}{\gamma^2 G^2 \delta^2} \left( \frac{1}{\tau_2} - \frac{1}{\tau_1} \right) \right]^2 + \frac{4}{\gamma^4 G^4 \delta^4 \tau_1 \tau_2} \right\}^{1/2} \right] \quad (11a)$$

$$D' = \frac{1}{2} \left[ D + D + \frac{1}{\gamma^2 G^2 \delta^2} \left( \frac{1}{\tau_1} + \frac{1}{\tau_2} \right) + \left\{ \left[ D - D + \frac{1}{\gamma^2 G^2 \delta^2} \left( \frac{1}{\tau_2} - \frac{1}{\tau_1} \right) \right]^2 + \frac{4}{\gamma^4 G^4 \delta^4 \tau_1 \tau_2} \right\}^{1/2} \right] \quad (11b)$$

and  $p'_1$  and  $p'_2$  are given by

$$p'_1 = -\frac{p_1 D_1 + p_2 D_2 - D_2}{D'_2 - D'_1} \quad (12a)$$

$$p'_2 = \frac{p_1 D_1 + p_2 D_2 - D'_1}{D'_2 - D'_1} \quad (12b)$$

If the displacement of the fluctuational motion of the network segment can be thought to follow Gaussian distribution, the  $\langle z^2 \rangle$  can be assumed to be comparable to  $(\kappa^{-1})^2$ . For the PDMAA gel, it was shown that the relationship between  $\kappa^{-1}$  and  $Q$  is given by  $\kappa^{-1} \sim Q^{0.71}$  and the  $\kappa^{-1}$  value for the PDMAA gel with  $Q=25$ , in which  $D/D_0 = \exp(-1)$ , is equal to the hydrodynamic radius of PEG ( $M_w=20,000$ ) of 4.2 nm [33, 57] as shown below. Thus, we have

$$\kappa^{-1} = 4.2 \text{ nm} \times \left(\frac{Q}{25}\right)^{0.71} \quad (13)$$

When the effect of the residual field gradient ( $G_r$ ) is not negligible, the echo signal intensity attenuation can be expressed in the form

$$\frac{A(\delta)}{A(0)} = \exp(T_{dis} + T_{resi}) \quad (14)$$

where  $T_{dis}$  is the term for the decay owing to the displacement, which is equal to  $-\gamma^2 G^2 D \delta^2 (\Delta - \delta/3)$  for a single-component diffusion, and  $T_{resi}$  is that owing to the effect of  $G_r$ . On the basis of the consideration that  $G_r$  is induced and decays with a single characteristic time,  $t_r$ ,  $T_{resi}$  is given by [39, 110]

$$\begin{aligned} T_{resi} &= -(\gamma G k t)^2 \exp \frac{-2\Delta + 1}{t} \left(1 - \exp \frac{-\Delta}{t}\right)^2 \left(\exp \frac{\delta}{t} - 1\right)^2 \\ &= -K \left(\exp \frac{\delta}{t} - 1\right)^2 \end{aligned} \quad (15)$$

where  $k$  is an apparatus constant and  $K$  is a constant when  $G$  and  $\Delta$  are fixed.

### 3. Diffusional Behavior of Synthetic Polymer Gels

(a) *Diffusional Behavior of Water in Poly(Methacrylic Acid) Gels.* In order to investigate changes in the translational motion of water contained in the PMAA gel by a change in the degree of cross linking, the diffusion coefficient of water molecules ( $D_{H_2O}$ ) in PMAA gels with the degree of swelling  $Q=3.4-105.8$  was determined by a PGSE  $^1\text{H}$  NMR method at 300 K, where  $Q$  is defined as the ratio of the weight of swollen gel ( $M_{swollen}$ ) to the weight of dried gel ( $M_{dry}$ ) [32]. As seen from this table,  $D_{H_2O}$  increases as  $Q$  is increased. This means that an increase in  $q$  leads to an increase in mobility of water molecules. If the  $D_{H_2O}$  increases are plotted against  $Q^{1/3}$ , it is seen from Figure 15 that  $D_{H_2O}$  increases linearly from  $1.37 \times 10^{-5}$  to  $2.19 \times 10^{-5} \text{ cm}^2 \text{ s}^{-1}$  with increasing  $Q^{1/3}$ . This shows that the translational molecular motion of water molecules in the PMAA gel increases



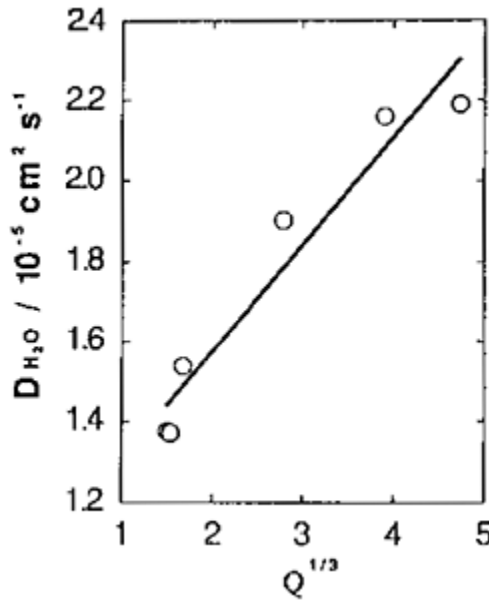


**FIG. 15** Plots of diffusion coefficient of water ( $D_{H_2O}$ ) in PMAA gel against  $Q^{1/3}$  at 300 K.

with an increase in the degree of swelling. The  $D_{H_2O}$  value of neat water at 300 K is  $2.5 \times 10^{-5} \text{ cm}^2 \text{ s}^{-1}$ . Therefore, it can be said that the translational molecular motion of water molecules in the gel is more restrained compared with that of neat water by the intermolecular interactions with the polymer network.

We are concerned with the reason why there exists a linear relationship between the  $D_{H_2O}$  and  $Q^{1/3}$ . The volume for the gel which contains network polymer and water may be associated with  $Q^{1/3}$ . Assuming that the volume for the gel is a cube with the length of an edge being  $r$ , the degree of swelling for the gel is rearranged as

$$Q = \frac{M_{\text{swollen}}}{M_{\text{dry}}} = \frac{(\rho_{\text{swollen}} \cdot V_{\text{swollen}})}{M_{\text{dry}}} = \left( \frac{\rho_{\text{swollen}}}{M_{\text{dry}}} \right) r^3 \quad (16)$$

where  $\rho_{\text{swollen}}$  is the density of swollen polymer gel and  $V_{\text{swollen}}$  the volume of swollen polymer gel. By rearranging Eq. (16), we obtain

$$r = A Q^{1/3} \quad (17a)$$

$$A = \frac{M_{dry}^{1/3}}{\rho_{swollen}} \quad (17b)$$

and  $M_{dry}$  is a constant. If  $Q$  is changed as a function of the degree of cross linking of the gel,  $\rho_{swollen}$  does not change greatly (at 300 K  $\rho_{swollen}=1.001 \text{ g cm}^{-3}$  at  $Q=3.4$  and  $\rho_{swollen}=0.997 \text{ g cm}^{-3}$  at  $Q=106$ ). Therefore, it can be said that the length of an edge of the volume of the gel ( $r$ ) is proportional to  $Q^{1/3}$ . This means that  $r$  of the volume containing a constant amount of network polymer increases with an increase in  $Q^{1/3}$ , and so the size of the polymer network in the gel expands the intermolecular distance between water molecules increases. For this, the molecular motion of molecules increases with an increase in  $Q^{1/3}$ . From the linear relationship between the  $D_{H_2O}$  and  $Q^{1/3}$ , it can be said that the molecular motion of water depends on intermolecular distance.

(b) *Diffusional Behavior of Water and Poly(Ethylene Glycol) in Poly(Dimethylacrylamide) Gels.* The diffusion coefficients of HDO ( $D_{HDO}$ ) and poly(ethylene glycol) (PEG) contained in poly(dimethylacrylamide) (PDMAA) gel were determined by the PFGSE  $^1\text{H}$  NMR method as described above 3 at 303 K varying  $Q$  and molecular weight ( $M_w$ ) of PEG [33]. The  $D_{HDO}$  values obtained were plotted against  $Q$  as shown in Figure 16. As seen from this figure,  $D_{HDO}$  increases as  $Q$  is increased, and it is almost independent of  $M_w$  of PEG contained in the gel. The change of  $D_{HDO}$  in the small  $Q$  region is much larger than that in the large  $Q$  region. The  $D_{HDO}$  value in the large  $Q$  region asymptotically approaches that for HDO in neat  $\text{D}_2\text{O}$  ( $2.22 \times 10^{-5} \text{ cm}^2 \text{ s}^{-1}$ ). Therefore, it can be said that the intermolecular interaction between water and polymer network, of which the strength depends on the size of a network, restrains translational motion of the water. There is almost no effect on the molecular motion of HDO by the change of  $M_w$  of PEG, indicating that the diffusion of HDO is independent of  $M_w$  of PEG.

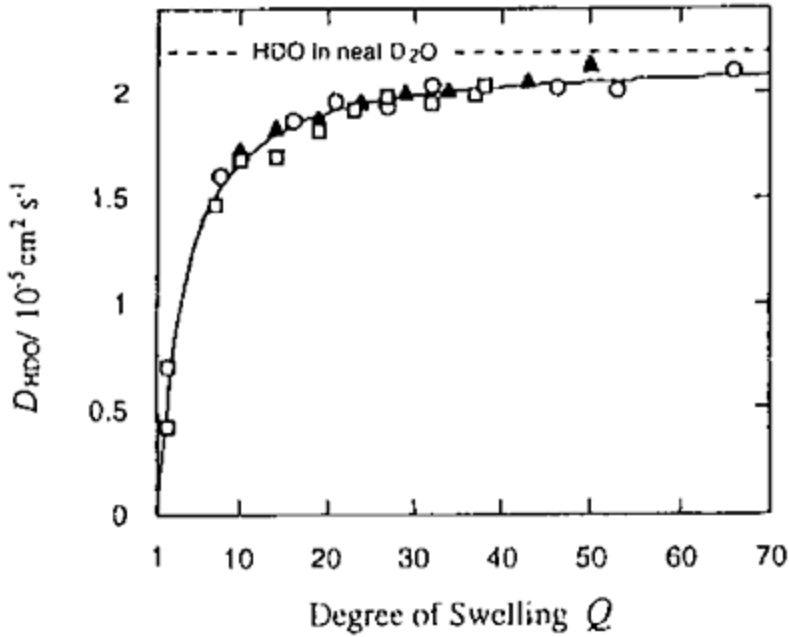


FIG. 16 Dependence of the diffusion coefficient of water molecules ( $D_{HDO}$ ) on the degree of swelling ( $Q$ ) in a PDMAA gel containing PEG with  $M_w = 4250$  ( $\square$ ), 10,890 ( $\blacktriangle$ ) and 20,000 ( $\circ$ ) at 303 K.

We can understand this diffusional behavior by using the modified free-volume theory proposed by Fujita [34–36]. The diffusion coefficient is related to the friction,  $\zeta$ , by the equation  $D = kT/\zeta$ , where  $k$  is the Boltzmann constant and  $T$  the absolute temperature [37]. The dependence of  $\zeta$  on solvent concentration is expressed as an exponential function of the fractional free volume,  $f$ . Then, the ratio of  $\zeta$  at any polymer concentration to  $\zeta$  at a reference concentration ( $\zeta_r$ ) is given by

$$\frac{\zeta}{\zeta_r} = \exp \left[ B \left( \frac{1}{f} - \frac{1}{f_3} \right) \right] \quad (18)$$

where  $f_r$  is  $f$  at a reference concentration and  $B$  is the minimum hole-size parameter required for the displacement of solvent, which is independent of the polymer concentration and is assumed to be 1. If  $f$  is linearly proportional to the increase of volume fraction of solvent at a constant temperature,  $f$  can be expressed in the form

$$f = f_r + \beta(v - v_r) \quad (19)$$

where  $v$  is the volume fraction of solvent,  $v_r$  the volume fraction of solvent at a reference

concentration, and  $\beta$  the proportionality constant. An assumption of Eq. (19) in the free-volume theory was originally introduced to the polymer-solvent mixtures in the sufficiently low solvent concentration region. However, the free-volume theory is used to elucidate the dependence of diffusion of solvent in polymer solution [38–40] and gel [41] on solvent concentration in the large solvent concentration region. Thus, by substituting Eq. (19) into Eq. (18), we have

$$\frac{\zeta}{\zeta_r} = \exp \frac{(v - v_r)}{f_r(f_r/\beta + v - v_r)} \quad (20)$$

From this equation, we have the following expression with the assumption that solvent in infinite swollen gel is chosen as a reference; that is,  $v_r=1$ .

$$D_{HDO} = D_{HDO}^0 \exp \frac{1 - v}{\{(1 - v)f_{solv} - f_{solv}^2/\beta\}} \quad (21)$$

where  $D_{HDO}^0$  and  $f_{solv}$  are the self-diffusion coefficient and the fractional free volume of deuterated water in infinite swollen gel, respectively. As the volume fraction of polymer may be approximated to be the same as the weight fraction of polymer,  $1-v \approx Q^{-1}$ . Thus, we have

$$D_{HDO} = D_{HDO}^0 \exp \frac{Q^{-1}}{(Q^{-1}f_{solv} - f_{solv}^2/\beta)} \quad (22)$$

The dynamical behavior of probe polymer in a gel can be analyzed by the ratio of the screening length of polymer network to the dimensional size of PEG. It is shown that the diffusion of a particle in semi-dilute polymer solution [42–44] and in a polymer gel [45] is followed by the following relation

$$\frac{D}{D^0} = \exp(-\kappa R) \quad (23)$$

where  $D^0$  is the diffusion coefficient of an isolated particle,  $R$  the radius of a particle, and  $\kappa^{-1}$  the dynamic screening length of polymer chain. When  $D/D^0=e^{-1}$ ,  $\kappa^{-1}$  is equivalent to  $R$ . This relation has also been employed for elucidating the self-diffusional behavior of random-coil polymers in solution [46] and gel [47] in which  $\kappa^{-1}$  is large enough for probe polymers to have the same motion as a hard sphere rather than the reptational motion. In these cases, the interchain hydrodynamic interactions more significantly contribute to the diffusion process compared with the topological constraints. For this, the hydrodynamic radius of a probe polymer can be replaced by  $R$ . When the topological constraint cannot neglect compared with the interchain hydrodynamic interactions,  $D_s$  become larger than the value expected from Eq. (23). When the diffusion coefficient of

an isolated PEG ( $D_{PEG}^0$ ) is determined from the diffusion coefficient of PEG in aqueous dilute solution ( $D_{PEG}^{soln}$ ), it is necessary to take into account the change of local friction of polymer which is estimated by the change for the diffusion coefficient of solvent [48]. Then,  $D_{PEG}^0$  is given by

$$D_{PEG}^0 = \frac{D_{PEG}^{soln}}{D_{HDO}^{neat}/D_{HDO}} \quad (24)$$

where  $D_{HDO}^{neat}$  is the diffusion coefficient of HDO in  $D_2O$ . In this work, the diffusional behavior of water and PEG in a PDMAA gel has been analysed by the above-mentioned Eqs. (23) and (24).

(c) *Diffusion Coefficient of HDO in a PDMAA Gel.* We can understand more clearly the dynamical behavior of water in the gel system using Eq. (23) obtained from the modified free-volume theory [35–37]. The solid curve obtained from a least-squares fitting to the experimental data using Eq. (23) is shown in Figure 17. The theoretical curve agrees well with the experimental data. From this result, the diffusion coefficient for HDO in infinite swollen gel ( $Q$ ) is obtained to be  $D_{PEG}^0 = 2.16 \times 10^{-5} \text{ cm}^2 \text{ s}^{-1}$ , which is lower than HDO in neat  $D_2O$  ( $2.22 \times 10^{-5} \text{ cm}^2 \text{ s}^{-1}$ ). This means that the diffusion coefficient for HDO in neat  $D_2O$  is different from the  $Q$ -extrapolated value to the infinite given by the modified free-volume theory for the diffusion concentration dependence [33]. The diffusion coefficient for an isolated HDO molecule in bulk PDMAA ( $Q=1$ )

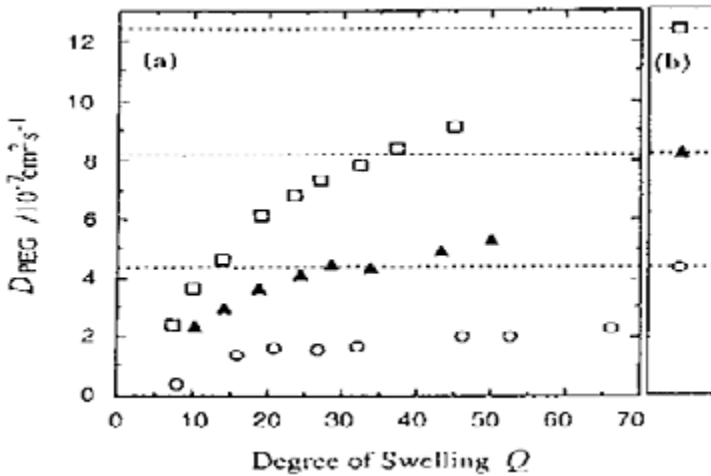


**FIG. 17** Dependence of the diffusion coefficient of PEG ( $D_{PEG}$ ) in PDMA gel on the degree of swelling ( $Q$ ) at 303 K (a). The diffusion coefficients of PEG in 1 wt% aqueous solution at 303 K (b).  $M_w$  of PEGs used are 4250 ( $\square$ ), 10,890 ( $\blacktriangle$ ), and 20,000 ( $\circ$ ).

obtained from Figure 16 was  $2.5 \times 10^{-7} \text{ cm}^2 \text{ s}^{-1}$ . It is seen that the translational motion of isolated water in bulk polymer is more strongly restrained compared to that in the gel. Further, it can be said that the rapid decrease of  $D_{HDO}$  in the small  $Q$  region can be explained by the decrease in free volume.

(d) *Diffusion Coefficient of PEG in a PDMAA Gel.* In order to investigate the translational motion of PEG contained in PDMAA gel as a probe polymer, the diffusion coefficient of PEG ( $D_{PEG}$ ) was determined by the PFGSE  $^1\text{H}$  NMR method at 303 K varying  $Q$  and  $M_w$  of PEG contained in the gel [33]. The  $D_{PEG}$  values obtained were plotted against  $Q$  in Figure 17a. It was found that  $D_{PEG}$  increases as  $Q$  is increased and also depends on the  $M_w$  of PEG. The  $D_{PEG}$  value in the gel is smaller than that at 1 wt% aqueous PEG solution ( $D_{PEG}^{soln}$ ) at 303 K as shown in Figure 17b. Therefore, it can be said that the translational motion of PEG in the gel is more restrained by large intermolecular interaction with polymer network as compared with PEG in aqueous solution and that PEG with higher  $M_w$  is more strongly restrained.

Next, we are concerned with the relationship between the degree of restraint in molecular motion of PEG in the gel and the ratio of the screening length of polymer network to the size of PEG. The dynamic behavior of PEG in the gel can be analyzed by using Eq. (23). The relationship between the dynamic screening length ( $\kappa^1$ ) and the concentration of network polymer ( $c$ ) or the degree of swelling ( $Q$ ) is expressed by

$$\kappa^{-1} \sim c^u = Q^{-u} \quad (25)$$

where  $u$  may be a constant in the range from  $-0.5$  to  $-1.0$ , but depends largely on the polymer species [43]. Substitution of Eqs. (24) and (25) into Eq. (23) gives

$$\frac{D_{PEG} D_{HDO}^{neat}}{D_{PEG}^{soln} D_{HDO}} = \exp(-Q^u R) \quad (26)$$

It is convenient to rewrite it in the form

$$\ln \left( -\ln \frac{D_{PEG} D_{HDO}^{neat}}{D_{PEG}^{soln} D_{HDO}} \right) = u \ln Q + \ln R \quad (27)$$

The log-log plot of the  $\ln[-\ln(D_{PEG} D_{HDO}^{neat}/D_{PEG}^{soln} D_{HDO})]$  value against  $Q$  using the experimental data (Fig. 17) has been shown in Figure 18. The three straight lines for PEG with different  $M_w$  have almost the same slope but different intercepts. As  $R$  in aqueous PEG solution is assumed to be the same as that in gel, we have

$$R = \frac{kT}{6\pi\eta_s D_{PEG}^{soln}} \quad (28)$$

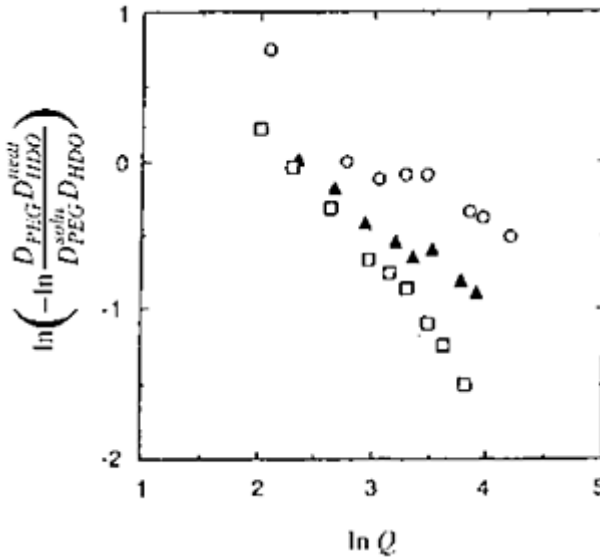


**FIG. 18** The plot of  $\ln[-\ln(D_{PEG}^{neat} D_{HDO}^{soln} / D_{PEG}^{soln} D_{HDO}^{neat})]$  against  $\ln Q$  at 303 K.  $M_w$  of PEGs used are 4250 ( $\square$ ), 10,890 ( $\blacktriangle$ ), and 20,000 ( $\circ$ ).

where  $\eta_s$  is the viscosity of solvent in solution. Substitution of Eq. (28) into Eq. (27) gives

$$\ln \left[ \left( -\ln \frac{D_{PEG}^{neat} D_{HDO}^{soln}}{D_{PEG}^{soln} D_{HDO}^{neat}} \right) D_{PEG}^{soln} \right] = u \ln Q + \ln \left( \frac{kT}{6\pi\eta_s} \right) \quad (29)$$

In Figure 19,  $\ln[(-\ln(D_{PEG}^{neat} D_{HDO}^{soln} / D_{PEG}^{soln} D_{HDO}^{neat})) D_{PEG}^{soln}]$  value calculated using the experimental data is plotted against  $\ln Q$ . A straight line with a slope of  $-0.71$  is obtained and so  $u = -0.71$ . Therefore, we have  $\kappa^{-1} \sim Q^{0.71} = c^{-0.71}$ . Depending on the nature of network and solvent, there are a variety of theoretical calculations for the concentration dependence of the dynamic screening length [43]. deGennes [49] proposed theoretically that for flexible polymer chains in a gel with good solvent, the relationship  $\kappa^{-1} \sim c^{-0.71}$  is obtained. This prediction is in agreement with the above experimental results.

(e) *Diffusional Behavior and Intermolecular Hydrogen Bond Between Probe Polymer and Network Polymer in (N,N-Dimethylacrylamide Acrylic Acid) Copolymer Gels.* The molecular dynamics of a probe polymer is strongly affected in polymer gel systems with various kinds of intermolecular interactions between the probe polymer and the network polymer, such as, for example, hydrogen bonding, hydrophobic, and Coulomb interactions. For example, by adding aqueous PEG solution into aqueous poly(acrylic acid) (PAA) solution, the complex between PEG and PAA is formed by the formation of hydrogen bonds between the oxygen atoms of PEG and the carboxyl groups of PAA

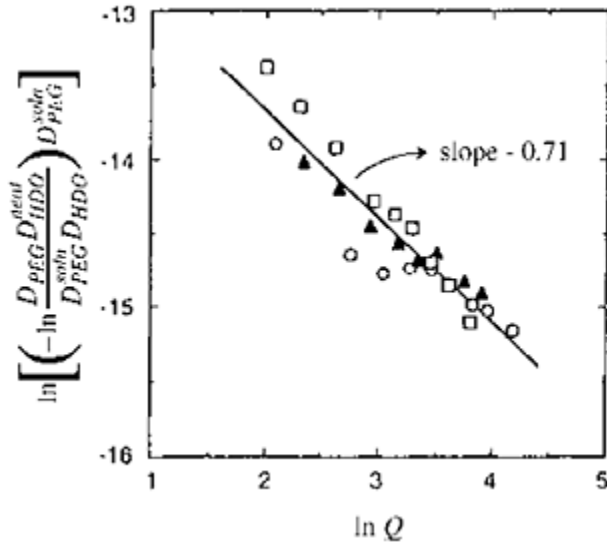


**FIG. 19** The plot of  $\ln\left[-\ln\left(D_{PEG} D_{HDO}^{neat} / D_{PEG}^{soln} D_{HDO}\right) D_{PEG}^{soln}\right]$  against  $\ln Q$  at 303 K.  $M_w$  of PEGs used are 4250 ( $\square$ ), 10,890 ( $\blacktriangle$ ), and 20,000 ( $\circ$ ).

[50, 51], and also in poly(methacrylic acid) (PMAA) hydrogel the complex between PEG and PMAA is formed by the same interaction [52]. The justification for the formation of such complexes have been carried out by macroscopic methods such as viscosity measurement for solutions and mass measurement for gels. Nevertheless, in order to clarify more clearly such an intermolecular interaction between the probe polymer and the network polymer in the gel systems, systematic studies by a microscopic method such as NMR spectroscopy are needed.

In this section, the effect of intermolecular hydrogen bond interactions between PEG (probe polymer) and network polymer in (*N,N*-dimethylacrylamide [DMAA]-acrylic acid (AA)) copolymer gel systems on the dynamic behavior by measuring diffusion coefficient and  $^1\text{H}$  spin-spin relaxation time ( $T_2$ ) by the PGSE  $^1\text{H}$  NMR method [22–29] and by the Carr-Purcell/Meiboom-Gill (CPMG)  $^1\text{H}$  NMR method [53–56], respectively, is clarified and, on the basis of its results, the formation of the loose complex is elucidated. Typical spin-echo  $^1\text{H}$  NMR spectra of a (DMAA-AA) copolymer ( $f_{AA}=0.5$ ) gel at  $Q=61$  containing PEG and HDO are shown as a function of field gradient pulse length ( $\delta$ ) in Figure 20 [57]. Peaks at 4.73, 3.72, and 2.93 ppm can be assigned to HDO, methylene protons of PEG, and methyl protons of DMAA unit, respectively, by using reference data on PEG solution and PDMAA gel without PEG. Peaks assigned to methylene and methine protons of DMAA unit and AA unit appear strongly in the NMR experiment with a single pulse and decay during echo time ( $2\tau$ ) because these protons are restrained in molecular motion and have short  $T_2$ . The plots of



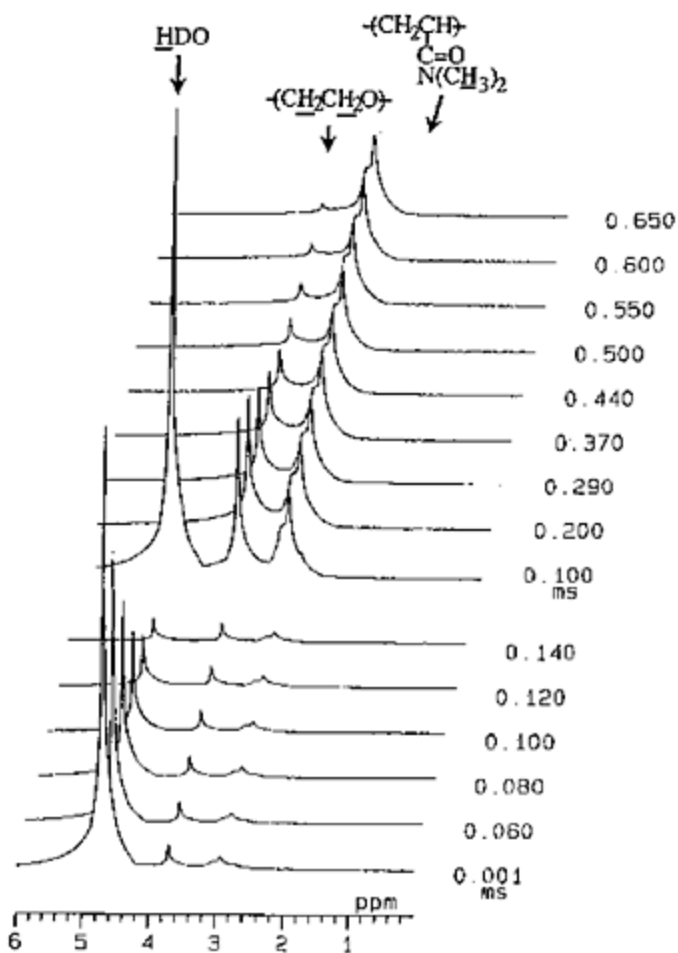


**FIG. 20** Spin-echo  $^1\text{H}$  NMR spectra of a (DMAA-AA) copolymer gel ( $Q=67$ , DMAA/AA=50 mol/50 mol) containing PEG with  $M_w=4250$  as probe polymer and HDO as solvent by varying field gradient pulse duration ( $\delta$ ).

$\ln[A(\delta)/A(0)]$  against  $\gamma^2 G^2 \delta^2 (\Delta - \delta/3)$  for peaks at 4.73 and 3.72 ppm show that the experimental data lie on a straight line. This means that the individual diffusant of HDO and PEG in the gel has a single-component diffusion during the observation time. Every measurement for diffusion coefficient in this study shows a single component diffusion.

(f) *Diffusion Coefficient of HDO in (DMAA-AA) Copolymer Gels.* The diffusion coefficients of HDO ( $D_{\text{HDO}}$ ) contained in PDMAA gels, PAA gels, and (DMAA-AA) copolymer gels with PEG were determined by PFGSE  $^1\text{H}$  NMR method at 303 K varying  $Q$  and  $f_{\text{AA}}$  [57]. The  $D_{\text{HDO}}$  values obtained were plotted against  $Q$  as shown in Figure 21. As seen in Figure 21,  $D_{\text{HDO}}$  increases as  $Q$  is

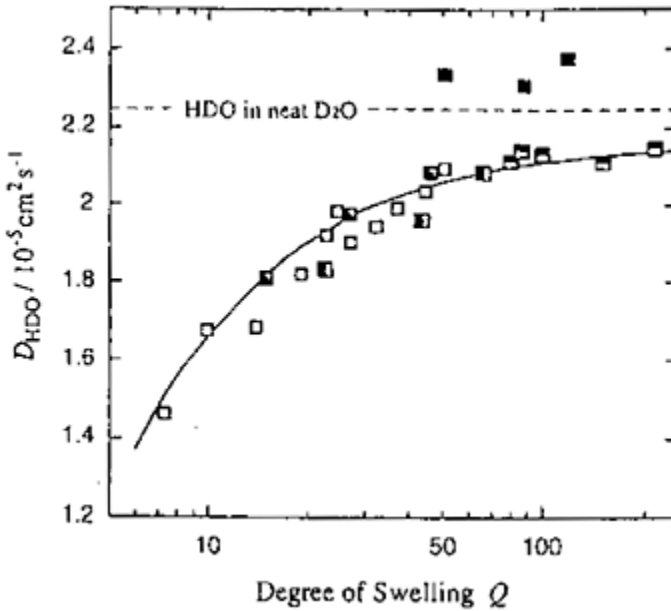


**FIG. 21** Dependence of the diffusion coefficient of water molecule ( $D_{HDO}$ ) on the degree of swelling ( $Q$ ) in (DMAA-AA) copolymer gels containing PEG with  $M_w$  of 4250 at 303 K. The mole fraction of AA gels,  $f_{AA}$ , is ( $\square$ ) 0 mol%, ( $\blacksquare$ ) 20 mol%, ( $\blacksquare$ ) 50 mol%, ( $\blacksquare$ ) 90 mol%, and ( $\blacksquare$ ) 100 mol%.

increased. The molecular motion of HDO is not affected by a change of  $f_{AA}$  in the region of  $f_{AA} < 0.9$ . This means that the translational motion of HDO molecule increases as the size of the network becomes large. The dynamical behavior of solvent in a gel can be analyzed by the modified free-volume theory [34–36]. As described above,  $D_{HDO}$  in a PDMAA gel can be expressed by Eq. (8). From a least-squares fitting to the experimental data for PDMAA gels using Eq. (8), we can determine  $D_{HDO}^0$ ,  $f_{solv}$ , and  $\beta$  to be  $2.16 \times 10^{-5} \text{ cm}^2 \text{ s}^{-1}$ , 0.178, and 0.079, respectively. The solid curve shown in Figure 21, which is calculated by using Eq. (8) and parameters obtained for PDMAA gels, agrees well with the experimental data obtained for (DMAA-AA) copolymer gels with an  $f_{AA}$  value less than 0.9. This indicates that the diffusion of HDO is independent of the concentration of carboxylic acid group in this region.  $D_{HDO}$ s in PAA gels are larger than those in (DMAA-AA) copolymer gels. This may be because the concentration of  $\text{H}^+$  ions dissociated from carboxylic acid groups in PAA gels, which diffuse faster than HDO, is higher than that in (DMAA-AA) copolymer gel.

(g) *Diffusion Coefficient of PEG in (DMAA-AA) Copolymer Gels.* In order to investigate the translational motion of PEG contained in PDMAA gels and PAA gels as the probe polymer, the diffusion coefficient of PEG ( $D_{PEG}$ ) was determined by the

PFGSE  $^1\text{H}$  NMR method at 303 K varying  $Q$  of the gel [57]. The obtained  $D_{\text{PEG}}$  values were plotted against  $Q$  as shown in Figure 22. The  $D_{\text{PEG}}$  value in PDMAA gel is smaller than that in aqueous 1 wt% PEG solution (*dashed line*), and increases as  $Q$  is increased. From the plot of  $\ln(-\ln(D/D_0))$  against  $\ln Q$ , it was shown that this behavior is followed by  $D/D_0 = \exp(-Q^u R)$ , and is similar to that mentioned above [45]. Therefore, it can be said that the translational motion of PEG in PDMAA gel is restrained by hydrodynamic interaction with polymer network. This means that the polymer network is working as only a spatial obstruction for the displacement of PEG. The  $D_{\text{PEG}}$  value in PAA gels is much smaller than that in PDMAA gel. This suggests that the loose complex of the PEG and PAA network is formed by intermolecular hydrogen bond interactions between the oxygen atoms of PEG and the carboxyl groups of PAA [51]. By addition of a small amount of HCl into the solution for the gel to be 0.15 mM in concentration, the gel shrinks and  $D_{\text{PEG}}$  is decreased as shown in Figure 22 (*arrows*). The complexation arises from an intermolecular hydrogen bond interaction between oxygen atoms of PEG and the carboxylic groups of AA units in the undissociated state as shown below. Therefore, it can be said that the addition of HCl leads to an increase in the amount of undissociated carboxylic groups and so enhances the formation of the complex and induces the shrinkage of the gel. This leads to slow diffusion of PEG. On the other hand, by

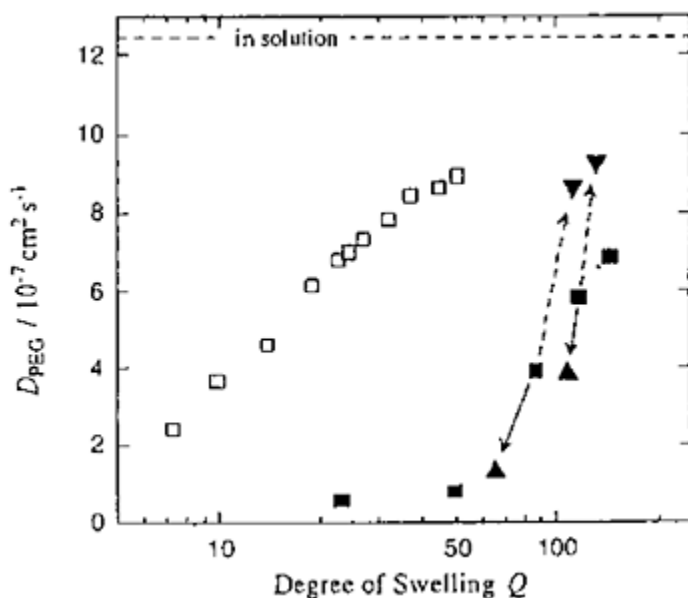


**FIG. 22** Dependence of the diffusion coefficient of PEG with  $M_w$  of 4250 ( $D_{\text{PEG}}$ ) in PDMAA gels ( $\square$ ), PAA gels ( $\blacksquare$ ), PAA gels soaked in 0.15 mM HCl ( $\blacktriangle$ ), and PAA gels soaked in 30 mM trimethyl amine ( $\blacktriangledown$ ) on the degree of swelling ( $Q$ ) at 303 K. The diffusion coefficient of PEG with  $M_w$  of 4250 in wt% aqueous solution at 303 K is indicated by the dashed line.

addition of trimethylamine (20 mM), the gel swells and  $D_{\text{PEG}}$  is increased as shown in Figure 22 (*arrows and dashed line*). It can be said that the addition of an amine decreases the amount of dissociated carboxylic group and so inhibits the formation of the complex. This leads to fast diffusion of PEG and the swelling of the gel.

For the detailed understanding of the complexation of PEG and gel network,  $D_{\text{PEG}}$  in (DMAA-AA) copolymer gels was measured and the obtained  $D_{\text{PEG}}$  values were plotted against  $Q$  as shown in Figure 23 [57]. It can be said that  $D_{\text{PEG}}$  has almost a constant value in the range of  $f_{\text{AA}} > 0.5$  and is drastically decreased in the range of  $f_{\text{AA}} > 0.9$  even though Figure 23 shows some scatter, which is probably caused by the inhomogeneity of the gels in the polymer concentration. From these results, it is suggested that when  $f_{\text{AA}}$  is small, that is, the AA unit is isolated in DMAA sequences, the molecular motion of PEG is not strongly restrained by the weak intermolecular interaction with AA units, but when  $f_{\text{AA}}$  is large, that is, consecutive AA units are distributed in the network, intermolecular interactions between PEG and consecutive AA segments are enhanced, and so the molecular motion of PEG is strongly restrained [58].

(h)  $^1\text{H}$   $T_2$  of PEG in (DMAA-AA) Copolymer Gels. The  $T_2$  value reflects the molecular motion [56, 59]. In the molecular motion of PEG in  $\text{D}_2\text{O}$  solution, the

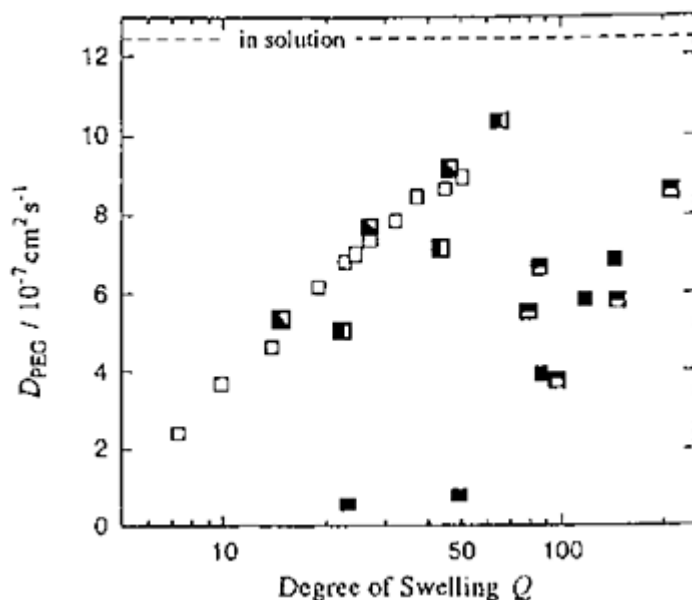


**FIG. 23** Dependence of the diffusion coefficient of PEG with  $M_w$  of 4250 ( $D_{\text{PEG}}$ ) in (DMAA-AA) copolymer gels on the degree of swelling ( $Q$ ) at 303 K. The diffusion coefficient of PEG with  $M_w$  of 4250 in 1 wt% aqueous solution at 303 K is indicated by the dashed line. The mole fraction of AA in gels,  $f_{\text{AA}}$ , is (□) 0 mol%, (◐) 20 mol%, (■) 50 mol%, (◑) 90 mol%, and (■) 100 mol%.

segmental motion is a dominant factor compared with the translational motion and rotational motion of a whole molecule. In order to investigate the segmental motion of PEG contained in PDMAA gels, PAA gels, and (DMAA-AA) copolymer gels,  $^1\text{H } T_2$  of PEG was measured by the CPMG method at 303 K varying  $Q$  and  $f_{AA}$  of the gel. Figure 24 shows the plot of the obtained  $^1\text{H } T_2$  values against  $Q$ . The  $^1\text{H } T_2$  values of PEG in (DMAA-AA) copolymer gels with  $f_{AA} < 0.5$  decrease as  $Q$  is decreased [57]. This means that the correlation time for the segmental motion of PEG molecule increases as the size of the network becomes small. It is thought that the segmental motion of PEG is restrained by hydrodynamic interaction with the polymer network in these gels, as the molecular motion of PEG is not strongly restrained by intermolecular hydrogen bonding interaction with AA units in the gels with  $f_{AA} < 0.5$  as indicated by the experimental data on  $D_{PEG}$ .

The  $^1\text{H } T_2$  value of PEG in (DMAA-AA) copolymer gels with  $f_{AA} > 0.9$  is much smaller than that with  $f_{AA} < 0.5$ , and this behavior is similar to that of  $D_{PEG}$ . Therefore, it can be said that the loose complex between PEG and AA units in the network polymer, which needs any specified consecutive units of AA, restrains the segmental motion of PEG as well as the translational motion of PEG. This suggests that there is not so strong a hydrogen bond interaction between a part of the segment in PEG and the polymer network that is enough to restrain the

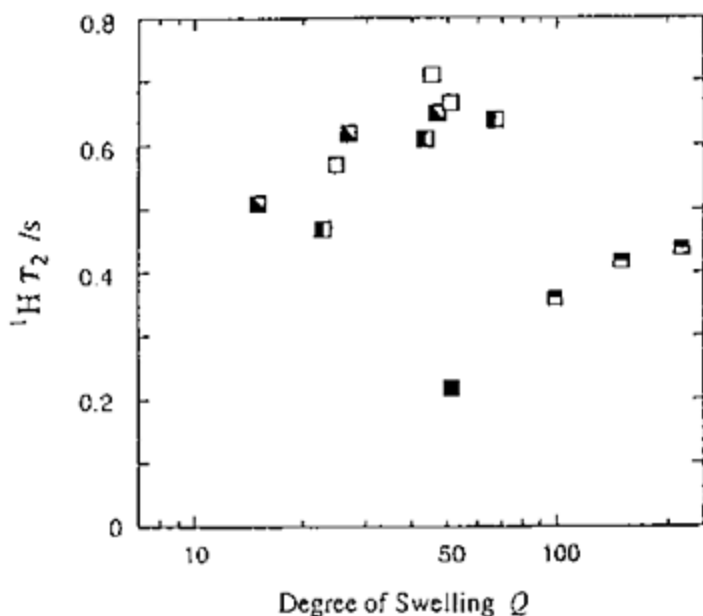


**FIG. 24** Dependence of  $^1\text{H } T_2$  of PEG with  $M_w$  of 4250 in (DMAA-AA) copolymer gels on the degree of swelling ( $Q$ ) at 303 K. The mole fraction of AA in gels,  $f_{AA}$ , is ( $\square$ ) 0 mol%, ( $\blacksquare$ ) 20 mol%, ( $\blacksquare$ ) 50 mol%, ( $\boxtimes$ ) 90 mol%, and ( $\blacksquare$ ) 100 mol%.

translational motion of PEG molecule, in this case the dominant parts of segments in PEG, which do not form a hydrogen bond, would undergo fast segmental motion. From the above results, it can be said that the complex is stabilized through hydrogen bondings between the whole of PEG chain and the consecutive AA units in the network polymer. This is consistent with the result of the diffusion coefficient measurement that  $D_{PEG}$  does not decrease in (DMAA-AA) copolymer gels with  $f_{AA} < 0.5$ .

It can be that the  $D$  and  $^1\text{H}$   $T_2$  values for PEG (probe polymer) in swollen (DMAA-AA) copolymer gels with various mole fractions of AA units were determined by using the PFGSE method and the Carr-Purcell/Meiboom-Gill method. From these experimental results, it was found that the  $D$  and  $^1\text{H}$   $T_2$  values for PEG in (DMAA-AA) copolymer gels with  $f_{AA} > 0.9$  are much smaller than those in (DMAA-AA) copolymer gels with  $f_{AA} < 0.5$  because of the loose complexation of PEG and consecutive AA units in the network. Further, it has been demonstrated that the  $^1\text{H}$  NMR methods are useful means for elucidating an intermolecular hydrogen bond interaction through the observation of molecular dynamics.

#### 4. Intermolecular Hydrophobic Interaction Between Probe Polymer and Network Polymer in (*N*-Stearyl Itaconamide—*N,N*-Dimethylacrylamide) Copolymer Gels

In the PGSE  $^1\text{H}$  NMR method, the observation time is clearly defined as the time interval between the two field gradient pulses in which the molecules are allowed to diffuse. Therefore, the analysis for the result of diffusion measurements varying the time interval makes it possible to elucidate the spatial and morphological structure of inhomogeneous gels and to determine the exchange time between the states of diffusant interacted and uninteracted with polymer network.

In this section, the effect of the diffusional behavior on the intermolecular hydrophobic interactions between PEG oleylether (PEG-Ole) as the probe polymer and the network polymer in stearyl itaconamide (SIA)-DMAA copolymer gel swollen with water is elucidated, in which the micelle of SIA is immobilized by copolymerization, through the diffusion coefficient determined by the PFGSE  $^1\text{H}$  NMR method, and  $^1\text{H}$   $T_1$  and  $T_2$  are determined by the  $^1\text{H}$  pulse NMR method. Furthermore, on the basis of the experimental results, we attempt to estimate the exchange time between two states of PEG-Ole aggregated and unaggregated with the micelle immobilized in the polymer network [60].

(a) *Diffusion Coefficient of HDO in SIA-DMAA Copolymer and PDMAA Gels.* The diffusion coefficients of HDO ( $D_{HDO}$ ) contained in SIA-DMAA copolymer gels and PDMAA gels with PEG-Ole and in SIA-DMAA copolymer gels with PEG were determined by the PFGSE  $^1\text{H}$  NMR method with  $\Delta$  of 30 ms at 303 K varying  $\delta$  from 0 to 0.05 ms, and were plotted against  $Q$  as shown in

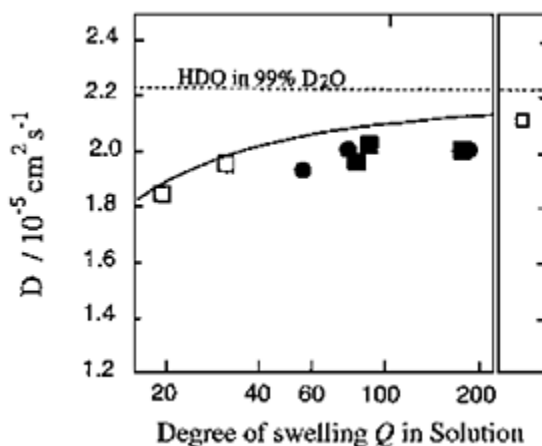


**FIG. 25** Dependence of the diffusion coefficient of water molecule ( $D_{HDO}$ ) on the degree of swelling ( $Q$ ) in a PDMAA gel containing PEG-Ole with  $M_w$  of 1200 ( $\square$ ), in a SIA-DMAA gel containing PEG with  $M_w$  of 1500 ( $\bullet$ ), in a SIA-DMAA gel containing PEG-Ole with  $M_w$  of 1200 ( $\blacksquare$ ), and in solution containing PEG-Ole with  $M_w$  of 1200 ( $\square$ ) at 303 K.

Figure 25. It has been reported that the  $D_{HDO}$  values in a PDMAA gel can be expressed by Eq. (12) based on the modified free-volume theory [33, 57]. The solid curve shown in Figure 25 was calculated by using Eq. (12) and parameters obtained from the  $D_{HDO}$  values in PDMAA gels. The  $D_{HDO}$  values in SIA-DMAA copolymer gels together with PEG and with PEG-Ole are below the solid curve. This result may be due to the structure of SIA-DMAA copolymer gels, in which the micelle of stearyl group acts as a spatial obstruction and HDO molecules diffuse by a roundabout way and the apparent value of  $D_{HDO}$  is reduced [61–63]. This effect of the gel structure on the apparent diffusion coefficient is clarified on the basis of the diffusion coefficients for probe polymers varying the interval of the field gradient pulse (observation time for the diffusion). The  $D_{HDO}$  values in PDMAA gels with PEG-Ole and in PEG-Ole solution are also slightly below the solid curve. This is due to the existence of the micelle of PEG-Ole which can be a spatial obstruction for the diffusion of HDO molecules.

(b) *Diffusional Behavior of Probe Polymers in SIA-DMAA Copolymer Gels.* The PFGSE  $^1\text{H}$  NMR spectra were measured with  $\Delta$  of 30 ms varying  $\delta$  from 0 to 0.108 ms for SIA-DMAA copolymer gels with PEG and PDMAA gels with PEG-Ole, and the plots of  $\ln[A(\delta)/A(0)]$  against  $\gamma^2 G^2 \delta^2 (\Delta - \delta/3)$  for the peak at 3.72 ppm were obtained as shown in Figure 26 [60]. It is seen that the experimental data lie on a straight line. This means that PEG in SIA-DMAA copolymer gels and PEG-Ole in PDMAA gels have single-component diffusions during the observation time.

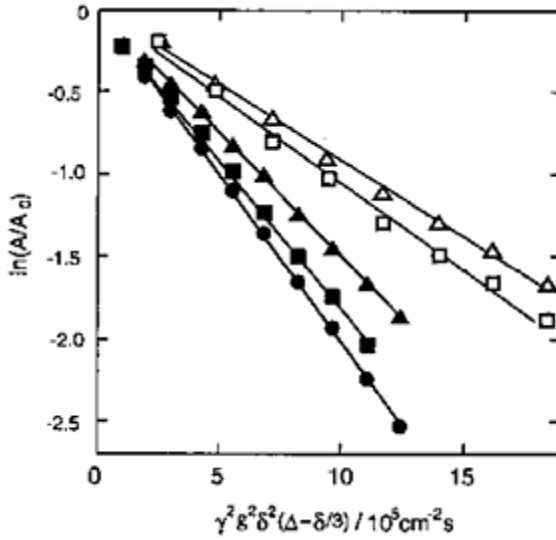


**FIG. 26** Diffusional spin-echo attenuation of PEG-Ole in PDMAA gel with the degree of swelling  $Q=19$  ( $\Delta$ ) and with  $Q=30$  ( $\square$ ) and that of PEG in SIA-DMAA gel with  $Q=53$  ( $\blacktriangle$ ), with  $Q=74$  ( $\blacksquare$ ), and with  $Q=177$  ( $\bullet$ ).

For SIA-DMAA copolymer gels with PEG-Ole, the plots of  $\ln[A(\delta)A(0)]$  against  $\gamma^2 G^2 \delta^2 (\Delta - \delta/3)$  for the peaks at 3.72 ppm for methylene protons of ethylene group in PEG-Ole and at 2.93 ppm for methyl protons of DMAA obtained from the spectra measured with  $\Delta$  of 30 ms varying  $\delta$  from 0 to 0.738 ms are shown in Figure 27.

The plots for methyl protons of DMAA in the polymer network is obviously decreased in the region of large  $\gamma^2 G^2 \delta^2 (\Delta - \delta/3)$  value, which may be caused by the fluctuation motion of the network segment or by the effect of the residual gradient ( $G_r$ ), because the network segment does not move by the translational diffusion. In order to estimate a distance for the displacement of the network segment by the fluctuational motion, the  $\kappa^{-1}$  can be used. The  $\kappa^{-1}$  values of SIA-DMAA copolymer gels with  $Q=78$  and 169 were obtained to be 9.3 and 16.0 nm, respectively, by using Eq. (13) obtained for PDMAA gels. Then, by using Eq. (4) and the assumption of  $\langle z^2 \rangle \sim (\kappa^{-1})^2$ , the corresponding  $\ln(A/A_0)$  values with  $\delta=0.738$  ms are estimated to be  $-0.0016$  and  $-0.0049$  for the gel with  $Q=78$  and 169, respectively. However, the plots for methyl protons of DMAA show a much larger decrease than those estimated values with the downward curvature. Therefore, it is considered that there is the effect of  $G_r$  on the reduction of the peak intensity under applying a high field gradient.

For the signal of DMAA in the network,  $T_{dis}$  is negligibly small as shown above, and so from Eqs. (14) and (15), the decay by  $G_r$  is given by

$$\ln \frac{A(\delta)}{A(0)} = T_{resi} = -K \left[ \exp\left(\frac{\delta}{t_r}\right) - 1 \right]^2 \quad (30)$$



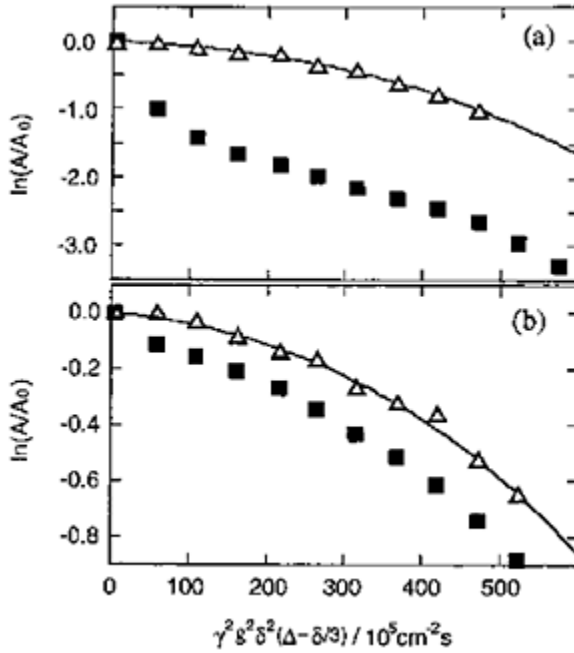


**FIG. 27** Spin-echo attenuation of PEG-Ole (■) and  $\text{CH}_3$  of DMAA (Δ) in SIA-DMAA gel with the degree of swelling  $Q=169$  (a) and  $Q=78$  (b). The solid curves are calculated by using Eq. (30).

The solid curves obtained from least-squares fittings to the experimental data using Eq. (30) are shown in Figure 27. The obtained curves agree well with the experimental data, and the  $t_r$  values are given as to be 0.40 and 0.42 ms for the gel with  $Q=78$  and 169, respectively.

The  $T_{dis}$  for PEG-Ole is given by subtracting the effect of  $G_r$  from the decay of the peak for PEG-Ole in the following way:

$$T_{dis} = \ln \frac{A(\delta)}{A(0)} - T_{resl} = \ln \frac{A(\delta)}{A(0)} + K \left[ \exp \left( \frac{\delta}{t_r} \right) - 1 \right]^2 \quad (31)$$

where  $K[\exp(\delta/t_r)-1]^2$  is given by using parameters obtained from least-squares fittings to the experimental data for DMAA in the same spectra. The  $T_{dis}$  values were plotted against  $\gamma^2 G^2 \delta^2 (\Delta - \delta/3)$  in Figure 28. The plot deviates from a straight line as seen in Figure 28. This means that PEG-Ole in SIA-DMAA copolymer gel has a complex component diffusion during the observation time. As a simple assumption for this diffusional behavior, we consider that a part of a PEG-Ole diffuses with  $D_2$  among micelles in the gel, and another aggregates with

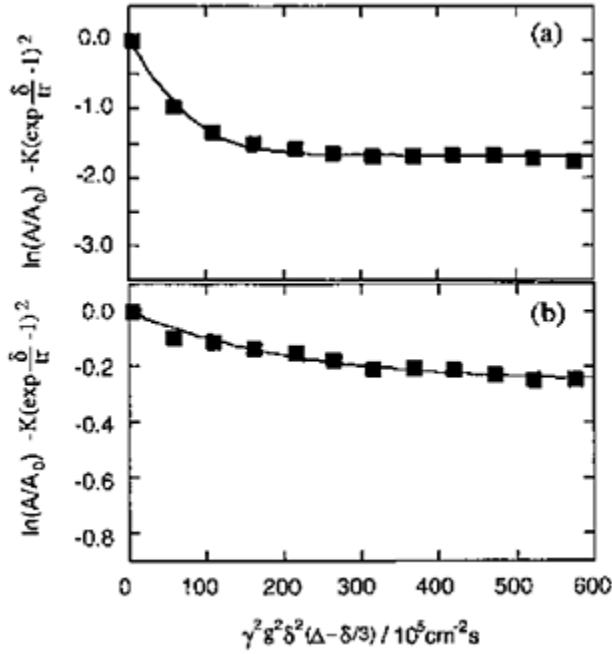


**FIG. 28** Diffusional spin-echo attenuation of PEG-Ole in SIA-DMAA gel with the degree of swelling  $Q=169$  (a) and  $Q=78$  (b) corrected by using Eq. (18). The solid curves are calculated by using Eq. (31).

micelles immobilized in the polymer network and does not diffuse, so  $D_1=0$  in Eq. (8), and we have

$$T_{dis} = (1 - p_2) + p_2 \exp[-\gamma^2 G^2 D_2 \delta^2 \frac{\Delta - \delta}{3}] \quad (32)$$

The solid curves obtained from least-squares fittings to the experimental data using Eq. (32) are shown in Figure 28. From these results, the  $D_2$  values are given to be  $5.42 \times 10^{-8}$  and  $2.23 \times 10^{-7} \text{ cm}^2 \text{ s}^{-1}$  for the gel with  $Q=78$  and  $169$ , respectively, and also  $p_2$  is given as to be  $0.82$  and  $0.23$ , which are the relative populations of diffusing components, respectively, when the difference in relaxation time between the components is negligible. Since the plots of  $\ln[A(\delta)A(0)] + K[\exp(\delta/t_r) - 1]^2$  against  $\gamma^2 G^2 D_2 \delta^2 (\Delta - \delta/3)$  for PEG-Ole in SIA-DMAA copolymer gels with  $Q=14$  and  $21$  show very small decay, which makes it difficult to analyze as two components, each of them was analyzed as a single component using Eq. (4) to be  $0.9 \times 10^{-8}$  and  $0.3 \times 10^{-8} \text{ cm}^2 \text{ s}^{-1}$ , respectively.

In order to clarify the effect of the hydrophobic interaction between the probe polymers and polymer networks on the diffusional behavior of the probe polymer, the  $D$  values obtained for PEG ( $D_{PEG}$ ) and PEG-Ole ( $D_{PEG-Ole}$ ) in SIA-DMAA

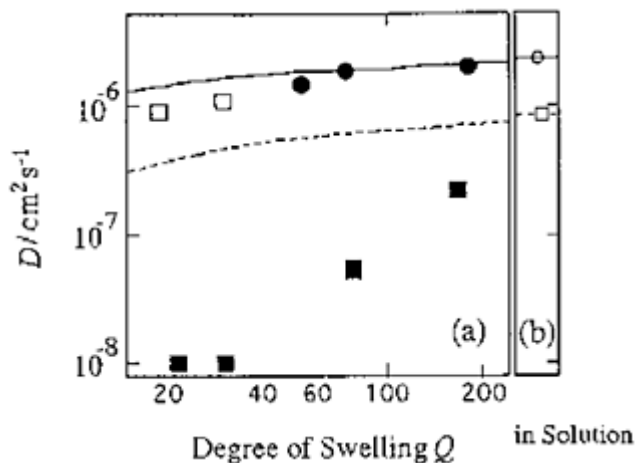


**FIG. 29** (a) Plots of the diffusion coefficient ( $D$ ) for PEG-Ole with  $M_w$  of 1200 in PDMAA gel ( $\circ$ ), for PEG with  $M_w$  of 1500 in a SIA-DMAA gel ( $\bullet$ ), and for PEG-Ole with  $M_w$  of 1200 in a SIA-DMAA gel ( $\blacksquare$ ) against the degree of swelling,  $Q$ , at 303 K. The solid line and dashed line are calculated by using Eq. (38) for PEG with  $M_w=1200$  and for micelle of PEG-Ole with  $D=5.45\times 10^{-7} \text{ cm}^2 \text{ s}^{-1}$  in solution, respectively. (b) Plots of the diffusion coefficient ( $D$ ) for PEG with  $M_w$  of 1500 in 0.5% solution ( $\circ$ ) and for PEG-Ole with  $M_w$  of 1200 ( $\square$ ) in 0.1% solution at 303 K.

copolymer gels and for  $D_{PEG-Ole}$  in PDMAA gel are plotted against  $Q$  as shown in Figure 29a. On the basis of the  $D$  value in solution (Fig. 29b), the solid line and the dashed line were calculated for PEG with  $M_w=1200$  and for the micelle of PEG-Ole, respectively, by using the following equation [33, 57], which is obtained for  $D_{PEG}$  in PDMAA gel,

$$D = \frac{D_{soln}}{D_{HDO,neat}/D_{HDO}} \exp - \frac{R}{Q^{0.71}} \quad (33)$$

where  $D_{soln}$  and  $D_{HDO,neat}$  are  $D$  of the probe polymer in dilute solution and  $D_{HDO}$  in neat  $D_2O$ , respectively.  $R=kT/6\pi\eta_s D_{soln}$ , where  $\eta_s$  is the viscosity of solvent. The  $D_{PEG}$  value in SIA-DMAA copolymer gel is almost the same as that calculated for PEG in PDMAA gel on the basis of the  $D$  value in 0.5% solution (*solid line*). Therefore, it can be said that there is no strong specific interaction between PEG and the network of SIA-DMAA copolymer gel except the hydrodynamic interaction. The slight lowering of the experimental points from the solid line may come from the micelle structure of SIA-DMAA copolymer gel, which makes PEG to diffuse by a roundabout way in a similar manner as described for the  $D_{HDO}$ . The  $D_{PEG-Ole}$  value in PDMAA gel is larger than that calculated for micelle of PEG-Ole in PDMAA gel on the basis of the  $D$  value in 0.1% solution (*dashed line*). Therefore, it is considered that PEG-Ole molecule exists as a

smaller micelle in PDMAA gel than in 0.1% solution. The  $D_{PEG-Ole}$  value in SIA-DMAA copolymer gel, which is obtained for the component diffusing among micelles of SIA, is much smaller than  $D_{PEG-Ole}$  in PDMAA gel. From this result, it is suggested that the hydrophobic interaction between the oleyl group of PEG-Ole and the stearyl group of SIA restrains the diffusion of PEG-Ole molecule during the diffusion of PEG-Ole among the micelles of SIA besides allowing the formation of comicelle of PEG-Ole and SIA.

### D. Diffusional Behavior of Polypeptide Gels

The NMR methods involving pulsed magnetic field gradients provide one of the most attractive techniques for studying molecular dynamics in polypeptide solution and gel systems. In particular, PFGSE NMR has been an invaluable tool in determining the anisotropic structures of polypeptide the lyotropic liquid crystalline phase. Almost two decades ago, the first lateral diffusion coefficient of an amphiphile in a lamellar liquid crystalline phase was measured directly with the PFGSE NMR method [64, 65]. In recent years, the range of applications of NMR diffusion techniques has been growing rapidly owing to the great improvements in the NMR equipment for the diffusion microscopy [23–31]. We concentrate here on the diffusion behavior of a solvent molecule in a polypeptide gel system with  $\alpha$ -helix-random coil transition and on the diffusion behavior of solvent and probe n-alkane molecules in the polypeptide gel system with highly oriented structures.

#### 1. Diffusion Behavior of Solvents in Unoriented Polypeptide Gels

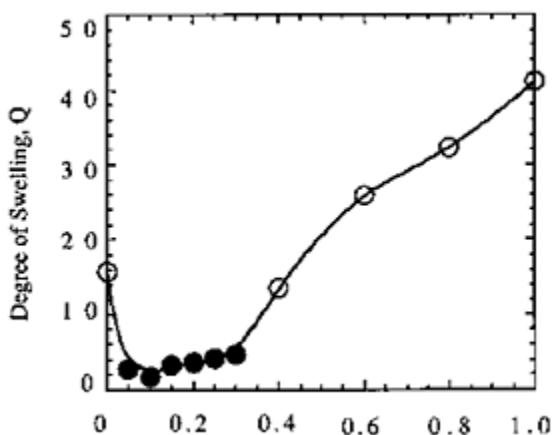
In high-resolution solid-state  $^{13}\text{C}$  NMR experiments on cross-linked poly-( $\gamma$ -methyl L-glutamate) (PMLG) gel, we have elucidated that the conformation of cross-linked PMLG with a mixture of chloroform ( $\text{CHCl}_3$ ) and trifluoroacetic acid (TFA) largely depends on the solvent composition [18, 66]. The increase of the volume fraction of TFA ( $f_{\text{TFA}}$ ) in a mixture of  $\text{CHCl}_3$  and TFA induces the  $\alpha$ -helix-random coil transition of the main chain of cross-linked PMLG.  $\text{CHCl}_3$  and TFA are sometimes so-called helix and coil solvents, respectively. It is significant for gel science in polypeptide gel systems to elucidate how the translational motion of these solvents is affected when the main chain of PMLG changes from the  $\alpha$ -helix form to the random coil form. In such system, the diffusion of solvent molecules contained in the polypeptide gel system strongly depends on the dynamics of polypeptide chains. As demonstrated above, the PFGSE NMR method gives very useful information about the diffusion process of the polymer gel system. From such a background, the dynamics of solvents in cross-linked PMLG gel with a mixture of  $\text{CHCl}_3$  and TFA ongoing from the  $\alpha$ -helix form to the random coil form through the diffusion coefficients were determined by PFGSE  $^1\text{H}$  NMR.

Spin-echo  $^1\text{H}$  NMR spectra of a PMLG gel containing a mixture of  $\text{CHCl}_3$  and TFA with  $f_{\text{TFA}}=0.10$  were measured as a function of magnetic field gradient pulse length ( $\delta$ ). In the spectra (not shown here), the two intense peaks at 6.9 and 9.1 ppm were straightforwardly assigned to the  $\text{CHCl}_3$  and TFA protons, respectively. The  $^1\text{H}$  chemical shift of  $\text{CHCl}_3$  almost does not change with an increase in TFA content, but, on the other hand, the  $^1\text{H}$  chemical shift of TFA is observed at 8.7 to 10.5 ppm with an increase in

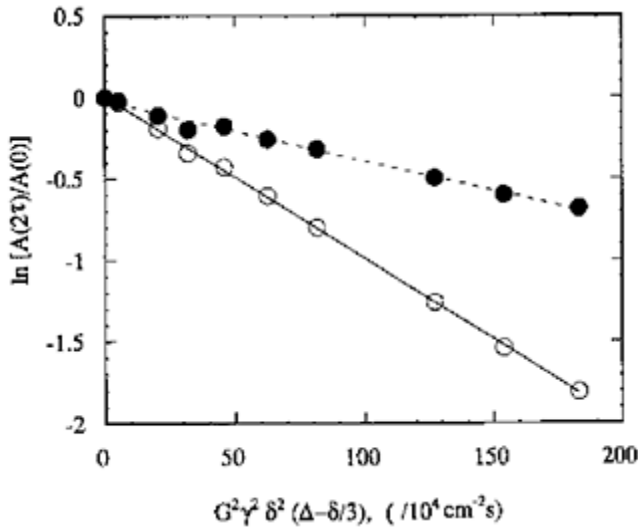
TFA content.

Figure 30 shows the degree of swelling ( $Q$ ) of PMLG gel in a mixture of TFA/  $\text{CHCl}_3$  against the TFA content ( $f_{\text{TFA}}$ : the volume fraction of TFA). A PMLG gel in  $\text{CHCl}_3$  is transparent. The degree of swelling decreases with increasing the TFA content from  $f_{\text{TFA}}=0.05$ –0.30 whereas the gel becomes turbid. In the TFA content from  $f_{\text{TFA}}=0.30$ –1.0, the degree of swelling of the PMLG gel increases with increasing the TFA content; meanwhile the gel becomes transparent again. This shows that the main chain of the PMLG gel underwent a conformation transition from  $\alpha$ -helix form to the random coil form. The mixture solvent with  $f_{\text{TFA}}=0.05$ –0.30 acts as a poor solvent to the random coil form; then the inhomogeneous aggregation occurs in the gel system. The mixture solvent with higher TFA content of  $f_{\text{TFA}}=0.30$ –1.0 acts as a good solvent to the random coil form.

The diffusion coefficients of TFA and  $\text{CHCl}_3$  contained in a PMLG gel were determined by the PFGSE  $^1\text{H}$  NMR method at 303 K varying the TFA content contained. The decays of TFA and  $\text{CHCl}_3$  lie on a straight line as shown in Figure 31. This means that the individual diffusants of TFA and  $\text{CHCl}_3$  in the PMLG gel have a single diffusion component during the observation time. From the slope of the intensity decay, the diffusion coefficients for TFA ( $D_{\text{TFA}}$ ) and  $\text{CHCl}_3$  ( $D_{\text{CHCl}_3}$ )



**FIG. 30** Dependence of the degree of swelling ( $Q$ ) of PMLG gel on the TFA content in a mixture of  $\text{CHCl}_3$  and TFA. (○), the gel is transparent (●), the gel is turbid.



**FIG. 31** Diffusional spin-echo attenuation of TFA (●) and CHCl<sub>3</sub> (○) in PMLG gel with  $f_{\text{TFA}}=0.10$  by varying field gradient pulse duration ( $\Delta$ ). From the slopes of the solid and dash straight line,  $D_{\text{TFA}}$  and  $D_{\text{CHCl}_3}$  were obtained to be  $0.37 \times 10^{-5}$  and  $1.00 \times 10^{-5} \text{ cm}^2 \text{ s}^{-1}$ , respectively.

can be determined by Eq. (1) to be  $0.37 \times 10^{-5}$  and  $1.00 \times 10^{-5} \text{ cm}^2 \text{ s}^{-1}$ , respectively. The diffusion coefficient of TFA is smaller than that of CHCl<sub>3</sub>. This means that the translational motion of TFA is more restrained by the PMLG network compared with CHCl<sub>3</sub>. The diffusion coefficients of TFA and CHCl<sub>3</sub> in PMLG gel were plotted against the TFA content in a mixture of TFA/CHCl<sub>3</sub> as shown in Figure 32. As seen from Figure 32  $D_{\text{CHCl}_3}$  largely decreases in the  $f_{\text{TFA}}$  range from 0 to 0.05. This tendency is very similar to that of the degree of swelling in Figure 30. This shows that the conformation of the PMLG gel changed from the  $\alpha$ -helix to the random coil on increasing the TFA content. The transition from the  $\alpha$ -helix form to the random coil form leads to the shrinkage of the PMLG gel owing to the decrease of the network size and leads to the decrease of diffusion coefficients of CHCl<sub>3</sub>. In the  $f_{\text{TFA}}$  range from 0.05 to 0.20,  $D_{\text{TFA}}$  and  $D_{\text{CHCl}_3}$  increase, although the degree of swelling is almost constant. It can be said that in the  $f_{\text{TFA}}$  range the helix-coil transition leads to such diffusional behaviors. After the helix-coil transition, the molecular motion of TFA and CHCl<sub>3</sub> is increased with an increase in  $f_{\text{TFA}}$ .

The plots of  $\ln D$  for TFA and CHCl<sub>3</sub> in PMLG gel are shown against the inverse of absolute temperature ( $1/T$ ) in Figure 33. The diffusion coefficients can be expressed against temperature as an Arrhenius-like equation:

$$D = \frac{a_0^2}{\tau_0} \exp\left(\frac{-E_a}{kT}\right) \quad (34)$$

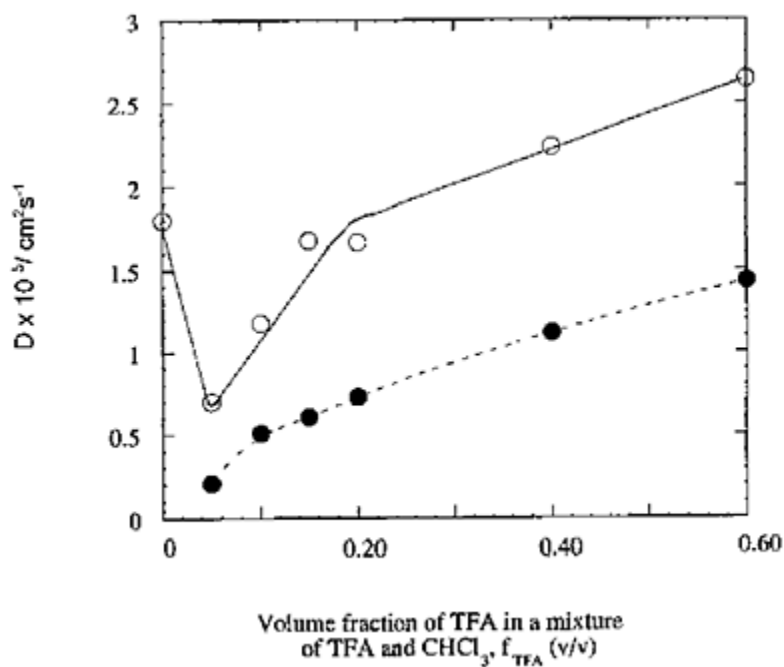


**FIG. 32** The plot of the diffusion coefficients for TFA (●) and  $\text{CHCl}_3$  (○) in PMLG gel against the TFA content in a mixture of TFA and  $\text{CHCl}_3$ .

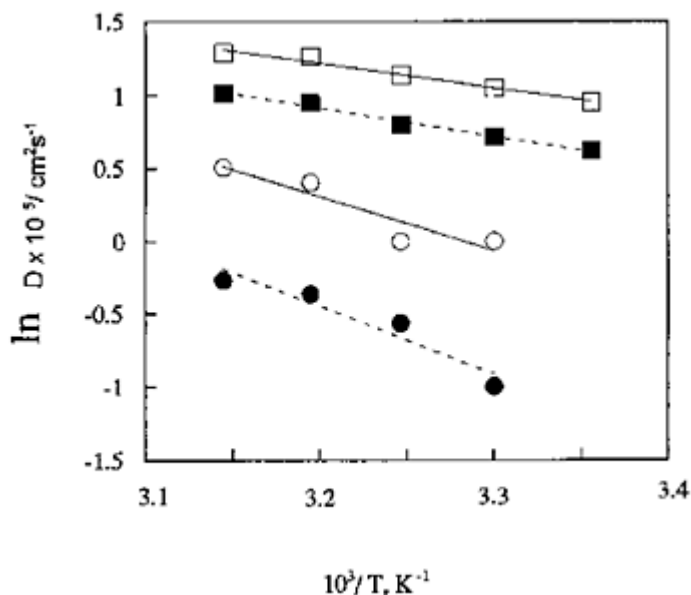


**FIG. 33** The plots of  $\ln D$  for TFA and  $\text{CHCl}_3$  in PMLG gel are shown against the inverse of absolute temperature ( $1/T$ ) at  $f_{\text{TFA}}=0.10$ . In PMLG gel system, (●) for TFA and (○) for  $\text{CHCl}_3$ , and in a mixture solvent of  $\text{CHCl}_3$  and TFA, (■) for TFA and (□) for  $\text{CHCl}_3$ .

where  $a_0$  is the interval of the diffusant,  $\tau_0$  the time of diffusing,  $k$  the Boltzmann constant, and  $E_a$  an activation energy for diffusion. From the slope for such plots, the activation energies for TFA and  $\text{CHCl}_3$  were obtained to be 38.7 and 30.5 kJ/mol, respectively. On the other hand, the activation energies for pure TFA and  $\text{CHCl}_3$  were obtained to be 16.2 and 13.5 kJ/mol, respectively. From these results in the gel system, it can be said that intermolecular interactions between solvent and polypeptide network are strong enough to restrain the translational motion.

## 2. Diffusion Behavior of Solvent and Probe Molecules in Highly Oriented Polypeptide Gels

As is well known, poly( $\gamma$ -benzyl L-glutamate) (PBLG) forms the lyotropic liquid crystalline state in good solvents such as, for example, dichloromethane, dioxane, and chloroform, and when the PBLG liquid crystalline solution is placed in a strong magnetic field, the main chain can be oriented in the direction of the magnetic field [67–76]. The molecular motion of solvent and PBLG in the liquid crystalline solution is considerably influenced by intermolecular interactions. By reacting highly oriented PBLG chains with a cross linker in a strong magnetic field, a cross-linked PBLG gel with the highly oriented  $\alpha$ -helical chains is expected to be prepared. We have been attracted to the problem of how is the diffusional process of solvent and  $n$ -alkanes with relatively extended



conformation in the gel with anisotropic structure because of the fact that *n*-alkanes are basic molecules for understanding structure and dynamics of linear polymer chains [6, 77, 78].

According to the work on the orientation of *n*-alkanes in a PBLG liquid crystalline solution by  $^1\text{H}$  NMR [79], in which PBL chains are highly oriented, *n*-alkanes being guest molecules are highly oriented to the magnetic field of an NMR magnet with the relatively extended conformation along the  $\alpha$ -helical PBLG chains. Also, as elucidated by the NMR method, *n*-alkanes in the rotator phase take on extended conformations and which are fastly rotating around the long axis [8,9], and the diffusion coefficients for the direction in parallel and perpendicular to the long axis are different from each other [80–83]. Samulski et al. [84] and Abe et al. [85] have studied conformational behaviors of deuterated *n*-alkenes in PBLG liquid crystalline solution by conformational analysis combining the rotational isomeric state model and  $^2\text{H}$  NMR spectral analysis. From these studies, the orientational behaviors of guest alkanes in a liquid crystalline solution have been clarified.

From such a background, cross linked PBLG gels with highly oriented  $\alpha$ -helical chains are prepared, and the diffusion coefficient of the solvent and *n*-alkanes in the gel for the directions parallel and perpendicular to the  $\alpha$ -helical PBLG axis by using the PFGSE  $^1\text{H}$  NMR method with a strong field gradient strength has been elucidated. In the liquid crystalline and gel states, the orientation of the PBLG chains can be determined by using high-resolution solid-state  $^{13}\text{C}$  NMR.

The poly( $\gamma$ -benzyl L-glutamate) (PBLG) ( $M_w=130,000$ ) used in this work was supplied by Ajinomoto Co. Ltd. Two kinds of samples were prepared, one is 25 wt% PBLG/1,4-dioxane lyotropic liquid crystalline solution/gel and the other is 25 wt% PBLG/*n*-alkanes/1,4-dioxane lyotropic liquid crystalline solution/gel. PBLG in the lyotropic liquid crystalline solution was cross linked with diaminoethane (20%/monomer unit) as a cross linker by the ester-amide exchange reaction to prepare its gel in the magnetic field (10.5T) used for the NMR [86, 87]. In the magnetic field, PBLG chains are highly oriented. When the cross linker was added to the PBLG solution in a NMR tube, the NMR tube was spun for several minutes in the NMR probe in order to homogenize the cross linker in the PBLC solution. Then the highly oriented PBLG gel obtained was swollen in 1,4-dioxane to remove the cross linker.

The diffusion coefficients of 1,4-dioxane as solvent and *n*-alkanes (*n*-pentane and *n*-decane) as probe molecules contained in the oriented PBLG gel were determined by the PFGSE  $^1\text{H}$  NMR method at 303 K. The experiments were carried out under two conditions: (1) the PBLG  $\alpha$ -helix axis is parallel to the magnetic field ( $D_{\parallel}$ ) and (2) the PBLG  $\alpha$ -helix axis is perpendicular to the magnetic field ( $D_{\perp}$ ). In the PFGSE system designed, the direction of the field gradient pulse cannot be changed, because the NMR probe system is designed such that it can generate a very strong field gradient. However, it can be said that during this experimental time, the measurement time of the PFGSE method is very short for obtaining the proton signal. The orientations of the PBLG chains in the gel sample do not change with a change of the orientation of the gel sample with respect to the magnetic field. Some crossed polarized microscopic photographs of these gels were taken. From these, it is clear that the PBLG chains in the polypeptide gel are highly oriented.

For the peak of 1,4-dioxane and n-alkanes in the oriented PBLG gel, plots of  $\ln[A(\delta)/A(0)]$  against  $\gamma^2 G^2 \delta^2 (\Delta - \delta/3)$  are a straight line (not shown). This shows that the diffusant, 1,4-dioxane and n-alkanes in the gel are single-component diffusion during the observation time. Then the diffusion coefficients,  $D$ , of 1,4-dioxane and n-alkanes in the oriented PBLG gel under the above-mentioned condition were determined from the slope of the straight line, and also the diffusion coefficients of those molecules in their neat liquid and in 25% PBLG liquid crystalline solution were determined. The determined diffusion coefficients,  $D$ , of 1,4-dioxane and n-alkanes in the above states are shown in Table 2. The diffusion coefficient of 1,4-dioxane in the neat liquid is  $1.06 \times 10^{-5} \text{ cm}^2 \text{ s}^{-1}$ , which is much larger than that in the 25 wt% PBLG/1,4-dioxane liquid crystalline solution that is  $5.8 \times 10^{-6} \text{ cm}^2 \text{ s}^{-1}$ . This means that in the liquid crystalline solution, the translational motion of the 1,4-dioxane molecule was strongly restrained by the interaction between the PBLG chains.

**TABLE 2** Determined-diffusion Coefficients of Dioxane and n-Alkanes in PBLG/1,4-Dioxane/n-Alkane Gel with Highly Oriented PBLG Chains, in the PBLG/1,4-Dioxane/ n-Alkane Liquid Crystalline solution, and Pure Liquid State at 30°C

Molecules	Diffusion coefficient $D \times 10^5 / \text{cm}^2 \text{ s}^{-1}$			
	Pure liquid	Liquid crystalline state	Gel state	
			$D_{\parallel}$	$D_{\perp} (D_{\parallel} + 2D_{\perp})/3$
1,4-Dioxane	1.06	0.58	0.540.45	0.48
n-Pentane (n-C <sub>5</sub> H <sub>12</sub> )	5.10	1.15	0.840.64	0.71
n-Decane (n-C <sub>10</sub> H <sub>22</sub> )	0.96	0.69	0.610.50	0.54

On the other hand, the diffusion coefficients of 1,4-dioxane in the oriented PBLG gels in which the PBLG chains orient parallel and perpendicular to the applied magnetic field are smaller than that in the PBLG/1,4-dioxane liquid crystalline solution. This means that the translational motion of 1,4-dioxane through the PBLG networks in the gel is restrained much more strongly than that in the liquid crystalline solution.

Next we are concerned with the diffusion process of the 1,4-dioxane molecule in the oriented PBLG gel. We obtained  $D_{\parallel}$  and  $D_{\perp}$  to be  $5.4 \times 10^{-6}$  and  $4.5 \times 10^{-6} \text{ cm}^2 \text{ s}^{-1}$ , respectively. This difference is significant because the experimental error for the  $D$  value is estimated to be less than 5%. It is shown that the diffusion coefficient of the 1,4-dioxane molecule along the  $\alpha$ -helical PBLG axis is significantly larger than that perpendicular to the  $\alpha$ -helical PBLG axis. The diffusion process is thus anisotropic. This is because as the degree of the cross linking is not so high, the obstacle for the translational displacement of 1,4-dioxane in the direction parallel to the  $\alpha$ -helical axis is much larger than that in the direction perpendicular to the  $\alpha$ -helical axis. From these experimental results in the oriented PBLG gel system, it can be said that the solvent dynamics is significantly influenced by the microstructure of the network polypeptide chains in the gel.

The diffusion coefficients of n-pentane and n-decane in the pure liquid state as measured by the PFGSE  $^1\text{H}$  NMR method are  $5.1 \times 10^{-5}$  and  $9.6 \times 10^{-6} \text{ cm}^2 \text{ s}^{-1}$ , respectively. The diffusion coefficient of n-pentane is much larger than that of n-decane. In the liquid crystalline state, the diffusion coefficients of n-pentane and n-decane are  $1.15 \times 10^{-5}$  and  $0.69 \times 10^{-5} \text{ cm}^2 \text{ s}^{-1}$ , respectively. It was found that the diffusion coefficients of these molecules are largely reduced in the liquid crystalline solution as compared with those in the pure liquid state.

The  $D_{\parallel}$  values of n-pentane and n-decane are  $0.84 \times 10^{-5}$  and  $0.61 \times 10^{-5} \text{ cm}^2 \text{ s}^{-1}$ , respectively. On the other hand, the  $D$  values of n-pentane and n-decane are  $0.64 \times 10^{-5}$  and  $0.50 \times 10^{-5} \text{ cm}^2 \text{ s}^{-1}$ , respectively. It is apparent that the diffusions of these molecules in parallel to the PBLG helical chain in the network are significantly faster than those perpendicular to the PBLG helical chain in the network, that is  $D_{\parallel} > D_{\perp}$ , and so the diffusion is anisotropic as expected.

As reported previously [82, 83], the diffusion coefficients of n- $\text{C}_{24}\text{H}_{50}$  were measured in a lamellar single crystal at a temperature of 49 in the rotator phase in the directions parallel and perpendicular to the long chain axis, which take an *all-trans* zigzag conformation. Then, the determined  $D_{\perp}$  and  $D_{\parallel}$  values were  $1.64 \times 10^{-6}$  and  $2.70 \times 10^{-6} \text{ cm}^2 \text{ s}^{-1}$ , respectively, and so  $D_{\perp} < D_{\parallel}$ . This result is opposite to the above result in the highly oriented gel. This means that the translational migration of extended n-alkane chains is largely interrupted by networks, which is different from the case of the diffusion in the rotator phase of pure n-alkane.

The measured diffusion coefficients,  $D$ , for the gel system with highly oriented chains can be calculated from

$$D = \cos^2 \theta D_{\parallel} + \sin^2 \theta D_{\perp} \quad (35)$$

for molecular chains oriented at the magnetic angle  $\sin^2 \theta = 2/3$ . Thus, we have

$$D = \frac{1}{3D_{\perp}} + \frac{2}{3D_{\parallel}} = \frac{(D_{\parallel} + 2D_{\perp})}{3} \quad (36)$$

as calculated by using the  $D_{\parallel}$  and  $D_{\perp}$  values may be compared with the diffusion coefficients in pure liquid state and liquid crystalline state. The  $(D_{\parallel} + 2D_{\perp})/3$  values of 1,4-dioxane, n-pentane and n-decane are  $0.48 \times 10^{-5}$ ,  $0.71 \times 10^{-5}$ , and  $0.54 \times 10^{-5} \text{ cm}^2 \text{ s}^{-1}$ , respectively. These averaged diffusion coefficients are much smaller than those in the pure liquid state and the liquid crystalline state. This means that in the gel system, the translational motion of these diffusants was more strongly restrained with interactions by the highly oriented PBLG chain network. Further, it can be said that an increase in the number of carbons of n-alkanes leads to the reduction of the diffusion coefficients. As the probe molecules move through the gel network, the diffusion of probe molecules is strongly influenced by the size of the probe molecules themselves.

### III. MACROSCOPIC STRUCTURE OF POLYMER GELS

#### A. Approaches by NMR Imaging

NMR imaging has been widely used for obtaining information on the spatial distribution of the spin density, the relaxation times, and the diffusion coefficient in living systems containing mobile components such as water (89, 90). The NMR imaging technique has been demonstrated to be a powerful means to characterize the spatial and macroscopic structures and dynamics of polymer samples [23, 91]. This technique may break new ground in characterizing and understanding polymer gels.

##### 1. Diffusion in Gels

Polymer gels are microscopically liquid and mobile components of them such as solvents, counterions, and dissolved molecules, and the network polymer migrates in them. It is important to study the diffusion process in gels to understand its dynamics, such as structural changes, mobility, interaction between molecules, and binding phenomena. The diffusion coefficients of mobile components in the gel samples are studied by the PGSE techniques. The gels, unlike solution samples, are heterogeneous systems microscopically and/or macroscopically and there is spatial distribution of chemical and physical properties. There may be distribution of the diffusion coefficient of mobile components in the gel. It is significant to study the spatial distribution of diffusion coefficients in the gel by NMR imaging. In this section, the diffusion process in the gel samples studied by NMR imaging are described.

The distribution of self-diffusion coefficient of methanol and acetone imbibed in cross-linked PMMA was measured [92, 93]. Dry PMMA rods were immersed in methanol or acetone at 30°C and images of the solvents absorbed in the PMMA were acquired with the STEAM. The self-diffusion coefficient of methanol in the swollen PMMA immersed for 20 days was calculated from the images obtained with changing the pulsed field gradient. The distribution of the self-diffusion coefficient of methanol in the sample were visualized as a two-dimensional image and the coefficient values were obtained from the image. The region within 100 mm of the glassy core of the PMMA exhibits a self-diffusion coefficient of  $(3.2 \pm 0.9) \times 10^{-7} \text{ cm}^2 \text{ s}^{-1}$  and the outer region of the swollen gel exhibits  $(9.2 \pm 0.9) \times 10^{-7} \text{ cm}^2 \text{ s}^{-1}$ . The self-diffusion coefficient of methanol measured by tracer technique at 30°C is  $2.5 \times 10^{-5} \text{ cm}^2 \text{ s}^{-1}$  [94]. The coefficient values for the methanol imbibed in the PMMA network polymer is smaller than that for the free state and the motion is strongly restrained. The STEAM method is suitable to measure a self-diffusion coefficient of such small values. It has been reported that the self-diffusion of methanol in the swollen PMMA shows case II-type characteristics [95–97]. The case II diffusion is characterized by a sharp diffusion front that is the interface between the swollen and the dry regions and constant solvent concentration in the swollen region. However, the results from the NMR imaging showed that self-diffusion coefficient of methanol is smaller near the glassy core of the PMMA and is larger at the outer region of the swollen gel. The investigations explained that the decreases in solvent self-diffusion coefficients

result from the influence of the polymer motions on the solvent mobility.

## 2. Stress-Strain Process in a PMAA Gel

Chemical reactions are caused in polymer gels by the mechanical energy applied. It was reported that ionization of the carboxylic groups of a water-swollen PMAA gel [98] and a PAA gel [99] occurs upon application of stress. These processes are energy conversion from a mechanical to a chemical one. Such interesting phenomena may come from the viscoelastic characteristics of the gels that are made up of an elastic network polymer and a liquid solvent. It is important to study the effect of the stress applied on a gel to understand its characteristics.

The spatial distribution of the  $^1\text{H}$  spin density and the  $^1\text{H}$   $T_2$  of water molecules in cross-linked water-swollen PMAA gel with applying stress were studied by  $^1\text{H}$  NMR imaging [100]. A cylindrical PMAA gel sample with the diameter of 15.0 mm and a height of 5.3 mm at the degree of swelling,  $Q=22$  was placed in a cylindrical sealed glass cell. The stress on the gel sample was applied with a glass piston, the top of which was circular with a diameter of 7.7 mm. Throughout the experiments, no  $^1\text{H}$  signals of the network polymer of the PMAA gel swollen with  $\text{D}_2\text{O}$  ( $Q=22$ ) was not able to be detected by the spin warp imaging owing to its short  $T_2$  and great dipolar broadening. On the other hand,  $^1\text{H}$  signals of water contained in the gel were successfully observed owing to its fast molecular motion.

Figure 34 shows the observed transverse  $^1\text{H}$  spin density image of water in the PMAA gel at  $Q=22$  without stress (Fig. 34a) and with stress of 4.8 kPa (Fig. 34a, c), where the direction of the cross-sectional profile is perpendicular to the direction of the stress applied. Figure 34c is the image sliced away from the top surface of the gel compared with Figure 34b. It is more convenient to show this by means of colors, but in this chapter, all of the NMR imaging patterns are in black and white. Thus, for example, the blue color is represented by black. The magnitude of  $^1\text{H}$  spin density is differentiated by 256 steps, and then the observed  $^1\text{H}$  spin density image is represented by colors from white, representing the highest density, to dark blue, representing the lowest density. The intensity scale indicated by colors is also shown in Figure 34.

The  $^1\text{H}$  spin density distribution of the obtained image of Figure 34a is approximately homogeneous. This shows that the water molecules which undergo fast molecular motion are homogeneously distributed in the gel. The blue circular portion in Figure 34b shows the compressed region to which stress is applied. As seen from Figure 34c, there are white regions at the top and the bottom of the image, and colored half-circular stripes appear toward the compressed region as white light pink, red-orange, bright orange, yellow. The yellow region appears in the compressed region and the blue one appears at the periphery of the gel. Further, the  $^1\text{H}$  spin density pattern as shown in Figure 34c is asymmetrical, and

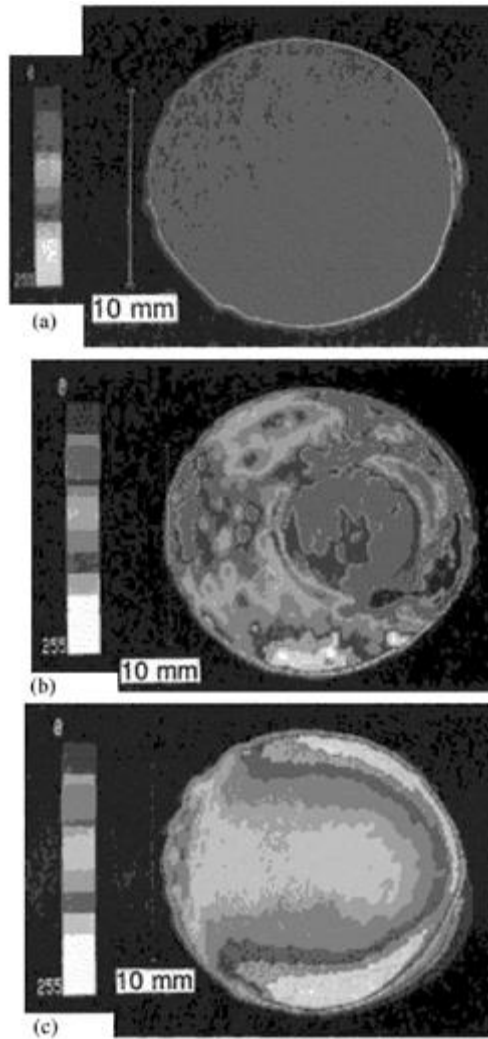


**FIG. 34** Observed transverse  $^1\text{H}$  spin density image for water in the PMAA gel ( $Q=22$ ). (a) Without stress at a depth of 1.9 mm from the top surface; (b) with stress of 4.8 kPa at depth of 1.0 mm; (c) with stress of 4.8 kPa at depth of 1.9 mm. The magnitude of the  $^1\text{H}$  spin density is differentiated by the color signal variation.

the  $^1\text{H}$  spin density of water in the right-hand part of the image (the white region) is higher than that in the left-hand one (the yellow and green regions). The fact that the stress was applied away from the center of the gel induces such an asymmetrical pattern.

The  $^1\text{H}$  spin density gradient in the gel is induced by stress, and the density of water molecules with higher molecular motion in the compressed region is lower than that in

the uncompressed region. On the other hand, the population of water molecules became higher in the white region and the uncompressed part of the top surface of the PMAA gel rose up slightly owing to deformation of the gel by the stress. This shows that water molecules excluded from the compressed region migrate to the surrounding region.

The  $^1\text{H}$   $T_2$  for water in the PMAA gel ( $Q=89$ ) compressed homogeneously was measured by means of 500-MHz  $^1\text{H}$  pulse NMR using the CPMG method. The obtained  $^1\text{H}$   $T_2$  values are plotted against the strength of the applied stress as shown in Figure 35. This shows that the  $T_2$  decreases with increasing stress and the  $T_2$  value under a stress of 17.6 kPa is half the value under no stress. The molecular motion of water in the PMAA gel is restrained by the strain induced by the stress.

Figure 36a-h shows coronal  $^1\text{H}$   $T_2$ -enhanced images of water in the PMAA gel at  $Q=22$ , where the word *coronal* means that the cross-sectional profile is parallel to the direction of the applied stress. In these images, the relative magnitude of the  $^1\text{H}$   $T_2$  value of the water is represented by colors. The white color shows the longest  $T_2$  value and dark blue the shortest one according to the color scale as shown in the Figure 36. Although the  $^1\text{H}$   $T_2$  distribution was almost homogeneous in the gel under no stress, a gradient pattern in the  $T_2$  distribution was obtained in the gel under a stress of 4.8 kPa, where the stress was applied away from the center of the gel. The  $T_2$  value of the top surface is short as indicated by dark blue or blue. The color in the compressed region changes from the top of the gel toward the bottom as dark blue, blue-green, light green, yellowish green, yellow, bright orange, orange, red-orange, bright orange-yellow, blue, dark blue. This indicates that the  $^1\text{H}$   $T_2$  value of water in the compressed region increases from the top surface of the gel toward the inner part and decreases from the inner part toward the bottom. The  $^1\text{H}$   $T_2$  value increases from

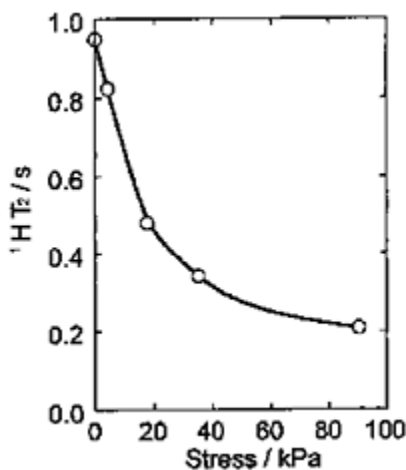


**FIG. 35** Dependence of the  $^1\text{H}$   $T_2$  for water in the PMAA gel ( $Q=89$ ) on the applied stress. The  $^1\text{H}$   $T_2$  was measured by the CPMG method.

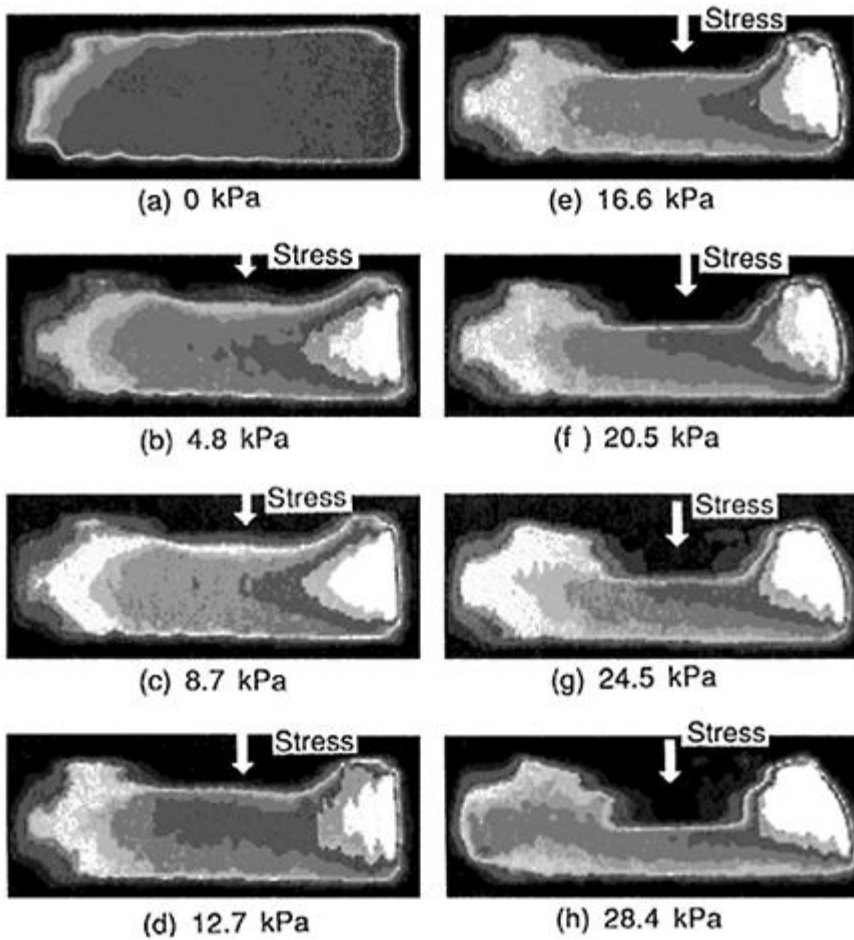


**FIG. 36** Observed coronal  $^1\text{H}$   $T_2$  enhanced image for the PMAA gel ( $Q=22$ ) as a function of stress.

the left end of the gel to the right end as indicated by dark blue, blue, green, light green, yellowish green, yellow, bright orange, orange, red, pink, light pink, and white. As seen from the results, the propagation of the strain in the gel can be observed as the  $T_2$  distribution.

The gradient pattern of spatial distribution on  $T_2$  changes with increasing stress as shown in Figure 36a–h. The red and orange regions in the compressed region become narrow with increasing stress, and the bright orange and yellow regions become wide. The white region becomes wide with an increase of the strength of stress from 12.7 to 28.4 kPa. The molecular motion of water molecules in the compressed region is more strongly restrained with an increase in stress. Further, in the uncompressed region (the right and left end parts of the gel), the population of water molecules that undergo



relatively fast molecular motion increases with increasing stress. This shows that the migration of water in the gel is increased with an increase of stress, and the difference in the molecular motion of water in between the compressed and the uncompressed regions becomes large.

The imaging study revealed that the spatial distribution of density and molecular motion of water in the PMAA gel is changed by the mechanical stress applied. These results demonstrate that the NMR imaging technique is useful to study the response of the gels to stimulation spatially.

### 3. Shrinkage Process of a PMAA Gel Under DC Electric Field

Water-swollen cross-linked polyelectrolyte gels deform by the application of an electric field [1, 2]. From the first observation of electric field-induced deformation for a polyelectrolyte gel [101], the phenomena termed chemomechanical reactions were studied from the fundamental or applicable point of view by many researchers. Although a great deal of effort has been made in studying the mechanism, it seems that a fundamental approach at the molecular level for the gel has rarely been taken. Therefore, it is important to clarify the structure and dynamics of small molecules, such as water in the gels, through microscopic observation at the molecular level.

The spatial distribution of  $^1\text{H}$  spin density and  $^1\text{H}$   $T_2$  of water molecules in a PMAA gel contracted under an electric field was studied to clarify the behavior of water molecules in the gel during the shrinkage process [102]. The application of an electric field to the PMAA gel leads to shrinkage of it with exhaustion of water. Shrinkage of the gel close to the positive electrode is larger than that of the negative one. The edge of the gel in contact with the negative electrode is swollen with time. Figure 37 shows the elapsed-time ( $T_e$ ) dependence for the shape and the spatial distribution of  $^1\text{H}$  spin density of the PMAA gel (diameter of 8.0 mm and a length of 25.0 mm) with and without the application of an electric field.

The  $^1\text{H}$  spin density images showing gradient at  $T_e=0$  represent there is a distribution gradient of the water in both gels at first. The density of water molecules increases going from the right end of the gels to the left as indicated by blue, green, light green, yellowish green, yellow, bright orange, orange, red, and white. The region occupied by yellow and red colors in the gel under an electric field of 3 V becomes large from left to right with time. At  $T_e=20$  min, the yellow region in the images of the both gels increases. The change in the magnitude of  $^1\text{H}$  spin density in going from the positive electrode to the negative electrode are indicated by white, red, orange, yellow, and white. At  $T_e=240$  min, the red region in the center area of the gel with a 3 V direct

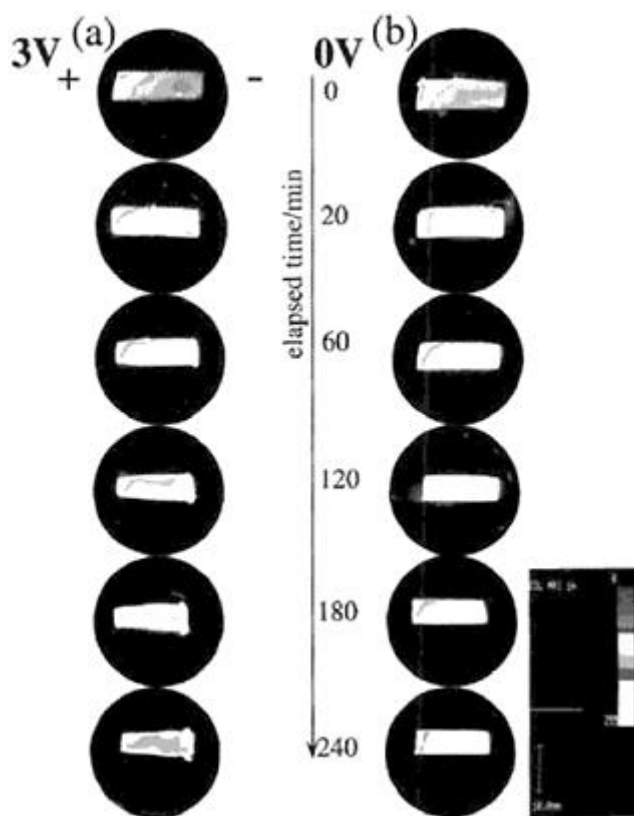


**FIG. 37** Elapsed-time dependence of images for the  $^1\text{H}$  spin density distribution of the PMAA gel ( $Q=36$ ) with (a) and without (b) the application of an electric field (3 V DC).

current (DC) electric field applied becomes large. The  $^1\text{H}$  spin density changes in going from the positive electrode to the negative electrode as indicated by white, red, orange, and white. In order to analyze clearly the  $^1\text{H}$  spin density in detail, the images for the  $^1\text{H}$  spin density distributions of the PMAA gel with and without the application of 3 V DC of an electric field are represented by a three-dimensional profile as shown in Figure 38. Although water contained in the gel without the application of an electric field decreases homogeneously in the gel with time, water in the gel under 3 V DC of electric field decreases and migrates from the positive side to the negative one. These results prove the hypothesis that water molecules in a polyelectrolyte gel migrate from the positive side to negative one with protonated water molecules under DC electric field based on an electroosmosis. The water migration is accompanied by shrinkage of the gel from the positive side and swelling at the edge of the gel of the negative side.

It is important to have information about the  $^1\text{H}$   $T_2$  value of water molecules in the PMAA gel in order to analyze the dynamic behavior of water molecules

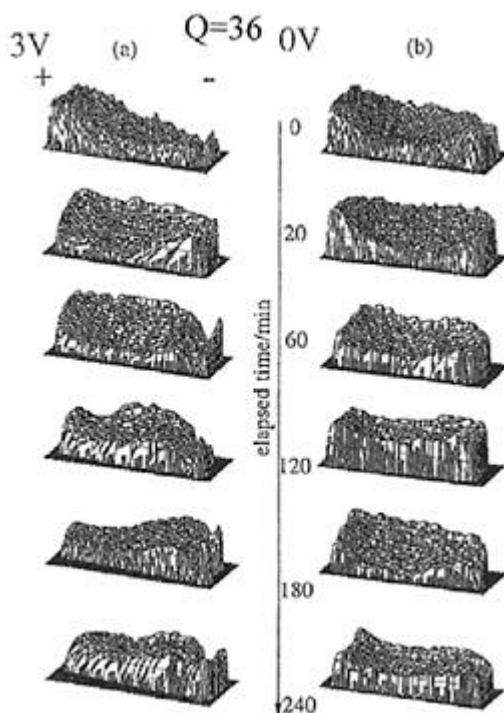


**FIG. 38** Three-dimensional histograms for the  $^1\text{H}$  spin density distribution of the PMAA gel with (a) and without (b) the application of an electric field.

under an electric field. The  $T_2$  distributions for the gel with and without the application of an electric field were measured. The  $T_2$  image experiment on the gel without the application of an electric field becomes reference data to clarify the shrinkage process of the gel with the application of an electric field. Figure 39 shows the  $^1\text{H}$   $T_2$  distribution images for the transverse slice of the PMAA gel under 3 V DC and under 0 V DC at elapsed time  $T_e=0$  h (initial state) and 4 h after the application of an electric field, where the figure shows  $T_2$  values for the part indicated by an open circle in the gel. Little change of the  $T_2$  value of water molecules in the gel (0V) is observed during the image experiment, whereas significant change in the  $^1\text{H}$   $T_2$  value of water molecules in the gel (3V) was observed during the experiment. The  $^1\text{H}$   $T_2$  values of water molecules around the positive side are decreased to a larger extent than those around the negative one by the application of an electric field. This means that the molecular motion of water molecules in the gel near the positive electrode was strongly restrained. The elapsed-time dependence of the  $^1\text{H}$   $T_2$  distribution change in the gel under the application of an electric field was measured as shown in Figure 40. Figure 40 shows that the molecular motion of water molecules in the gel is restrained with elapsed time as seen from the observation of the decrease of the  $^1\text{H}$   $T_2$  value.

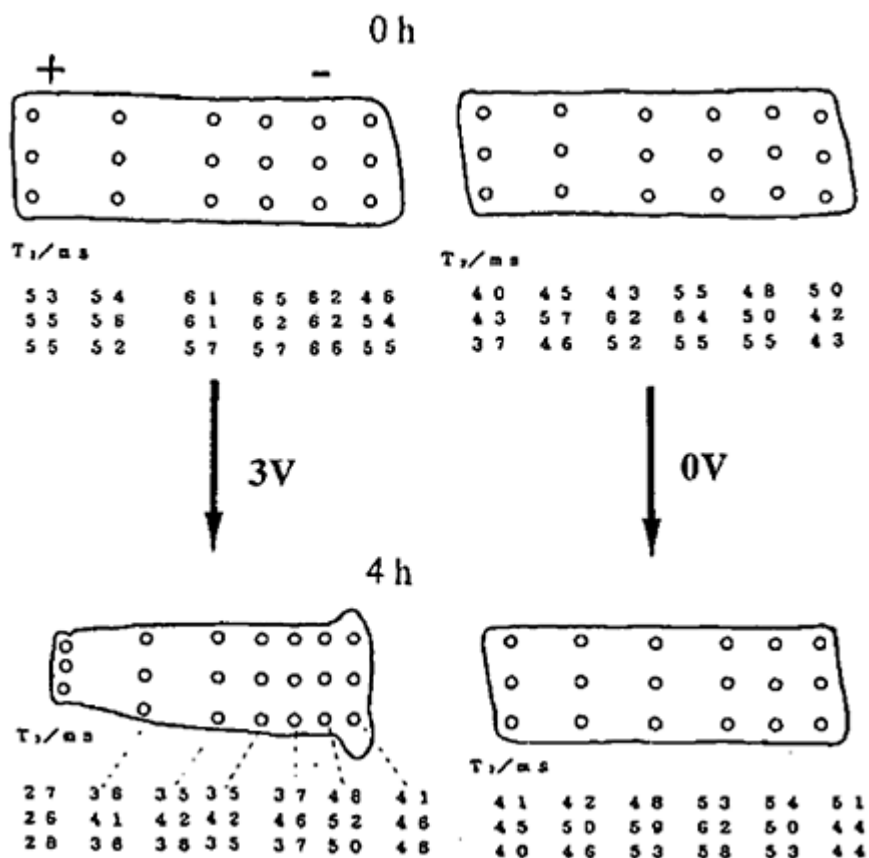
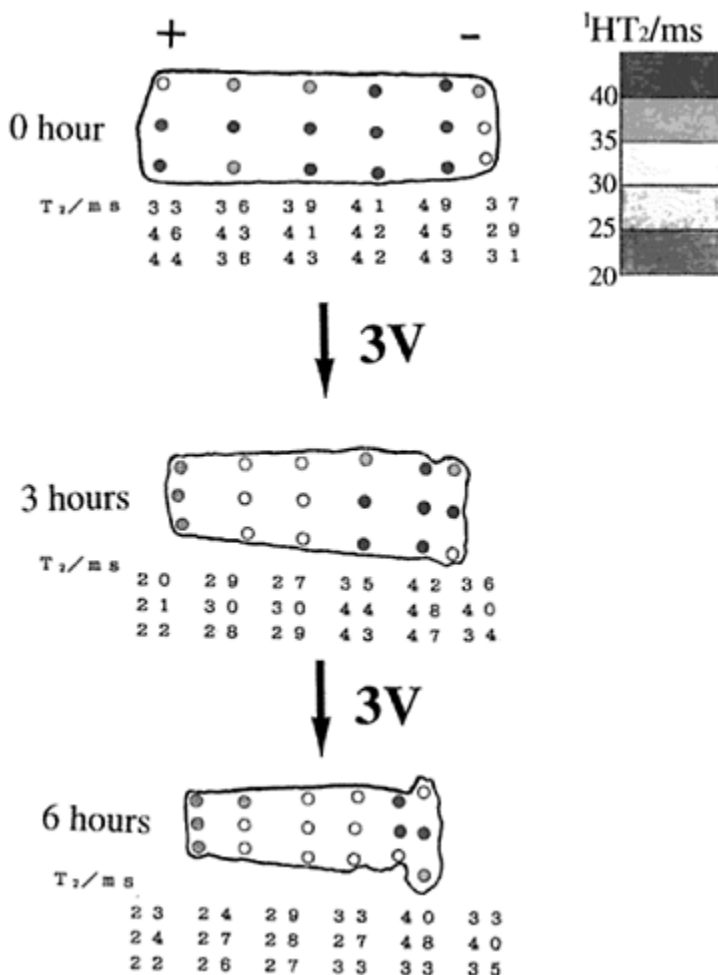


FIG. 39  $^1\text{H}$   $T_2$  distribution for transverse slice of the PMAA gel ( $Q=36$ ) at  $T_e=0$  h and at 4 h with and without the application of an electric field (3 V DC).

From these results, the profile of the  $T_2$  distribution image can be divided into four regions in a manner similar to the  $^1\text{H}$  spin density distribution image. For convenience, a rough schematic representation for the  $^1\text{H}$   $T_2$  distribution image is represented in Figure 41. Water molecules in the region with large shrinkage in the gel shows low mobility, but at region 3 in the Figure 41, the mobility of water molecules is high, although the density of network is high. These results are interesting from the viewpoint of the structure and dynamics of the gel, which show the network polymer in the gel under an electric field may form a complicated structure of which interaction with water molecules is different from that of normal linear polymer.



**FIG. 40**  $^1\text{H}$   $T_2$  distribution for transverse slice of the PMAA gel at  $T_e=0, 3$ , and 6h with the application of an electric field (3 V DC).

It is also interesting to study the shrinking process of a polyelectrolyte gel under an electric field, which has macroscopically inhomogeneous structure. Such a hydropolymer gel is a good model to investigate the response of a human body to an electric stimulus, because the body is an inhomogeneous hydros swollen gel. The shrinking process of a composite hydros swollen PMAA gel which is a double cylindrical rod under an electric field is shown in Figure 42 [103]. The degree of swelling of the outside and inside parts of the gel are different with each other. The amount of cross-linking reagent used during polymerization of the inside network of the gel was different from that of outside one.

The observed  $^1\text{H}$  spin density images of the PMAA gel (Q for the inside part is 26, the outside 28) as a function of elapsed time,  $T_e$ , after the application of an

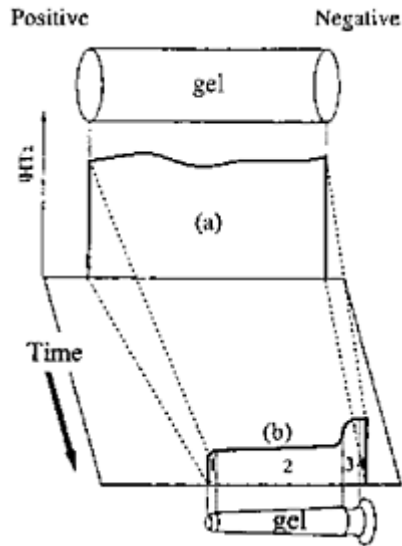


**FIG. 41** Schematic diagram for change in the  $^1\text{H}$   $T_2$  distribution image in the PMAA gel  $T_e=0$  h (a) and  $T_e=6$  h (b).

electric field (3 V DC) are shown in Figure 43. The  $Q$  for the outside part of the gel is larger than that for the inside one. It is shown that at  $T_e=0$  min most of the inside gel region is represented by a yellow color and the outside gel region is represented by a red color. This indicates that the  $^1\text{H}$  spin density of the outside gel is higher than that of the inside gel. The experimental result is consistent with the fact that the degree of swelling of the inside and outside gels are 26 and 28, respectively. Most of the inside and outside regions are represented by red except for the gel parts in contact with the negative and positive electrodes at

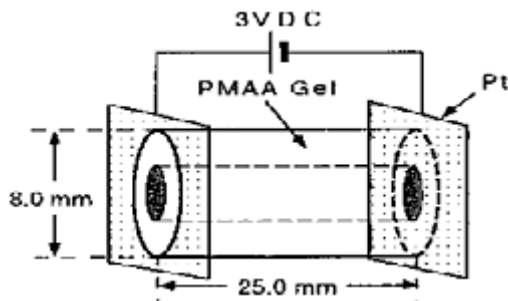


**FIG. 42** Structural scheme of the composite PMAA gel consisting of the inside part (shadowed part) and the outside part (light part). The degrees of swelling of the inside and outside gels are different from each other.

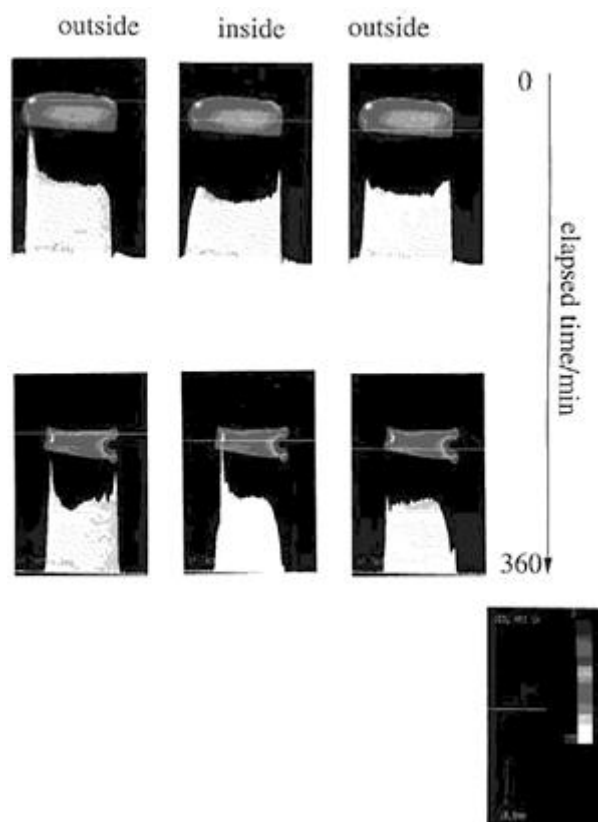


**FIG. 43** Elapsed-time dependence of images for the  $^1\text{H}$  spin density distribution and two-dimensional intensity histogram of the composite PMAA gel with the application of an electric field (3 V DC). The  $Q$  values of the inside and outside gels are 26 and 28, respectively.

Te=360 min. The  $^1\text{H}$  spin density distributions for the inside and outside of the gel, of which positions are indicated by a white line on the image, are also indicated by two-dimensional histogram in Figure 44. The shrinking rate of the inside gel, of which  $Q$  is smaller than that of the outside gel, is faster compared with the outside gel. This result is very interesting, because it is discrepant from the results that the shrinking rate of the gel under an electric field increases with an increase in  $Q$  (103). The inhomogeneous structure of the composite PMAA gel may give various effects to the migration of water and ions, the distribution of electric current, and the motion of the network polymer in the gel. It can be predicted easily that the interface between the two kinds of networks in the composite gel also plays an important role in the phenomenon. The schematic diagrams for the  $^1\text{H}$  spin density distribution of the gel under the shrinkage process are illustrated in Figure 44a. The trend of the shrinkage process and the  $^1\text{H}$  spin density distribution for

a homogeneous PMAA gel by the application of

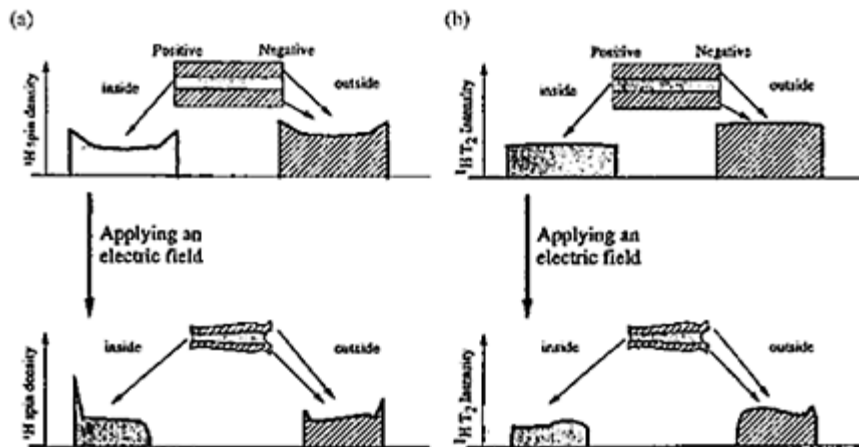


**FIG. 44** Schematic diagrams of the shrinking process of the composite PMAA gel by the application of an electric field as viewed by the  $^1\text{H}$  spin density images (a) and the  $^1\text{H}$   $T_2$ -weighted images (b).

an electric field, as described above, is similar to that of the outside gel rather than the inside gel. However, the whole shape of the shrunk composite gel is very different from that of the homogeneous gel that shrinks to form a wine stopper-like shape.

The three-dimensional histograms of elapsed-time dependence of the  $^1\text{H}$   $T_2$ -weighted image of water in the gel after the application of an electric field are shown in Figure 45 with the three-dimensional histograms of  $^1\text{H}$  spin density in the gel. The corresponding schematic diagrams are illustrated in Figure 44b. Before the application of an electric field, the  $^1\text{H}$   $T_2$ -weighted intensity is almost constant in the whole region of the gel. This means that the mobility of water in the whole region of the inside and outside of the gel is almost the same. However, at a long elapsed time after the application of an electric field, the  $^1\text{H}$   $T_2$ -weighted intensity in the region around the negative electrode in both of the inside and outside gels is somewhat higher than that around the positive electrode. The molecular motion of water in the gel around the negative electrode is faster than that in the other region. The trend is very similar to that for the case of a homogeneous PMAA gel discussed above. The shrinkage process of a composite gel for which the  $Q$  of the inside and outside gels are 28 and 26, respectively, was also studied as the contrasting case with [103].

#### 4. Migration of $\text{Mn}^{2+}$ Ions in a PMAA Gel

(a) *A Homogeneous PMAA Gel.* In order to elucidate the spatial distribution of paramagnetic  $\text{Mn}^{2+}$  ions in a PMAA gel swollen in an aqueous manganese(II)



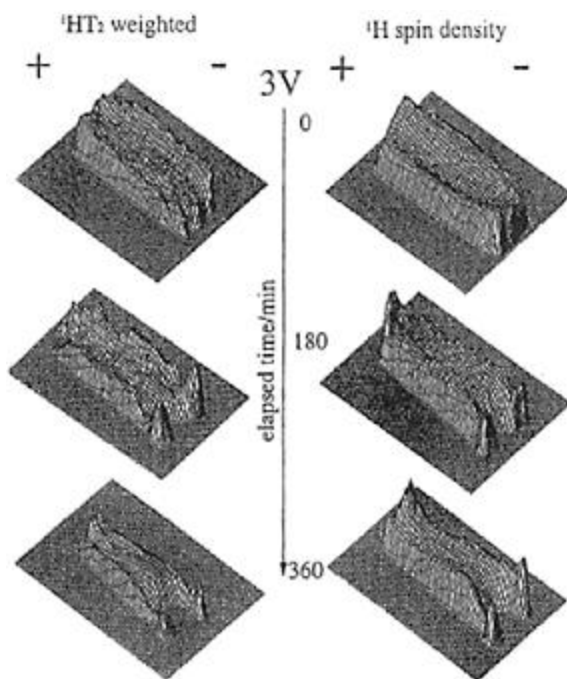


**FIG. 45** Three-dimensional histograms of elapsed-time dependence for the  $^1\text{H}$   $T_2$ -weighted images and the  $^1\text{H}$  spin density images of the composite PMAA gel with the application of an electric field.

sulfate solution with the application of a 3-V DC electric field, the images of the spatial distribution of the  $^1\text{H}$   $T_2$  value were measured by a  $^1\text{H}$  NMR imaging method [104]. The logarithm of the  $^1\text{H}$   $T_2$  value of water decreases linearly with an increase of the concentration of paramagnetic  $\text{Mn}^{2+}$  ion. From the  $^1\text{H}$  pulse NMR experiments on the gel containing  $\text{Mn}^{2+}$  ion, the relationship between the  $^1\text{H}$   $T_2$  value of water and the concentration of  $\text{Mn}^{2+}$  ions ( $C \text{ mol L}^{-1}$ ) in the gel [105] was obtained as shown in Figure 46 and is expressed by

$$T_2(^1\text{H}) = 7.24 C^{-0.163} \quad (36)$$

This means that the concentration of  $\text{Mn}^{2+}$  ions in the gel can be determined through the observation of the  $^1\text{H}$   $T_2$  value of water in the gel. The application of an electric field to a PMAA gel leads to shrinkage of the gel with exhaustion of water. Shrinkage around the positive electrode is larger than that around the negative electrode. The gel part in contact with the negative electrode is swollen.

The  $^1\text{H}$  spin density images for a transverse slice of a PMAA gel swollen in manganese (II) sulfate solution measured as a function of the elapsed time ( $T_e$ ) under a 3-V DC

electric field are shown in Figure 47 [104]. It is shown that at elapsed time  $T_e=0$  min most of the gel is occupied by the blue region. At

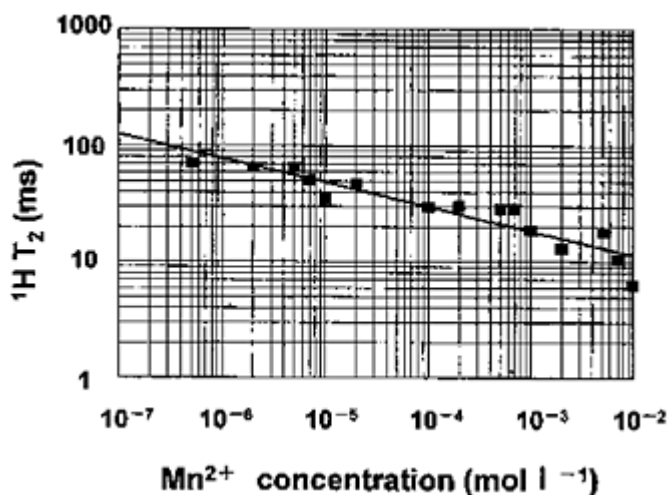


**FIG. 46** The dependence of  $^1H T_2$  of water in the PMAA gel on  $Mn^{2+}$  concentration.

$T_e=15$  min, the magnitude of  $^1H$  spin density increases in going from the positive electrode to the negative electrode as indicated by blue, green, blue, and violet. At  $T_e=30$  min, the  $^1H$  spin density changes as indicated by blue, violet, white, violet, blue, green, blue, and red. After  $T_e=60$  min, the white region increases. The  $^1H$  spin density image experiments for PMAA gel (0 V) is represented in Figure 47b. It has been shown that at elapsed time  $T_e=0$  min most of the gel is occupied by the blue region. Each image of  $^1H$  spin density from  $T_e=15$  min to  $T_e=120$  min, the magnitude of  $^1H$  spin density is occupied by green region and red regions. There is little change in the  $^1H$  spin density image for PMAA gel (0 V).

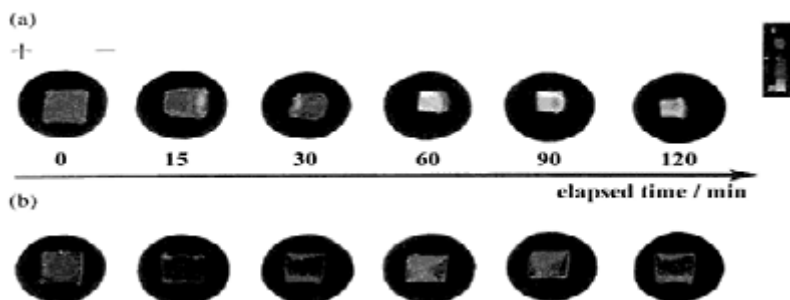


**FIG. 47** Elapsed-time dependence of image for the  $^1H$  spin density of PMAA gel swollen by an aqueous manganese(II) sulfate solution with (a) and without (b) the application of an electric field.

It is important to have information about the  $^1\text{H}$   $T_2$  value of water molecules in a PMAA gel in order to analyze the distribution of paramagnetic  $\text{Mn}^{2+}$  ions in the gel under an electric field. The  $^1\text{H}$   $T_2$  value of water molecules in a PMAA gel (3 V) is represented in Figure 48a. At  $T_e=0$  min, the  $^1\text{H}$   $T_2$  value of water molecules in a PMAA gel (3 V) distributes homogeneously in the gel. At  $T_e=15$  min, the  $^1\text{H}$   $T_2$  value of water molecules in a PMAA gel (3 V) decreases from the positive electrode to the negative electrode as indicated by 32, 33, 32, 27, 15, and 10 ms. At  $T_e=30$  min, the  $^1\text{H}$   $T_2$  value of water molecules in a PMAA gel (3 V) changes as indicated by 41, 44, 45, 39, 27, and 14 ms. At  $T_e=45$  min, 45, 48, 45, 39, 29, and 14 ms. At  $T_e=60$  min, 56, 73, 67, 62, 42, and 21 ms. At  $T_e=90$  min, 71, 83, 93, 65, 37, and 20 ms. At  $T_e=120$  min, 55, 54, 48, 36, 26, and 17 ms.

The  $^1\text{H}$   $T_2$  value of water molecules in the PMAA gel (0 V) is represented in Figure 48b. As seen from this diagram, the  $^1\text{H}$   $T_2$  values of water molecules in a PMAA gel (0 V) are almost about 18 ms without changing from  $T_e=0$  to  $T_e=120$  min. The  $^1\text{H}$   $T_2$  value is influenced not only by the  $\text{Mn}^{2+}$  ion concentration but also the mobility of water molecules in a PMAA gel.

The  $\text{Mn}^{2+}$  ions in a PMAA gel (3 V) move from the positive electrode side to the negative electrode side. The  $^1\text{H}$   $T_2$  distribution images can be converted to the  $\text{Mn}^{2+}$  ion distribution images. Their three-dimensional profiles of the spatial distribution of the paramagnetic  $\text{Mn}^{2+}$  ion concentration in a PMAA gel swollen by an aqueous manganese (II) sulfate solution with (a) and without (b) the application of an electric field were shown in Figure 49. At  $T_e=0$  min, the  $\text{Mn}^{2+}$  ion distributes homogeneously in the gel. The concentration of the  $\text{Mn}^{2+}$  ions in the gel is about  $3.8 \times 10^3 \text{ mol L}^{-1}$ . As the elapsed time is increased, the

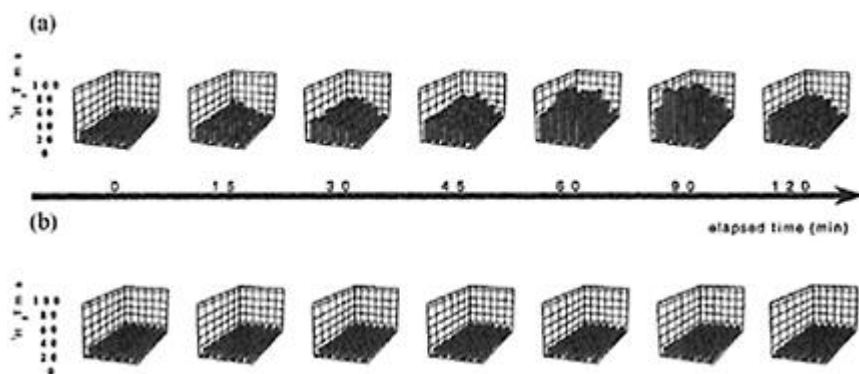


**FIG. 48** Elapsed-time dependence of the  $^1\text{H}$   $T_2$  distribution for a transverse slice of a PMAA gel swollen by an aqueous manganese(II) sulfate solution with (a) and without (b) the application of an electric field.

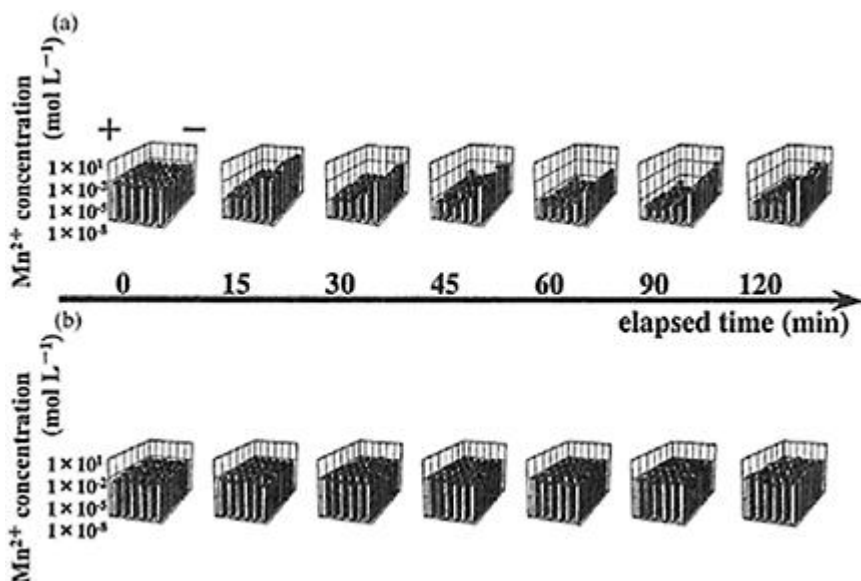


**FIG. 49** Elapsed-time dependence of the spatial distribution of the paramagnetic  $Mn^{2+}$  ion concentration in a PMAA gel swollen by an aqueous manganese(II) sulfate solution with (a) and without (b) the application of an electric field.

$Mn^{2+}$  ions migrate from the positive electrode side to the negative electrode side. The concentration of the  $Mn^{2+}$  ions in the gel at the positive electrode side becomes lower compared with that at the negative electrode side. The  $Mn^{2+}$  ions exhaust from the negative electrode side of the gel.

The  $^1H\ T_2$  of water molecules close to  $Mn^{2+}$  ions in the PMAA gel is decreased by the presence of  $Mn^{2+}$  ions in a gel. As a PMAA gel swollen by an aqueous manganese(II) sulfate solution is applied with an electric field,  $Mn^{2+}$  ions in the gel move toward the negative electrode side and the concentration of  $Mn^{2+}$  ions have a characteristic spatial distribution. The spatial distribution of the paramagnetic ions in a PMAA gel with application of an electric field is converted by the images of the spatial distribution of the  $^1H\ T_2$  values obtained by the  $^1H$  NMR imaging method.

*(b) A Composite PMAA Gel*

Formation process of a composite PMAA gel and the  $^1H$  NMR images with polymerization time. In order to elucidate the preparation process of a composite PMMA gel, a reaction solution corresponding to the part B (the degree of cross linking =  $4.8 \times 10^{-3}$  mol%) was put into an NMR tube with an outside diameter of 10 mm, and then its NMR tube was immediately placed in a  $^1H$  NMR imaging

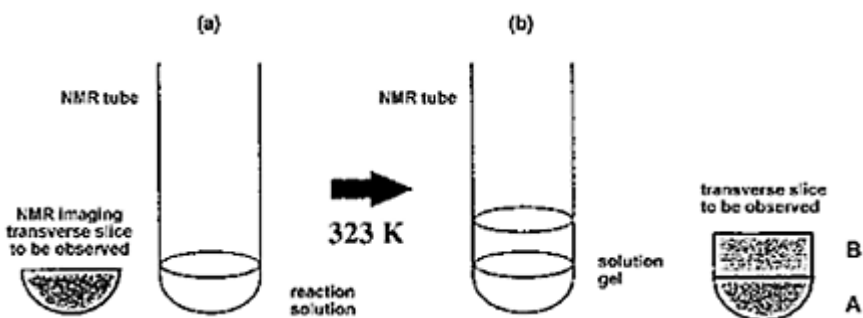


**FIG. 50** Schematic diagram for forming a composite PMAA gel consisting of two parts A and B with different degree of cross-linking (a) and the NMR imaging transverse slice to be observed (b).

probe at 323 K and the polymerization was started (see Fig. 50) [106]. The polymerization process was monitored by  $^1\text{H}$   $T_2$  image and the  $^1\text{H}$  spin density image as shown in Figure 51 a and b, respectively. The round shape in the images comes from the shape of the bottom of the NMR tube. Both of the  $^1\text{H}$  spin density image and  $^1\text{H}$   $T_2$  image are changing with an increase in polymerization time. At  $t=0$  h, the reaction system is a nonviscous solution, and so the  $^1\text{H}$   $T_2$  is very long (approximately 300–400 ms). In the  $^1\text{H}$   $T_2$  image the white region corresponding to the longest  $T_2$  occupies as a whole. The yellow, red, and blue regions slightly appear. The  $T_2$  value for these regions is not so different from that

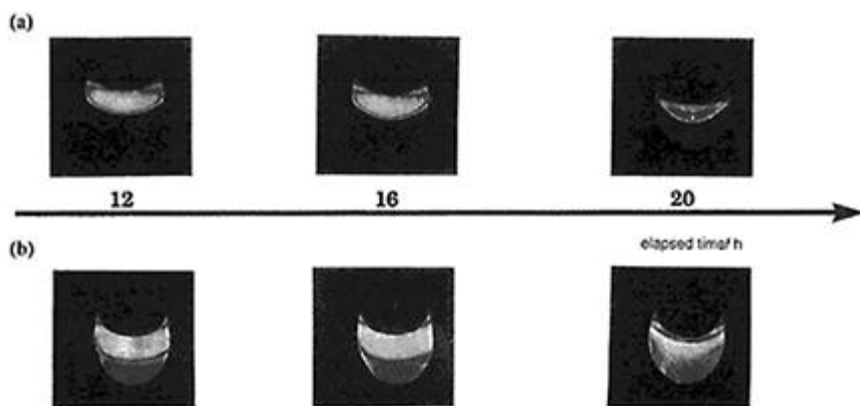


**FIG. 51** Polymerization process monitored by  $^1\text{H}$   $T_2$  image (a) and the  $^1\text{H}$  spin density image (b). The reaction solution system is corresponding to part B (the degree of cross linking  $= 4.8 \times 10^{-3}$  mol%) in a composite gel. The round-shaped bottom in the images comes from a shape of the bottom of the NMR tube.

of the white region. At 4 and 8 h, the reaction system becomes gradually viscous, because the gelation was advanced. The  $T_2$  value in the whole region becomes about 100–200 ms. The white and red regions change to the blue region. At that time on the surface of the reaction system, a thin liquid-like region appears, and so the color becomes red or white.

On the other hand, the  $^1\text{H}$  spin density image does not change almost with polymerization time. This shows that the gelation is homogeneously advanced.

As described in the experimental section, the reaction solution corresponding to part A (the degree of cross linking =  $2.2 \times 10^{-3}$  mol%) in a composite gel was added into the NMR tube. The polymerization process was monitored by the  $^1\text{H}$   $T_2$  image and the  $^1\text{H}$  spin density image as shown in Figure 52a and b, respectively. The added reaction solution has a very long  $^1\text{H}$   $T_2$ , and so the  $^1\text{H}$   $T_2$  image was observed as a white region. However, the part B-made gelation was observed, because the  $^1\text{H}$   $T_2$  value is very much shorter compared with that for the added reaction solution. However, in the  $^1\text{H}$  spin density image, the added reaction solution appears as a white region. Naturally, the  $^1\text{H}$  spin density for the solution is much higher than that in the part B to be gel. After 12 h, even in the added reaction solution system the polymerization is very slowly advanced. At 20 h, the polymerization is clearly advanced so that the color for the added reaction system becomes red and also the part B is observed as a slight blue

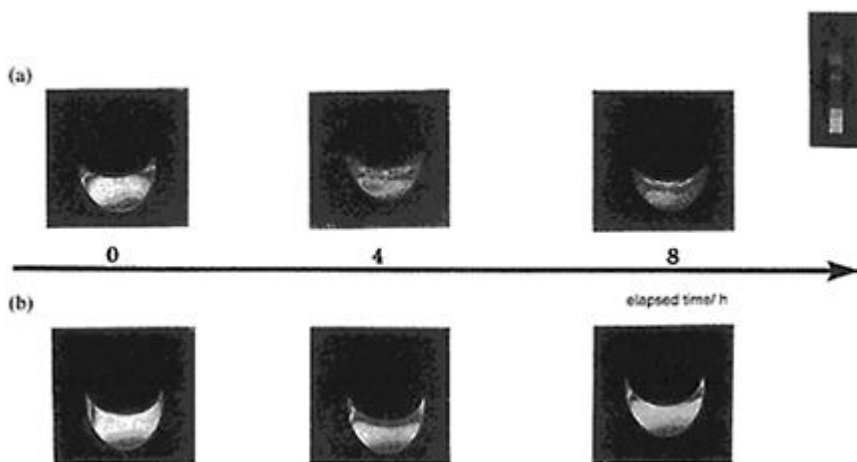


**FIG. 52** Polymerization process monitored by  $^1\text{H}$   $T_2$  image (a) and the  $^1\text{H}$  spin density image (b). The reaction solution corresponding to part A (the degree of cross linking =  $2.2 \times 10^{-3}$  mol%) in a composite gel was added into the part B system formed in the NMR tube (as shown in Fig. 51). The round-shaped bottom in the image comes from a shape of the bottom of the NMR tube.

region. In the  $^1\text{H}$  spin density image, both of the two regions are clearly observed. In the interfacial region between them the  $^1\text{H}$   $T_2$  value becomes 70 ms, which is shorter compared with that in the part B because of faster polymerization. This means that the degree of cross linking for the interfacial region is very high and is different from the two

regions.

(c)  $^1\text{H } T_2$  NMR Images of a Composite PMAA Gel Containing  $\text{Mn}^{2+}$  Ions. The  $^1\text{H } T_2$  NMR images of a composite PMAA gel containing  $\text{Mn}^{2+}$  ions in the transverse slice to be observed were measured as a function of the elapsed time (Te) for 120 min after the application of a 3-V DC electric field [105]. In such experiments, the DC current in the gel was 0.1 mA. In Figure 53 the three-dimensional histograms of the  $^1\text{H } T_2$  NMR images are shown as a function of the elapsed time with (a) and without (b) the application of an electric field. The magnitude of the  $^1\text{H } T_2$  value is differentiated 256 steps between the lowest and highest values.

We must be concerned with the shrinkage of a composite PMAA containing  $\text{Mn}^{2+}$  ions by the application of an electric field. The application of an electric field to a PMAA gel leads to shrinkage of the gel with exhaustion of water from the negative electrode. This is the same as the shrinkage process of a PMAA gel swollen in deionized water reported previously (2,4). At  $T_e=0$  min, the  $^1\text{H } T_2$  values in part A and part B in a composite gel are about 40 and 20 ms, respectively, and the interfacial region is clearly recognized. The degree of

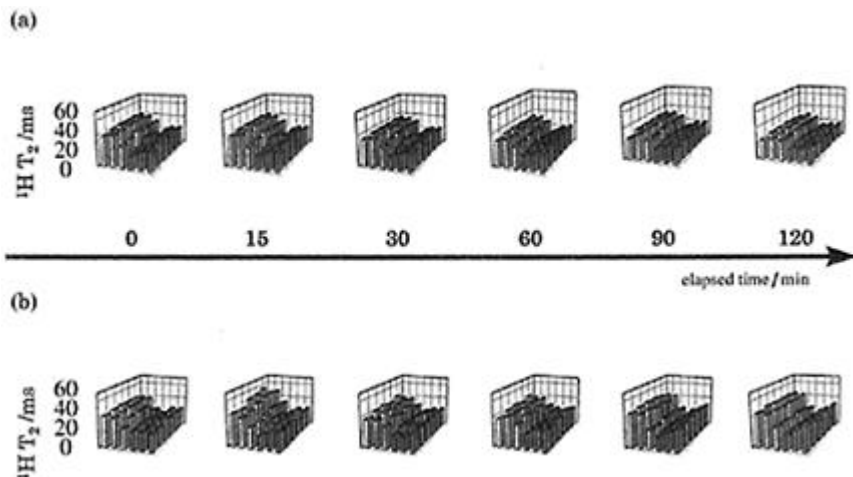


**FIG. 53** Three-dimensional histogram of the elapsed time dependence of the shapes (a) and  $^1\text{H } T_2$  distribution for a transverse slice of a composite PMAA gel swollen by aqueous manganese(II) sulfate solution with (b) and without (c) the application of a DC 3-V electric field.

cross linking for part B is much higher than that for part A. Thus, this means that the  $\text{Mn}^{2+}$  ion concentration in the former is much higher than that in the latter. As seen from the  $^1\text{H } T_2$  NMR image experiments without the application of an electric field (Figure 53b), there is little change in the three dimensional histogram patterns with a change in the elapsed time.

On the other hand, in the  $^1\text{H } T_2$  NMR image experiments with the application of an electric field (Figure 53a), the  $^1\text{H } T_2$  values in part A and part B in a composite gel

increase and decrease with an increase in the elapsed time, respectively. At  $T_e=60$  min, the  $^1\text{H}$   $T_2$  values in part A and part B become about 60 and 10 ms, respectively. The difference in  $^1\text{H}$   $T_2$  between parts A and B becomes much larger with an increase in the elapsed time. The interfacial region is clearly recognized. At  $T_e=120$  min, the  $^1\text{H}$   $T_2$  value in the gel decreased linearly in going from the positive electrode to the negative electrode. The interfacial region is recognized. Here it must be said that the change of the spatial distribution of the  $^1\text{H}$   $T_2$  of water is influenced not only by the  $^1\text{H}$   $T_2$  value which is accompanied by the shrinkage of a composite PMAA gel with the application of an electric field is much smaller than that of the  $^1\text{H}$   $T_2$  value by the influence of paramagnetic ions as reported previously (4).

By using the relationship between the  $^1\text{H}$   $T_2$  of water in the gel and the  $\text{Mn}^{2+}$  ion concentration as expressed by Eq. (36), the profile  $^1\text{H}$   $T_2$  images obtained were converted to the  $\text{Mn}^{2+}$  ion concentration images as shown in Figure 54. Without the application of an electric field, the spatial distribution pattern of the

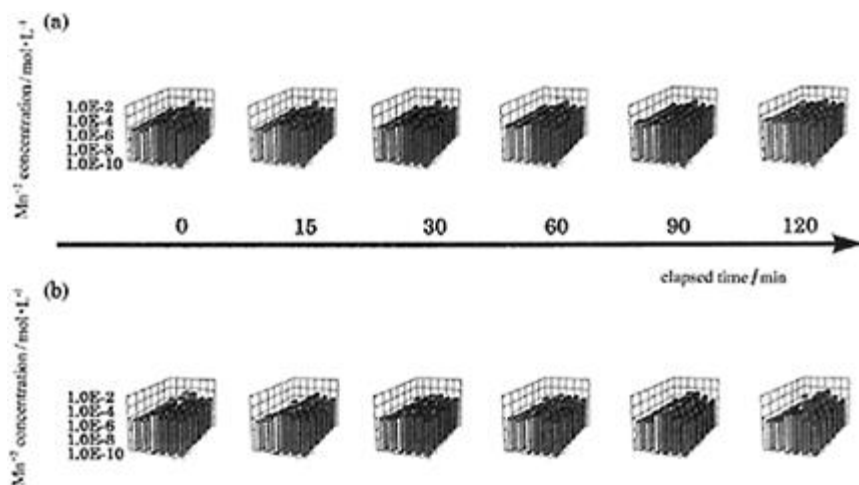


**FIG. 54** Three-dimensional histogram of the elapsed time dependence of the spatial distribution of the paramagnetic  $\text{Mn}^{2+}$  ion concentration for a transverse slice of a composite PMAA gel swollen by aqueous manganese(II) sulfate solution with (a) and without (b) the application of a DC 3-V electric field.

$\text{Mn}^{2+}$  ion concentration in the gel does not change with the elapsed time. At  $T_e=0$  min, the  $\text{Mn}^{2+}$  ion concentration in part A of a composite gel is much lower than that in part B. The interfacial region between them can be clearly recognized. Under the application of an electric field, with an increase in the elapsed time, the  $\text{Mn}^{2+}$  ion concentration in part A decreases and, on the other hand, that in part B increases. This means that the  $\text{Mn}^{2+}$  ions migrate from part A to part B through the interfacial region. At  $T_e=15$ , 30, and 60 min, the  $\text{Mn}^{2+}$  ion concentration at the interfacial region is clearly increased. The  $\text{Mn}^{2+}$  ions exhaust from the negative electrode side of the gel and then the total amount of the



$\text{Mn}^{2+}$  ions in the gel is decreased with the elapsed time. At  $T_e=120$  min, even the difference in the amount of the  $\text{Mn}^{2+}$  ions between part A and part B is observed, and so the interfacial region is clearly recognized. This means that the migration rate of the  $\text{Mn}^{2+}$  ions in part A in going from the positive electrode to the negative electrode is transitionally decreased at the interfacial region because of the higher degree of cross linking in the interfacial region. In part B, the  $\text{Mn}^{2+}$  ion concentration gradient appears like the previous results in a homogeneous PMAA gel under a DC electric field [105]. From such an experimental finding, it can be said that the spatial distribution images of the  $\text{Mn}^{2+}$  ions in a composite gel leads to useful information about the spatial distribution about the degree of cross linking in the gel.

Finally, it can be concluded that the migration process of the  $\text{Mn}^{2+}$  ions in a composite gel under the application of a DC electrical field was elucidated through the observation of the spatial distribution images of the  $\text{Mn}^{2+}$  ions by the  $^1\text{H}$  NMR imaging method. In addition, the formation process of a composite PMAA gel was successfully observed with polymerization time by means of  $^1\text{H}$  NMR imaging and was elucidated.

### 5. Shrinkage of PNIPAM Gel in Response to the Change in Temperature

The PNIPAM gel is a well-known thermoshrinking gel which collapses at the transition temperature around  $33^\circ\text{C}$  by heating (1, 2, 2107–109). During the shrinking process in response to the increase in temperature, PNIPAM gels often form the so-called structure in which the inner unshrunk layer is surrounded by the outer shrunken layer. It has been shown that two components of  $^1\text{H}$   $T_2$  for a PNIPAM gel are observed by heating: a short  $T_2$  component corresponding to the outer shrunken layer and a long  $T_2$  component corresponding to the inner unshrunk layer (10). It would be interesting to have spatial information about the molecular mobility during the shrinkage process of the gel with skin structure. Figure 55 shows a  $^1\text{H}$   $T_2$ -enhanced image for the gel ( $Q=43.6$  at  $20^\circ\text{C}$ ) in water after a rapid increase in temperature (10). The region with a short  $T_2$  was observed in the outer layer of the gel. It is clear that the molecular motion in the outer layer is much more restrained than that in the inner layer where the polymer networks swells. NMR imaging is a very powerful tool

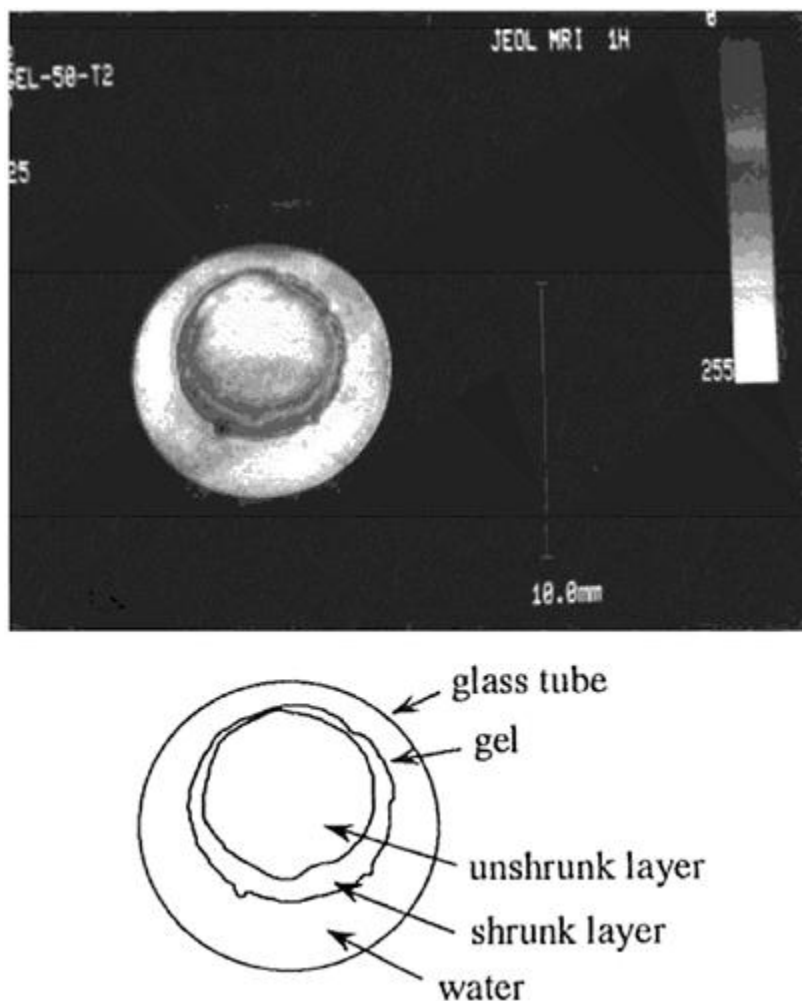


**FIG. 55** Observed  $^1\text{H}$   $T_2$ -weighted image of the PNIPAM gel ( $Q=40$ ) after rapid temperature change from 20 to 40°C.

for investigating such kinds of inhomogeneous reaction occurred in polymer gels giving information on the spatial distribution of molecular motion.

#### IV. SUMMARY

It has been demonstrated that NMR methodologies as developed recently in NMR spectroscopy provide useful information about the microscopic and macroscopic structures and the dynamics of polymer gel systems. From this, the structure/ dynamics-

property relation for polymer gels to be complicated soft-materials will be completely elucidated microscopically and macroscopically in near future.

## REFERENCES

1. Osada Y. *Adv Polym Sci* 82:1, 1987.
2. DeRossi D, Kajiwarra K, Osada Y, Yamauchi A (eds). *Polymer Gels—Fundamentals and Biomedical Applications*. Plenum Press, New York, 1991.
3. Yasunaga H, Kobayashi M, Matsukawa S, Kurosu H, Ando I. *Ann Rept NMR Spectrosc* 34:39, 1997.
4. Ando I, Asakura T (ed). *Solid State NMR of Polymers*. Elsevier, Amsterdam, 1998.
5. Ando I, Kurosu H, Matsukawa S, Yamazaki A, Hotta Y, Tanaka N. In: *The Wiley Polymer Networks Review Series*. Vol 1, ed. Nijenhuis K, Mijs WJ, eds. Wiley, New York, 1998, pp 331–346.
6. Ando I, Kobayashi M, Kanekio M, Kuroki S, Ando S, Matsukawa S, Kurosu H, Yasunaga H, Amiya S. *Experimental Methods in Polymer Science*. Wiley, New York, 1999, pp 261–483.
7. Bleombergen N, Purcell EM, Pound RV *Phys Rev* 73:679, 1948.
8. Heskins M, Guillet JE. *Macromol Sci Chem* A2:1441, 1986.
9. Ohta H, Ando I, Fujishige S, Kubota K. *Polymer Sci B* 29:963 1991.
10. Tanaka N, Matsukawa S, Kurosu H, Ando I. *Polymer* 39:4703, 1998.
11. Paul DR. *J Appl Polym Sci* 11:439, 1976.
12. Takahashi A, Hiramitsu S. *Polymer J* 6:103, 1974.
13. Kobayashi M, Ando I, Ishii T, Amiya S. *Macromolecules* 28:6677, 1995.
14. Terao T, Maeda S, Saika A. *Macromolecules* 16:1535, 1983.
15. Kobayashi M, Ando I, Ishii T, Amiya S. *J Mol Struct* 440:155, 1998.
16. Torchia DA. *J Magn Reson* 30:613, 1978.
17. Kobayashi M, Ando I, Ishii T, Amiya S. *Polym Gels Networks* 6:425, 1998.
18. Zhao C, Matsukawa S, Kobayashi M, Ando I. *J Mol Struct* 442:235, 1998.
19. Saito H, Ando I. *Ann Rept NMR Spectrosc* 21:210, 1989.
20. Ando I, Yamanobe T, Asakura T. *Prog NMR Spectrosc* 22:349, 1990.
21. Shoji A, Ando S, Kuroki S, Yoshimizu H, Ando I, Webb GA. *Ann Rept NMR Spectrosc* 26:55, 1993.
22. Tanner JE, Stejskal EO. *Chem Phys* 48:1768, 1968.
23. Callaghan PT. *Principles of Nuclear Magnetic Resonance Microscopy*. Clarendon Press, Oxford, UK, 1991.
24. Kimmich R. *NMR: Tomography, Diffusometry, Relaxometry*. Springer, Berlin, 1997.
25. Karger J, Pfeier H, Heink W. *Adv Magn Reson* 12:1, 1988.
26. Price WS. *Ann Rep NMR Spectrosc* 32:51, 1996.
27. Price WS. *Ann Rep NMR Spectrosc* 35:139, 1998.
28. von Meerwall ED. *Adv Polym Sci* 54:1, 1984.
29. Nose T. *Ann Rep NMR Spectrosc* 27:217, 1993.
30. Kanekiyo M, Kobayashi M, Ando I, Kurosu H, Ishii T, Amiya S. *J Mol Struct* 447:49, 1998.
31. Matsukawa S, Yasunaga H, Zhao C, Kuroki S, Kurosu H, Ando I. *Prog Polym Sci* 24:995, 1999.
32. Yasunaga H, Ando I. *Polym Gels Networks* 1:83, 1993.
33. Matsukawa S, Ando I. *Macromolecules* 29:7136, 1996.

34. Fujita H. *Adv Polym Sci* 3:1, 1961.
35. Fujita H, Kishimoto A. *J Chem Phys* 5:393, 1961.
36. Fujita H, Kishimoto A, Matsumoto K. *Trans Faraday Soc* 56:424, 1960.
37. Muhr AH, Blanshard JMV *Polymer* 23:1012, 1982.
38. Boss BD, Stejska EO, Ferry JD. *J Phys Chem* 71:1501, 1967.
39. von Meerwall ED, Amis EJ, Ferry JD. *Macromolecules* 18:260, 1985.
40. Muhr AH, Blanshard MV *Polymer* 23:1012, 1982.
41. Yasuda H, Lamaze CE, Peterlin A. *J Poly Sci* 9:1117, 1971.
42. Langevin D, Rondelez FP. *Polymer* 19:875, 1978.
43. Cukier R. *Macromolecules* 17:252, 1984.
44. Phillies GD, Malone C, Ullmann K, Ullmann G, Rollings J, Yu L. *Macromolecules* 22:2280, 1987.
45. Cameron RE, Jalil MA, Donald AM. *Macromolecules* 27:2708, 1994.
46. Wheeler LM, Lodge TP. *Macromolecules* 22:3399, 1989.
47. Nemeto N, Kojima T, Inoue T, Kishine M, Hiriyama T, Kurata M. *Macromolecules* 22:3793, 1989.
48. Nemoto N, Landry MR, Noh I, Kitano T, Wesson J, Yu H. *Macromolecules* 18:308, 1985.
49. de Gennes PG. *Macromolecules* 9:594, 1976.
50. Smith KL, Winslow AE, Petersen DE. *Ind Eng Chem* 51:1361, 1959.
51. Tsuchida E, Abe K. *Adv Polym Sci* 45:2, 1982.
52. Philippova OE, Karibyant NS, Starodubtzev SG. *Macromolecules* 27:2398, 1994.
53. Hahn, EL. *Phys Rev* 80:580.
54. Carr HE, Purcell EM. *Phys Rev* 94:630, 1954.
55. Meiboom S, Gill D. *Rev Sci Instr* 29:688, 1958.
56. Farrar TC, Becker ED. *Pulse and Fourier Transform NMR. Introduction to Theory and Methods*. Academic Press, New York, 1971.
57. Matsukawa S, Ando I. *Macromolecules* 30:8310, 1997.
58. Illiopoulos I, Audebert R. *Macromolecules* 24:2566, 1991.
59. McConnell J. *The Theory of Nuclear Magnetic Relaxation in Liquids*. Cambridge University Press, Cambridge, UK, 1987.
60. Matsukawa S, Ando I. *Macromolecules* 31:1865, 1999.
61. Ohtsuka A, Watanabe T, Suzuki T. *Carbohydr Polym*, 24:95, 1994.
62. Yoon H, Kim H, Yu H. *Macromolecules* 22:848, 1989.
63. Muhr AH, Blanshard MV *Polymer* 23:1012, 1982.
64. Lindblom G, Rilfors L. *Biochim Biophys Acta* 988:221, 1989.
65. Lindblom G, Wennerstrom H. *Biophys Chem* 6:167, 1977.
66. Zhao C, Matsukawa S, Kurosu H, Ando I. *Macromolecules* 31:3139, 1998.
67. Robinson C. *Trans Faraday Soc* 52:571, 1956.
68. Robinson C, Ward JC. *Nature* 180:1183, 1957.
69. Robinson C, Ward JC. *Discussion Faraday Soc* 25:29, 1958.
70. Robinson C. *Tetrahedron* 13:219, 1961.
71. Elio A, Ambrose ET. *Discussion Faraday Soc* 29:246, 1958.
72. Sobajima S. *J Phys Soc Jpn* 23:1070, 1967.
73. Panar M, Phillips WD. *J Am Chem Soc* 90:3859, 1968.
74. Orwell RD, Vold RL. *J Am Chem Soc* 93:5335, 1971.
75. Samalski ET, Tobolsky AV *Mol Cryst Liq Cryst* 7:433, 1969.
76. Fung BM, Gerace MJ, Gerace LS. *J Phys Chem* 74:83, 1983.
77. Flory PJ. *Statistical Mechanics of Chain Molecules*. Interscience, New York, 1969.

78. Doi M, Edwards SF. *The Theory of Polymer Dynamics*. Clarendon Press, Oxford, UK, 1986.
79. Ando I, Hirai T, Fujii Y, Nishioka A. *Makromol Chem* 184:2581, 1983.
80. Ishikawa S, Kurosu H, Ando I. *J Mol Struct* 248:361, 1991.
81. Ishikawa S, Ando I. *J Mol Struct* 273:227, 1991.
82. Yamakawa H, Matsukawa S, Kurosu H, Kuroki S, Ando I. *Chem Phys Letts* 283:333, 1998.
83. Yamakawa H, Matsukawa S, Kurosu H, Kuroki S, Ando I. *J Chem Phys* 111:5129, 1999.
- 84a. Photinos DJ, Samulski EJ, Torium H. *J Phys Chem* 94:4688, 1990.
- 84b. Photinos DJ, Samulski EJ, Toriumi H. *J Chem Phys* 95:2758, 1991.
- 85a. Sasanuma Y, Abe A. *Polymer J* 23:117, 1991.
- 85b. Abe A. *Macromol Chem, Macromol Symp* 53:13, 1992.
86. Zhao C, Zhang H, Yamanobe T, Kuroki S, Ando I. *Macromolecules* 32:3389, 1999.
87. Zhao C, Kuroki S, Ando I. *Macromolecules* 33:4486, 2000.
88. Gao Z, Schlick S, Matsukawa S, Ando I, Rossi G. *Macromolecules* 32:3289, 1999.
89. Mansfield P, Morris PG. *NMR Imaging in Biomedicine. Advances in Magnetic Resonance Supplement 2*. Academic Press, New York, 1982.
90. McCready VR, Leach M, Ell PJ (eds). *Functional Studies Using NMR*. Springer-Verlag, Berlin, 1987.
91. Mansfield P, Hahn EL (eds). *Phil Trans R Soc Lond A*, 333:401, 1990.
92. Weisenberger LA, Koenig JL. *Polym Sci Polym Lett* 27:55, 1989.
93. Weisenberger LA, Koenig JL. *Macromolecules* 23:2445, 1990.
94. Rathbun RE, Babb AL. *J Phys Chem* 65:1072, 1961.
95. Thomas NL, Windle AH. *Polymer* 23:529, 1982.
96. Hui C-Y, Wu K-C, Lasky RC, Kramer EJ. *J Appl Phys* 61:5129, 1987.
97. Hui C-Y, Wu K-C, Lasky RC, Kramer EJ. *J Appl Phys* 61:5137, 1987.
98. Osada Y, Kishi R, Hasebe M.J. *Polym Sci: Part C: Polym Lett* 25:481, 1987.
99. Sawahata K, Gong J-P, Osada J. *Macromol Rapid Commun*, 16:713, 1995.
100. Yasunaga H, Kurosu H, Ando I. *Macromolecules* 25:6505, 1992.
101. Tanaka T, Osada Y, Ross-Murphy SB, Siegel RA (eds). *Polym Gels Networks*, 1994.
102. Shibuya T, Yasunaga H, Kurosu H, Ando I. *Macromolecules* 28:4377, 1995.
103. Kuros H, Shibuya T, Yasunaga H, Ando I. *Polym J* 28:80, 1996.
104. Gong JP, Nitta T, Osada Y. *J Phys Chem* 98:9583, 1994.
105. Yamazaki A, Hotta Y, Kurosu H, Ando I. *Polymer* 39:1511, 1998.
106. Yamazaki A, Hotta Y, Kurosu H, Ando I. *J Mol Struct*. 2000, in press.
107. Fujishige S, Kubota K, Ando I. *J Phys Chem* 93:311, 1989.
108. Bae YH, Okano T, Kim SW. *J Polym Sci Polym Phys*, 28:923, 1990.
109. Yoshida R, Uchida K, Kaneko Y, Sakai K, Kikuchi A, Sakurai Y, Okano T. *Nature* 374:240 1995.
110. von Meerwall E, Kamat M. *J Magn Reson* 83:309, 1989.



# Electrical and Magnetic Field-Sensitive Smart Polymer Gels

**MIKLÓS ZRÍNYI, DÉNES SZABÓ, GENOVÉVA FILIPCSEI, and  
JÓZSEF FEHÉR** *Budapest University of Technology and Economics,  
Budapest, Hungary*

## I. INTRODUCTION

### A. Scope of the Review

The idea of intelligent and smart materials evolved in the late 1980s with the purpose of establishing a new area in material science to take into account the interrelation between materials and the natural (external) environment [1–4]. The term *smart materials* refers to a class of monolithic and composite media having inherent intelligence together with self-adaptive capabilities to external stimuli. This newly developed concept aims to create artificially designed systems possessing sensor, processor, and actuator functions internally in the material itself. Electrical field- and magnetic field-responsive materials are a specific subset of smart materials which can adaptively change their physical properties in an external electrical or magnetic field, respectively. At present, there are several adaptive materials that can actuate or alter their properties in response to a changing environment. Certain polymer gels represent one class of these materials [5, 6]. Their unique properties based on volume phase transition as a response to a small change in external conditions make such systems useful. Application of the principles in engineering promises new materials and technologies with a broad spectrum of biomedical and chemical applications including muscle-like soft linear actuators in advanced robotics, micromachines, biomimetic energy-transducing devices, selective absorbents, sensors, and controlled drug-delivery systems.

Among the synthetic responsive polymer gels best known and studied are those which have hydrophobic side chains like, for instance, poly-N-isopropylacrylamide. The main characteristic of fully or partly hydrophobic network chains is that at lower temperature they are more hydrated and more expanded. Hence, they can convert thermal energy directly into work by swelling or collapsing. The temperature range over which this conversion occurs can be controlled by the chemical composition of the network backbone. Today, the stimuli that have been demonstrated to induce discontinuous volume changes are diverse and include temperature, pH, solvent or ionic composition, electrical field, light intensity as well as introduction of specific ions [6–12].

Electrical field- and magnetic field-sensitive polymer gels are soft smart materials whose elastic and thermodynamic properties are a strong function of the field strength

imposed upon them. Since electrical and magnetic fields are convenient stimuli from the point of signal control, it is of great importance to develop and study such gel systems. For the sake of clarity, this chapter will use the *term field* to include either an electrical or magnetic field. No other field, namely, gravitational field, effects are the subjects of this study. We also use the *term field-responsive gels* to refer to electrical field- and magnetic field-sensitive smart gels.

The main purpose of this chapter is to report on recent advances in the development of field-responsive polymer gels. Since these gels are being developed mainly for actuator purposes, the study of motion and deformation induced by external fields is our primary interest.

We consider here polymer gels as active mechanochemical devices that can store energy. Under certain conditions, the stored energy can be converted into mechanical movement, which manifest itself as swelling, shrinking, or shape transformation. Kuhn et al. were the first to realize that certain water-swollen polymers can be chemically contracted similar to muscle [16]. Since their pioneering work various chemically active polymers, as well as their composites, have been studied in order to develop an artificial muscle for biomechanics and technical applications. Several authors have given extensive reviews of these materials [5, 6, 9, 11–15, 17].

In the first part of this chapter, we introduce a new concept to classify responsive polymer gels. This is followed by a brief summary of the main effects on swelling induced by electrical fields. The response of filler-loaded gels to electrical field is the next to be discussed. Later sections follow on magnetic polymer gels. The mechanical properties under uniform and nonuniform external magnetic fields are described. A final section is concerned with the kinetics of deformation and swelling behavior.

## B. Characterization of Responsive Gels by the Origin of the Force

It is well known that polymer gels are able to provide the motive force for movement. Their swelling and shrinking behavior is a manifestation of an active three-dimensional mechanochemical spring. They can produce motion, lift weights, and perform work. Volumetric change is not the only way to transform the energy stored in the gel into mechanical work. Elongation or contraction at constant volume may also produce useful work.

Because polymer gels convert some form of energy to motion, a natural basis for their understanding arises from the laws of thermodynamics. To determine the nature of the force generated by a polymer gel, one must consider all the relevant interactions that contribute to the force or displacement. We learned from the thermodynamics of rubber elasticity that the molecular mechanism of force,  $f$ , generation in the network chains is made up of two different contributions. In general, energetic and entropic effects must be taken into account.

$$f = \frac{\partial A}{\partial l} = \frac{\partial U}{\partial l} - T \frac{\partial S}{\partial l} = f_U + f_S \quad (1)$$

Where  $A$ ,  $U$ , and  $S$  represent the free energy, internal energy, and entropy, respectively  $f_U$



and  $f_s$  denote the derivative of internal energy and entropy with respect to displacement,  $l$  in order to yield force components. On the basis of Eq. (1), one can classify the gels as:

1. Swelling or shrinking of polymer gels is due to imbalance between osmotic and entropic forces. The mechanical stress is generated mainly by continuous conformational changes, or volume-phase transition of LCST or UCST type [18]. In either case, the volume change is entropically driven. This means that conventional polymer gels, which swell or shrink as a consequence of certain stimuli, can be considered as *entropy-driven responsive gels*. This is not the only possibility to induce deformation or release work.
2. The new generation of responsive gels exploit energetic effects to create force or work. These gels are either composite gels or networks swollen by a liquid that can change its dielectric properties drastically under external field. We call this kind of gels *energy-driven responsive gels*, because the network chains deform as a result of strong energetic interactions.

There are significant differences when comparing the mechanism of force generation occurring in responsive gels of these two kinds. In the case of entropy-driven gels, the force is due to volume change, whereas in the case of energy-driven polymer gels, there is no volume change, but shape change occurs. Consequently, the response rate is also very different. Electric or magnetic polarization that induces the deformation of field-responsive gels is much faster than swelling or shrinking, which are controlled by a much slower diffusion mechanism. Another substantial difference is the nature of the response. In the case of energy-driven gels, both the stimulus and the response are directed, whereas in the case of volume change, it is difficult to localize the volume change to certain parts of the gels, and hence to produce directed motion.

### C. Conventional Smart Gels in an Electrical Field

Since the interactions of an electrical field with charges are much stronger than those with neutral materials, it is not surprising that the conformational changes in the responsive gels are related to either polyelectrolyte gels or charged mobile molecules that can bind to the network chains influencing the hydrophil-hydrophobic balance. The effects of an electrical field on the shape and motility of polyelectrolyte gels have been the subject of many discussions. Excellent reviews on the deformation and viscoelastic behavior of polymer gels in an electrical field have appeared in the literature [11, 12, 19–21].

The influence of the electrical field on the mechanical, swelling, and thermo-dynamical properties can be classified into three main groups:

- Electrical field-induced collapse transition
  - Electrochemical reaction
  - Electrically activated complex formation

Polymer gels containing ionic groups become deformed when an electrical field is applied through the gel [20, 21]. The deformation is due to swelling or shrinking of a certain part of the gel. This is the result of the migration of charged ions that are pushed

to the anode or cathode side of the gel by the electrical field. An infinitesimal change in electrical potential across the polyelectrolyte gel can induce an abrupt reversible volume change. This first-order-like phase transition is often referred to as collapse transition.

Electrochemical reactions performed in a polymer gel can also significantly influence the swelling degree. When changing the amount of oxidizing and reducing compounds in a gel by control of the applied potential, the pH of the gel changes. Accordingly, the shape and swelling degree of a pH-sensitive polymer gel can be controlled by electrochemical stimuli [22, 23].

Complex formation can also be used to modify the degree of swelling. Polyelectrolyte gels can bind oppositely charged surfactant molecules [24–26]. By using an electrical field, it is possible to direct the binding of surfactant molecules selectively to one side of the gel. Owing to the presence of surfactant molecules, a local anisotropic shrinkage occurs. Reversing the direction of the field results in contraction of the opposite side. If the polarity of the electrical field is reversed periodically, the gel shows repeated curvature.

So far, we have outlined the main mechanism of entropy-driven deformations. In each case, the deformation or displacement is due to volume change. Any technical application critically depends on the response rate. Efforts to develop responsive gels are often complicated by the fact that structural changes are kinetically restricted by diffusion of liquid molecules into or out of the polymer matrix, respectively. The formation of a collapsed polymer skin layer on the surface of the gel also blocks the outflux of entrapped water. The swelling or shrinkage rate is rather small, and it strongly depends on the geometry and the size of the gel sample. The rate of volume change has been found to be inversely proportional to the square of the smallest dimension of the gel. This disadvantage often hinders efforts to design an optimal gel for different application purposes.

## II. THE EFFECT OF AN ELECTRICAL FIELD ON NEUTRAL POLYMER GELS

The change in length of a sample in the presence of an electrical field is a common phenomenon in several materials, and the phenomenon is called electrostriction. Most of the electrostrictive materials are solids, which undergo a mechanical distortion when subjected to an external electrical field. Certain polymer dielectrics and highly swollen gels have been found to show electrostriction. At high uniform fields, these materials generate a large electrostatic force when sandwiched between two compliant electrodes. Owing to electrostriction, the dielectric polymer becomes compressed. The response to an electrical field is fast and remarkable.

The *electrostrictive soft materials* can be divided into two main groups:

The first main group includes a dielectrical polymer dielectrics sandwiched between two compliant electrodes [27–30]. At high uniform fields, a large electrostatic force is generated between the electrodes, which compresses the dielectrical polymer as shown schematically in Figure 1. Polyurethane elastomers have been investigated in more detail.

The other group is related to chemically cross-linked polyvinyl alcohol gels swollen by dimethyl sulfoxide, between two electrodes placing them on the gel surfaces [31–34].

The stress,  $\sigma_E$ , that is exerted perpendicular to the gel surfaces can be expressed with the dielectrical constant and field intensity as follows:

$$\sigma_E = \chi \cdot \epsilon_0 \cdot E^2 \quad (2)$$

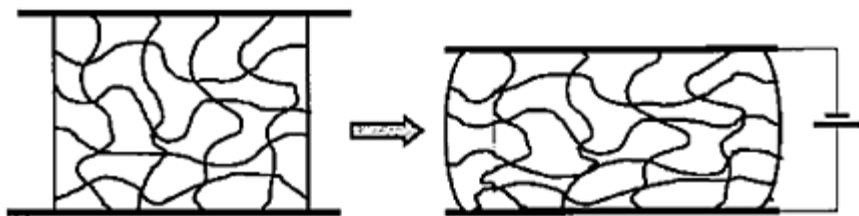


**FIG. 1** Schematic representation of compression due to an electrostrictive effect.

where  $\epsilon_0$  is the permittivity of vacuum and  $\chi$  denotes the relative permittivity (dielectrical constant) of the material, either the polymer (in the first group) or the solvent (in the second group), respectively.  $E$  denotes the electrical field across the thickness of the electrostrictive material. On the basis of Eq. (2), one can establish that the electrostrictive stress is proportional to the dielectrical constant and scales with the square of the uniform field strength. It must be mentioned that in the case of a fluid system, the electrostrictive stress is often referred to as electrical pressure, which can exceed a value of  $\sigma_E \sim 10$  kPa that allows a wide range of applications.

Electrostrictive gels are fast-motion gels compared to entropy-driven poly-electrolyte-responsive gels. The response time can approach the order of a millisecond. Unfortunately, the measure of deformation or displacement is rather small, which entails several restrictions in applications.

The *electroconvection*, or electrohydrodynamic, effect may also be used to induce deformation of a neutral polymer gels. When a gel swollen by a dielectrical fluid with very low conductivity is subjected to a high electrical field, convection of solvent inside the gel occurs [36]. Charge carriers in the weakly conductive dielectrical liquid are created either by bulk dissociation of chemical impurities or by injection of ions from the metallic electrodes [43]. Above a critical field strength, the Coulomb force acting on the free charges can put the liquid into motion. The electroconvective motion of liquid inside the gel can be used to perform large and reversible deformation (see Fig. 2).

Hirai et al. have investigated highly swollen polymer gels between two electrodes placed on the gel surfaces [35, 36]. In this case, a nonionic polymer network swollen to equilibrium with a solvent of high dielectrical constant is actuated by an external electrical field. Bending as well as flapping of a wing were

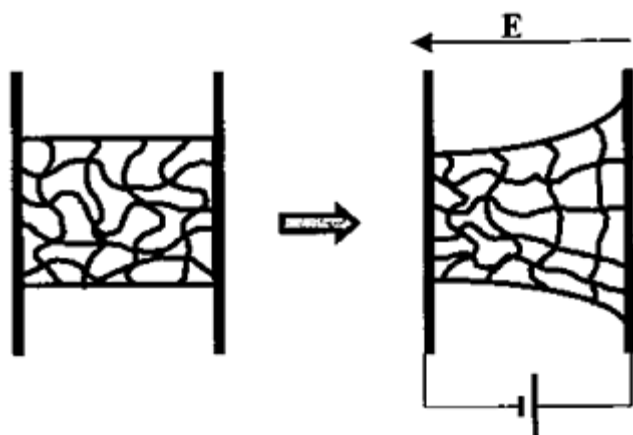


**FIG. 2** Schematic representation of deformation to electroconvection.

demonstrated. The deformation was induced by directed charge-injected solvent drag.

Low molecular mass liquid crystals can easily rearrange their orientation under an electrical or magnetic field. If a flexible polymer network is swollen by such liquid crystalline fluid, the microscopic rearrangement of the molecules can be transmitted to macroscopic and quick deformation of the polymer gel. Kishi et al. have studied the electrical deformation of thermotropic liquid crystalline polymer gels [37]. They found that the deformation of the gel was attributed to the electrical reorientation of mesogenic groups. Unfortunately, the observed bending was rather small. A theoretical analysis was provided recently [38].

### A. Composite Gels

Many useful engineering materials as well as living organisms have a heterogeneous composition. The components of composite materials often have contradictory, but complementary, properties. We use the term *composite gel* to indicate that, in addition to the polymer network and swelling agent, a third component is present as a filler. Fillers are usually solid additives that are incorporated into the polymer networks to modify the physical properties. Fillers can be divided into three categories: those that reinforce the polymer gel and improve its mechanical performance, those that are used to take up space, and thus reduce material cost. The third, less common category is when filler particles are incorporated into the gel to improve its electrical or magnetic properties. The size of the filler material varies from several nanometers to micrometers. They can be built into a network either as individual particles or as aggregates. Filler particles can also form ordered structures. If there are strong attractive interactions between the network polymers and the surface of the solid particles, this provides a coupling between forces acting on the solid particles and conformational change of the surrounding macromolecules.

All neutral materials experience force or torque when subjected to an electrical field.

The field can polarize a substance by inducing new dipolar moments, realigning existing dipoles, or altering their magnitude. Furthermore, the dipoles in the material interact with each other. These mutual interactions are strong in certain solids but rather weak in fluid systems. In order to enhance the influence of external fields on solution and/or gel properties, it is necessary to combine solid-like and fluid-like behaviors. New colloidal solutions, termed *complex fluids*, have been introduced. Electrorheological fluids, magnetorheological fluids, and ferrofluids contain small, dispersed particles in the size range from nanometers to micrometers [39–41]. These fluids respond to an applied field by rapidly changing their apparent viscosity and yield stress. Since polymer gels contain a substantial amount of liquid as a swelling agent, it is possible to fabricate field-sensitive gels by using a polymer network swollen by a complex fluid. The incorporated colloidal particles, characterized by strong adsorptive interactions with the polymer chains, couple the shape and physical properties of the gel to the external field. Since the particles are attached to the gel matrix, all forces acting on the particles are transmitted directly to the polymer chains resulting in either locomotion or macroscopic deformation of the gel. Here we consider such filler-loaded gels in which the filler particles have strong electrical magnetic properties. The stronger field attracts the particles, and owing to their small size and strong interactions with molecules of dispersing liquid and polymer chains, they all move together. Because of the cross-linking bridges in the network, changes in molecular conformation can accumulate and lead to macroscopic shape changes or/and motion. In this case, the polymer network plays the role of a mechanical amplifier.

### III. ELECTRICAL FIELD-SENSITIVE COMPOSITE GELS

#### A. Electrophoretic Effects

The terms *electrophoresis* and *dielectrophoresis* imply the interplay between electrical phenomena and motion. Electrophoresis is the migration of a charged particle due to a uniform or nonuniform electrical field. It is typical for charged colloidal particles. If the charged particles are considerably separated within the system, carry relatively small charges, and the electrostatic force between the particles can be neglected, then the only electrophoretic force,  $f_{EP}$ , to be considered is the one caused by the external electric field:

$$f_{EP} = q \cdot E \quad (3)$$

Where  $q$  represents the free charges present and  $E$  denotes the electrical field strength. The direction of the electrical field plays a decisive role in the motion.

#### B. Dielectrophoretic Effects

Dielectrophoresis is the migration of neutral particles in nonuniform electrical field due to polarization (Fig. 3b). Although polarization effects are often considered to be weak, there are several examples where they are far more effective than Coulomb forces, since

polarization forces can act directly on an uncharged particle.

Two distinct types of interactions can be identified: *field-partide* and *particle-particle* interaction. If the field is nonuniform, then the field-particle interactions are dominant. Particles experience a dielectrophoretic force,  $f_{DEP}$ . They are attracted to regions of stronger field intensities when their permittivity exceeds that of the suspension medium [41, 42]:

$$f_{DEP} = 2\pi\epsilon_1 R^3 K \nabla E^2 \quad (4)$$

Where  $\epsilon_1$  denotes the dielectrical permittivity of the solvent,  $R$  denotes the radius of the colloidal particle. The symbol  $\nabla$  represents the gradient operator. The quantity  $K$ , known as the Clausius-Mossotti function, provides a measure of the strength of the effective polarization of the spherical particle with a dielectrical permittivity of  $\epsilon_2$ :

$$K(\epsilon_1, \epsilon_2) = \frac{\epsilon_2 - \epsilon_1}{\epsilon_2 + 2\epsilon_1} \quad (5)$$

Eq. (4) reveals the most important feature of dielectrophoretic effects. It shows that the dielectrophoretic force is proportional to the volume of the individual particles dispersed in the swelling liquid.  $f_{DEP}$  is also proportional to the dielectrical permittivity of the medium in which the colloidal particles are suspended. It is important to mention that the dielectrophoretic force vector is directed along the gradient of the square of electrical field intensity,  $\nabla E^2$ , which is in general not parallel to the electrical field vector,  $E$ . It is also seen that  $f_{DEP}$  depends on the sign and magnitude of the Clausius-Mossotti function. In case of  $K > 0$  the colloidal particles are attracted to electrical field intensity maximums and repelled from minima. The dielectrophoretic force not depend on the polarity of the electrical field, and it is observed with alternating current (AC) as well as direct current (DC) excitation. The direction of the field does not play any role.

### C. Electrorheological Effects

Electrorheology is defined as the electrical field-induced change in rheological properties, which is typically observed in suspensions [39–42]. This phenomenon is the manifestation of field-induced electrostatic stress. A typical electrorheological fluid consists of a suspension of fine dielectrical particles in the size range from nanometers to micrometers in a liquid of low dielectrical constant. In uniform fields, because of the lack of a field gradient, there are no attractive or repulsive field-particle interactions; therefore particle-particle interactions become dominant. The imposed field induces electrical dipoles. If the particles are spaced closely enough, so that their field can reach their neighbors, mutual particle interactions occur. These interactions can be very strong leading to a significant change in the structure of the particle ensemble. The particles attract each other when aligned end to end and repel each other when placed side by side. Owing to the attractive forces a pearl chain structure may develop, as shown in Figure 3a.

As a result, the viscosity of the suspension increases dramatically,

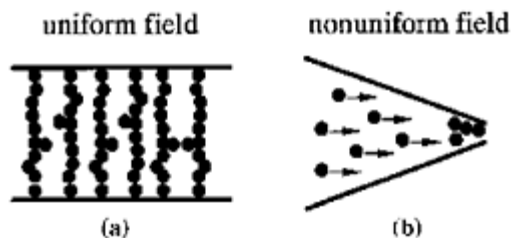


**FIG. 3** Electrorheological (a) and dielectrophoretic effects (b) of neutral particles under uniform and nonuniform electrical fields.

and when the field intensity exceeds a critical value, the electrorheological fluid turns into a solid.

#### D. Responsive Gels Based on Electrorheological Effects

Since polymer gels contain a substantial amount of liquid, it is possible to fabricate electrical field-sensitive gels. An *electrorheological gel* is a flexible polymer network swollen by an electrorheological liquid. The imposed electrical field induces dipoles in the filler particles. Two distinct types of electrorheological interactions can be identified depending on the nature of the applied field.

In a uniform electrical field the mutual particle interactions are dominant. The applied electrical field usually increases the value of the modulus [44], in a mechanism shown schematically in Figure 4. It was found that the shear storage modulus scales with the square of the electrical field intensity [45]. Unfortunately, there is little experimental evidence concerning this effect. Bohon et al. have found that in a uniform field unidirectional compression occurs [46]. The electrorheological gels are fast-motion gels: The response time can approach the order of a millisecond [45, 46].

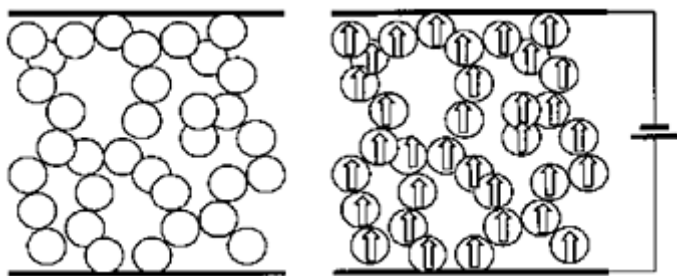


**FIG. 4** Schematic representation of an increase of modulus due to mutual particle interactions. This phenomenon is a demonstration of field-induced electrostatic stress. The arrows indicate the induced electrical dipoles.

In a nonuniform field, owing to the electrophoretic force and coupling between the polymer chains and solid particles, either locomotion or deformation is expected. Unfortunately, until now, no experimental evidence has been provided for the deformation of polymer gels due to dielectrophoretic forces.

### E. Responsive Gels Based on Electrophoretic Effects

An electrostatic charge is often a result of the excellent insulation properties of polymers. Certain solid materials may produce charges under an external electrical field. Colloidal semiconductor particles like  $\text{TiO}_2$  have been used as a photocatalyst in a number of reactions [47]. When these particles are embedded in a nonconducting polymer gel and placed in a strong DC field, electrons are emitted from the surface and the particles become positively charged [48]. The particles can release their surface charge only when they touch another body which is inversely charged. Since polymers are poor conductors, and the volume fraction of the dispersed particles does not exceed the percolation threshold, the charge displacement cannot equalize. As a result, the gel interacts with the applied electrical field. If the particles are considerably separated within the gel, carry relatively small charges, and the electrostatic force between the particles can be neglected, then the only electrostatic force to be considered is the one caused by the external electrical field. This force is given by Eq. (3).

The  $\text{TiO}_2$ -loaded PDMS gel cylinder, suspended in silicon oil, shows significant and rapid bending toward the cathode when an external electric field is applied. This behavior is reversible when positive and negative electrodes are alternated. Figure 5 shows the bending of a  $\text{TiO}_2$ -loaded PDMS gel measured at a different uniform electrical field strength. The  $\text{TiO}_2$  content of the gel was 10 wt%. When applying an external electrical field, the gel cylinder gradually

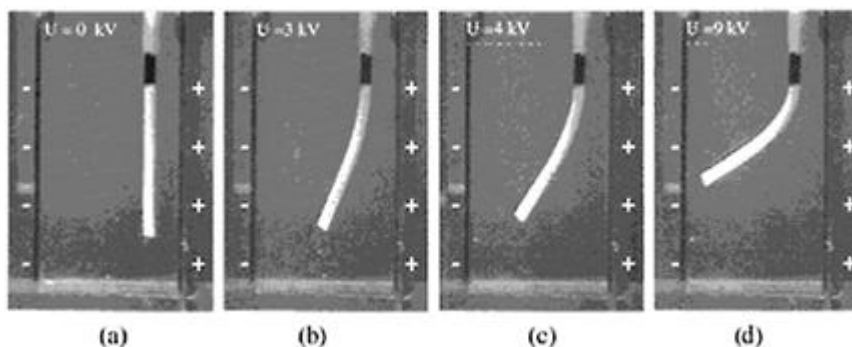


**FIG. 5** Deflection as a function of the electrical field strength [48]. The applied voltage is indicated on the figure. The gap distance is 3 cm. The polarity of the electrodes is also indicated.

bends toward the cathode. The displacement of the free bottom end of the gel depends on the strength of the electrical field. These experimental results have shown that in an



electrical field the gel accumulates positive charges and the measure of the electromechanical response is proportional to the DC field strength.

It was found that the spatial distribution of the electrical field does not play a significant role; thus the effect of a possible gradient force can be neglected [48, 49]. It is worth mentioning that the measured current was less than 0.8  $\mu\text{A}$  in each case. This means that, despite the high voltage, the input energy is rather small, offering a great promise in application as actuator devices. It has to be mentioned that the bending was rapid and the final equilibrium shape was reached within 5 s.

The experimental results suggest that the bending of suspended gel cylinders toward the cathode is the consequence of the interaction of a charged gel with the external electrical field. The net electrostatic force can in principle be obtained by summation of all forces exerted on the gel. The linear force density,  $\rho_f$  involves the Coulomb forces acting on the unit length of the suspended gel perpendicular to the axis of a freely pendent gel. The condition of mechanical equilibrium can be given by the following differential equation [49]:

$$\frac{d^4 u(z)}{dz^4} = \frac{\rho_f}{E_m \cdot \Theta} \quad (6)$$

where  $u(z)$  stands for the deflection at the point  $z$ ,  $E_m$  denotes the Young modulus of the gel, and  $\Theta$  is the moment of inertia,  $\Theta = \pi r^4/4$ . Here  $r$  represents the radius of the cylindrical gel. The solution of this differential equation with the boundary condition  $u(z=0)=0$  is:

$$u(z) = \frac{c \cdot V^2}{E_m \cdot \Theta} z^2 (z^2 - 4zl + 6l^2) \quad (7)$$

where  $l$  represents the length of the gel cylinder, and the constant  $c$  includes the capacitance and concentration of solid particles, as well as the gap distance. Eq (7) provides us the shape of a pendant, electrically stimulated gel. We have compared the prediction of Eq. (7) with a real experiment [49, 50]. It was found that close to the upper fixed point of the gel, the agreement is quite good. However, a significant deviation occurs at the lower end of the gel. This deviation may be due to the neglected gravitational effect. On the basis of Eq. (7), it is easy to determine the deflection of the free end of the gel,  $u(l)$ :

$$u(l) = \frac{3 \cdot c \cdot l^4}{E_m \cdot \Theta} \cdot V^2 \quad (8)$$

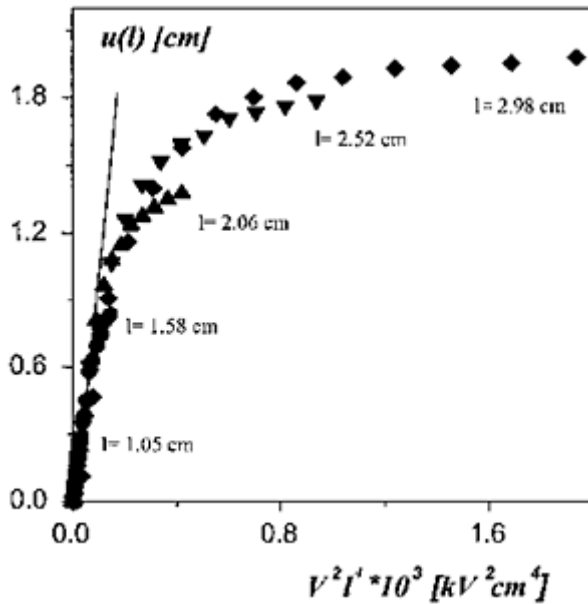


**FIG. 6** Deflection of the free end of the gel as a function of the product of  $V^2 \cdot l^4$ . The numbers indicate the length of the pendant gels.

Eq. (8) predicts that the deflection scales with the square of the electrical field and the magnitude is strongly influenced by the length of the gel.

On the basis of Eq. (8), we expect a unique function between  $u(l)$  and the product of  $V^2 \cdot l^4$  for a given gel. This relationship is plotted in Figure 6. It may be established that within the experimental accuracy this prediction seems to be valid. The experimental points scatter around the same line. From the initial part of this dependence we have determined the value of  $(3 \cdot c)/(E_m \cdot \Theta)$ . It was found to be  $9.1 \cdot 10^{-3} \text{ kV}^{-2} \text{ cm}^{-3}$ . The shape of the  $u(l) - V^2 l^4$  curve, which is not a straight line as predicted by Eq. (8), suggests that a simple linear capacitance relation that was assumed between the charge and voltage has a limited validity. For higher field intensities, a saturation effect must be taken into account.

We were able to produce several subsequent bending deformations of the gels by a modulated electrical field. In Figure 7, one can see three pairs of parallel plate electrodes, respectively. We have varied the direction of the field by changing the polarity of the subsequent electrode pairs to the opposite sign as shown in Figure 7. Since the negative electrodes attract the gel and the positive ones repel it, as a result, the gel forms a wave shape. If we change the polarities, undulation occurs. The undulation can be very fast as shown in Figure 7. To destroy and build up a new wave form in the opposite direction requires 264 ms. This corresponds to an undulation frequency of 3.8 Hz. It is worth mentioning that the kinetics of undulation is strongly influenced by the electrical field intensity, the diameter of the pendant gel, as well as the viscosity of the liquid.

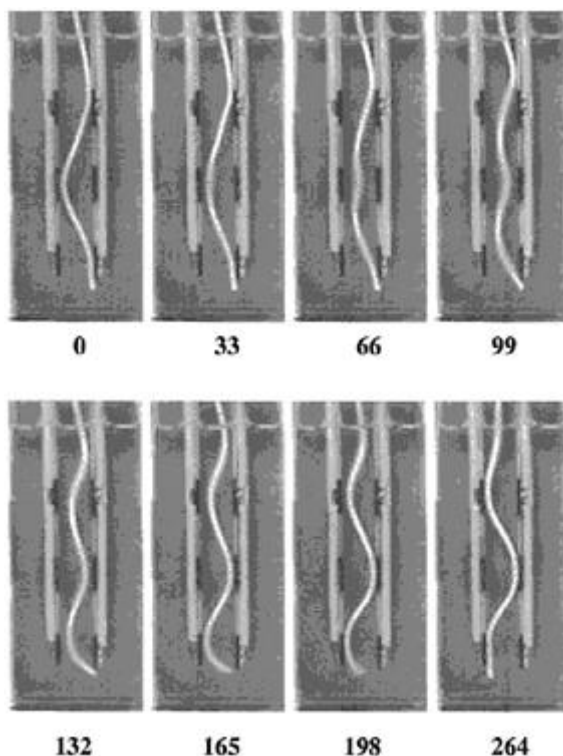


**FIG. 7** Undulation of a neutral polymer gel due to polarity change.

The rate of the electromechanical response was found to be proportional to the DC field strength. For any technical application, besides the fast response, it is important to have large forces and large displacement. The force derives from the interaction of charges with the external electrical field. The maximum charge before breakdown depends on both the voltage and electrical field. The magnitude of the electrical field, in practical applications, is usually confined in the range of 0.1–50 kV/mm [43].

The lower limit is usually considered too weak to move macroscopic objects, whereas the upper one is set by the occurrence of the electrical breakdown. A higher value of electrical fields, far beyond the value, which causes the break-down in macroscopic cases, is typical of very small devices. It is the main reason why electrostatics tend to become more important on small size scales, where fields, and hence forces, can be relatively high. Thus, scaling down the size of the electrical field-sensitive gels gives hope for the development of a new type of soft microelectromechanical actuator.

## IV. MAGNETIC FIELD-SENSITIVE POLYMER GELS

### A. Magnetostriction

Magnetostriction and magnetoelastic effects are fundamental to all ferromagnetic and ferrimagnetic materials [51]. Although there are several magnetostrictive effects, for example, volume and torsional changes, we shall consider only the longitudinal effect; that is, changes in the length. This is a common phenomenon in several materials, and it is called linear magnetostriction. Most of the magnetostrictive materials are solids which develop mechanical deformation when subjected to an external magnetic field. This phenomenon is attributed to the rotation of small magnetic domains in the solid body. In the absence of a magnetic field, the domains are randomly oriented. The imposition of an external magnetic field results in alignment of these domains and consequently a strain field occurs. As the intensity of magnetic field is increased, more and more magnetic domains orient themselves so that their principal axes of anisotropy become colinear with the magnetic field. At high field strength, all magnetic domains align along the direction of the field and as a result the magnetization saturates. In a material exhibiting magnetostriction, the dimension along the magnetization is elongated, whereas the dimension perpendicular to it is shortened, keeping the volume constant.

Until recently, the observed magnetostrictive deformations were quite small. For iron, nickel, and cobalt, the strain is of the order of  $10^{-5}$ . The largest magnetostriction has been found in the rare earth metals and compounds. Terbium-dysprosium-iron alloys offer strains up to 0.002. Although the magnetostrictive dimensional changes are small, they are driven by strong interatomic forces; therefore traditional magnetostrictive materials find application where very strong forces, but not large movements, are required.

### B. Ferrogels: Magnetostrictive Soft Materials

Magnetic field-sensitive gels, or as we will call them, ferrogels, are chemically cross-linked polymer networks swollen by a ferrofluid [52–69]. A ferrofluid or a magnetic fluid is a colloidal dispersion of monodomain magnetic particles with a typical size of about 10 nm [39, 40, 42].

Preparation of ferrogels does not require a special polymer or a special type of magnetic material. As a polymer network one may use very flexible chain molecules which can be cross linked. The magnetic filler particles can be prepared from ferromagnetic or ferrimagnetic materials. An important requirement is the strong adsorptive interaction between the solid particles and polymer network chains. One can prepare both magnetic hydrogels and networks swollen by organic ferrofluid. The magnetoelastic properties of ferrogels can be influenced in a wide range by chemical means. During the preparation it is possible to vary the initial polymer concentration, the degree of cross linking, as well as the amount of magnetic particles incorporated into the gel.

The degree of equilibrium swelling and the elastic modulus of the gel are strongly influenced by the initial polymer concentration and the degree of cross linking. The

magnetic properties are determined mainly by the quality and the size of dispersed magnetic material as well as the concentration of them. It is worth mentioning that in order to maintain the highest possible elasticity of gels the concentration of magnetic particles must be below the percolation threshold.

In this chapter, mainly chemically cross-linked poly(vinyl-alcohol) (PVA) hydrogels filled with magnetite ( $\text{Fe}_3\text{O}_4$ ) particles are discussed. A description of the chemical procedure can be found in our previous work [53–55].

### **C. Effect of a Magnetic Field on the Shape of Ferrogels as Seen by Naked Eyes**

In a uniform magnetic field, a ferrogel experiences no net force. When it is placed into a spatially nonuniform magnetic field, forces act on the magnetic particles and the magnetic interactions are enhanced. The stronger field attracts the particles, and owing to their small size and strong interactions with molecules of dispersing liquid and polymer chains, they all move together. Changes in molecular conformation can accumulate and lead to shape changes. The principle of the ferrogel's shape transformation and motility lies in an unique magneto-elastic behavior. The magnetic field drives and controls the displacement and the final shape is set by the balance of magnetic and elastic interactions. The shape change can be bending, elongation, contraction, and a combination of these basic distortions. This is demonstrated in Figure 8. The magnetic field-sensitive gels can be made to bend and straighten, as well as to elongate and contract repeatedly many times without damaging the gel. The response time to obtain the new equilibrium shape was found to be less than a second, and this seems to be independent of the size of the gel. It must be mentioned that all the shape changes reported here are completely reversible.

A peculiarity of ferrogel's shape distortion is the nonhomogeneous deformation which can be seen in Figure 8b and c. The gels were marked along their height by stripes perpendicular to the gel axis. The distance between subsequent stripes was constant. In a nonuniform magnetic field, the displacement of subsequent stripes does not remain the same as in the case of homogeneous deformation but varies along the gel axis, indicating the importance of nonhomogeneous shape distortion, which will be discussed in detail in Chapter 6.

### **D. Magnetic Properties of Ferrogels**

In a ferrogel, the finely distributed nanosized magnetic particles are located in the swelling liquid and are attached to the flexible network chains by adhesive forces.

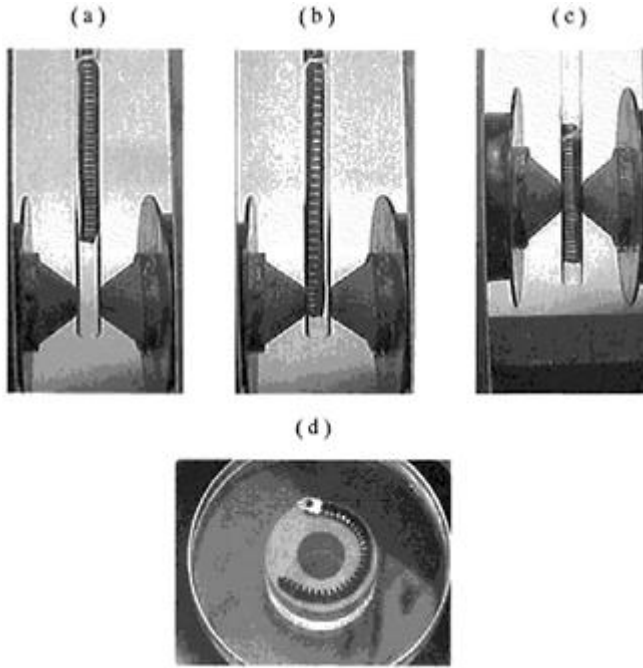


**FIG. 8** Shape distortion of ferrogels due to a nonuniform magnetic field. (a) No external magnetic field. (b) The maximal field strength is located under the lower end of the gel. (c) The maximal field strength is focused in the middle of the gel along its axis. (d) Bending induced by a permanent magnet.

The solid nanoparticles are the elementary carriers of a magnetic moment. If the concentration of magnetic particles is below the percolation threshold, the gel contains a collection of single-domain particles. From the magnetic viewpoint, the ferrogel is a dilute ensemble of noninteracting magnetic moments. Similar to ferrofluids, at elevated temperatures, the ferrogel should show superparamagnetic characteristics. But in contrast to magnetic fluids, the position of the particles built into the gel are rigidly fixed; thus the moments of the blocked particles cannot rotate toward the direction of the external field if the Zeeman energy is smaller than the anisotropy energy (this is the situation in fields smaller than 0.5 T).

In the absence of an external magnetic field, the moments are randomly oriented, and thus the gel has no net magnetization. As soon as an external field is applied, the magnetic moments tend to align with the field and produce a bulk magnetization,  $M$ :

$$M = \frac{\langle \mathbf{M} \cdot \mathbf{H} \rangle}{H} = M_S \langle \cos \theta \rangle \quad (9)$$

where  $\theta$  is the angle between the magnetic field and the magnetic axis of a particle,  $M_s$ , is the saturation magnetization,  $H$  is the external field, and an average,  $\langle \cos \theta \rangle$ , is taken over all the particles. With ordinary field strengths, the tendency of the magnetic moments to align with the applied field is partially overcome by thermal agitation, such as with the molecules of para-magnetic gas. As the strength of the field increases, all the particles eventually align their moments along the direction of the field, and as a result, the magnetization saturates. The single-domain particles are therefore the most efficient magnets.

If the field is turned off, the magnetic dipole moments begin to randomize, and thus the bulk magnetization reduces. Depending on the temperature and size of particles, there are two mechanisms for the relaxation of magnetization [70]:

1. The Brownian rotation, at which the rotation of the magnetic moments take place together with the rotation of the individual particles with a relaxation time,  $\tau_B$ .
2. The Néel relaxation, which is a rotation of the magnetic moments inside the particles; the Néel mechanism can be described by another relaxation time,  $\tau_N$ .

In ferrogels, the magnetic particles are trapped by the polymer network; therefore the Brownian rotation is supposed to be restricted and the Néel relaxation is expected to become more effective.

On the basis of relaxation times one can define a blocking temperature,  $T_B$ . At temperature  $T < T_B$ , the magnetic material exhibits ferromagnetic characteristics with hysteresis and remanent magnetization. With increasing temperature, the ferromagnetic characteristics decrease and vanish at the blocking temperature. Above  $T_B$ , all apparent ferromagnetic characteristics disappear even though within each particle the magnetic moments remain ferromagnetically aligned. It is worth mentioning that the blocking temperature is proportional to the volume of the magnetic particles, which means even a modest increase in particle size can result in a significant increase in the value of  $T_B$ . At  $T > T_B$ , the magnetic nanoparticles exhibit superparamagnetic behavior with a giant magnetic moment, which is about  $10^4$  times larger than the individual atomic moment.

The magnetic behavior of superparamagnetic material can be described by the Langevin function. Assuming the magnetization of individual particles in the gel to be equal to the saturation magnetization of the pure ferrimagnetic material, the magnetization,  $M$ , of a ferrogel in the presence of an applied field can be expressed as

$$M = \Phi_m M_s L(\xi) = \Phi_m M_s \left( \coth \xi - \frac{1}{\xi} \right) \quad (10)$$

where  $\Phi_m$  is the volume fraction of the magnetic particles in the whole gel, and the parameter,  $\xi$ , of the Langevin function,  $L(\xi)$ , is defined as

$$\xi = \frac{mH}{k_B T} \quad (11)$$

where  $\mu_0$  is the magnetic permeability of the vacuum,  $m$  is the giant magnetic moment of nanosized magnetic particles,  $k_B$  denotes the Boltzmann constant, and  $T$  denotes the temperature.

According to Eq. (10), the magnetization of a ferrogel is in direct proportion to the concentration of magnetic particles and their saturation magnetization. It is worth mentioning that the Langevin approach can be used either

If the particles are rigidly fixed in the gel and the energy barriers between the easy axeses for spin alignment are smaller than the thermal energy

Or the direction of the magnetization within the particle is fixed, but the rotation of particles in the gel is allowed.

The static properties are in either case the same, but the relaxation times are different. On the basis of Eq. (10), one may conclude that two experimental features should characterize superparamagnetism:

There is no hysteresis in the field dependence of the magnetization ( $M$  is a single valued function of  $H$ ).

The magnetization is a universal function of  $H/T$ .

Generalization of Eq. (1) to a polydisperse particle system is:

$$M = \int_0^\infty f(V) \Phi_m M_S L\left(\frac{M_S V H}{k_B T}\right) dV \quad (12)$$

where  $V$  represents the particles volume and  $f(V)$  is the normalized volume distribution function. Assuming the particles are spherical, a simple relation between volume and size exists, and the volume distribution can easily be converted to size distribution and vice versa.

The reduced magnetization is the magnetization divided by its saturation value,  $M_r = M/M(H \rightarrow \infty)$ . The reduced magnetization-magnetic field plot is commonly used for comparison of the size distribution of magnetic nanoparticle systems. The advantage of this plot compared to the regular magnetization plot (magnetization against magnetic field) is the independence on the amount of filler particles. Therefore, the shape of the reduced magnetization curve is determined by the magnetic size distribution of the particles. In case of ferrogels, the reduced magnetization is:

$$M_r = \int_0^\infty f(V) L\left(\frac{M_S V H}{K_B T}\right) dV \quad (13)$$



This equation provides a quantitative relationship between the magnetization and the size distribution function. Measuring the reduced magnetization, we can estimate the size distribution of the particles, or assuming or measuring the size distribution function (this is in most cases the geometrical size), we can determine the related magnetization curve. We also determined the geometrical size distribution from electronmicroscopy analysis. The possible difference between the size distributions indicates the existence of a magnetically dead layer [71].

Figure 9 shows a typical reduced magnetization curve of ferrogel. The size distribution of the particles was determined by electron microscopic analysis (*dotted line*). It is seen in Figure 9 that this theoretical curve is not a satisfactory fit to the experimental data. This indicates that magnetic size distribution is different from the geometrical one. We also plotted (*solid line*) the reduced magnetization correcting the Langevin function with a log normal size distribution with parameters  $D_m=9.8$  nm and  $\sigma=0.38$ . We obtained a perfect fit with experimental data (*solid line* in Figure 9).

It is important to mention that within experimental accuracy, no hysteresis loop has been observed. This means that no remanent magnetization takes place in ferrogels at room temperature. This is an important result indicating that in an alternating magnetic field the transformation of magnetic into thermal energy is rather small. For this reason, devices made of ferrogels and subjected to an alternating magnetic field are characterized by a small energy loss per cycle.

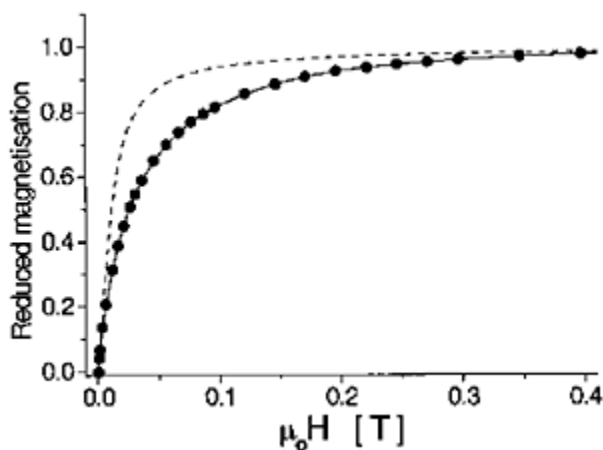


FIG. 9 Magnetization as a function of magnetic field intensity.

### E. Ferrogels in a Nonuniform Field

From the viewpoint of macroscopic deformations, the ferrogel can be regarded as a magnetic continuum. Hence, placed in a nonuniform magnetic field, the magnetic force density,  $\mathbf{f}_m$ , acting on a piece of ferrogel can be written as

$$\mathbf{f}_m = \mu_0(\mathbf{M}\nabla)\mathbf{H} \quad (14)$$

where  $\mu_0$  means the magnetic permeability of vacuum,  $\mathbf{M}$  represents the magnetization, and  $\nabla H$  takes into account the gradient of magnetic field,  $\mathbf{H}$ . It should be kept in mind that the magnetic force density vector varies from point to point in accordance with the position dependence of the product  $(\mathbf{M}\nabla)\mathbf{H}$ . In a nonaccelerating system, the force density manifests itself as a stress distribution which must be balanced by the network elasticity. A completely balanced set of forces is in this respect equivalent to no external force at all. However, they affect the gel internally, tending to change its shape or size, or both.

In general, the deformation induced by a magnetic field can not be considered to be homogeneous, since the driving force  $(\mathbf{M}\nabla)\mathbf{H}$  varies from point to point in space. However, one can find a special distribution of a magnetic field, where the deviation from the homogeneous case is not significant. In this case, the condition for uniaxial deformation of a ferrogel cylinder can be written as follows [58, 59]:

$$\lambda_H^3 - \beta(H_h^2 - H_m^2)\lambda_H - 1 = 0 \quad (15)$$

where  $\lambda_H$  denotes the deformation ratio due to field-induced strain. The parameter  $\beta$  is defined as

$$\beta = \frac{\mu_0\chi}{2G} \quad (16)$$

where  $\chi$  stands for the initial susceptibility of the ferrogel and  $H_h$  and  $H_m$  represent the magnetic field strength at the bottom and the top of a suspended ferrogel cylinder, respectively. Eq. (15) can be considered to be a basic equation for describing the unidirectional magnetoelastic properties of ferrogels. It shows that if we suspend a gel in a nonhomogeneous magnetic field in such a way that  $H_h > H_m$ , then elongation occurs. In the opposite case when the field intensity is higher on top of the gel, that is,  $H_h < H_m$ , Eq. (13) predicts unidirectional compression.

### 1. Unidirectional Magnetoelastic Measurements

We have studied the dependence of elongation on the steady current intensity required by the electromagnets to produce an external magnetic field. A cylindrical ferrogel was suspended in water to prevent evaporation of swelling liquid and to balance the weight of gels by the buoyancy. The experimental arrangement is shown in Figures 10 and 11.

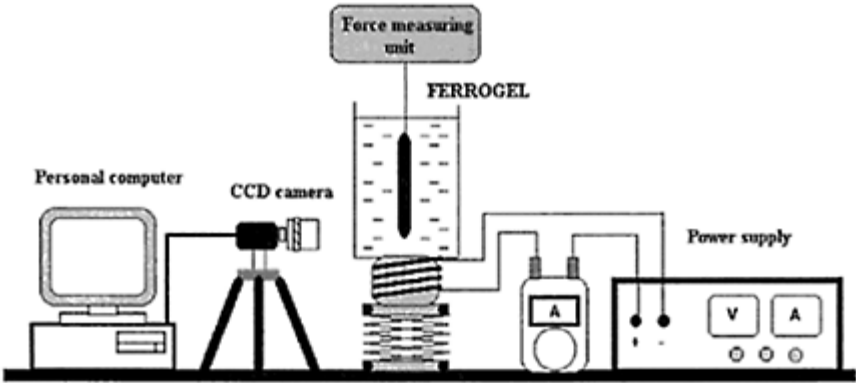


**FIG. 10** Experimental arrangement to measure the stress and strain induced by a magnetic field.

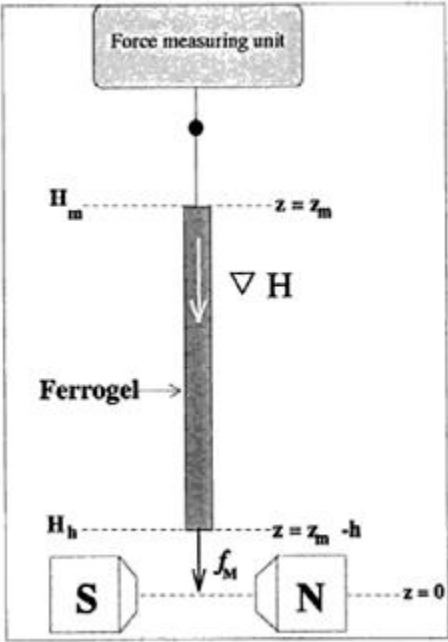


**FIG. 11** Schematic diagram of experimental setup to study the magnetoelastic properties of ferrogel cylinders.

We have also studied the magnetoelastic properties of ferrogel cylinders suspended in water vertically between plan-parallel poles of electromagnets as shown in Figures 8, 10, and 11. Figure 12a shows the effect of a magnetic field on the deformation of ferrogel. The relative displacement is plotted against the steady current intensity. It can be seen

that the displacement of the lower end of the ferrogel, due to magnetic force, is rather significant. A giant magnetostriction takes place. In many cases, we were able to produce an elongation of 40% of the initial length by applying a nonuniform magnetic field. It may be seen that at small current intensities the displacement slightly increases. However, at a certain current intensity, a comparatively large, abrupt elongation occurs. This noncontinuous change in the size appears within an infinitesimal change in the steady current intensity. A further increase in the current intensity results in another small extension.

We have found that by decreasing the current a contraction takes place. Similarly to the extension, the measurement of the contraction was found to have a noncontinuous dependence on current intensity. It is worth mentioning that the discrete shape transition occurred within a time interval of 1 s, independently from the gel size. Not only the relative displacement but also the measured force shows similar dependence characterized by both an abrupt change in magnitude and hysteresis. This is demonstrated in Figure 12b. The peculiar property of ferrogel's magnetoelasticity is the hysteresis which characterizes the extension-

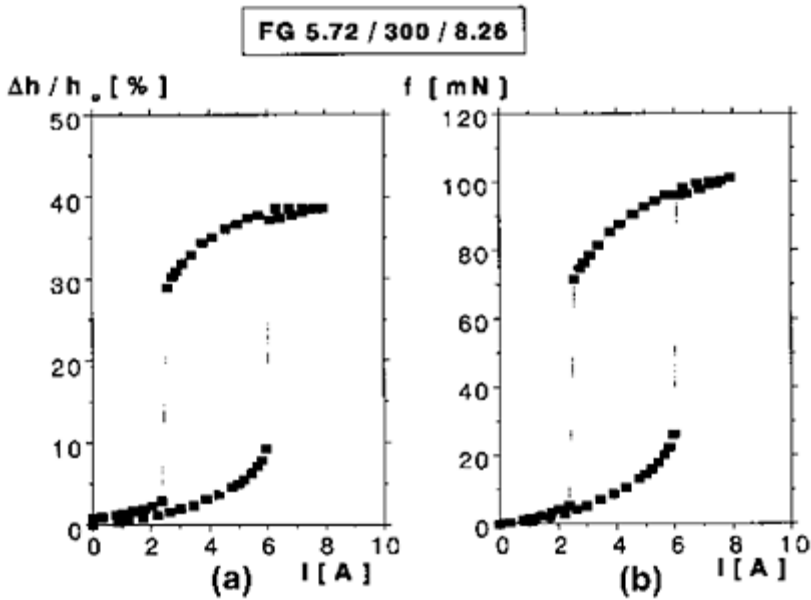


**FIG. 12** The noncontinuous magnetoelastic behavior of a ferrogel. (a) Relative displacement as a function of steady current. (b) Force induced by a magnetic field as a function of steady current.

contraction process. Despite its irreversible nature, this process is time independent under ordinary conditions. It must be emphasized that the observed hysteresis phenomena is not a consequence of the well-known magnetic hysteresis of ferromagnetic materials, since according to our measurements, the ferrogels exhibit no magnetic hysteresis at all.

By variation of the experimental conditions, we have found a crossover between continuous and discontinuous shape transitions. The initial position in the nonuniform magnetic field seems to play an essential role in the mode of stretching (Fig. 13). The crossover between continuous and noncontinuous

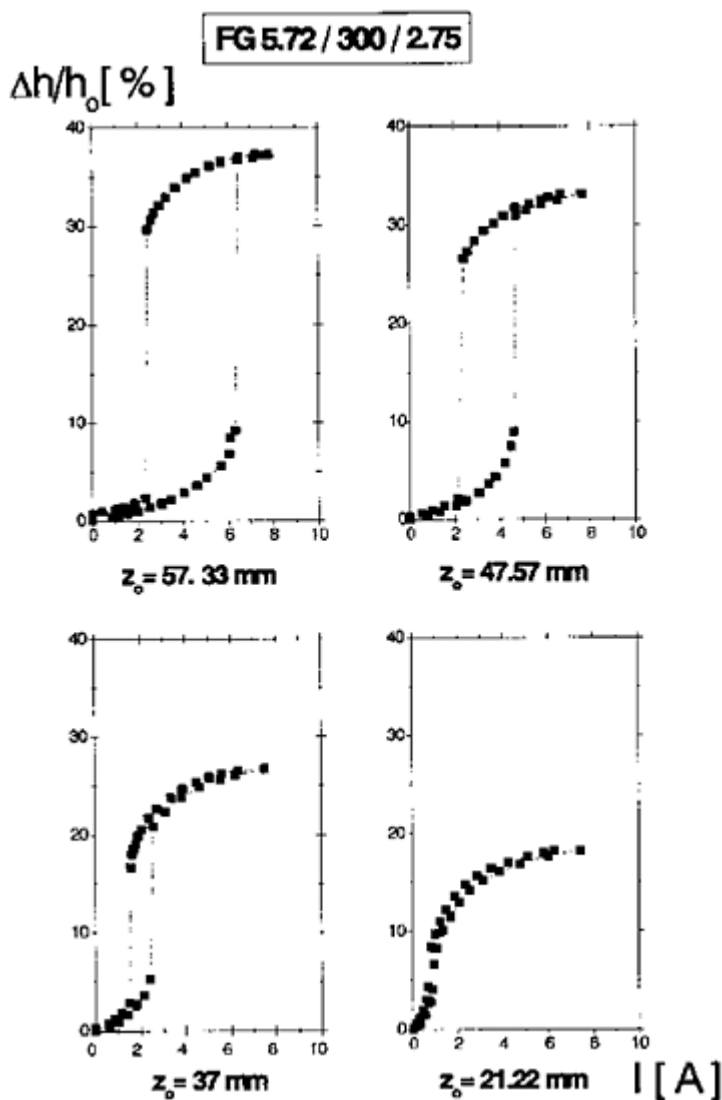


FIG. 13 The effect of the initial position of the discontinuous shape transition.  $h_0=163 \text{ mm}$  and the values of  $z_0$  are indicated.

transitions seems to be determined by the position of the gel only. A similar observation has been made for other ferrogels having a much smaller amount of magnetite. We have

varied the magnetite concentration of ferrogels in a wide range between 2.75 and 12.6 w%. For each gel's similar abrupt shape transition have been observed [57–59].

## 2. Interpretation of Noncontinuous Shape Transition

It is possible to interpret the abrupt shape transformation and hysteresis phenomena on the basis of Eq. (15). In order to find the dependence of elongation on the steady current intensity, first we have to relate the magnetic field strengths,  $H_h$  and  $H_m$ , to the steady current intensity. Let us assume that the magnetic field strength varies along the gel axis as

$$H(z) = H_{max} h(z) \quad (17)$$

where  $H_{max}$  represents the maximal field strength at the position  $z=0$  and  $h(z)$  is a unique function characterizing the experimental arrangement (geometry of poles and gap distance). It was found that the  $z$ -directional distribution of magnetic field strength can be satisfactorily approximated by the following forms, as shown in Figure 14:

$$h(z) = \begin{cases} 1 - kz^2 & \text{if } |z| < \delta \\ (1 - k\delta^2)e^{-\gamma(|z|-\delta)} & \text{if } |z| \geq \delta \end{cases} \quad (18)$$

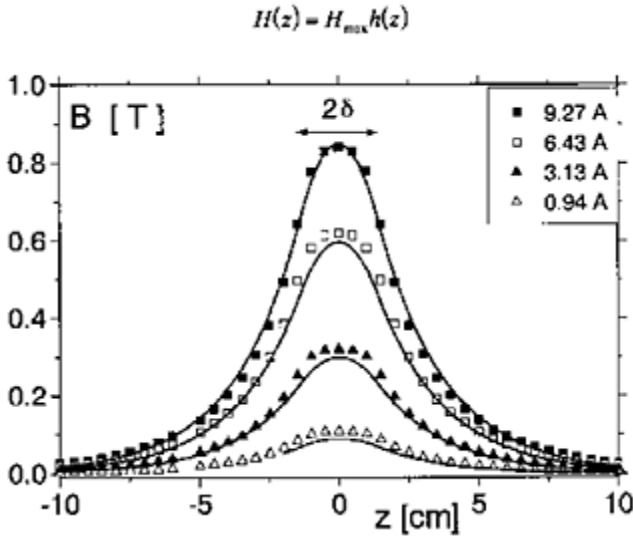


**FIG. 14** Magnetic field distribution used for the experiments. The magnetic induction  $B = \mu_0 H$  is plotted against the distance measured from the center of the face-to-face planparallel magnetic poles of the electromagnet. The solid line was calculated from Eqs. (17) and (18).

where  $\gamma$  is a characteristic constant describing the exponential decay of field strength at larger distances,  $\delta$  denotes the radius of poles, and the constant  $k = \gamma/(2\delta + \gamma\delta^2)$  was determined by taking into account the same slope of  $h(z)$  curves at distance  $r = \delta$ , where the functions [in Eq. (18)] meet each other.

According to the Biot-Savar law,  $H_{\max}$  can be written as  $H_{\max} = k_I I$ , where  $k_I$  means a proportionality factor and  $I$  is the steady current intensity. It must be mentioned that the value of parameter  $k_I$  strongly depends on the quality of the electromagnet.

The numerical solution of Eq. (15) provides the  $\lambda$  dependence which is shown in Figure 15. In contradistinction to the state of equilibrium, the internal parameter (deformation ratio) is not a single-valued function of the external parameter (current intensity); that is, metastability develops with abrupt non equilibrium transition. The transition from A  $\rightarrow$  B takes place at a different value of current intensity from that for C  $\rightarrow$  D. An area ABCD remains as a kind of hysteresis loop. This cycle depicted in Figure 15 is time independent and may be repeated several times. Here a macroscopic energy barrier is provided by magnetic interactions and this energy barrier compels the ferrogel to go around it at a higher or lower current than the equilibrium value. A thermodynamic analysis of this abrupt shape transition was also provided [59]. It was shown that noncontinuous shape transition is due to a shift of the equilibrium state from one local minimum to another one similar to a first-order phase transition.

We have also studied the influence of parameters  $z_0$  on the shape of  $\lambda(I)$  dependence. These results are summarized in Figure 16. One can see that with increasing  $z_0$ , both the measure of abrupt transition and hysteresis increases. This finding is in accordance with our experimental results (Fig. 13). The parameter  $\gamma$  which controls the gradient of the field strength also plays an essential role. It is

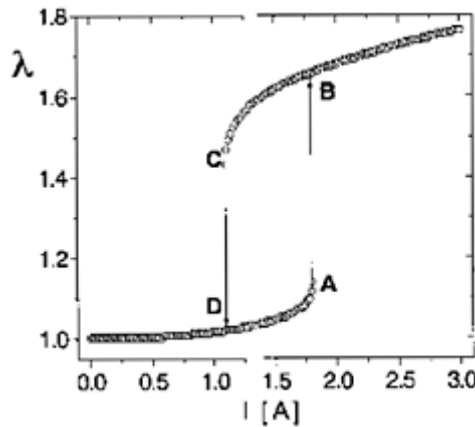


**FIG. 15** Dependence of deformation ratio,  $\lambda$ , on the steady current intensity as calculated on the basis of Eq. (15). For the calculation,  $h_0 = 10$  cm,  $z_0 = 5$  cm, and  $\gamma = 0.4$  were used.

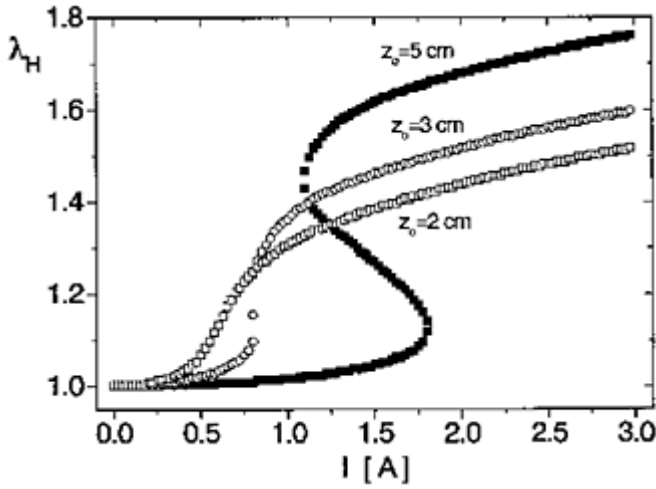


**FIG. 16** Dependence of deformation ratio,  $\lambda$ , on the steady current at different initial positions of the gel.

that the necessary condition for realizing an abrupt transition requires a value of  $\gamma > 0.15$ . Below this value, no discontinuous transition occurs if  $h_0 = 10$  cm and  $z_0 = 5$  cm.

In order to discuss the nature of this transition in a thermodynamic context, it is convenient to shift our attention to the thermodynamic potential which characterizes the system.

A description of the effect of a magnetic field on the thermodynamic properties requires the adoption of the magnetic energy as an additional interaction energy:

$$W_M = \frac{1}{2} \int_W \mathbf{M} \mathbf{H} dV \quad (19)$$

Here the integration is over the total volume of magnetic body placed into the field. In our case, the magnetic potential energy of the ferrogel cylinder having a cross-sectional area of  $a_0$  and a susceptibility of  $\chi$ , can be written as

$$W_M(\lambda_z) = \frac{\mu_0 \chi a_0}{2\lambda_z} \int_{z_M}^{z_M - h_0 \lambda_z} H^2(z) dz \quad (20)$$

The elastic contribution of the energy,  $W_{el}(\lambda_z)$ , can be obtained from the theory of rubber elasticity:

$$W_{el}(\lambda_z) = \frac{1}{2} GV \left( \lambda_z^2 + \frac{2}{\lambda_z} - 3 \right) \quad (21)$$



In order to study the noncontinuous magnetoelastic behavior of ferrogels and the mechanical instability, we have plotted the whole energy of the magnetic gel,  $W$  (which includes the elastic and magnetic energy as well), against all possible deformation ratios. Only the case of unidirectional extension (i.e.,  $H_h > H_m$ ) is taken into consideration.

$$W(\lambda_z) = W_e(\lambda_z) + W_M(\lambda_z) \quad (32)$$

The equilibrium position corresponds to the minimum of the  $W(\lambda_z)$  function. Figure 17 shows the  $W(\lambda_z)$  dependence at different steady current intensities calculated on the basis of Eq. (22). It is difficult to see that at small current intensities there is a minimum which corresponds to the stable equilibrium. Increasing the current intensity above a certain value ( $I=6A$ ), the single equilibrium state bifurcates into two minima. These two minima are separated by an energy gap. If the potential has the form shown in Figure 17 for  $I > 6A$ ,

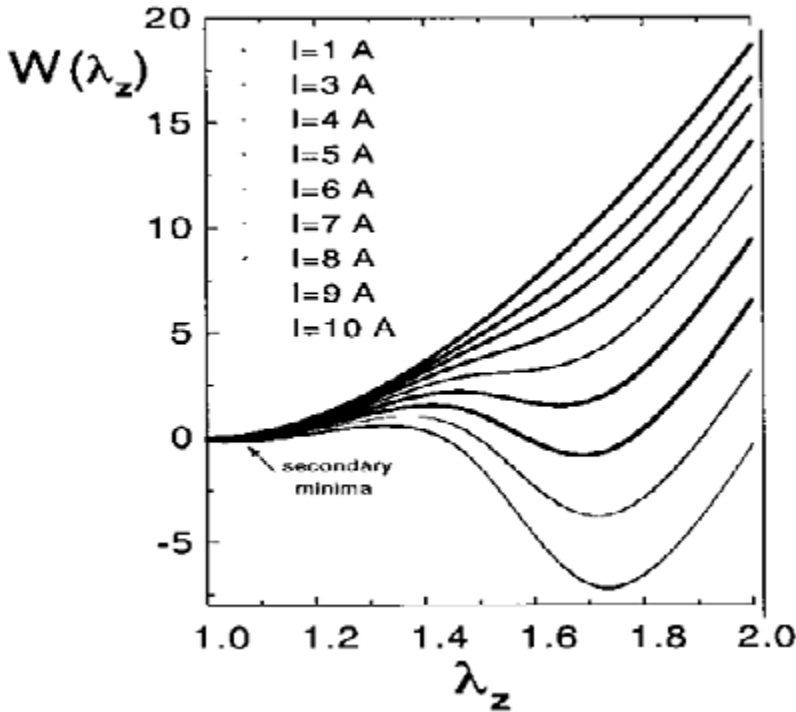


**FIG. 17** Dependence of free energy of a ferrogel as a function of a possible deformation ratio at different magnetic field distributions. The current increases from top to the bottom on the functions.

the system is stable in the lower minimum. Let us consider that system is in the secondary minimum. A relative small fluctuation is all that is required to overcome the

shallow energy barrier at the secondary minimum. As a result, the ferrogel quickly turns to its stable state. Inversely, the absolute minimum is separated from the secondary minimum by a much higher energy barrier. The fluctuation from here into the other minimum is very impossible, since the probability of such transition decreases exponentially with the height of the intermediate energy barrier.

### 3. Nonhomogeneous Deformation

The description of the macroscopic deformations of ferrogels requires a special treatment owing to the complex nature of the mechanism of magnetic field-induced deformations. The nonlinear character of both elastic and magnetic interactions results in some novel features of the deformation process. However, not only the high degree of nonlinearity of the governing equations but also the nonhomogeneity of the resulting deformations makes the treatment special and fairly complicated. As a body force, the magnetic field induces deformations with a unique pattern never seen in deformations induced by surface tractions.

In the conventional theory of elasticity [72], a linear relationship between stress and strain is assumed. In this way, the elastic nature of a material is fully described by a tensor of the elastic moduli. For most solids in ordinary situations, this approximation is acceptable, since the deformations are small. Most of the magnetism-related elastic effects, such as magnetostriction, can be treated in the frame of the linear theory. The reason for this is that materials with significant magnetic susceptibility (i.e., ferro-, antiferro-, and ferrimagnetic materials) are hard solids, consequently are unable to sustain large deformations even in fields as high as several tesla. In ferrogels, however, superparamagnetism provides a fair amount of magnetic susceptibility, and the extremely high elasticity of the polymer network results in a material capable of undergoing giant deformations (the strain can reach 1.5) in an ordinary magnetic field. It is clear that for ferrogels we need to employ the generalized, nonlinear theory in order properly to describe the deformation process in the whole deformation range.

In the theory of nonlinear elasticity, a material body is regarded as a set of elastically joined material points. The forces are considered to act on the material points and the condition of mechanical equilibrium is characterized by the balance between external and elastic forces. External forces are classified by means of their nature as surface tractions and body forces. Surface tractions act only on surface points, whereas body forces act on each material point. Naturally, body forces can be generated only by fields of which the most common is gravity, which acts universally and homogeneously on each material element. Although at first glance the treatment of gravity in the theory of elasticity seems to be quite straightforward, nevertheless, the resulting deformation is always nonhomogeneous; that is, the displacement of material points during the deformation varies point by point. The reason for the nonhomogeneity is that the stress changes vertically analogous to hydrostatic pressure.

As two popular examples of gravity-induced deformations, which can be found in any textbook on elasticity, we refer to the bending of a stick and the distortion of a standing column under their own weight. The other two fields, namely, electrical, and magnetic fields, can induce even more interesting deformation patterns. Unlike gravity, these fields

might have a complex distribution in space. Since the field, and the force alike, is nonuniform, different material points experience forces of different strength and direction, which leads to a nonhomogeneous deformation often with a complex deformation pattern. As an illustrative example of the complex deformation that ferrogels can achieve in a magnetic field, we present the two-dimensional deformation of a ferrogel sheet in Figure 18. The gel sheet is shown in the undeformed (a) and deformed (b) states, respectively. The sample was placed in between two glass plates so that no perpendicular deformations were allowed. The magnetic field was induced by

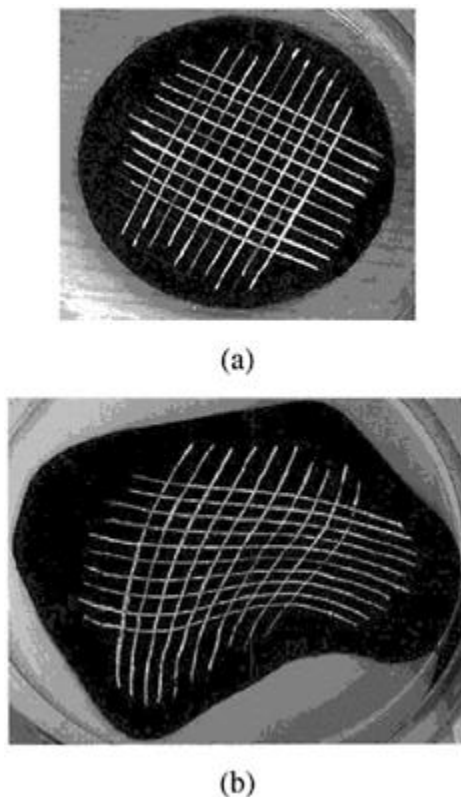


**FIG. 18** Illustration of the complex nonhomogeneous deformation of a ferrogel sheet. Undeformed (a) and deformed (b) states. The magnetic field was induced by permanent magnets placed around the gel.

a couple of permanent magnets placed around the gel. The complexity and nonhomogeneity of the deformation is well demonstrated on the distortion of the grid that was painted on the surface of the gel.

In order to point out the essential difference between deformations induced by body forces and surface tractions, we recall Ericksen's theorem [73]. The theorem states that homogeneous deformations are the only deformations, which can be achieved by the

application of surface tractions alone, considering a homogeneous and isotropic material characterized by an arbitrary strain-energy function. In other words, we cannot induce diverse nonhomogeneous deformations with surface tractions. In contrast to surface tractions, application of fields that act as body forces leads to nonhomogeneous deformations without any additional constraints for the material.

Not only the nature of the resulting deformation but also the treatment of body forces is different from that of surface tractions. Many well-established and successful methods of nonlinear elasticity (e.g., inverse method, diagonalization of the deformation tensor) are not applicable owing to the nonhomogeneity of the deformation. How to describe magnetic field-induced nonlinear deformations of a hyperelastic, incompressible magnetic continuum characterized by Langevin-type magnetization and a neo-Hookean strain-energy function is discussed elsewhere [74]. This latter is frequently used for swollen polymer gels. Although we concentrate on the deformations of ferrogels, the presented theory is general in a sense that it is applicable for electrical field-induced deformations as well.

As we point elsewhere [74], owing to the relatively complex form of the Langevin-type magnetization and the magnetic force density, even in simple magnetic field distributions, it is not possible to achieve an analytical solution of the driving equations. In order to demonstrate the characteristics of the magnetic field-induced deformations of a magnetic continuum, it is worth examining a simple one-dimensional situation.

Let us consider a very simple physical situation similar to our unidirectional experiments discussed in the previous section. Namely, a long and thin ferrogel cylinder is suspended in water vertically. The magnetic field is induced by a solenoid-based electromagnet placed under the gel. The axis of the gel cylinder ( $z$ ) is parallel with the magnetic field and its gradient. In this case, the deformation of the gel is uniaxial and can be considered to be one dimensional.

The governing equation for this situation describing the displacement of each point of the gel along the  $z$ -axis is the following second-order, nonlinear ordinary differential equation [75]:

$$G \left[ \frac{d^2 u_z(Z)}{dZ^2} + \frac{2}{(du_z(Z)/dZ)^3} \frac{d^2 u_z(Z)}{dZ^2} \right] + M[u_z(Z)] \frac{dH[u_z(Z)]}{dZ} = 0 \quad (23)$$

where  $u_z(Z)$  represents the displacement given in the reference, undeformed, configuration,  $G$  is the shear modulus of the gel,  $M$  denotes the magnetization,

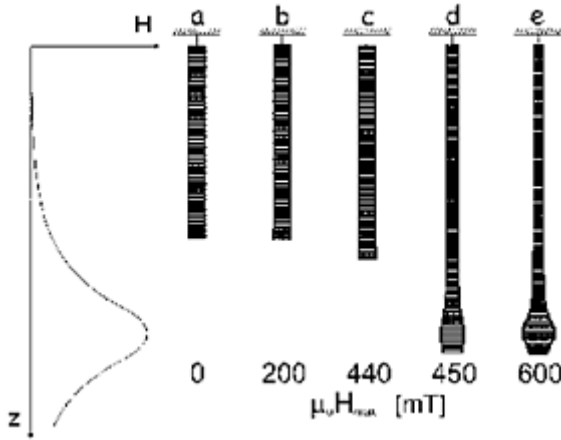


**FIG. 19** Schematic representation of the uniaxial deformation of a ferrogel cylinder calculated numerically from Eq. (1). The external magnetic field distribution described by Eqs. (28)–(30) is also indicated. The gel on the left-hand side is undeformed ( $B=0$ ). The others represent the abrupt transition within a slight increase of the field intensity.

and  $H$  denotes the magnetic field strength. As boundary conditions, the displacements and/or the surface tractions must be prescribed on the two ends of the gel cylinder. In our particular case, the position of the top surface of the gel cylinder was fixed by a rigid, nonmagnetic copper thread, whereas the bottom surface was free and unloaded. Accordingly:

$$u_z(0)=0, t(Z_m)=0 \quad (24)$$

where 0 and  $Z_m$  represent the positions of the top and bottom ends of the gel, respectively.

Based on Eq. (23) with boundary conditions given by Eq. (24), we calculated the unidirectional deformation of a ferrogel cylinder. This is shown in Figure 19. On the left-hand side, the magnetic field strength along the  $z$ -axis is plotted. The distribution of the field we employed in the calculations was similar to that in real experiments. As one can see, the gel elongates eventually as the magnetic field intensity increases. At a certain field intensity, the gel falls abruptly into a new equilibrium position similar to what we observed experimentally. The white lines on the gel body demonstrate the nonhomogeneity of the deformation. The different distance between adjacent lines indicates a different degree of deformation. The high degree of nonhomogeneity is well seen. At lower field intensities (gels b and c), the upper part of the gel elongates to a greater extent than the lower part, whereas at higher field intensities (gels d and e), the lower part of the gel contracts while the upper part elongates.

In order to test the validity of our model, we compared theoretical calculations with the

results of unidirectional experiments. In Figure 20, the strain of the

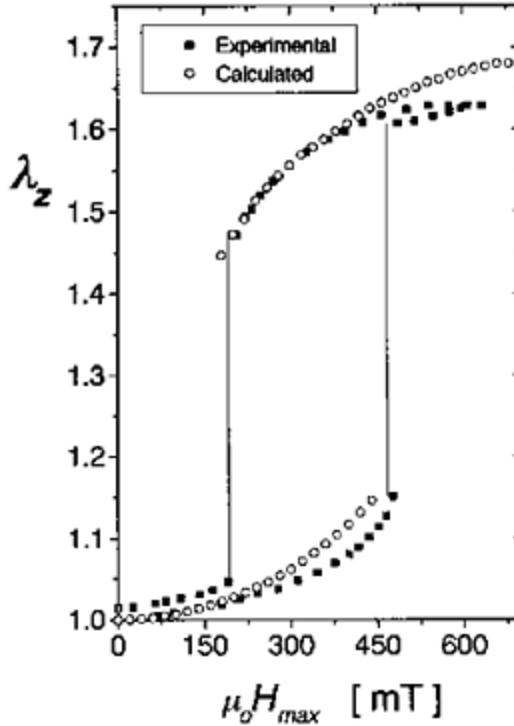


**FIG. 20** Uniaxial elongation of a ferrogel cylinder. The points represent the displacement of the bottom end of the gel. The blank points were calculated on the basis of Eq. (26) with boundary conditions and magnetic field distribution given by Eq. (27) and Eqs (28)–(30), respectively.

bottom end of the gel is plotted against the maximum field intensity. Both experimental and calculated points are shown. The calculated points fit quite well to the measured ones, indicating that our model is able to reproduce not only the noncontinuous characteristic of the deformation process but also provides accurate, realistic numerical values.

As mentioned previously, the analytical determination of the displacement field is generally extremely complicated; therefore, a numerical procedure is necessary to calculate the deformation. Nowadays the finite element method (FEM) is prevalent in solid mechanics and provides a useful tool to study realistic, three-dimensional nonlinear deformations. However, magnetic body forces are not commonly applied in engineering; consequently, they cannot be simply considered with the usual FEM systems. Some FEM programs allow us to extend the program with user-defined subroutines for modeling various material behaviors, load types, or other special effects. The FEM system MARC [75] has been chosen for the calculations, because it was developed for modeling

nonlinear mechanical deformations and it can be extended with the aforementioned user subroutines. As an illustrative example of three-dimensional deformation of ferrogels, in Figure 21, we present the deformation of a ferrogel block whose ends are fixed to a wall. The magnetic field is uniaxial and has a Gaussian distribution along the gel axis as shown on the top of Figure 21. The arrows indicate the location of the maximum field intensity. We represented the deformation of the block at different field intensities. Looking at the set of pictures one may associate with the motion of a living worm. This indicates that the deformation and motion of ferrogels have a close relationship with those of

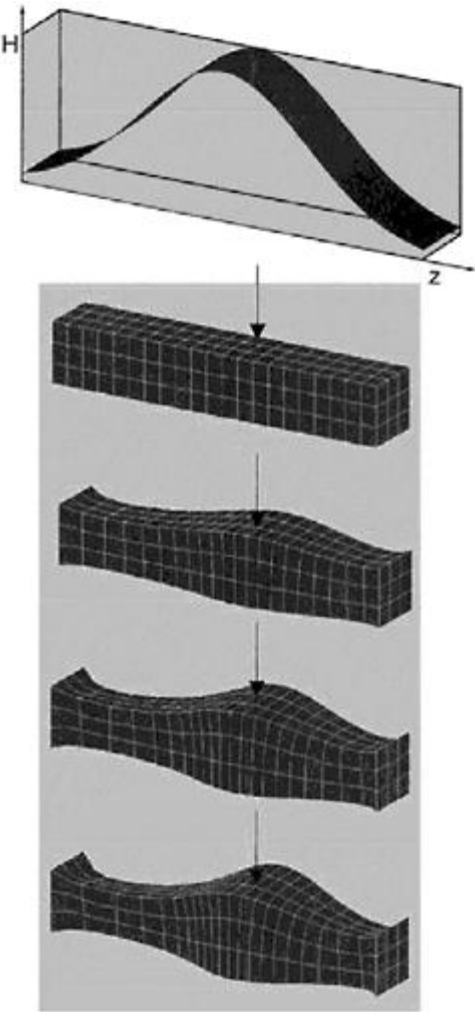


**FIG. 21** FEM calculation of the deformation of a ferrogel block in a uniaxial magnetic field at different field intensities. The magnetic field strength has a Gaussian distribution along the block as shown. The position of the field maximum is indicated by arrows.

simple living organisms. This is due to the complexity and nonhomogeneity of the magnetic field-induced deformations.

#### 4. Theoretical Basis for Design of Ferrogel Actuators

The shape change of ferrogels induced by a nonuniform magnetic field can be exploited to construct soft actuators which convert energy from magnetic to mechanical work. We consider here a vertically suspended cylindrical ferrogel as a linear actuator by means of which a nonmagnetic load can be lifted up. The position of the upper surface of the gel is fixed. First the gel is preloaded with a mass,  $M$ . As a consequence, a passive strain,  $\lambda_M$ , develops. The magnitude of the extension due to the passive strain can be calculated on the basis of the rubber elasticity theory. The neo-Hookean law of rubber elasticity can be written as follows:

$$\lambda_M^3 - \alpha \lambda_M^2 - 1 = 0 \quad (25)$$

The dimensionless quantity,  $\alpha$ , includes the ratio of nominal stress,  $\sigma_n$ , and the modulus,  $G$ . The nominal stress due to the load of mass of  $M$  can be given as  $Mg/a_0$ , where  $g$  represents the gravitational constant and  $a_0$  denotes the undeformed cross-sectional area of the gel at rest.

$$\alpha = \frac{\sigma_n}{G} = \frac{Mg}{a_0 G} \quad (26)$$

Eq. (25) tells us how the deformation ratio depends on the applied mechanical stress and modulus. It is obvious that, in the presence of a load, the pendant gel elongates; that is,  $\lambda_M > 1$ .

When an external magnetic field is applied, due to the strong magnetostrictive effect, the strain will be changed to  $\lambda_{M,H}$ . This quantity can be obtained from Eq. (27) [69]:

$$\lambda_{M,H}^3 - \alpha \lambda_{M,H}^2 - \beta (H_h^2 - H_m^2) \lambda_{M,H} - 1 = 0 \quad (27)$$

Eq. (27) shows that if we suspend a ferrogel in a nonhomogeneous magnetic field in such a way that  $H_h > H_m$ , then elongation occurs  $\lambda_{M,H} > \lambda_M > 1$ . When the field is turned off, the load is lifted up. In the opposite case,  $H_h < H_m$ , work is released when the magnetic field is applied,  $\lambda_M > 1$ , but  $\lambda_{M,H} < \lambda_M$ . We have found that the displacement of the end of the gel is much more significant at elongation than at contraction. An expression for the mechanical work can be derived:

$$W = Mg \Delta h = Mg h_0 (\lambda_{M,H} - \lambda_M) \quad (28)$$



where  $h_0$  denotes the undeformed length of the magnetic gel.

For such a case, as a representative example, we have calculated the mechanical work as a function of current intensity at different applied loads. We have

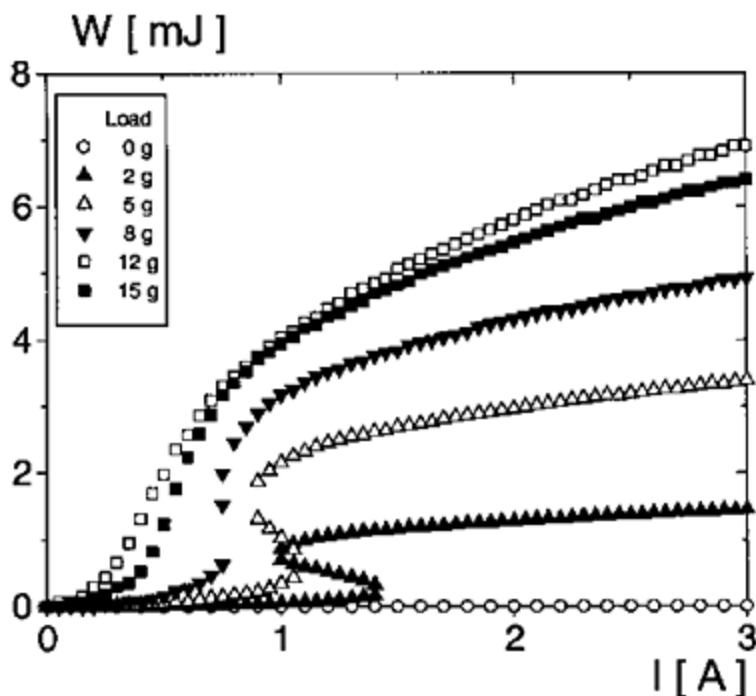


**FIG. 22** The mechanical work at different applied loads as calculated on the basis of Eq. (28). The mass of the load is indicated.

considered a cylindrical gel with a length of 10 cm and a volume of  $7.8 \text{ cm}^3$ . This gel contains 0.39 g polymer and 0.31 g magnetite. The results are shown in Figure 22. It is obvious that the mechanical work strongly depends on the applied load. One can see that at small loads the work increases with the load.  $M=12 \text{ g}$  represents the highest mechanical work. It is also seen that, above a certain value, if the load is comparatively heavy, the work decreases with increasing mass. Similar results have been found for mechanical work produced by swelling [76]. Any other experimental situation can be studied with the aid of Eqs. (27) and (28).

## 5. Kinetics of the Shape Change

Any technical application of magnetic field-sensitive polymer gels critically depends on the response time. It is therefore of primary interest to investigate the deformation behavior of ferrogels in response to the magnetic stimulus. Since the magnetic field is created by electromagnets, it is easy to achieve dynamic conditions by modulated current intensity. We applied stepwise and sine wave modulation by a function generator in the

frequency range of 0.01–100 Hz. A cylindrical gel sample characterized by a height of 8.0 mm and radius of 4.5 mm was put onto the upper surface of a standing electromagnet [62, 76]. The position of the top surface of the gel was measured by a light beam and the displacement was monitored with the aid of a light diode as a voltage signal. Owing to the experimental arrangement, a contraction takes place when current flows through the solenoid. When the current is turned off, the gel expands and its equilibrium shape is recovered. We have measured the elastodynamic response of ferrogels at different frequencies. Owing to technical reasons, the elastodynamic response at higher frequencies can be more conveniently studied by sine wave modulation of the current. According to Eq. (14), the measure of deformation is determined by the square of current intensity. The direction of the magnetic field does not play any role. Consequently, the frequency of created magnetic force and the frequency of the current is not the same. As a result, within one period of current change, we expect two periods of magnetic force as well as two cycles of deformation. Figure 23 shows the frequency dependence of the elastodynamic characteristics of a ferrogel. It can be seen that up to 40 Hz, the magnetic stimulus and the elastic response are strongly coupled. Neither phase shift nor significant mechanical (nor magnetic) relaxation takes place. It is important to mention that above 40 Hz, no elastodynamic response has been observed.

### F. Ferrogels in a Uniform Magnetic Field

As discussed earlier, unlike conventional magnetostrictive materials, ferrogels do not become deformed in uniform fields. The reason for this is that the small superparamagnetic particles embedded in the polymer matrix experience no force in a uniform magnetic field. Similar to the chain formation in magnetorheological, and electrorheological fluids, one might expect some kind of alignment of the nanoparticles as a result of the anisotropic nature of magnetic dipole-dipole interaction. In the case of ferrogels, however, since the particles are bond to the polymer network, and consequently are restricted in their motility, no movement or alignment of the particles takes place.

The only process taking place when a uniform magnetic field is imposed on a ferrogel is the rotation of the magnetic dipole moment of the individual particles. This results in a considerable macroscopic magnetization of the gel. As a consequence of the magnetization, a demagnetizing field will be formed, reducing the effective field inside the gel:

$$H_{eff} = H_{app} - H_{dem} = H_{app} - NM \quad (29)$$

Here  $H_{eff}$ ,  $H_{app}$ , and  $H_{dem}$  denote the effective, applied, and demagnetizing field, respectively,  $N$  represents the demagnetizing coefficient that is related to the shape of ferrogel, and  $M$  is the magnetization of ferrogel.

The magnetic energy,  $W_M$  of a piece of ferrogel is related to the effective field:

$$W_M = \mu_0 M H_{eff} \quad (30)$$

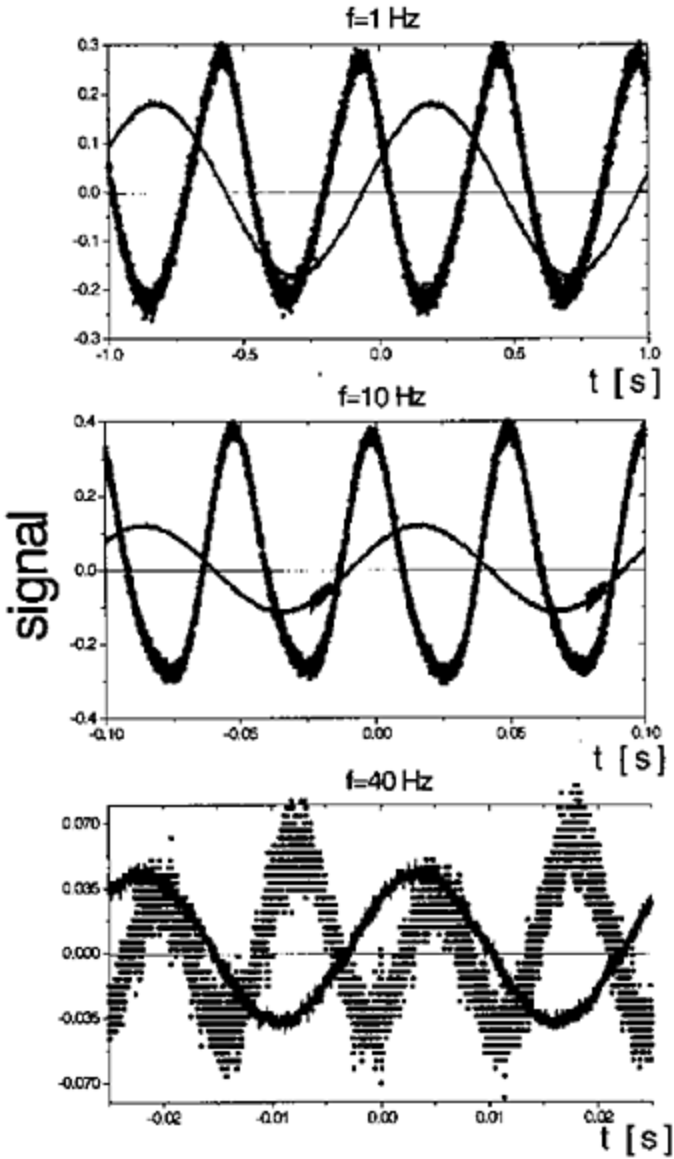


**FIG. 23** Elastodynamic response of a ferrogel at different frequencies of sine wave modulation. Solid line represents the modulated current, dotted line corresponds to the elastic response. The frequency,  $f$ , is indicated.

Let us consider how the magnetic energy of a piece of ferrogel changes when it becomes deformed. For the sake of simplicity, let us consider a unidirectional deformation parallel

to the applied field. Deformation of the ferrogel sample involves a change in the geometry, and thus results in a change of the demagnetizing coefficient. As a consequence of the change in the demagnetizing coefficient, both the effective field and magnetization will change, resulting in a change of the magnetic energy. This means that deformation of a ferrogel requires more or less energy in a uniform magnetic field, since one must overcome the change in the elastic and magnetic energy as well. In practice, the magnetic effect manifests itself as an increase or a decrease in the elastic modulus of a ferrogel. Whether the gel becomes apparently stiffer or softer depends on the relative direction of the applied field and deformation, respectively

From an application point of view, there are two convenient arrangements. First, the axis of deformation and the applied field are parallel. In this case, compression of the ferrogel sample results in a decrease of the magnetic energy, and thus a smaller compression modulus. Elongation of the gel, however, involves an increase in the magnetic energy, so that there is a higher elastic modulus. In the second arrangement, the axis of deformation and the direction of the applied field are perpendicular. In this case, the compression modulus increases, whereas elongation of the gel will become easier.

In the case of a unidirectional deformation, the accessory “magnetic” modulus of a ferrogel can be easily calculated from the change of magnetic energy due to distortion of the gel. It is convenient to introduce a magnetic stress,  $\sigma_M$ , so that the total stress is expressed as a sum of elastic,  $\sigma_{el}$ , and magnetic contributions:

$$\sigma = \sigma_{el} + \sigma_M \quad (31)$$

The elastic stress corresponds to pure mechanical stress with no field applied. It is widely accepted that unidirectional deformation of highly swollen polymer gels can be described by a neo-Hookean stress-strain dependence:

$$\sigma_{el} = G \left( \gamma - \frac{1}{\gamma^2} \right) \quad (32)$$

where  $\gamma$  represents the strain measured in the direction of the applied stress and  $G$  denotes the elastic modulus of the gel. It can be defined as

$$G = \frac{1}{3} \lim_{\gamma \rightarrow 1} \left( \frac{\partial \sigma}{\partial \gamma} \right) \quad (33)$$

It is worth mentioning that in the small strain regimen, one can approximate the experimental data by Hooke’s law with a modulus of  $E=3G$ .

The magnetic stress can be calculated from the magnetic energy density:

$$\sigma_M = \frac{\partial W_M}{\partial \gamma} \quad (34)$$

$W_M$  depends on  $\gamma$  through both  $M$  and  $H_{eff}$  since according to Eq. (29), the effective field depends on the demagnetizing coefficient which is related to the shape; that is, to the deformation of the gel. The accessory magnetic modulus,  $G_M$ , can be calculated similar to Eq. (33):

$$G_M = \frac{1}{3} \lim_{\gamma \rightarrow 1} \left( \frac{\partial^2 W_M}{\partial \gamma^2} \right) \quad (35)$$

Let us consider now a simple situation similar to our experiments shown in Figure 24. For further details on the experiments please refer elsewhere [63]. A cylindrical piece of ferrogel is deformed along the symmetry axis and magnetized perpendicularly to it. In the undeformed, equilibrium state, the ferrogel has a Langevin-type magnetization related to the effective field. During the compression of the ferrogel cylinder, its height and diameter will become smaller and bigger, respectively. For the sake of simplicity let us assume that the shape of the sample will remain a regular cylinder. This involves a decrease in the demagnetizing coefficient which finally results in an increase of both the effective field and magnetization. Consequently, the compression of the gel involves an increase of the magnetic energy. This also means that the force required to compress the

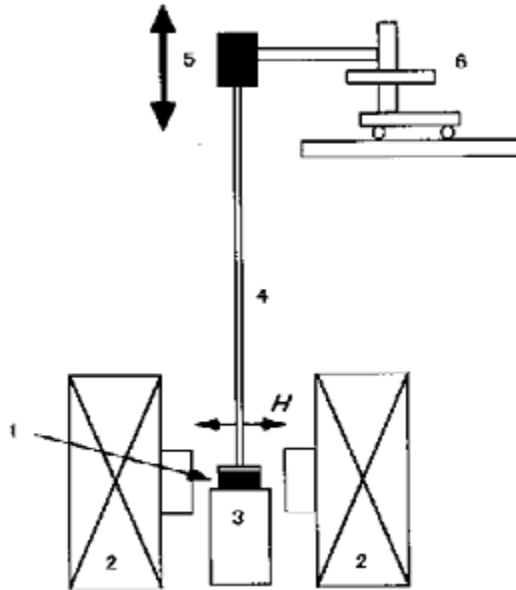


**FIG. 24** The apparatus for the compressive modulus measurement. (1) Ferrogel sample, (2) electromagnet, (3) sample stage, (4) silver rod, (5) strain gauge, (6) reading microscope.

sample, and hence the compression modulus, increases when a magnetic field is applied.

The analytic calculation of the excess modulus is complicated by two aspects: (1), the

complex form of the Langevin function and (2), the demagnetizing coefficient cannot be given in an analytic form. However, it is possible to derive an analytic formula for the magnetic contribution to the modulus indifferent applied fields if, on one hand, we use an approximation formula for the demagnetizing coefficient and, on the other hand, we examine the asymptotic values of the Langevin function; that is, the magnetization of ferrogel at low and high field intensities.

The demagnetizing coefficient of a cylindrical (with a diameter twice as big as the height) piece of magnetic substance can be approximated by [76, 66]:

$$N(\gamma)=0.06+0.18\gamma^{3/2} \quad (37)$$

At low field intensities ( $H_{eff} < 400$  Oe), the Langevin function can be approximated by a linear curve; hence, the magnetization is proportional to the effective field strength:

$$M=\chi H_{eff} \quad (38)$$

The proportionality factor is the magnetic susceptibility of which  $\chi=0.03$  is usual for ferrogels. Combining Eqs. (36) and (37), the magnetic energy density in low fields can be written as follows:

$$W_M = H_0 \chi \frac{H_{app}^2}{[1 + N(\gamma)\chi]^2} \quad (38)$$

From Eq. (35), the excess modulus:

$$G_M = 2 \cdot 10^{-4} H_{app}^2 \quad (39)$$

that is, at low field intensities,  $G_M$  is proportional to the square of the applied field. It is worth mentioning that this field dependence of  $G_M$  differs from that of  $M$  and it is in good agreement with the experimental results shown in Figure 25.

At high field intensities, the magnetization of ferrogel saturates, so that for  $H > 5000$  Oe, the magnetization can be considered as being independent of the applied field. In this case, the magnetic energy density can be expressed as

$$W_M = \mu_0 M_{sat} [H_{app} - N(\gamma) M_{sat}] \quad (40)$$

where  $M_{sat}$  denotes the saturation magnetization and is approximately 50 emu/g. After calculating  $G_M$ , we obtain

$$G_M = 88 \text{ Pa}$$

(41)

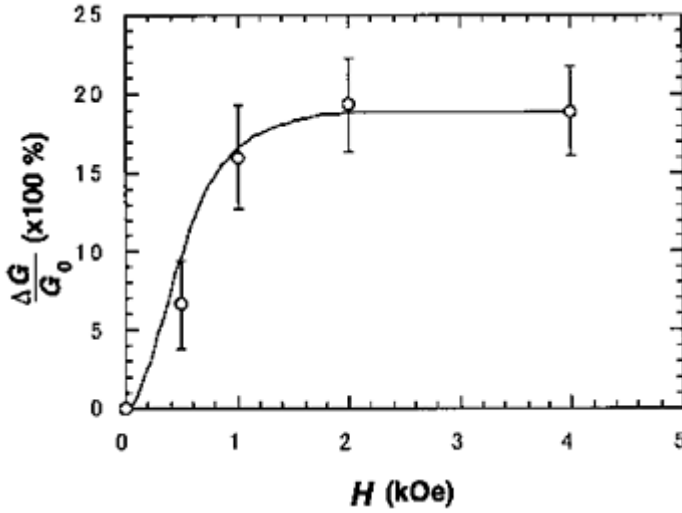


**FIG. 25** Magnetic field dependence of a compression modulus [63]. The excess modulus normalized to the modulus without field is plotted against the applied magnetic field. The solid line shows the theoretical curve calculated on the basis of Eq. (42).

that is, at high field strengths,  $G_M$  is independent of the applied field similar to the magnetization. This is also in agreement with our experimental results (see Fig. 25).

In the general case (in the range of  $200 \text{ Oe} < H_{app} < 5000 \text{ Oe}$ ), the magnetization is described by the Langevin function and the magnetic energy density has a complex form:

$$W_M = \mu_0 M_{sat} \coth \left( \frac{\mu_0 m H_{eff}}{kT} - \frac{kT}{\mu_0 m H_{eff}} \right) \times \left[ H_{app} - N(\gamma) M_{sat} \coth \left( \frac{\mu_0 m H_{eff}}{kT} - \frac{kT}{\mu_0 m H_{eff}} \right) \right] \quad (42)$$

Based on this expression, we calculated  $G_M$  numerically. The result, together with experimental data, is shown in Figure 25.

We must emphasize that the shape of the sample plays an essential role. Although it is expected to alter the moduli magnitudes, it is not expected to alter the qualitative behavior presented here. In our experiments, the maximum change in the compression modulus was found to be around 20%, which can be probably further increased by properly choosing the shape of the ferrogel sample. We believe that already the

preliminary investigations presented here suggest that ferrogels have many potential applications as tuned vibration absorbers, stiffness tunable mounts, and suspensions.

### G. Swelling Behavior of Magnetic Gels

Poly(N-isopropylacrylamide) hydrogel, abbreviated as NIPA gel, is one of the most frequently studied temperature-responsive gels. It exhibits a remarkable volume change in response to temperature changes. The transition temperature above which the network chains are in the collapsed state is called the lower critical solution temperature (LCST). For NIPA gels swollen in water, LCST has been found to be 34°C. There are several other gels showing reversible swelling and shrinking transition with a different LCST or UCST. The temperature sensitivity is an important property for several applications; for example, controlled drug release. These gels are often used to immobilize enzymes and as carriers of certain functional groups important for biochemical or biomedical applications [79]. Usually, small gel beads in the size range from approximately 0.1  $\mu\text{m}$  to several millimeters are used. These gels are heated by a surrounding heat source to control the degree of swelling. A more efficient type of heating was proposed recently by application of magnetic heating. Takahashi and his coworkers immobilized needle-like  $\gamma\text{-Fe}_2\text{O}_3$  powders with 0.5–0.8  $\mu\text{m}$  length into polymer gels [80, 81]. Owing to the hysteresis loss of the hard magnetic material in the presence of an alternating magnetic field, the magnetic energy is converted into heat inside the gel, which increases the temperature. Thus, warming up the gel beads only is an energetically more efficient method than heating the whole environment.

The magnetic properties of  $\gamma\text{-Fe}_2\text{O}_3$  powder and  $\text{Fe}_3\text{O}_4$  nanoparticles are quite different.  $\gamma\text{-Fe}_2\text{O}_3$  is a magnetically hard material showing a hysteresis loop on the magnetization curve. The shape of the hysteresis curve is dependent upon the hardness of the material as well as the magnitude and rate of the change of the applied field. Hysteresis makes possible permanent magnetism, but it also represents an energy loss mechanism producing heat.

Owing to the significant difference between soft and hard magnetic particles incorporated into a gel matrix, the properties of magnetic gel beads are also different. If the gel is loaded with a magnetically hard filler material, it behaves like a permanent magnet. As a consequence, owing to the magnetic interactions, the gel beads form aggregates even with the lack of external magnetic field. In order to counterbalance the magnetic interactions, intensive stirring is required to maintain individual gel beads. If magnetically soft particles are introduced into the gel, then the beads have no permanent magnetization and as a result they form aggregates only in the presence of an external magnetic field.

We have prepared magnetically soft NIPA gel (abbreviated as MNIPA gel) [68]. During preparation we have built in individual magnetic nanoparticles into the NIPA gel matrix. By incorporation of magnetite particles into poly(N-isopropylacrylamide) hydrogels, we are able to target and separate the gel beads by a magnetic field. It was established that the presence of magnetic



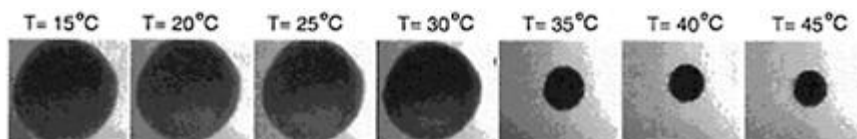


**FIG. 26** Collapse transition of a MNIPA gel bead. The diameter of the gel bead is 1.87 mm and 1.00 mm before and after the collapse transition, respectively.

material does not modify the temperature sensitivity of these gels. It was found that similar to the nonmagnetic NIPA gels, an abrupt volume change in response to a temperature change has been observed. This is demonstrated in Figures 26 and 27.

Magnetizable particles, like MNIPA gel beads, experience a force in a nonuniform magnetic field. The beads are attracted to magnetic field intensity maximums and repelled from minima. As a consequence, all the beads gather where the field intensity has the highest value. On the basis of this principle, it is possible to target the temperature- and magnetic field-sensitive gels to certain positions by using magnetophoretic interactions.

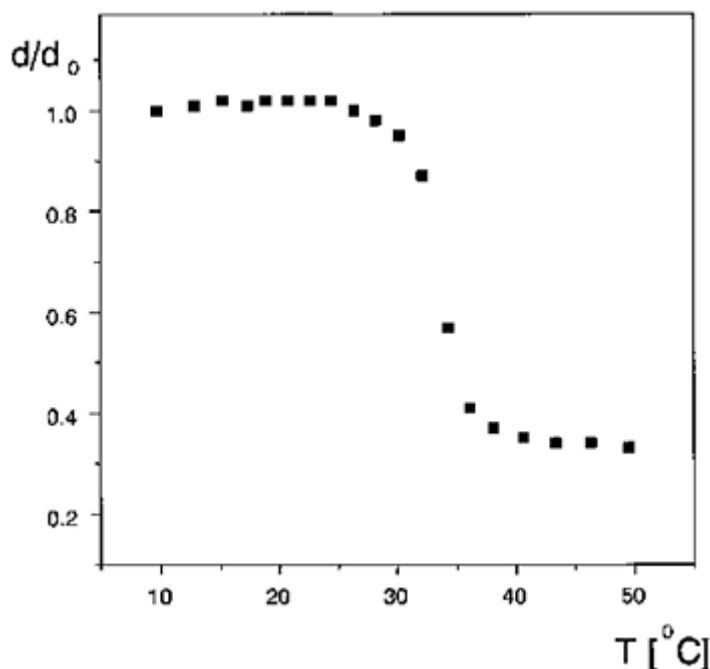


**FIG. 27** The dependence of the relative diameter of an MNIPA gel bead as a function on the temperature.

## V. FUTURE ASPECTS

The ability of electrical field- and magnetic field-sensitive gels to undergo a quick controllable change of shape can be used to create an artificially designed system possessing sensor and actuator functions internally in the gel itself. Their unique magnetoelastic properties may be used to create a wide range of motions and to control the shape change and movement that are smooth and gentle similar to that observed in muscle. Thus, application of field-sensitive gels as soft actuators for robots and other devices with enhanced properties in comparison with existing analogues has special interest. An understanding of coupling of elasticity with external fields in gels will hasten the gel engineering to switches, sensors, micromachines, biomimetic energy-transducing devices, and controlled delivery systems.

## ACKNOWLEDGMENTS

This chapter is based on research supported by a series of grants. This work was supported by the Hungarian Academy of Sciences under the contract of OTKA T 030654; by the European Commission, Directorate-General XII Science, Research and Development; Grant No. IC 15 CT 96-0756 by the Hungarian-Japanese Intergovernmental Cooperation T  T: 25/98; and by the J.Varga Foundation. The authors are deeply grateful for their support. A visitor professorship granted to M.Z. by the Canon Foundation, as well as the Yamagata University, Venture Business Laboratory provided the opportunity to complete the manuscript. One of the authors (D.S.) thanks Monbusho (Japanese Ministry of Education, Science and Culture) for making his stay and research possible in Japan.

## REFERENCES

1. MV Gandhi, BS Thompson. *Smart Materials and Structures*. Chapman & Hall, London, 1992.
2. *Proceedings of Third Conference of Intelligent Materials*, Lyon, France, 1996.
3. AS Hoffman. *Macromol Symp* 98:645, 1995.
4. Y Osada, SB Ross-Murphy. *Sci Am*, May, 1993.
5. De Rossi, K Kawana, Y Osada, A Yamauchi. *Polymer Gels, Fundamentals and Biomedical Applications*. Plenum Press, New York, 1991.
6. RS Harland, RK Prud'homme (eds). *Polyelectrolyte Gels ACS, Symposium Series* 480, 1992.
7. T Tanaka. *Science* 218:467, 1982.
8. T Tanaka. *Phys Rev Lett* 40:820, 1978.
9. Y Osada. *Adv Polym Sci* 82:1, 1987.
10. Y Osada, H Okuzaki, JP Gong. *Trends Polym Sci* 2:1994.
11. *Adv Polym Sci* 109:1993.
12. *Adv Polym Sci* 110:1993.

13. NA Peppas, RW Korsmeyer (eds). *Hydrogels in Medicine and Pharmacology*. CRC Press, Boca Raton, FL, 1987.
14. Y Osada, DE Rossi (eds). *Polymer Sensors and Actuators*. Springer-Verlag Berlin, 1999.
15. M Shahinpoor, Y Bar-Cohen, JO Simpson, J Smith. *Smart Mater Struct* 7:R15, 1998.
16. W Kuhn, B Hargitay, A Katchalsky, H Eisenberg. *Nature* 165:514, 1950.
17. DW Urry. *Angew Chem Int Ed Eng* 32:819, 1993.
18. IC Sanchez, MT Stone. *Polymer Blends*. Vols 1, 16. John Wiley, New York, 2000.
19. T Shiga. *Adv Polym Sci* 134:132, 1997.
20. T Tanaka, I Nishio, S Sun, SU Nishio. *Science* 218:467, 1982.
21. M Doi, M Matsumoto, Y Hirose. *Macromolecules* 25:5504, 1992.
22. D de Rossi, P Chiarelli, G Buzzigoli, C Domenichi, L Lazzeri. *Trans Am Soc Artif Int Org XXII*: 157, 1986.
23. S Shinohara, N Tajima, K Yanagisawa. *J Intell Mater Syst Struct* 7:254, 1996.
24. Y Osada, H Okuzaki, H Hori. *Nature* 355:242, 1992.
25. Y Osada, H Okuzaki, JP Gong. *Trends Polym Sci* 2:2, 1994.
26. H Okudazaki, Y Osada. *J Biomater Sci Polym Ed* 5:485, 1994.
27. RD Kornbluh, R Pelrine, J Joseph, R Heydt, Q Pei, S Chiba. *Proceedings of SPIE Conference on Electroactive Polymer Actuators and Devices*, Newport Beach, CA, 1999, p 149.
28. T Hirai, H Sadato, S Hayashi, Y Amemiya, T Ueki, M Hirai. *Rep Prog Polym Phys Jpn* 37:417, 1994.
29. T Hirai, H Sadato, T Ueda, T Kasazaki, Y Kurita, M Hirai, S Hayashi. *Die Angewandte makromolekulare Chemie* 240:221, 1996.
30. M Watanabe, M Yokoyama, T Ueda, T Kasazaki, M Hirai, T Hirai. *Chem Lett* 773, 1997.
31. T Shiga, T Kurauchi. *J Appl Polym Sci* 39:2305, 1990.
32. T Hirai, H Nemoto, M Hirai, S Hayashi. *J Appl Polym Sci* 53:79, 1994.
33. M Hirai, T Hirai, A Sakumoda, H Nemoto, Y Amemiya, K Kobayashi, T Ueki. *J Chem Soc Faraday Trans* 91:473, 1995.
34. J Shan, J Chen, X Shen, R Chen. *Chem Lett* 427, 1999.
35. T Hirai, J Zheng, M Watanabe. *Proceedings of SPIE Conference on Electroactive Polymer Actuators and Devices*, Newport Beach, CA, 1999, p 209.
36. J Zheng, M Watanabe, H Shirai, T Hirai. *Chem Lett* 500, 2000.
37. R Kishi, Y Suzuki, H Ichijo, O Hirasa. *Chem Lett* 2257, 1994.
38. M Hebert, R Kant, P-G de Gennes. *J Phys I France* 7:909, 1997.
39. RE Rosenweig. *Ferrohydrodynamics*. Cambridge University Press, Cambridge, UK, 1985.
40. M Nakano, K Koyama. *Electro-rheological Fluids, Mageto-rheological Suspensions and Their Applications*. World Scientific Publishing, 1997.
41. R Thao, GD Roy. *Electrorheological Fluids*. World Scientific Publishing, 1994.
42. TB Jones. *Electromechanics of Particles*. Cambridge University Press, Cambridge, UK, 1995.
43. JM Crowley. *Fundamentals of Applied Electrostatics*. Wiley, New York, 1984.
44. T Shiga, A Okada, T Kurauchi. *J Mater Sci Lett* 14:514, 1995.
45. T Shiga, A Ohta, T Hirose, Y Okata, T Kurauchi. *J Mater Sci Lett* 28:1293, 1993.
46. K Bohon, S Krause. *J Polym Sci* 36:1091, 1998.
47. C Boxal. *Chem Soc Rev* 137, 1994.
48. M Zrínyi, J Fehér, G Filipcsei. *Macromolecules* 33:5751, 2000.

49. G Filipcsei, J Fehér, M Zrínyi. *J Mol Struct* 554(1): 109, 2000.
50. J Fehér, G Filipcsei, J Szalma, M Zrínyi. *Colloid and Polymer Science* (in press).
51. JB Restorf. *Encycl of Appl Phys* 9:22, 1994.
52. M Zrínyi, L Barsi, A Büki. *Europhysics Conference on Gels, Balatonszeplak, Hungary, Sept 25–29, EPS Conference Abstract, Vol 19G, 1995, p 400.*
53. L Barsi, A Büki, D Szabó, M Zrínyi. *Prog Colloid Polym Sci* 102, 1996.
54. M Zrínyi, L Barsi, A Büki. *J Chem Phys* 104:8750, 1996.
55. M Zrínyi, L Barsi, A Büki. *Polym Gels Netw* 5:415, 1997.
56. D Szabó, L Barsi, A Büki, M Zrínyi. *Models Chem* 134:155, 1997.
57. M Zrínyi. *Trends Polymer Sci* 5:280, 1997.
58. M Zrínyi, L Barsi, D Szabó, H-G Kilian. *J Chem Phys* 108:5685, 1997.
59. D Szabó, G Szeghy, M Zrínyi. *Macromolecules* 31:6541, 1998.
60. L Barsi, M Zrínyi. *ACH Models Chem* 153:241, 1998.
61. M Zrínyi, D Szabó, L Barsi. *J Intell Mater Syst Struct* 9:667, 1998.
62. M Zrínyi, D Szabó, H-G Kilian. *Polym Gels Netw* 6:441, 1999.
63. T Mitsumata, K Ikeda, JP Gong, Y Osada, D Szabó, M Zrínyi. *J Appl Phys* 85:1, 1999.
64. M Zrínyi. *Colloid Polym Sci* 27:98, 2000.
65. D Szabó, T Czako-Nagy, M Zrínyi, A Vertes. *J Colloid Interface Sci* 221:166, 2000.
66. Gy Török, VT Lebedev, L Cser, M Zrínyi. *Physica B* 276–278:396, 2000.
67. M Zrínyi. *Colloid Polym Sci* 27:98–103, 2000.
68. M Xulu, G Filipcsei, M Zrínyi. *Macromolecules* 33:1716, 2000.
69. M Zrínyi, D Szabó, L Barsi. *Magnetic field sensitive polymeric actuators. In: Polymer Sensors and Actuators. Y Osada, DE Rossi, eds. Springer-Verlag, Berlin, 1999, p 385.*
70. L Néel. *Ann Geophys* 5:99, 1949.
71. D Szabó, I Czako-Nagy, M Zrínyi, A Vertes. *J Colloid Interface Sci* 221:166, 2000.
72. LD Landau, EM Lifshitz. *Theory of Elasticity*. 3rd ed. Pergamon Press, Oxford, UK, 1986.
73. RW Odgen. *Non-linear Elastic Deformations*. Ellis Horwood, Chichester, UK, 1984.
74. D Szabó, A Meggyes, JP Gong, Y Osada, M Zrínyi (submitted to *Physica D*).
75. *MARC User Manual*, MARC Analysis Research Corporation, 1997.
76. RM Bozoth, DM Chapin. *J Appl Phys* 13:320, 1942.
77. JA Osborn. *Phys Rev* 67:351, 1945.
78. M Zrínyi, F Horkay. *J Intell Mater Syst Struct* 4:190, 1993.
79. T Okano (ed). *Biorelated Polymers and Gels*. Academic Press, New York, 1998.
80. F Takahashi, Y Sakai, Y. Mizutani. *J Ferment Bioeng* 83:152, 1997.
81. N Kato, Y Takizawa, F Takahashi. *J Intell Mater Syst Struct* 8:588, 1997.



# Rhythmically Pulsing Gels Based on Chemomechanical Feedback Instability

RONALD A.SIEGEL, GAURI P.MISRA, and ANISH P.DHANARAJAN

*University of Minnesota, Minneapolis, Minnesota*

## I. INTRODUCTION

It has been known for many decades that cross-linked polymer gels are capable of responding mechanically to chemical stimuli. Starting with the early work of Kuhn et al. [1], numerous investigators have investigated the ability of polyelectrolyte gels to convert chemical changes, such as changes in pH or ionic environment, into mechanical work [2–6]. It has also been noticed that changes in swelling of gels can be exploited to modulate the transport of solutes, and this has given rise to numerous studies of chemically responsive drug-delivery systems [7–9].

The earlier work on polyelectrolyte gels primarily involved compositions with a large number of ionizable side chains, such as cross-linked poly(methacrylic acid). The mechanism of volume change and chemomechanical energy conversion was explained primarily in terms of shielded electrostatic repulsions between fixed charges on the gel [2, 10, 11], or equivalently to osmotic forces due to the difference in mobile ion concentrations inside and outside the gel which arise in order to maintain electroneutrality in the gel [12].

Two breakthroughs occurring in the 1970s and 1980s moved the field of chemically responsive gels forward. First was the discovery by Tanaka of the first-order swelling phase transition [13]. The second was the discovery of the thermally based transition of poly(N-isopropylacrylamide) (NIPA) gels, which undergo first-order volume transitions as a function of temperature [14]. This transition occurs in essentially uncharged NIPA gels, so it cannot be explained by an electrostatic/osmotic mechanism. The transition in neutral NIPA gels has been explained in terms of hydration and dehydration of NIPA side chains, with hydration, and hence swelling, being favored at low temperatures and dehydration and gel collapse arising at high temperatures [15]. A well-defined temperature separating the swollen and collapsed regimen exists; that is, the swelling phase transition temperature.

It was soon shown that the swelling phase transition in NIPA gels can be manipulated chemically by incorporating a small fraction of comonomers containing chemically switchable side chains. These monomers can drastically shift the balance of forces governing hydration and dehydration, and the shift depends on the charge state of the side chain. For example, copolymerization of NIPA with a small fraction of ionizable groups such as acrylic acid (AA) or methacrylic acid (MAA) leads to gels whose volume

transition temperature depends on pH and ionic strength [16–19]. Conversely, when temperature and ionic strength are held constant, a volume transition can be induced by a pH change in the surrounding medium [17, 20, 21]. Such thermally based, chemically modulated transitions can be brought about with a smaller density of ionizable groups than is typically needed for the earlier studied gels which depended on electrostatic/osmotic mechanisms [19]. They are also less affected by ionic strength.

Most efforts toward applications of gel swelling transitions have assumed the gel to be a responsive element. Thus, “artificial muscles” [2–6] and responsive drug-delivery systems [7–9, 17] are usually controlled by an external stimulus such as a change in temperature or pH. Other chemical stimuli have also been investigated. For example, considerable interest has been shown in systems that respond to changes in glucose concentration either using pH-sensitive systems in conjunction with glucose oxidase, which converts glucose to gluconic acid and hence lowers the local pH [22–24], or using phenylboronic acid-based hydrogels whose charge states are altered directly by the binding of glucose [25]. These systems are intended for the automatic delivery of insulin in type I diabetes.

In this chapter, we discuss a hydrogel/enzyme system that pulsates rhythmically in the presence of a *constant* level of glucose. This behavior is attributed to a nonlinear chemomechanical feedback instability between the gel and the enzyme reaction. A potential application is the rhythmic delivery of hormones other than insulin in patients whose blood glucose is well controlled. For example, it is now accepted that the endogenous release of gonadotropin hormone-releasing hormone (GnRH) exhibits ultradian rhythms in both men and women, and that the induction or restoration of normal reproductive function in GnRH-deficient individuals requires that not only the average level of GnRH but also the periodicity of release be restored [26, 27].

In Section II, we outline the design principles for the rhythmic gel/enzyme system, review our previous efforts, and identify the innovations of the present work. Details of the experimental system are presented in Section III, and experimental results appear in Section IV. In Section V, we propose some methods to improve the system’s performance, and then discuss the relationship between the present system and various chemical, biochemical, and membrane oscillators that have been studied.

## II. BACKGROUND

The principles behind the autonomous pulsing system have been discussed previously [28–32], and they are embodied in Figure 1a. Briefly, the system consists of a chamber containing the enzymes glucose oxidase, gluconolactonase, and catalase. The chamber is placed in an external environment containing glucose at constant concentration and at physiological pH. The chamber and environment communicate through an acidic hydrogel membrane whose permeability to glucose depends on the pH inside the membrane. The gel is a copolymer of NIPA and MAA. At high intrachamber pH values, the acidic side chains on the gel are ionized and the membrane is in its swollen, permeable state. At lower intrachamber pH, these side chains are protonated and electrically neutral, and the hydrophobicity of the NIPA dominates, causing collapse of

the gel and shutdown of glucose permeability.

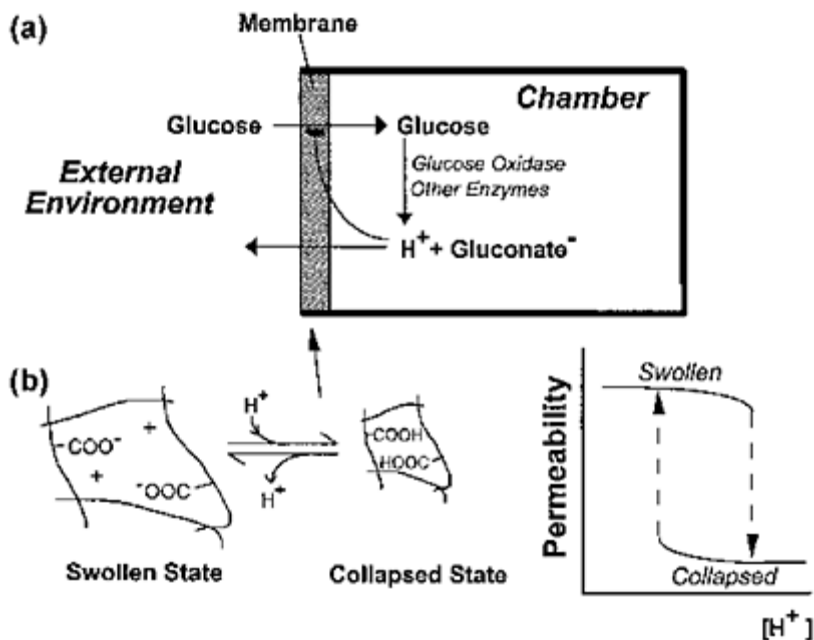
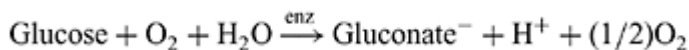


**FIG. 1** (a) Schematic drawing of rhythmically pulsing gel/enzyme system. "Other enzymes" refers to catalase and gluconolactonase. (b) Illustration of hysteretic collapse and reswelling of gel membrane and change in permeability to glucose as a function of hydrogen ion concentration inside the chamber,  $[H^+]$ .

If the system starts out in the high-permeability state, glucose enters the chamber through the membrane and is converted to hydrogen ions through the action of the enzymes:



Some of these hydrogen ions serve to lower pH inside the chamber, whereas others bind to the membrane, causing collapse. At this point, glucose entry into the chamber is attenuated, and production of hydrogen ions by the enzyme reaction is slowed. The hydrogen ions that have accumulated in the chamber and membrane eventually diffuse irreversibly into the environment, causing the pH in the chamber to increase and the membrane to recharge and reswell. The system has thus returned to its original state, and further cycles of gel collapse and reswelling ensue.

Although the sequence of events described above is intuitively clear, certain extra conditions must be operative for the rhythmic swelling/deswelling behavior to occur. First, it is extremely useful [30], though not completely necessary [29], that the characteristic relating glucose permeability (i.e., swelling) of the membrane to



intrachamber pH should exhibit hysteresis, so that the pH at which collapse occurs is lower than the pH at which reswelling occurs. Such a characteristic is illustrated in Figure 1b. Second, oscillations will occur only within a finite range of external glucose concentrations. If the external glucose concentration is too low, then the system will never be able to reach a low enough intrachamber pH to cause gel collapse. If the external glucose concentration is too high, there will be sufficient influx of glucose into the device even after collapse that the intrachamber pH will be maintained low at all times, and gel reswelling will not occur.

In earlier work using a diffusion cell with controllable pH gradient, we established that the permeability to glucose of poly(NIPA-co-MAA) gel membranes can be reduced more than 10-fold in response to a lowering of pH on one side of the membrane, and that this transition is first order in character [31, 33]. Importantly, it was shown that the desired hysteresis exists in this permeability transition. However, permeability to hydrogen ions was not significantly affected by the transition [31]. Based on these results, along with measurements of membrane permeability parameters and a simplified model of the system, an attempt was made to include such membranes in an experimental prototype designed to mimic the device scheme illustrated in Figure 1. Rhythmic swelling and deswelling of the membrane would be signaled by pH oscillations in the prototype compartment which corresponded to the chamber in Figure 1. Unfortunately, the prototype only exhibited a couple of upward and downward swings in “intrachamber” pH, and then it came to rest at a constant, steady-state pH value. The system could be restimulated by spiking HCl into the “chamber,” leading to extra downswings and upswings in intrachamber pH. From this last observation it was concluded that the cessation of pH oscillations was not due to fatigue of the membrane or loss of enzyme activity.

In these unsuccessful experiments, the observed rates of change in intrachamber pH were very slow. It was hypothesized that such slow changes allow the membrane to adjust to states of intermediate glucose permeability that would drive the system to a steady state, where glucose influx and hydrogen ion efflux rates are balanced and intrachamber pH is constant [32]. In order to test this notion, it was necessary to find ways to accelerate the pH changes, thus disallowing the membrane’s relaxation to the intermediate glucose permeability state. It was also necessary to introduce methods of acceleration that preserve the autonomous nature of the chemomechanical system. For example, manual or computer-controlled addition of extra acid and/or base into the chamber would not be regarded as being acceptable.

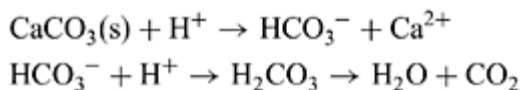
The most obvious method to accelerate pH swings is to increase the ratio of membrane area to chamber volume. This method was found to be ineffective, however, since the source of slow pH change is the buffering of intrachamber hydrogen ions by the carboxylate groups attached to the gel.

An alternative means of accelerating pH swings is to increase the external glucose concentration and include a “shunt” pathway for removal of hydrogen ions before binding to the membrane. To explain this strategy, consider the task of filling a bucket with a hole in the bottom to a desired water level. The time constant for this filling process is (see Appendix) inversely related to the diameter of the hole. Adding an extra hole will decrease this time constant. However, water has to be added more quickly in

order to fill the bucket to the same level as before. Similarly, an extra hole causes the water level to fall faster when the rate of inflow of water is reduced.

In the gel enzyme system, the water level corresponds to intrachamber  $H^+$  concentration, the original hole corresponds to the membrane, through which  $H^+$  exits from the chamber, the added hole corresponds to the shunt pathway for removal of  $H^+$ , and the product (external glucose concentration)  $\times$  (membrane permeability to glucose) corresponds to the rate of water addition to the bucket.

A shunt pathway for removal of  $H^+$  is provided by  $CaCO_3$  in the form of solid marble through the reactions [34]



The first of these reactions is heterogeneous and is assumed to be rate limiting at the pH values of interest.

In the following, we show that a new prototype of the device in Figure 1, with marble included, is indeed capable of rhythmic behavior for periods of several days, with pH oscillations exhibiting periods of a few hours. The present design does not exhibit oscillations over infinite duration, however, and we will consider some explanations for this observation.

### III. EXPERIMENTAL METHODS

#### A. Preparation of Hydrogel Membranes

Prepolymer solutions were prepared consisting of NIPA, MAA, and tetraethylene glycol dimethacrylate (TEGDMA), in mole ratio 90/10/0.7, all dissolved in water and methanol, with the weights of each solvent being equal to the total liquid weight of the monomers. Total volume of prepolymer solutions was 1.3 mL. To this was added 5 mg ammonium persulfate (initiator) and 20  $\mu$ L tetraethylmethylenediamine (TEMED, accelerator). Solutions were introduced between two glass plates separated by 250  $\mu$ m spacers and polymerized for 1 h at 10°C. After polymerization, disc-shaped gels were removed and washed extensively first in methanol, then in a series of water/methanol solvents, and finally in saline solution to which was added 0.01 w% bronopol (a preservative).

#### B. Test Cell (Prototype)

A water-jacketed (37°C), magnetically stirred side-by-side diffusion cell, with chamber volumes 80 mL, served as a prototype for the device in Figure 1. Figure 2

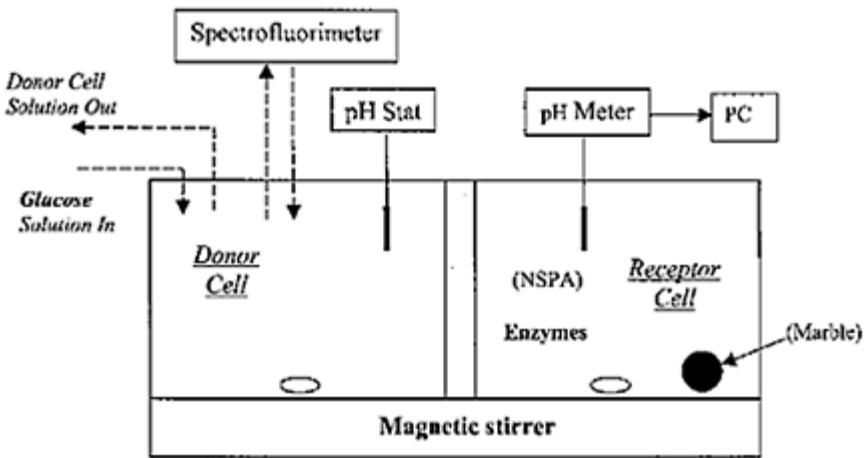


**FIG. 2** Schematic drawing of a test cell which mimics the system in Figure 1. See Section III.B for details. Parentheses around “NSPA” and “Marble” indicate that these components are not present in all experiments.

shows a schematic of this test cell. The donor cell, which mimicked the external environment, was fed continuously (1.37 mL/min) with saline solution (0.05 NaCl) containing glucose at specified constant concentration, and its contents were drained out through a separate line at the same flow rate as the feed. The donor cell was held at pH 7 by pH-stat, and the glucose solution was kept sterile with bronopol. The receptor cell, mimicking the device chamber, contained saline solution in which was dissolved 20 mg glucose oxidase (234 IU/mg) and 2mg catalase (10,700 IU/mg). (Gluconolactonase was also present as an impurity in the glucose oxidase preparation.) When appropriate, a 12.5-g piece of marble was added to the receptor cell. The transport aperture between the cells was of radius 1 cm.

(Note, the test cell is very similar to cells used in the previous work cited above, the main difference being the presence of marble [31, 32]. Thus, the receptor cell corresponds to the “chamber” in Section II.)

### C. Experimental Procedures

Before running an experiment, the gel was mounted and clamped between the donor and receptor cells, which were then filled with saline at pH 7 and 6, respectively. No glucose, enzyme, or marble was present at this point. After a few hours, enzymes were introduced into the receptor cell and pH was lowered and held constant by pH-stat for 45 min. To begin an experimental run, the pH-stat was removed from the receptor cell and replaced by a pH-electrode. Glucose solution was introduced into the donor cell and the feed and drain pumps were started. During a run, the time course of pH in the receptor cell was recorded on a personal computer.

Experiments were carried out at different glucose concentrations and in the presence and absence of marble in the receptor cell. When marble was included, it was added at the starting point of a run.

In order to confirm that pH oscillations are due to repeated swelling and collapse of the hydrogel membrane, in one experiment the transport of the neutral (actually zwitterionic) *n*-(3-sulfopropyl) acridinium inner salt (NSPA: MW 304.1) across the membrane was monitored by spectrofluorimetry ( $\lambda_{\text{ex}}=420$  nm,  $\lambda_{\text{em}}=490$  nm).

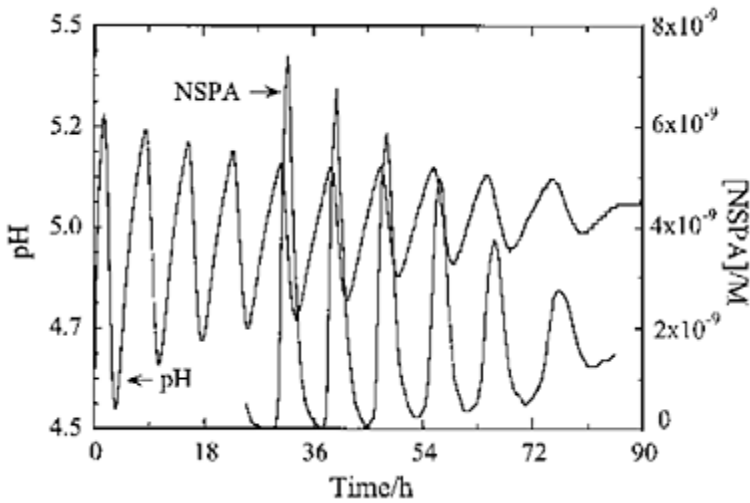
#### IV. RESULTS

In the previous work with a prototype system similar to that used here, but in the absence of marble, at most a couple of downswings and upswings in pH were observed. The upstream glucose concentration providing the best results was 1.5 mM. The swings in pH were very slow, requiring days to complete. Our hypothesis is that by accelerating pH swings, owing to the presence of marble and a compensating increase in donor glucose concentration, oscillations can be sustained indefinitely.

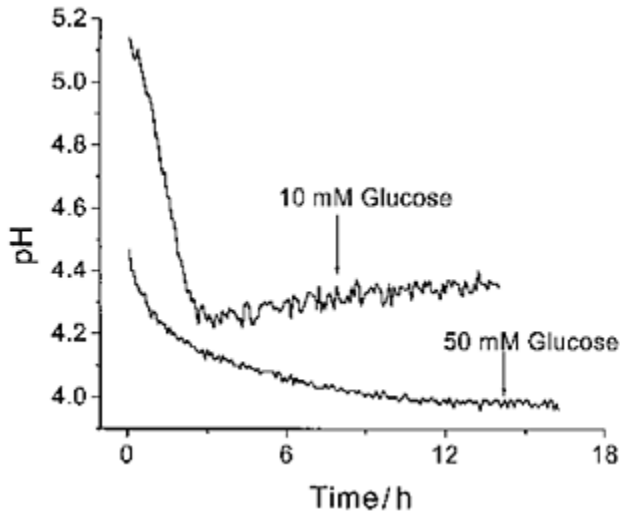
Figure 3 illustrates sustained oscillations in pH in the receptor cell when marble is present in the receptor cell and 50 mM glucose flows through the donor cell. Numerous oscillations are observed, with periods of a few hours and lasting over several days. During the oscillatory phase, NSPA was spiked into the receptor cell, and its appearance in the donor cell was monitored. A series of NSPA peaks in the donor cell is observed. Peak amplitude decreases with time, most likely due to depletion in the receptor cell. (Note that the roles of “donor” and “receptor” cells are reversed with respect to NSPA.) The presence of peaks instead of ramps and plateaus in NSPA concentration is due to drainage of solution from the donor cell.

Figure 4 illustrates control runs in which marble was not included. Two donor glucose concentrations, 10 and 50 mM, were tested. At the lower glucose concentration, pH drops to about 4.3 after about 3 h and remains near that value through the rest of the run. At the higher glucose concentration, pH initially falls very rapidly, reaching 4.3 after just 1 h. Thereafter follows a slower descent in pH, with a final pH value approximately 4. Evidently, raising the glucose concentration without including marble merely drives the membrane into the collapsed state. It is worthy of note, however, that even in the collapsed state there is an apparent residual permeability to glucose. This is evidenced by the slow phase of pH decline at 50 mM glucose, and the differing final pH values attained for the two glucose levels.

The experimental run shown in Figure 5 starts with marble in the system. When donor glucose concentration is 10 mM, the system exhibits only a couple



**FIG. 3** Demonstration of pH oscillations in a receptor chamber and oscillations of NSPA flux across hydrogel membrane. Donor glucose concentration is 50 mM.



**FIG. 4** Lack of pH oscillations in the receptor chamber when marble is absent, with donor glucose concentrations 10 and 50 mM.

of pH swings and then comes to rest. When the donor glucose concentration is then raised to 50 mM, numerous pH oscillations ensue. Apparently, the presence of marble, which accelerates pH changes, must be accompanied by a significant increase in the donor glucose level in order to induce multiple oscillations.

To date, it has not been possible to demonstrate pH oscillations for an indefinitely long duration. A close look at Figures 3 and 5 reveals that, with

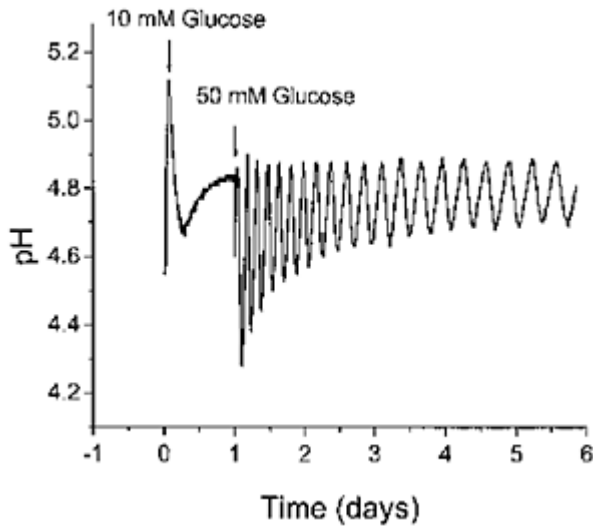


**FIG. 5** Effect of the donor glucose concentration on the ability of the system to oscillate in the presence of marble in the receptor cell. The system does not oscillate when the donor glucose concentration is 10 mM, but oscillations commence when the donor glucose concentration is changed to 50 mM.

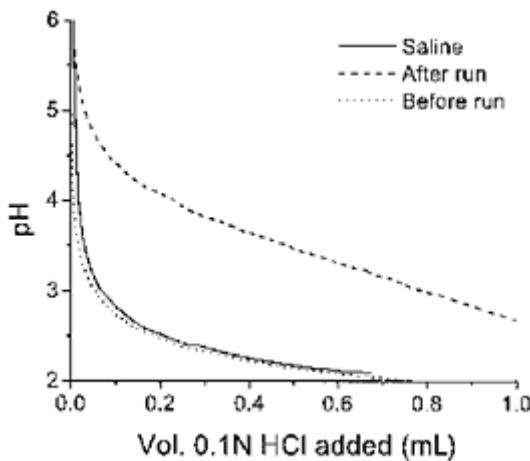


**FIG. 6** pH titrations of receptor medium before (*dots*) and after (*dashes*) an oscillating run. For comparison, a titration of the medium without enzyme is shown (*solid line*). The donor glucose concentration is 50 mM.

time, the period between pH peaks increases, and the downswings and upswings become progressively more sluggish. We believe that oscillations ultimately cease, because the swings eventually become sufficiently slow that the gel is allowed sufficient time to find its intermediate permeability state, as in the case where marble is absent.

The mechanism for this increased sluggishness in pH behavior with time is not well understood at present. One possibility is that gluconate accumulates in the receptor cell with time, and this species buffers changes in pH in that cell. Figure 6 shows the results of pH titrations of receptor cell medium before and after a run along with a titration of an enzyme-free control solution. There is little difference in titration behavior between the "before" medium and the control, so the enzyme seems to play a limited role in buffering the receptor cell solution. However, the medium collected after the run requires substantially more added acid to lower pH, which suggests that a buffering species has accumulated. Figure 7 shows that 50 mM gluconate added to the receptor cell in the middle of an oscillation substantially slows down the rate of pH change to such an extent that oscillations cease. Figures 6 and 7 together suggest that accumulated gluconate may play an important role in the slowing and ultimate quenching of pH oscillations in the present system.

## V. DISCUSSION

### A. Experimental Results

Although the present work represents an advance in efforts to obtain the sustained, autonomous rhythmic swelling and deswelling of gels, periodic behavior does not persist indefinitely. Moreover, a number of the observed

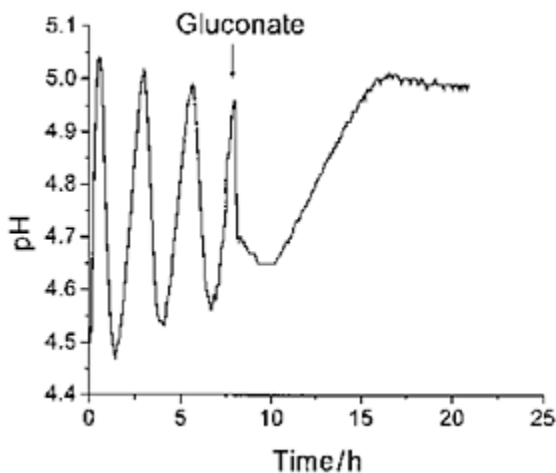


**FIG. 7** Quenching effect of 50 mM gluconate added to receptor cell on pH oscillations in the receptor cell. The donor glucose concentration is 50 mM.

phenomena are not completely understood. Although we have just suggested that gluconate may contribute to the cessation of oscillations, we presently do not know the rate of accumulation of this buffering species. Also unclear is the interaction of gluconate with  $\text{Ca}^{2+}$  released from marble. This divalent cation also accumulates with time, and its effect on the gel membranes swelling and permeability is unknown at present.

Improvement in the system's performance may require methods for limiting gluconate levels in the receptor cell and for eliminating marble from the system. The gluconate level is determined largely by the concentration of glucose in the donor cell, and this concentration had to be increased to 50 mM to compensate for the marble. Incidentally, this level of glucose is far above the normal physiological glucose range (5–10 mM), which is a further disadvantage if this system is to see applications in drug delivery.

The required level of donor glucose could be reduced by moving the operating pH range of the gel membrane in the alkaline direction, since fewer hydrogen ions would have to be produced. Preliminary results (not shown) suggest that this can be accomplished by reducing the fraction of MAA groups in the copolymer. Further alkaline shifts in the membrane's operating range may be achieved by replacing MAA in the membrane with acidic comonomers bearing a higher  $\text{pK}_a$  value [35]. The rate of pH downswings and upswings may also be accelerated by these means, as fewer hydrogen ions are involved in the phase transition. This latter aspect may help eliminate the need for marble.

If the present system is to be converted to a device for biomedical applications, its behavior in buffered physiological media must be studied. Such buffering is normally considered to be an obstacle in pH-modulated drug delivery from implantable devices. It is interesting to point out, however, that in acidic pH regions the primary physiological buffer is bicarbonate, which is also a product of the marble- $\text{H}^+$  reaction. The possibility arises, then, that this physiological buffer could replace marble as the hydrogen ion scavenger. Of course, this is merely a conjecture which will require intensive study.

A final item that is not well understood pertains to the phase relation between peaks in NSPA appearing in the donor cell and pH oscillations in the receptor cell. At first glance, these two features are well correlated in their periodicity, and slowing of pH oscillations is matched by broadening of NSPA peak. We would expect that NSPA transport across the membrane should be maximal when the gel membrane is swollen and minimal when the membrane is collapsed. A close look at Figure 3, however, reveals that NSPA in the donor cell starts to rise while pH in the receptor cell is increasing; that is, when the gel is supposed to be still in its collapsed state, the NSPA concentration starts to fall while pH is decreasing and the membrane is supposedly swollen. The precise temporal relationships between gel swelling/deswelling, receptor cell pH and NSPA permeability through the membrane apparently needs further clarification.

(Note: one may obtain the rate of delivery of NSPA into the donor cell by deconvoluting the NSPA curve by the residence time distribution of the fluid in the donor cell. The latter is monoexponential with the time constant of approximately 1 h. The result would be a sharper set of peaks in NSPA flux across the membrane, with an overall phase shift to the left. Carrying out such a deconvolution procedure would not alter the conclusions of the previous paragraph.)



## B. Relation to Other Oscillators

The present system may be regarded as a chemomechanical analogue of chemical oscillators such as the well-known Belousov-Zhabotinsky (BZ) reaction [36–41], biochemical/genetic systems associated with oscillations in glycolysis, intracellular calcium levels, the embryonic cell division cycle and circadian rhythms [42–44], and artificial membrane systems such as the Teorell oscillator [45–51]. These systems, in turn, are analogous to nonlinear voltage-controlled oscillators which are components of electrical circuits.

Although the details of these disparate systems vary greatly, they share certain design principles [37, 39, 50]. First, they are all far from equilibrium. Second, they contain at least one bistable element which affects (directly or indirectly) the rate of change of other system variables. Third, one of these variables provides feedback to the bistable element, causing it to flip back and forth between its stable states. It may be said that the feedback variable destabilizes the system, preventing it from remaining in either state set by the bistable element. The ability of systems that incorporate these principles to oscillate depends also on the relaxation times associated with the bistable element and the other system variables [40, 41, 52].

The present system is far from equilibrium, since it irreversibly converts external glucose to hydrogen ions that are removed once they are released into the external environment. The gel membrane, whose swelling and permeability to glucose can take on two stable values over a range of intrachamber (receptor cell) hydrogen ion concentrations (see Fig. 1b), is the bistable element. Hydrogen ions enzymatically produced from glucose represent the feedback variable.

The previous difficulties in obtaining multiple oscillations appear to have stemmed from the slow relaxation time of the receptor cell  $H^+$  concentration. As discussed previously, this may have permitted the membrane sufficient time to find an intermediate permeability state consistent with a stable steady state. Incorporation of marble into the system accelerates changes in  $H^+$  concentration, allowing it to move rapidly enough to effect a phase transition before the intermediate permeability state can be reached.

Before concluding, we note that other strategies for producing chemomechanically based oscillations in gel swelling have been reported. In one study [53], a poly(NIPA-co-AA) gel was suspended in a continuous stirred tank reactor which supports a chemical pH oscillator derived from a peroxide-sulfite-ferrocyanide reaction. Swelling/deswelling cycles of the gel followed upswings and down-swings in reactor pH. In a second system [54, 55], a catalytic component of the BZ reaction was incorporated into side chains of a gel, and the gel exhibited low-amplitude swelling oscillations when immersed in a medium containing BZ reactants. These oscillations are due to cyclic changes in the redox state, and hence the electrical charge, of the immobilized catalyst.

In both systems described in the previous paragraph, swelling oscillations are driven primarily by the chemical oscillator, and the mechanical swelling and deswelling of the gel is not essential to the mechanism. However, the oscillating gel may provide a fluctuating mass transfer resistance to the reactants in the second system [53], thereby perturbing and providing some feedback to the chemical reaction kinetics. (Also, subtle geometrical effects can lead to interesting chemical waves inside the gel [54].) In the

present system, the chemical (hydrogen ion production) and mechanical (hysteretic swelling and deswelling) components play equal and essential roles in the production of oscillations.

Finally, we note that, in contrast to these other chemomechanical systems, whose mechanisms rely on a complex of redox reactions involving toxic species which must be supplied and removed continuously, the present system is driven by glucose, an endogenous compound. This feature is advantageous for biomedical applications.

## VI. SUMMARY

In this chapter, we have demonstrated that numerous autonomous oscillations in pH can be achieved in a gel/enzyme system, and that previous failures were probably due to sluggishness of the system response. Work remains, however, in understanding why the system eventually stops oscillating. Also, methods for controlling system periodicity need to be explored in more detail. These basic studies of rhythmically pulsing gel systems are necessary if such systems are to be used in the future for biomedical applications such as drug delivery.

## ACKNOWLEDGMENTS

This work was supported by NIH grant CHE-9996223 and by the University of Minnesota. The authors thank Mr. Yuandong Gu for helpful discussions.

## APPENDIX

In this appendix, we present a simple mathematical description of the “bucket and hole” analogy used to explain how introducing the marble shunt pathway for hydrogen ions can reduce the time constant associated with pH changes in the device chamber.

Consider a cylindrical bucket of base area  $B$  into which water is poured at rate  $R_1$  L/min. The bucket has a hole of area  $A_1$ . If at a given time,  $t$ , the water level in the bucket is given by  $y(t)$ , then one may write the following differential equation for  $y$ :

$$B \frac{dy}{dt} = R_1 - kA_1 y$$

where  $k$  is a constant of proportionality. If the initial water level at time 0 is  $y_0$ , then the differential equation's solution is

$$y(t) = y_0 + \left( \frac{R_1}{kA_1} - y_0 \right) e^{-(kA_1/B)t}$$

The final water level is therefore  $y_{\infty} = R_1/kA_1$  and the "time constant" for reaching this level is  $B/kA_1$ .

Suppose a second hole of area  $A_2$  is placed in the bottom of the bucket, so the total hole volume is  $A_1 + A_2$ . The time constant is now reduced to  $B/k(A_1 + A_2)$ . However, to attain the same final level  $y_{\infty}$  as before, water must be poured into the bucket at rate  $R_2 = R_1(A_1 + A_2/A_1)$ . Notice that this is true whether the target level is above or below the initial level.

In conclusion, a reduction in the time constant must be accompanied by an increase in the rate of the addition of water to the bucket if one wishes to reach the same target level. Analogously, introduction of the marble shunt for hydrogen ion removal serves to decrease the time constant for pH change, but in order to reach pH values necessary for the desired phase transitions, the source of  $H^+$ , namely, the external glucose, must increase in concentration.

## REFERENCES

1. W Kuhn, B Hargitay, A Katchalsky, H Eisenberg. *Nature* 165:514–516, 1950.
2. A Katchalsky. *Prog Biophys Chem* 4:1–59, 1954.
3. A Katchalsky, M Zwick. *J Polym Sci* 16:221–234, 1955.
4. Y Osada. *Adv Polym Sci* 1–46, 1987.
5. M Suzuki, O Hirasa. *Adv Polym Sci* 110:241–261, 1993.
6. DW Urry, RD Harris, KU Prasad. *J Am Chem Soc* 110:3303–3305, 1988.
7. RA Siegel, M Falamarzian, BA Firestone, BC Moxley. *J Controlled Release* 8:179–182, 1988.
8. A Khare, NA Peppas. *J Biomater Sci Polym Ed* 4:275–289, 1993.
9. J Cornejo-Bravo, V Arias-Sanchez, A Alvarez-Angyuiano, RA Siegel. *J. Controlled Release* 33:223–229, 1995.
10. J Hasa, M Ilavsky, K Dusek. *J Poly Sci* 13:253–262, 1975.
11. MD Buschmann, AJ Grodzinsky. *J Biomech Eng* 117:179–192, 1995.
12. PJ Flory. *Principles of Polymer Chemistry*. Cornell, Ithaca, NY, 1953.
13. T Tanaka, D Fillmore, ST Sun, I Nishio, G Swislow, A Shah. *Phys Rev Lett* 45:1636–1639, 1980.
14. Y Hirokawa, T Tanaka. *J Chem Phys* 81:6379–6380, 1984.
15. S Sasaki, H Kawasaki, H Maeda. *Macromolecules* 30:1847–1848, 1997.
16. S Hirotsu, Y Hirokawa, T Tanaka. *J Chem Phys* 87:1392–1395, 1987.
17. L-c Dong, AS Hoffman. *J Controlled Release* 15:141–152, 1991.
18. H Kawasaki, S Sasaki, H Maeda. *J Phys Chem* 101:4184–4187, 1997.
19. H Kawasaki, S Sasaki, H Maeda. *J Phys Chem B* 101:5089–5093, 1997.
20. CS Brazel, NA Peppas. *Macromolecules* 28:8016–8020, 1995.
21. R Yoshida, H Ichijo, T Hakuta, T Yamaguchi. *Macromol Rapid Commun* 16:305–310, 1995.
22. K Ishihara, K Matsui. *J Polym Sci: Polym Lett Ed* 24:413–417, 1986.
23. G Albin, TA Horbett, SR Miller, NL Ricker. *J Controlled Release* 7:267–291, 1987.
24. LA Klumb, TA Horbett. *J Controlled Release* 18:59–80, 1992.
25. K Kataoka, H Miyazaki, M Bunya, T Okano, Y Sakurai. *J Am Chem Soc* 120:12694–12965, 1998.
26. N Santoro, M Filicori, WFJ Crowley. *Endocr Revs* 7:11–23, 1985.

27. E Knobil. *N Engl J Med* 305:1582–1583, 1991.
28. RA Siegel, CG Pitt. *J Controlled Release* 33:173–186, 1995.
29. RA Siegel. In: *Controlled Release: Challenges and Strategies*. K Park, ed. American Chemical Society, Washington, DC, 1997, pp 501–527.
30. X Zou, RA Siegel. *J Chem Phys* 110:2267–2279, 1999.
31. J-C Leroux, RA Siegel. In: *Intelligent Materials and Novel Concepts for Controlled Release Technologies*. J DeNuzzio, ed. American Chemical Society, Washington, DC, 1999, pp 98–111.
32. J-C Leroux, RA Siegel. *Chaos* 9:267–275, 1999.
33. JP Baker, RA Siegel. *Macromol Rapid Commun* 17:409–415, 1996.
34. G Rábai, I Hanazaki. *J Phys Chem* 100:10615–10619, 1996.
35. JL Thomas, H You, DA Tirrell. *J Am Chem Soc* 117:2949–2950, 1995.
36. AM Zhabotinsky. *Biofizika* 9:306–311, 1964.
37. IR Epstein, K Kustin, P DeKepper, M Orbán. *Sci Am* 248:112–123, 1983.
38. IR Epstein, K Showalter. *J Phys Chem* 100:13132–13147, 1996.
39. IR Epstein, JA Pojman. *An Introduction to Nonlinear Chemical Dynamics*. Oxford University Press, New York, 1998.
40. KLC Hunt, PM Hunt, J Ross. *Ann Rev Phys Chem* 41:409–439, 1990.
41. P Gray, SK Scott. *Chemical Oscillations and Instabilities*. Clarendon, Oxford, UK, 1990.
42. JD Murray. *Mathematical Biology*. Springer-Verlag, Berlin, 1989.
43. A Goldbeter. *Biochemical Oscillators and Cellular Rhythms*. Cambridge University Press, Cambridge, UK, 1996.
44. JJ Tyson. *Proc Natl Acad Sci* 88:7328–7332, 1991.
45. A Katchalsky, R Spangler. *Q Rev Biophys* 2:127–175, 1968.
46. T Teorell. *J Gen Physiol* 42:831–845, 1959.
47. Y Kobatake, H Fujita. *J Chem Phys* 40:2219–2222, 1964.
48. P Meares, KR Page. *Proc R Soc Lond A* 339:513–532, 1974.
49. H-S Hahn, A Nitzan, P Ortoleva, J Ross. *Proc Natl Acad Sci USA* 71:4067–4071, 1974.
50. R Larter. *Chem Revs* 90:355–381, 1990.
51. N Minoura, M Higuchi, TY Ohmori. *Biochem Biophys Res Comm* 249:601–604, 1998.
52. J Boissonade, P De Kepper. *J Phys Chem* 84:501–506, 1980.
53. R Yoshida, T Takahashi, T Yamaguchi, H Ichijo. *J Am Chem Soc* 118:5134–5135, 1996.
54. R Yoshida, M Tanaka, S Onodera, T Yamaguchi, E Kokufuta. *J Phys Chem* 104:7549–7555, 2000.
55. K Miyakawa, F Sakamoto, R Yoshida, E Kokufuta, T Yamaguchi. *Phys Rev E* 62:793–798, 2000.

# Index

ABA, 230  
ABC, 230  
Absolute temperature (T), 262  
Accelerator, 222  
Acceptor molecule, 205  
Acetone, 288  
Acryl amide (AAm), 209  
Activation energy, 182, 190, 205  
Adsorption energy, 217  
Agar(ose), 38  
 $\text{AgNO}_3$ , 107  
n-alkane, 280  
Alkyltrimethylammonium bromide ( $\text{C}_n\text{TAB}$ ,  $n=10-16$ ), 71, 222, 223  
Amide C=O carbon, 254  
N-(3-aminopropyl) metharylamide hydrochloride (NAPMAC), 221  
Ammonium persulfate (APS), 222  
Amonton's law, 178, 206  
Amorphous halo, 225  
    network, 206  
Amphiphile, 280  
Amphiphilic molecules, 82  
AMUR-K, 114  
Amylopectin, 38  
Amylose, 38  
Angstrom-length, 221  
Anionic gel, 103  
    surfactants, 221  
Anisotropic contraction, 191  
    energy, 330  
Anisotropic structure, 285  
Anomalous correction, 123  
    dispersion correction, 122  
    SAXS (ASAXS), 112  
Apparatus constant (K), 259  
Arrhenius, 280  
    formula, 190  
Artificial joint, 218  
Associative phase separation, 69  
Atomic scattering, 122  
Attraction energy, 48

Autonomous pulsing system, 364

Belousov-Zhabotinsky reaction, 373

Bending constant (bending modulus), 78

Bilayer, 73, 92

Biological macromolecule, 28

Biomedical application, 373

Biopolymer, 82

gel, 28

Biot-Savar law, 339

Block copolymer, 101, 221

Boembergen-Purcell-Pound (BPP) theory, 239, 254

Boltzmann constant, 78, 178, 214, 261, 284

distribution, 179

Bound counterion, 184, 186, 188, 190

water, 199

Branched polymers, 1

Branching degree, 19

model, 35

Brownian motion, 93

rotation, 331

Calcium alginate gel, 202

Carboxyl group, 267, 271

Cardiolipin, 92

Carr-Purcell/Meiboom-Gill (CPMG)  $^1\text{H}$  NMR method, 268, 291

Carrageenan, 38

Cascade formalism, 1, 7, 15, 26

Catanionic surfactant, 72

Cationic gel, 103

polyelectrolyte gels, 221

Cetylpyridinium chloride (CPC), 104

Cetyltrimethylammonium bromide (CTAB), 93

Chain-packing interaction, 72

Charge density, 177, 179, 196, 197, 209, 213, 215, 216, 223, 226

polymer system, 58

surfactant micelle, 70

Chemical energy, 238

free energy, 200

network, 28

oscillator, 374

shift value ( $\delta$ ), 239, 248, 251

Chemically responsive gel, 363

Chemomechanical contraction, 177

energy conversion, 363

reaction, 293

system, 200

Chloroform:

- CHCl<sub>3</sub>, 252, 280
- <sup>13</sup>C NMR, 245
- C<sub>n</sub>TAB, 70, 222, 223
- Coefficient of viscosity, 196
- Coil-globule transition, 83
- Coliphage T4 DNA, 93
- Collagen, 36
- Collapse transition, 165, 317
- Colloidal particle network, 34
- Compact globular conformation, 93
- Complete miscibility, 69
- Concentration of network polymer (*c*), 265
- Cooperative binding, 68
- Copolymer, 222
- Correlation time (*T<sub>c</sub>*), 238
- Coulomb interaction, 267
- Counterion density, 214
  - fluctuation, 186
  - mobility, 182
- CrCl<sub>3</sub>, 102
- Critical aggregation concentration (CAC), 67, 68, 70, 71
  - gel concentration, 33
  - micellar concentration (CMC), 68, 70, 71, 72, 82, 223
- Cross-linked polyelectrolyte gel, 180
  - polymer network, 206
- Cross-linker density, 102, 232
- Cross-linking density, 179, 180, 186, 188, 191
  - point, 177, 180, 186, 191, 195, 199
- Cross-polarization (CP) method, 246
- Cryo-TEM, 89, 91, 93
- Cryo-transmission electron microscopic (cryo-TEM), 67
- Crystalline phase, 127
  - structure, 180
- Crystallography, 222
- Cubic liquid crystalline phase, 75
- Cubic phase, 76
- Curvature energy, 77, 78
  - free energy, 78
- Cylinder form factor, 225
  
- DDAB, 75, 79, 92
- Debye-Brinkman equation, 211
- Debye-Bueche-type, 19, 24
- Debye-Huckel atmosphere, 182
- Decay during echo time (*T<sub>2</sub>*), 268
- Deep electrostatic potential well, 180
- Deep potential valley, 179
  - well, 179, 180, 190

- deGeness, 266
- Degree of cross linking, 205
  - of disorder, 126
  - of polymerization, 185
  - of swelling, 193, 197, 198, 199, 209, 215, 216
- Density of swollen polymer gel ( $\rho_{\text{swollen}}$ ), 260
- $D_{H_2O}$ , 259, 288
- Dialkyldimethylammonium, 79
- Diaminododecane, 252
- Dichloromethane, 284
- Didodecyldimethylammonium bromide (DDAB), 73
- Dielectric constant, 164
  - relaxation, 183
- Diffusion coefficient, 254
  - constant, 185, 186, 188, 191
  - in gel, 288
  - time ( $T_d$ ), 256
- Dimethyl acryl amide (DMAA), 267
- N,N-dimethylformamide (DMF), 205
- Dioxane, 284
- Dipolar attraction, 166
- Dipolar interaction, 239
- Dipole-dipole attraction, 163
  - interaction, 239, 246
- Direct current conductivity measurement, 183
  - electric field, 293
- Disorder-order transition, 30
- Disorderd phase (DIS), 225
- DNA, 82, 221
  - globule, 94
  - molecules, 93
    - amphiphile interaction, 82
- Donnan equilibrium, 202
- Double-chained surfactant, 77
- Drug-delivery system, 82, 202, 363
- Dynamic mechanical analysis, 17, 19
  - screening length of polymer chain, 263
- Echo signal attenuation, 257
- Effective attraction energy, 217
  - surfactant parameter, 75
- Egg-box model, 37
- Elapsed-time ( $T_e$ ), 292, 307
- Elastic cross-linked network, 177
  - energy, 217
  - force, 210
  - modulus, 213



- network polymer, 288
- Electrical conductance, 177, 180
  - conduction, 181
  - conductivity, 190
  - contraction, 195
  - drift, 182
- Electro field-sensitive, 315
- Electrochemical response, 325, 327
- Electroconductive organogel, 205
- Electroconvection, 319
- Electrohydrodynamics, 319
- Electrokinetic contraction model, 199
  - transportation, 177
- Electrophoretic, 199
- Electrorheological fluids, 350
- Electrorheology, 322
- Electrostatic attraction, 76, 208
  - force, 321, 324
  - interaction, 8, 71, 76, 82, 92, 93, 103, 180, 188, 221, 227, 231, 236
  - potential, 200
    - distribution, 178
    - energy, 179
    - energy distribution, 178
    - well, 186
  - repulsion, 93, 209, 213, 216
- Electrostriction, 318
- Energy barrier, 188
- Energy-driven, 316
- Entropy-driven, 316
- Equivalent conductance, 180, 181
- Ester carbonyl carbon, 252, 280
- Ester-amide exchange reaction, 252
  
- f*-functional monomers, 5, 6
  - random polycondensates, 6, 7, 8, 10, 15
- Face-centered cubic (FCC), 229, 230, 236
- Faraday's law, 195
- Ferrogel, 102, 328
- Filler, 320
- Finite element method (FEM), 346
- Flat bilayer state, 77
- Flory-Huggins-type interaction, 221
- Flory-Stockmayer model, 1, 21, 22, 24, 26
- Fluorescence microscopy, 83, 93
  - relaxation, 173
- Fluorescently labeled DNA, 93
- Fractional proton number ( $P_i$ ), 257
- Free counterion, 182

- energy, 78
- induction decay (FID), 239
- radical copolymerization, 222
- volume theory, 261, 264, 270, 275
- water, 199
- Freeze-dried, 233
- Freeze-thaw cycle, 248
- Frictional coefficient, 178, 206, 209
  - force, 178, 195, 206, 209, 210, 216
- Gaussian distribution, 256
- Gaussian subchains, 9, 10, 13
- Gel friction, 208
  - point, 28
  - preparation, 222
- Gel-surfactant, 236
- Gellan, 39, 206
- Gene therapy, 82, 221
- Gibbs' phase rule, 73
- Globular protein, 29
- GNOM, 106, 115
- Good's theory, 1
- Gradient pulse interval ( $\Delta$ ), 256
- Gyromagnetic ratio of proton ( $\gamma$ ), 256
- $\text{H}_2\text{Pt}(\text{OH})_2\text{Cl}_4$ , 115
- $\text{H}_2\text{PtCl}_6$ , 106, 118
- $\text{HAuCl}_4$ , 114
- HCPC, 226, 233
- HCPC-DIS transition, 225
- HCPCs, 225, 235
- $^1\text{H}$  decoupling, 248
- HDO, 261
- Head group interaction, 93
- Heat-induced gelation, 39
- Helix-coil transition, 254
- $\alpha$ -helix conformation, 38, 252, 280
- Heterostructural chain, 29
- Hexagonal phase, 75
- Hexagonally close-packed system of spheres (HCPS), 230, 235
- High-frequency relaxation, 182
- High-resolution solid-state  $^{13}\text{C}$  NMR method, 238, 245, 252
- Highly ordered macrolattices, 221
- HMR 68, 71
- $^1\text{H}$  NMR imaging method, 238, 308
- $^2\text{H}$  NMR spectral, 284
- Hooke's law, 352
- Hookean solid, 32

- $^1\text{H}$  pulse NMR method, 238, 291
- $^1\text{H}$  spin density, 288, 292, 299
- $^1\text{H}$  spin-echo signal, 243
- Hydrodynamic radius, 258
  - interaction, 263
  - lubrication, 212
  - resistance, 209
- Hydroelectrolyte gel, 238
- Hydrogen bond, 93, 239, 245, 248, 254, 267, 271
- Hydrophobic interaction, 71, 82, 92, 93, 103, 112, 226, 231, 267, 271, 273, 278
  - surfactant, 221, 224
- Hydrophobically modified copolymer, 92
  - polycation, 90
  - polyelectrolyte, 71
  - polymer (HMP), 67, 90
- Hydrostatic pressure, 343
- Hydroxy group, 248
- Hydroxyethylcellulose, 72, 84
  
- Immobile region, 244
- Inhomogeneous aggregation, 281
- Initiator, 222
- Insoluble complex, 92
- Intensity,  $I(S)$ , 104
- Interconnected vesicle, 90
- Interdomain interaction, 14
- Interfacial free energy, 212
  - interaction, 208
  - region, 244
- Intermolecular excluded volume interaction, 47
  - junction, 43
  - network, 29
- Internal ordered microstructure, 48
- Intrabilayer effect, 90
- Intraglobular hydrophobic residue, 39
- Ion transportation, 180
- Ionic conduction, 205
  - strength, 69, 210
  - surfactant, 67
- Ionizable group, 166
- Ionomer multiplet structure, 164
  - system, 29
- Isoelectric point, 40
- N-Isopropylacrylamide (NIPAAm), 222
- Isotactic polymer, 29
- Isotropic phase, 89
- $i$ th region ( $\psi_i$ ), 257

- Jump-like fashion, 53
- Jumpwise collapse, 169
- Junction zone, 29
  
- Kramers' theorem, 7
  
- Lamellar, 236
  - liquid crystalline phase, 280
  - morphology (LAM), 225, 227
  - phase, 73, 75, 76, 77
- Langevin function, 331
  - type magnetization, 344, 353
- Laser-aided prealigned pinhole collimator, 224
- Liebmann's method, 179
- Lifshitz point, 59
- Linear polymer, 180
- Lipid bilayer, 92
  - membrane, 82
- Liposome, 82
- Liquid crystal, 284, 286, 320
  - crystalline phase, 72, 94
- Liquid-liquid phase separation, 87
- Long-chain surfactant, 70
- Long-range electrostatic interaction, 221
- Lorenzian form, 13
- Loss modulus, 32
- Low-frequency dielectric relaxation, 177
  - relaxation, 183, 190
- Lower critical solution temperature (LCST), 357
- Lyotropic liquid crystalline phase, 280, 284
  
- Macrolattice, 227, 232, 236
- Magnetic angle spinning (MAS), 246, 251
  - dipole-dipole-interaction, 350
  - energy, 352
  - field gradient pulse length ( $\delta$ ), 280
  - field-sensitive, 315, 327, 357
- Magnetoelasticity, 336
- Magnetorheological fluids, 350
- Magnetostriction, 328, 342
- Mean-square radius, 7
- Mechanical energy, 238
- Mechanochemical system, 200
- Membrane adsorption, 95
- Mesoscopic length, 224
- Metal-containing polymer gel, 101
- Methacrylic acid (MAA), 222
- Methanol, 288

- N,N'-methylenebisacrylamide (BIS), 232
- Micellar phase, 77
- Micelle formation, 57
- Microemulsion, 221
- Microphase separation, 102
- Microphase-separated macrolattices, 221
- Mixed colloidal system, 82
- Mobile region, 244
- Molar interaction parameter, 72
- Molecular motion, 265
  - weight ( $M_w$ ), 261
- Morphology, 236
- Multilamellar vesicle, 80
- Multivalent counterion, 169
  
- $N_2H_4 \cdot H_2O$ , 106
- $NaBH_4$ , 107
- $NaPtCl_6$ , 118
- Necklace-like conformation, 55
- Neel relaxation, 331
- Neo-Hookean, 344, 348, 352
- Network charge density, 208
- Network-counterion interaction, 183
- Neutral (noncharged) hydrogel, 191
- Newton equation, 211
- Newton's law, 211
- Newtonian liquid, 32
- $(NH_4)_2PtCl_4$ , 118
- Nisopropyl acrylamide (NIPA), 102
- NMR method, 238
- Nonadsorbing polymer, 82
- Nonionic surfactant, 82
- Nuclear magnetic resonance (NMR), 67, 92, 238
  - overhauser effect (NOE), 246
- Number-average, 2
  
- Omstein-Zernick form, 13
- Oppositely charged bilayer, 91
  - lipid, 92
  - polyelectrolyte, 92
  - surfactant, 103
- Order-disorder transitions, 235
- Order-order-transitions, 235
- Organic/inorganic hybrid gels, 15
- Osmotic pressure, 212
- Ovalbumin, 40
- Oxygen atom, 267, 271

- P(MAA/NIPAM), 222, 228, 231
  - gel- $C_n$  TB complex, 223, 229, 230
  - polyelectrolyte gel, 229
- P(NAPMACI/NIPAM), 222, 224, 225, 231
- Path-weighted function, 7
  - generating function, 3, 8
- Pectin, 37
- n-pentane, 285
- Phase separation, 67, 69, 70, 71, 85, 87, 89, 90, 92
- Phase transitions, 236
- Phosphatidylcholine vesicle, 92
- Phospholipid, 78, 82
- Photoemission diode, 202
- Physical network, 28
- Physiological buffer, 373
  - media, 372
- PMA carboxylic group, 112
- Poisson equation, 195, 212, 216
- Poisson-Boltzmann equation, 177, 178, 195
- Poly(2-acrylamido-2-methylpropane sulfonic acid) (PAMPS), 178, 180, 181, 193, 199, 206
- Poly(acrylic acid) (PAA), 177, 266, 288
- Poly(diallyldimethylammonium chloride) (PDADMACI), 104, 110, 111, 113
- Poly(dimethyl acryl amide) (PDMAA) gel, 258, 260
- Poly(ethylene glycol) (PEG), 82, 258, 260
- Poly(ethylene glycol) oleylether (PEG- Ole), 274
- Poly(methacrylic acid) (PMAA) (PMA), 222, 223, 259, 267, 288, 293
- Poly(N-isopropylacrylamide) (PNIPAM), 239, 309, 315, 357
- Poly(vinyl-alcohol) (PVA), 245, 328
- Poly( $\gamma$ -methyl L-glutamate) (PMLG), 250, 280, 284
- Poly[(dimethyl amino) propylacrylamide] (PDMAPAA), 205
- Poly(sodium p-styrenesulfate) (PNaSS), 209
- Poly(styrene sulfonate) (PNaPSS), 186
- Polydispersity, 88, 89
- Polyelectrolyte charge density, 236
- Polyelectrolyte, 67, 70
  - gel, 101, 127, 177, 182, 186, 190, 200, 205, 208, 221, 292
    - micelle, 67
    - surfactant, 236
    - surfactant complex (PSCs), 221, 235
    - vesicle, 67
- Polymer chain, 179, 188
  - entropy, 221
  - segment, 187
    - coiling effect, 181
- Polymer network, 186
  - concentration, 209
  - density, 216
- Polymer volume fraction, 48

- Polymer-solid surface adsorption, 210
  - repulsion, 211
- Polymer-surfactant complex, 70, 71
  - interaction, 68, 69
- Polymer-vesicle interaction, 93
  - system, 82
- Polymerization, 101
- Polypeptide, 254, 280
- Polysaccharide, 82
- Probability-generating function, 1, 2, 3, 5, 6, 7
- Probe molecular, 254, 287
  - polymer, 274, 278
- Protein, 82
- Proton decoupling, 246
- Pulse field gradient parameter, 254
  - saturation transfer (PST), 246, 252
    - field gradient spin-echo NMR (PFGSE) method, 238, 254, 256, 265, 268, 274, 280
  
- Quattrisoft LM200, 84
  
- Radical polymerization, 232
- Radio frequency (rf) pulse, 238
- Radius of a particle ( $R$ ), 263
  - of gyration ( $R_g$ ), 106
- Random coil, 92, 254, 263, 280
  - flight chain, 10
- Rayleigh problem, 49
- Reciprocal space, 222
- Recrystallization, 221
- Relaxation time, 183, 189
- Repulsive osmotic pressure, 215
- Residual field gradient (Gr), 259, 275
- Resonance frequency:
  - $\omega$ , 239, 254
- Reswelling, 233
- Reversed hexagonal phase, 76
- Reversible gelation, 57
  - junction, 47
- Rhythmic gel/enzyme system, 363
- Rod-like polymer chain, 194
  
- Saddle-splay modulus, 78
- Salt-induced collapse, 169
- SAXS measurement, 223
- SAXSFCC, 231
- Scaling rule, 215
  - theory, 213
- Scattering techniques, 221

- surfactant, 231
- Screening effect, 90
- Segregative interaction, 41
  - phase separation, 69
- Self-assemble, 221
  - structure, 89
- Self-associate, 68
- Self-diffusion coefficient (ID), 238, 256, 263
- Shear loss modulus, 87
  - storage, 87
    - induced structure, 63
    - reversible network junction, 34
    - thickening effect, 61
- Single linear DNA, 94
- Small angle scattering, 221
- Small angle x-ray scattering (SAXS), 17, 103, 104, 112
- Smart materials, 315
- Smoluchowski equation, 10
- Sodium alkyl sulfate (SCnS,  $n=9-16$ ), 222, 224
  - dodecylbenzenesulfonate (SDBS), 104, 110
  - dodecylsulfate (SDS), 73 75, 79, 85, 104
  - hyaluronate, 71
  - octyl sulfate (SOS), 93
- Soft mechanoelectrical system, 202
- Solid-state nuclear magnetic resonance (NMR) method, 238
- Solution NMR, 238, 246
- $\theta$ -solvent, 55
- Spherical structure, 230
- Spin lattice time ( $T_1$ ), 238
- Spin-echo  $^1\text{H}$  NMR spectra, 280
- Spin-spin relaxation time ( $T_2$ ), 238, 268
- Sponge phase, 77
- Starch, 37
- Stearyl itaconamide (SIA), 274
- Stereochemical configuration, 248
- Steric interaction, 76
- Stoichiometric quantities, 221
- Stokes' law, 190
- Storage modulus, 32
- Stress generates potential (SGP), 200
- Strict limitation, 102
- Strong polyelectrolyte gel, 180
  - $\pi$ - $\pi$  interaction, 112
- Structural transition, 231
- Structured liquid, 34
- Supramolecular, 221
- Surface charge density, 178
  - frictional property, 177



- Surfactant, 221
- Surfactant aggregate, 91
  - micelle, 68
  - parameter, 73
- Swelling phase transition, 363
  - ratio, 208, 209
- Synchronized dynamic segmentational motion, 206
  
- Tactile-sensing system, 202
- Telechelic polyelectrolyte, 47
- TEM, 89, 102
- Temperature-sensitive, 357
- Teorell oscillator, 374
- Ternary phase diagram, 69
- 7,7,8,8 -tetracyanoquinodimethane (TCNQ), 205
- Tetraethoxysilane (TEOS), 15, 16, 17, 19, 21, 24
- N,N,N',N' -tetramethylethylenediamide (TEMED), 222
- Thermodynamic incompatibility, 41
- Three-dimensional long-range order, 221
- Toluene/hexane mixture, 222
- Topological interaction, 32
- Translational entropy, 163
- Triethoxysily-terminated poly(oxytetramethylene) (ET-PTMO), 15, 21
- Trifluoroacetic acid (TFA), 252, 280
- Triple-helix, 36
- Two-dimensional nonhexagonal packing, 235
  - detection, 224
  - packing, 235
  
- Ubiquitous body-centered cubic (BCC), 229
- Unilamellar vesicle, 80
  
- van der Waals attraction force, 216
  - interaction, 213
- Vesicular aggregates, 67
- Viscoelastic character, 87
  - characteristic of the gel, 288
- Viscosity, 68
- Viscous drag, 190
  - friction, 209
- Volume fraction of solvent ( $v$ ), 263
  - of swollen polymer gel ( $V_{swollen}$ ), 260
  - phase transition, 315
  - transition, 363
  
- Water transportation, 195
  - soluble polymer, 67
- Wave vector, 59

WAXS, 102

Weak polyelectrolyte gel, 177

Weight fraction-generating function, 5, 6, 8

average, 2

fraction, 5

Wet piezoelectric material, 200

X-ray, 104

Xanthan, 34

z-average, 2

Zeeman energy, 330

Zernicke-type, 19

Zwitterionic lipid, 82

### about the book . . .

This versatile reference offers an in-depth look at the properties, thermodynamic formation, structure, **latest** trends, and scientific applications of bio- and synthetic polymer gels—discussing both fundamental concepts and potential uses of gel technology.

Written by nearly **40** international experts from industry and academia, ***Polymer Gels and Networks*** illustrates the utility of gels in biomedical, pharmaceutical, cosmetics, toiletry, and chemical engineering...describes the use of **hydrogels** as superabsorbents, carriers for controlled drug release, membranes with regulated permeability, sensor devices, and artificial muscles...details the incorporation of hydrophobic- or temperature-sensitive monomer units and the addition of surfactants and linear polymers to enhance hydrophobic interactions...examines cross-linked polymer gels as well as gels with embedded metal nanoparticles or surfactant molecules...covers theoretical modeling of network constitution, scaling theory, and kinetic approaches to the phase transition of gels...identifies the features of biological and responsive gels, including topics in chemical processing, dynamics, and rheology...synthesizes interdisciplinary viewpoints to extend applications of gel science beyond biomedicine...and more.

### about the editors . . .

**YOSHIHITO OSADA** is Dean and Professor of the Graduate School of Science, Hokkaido University, Sapporo, Japan. The author, editor, or coeditor of over 300 scientific papers and three books, including *Membrane Science and Technology* (Marcel Dekker, Inc.), and a board member of several international journals, he is a member of the Chemistry Society of Japan, the Society of Polymer Science (Japan), the American Chemical Society, and the Materials Research Society (Japan). Dr. Osada received the Ph.D. degree (1970) in chemistry from Moscow State University, Russia.

**ALEXEI R. KHOKHLOV** is Full Professor and Chairman of Polymer Physics and Crystallophysics, Physics Department, Moscow State University, Russia. An editorial board member of numerous publications, including *Biomacromolecules*, the *International Journal of Polymer Materials*, and the *Polymer Journal*, he is the author, editor, or coeditor of over 250 scientific papers, books, and review articles. Dr. Khokhlov received the B.S. (1977), Ph.D. (1979), and D.Sc. (1983) degrees in physics from Moscow State University, Russia.

*Printed in the United States of America*

MARCEL DEKKER, INC.  
NEW YORK • BASEL

ISBN 0-8247-0669-2



9 780824 706692